Organised By:

THE HONG KONG INSTITUTION OF ENGINEERS
香港工程師學會
Geotechnical Division
岩土分部

Supported By:

HKGES HONG KONG GEOTECHNICAL SOCIETY
香港岩土工程學會

THE HONG KONG INSTITUTION OF ENGINEERS
香港工程師學會
Civil Division
土木分部

THE HONG KONG INSTITUTION OF ENGINEERS
香港工程師學會
Structural Division
結構分部

The HKIE Geotechnical Division 45th Annual Seminar

9 May 2025

Advancing Geotechnical Practice : Sustainable Solutions to Land & Infrastructure Developments


SJ
Grounded in excellence, driving transformational infrastructure worldwide.
SJ is a diverse collective of problem solvers for the built environment, continually reimagining ways to create a smart and sustainable future.


AECOM
Unlocking Cavern Potential with Geotechnical Engineering Innovations
AECOM is pushing the envelope for modular integrated construction (MiC) design and planning by pioneering Asia's first MiC cavern project for the Joint Cavern Development at Anderson Road Quarry Site. This innovative initiative will free up land for housing and waterfront open space development in East Kowloon.
To address the various constraints of building inside the caverns, MiC and design for manufacture and assembly (DfMA) have been introduced. A 4D BIM model is also adopted to enhance buildability and ensure safe site operations.
*Reference design in investigation stage
Learn more
Delivering a better world
aecom.com

Image Source: Tseung Kwan O Interchange & Lam Tin Tunnel (HKIE SD - SEA2024 Grand Award)

About Aurecon

Aurecon is an engineering, design and advisory company. We are dedicated to elevating Hong Kong's infrastructure through innovative building designs, integrated transportation systems, strategic advisory advices, and sustainable urban practices, all aimed at delivering exceptional projects that exceed expectations and promote a resilient, sustainable future.

Multi-Disciplinary Expertise

- Geotechnical Enginnering Tunnelling &
- Caverns Building Structures & Civil
- Structures Building Services Information &
- Communication Technology
- Transportation, Land & Water Environment
- & Sustainability Advisory Project
- Management

Iconic Projects

- Tseung Kwan O Interchange & Lam Tin Tunnel
- Central Kowloon Route
- Lok Ma Chau Loop and Western Connection Road

aurecon

Bringing ideas to life

Discover More







C M WONG & ASSOCIATES LTD
黃志明建築工程師有限公司

11/F Universal Trade Centre
3-5A Arbuthnot Road, Hong Kong
Tel: (852)2522-1068
Fax: (852)2526-3111
www.cmwal.com
cmwal@cmwal.com

C M Wong & Associates Ltd is a Hong Kong based consulting engineer in providing a full range of professional services including feasibility studies, planning, design and supervision in relation to building and infrastructure projects. Our clients include various Hong Kong Government departments, institutions and major developers.

We adopt a flexible approach to suit clients' needs. We are also renowned for providing innovative engineering solutions for challenging projects especially for those with difficult ground conditions.

ISO 9001 : 2015
Certificate No.: CC 801

ISO 14001 : 2015
Certificate No.: CC 5408

ISO 45001 : 2018
Certificate No.: CC 7033

中國建築工程(香港)有限公司
CHINA STATE CONSTRUCTION ENGINEERING (HONG KONG) LIMITED

慎微篤行 精築致遠

EXERCISE CAUTION IN DETAILS AND IMPLEMENTATION
BUILD A STRONG FOUNDATION TO SEEK GREATER SUCCESS

www.cscechk.com


新界西堆填區擴建計劃
West New Territories Landfill Extension


將軍澳海水化淡廠第一階段
First Stage of Tseung Kwan O Desalination Plant


香港國際機場三跑道系統項目-北跑道改建工程
Hong Kong International Airport Three Runway System Project - North Runway Modification Works

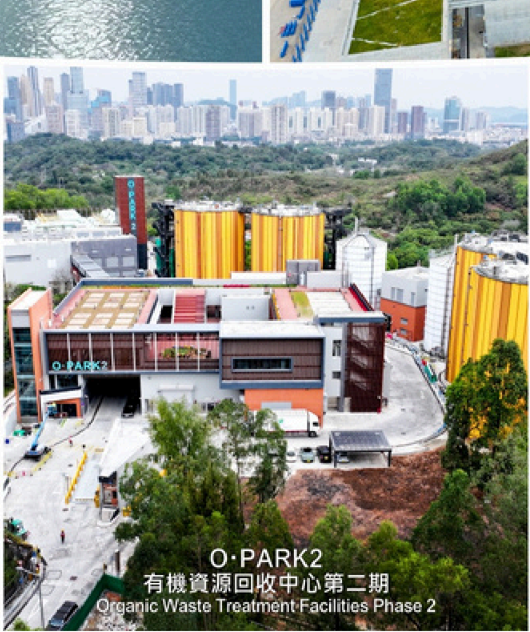

O·PARK2
有機資源回收中心第二期
Organic Waste Treatment Facilities Phase 2


元朗防洪霸及明渠改善計劃
Yuen Long Barrage and Nullah Improvement Schemes


RETAIN
· MSE retaining walls
· Precast retaining walls
· Reinforced Soil Slopes
· Dams and dikes
· Quays and jetties
· River training
· Reservoirs and canals
CROSS
· Bridge abutments
· Buried bridge structures
· Box bridges
· Tunnels and underground structures
GEOQUEST
(formerly known as Reinforced Earth)
New name, Proven expertise, Diverse solutions.
STRENGTHEN
· Embankments over soft soils, piles & subsidence
· Soil reinforcement
· Geosynthetic solutions and products supply: geogrids, geotextiles, geocells, drainage geocomposites
PROTECT
Natural risks protection
· Erosion
· Avalanche
· Rockfall & debris flow
· Slope stabilization
· Floods & Coastal
Industrial risks protection
· Waste storage
· Spill containment
· Blast protection
· Noise mitigation
· Secured storage
GEOQUEST HONG KONG LIMITED
Unit 705-706, 7/F, Tower 1, Cheung Sha Wan Plaza, 833 Cheung Sha Wan Road, Kowloon, Hong Kong
Tel: +852 2794 0322
Email: infohongkong@geoquest-group.co.hk
www.geoquest-group.com.hk

Facebook | LinkedIn | Instagram

Meinhardt China

With a dedicated team of 1,200 professionals in Hong Kong and China, we provide exceptional mechanical, electrical, civil, and structural design services for a wide range of construction projects. Our expertise includes project management and infrastructure development in areas such as bridges, tunnels, highways, ports, and water services. We also offer standout environmental consultancy, both integrated with our projects and as standalone services. Our specialists focus on innovative building façades, including curtain wall design and concrete refurbishment.

Additionally, our geospatial services are essential for advancing smart city development. Our clients include government bodies, agencies, private developers, and end-users across various industrial and commercial sectors, all relying on our commitment to excellence and proven results.

Our award-winning projects have garnered recognition internationally and these awards serve to affirm our unrivalled reputation for innovative and inspiring engineering solutions.

Our Projects

Hong Kong Children's Hospital
(Civil & Structural)

Cross Bay Link, TKO
(Infrastructure & Environment)

Northwest Kowloon Long Span Footbridge
(Infrastructure & Environment)

Grand Central & Yue Man Square
(Mechanical & Electrical)

Hong Kong West Kowloon Station High Speed Rail
(Mechanical & Electrical)

HKSTP Advanced Manufacturing Centre
(Civil & Structural)

10/F, Genesis, 33-35 Wong Chuk Hang Road, Wong Chuk Hang, Hong Kong
www.Meinhardt-china.com | www.meinhardtgroup.com

VIBRO 惠保

周大福創建集團成員
Member of CTFS Group

COMMITTED
PROFESSIONAL
UNITED

New Acute Hospital at Kai Tak Development Area

Road Improvement Works in West Kowloon Reclamation Development

WWW.VIBRO.COM.HK

Proceedings of the 45th Annual Seminar
Geotechnical Division, The Hong Kong Institution of Engineers

Advancing Geotechnical Practice: Sustainable Solutions to Land & Infrastructure Developments

9 May 2025
Hong Kong

Organised by:
Geotechnical Division, The Hong Kong Institution of Engineers

Supported by:
Hong Kong Geotechnical Society
Civil Division, The Hong Kong Institution of Engineers
Structural Division, The Hong Kong Institution of Engineers

ORGANISING COMMITTEE

Chairman
Ir Prof Warren DOU

Members
Ir Ray CHAN
Ir Angela CHAO
Ir Florence CHU
Ir Ellen LEE
Dr Andy LEUNG
Ir Abby LIU
Mr John WU
Ms Connie YAM
Ir Terence YAU

Published by:
Geotechnical Division
The Hong Kong Institution of Engineers
9/F., Island Beverley, 1 Great George Street, Causeway Bay, Hong Kong

Tel: 2895 4446
Fax: 2577 7791
Prepared in Hong Kong

FOREWORD

This year marks the 45th Anniversary of HKIE Geotechnical Division Annual Seminar, which was born in 1980 the same year when the Hong Kong government authorised the construction of first Mass Transit Railway (MTR) Island Line. The signature Annual Seminar will continue running uninterrupted, in a similar manner to MTR trains running in tunnels and underground stations built by geotechnical engineers.

We, geotechnical engineers, have been at the forefront of innovation in engineering to provide a quality standard of life for both present and future generations. The two keynote speakers Prof Chu Jian from the Nanyang Technological University, Singapore and Ir Dr Julian Kwan from the Civil Engineering and Development Department, Hong Kong will elucidate how smart geotechnology can strike a balance between the environment, society and economy in two most vibrant cities in the world. It is an opportune time to form borderless collaborations for an ecosystem of common prosperity.

The 45th Annual Seminar themed "Advancing Geotechnical Practice: Sustainable Solutions to Land & Infrastructure Developments" demonstrates our unwavering commitment to adopting Innovation & Technology (I&T) in shaping the future of Hong Kong. A variety of quality papers have been contributed by the government, academia and industry, achieving synergy between main stakeholders in sustainable development and between humans and nature. Resilience amid economic uncertainty is key to our success in embracing low-altitude economy, by utilising artificial intelligence (AI). Applications of AI in ground engineering is growing by leaps and bounds, cultivating expertise, and making Hong Kong an international hub for digital talent pool.

Organising the Annual Seminar is a gargantuan task, taking months of preparation by a team of dedicated members. I sincerely express my heartfelt gratitude to Ir Prof Warren Dou and his Organising Committee for successfully producing the proceedings and holding the hybrid Seminar. Also, to our Sponsors who have been supporting the Geotechnical Division for so many years through thick and thin.

Lastly, audience and readers of the proceedings are key drivers of the Seminar. The Geotechnical Division hopes that the skills and knowledge presented herein will inspire you to reach greater heights.

Thank you.

Ir Dr LEE Siew Wei
Chairman, Session 2024/25
HKIE Geotechnical Division

ACKNOWLEDGEMENTS

The Organising Committee would like to acknowledge the support of the following sponsors for their generous support of the Seminar:

Platinum Sponsor:
SMEC Asia Limited

Gold Sponsors, in alphabetical order:
AECOM Asia Company Ltd.
Asia Infrastructure Solutions Ltd
Aurecon Hong Kong Limited
Binnies Hong Kong Limited
C M Wong & Associates Ltd
China State Construction Engineering (HK) Ltd.
Fugro (Hong Kong) Ltd.
G and E Company Ltd
GEOQUEST Hong Kong Limited
Intrafor Hong Kong Limited
Meinhardt Consulting Engineers
Ove Arup & Partners Hong Kong Ltd.
VIBRO (H.K.) Limited

Silver Sponsors, in alphabetical order:
Adrian Construction Limited
AtkinsRealis Asia Limited
Bachy Soletanche Group Limited
China Road and Bridge Corporation (Hong Kong & Macau)
Chun Wo Construction Holdings Company Limited
Fong On Geotechnics Limited
Gammon Construction Limited (Foundations and Lambeth)
Sixense Limited
Tony Gee and Partners (Asia) Ltd
Tysan Foundation Ltd

TABLE OF CONTENTS

Influence of Fracture Characteristics and the Use of Network Connectivity Index on Synthetic Rock Mass Strength Characterisation of Moderately Jointed Granite in Hong Kong

I.S. Haryono
NOMA Consulting, Brisbane, Australia

ABSTRACT

Studies by Elmo & Stead (2010) and Stavrou et al. (2019) demonstrated that rock mass strength can be quantitatively characterised and directly linked to fracture characteristics. However, to date, rock mass classification and strength characterisation processes remain largely inductive, relying on empirical methods. It has been identified that this process is influenced by subjectivity and engineering judgement. With the rise of computing power and numerical modelling tools, engineers tend to apply and extend the use of rock mass classification system to determine rock mass strength and parameters in more advanced analyses. Typically, assessment of rock mass strength is undertaken by correlating different rock mass classification systems with the Hoek- Brown criterion for engineering and design purposes. Fracture characteristics; in terms of intensity and trace lengths, are rarely analysed in detail. This study addresses this gap by evaluating the influence of fracture characteristics on rock mass strength. The focus is on the assessment of unconfined compressive strength (UCS) of moderately jointed granite, based on actual tunnel face mapping records. Virtual large scale UCS tests on Synthetic Rock Masses (SRM), which consist of Voronoi Grain-Based Models (GBM) and explicit fractures, are undertaken to determine the rock mass strengths. The results indicate that fracture characteristics poses significant influence on the SRM strengths and demonstrate that rock mass strength characterisation can be directly assessed through the Network Connectivity Index (NCI, Elmo et al. (2021), which considers explicit assessment of fracture intensity & trace lengths. Through clear correlations between rock mass strength and NCI values, this paper demonstrates that NCI provides a more robust and objective alternative to the commonly used Q'-GSI correlations in deriving rock mass strength. The findings demonstrate the importance of integrating detailed fracture assessment into rock mass classification and mapping processes, to improve reliability of rock mass strength and parameters prediction for engineering purposes.

1 INTRODUCTION

Putting a number to geology in assessing rock mass strength and behaviour is considered an important step by engineers for rock engineering and design purposes. This certainly requires rigorous assessment to characterise rock mass condition and to determine appropriate rock mass parameters that can reflect its behaviour. This is particular important given the increasing reliance on numerical modelling in rock engineering projects. Errors in parameter input may affect engineering solutions in both safety and economical spectrum. In moderately jointed, strong rock mass like Hong Kong granite; rock mass characterisation and parameters determination present a significant challenge, which may not be able to be addressed solely based on conventional method.

Based on Middleton Mine data and through a series of numerical analyses adopting Discrete Fracture Network (DFN) and Finite-Discrete Element Method (FDEM), Elmo & Stead (2010) has demonstrated that existing natural fractures (discontinuities) control the potential failure modes and peak strengths of moderately jointed, slender, hard rock mine pillars in low confinement conditions. Their study showed that pillars with higher areal fracture intensity (P21 = total fracture lengths / mapping window area) exhibited lower axial strengths. The strengths of slender pillars are also significantly influenced by the orientation of the discontinuities relative to the loading direction, particularly when inclined discontinuities are present. The FDEM results further indicated that P21 values could serve as an indicator of the structural character of the rock mass and reliable measure of rock mass strength within the GSI approach. In separate works, Stavrou et al. (2019) also demonstrated the importance of fracture intensity in the moderately jointed rock with incomplete discontinuities in understanding the complete rock mass failure mode in this situation. Their numerical analysis of the large-scale Uniaxial Compressive Strength (UCS) tests demonstrated that there is a progressive strength reduction with increasing fracture intensity & persistence and decreasing fracture strength. These findings emphasise the importance of collecting detailed fracture data during site investigation and face mapping. Detailed assessment of natural fractures (e.g., discontinuities, joints) provides a more objective and quantitative approach to determining rock mass strength determination, it is directly linked to fracture characteristics. This method provides greater reliability compared to indirect assessments and secondary indicators, such as RQD or block size estimation.

Building on the extensive analyses by Elmo & Stead (2010), Elmo et al. (2021) introduced Network Connectivity Index (NCI) as a more quantitative and objective alternative for rock mass classification; based on as-mapped fracture intensity and density, and intersection density observed in rock masses. The NCI serves as an analogue to the blockiness descriptors in other systems, e.g. RQD/Jn in the Q-system, joint spacing in the RMR system, and the vertical axis in the GSI system. By relying on directly mapped fracture data, the need for interpretation and subjective judgment associated with empirical methods can be minimised and reliability of rock mass characterisation process can be improved.

The paper investigates the effect of fracture characteristics and the applicability of NCI method in the rock mass strength characterisation process through a series of virtual large scale Unconfined Compressive Strength (UCS) tests on Synthetic Rock Masses (SRM) of moderately jointed granite based on actual tunnel face mapping data. The results of the study indicate that NCI offers a more robust approach to rock mass strength characterisation process, indicated by clear correlation between NCI and SRM strengths (thus, interpreted GSI values). The paper also highlights the limitations of conventional method relying on Q'-GSI correlations for estimating rock mass strength. The absence of a correlation between as-mapped Q' values and SRM strengths demonstrates the disconnect in the rock mass characterisation process and the influence of subjective interpretation, raising concerns about the reliability of traditional approaches and emphasising the need for an alternative approach.

2 VIRTUAL UCS TEST ON MODERATELY JOINTED GRANITE

2.1 Assessed Rock Mass Conditions

The study in this paper focuses on typical moderately jointed granite in Hong Kong and the adopted conditions are based on actual tunnel face mapping results on site. The representative data are obtained from a 100-m stretch of tunnelling, excavated with Drill & Blast (D&B) method with typical advance length of 5 m. This results to twenty (20) tunnel faces and mapping records, shown in Figure 1. The span and the height of the tunnel is 16.7 m and 11.4 m, respectively. Table 1 provides the results of geotechnical mapping on site and the resulting Q-values of each face.

2.2 Calibration of the Grain Based Model (GBM) and Natural Fracture (Joint) Shear Strength

Virtual UCS tests are undertaken adopting the SRM model based on the as-mapped conditions, assuming pillar scenario with a width-to-height ratio of 0.4. The pillar size shown as blue in Figure 1 is 4 x 10 m (width x height). This condition is chosen since it is essentially consistent with standard laboratory UCS samples of which the results are utilised to determine σ_{ci} of the Hoek-Brown criterion, one of the first few steps and a key element to derive rock mass strength. Also, in such slender pillars, failure is predominantly controlled by naturally occurring discontinuities, in contrast to wider pillars, where failures are more complex with a combination of brittle and shearing processes (Elmo & Stead, 2010). The virtual UCS tests for this study are carried out using UDEC ver. 6.0 (Itasca, 2019). For the SRMs, the intact rock is modelled as Voronoi Grain- Based Model (GBM), and the mechanical behaviour and presence of fractures are explicitly represented.

The GBM aims to model the intact rock conditions using 2D voronoi tessellations (random poly-crystals) to simulate crack damage development through initiation and propagation of micro fractures along the grain boundaries (Ghazvinian et al., 2014). To allow for failure to occur only at contacts between the grains, elastic grains are assumed (Itasca, 2011). The grain size is 250 mm, and the grain contacts are modelled using simple Coulomb slip joint model. Iterative processes in determining micro properties according to Potyondy & Cundall (2004) are adopted until the desired macro properties are achieved. In addition to this, the micro properties are also determined to simulate Cohesion-Weakening-Friction-Strengthening (CWFS) behaviour. Published lab-scale UCS data by Wan (2018) has been used as a benchmark. For further virtual analyses of the SRMs, the intact rock strength and σ_{ci} in such large rock pillar is assumed to be the same as the lab-scale UCS result reported by Wan (2018), with no correction due to size-effect.

Table 2 presents the calibrated parameters of GBM. The virtual UCS test set up as well as the failed state and associated crack coalescence are presented in Figure 2. Figure 3(a) shows a reasonably good agreement between the stress-strain curve of the intact pillar and the curve obtained by Wan (2018) using PFC. The CWFS behaviour can be observed in Figure 3(b), particularly where the crack initiation and crack coalescence occur. The stress level for Crack Initiation level and Crack Damage are consistent with typical brittle rocks.

Table 1 Mapping Records of the Tunnel Faces

Models	RQD	Jn	Jr	Ja	Jw	SRF	Q
Model 01	90.0	6.0	1.5	1.5	1	1	15.00
Model 02	90.0	6.0	1.5	1.5	1	1	15.00
Model 03	95.0	6.0	1.5	1.5	1	1	15.83
Model 04	95.0	6.0	1.5	1.5	1	1	15.83
Model 05	90.0	6.0	1.5	1.5	1	1	15.00
Model 06	95.0	9.0	1.5	1.5	1	1	10.56
Model 07	95.0	6.0	1.5	1.5	1	1	15.83
Model 08	95.0	6.0	1.5	1.5	1	1	15.83
Model 09	95.0	6.0	1.5	1.5	1	1	15.83
Model 10	95.0	6.0	1.5	1.5	1	1	15.83
Model 11	100.0	6.0	1.5	1.5	1	1	16.67
Model 12	100.0	12.0	1.5	1.5	1	1	8.33
Model 13	100.0	6.0	1.5	1.5	1	1	16.67
Model 14	95.0	6.0	1.5	1.5	1	1	15.83
Model 15	85.0	12.0	1.5	1.5	1	1	7.08
Model 16	90.0	12.0	1.5	1.5	1	1	7.50
Model 17	90.0	12.0	1.5	1.5	1	1	7.50
Model 18	95.0	12.0	1.5	1.5	1	1	7.92
Model 19	100.0	6.0	1.5	1.5	1	1	16.67
Model 20	100.0	6.0	1.5	1.5	1	1	16.67

Table 2 Calibrated Parameters of the GBM in This Study

Micro Parameters (Grain Contacts)								Grain Parameters	
kn [GPa/m]	ks [GPa/m]	c_p [MPa]	c_r [MPa]	T_p [MPa]	T_r [MPa]	φ_p [^{0}]	φ_r [^{0}]	E [GPa]	ν
4,000	3,000	123	0	18	0	5	10	24	0.2

Laboratory Macro Properties (Wan, 2018)	
UCS [MPa]	189.42
Young's Modulus [GPa]	22.0

Natural fractures (joints) based on mapping records are explicitly modelled in the subsequent virtual tests on the SRMs. The adopted shear strength of the fractures is derived considering various Direct Shear (DS) tests around the tunnels. Back-analyses of the lab-scale DS tests are performed to determine the parameters. Continuously-Yielding-Joint Model (CYJM) (Cundall & Hart, 1984) is adopted to simulate fracture behaviour under DS tests. The CYJM is considered more realistic than the standard Mohr-Coulomb joint model, as it considers some nonlinear behavior observed in physical tests. Table 3 summarises the calibrated parameters. Figure 4 presents both the comparisons between stress-displacement curves obtained from the model and lab-scale DS tests (a), and comparisons between shear strength envelopes of the model and various shear strengths from lab tests (b).

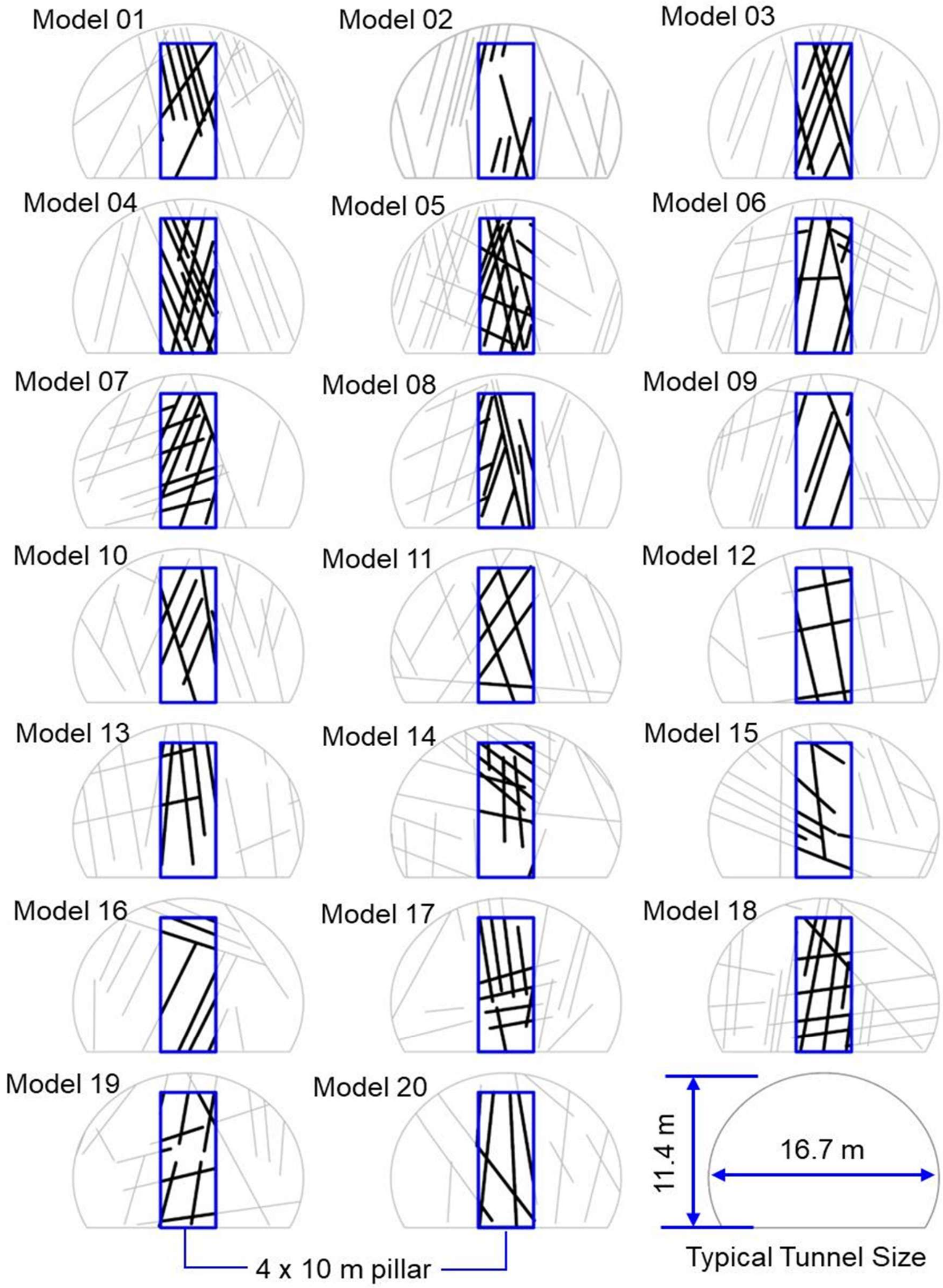

Figure 1: As-Mapped Tunnel Face and Adopted SRMs for Virtual UCS Tests (Highlighted in Blue)

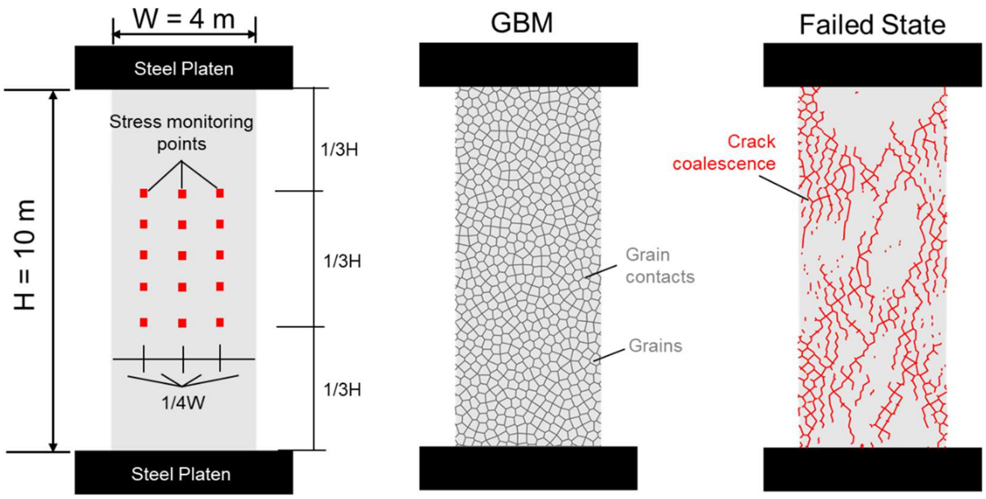

Figure 2: Virtual UCS Test Setup, the GBM and the Failed State of Intact Rock Pillar for Calibration

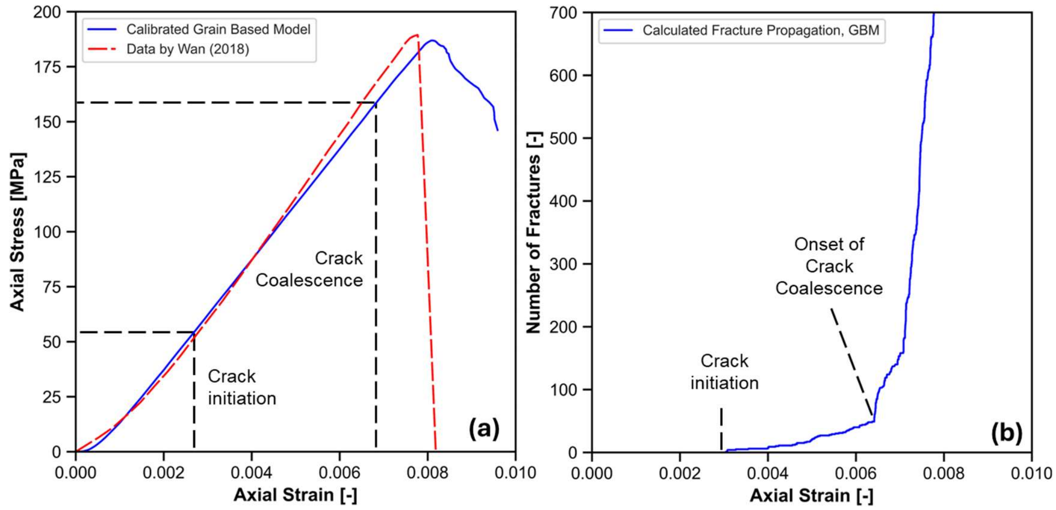

Figure 3: Stress-Strain & Fracture Propagation Plots of the Calibrated GBM (Intact Rock Pillar)

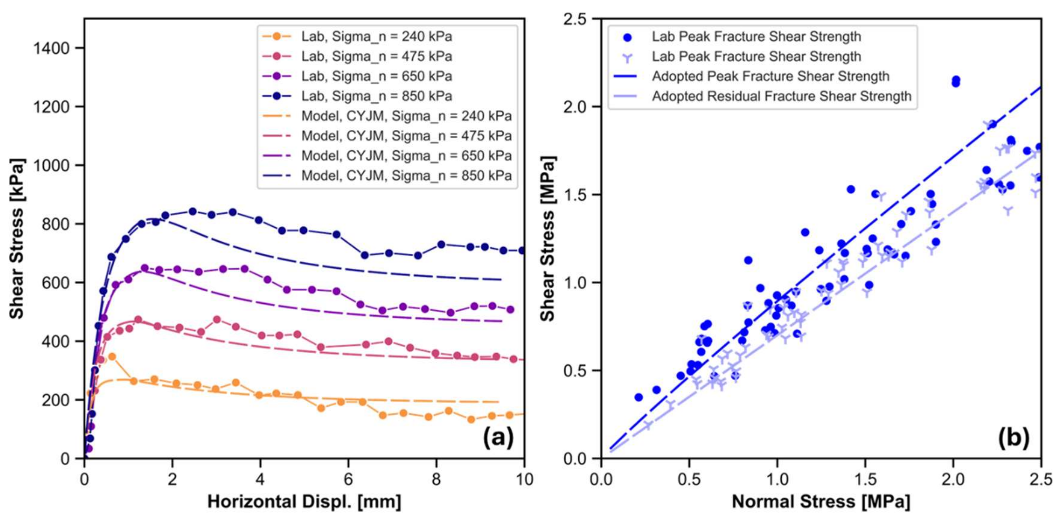

Figure 4: Fracture Shear Strength Calibration (a) and Adopted Peak and Residual Fracture Shear Strength (b)

Table 3 Calibrated CYJM Parameters for Fracture Shear Strength

kn [MPa/m]	ks [MPa/m]	c_p [MPa]	c_r [MPa]	φ_i [^{0}]	φ_r [^{0}]	roughness [m]
20,000	2,000	0	0	48	35	0.003

2.3 Virtual UCS Test Results and Comparisons with Rock Mass Quality Ratings

Following the calibrations, large scale UCS tests on 20 SRMs with explicit as-mapped fractures based on mapping results are undertaken, as discussed in Section 2.1. The sample is loaded at a rate of 50 mm/s in unconfined conditions. Both axial strain and peak unconfined axial stresses of the SRMs (UCSrm) are monitored and assessed. Upon obtaining the peak rock mass strengths, back-analysis is carried out to determine the associated GSI values for each SRM model. It should be noted that this process involves direct conversion from the obtained peak axial stress to associated GSI values, and no interpretation or engineering judgement is involved.

Figure 5 shows the post-peak conditions of the pillars and the resulting crack coalescence after virtual tests. This figure highlights the variability in failure modes across different SRM samples, which manifests as splitting (e.g. Model 13), shearing (e.g. Model 08), or combination of both (e.g. Model 02). However, it can be observed that majority of the failure modes are mostly driven by the natural fractures, which can be primarily attributed to the distribution, orientation, and intensity of natural fractures. Figure 6(a) summarises all the estimated rock mass strengths (UCSrm) from the virtual tests, including the interpreted GSI values; and Figure 6(b) presents the typical stress-strain curves of different SRMs with different interpreted GSI values. The use of NCI for rock mass strength characterisation are subsequently evaluated below.

3 INVESTIGATING THE INFLUENCE OF FRACTURE CHARACTERISTICS AND POTENTIAL USE OF THE NETWORK CONNECTIVITY INDEX (ELMO ET AL., 2021)

The Discrete Fracture Network (DFN) method is widely used for modelling rock masses, as it explicitly represents geological fractures, allowing for the estimation of potential block sizes within the rock mass. Miyoshi et al. (2018) demonstrated the application of DFN and block size analysis in estimating the blockiness axis of the GSI system (vertical axis). Haryono et al. (2024) demonstrated that it is possible to adopt DFN in the early design stage to estimate rock mass condition in terms of its fracture intensity and block sizes, and their study highlighted the benefits of DFN in improving reliability and enhancing the rock mass characterization process for underground engineering projects. Fracture intensity plays a crucial role in DFN modelling, as it directly influences the blockiness of a rock mass and, consequently, its mechanical behaviour. Fracture intensity is expressed as *Pij*, where *i* refers to the dimension of the measurement region and *j* refers to the dimension of the sampling region (Dershowitz, 1998). For a 2D mapping region, P_{21} refers to areal fracture intensity that represents the summation of fracture lengths per sampling area.

By explicitly assessing the fractures and characterising UCSrm from Figure 6(a) based on P_{21}, inverse relationship between fracture intensity and the rock mass strength can be observed, as shown in Figure 7. Higher P_{21}, indicating higher degree of jointing, leads to lower rock mass strength and These results demonstrate the effect of rock mass fracture characteristic to the rock mass strength, similar to the findings by Elmo & Stead (2010). These findings will certainly benefit rock mass characterisation process on site as it eliminates the need for estimating RQD or block size, which involves convoluted processes. However, the resulting P_{21}-UCSrm relationship presented herein are based on specific load setup relative to the fracture orientations for this study. Elmo & Stead (2010) have demonstrated that rock mass behaviour is influenced by the relative orientation of the fracture and applied load. Rotation of loading axis relative to the general fracture orientation will change the failure modes and estimated UCSrm. Therefore, relying solely on P_{21} values is not ideal.

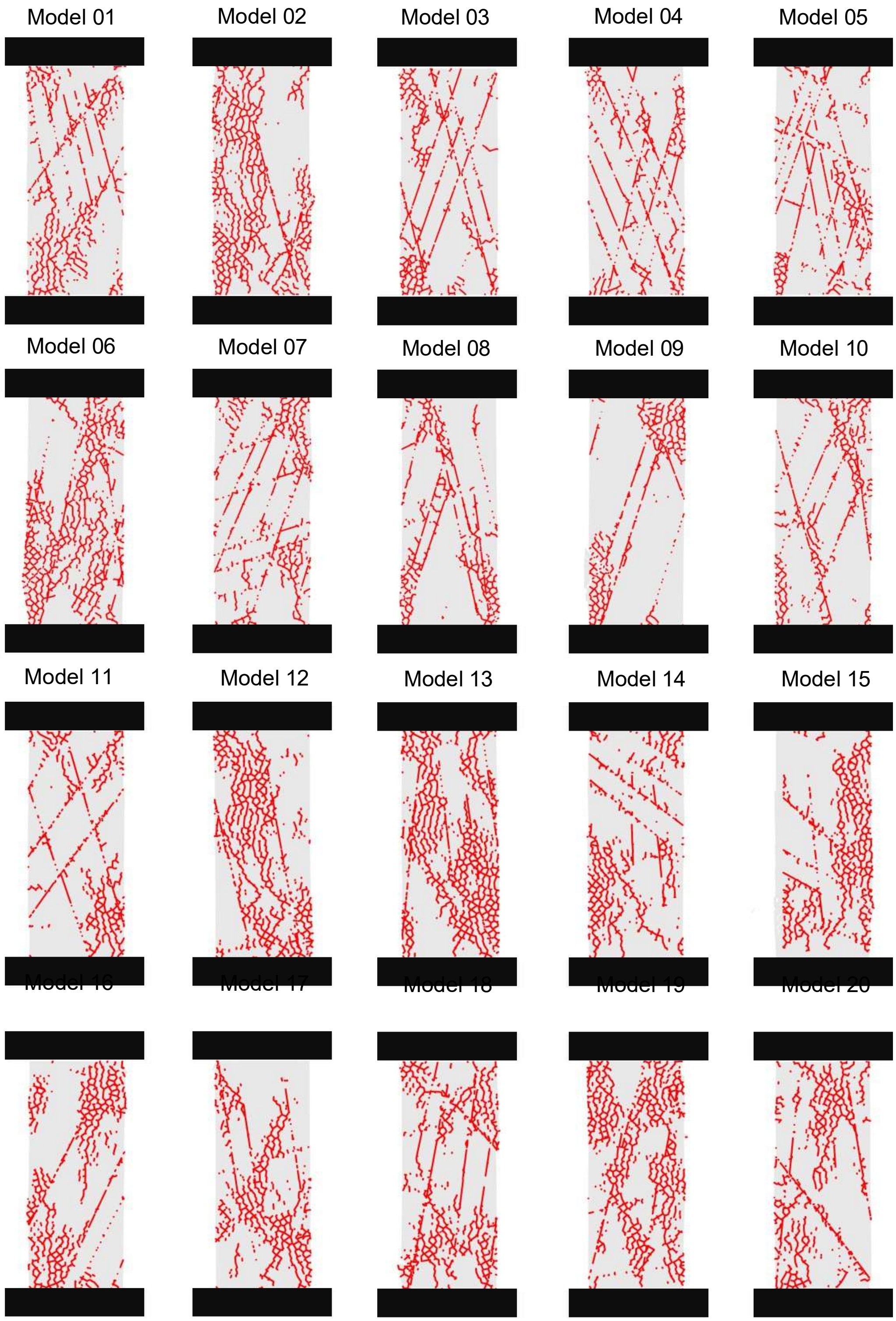

Figure 5: Crack Coalescence Observed in Post-Peak Condition After Virtual UCS Tests

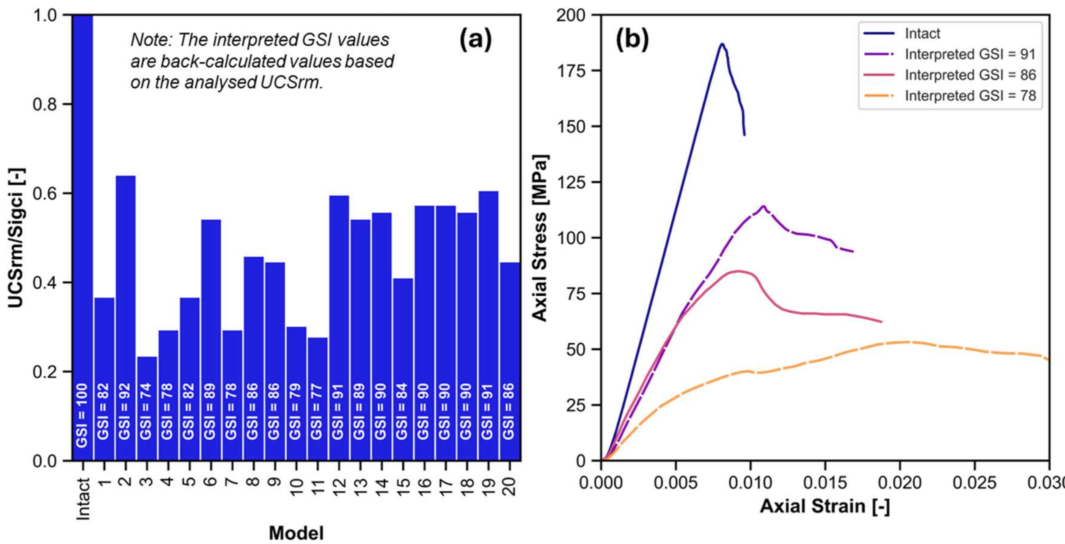

Figure 6: Estimated Strengths of All SRMs and Typical Stress-Strain Curves for Different SRMs with Different Interpreted GSI

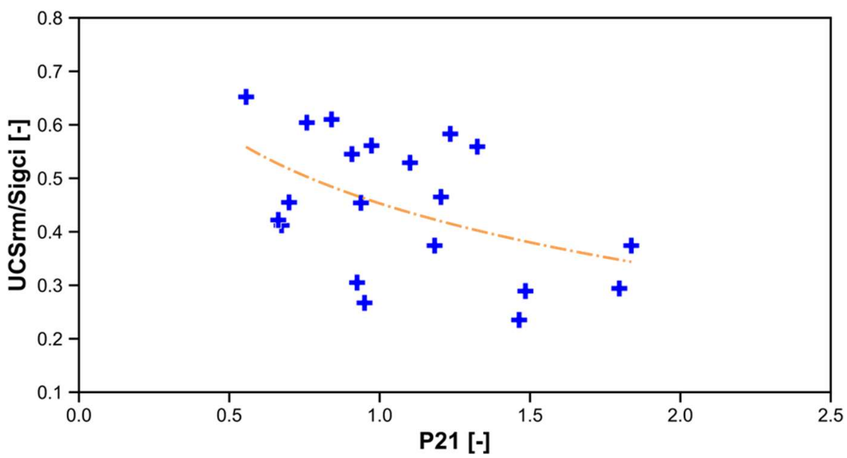

Figure 7: Relationship Between P_{21} and SRM Strengths

Xu et al. (2006), Alghalandis et al. (2015), and Sharif et al. (2019) highlighted the importance of considering fracture connectivity and intersections for rock mass characterisation. Based on this, Elmo et al. (2021) proposed to use the Network Connectivity Index in 2D (NCI_{2D}) for rock mass characterisation. NCI in 3D space (NCI_{3D}) has been conceptualised by Elmo (2023), however it is not discussed in this paper. NCI_{2D} relies on three basic parameters, including P_{21}, P_{20}, and I_{20}; where P_{20}, and I_{20} are the areal fracture density and areal fracture intersection, respectively. The determination of this parameters is shown in Figure 8. The term 'X' refers to the number of fracture intersections at different locations. The NCI_{2D} serves as an analogue to the blockiness descriptors in other systems, e.g. RQD/Jn in the Q-system, spacing in the RMR system, and the vertical axis in the GSI system., scale, size effects, and loading orientation are accounted in the NCI.

Combining the virtual test results, the back-calculated GSI, and the assessed NCI_{2D}, allows us to correlate GSI and NCI, as shown in Figure 9(a). The relationship demonstrates the effectiveness of using NCI for rock mass characterisation. The determination of the associated GSI ranges of a mapped face condition can be directly determined by collecting detailed fracture data and deriving the NCI values. Given the interpreted GSI values, a range of UCSrm for certain rock mass condition can also be directly determined, as shown in Figure 9(b). This approach is considered more objective and simplifies the classification process while reducing reliance on subjective & convoluted interpretation. It also enhances consistency and reliability in rock mass strength estimation.

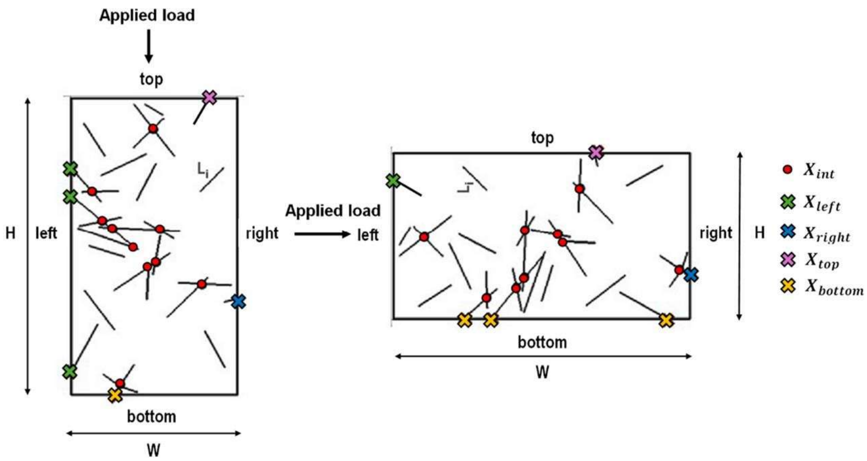

$$I_{20} = \frac{X_{int} + \frac{X_{top}}{W:H} + \frac{WX_{right}}{H} + \frac{WX_{left}}{H} + \frac{X_{bottom}}{W:H}}{Area} \qquad NCI_{2D} = \frac{P_{21}}{P_{20}} I_{20}$$

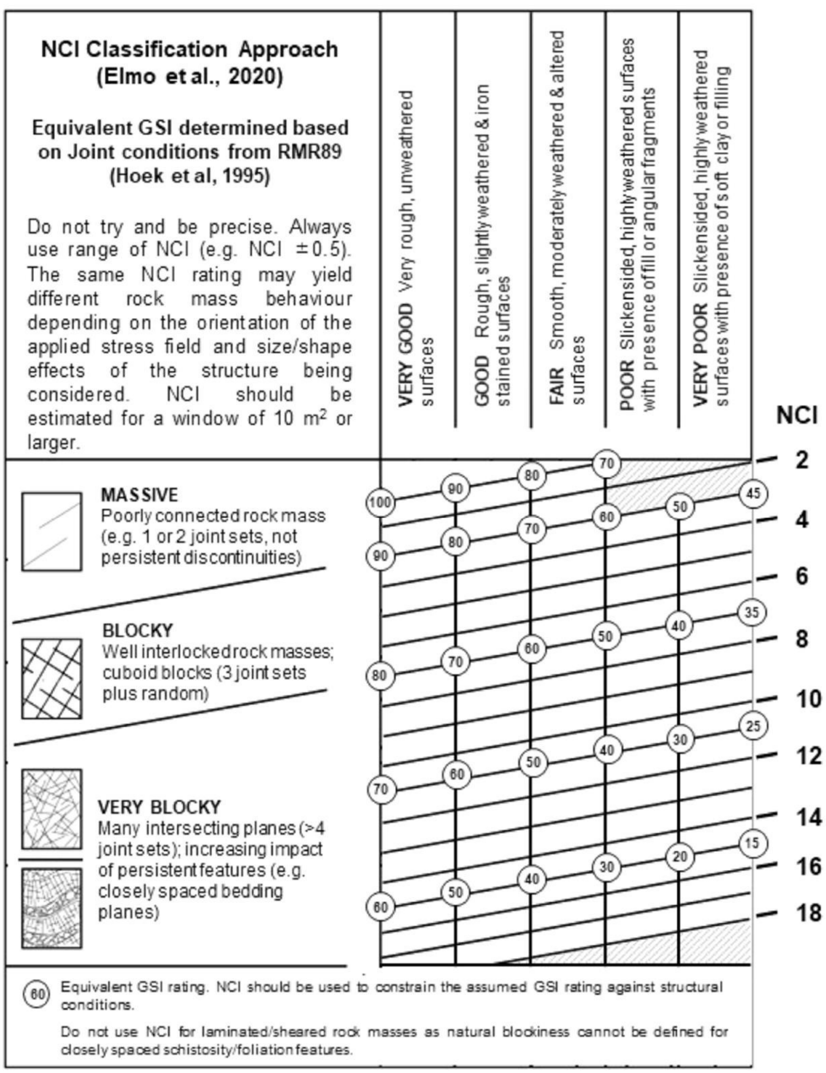

Figure 8: the Network Connectivity Index in 2D (NCI_{2D}) (Elmo et al., 2021)

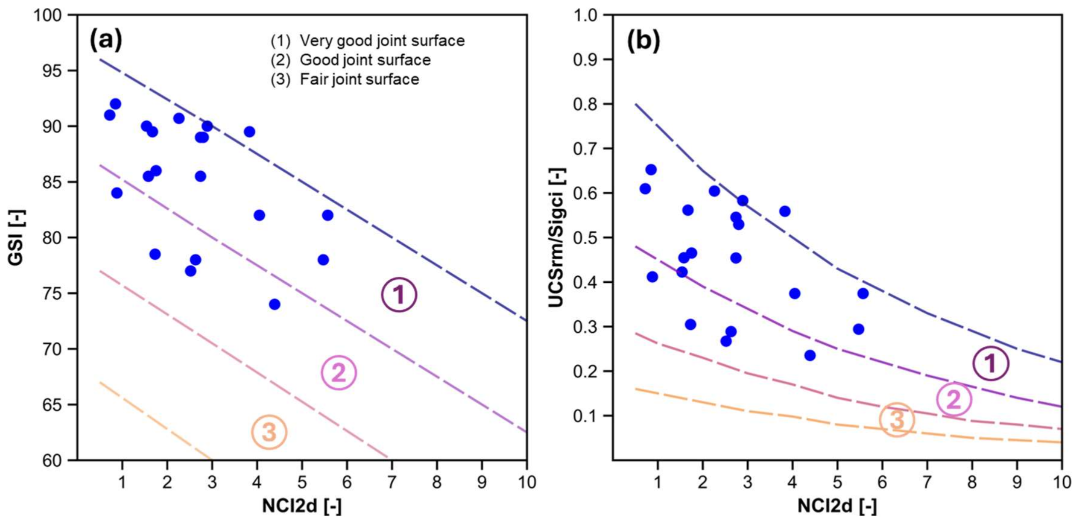

Figure 9: Relationship Between NCI_{2D} and GSI, and Between NCI_{2D} and Rock Mass Strengths

4 COMPARISON WITH CONVENTIONAL ROCK MASS CHARACTERISATION APPROACH IN DETERMINING ROCK MASS STRENGTH

Traditionally, typical underground engineering projects in Hong Kong adopt Q-values and Q-GSI conversion to determine rock mass parameters and strength for various analyses including numerical modelling. The correlation GSI=9lnQ'+44 (Hoek, 1994) remains widely adopted, while for Hong Kong's volcanic rocks, Wu et al. (2025) recently proposed GSI=15lnQ'+42. While both systems are based on similar descriptors; i.e. blockiness and joint conditions; their underlying concept, essence, geological database, parameters and ratings differ (Yang et al., 2022). Q-system (Barton et al., 1974) was specifically developed as a rock mass characterisation and tunnel support design tool. Unlike the Q-system, GSI was originally to link the constants *m* and *s* of the Hoek-Brown failure criterion to rock mass conditions observed on site, and to determine representative Hoek-Brown parameters (Hoek, 1994; Hoek & Brown, 2018). The GSI system was developed without considering Rock Quality Designation (RQD) and place a greater emphasis on assessment of the lithology, structure, and condition of discontinuity surfaces obtained from visual examination. The heart of the GSI system is careful engineering geology description, which is essentially qualitative (Marinos et al, 2005). Despite the widespread adoption of Q-GSI conversions, there is no established equivalency criterion to validate their accuracy. Quoting Yang et al. (2022), *"Classification systems are not universal, and their validity should not be set as default in every new project. Furthermore, empirical correlations potentially introduce more human and parameter uncertainties in the design process."*. Given these concerns, the assumption that the conventional classification ratings and conversions can be directly linked to rock mass physical properties, may be misleading and may influence the outcomes significantly.

Figure 10(a) demonstrates a counterintuitive trend and disconnect between as-mapped Q-values (Table 1) and rock mass strengths obtained from the virtual tests on the SRM models. It is naturally expected that lower Q-values are associated with lower rock mass strength due to increasing blockiness, however, the opposite trend emerges. This issue may stem from the inductive nature of the classification process and the influence personnel judgement during mapping, resulting in subjective results. Based on the parameters presented in Table 1, the main issues possibly arise the determination of the blockiness parameters (RQD/Jn). This has been highlighted by others, e.g. Erharter (2024). Additionally, many have pointed out several limitations of the use of RQD in rock mass characterisation, e.g Pells et al. (2017); which might further contribute to the inconsistencies. This underscores the setbacks of the conventional process and raises concerns about the reliability of Q'-GSI approach in determining rock mass strength. Figure 10(b) illustrates the limitations of this method and demonstrates inconsistencies in the estimated rock mass strengths. Regardless which correlation is adopted, notably, deviation in UCSrm values for a certain GSI deviate by more than 50%. It can also be observed that the trend in rock mass strength classified based on Q'-GSI approach differ significantly from the theoretical line. In contrast, Figure 9 and process outlined in Section 3 provides more robust and objective framework for rock mass characterisation.

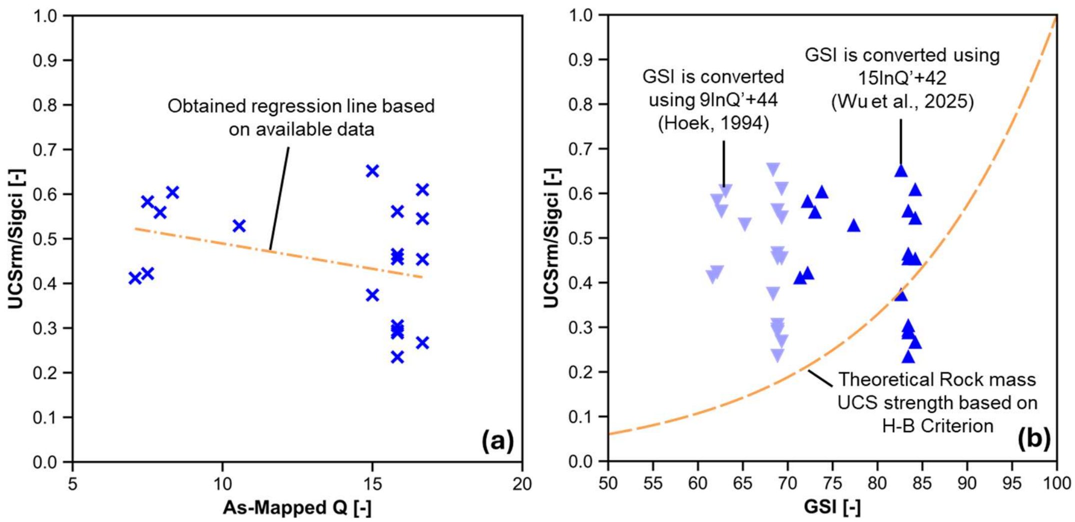

Figure 10: Counterintuitive Relationship Between Analysed SRM Strengths & Rock Mass Ratings (Q & GSI)

CONCLUSION

Through a series of virtual UCS tests on Synthetic Rock Masses (SRM) that incorporate actual as-mapped rock conditions, this study demonstrates that rock mass strength is fundamentally influenced by fracture characteristics. The results of this study confirm that rock mass strength can be reliably characterised using fracture-based descriptors. This is demonstrated by clear trend and correlations between P_{21}, NCI (Elmo et al, 2021), and rock mass strengths described above. By integrating detailed assessment of fracture intensity, density, and connectivity; it is possible to establish a more objective and quantitative rock mass characterisation framework. The determination of GSI and associated rock mass strength through NCI method becomes more straightforward and robust; improving reliability in workflow and minimising the influence of convoluted and inductive process.

In contrast, this paper also demonstrates the limitations of traditional rock mass strength characterisation relying on Q'-GSI conversion. Despite its convenience, its dependence on subjective interpretation and engineering judgment coupled with input uncertainties, increases the risk of inaccurately determining rock mass parameters. The absence of clear trend and the disconnect between the analysed SRM strengths and as- mapped rock mass ratings, including the converted GSI, highlights the concerns about the reliability of Q'- GSI approach in determining rock mass strength. As the equivalency criterion between the two systems is not well established, this paper argues that rock mass classification and strength determination process should avoid the conventional approach (correlations between rock mass systems) as their application could affect engineering outcomes significantly. Ultimately, it should be recognised that different classification systems are established based on different concepts, parameters and ratings. Kaiser (2019) noted that these systems should be used independently of each other and not based upon correlations derived under different geological conditions.

It should be noted that this study focuses on uniaxial problems. For underground engineering projects, stress path around underground openings is more complex and rock mass strength is influenced by different stress in minor and major principal stress directions. Further studies are required to account for this condition.

REFERENCES

Alghalandis, Y.F., Dowd, P.A. and Xu, C., 2015. Connectivity field: a measure for characterising fracture networks. Mathematical Geosciences, 47(1), pp.63-83.

Barton, N., Lien, R. and Lunde, J.J.R.M., 1974. Engineering classification of rock masses for the design of tunnel support. Rock mechanics, 6, pp.189-236.

Barton, N.R., 1988. Rock mass classification and tunnel reinforcement using the Q-system. In: Kirkaldie L. (ed.) Rock Classification Systems for Engineering Purposes, ASTM STP 984. American Society for

Testing and Materials, Philadelphia, PA, 59–88. Barton, N.R., 2015. Forty years with the Q-system – lessons and development. Keynote Lecture, Underground Design and Construction Projects, Hong Kong Institute of Materials, Minerals & Mining.

Cundall, P. A., and Hart., R.D., 1984. Analysis of block test no. 1 inelastic rock Mass behavior: phase 2 – a characterization of joint behavior (final report). Itasca Consulting Group Report, Rockwell Hanford Operations, Subcontract SA-957.

Dershowitz, W.S., 1998. FracMan interactive discrete fracture feature data analysis, geometric modelling and exploration simulation. User Documentation.

Elmo, D. and Stead, D., 2010. An integrated numerical modelling–discrete fracture network approach applied to the characterisation of rock mass strength of naturally fractured pillars. Rock Mechanics and Rock Engineering, 43, pp.3-19.

Elmo, D., Yang, B., Stead, D. and Rogers, S., 2021. A discrete fracture network approach to rock mass classification. In Challenges and Innovations in Geomechanics: Proceedings of the 16th International Conference of IACMAG-Volume 1 16 (pp. 854-861). Springer International Publishing.

Elmo, D., 2023. The Bologna Interpretation of Rock Bridges. Geosciences, 13(2), pp.33–33.

Erharter, G.H., 2024. Rock mass structure characterization considering finite and folded discontinuities: A parametric study. Rock Mechanics and Rock Engineering, 57(7), pp.5229-5249.

Ghazvinian, E., Diederichs, M.S. and Quey, R., 2014. 3D random Voronoi grain-based models for simulation of brittle rock damage and fabric-guided micro-fracturing. Journal of Rock Mechanics and Geotechnical Engineering, 6(6), pp.506-521.

Haryono, I.S., Rogers, S.F., Barrett, S.V.L. and McQueen, L.B., 2024. Improved reliability in rock mass characterisation for underground support design–Discrete fracture network model and site observation. Tunnelling and Underground Space Technology, 147, p.105740.

Hoek, E. 1994. Strength of rock and rock masses. ISRM News Journal, 2, 4–16.

Hoek, E., Carranza-Torres, C. and Corkum, B., 2002. Hoek-Brown failure criterion-2002 edition. Proceedings of NARMS-Tac, 1(1), pp.267-273.

Hoek, E. and Brown, E.T., 2019. The Hoek–Brown failure criterion and GSI–2018 edition. Journal of Rock Mechanics and Geotechnical Engineering, 11(3), pp.445-463.

Itasca Consulting Group, Inc. (2019) UDEC — Universal Distinct Element Code, Ver. 6.0. Minneapolis: Itasca.

Itasca, 2011. Long-term geomechanical stability analysis: OPG's deep geological repository for low & intermediate level waste. Technical Report, NWMO DGR-TR-2011-17.

Kaiser, P.K., 2019. From common to best practices in underground rock engineering. Proceedings of the 14th International Congress on Rock Mechanics and Rock Engineering (ISRM 2019). CRC Press, Boca Raton, FL, 141–182.

Miyoshi, T., Elmo, D. and Rogers, S., 2018. Influence of data analysis when exploiting DFN model representation in the application of rock mass classification systems. Journal of Rock Mechanics and Geotechnical Engineering, 10(6), pp.1046-1062.

Pells, P.J., Bieniawski, Z.T., Hencher, S.R. and Pells, S.E., 2017. Rock quality designation (RQD): time to rest in peace. Canadian Geotechnical Journal, 54(6), pp.825-834.

Potyondy, D.O. and Cundall, P.A., 2004. A bonded-particle model for rock. International journal of rock mechanics and mining sciences, 41(8), pp.1329-1364.

Sharif, L.K., Elmo, D. and Stead, D., 2019. Improving DFN-geomechanical model integration using a novel automated approach. Computers and Geotechnics, 105, pp.228-248.

Stavrou, A., Vazaios, I., Murphy, W. and Vlachopoulos, N., 2019. Refined approaches for estimating the strength of rock blocks. Geotechnical and Geological Engineering, 37, pp.5409-5439.

Yang, B., Mitelman, A., Elmo, D. and Stead, D., 2022., Why the future of rock mass classification systems requires revisiting their empirical past. Quarterly Journal of Engineering Geology and Hydrogeology, 55(1), pp.qjegh2021-039.

Wan, H.L.A, 2018. Numerical Simulation of UCS Test of Rocks Based on PFC3D Modelling. MSc. Thesis. The University of Hong Kong.

Wu, P.K.K., Chan, C.T.H. and Tsui, R.W.S., 2024. A review of the Q-system and the GSI based on recent tunnel and cavern projects in Hong Kong. Rock Mechanics and Rock Engineering, pp.1-13.

Xu, C., Dowd, P.A., Mardia, K.V. and Fowell, R.J., 2006. A connectivity index for discrete fracture networks.

Mathematical geology, 38, pp.611-634.

The Application of GEO Publication No. 1/2023 to a Deep Excavation in Hong Kong

Gavin S.H. Toh, S.S. To, T.S. Ho, Y.L. Yeung & M.C. Fok
Lambeth Associates Limited, Hong Kong

ABSTRACT

This paper offers an overview of the implementation of the GEO Publication No. 1/2023 revamped monitoring scheme at an excavation and lateral support project (ELS) in Kwai Chung, New Territories. Introduced by the Geotechnical Engineering Office (GEO) in late 2023, this publication features significant differences from the monitoring practices commonly used across Hong Kong today, particularly regarding ground settlement. Adoption of design assumptions and guidelines from this publication in ELS submissions of the Project were made to the Buildings Department by the end of 2024 to replace the previous 3A monitoring with the new 5A trigger level, which received approval from government authorities as well as agreement from utilities companies. This paper will explore the distinctions between the new 5A levels and the traditionally used 3A levels outlined in the Practice Note for Authorized Person (PNAP) APP-137, while also considering the design water levels suggested and comparing with the common approach in Hong Kong. By examining these differences, the study aims to provide insights into the implications and benefits of adopting this newly released monitoring scheme for large-scale excavation and infrastructure projects in the region.

1 INTRODUCTION

Before the release of GEO Publication No. 1/2023, the most recent reference document for ELS design in Hong Kong was GCO Publication No. 1/90, published in March 1990. Over the past thirty years, advancements in technology and modelling methods, along with industry experience, professional feedback, and trends from international practices regarding partial factors, led to the publication of GEO Publication No. 1/2023 in December 2023. This update aims to achieve more economically efficient designs for ELS works, reduce construction time, and enhance ground deformation monitoring and control.

Considering the Project's location in a relatively suburban area with fewer sensitive receivers, the project team submitted the ELS package with the application of the GEO Publication No. 1/2023. Following further discussions and meetings with government and private stakeholders, the ELS design was approved in 2024, making this project one of the first in Hong Kong to implement GEO Publication No. 1/2023. This paper will primarily focus on ground settlement monitoring and updates to design groundwater levels in the Project, facilitated by GEO Publication No. 1/2023 (referred as the Publication in this paper).

Lastly, measured data from inclinometers and strain gauges installed on site will be reviewed and discussed.

2 PROJECT BACKGROUND

The project involves extensive deep excavation work with a depth of approximately 14m with an area of approximately 260 meters by 95 meters. This excavation features sheet pile and clutched pipe pile walls, supported by four layers of struts. Located on flat, reclaimed land in Kwai Chung, the site was developed as part of the container terminal expansion in the early 1990s.

The geological profile of the site comprises a sequence of fill, alluvial clay, alluvial sand/silt, completely to highly decomposed granite, and moderately to slightly decomposed granite. Refer to Figure 1 for soil profile. The fill from the reclamation is found to be between 22 meters and 34.5 meters thick, meaning that most of the excavated material consists of the sandy, compacted fill used for reclamation. Located just over 200 meters from the seaside, the site is surrounded by container yards and a car park, covering an area of about 55,245 square meters.

Adjacent to the site are existing utilities from various service providers, including the Water Services Department (WSD), Drainage Services Department (DSD), China Light and Power Limited, The Hong Kong and China Gas Limited, Hong Kong Telecommunications Limited. The diameter of the underground utilities range between 0.1meters and 1.65meters.

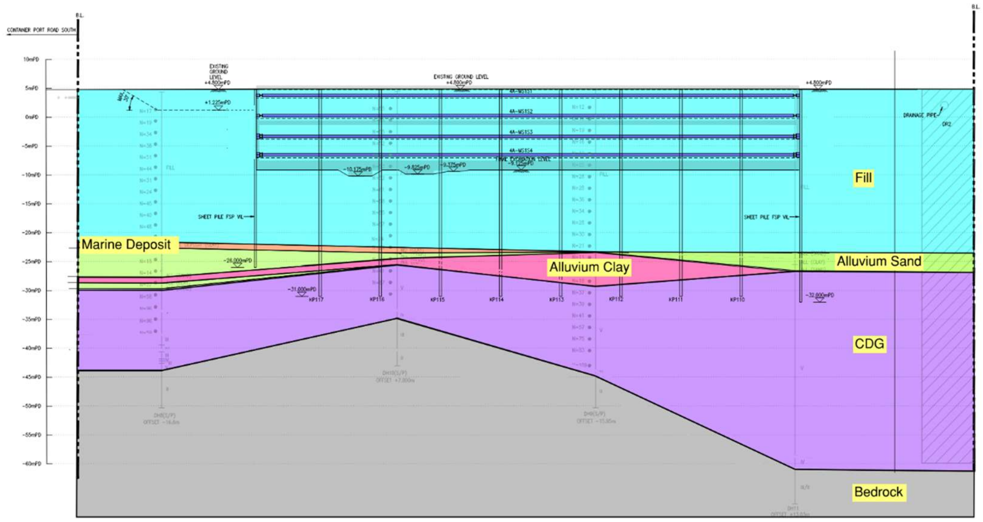

Figure 1: Section drawing of soil profile

3 GROUND SETTLEMENT

3.1 Original monitoring scheme

Prior to the introduction of the new publication, the ground settlement limit at the Site was set at 25mm, a standard commonly used across Hong Kong, primarily based on PNAP APP-137. The alert, alarm and action (AAA) level of ground settlement are detailed in Table 1.

Table 1: Alert, alarm and action (AAA) level of ground settlement suggested in PNAP APP-137 (October 2018 revision)

Instrument	Criterion	Alert (mm)	Alarm (mm)	Action (mm)
Ground settlement marker	Total settlement	12	18	25

According to PNAP APP-137 (October 2018 revision), titled "Ground-borne Vibration and Ground Settlement Arising from Pile Driving and Similar Operations," a 25mm empirical ground settlement action limit is recommended and widely adopted throughout Hong Kong. The alert, alarm and action levels were set at 50%, 70% and 100% of the 25mm value. PNAP APP-137 addresses vibrations and settlements that may occur due to foundation and excavation activities, maintaining the same limit regardless of excavation depth or the type of construction work performed.

3.2 Ground settlement trigger level in GEO Publication No. 1/2023

With the introduction of the Publication, the 5A trigger values have been recommended, with the highest-level set at 0.5% of the retained height (He) as shown in Table 2 below.

Table 2: Recommended trigger values for ground settlement monitoring in 5A Approach by GEO

Instrument	Criterion	Alert (mm)	Alarm (mm)	Action (mm)		
				Level 1	Level 2	Level 3
Ground monitoring marker	Total settlement	10	15	20	0.3%He* subject to a range of 25mm to 60mm	0.5%He* subject to a range of 30mm to 100mm

*He = the maximum excavation depth

Unlike the previously adopted PNAP APP-137 guidelines, the maximum values in the 5A trigger levels now vary based on the excavation depth. For this project, 0.5%He equates to a settlement limit of 69mm, given the retained height of 13.925m—significantly larger than the previous 25mm settlement limit. This increase in allowable settlement enables a substantial reduction in the preloading force required on site. Consequently, a submission incorporating the 5A trigger levels and the reduced preloading value was made to the Buildings Department (BD).

3.3 Ground settlement comparison between 3A and 5A trigger levels

Although the largest allowable ground settlement has been increased from 25mm to 0.5%He, the updated 5A trigger level encourages a quicker response from the project team to any measured ground settlement. A comparison between the 3A and 5A trigger levels, for this Project, is detailed in Table 3.

From this table, it is evident that the alert, alarm, and action level 1 in the Publication have lower settlement values compared to PNAP APP-137. Additionally, the Publication recommends earlier inspections and necessary measures when the first action level is reached. Consequently, the new ground settlement allowance ensures that potential issues are addressed promptly, minimising risks associated with settlement.

Table 3: Trigger values comparison in 3A and 5A approaches in monitoring ground settlement in Kwai Chung

Instrument	Criterion	Approach of Setting Trigger Values	Alert (mm)	Alarm (mm)	Action (mm)		
					Level 1	Level 2	Level 3
Ground monitoring marker	Total settleme nt	3A Approach (PNAP APP-137)	12	18	25		
		5A Approach (GEO Publication No. 1/2023)	10	15	20	41*	69*

*= the calculated trigger value is rounded to nearest integer

In the most recent update to PNAP APP-137, which was revised and published in November 2024, the monitoring control table has been expanded to include 5As instead of the previous 3As. However, the highest action level, Level 3, remains an empirical value of 25mm, consistent with the suggested value in the previous version, as shown in Table 4.

Table 4: Recommended 5A values for ground settlement monitoring in PNAP APP-137 (November 2024 revision)

Instrument	Criterion	Alert (mm)	Alarm (mm)	Action (mm)		
				Level 1	Level 2	Level 3
Ground monitoring marker	Total settlement	12	18	20	22	25

PNAP APP-137 also mentions that the engineering approach for assessing ground settlement is an alternative to the empirical 25mm limit. Site-specific limits can be established by referring to Appendix C of PNAP APP-24, which primarily addresses works related to railway structures and facilities. However, Appendix C of PNAP APP-24 indicates that the suggested monitoring control mechanism is still based on the 3A system, which is different to the updated 5A monitoring control mechanism detailed in GEO Publication No. 1/2023.

4 SERVICE/ BUILDING MONITORING LIMIT

In addition to ground settlement, GEO Publication No. 1/2023 also addresses service/building monitoring limits. However, the limits for alerts, alarms, and actions remain unchanged. Table 5 provides a comparison of the AAA/trigger levels between PNAP APP-137 and the Publication.

Section 9.2.2.4 of the Publication highlights that the suggested action level 1 to 3 suggested have been set in alignment with recent WSD guidelines. For water mains made of different materials, deformation should be controlled within a range of 1:400 to 1:200. As a result, the updated action limits for Levels 1, 2, and 3 are set at 1:400, 1:350, and 1:300, respectively.

These updated action levels promote a quicker response from the contractor and mandate more frequent reviews once action level 1 is reached. This proactive approach aims to ensure that any potential issues are addressed swiftly, enhancing the project's safety and efficiency.

Table 5: Trigger values comparison in 3A and 5A approaches in monitoring services

Instrument	Criterion	Approach of Setting Trigger Values	Alert	Alarm	Action		
					Level 1	Level 2	Level 3
Services monitoring marker	Angular distortion	3A Approach (PNAP APP-137, Oct 2018)	1:600	1:450	1:300		
		5A Approach (GEO Publication No. 1/2023)	1:600	1:500	1:400	1:350	1:300
Building monitoring marker		3A Approach (PNAP APP-137, Oct 2018)	1:1000	1:750	1:500		
		5A Approach (GEO Publication No. 1/2023)	1:1000	1:750	1:600	1:550	1:500

5 DESIGN GROUNDWATER LEVEL

5.1 Original design water levels

Before the release of the Publication, the common approach for determining design groundwater levels (DGWL) was as follows:

For the design groundwater level, the usual practice was to use the greater of either the highest measured groundwater level plus 2 meters or one-third of the retained height. GCO Publication No.1/90 did not provide specific guidance on DGWL, which led some Engineers to refer to Geoguide 1 for suggestions. According to Section 8.2.1 of Geoguide 1, the design for retaining walls should consider the worst credible groundwater conditions that might occur during extreme events such as heavy rainfall, flooding, or water main bursts. However, Geoguide 1 primarily addresses permanent works, with DGWL intended for a much longer design life than that of ELS design.

In this Project, before implementing GEO Publication No. 1/2023, the Serviceability Limit State (SLS) water level and Ultimate Limit State (ULS) water levels were set at +3.03mPD and +3.66mPD, respectively. The SLS water level was used for assessing deflection, while the ULS water level was applied for structural and stability checking. The +3.03mPD level represents the extreme sea level at Victoria Harbour with a five-year return period, measured at the Quarry Bay/North Point station. Meanwhile, the +3.66mPD level corresponds to the extreme sea level with a fifty-year return period at the same location. The ULS water level is also approximately 2meters above the measured highest groundwater level +1.87mPD. These levels were agreed upon in discussions with the GEO, considering the site's proximity to the sea.

The predicted tidal levels at Kwai Chung in 2024 indicate that the highest tide level, reaching +2.8mPD, was expected to occur in November.

5.2 Design groundwater levels in GEO Publication No. 1/2023

In the Publication, three design groundwater levels are recommended, as shown in Figure 2 below: the DGWL for ULS and two DGWL for SLS. The two SLS levels are the design high groundwater level (DHGWL) and the design low groundwater level (DLGWL).

The DHGWL should be based on a realistic estimation of the highest groundwater level and is used for assessing wall deflection and settlement caused by excavation. The DLGWL is utilised to determine acceptable ground settlement resulting from groundwater level drawdown outside of the excavation area.

As outlined in section 6.5 of the Publication, the DGWL should reflect possible scenarios that may occur during the temporary nature of ELS works. It is not necessary to account for effects from long-term and extreme events, such as those due to climate change. The Publication also advises against setting the SLS level too high for projects that involve preloading of struts to control wall deflection. This caution is due to the potential for adverse effects at higher-level struts when lower-level struts are preloaded excessively high. Furthermore, section 4.4.1 notes that excessive preloading can be counterproductive, as it may damage grout curtains, nearby utilities, and underground structures.

Additionally, the Publication notes that in reclaimed land, groundwater levels can be significantly influenced by tidal variations, with attenuation and lag depending on the permeability of the fill material, storage capacity, and horizontal distance from the shoreline.

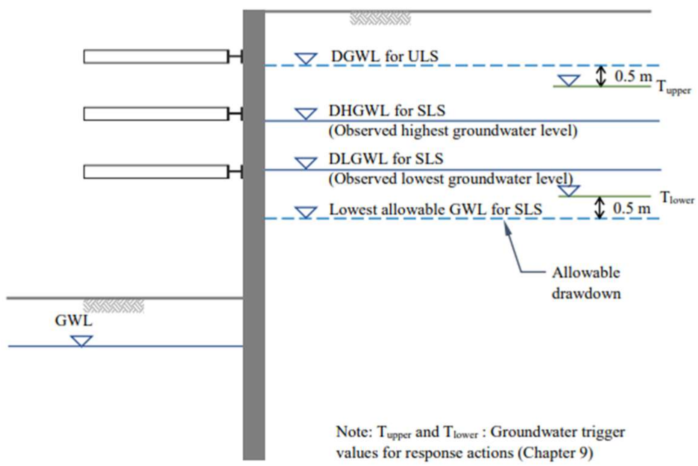

Figure 2: Recommended designed groundwater level by GEO for impact assessment. Extract of Figure 6.7 of GEO Publication No. 1/2023

During the site investigation period of the Project, standpipes were installed, and monitoring was conducted over a seven-day period. Additionally, before the contractor Gammon Construction Limited (GCL) was awarded, a comprehensive groundwater monitoring program was conducted over a nine-month period from January 2023 to October 2023, capturing data during typhoon and black rain storm event in early September 2023.

Once GCL commenced construction, daily groundwater monitoring was performed using standpipes installed on site. Overall, intensive monitoring was carried out over a 12-month period from August 2023 to August 2024 following contract award. Figure 3 provides a sample overview of the groundwater measurements.

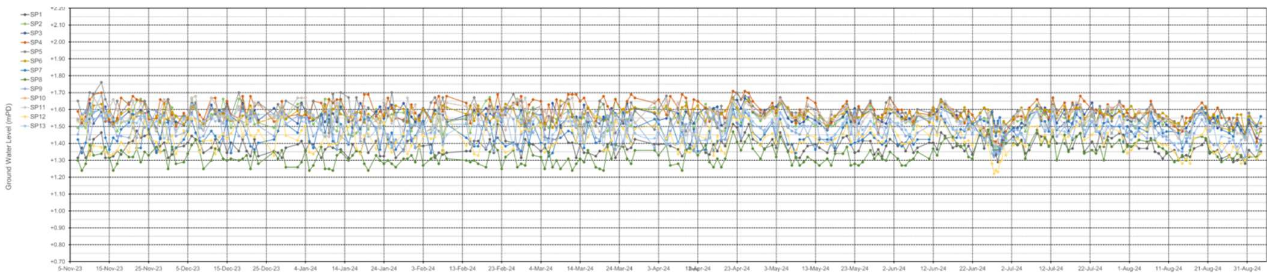

Figure 3: Sample overview of groundwater measurement on site

The measured groundwater levels on site generally ranged between +1.2mPD and +1.8mPD. Thus, by the time GEO Publication No. 1/2023 was applied and submitted to government authorities, a 21-month monitoring period had been completed, from January 2023 to September 2024, covering two wet seasons with typhoons and heavy rains.

With the highest recorded groundwater level being +1.87mPD throughout this long 21-month period, including during wet seasons with typhoons and heavy rain, the submission proposed a DHGWL for SLS of +1.9mPD, which received approval.

With sufficient data obtained from the 21-month groundwater monitoring period, the SLS water level was successfully reduced from +3.03mPD to +1.9mPD. This demonstrates the advantages of maintaining comprehensive groundwater monitoring records prior to the project's commencement. The reduction in DGWL and the increase in the settlement limit allowed for a considerable decrease in the preloading value (up to 80-90% at lower level) of the struts, as well as a reduction in the size of the struts required, if materials have not been purchased. Additionally, it provided greater flexibility in the sequence of strut removal, facilitating safer and easier construction of the permanent slabs. For instance, it became possible to remove more than 1 layer of struts before the construction of permanent slabs above them.

6 APPROVAL PROCESS

During the submission of the ELS packages, which included a proposal for a higher settlement limit and an updated DGWL, stakeholders across the project area had varied responses. Since GEO Publication No. 1/2023 is relatively new to approval bodies, public and private stakeholders, the design team had to put in extra effort to explain the changes and guidelines outlined in the document. Despite receiving governmental approval from BD, GEO, WSD, DSD and Highways Department, the project team still needed to engage with all utilities stakeholders to secure their approval or ensure no adverse comments regarding the higher settlement limit.

As the project team reached out to various utility providers, they received acceptance of the higher settlement limit from all public entities. Among the three private or semi-private stakeholders surrounding the sites, two accepted or conditionally accepted the proposal without significant issues. However, one stakeholder expressed concerns about their services and would not agree to increase the settlement limit beyond 25mm. Consequently, additional settlement points were established for the concerned party, ensuring that the settlement limit for their installed services remained at 25mm, while other utilities can be monitored under the new 5A scheme.

7 MEASURED DATA AND PREDICTION

In this project, the horizontal support system consists of flying struts, corner struts, and trusses. The design team has reviewed monitoring data, including ground settlement, utility measurements, inclinometer readings, and strain gauge recordings. This section briefly discusses the ground settlement data before focusing on the analysis and interpretation of inclinometer data near the flying struts, as well as strain gauge measurements installed on these struts. The findings from these instruments offer insights into the support system's performance, allowing for comparison between predicted and observed behaviour during preloading and excavation. Figure 4 presents the layout of the ground settlement markers, inclinometers, and strain gauges discussed in the subsequent sections.

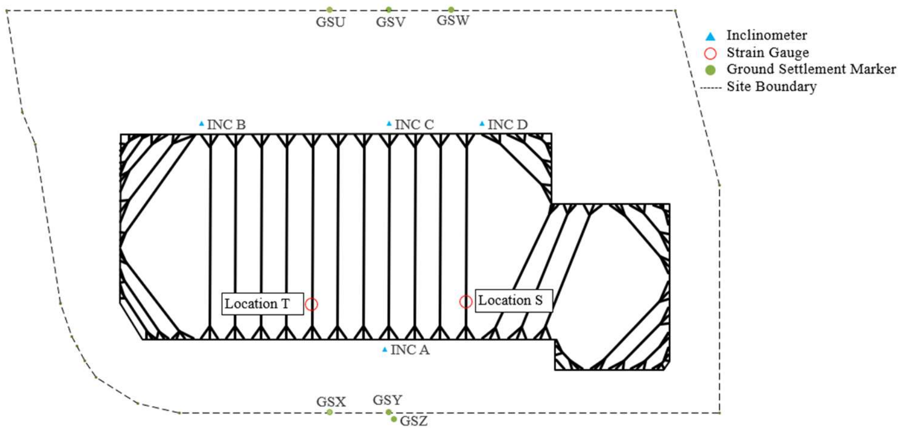

Figure 4: Schematic layout plan of ground settlement markers, inclinometers and strain gauge. Tie/Bracing has been omitted for clarity

7.1 Ground Settlement

Although the approved 5As settlement criteria permit settlements of up to 69mm, the predicted settlement exceeded 40mm in only a few isolated locations. As illustrated in Figure 4, the ground settlement markers on this site were installed at a considerable distance from the piled wall, primarily near the site boundary, which is at least 30 m away from the excavation. The predicted settlement at the final excavation stage was approximately 15 mm and the measured settlement at those markers was around 5 to 6 mm.

7.2 Inclinometers

Nine inclinometers have been installed around the excavation area, with approximately half positioned near flying struts. Figure 5 below illustrates the normalised predicted wall movement (to maximum value) at Inclinometer INC-A alongside the actual inclinometer measurements' normalised shape at each stage of excavation from Layer 2, until the final excavation level (FEL) is reached. The predicted wall movements were derived from a Plaxis 2D model, providing a comparative basis for assessing the accuracy of the design assumptions and the actual behaviour of the excavation support system.

The comparison in Figure 5 reveals that the measured displacements at the top of the wall consistently exceed the predicted values, likely due to additional surcharge loads at ground level, such as those induced by traffic or construction plant activity. In contrast, the recorded displacements at the base of the inclinometer are notably smaller than those predicted by the Plaxis model. This discrepancy may result from the presence of stiffer material at the wall toe, leading to less mobilisation of the lower wall section compared to the model's predictions.

Although not illustrated in Figure 5 for clarity, the data indicates that the wall experienced a measurable but not significant reduction of wall's deflection compared to the values predicted by the numerical model. This discrepancy suggests that while the preloading process restrained wall deflection, the actual behaviour of the wall deviates slightly from the modelled assumptions, potentially due to factors such as soil-structure interaction or variations in ground conditions.

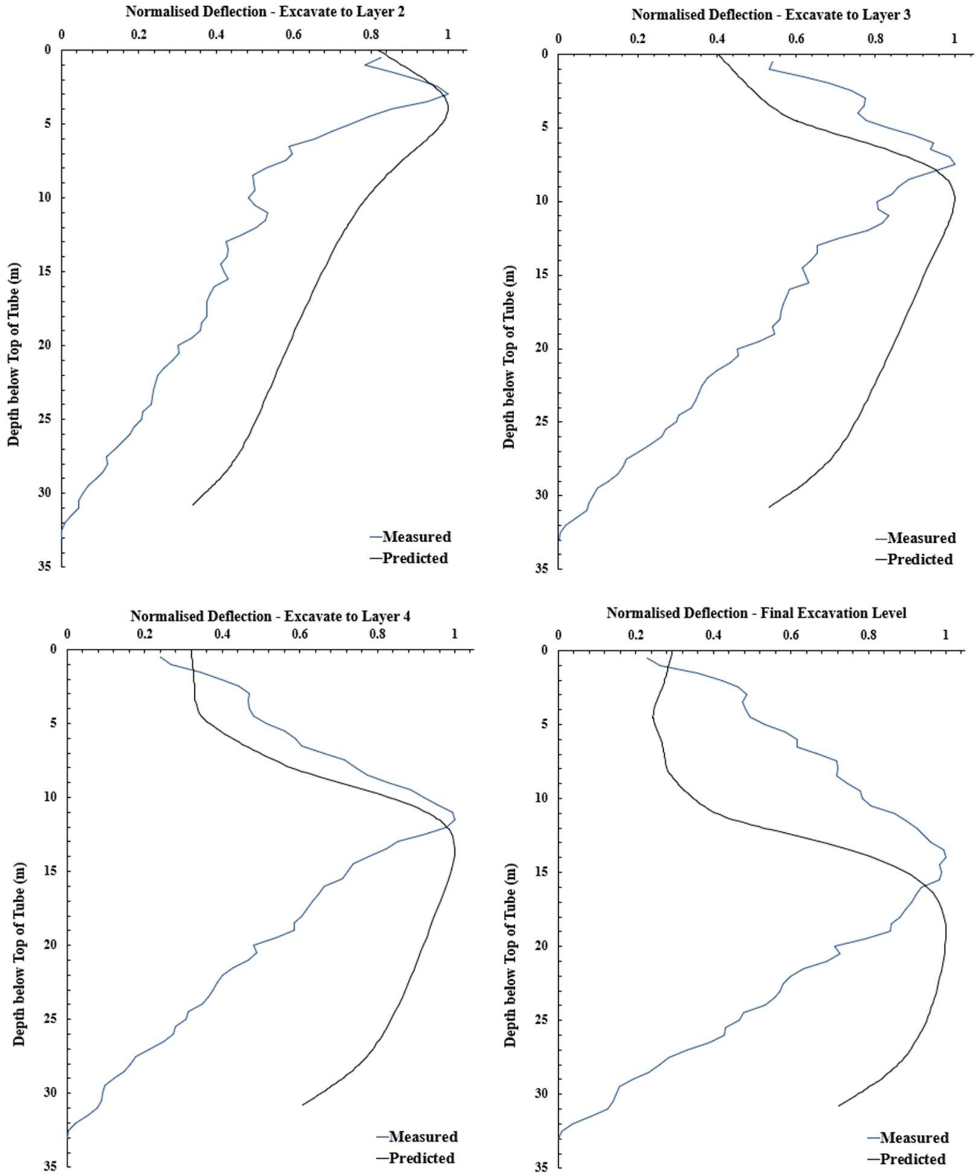

Figure 5: Inclinometer A's predicted shape and measurements at excavation to Layer 2, Layer 3, Layer 4 and FEL

Following the final excavation stage, the inclinometer readings from four inclinometers (INC A to INC D) adjacent to the flying struts are presented below in Figure 6. For majority of the inclinometers, the top of the wall exhibits larger deflections than predicted. In contrast, the bottom of the inclinometers remains relatively stable, showing minimal displacement, contrary to the expected behaviour, as mentioned previously.

All struts exhibited the largest deflection around the Layer 4 excavation level, although the observed behaviour differs slightly from the Plaxis model predictions, which indicated peak deflection at or below final excavation level. The soil below the excavation level may be stiffer than predicted, enhancing wall stabilisation, effectively limiting substantial outward displacement beneath the excavated zone, a finding consistent with INC A's earlier observation.

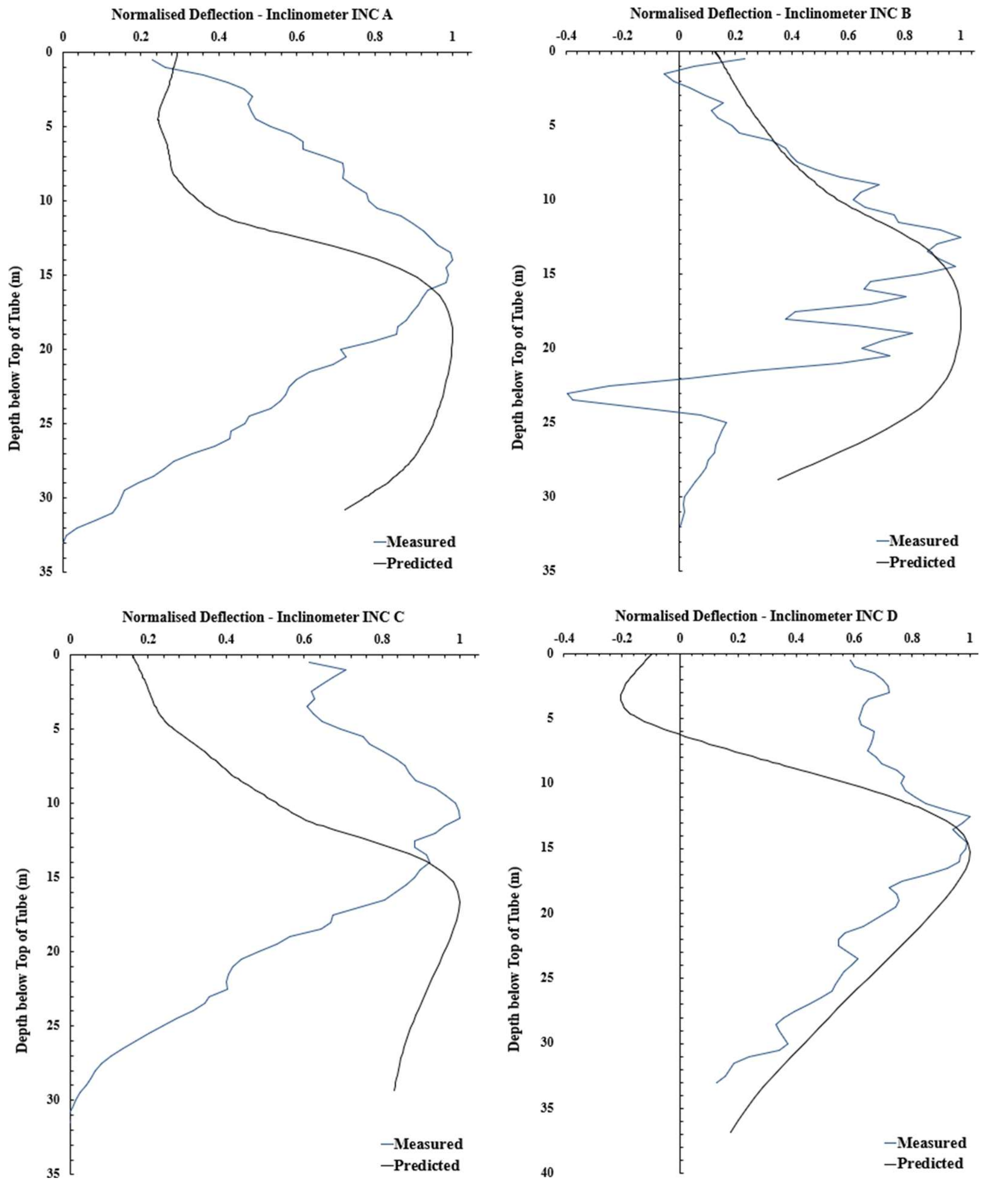

Figure 6: Inclinometer predicted shape and measurements at final excavation stage for INC A, INC B, INC C and INC D

In the case of inclinometer INC B, which recorded displacement in the opposite direction, the unusual readings are likely due to instrument damage or malfunction, as they deviate significantly from the expected trends and the behaviour observed in other inclinometers. These findings highlight the importance of cross-verifying instrument data and considering potential anomalies when interpreting results.

7.3 Strain gauges

Strain gauges have been installed on selected struts across the cofferdam, with data from those placed on the flying struts presented below. By analysing the strain gauge data, it is possible to determine whether the preloading value is maintained within the strut and whether the actual strut load deviates from the anticipated values.

The plots in Figure 7 present strain gauge measurements converted to strut load for the first to fourth layers, comparing them against the predicted SLS design loads at Location S. The plots reveal that strut loads fluctuate with daily temperature variations. Frequent strain gauge readings are especially valuable for verifying preloading values during preloading stage. Table 6 summarises the comparison between measured and predicted strut loads, especially during the FEL stage, along with key observations on strut load behaviour.

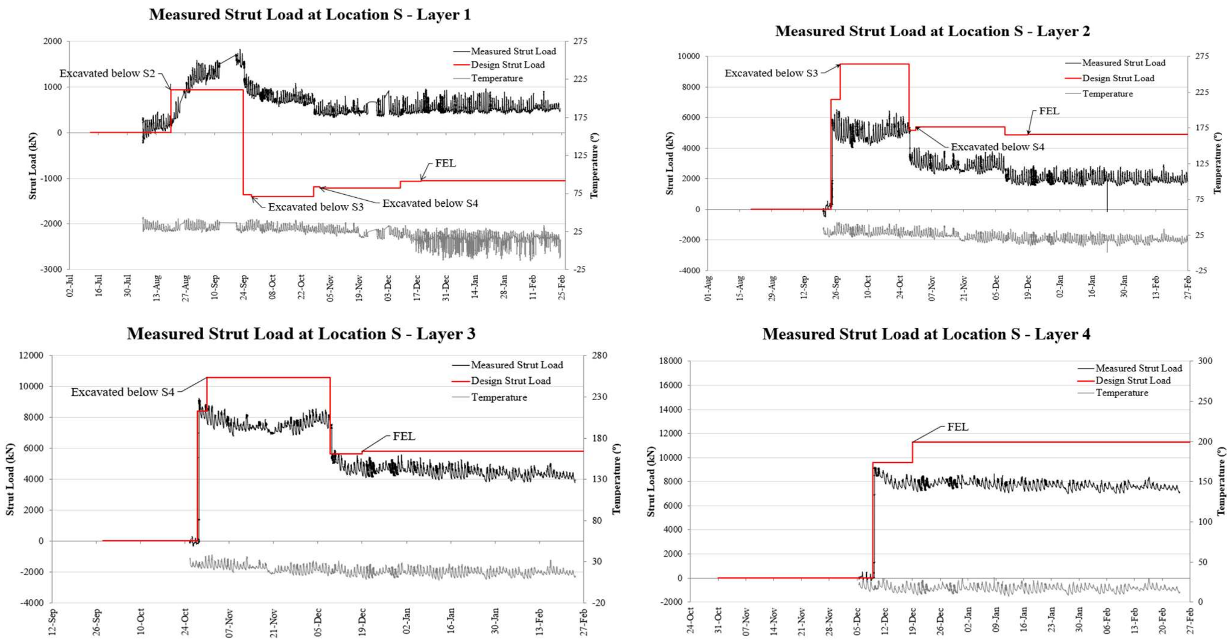

Figure 7: Strain gauge reading at Location S

Table 6: Comparison between measured and predicted strut load at Location S

Layer	Preload	Measured Load vs Predicted Load at FEL	Observation
1	No	Measured: 750kN Predicted: -1050kN	- Predicted tension not achieved - Possible due to additional surcharge on ground
2	Yes	Measured: 2000kN Predicted: 4900kN	- Lower load maybe due to higher than anticipated load in Layer 1 - Measured load at FEL is 41% of predicted value
3	Yes	Measured: 4200kN Predicted: 5810kN	- Strut load remained relatively stable for further excavation - Measured load at FEL is 72% of predicted value
4	Yes	Measured: 7600kN Predicted: 11270kN	- Strut load remained relatively stable for further excavation - Measured load at FEL is 67% of predicted value

Figure 8 illustrate the measured strut loads for the first to fourth layers at Location T compared to their SLS design loads. The load pattern at this location differs slightly from that observed at Location S.

Table 7 provides a summary of the comparison between measured and predicted strut loads at FEL, along with key observations on their behaviour.

Overall, the strain gauge measurements from both Location S and Location T closely align with the design predictions. Majority of the measured strut loads are consistent with the anticipated values and the measured strut loads did not exceed their ultimate structural capacity at any stage. Notably, both strain gauges recorded higher-than-predicted strut loads immediately following the installation of the Layer 1 strut. However, as excavation levels progressed, the strut load in Layer 1 gradually decreased.

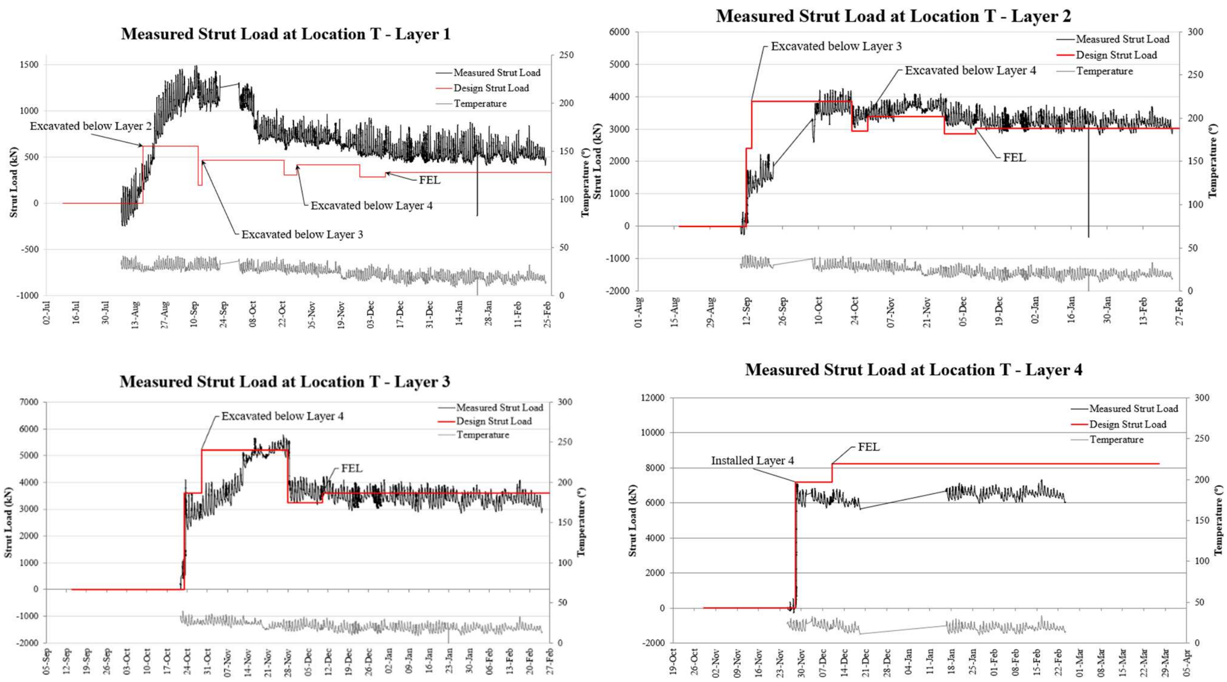

Figure 8: Strain gauge reading at Location T

Table 7: Comparison between measured and predicted strut load at Location T

Layer	Preload	Measured Load vs Predicted Load at FEL	Observation
1	No	Measured: 550kN Predicted: 330kN	- Measured values remained within structural capacity - Measured load at FEL is 60% of predicted value
2	Yes	Measured: 3200kN Predicted: 3010kN	- Temporary loss of connection - Measured load at FEL is 94% of predicted value
3	Yes	Measured: 3200kN Predicted: 3600kN	- Measured load at FEL is 89% of predicted value
4	Yes	Measured: 6300kN Predicted: 8230kN	- Measured load at FEL is 77% of predicted value

Regarding the higher-than-anticipated Layer 1 strut loads, comparison with results from a conventional empirical formula (as specified in the Publication Section 7.6.3 for multi-level strutted wall and illustrated in Figure 9) reveals close agreement between calculated and measured values. The observed discrepancy between the measured loads and the numerical model predictions, yet similarity with the values derived from the formula, can likely be attributed to lack of soil interaction with the piled wall in actual condition. In this early stage of excavation, a greater portion of the lateral load is transferred to the strut compared to the distribution along the piled wall predicted by the numerical model.

Despite this, the strain gauge results from both locations, aside from the higher-than-expected Layer 1 measured load, demonstrate a strong correlation with the design assumptions. Additionally, each strut experienced its peak load during the excavation phase, prior to the installation of the subsequent strut layer. This pattern underscores the importance of timely installation and the redistribution of loads as excavation advances. The observed behaviour further validates the design approach and provides confidence in the structural performance of the system.

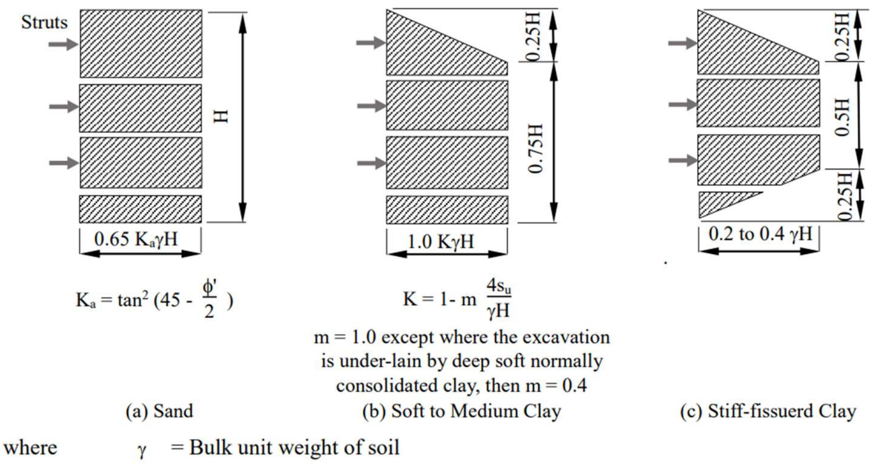

Figure 9: Apparent pressure diagram for computing strut loads in strutted excavations. Extract of Figure 7.20 of GEO Publication No. 1/2023

8 CONCLUSION

The recently published GEO Publication No. 1/2023 aims to promote more economical designs for ELS works, reduce construction time, and enhance ground settlement monitoring and control. At the Project, ELS submissions incorporating the new publication were successfully approved, resulting in more efficient designs. Monitoring data from inclinometers and strain gauges adjacent to flying struts generally align well with design assumptions, though minor discrepancies were observed in some instances. As more projects in Hong Kong adopt the guidelines from GEO Publication No. 1/2023 and contribute performance data and insights, the industry can further refine these guidelines to develop more sustainable solutions for ELS construction.

ACKNOWLEDGEMENTS

The authors would like to thank the whole project team for the support, contribution and participation on the project.

REFERENCES

Buildings Department (BD). 2022. *PNAP APP-24 – Railway Protection under Railways Ordinance, Mass Transit Railway (Land Resumption and Related Provisions) Ordinance and Area Number 3 of the Scheduled Areas in Schedule 5 to the Buildings Ordinance*. Buildings Department, Hong Kong Special Administrative Region Government.

Buildings Department (BD). 2018. *PNAP APP-137 – Ground-borne Vibrations and Ground Settlements Arising from Pile Driving and Similar Operations*. Buildings Department, Hong Kong Special Administrative Region Government.

Buildings Department (BD). 2024. *PNAP APP-137 – Ground-borne Vibrations and Ground Settlements Arising from Pile Foundation and Excavation and Lateral Supports Work*. Buildings Department, Hong Kong Special Administrative Region Government.

Geotechnical Control Office (GCO). (1990). GCO Publication No. 1/90, *Review of Design Methods for Excavations*. Geotechnical Engineering Office, Civil Engineering and Development Department, Hong Kong Special Administrative Region Government.

Geotechnical Engineering Office (GEO). (2020) Geoguide 1 *Guide to Retaining Wall Design* (2020 Version). Geotechnical Engineering Office, Civil Engineering and Development Department, Hong Kong Special Administrative Region Government.

Geotechnical Engineering Office (GEO). (2023) GEO Publication No. 1/2023, *Deep Excavation Design and Construction*. Geotechnical Engineering Office, Civil Engineering and Development Department, Hong Kong Special Administrative Region Government.

Constant Rate of Strain Consolidation Tests on a Marine Clay from the Central Waters near Kau Yi Chau

Philip W.K. CHUNG & Yiyi JIN
Department of Earth Sciences, The University of Hong Kong

Yumi Y.M. CHU
Geotechnical Engineering Office, CEDD, HKSAR Government

ABSTRACT

The constant rate of strain (CRS) consolidation tests offer several advantages over the conventional incremental loading oedometer tests. These include generating a continuous void ratio-effective vertical stress curve, completing a test typically within 2 days, full saturation of the specimen, and the ease of instrumentation for automated data collection. A new CRS testing system was recently established at the Public Works Central Laboratory, featuring full automation and accurate calibration. Different strain rate values were selected and applied in the CRS testing on undisturbed marine clay specimens from the Central Waters near Kau Yi Chau. Data analysis involved applying Wissa's modified linear theory to derive essential consolidation parameters. The study also examined the effects of strain rate on the void ratio-effective vertical stress curve, preconsolidation pressure, coefficient of consolidation, and base excess pore pressure, with initial findings presented in this paper.

1 INTRODUCTION

1.1 Historical notes

The constant rate of strain (CRS) testing technique, with specimens loaded continuously under controlled rates of strain, was first introduced by Hamilton and Crawford (1959) to better determine the consolidation characteristics of clayey soils. Strictly speaking, it is a constant rate of deformation test. Smith and Wahls (1969) demonstrated the detailed CRS test procedures and first established a mathematical model to interpret the test results, and a complete solution was achieved by Wissa et al. (1971) based on the small strain theory. Lee (1981) reviewed the model of Wissa et al. (1971) and proposed a moving boundary theory of consolidation that is suitable for both small and large strain conditions.

Gorman et al. (1978) conducted a sequence of CRS tests on three soil samples collected from Kentucky, the U.S., using strain rates ranging from 0.23–5.22%/hr. This study confirmed the reliability of the CRS test, for the results were comparable to those obtained from the conventional incremental loading (IL) oedometer tests and controlled gradient tests and showed that the CRS test required the shortest time (1.9 days on average) and was the easiest to perform. Further research by Gorman (1981) focused on the effect of strain rate on CRS test results and the strain rate selection scheme. It was suggested that the strain rate can be determined based on the soil's liquid limit and initial degree of saturation (Gorman, 1981). Leroueil et al. (1985) compared the results of a series of CRS tests on the Champlain Sea clay deposits of Eastern Canada with those of three other types of one-dimensional consolidation tests and discussed the strain rate effects on stress-strain relationship and preconsolidation pressure.

The CRS test was studied and applied in Sweden as early as 1975 (Sällfors, 1975), and a Swedish national standard containing step-by-step instructions on the CRS test was released in 1991 (Svensk Standard, 1991). The Swedish standard recommends the rate of strain to be set to 0.0025 mm/min, which generates a deformation of roughly 18% in 24 hours for a 20 mm-high specimen (i.e., 0.75%/hr). If the tested specimen is very soft or muddy clay, a lower rate could be applied so long as the measured base excess pore water pressure u_b does not exceed 10% of the vertical total stress σ_v, yet u_b is allowed to be higher during some parts of the test, but not over 20% of σ_v (Svensk Standard, 1991, cited in Holm, 2016).

The American Society for Testing and Materials (ASTM) standardized the CRS test in 1982 with the designation D4186-82, which suggests the strain rate be selected based on the specimen's liquid limit, as shown in Table 1 (ASTM, 1982). The recommendation (ASTM, 1991) was revised in 1989 to maintain the absolute value of the base excess pressure ratio, $R = u_b/\sigma_v$, between 3% and 30% at any time during the test. In 2006, ASTM further changed the recommendation to keep an R value between 3% and 15% in the normally consolidated range during the loading phase of the test (ASTM, 2008). A Chinese standard on the CRS test can be found in the designation GB/T 50123-2019, where the method for estimating the strain rate is similar to the recommendation of ASTM D4186-82 (Chinese Standard, 2019). The International standard (ISO) or European standard (EN) for the CRS consolidation test is not available so far (as of 2024).

Table 1: Liquid limit-based strain rate selection for the CRS consolidation test suggested by the ASTM (1982) standard D4186-82.

Liquid limit (%)	Rate of strain (%/min) / (%/hr)
< 40	0.04 / 2.4
40–60	0.01 / 0.6
60–80	0.004 / 0.24
80–100	0.001 / 0.06
100–120	0.0004 / 0.025
120–140	0.0001 / 0.006

Some CRS tests conducted in Hong Kong were found in Premchitt et al. (1996) using the Rowe cell, aiming to determine the preconsolidation pressure of a stiff alluvial clay sample collected near the Chek Lap Kok airport. In this study, three strain rate levels of 0.3, 0.6, and 6%/hr were attempted, and the curves of void ratio, excess pore water pressure, coefficient of consolidation, and constrained modulus ($1/m_v$) against the logarithm of applied effective stress obtained under different strain rates were compared. However, though the plots clearly presented the strain rate effects on these consolidation parameters, the CRS test results in this report lack detailed interpretation. In addition, the limitations of the Rowe cell equipment when applied in the CRS test were not adequately analysed. Based on the assemblage of the Rowe cell, the stresses may not be uniformly distributed over the sample's cross-section, and the accuracy of the pore water pressure measurements was in doubt, which leads to errors when interpreting the test results using prevailing theories.

1.2 Characteristics of the CRS test

The CRS testing method offers several advantages over the conventional IL oedometer test. First, depending on the applied strain rate, the time required to complete a CRS test is usually significantly less than a conventional oedometer test. An IL oedometer test takes approximately two weeks, while a CRS test typically can be finished within two days.

Second, in conventional tests, a sequence of loading is applied to the specimen in discrete stages, so the consolidation properties at the applied pressures between loading steps can only be inferred. In contrast, the CRS test is performed as a continuous process, during which the vertical stress, axial deformation, and pore water pressure at the bottom of the specimen are measured continuously by the testing system. Hence, the CRS test results can be presented in practically continuous plots (e.g., the void ratio-effective vertical stress and pore water pressure-effective vertical stress curves), which favours more reliable estimates of the consolidation parameters, especially the preconsolidation pressure. It has been argued by Premchitt et al. (1996) that doing a CRS test is probably the only way to accurately determine the preconsolidation pressure of stiff clays because the e-log σ'_v curve obtained from a conventional test would be too flat to identify the break in the curve.

Third, Stolle and Stolle (2011) pointed out that standard incremental loading tests generate high gradients of pore water pressure in the specimens that may not realistically develop in prototype applications. The CRS test, as an alternative approach, allows a smoother and more representative loading process, which is beneficial for characterising the consolidation parameters and minimizing sample disturbance.

Additionally, the CRS test can be instrumented to achieve full automation in terms of equipment setup, test procedures and data acquisition. The automation significantly enhances testing efficiency. The digitally recorded data are especially valuable for data analysis in research projects and streamline procedures in routine testing. By contrast, conventional oedometer testing relies on manual incremental loading which involves lifting the heavy metal discs onto the loading system, and manual recording data. These procedures are labor-intensive and prone to human error.

It is also worth noting that there is no provision for specimen saturation in the conventional oedometer tests. The specimen is merely soaked under a seating pressure of 5 kPa and assumed to be saturated during the test. In the CRS setting, a back pressure is applied to saturate the soil specimen, and this step is critical for accurately measuring the pore water pressure at the bottom of the specimen.

Though high-quality data can be obtained from the CRS test, a theory must be established before proceeding with the data reduction and interpretation, and the interpretation of the results requires more effort compared with the standard IL oedometer testing method. The IL oedometer test has long been a routine consolidation test with well-known and widely accepted methods and procedures to estimate the effective vertical stress, σ'_v, void ratio, e, coefficient of consolidation, c_v, hydraulic conductivity, k, coefficient of volume compressibility, m_v, and preconsolidation pressure from the results. However, the CRS test has been plagued by two major problems. One is that the distribution of (excess) pore water pressure throughout the height of the specimen varies, and the exact pattern, from zero at the drainage boundary at the top to a measured value at the bottom, is unknown, which poses challenges in calculating the average pore pressure and thus the average effective axial stress in the specimen. Another difficulty is selecting an appropriate strain rate at which to carry out the test for the type of soil specimen being tested. On one hand, a rate too fast would induce to much excess pore water pressure in the specimen so that results could not be interpreted correctly. On the other hand, if the deformation rate is too slow, the advantage of using the CRS test as a quick testing method is defeated, and it causes troubles in determining the primary consolidation properties due to the prominent secondary compression effects. Moreover, the excess pore water pressure generated under a very low strain rate is insignificant, causing problems in applying the equations for the consolidation parameters according to the available theories.

1.3 Theories of CRS result interpretation

The most popular theories for interpreting the CRS data are the linear theory of Smith and Wahls (1969) and the modified linear theory and nonlinear theory developed by Wissa et al. (1971). The theories of Wissa et al. (1971) was first adopted by ASTM. From 1982 to 2005, ASTM suggested the nonlinear theory to be used; since 2006, the modified linear theory has been recommended, with the equations of the nonlinear model provided in the appendix of the ASTM D4186, and the use of the nonlinear theory equations is not regarded as a non-conformance with the CRS test method.

The linear theory is established based on assumptions that the coefficient of volume compressibility, m_v, is constant, i.e., the relationship between the strain and effective stress is linear, and that the distribution of excess pore water pressure is linear throughout the height of the specimen. The nonlinear theory is based on assumptions that the virgin compression index, C_c, is constant, i.e., there is a linear relationship between the strain and log effective stress, and that the distribution of excess pore water pressure is parabolic.

The equations for estimating the effective vertical stress σ'_v, coefficient of consolidation, c_v, hydraulic conductivity, k, and coefficient of volume compressibility, m_v from CRS test are given in the latest version of ASTM D4186 under both linear and nonlinear models, with the linear model as the preferred method.

1.4 Research objectives

A CRS apparatus was recently procured by the Public Works Central Laboratory (PWCL) of GEO/CEDD. A collaborative research project was conducted by the Department of Earth Sciences of HKU and GEO with the following objectives:

(1) Assemble the apparatus with full automation and calibration;
(2) Establish the testing procedures based on the current ASTM (2020) standard D4186/D4186M–20$^{\varepsilon 2}$;
(3) Perform a series of trial tests on different types of soil with different specimen preparation: remoulded kaolin, reconstituted kaolin, remoulded kaolin with preconsolidation, and undisturbed marine clay obtained from the Central Waters near Kau Yi Chau;
(4) Study the data reduction and interpretation of the test results, including the application of linear and nonlinear equations provided in D4186/D4186M–20$^{\varepsilon 2}$; and

(5) Investigate the selection of appropriate strain rates and their impact on the interpretation of various consolidation parameters.

This paper presents some details of objectives (1) and (2) and some test results of undisturbed marine clay under objectives (3) and (4).

2 NEW CRS SETUP IN THE PUBLIC WORKS CENTRAL LABORATORY

2.1 Apparatus, test procedures and calibration

The new CRS testing system at the PWCL (Figure 1) is assembled using VJ Tech's TriSCAN-50 Pro Advanced Triaxial Load Frame, Multi-Purpose Consolidation Cell, and APC Pro Automatic Pressure Controller. It can be noticed from the schematic diagram in Figure 1 that the soil specimen, laterally constrained by the confinement ring, is submerged in the chamber together with a load cell that measures the axial force applied to the top of the specimen during the test. In each test, after the apparatus and soil specimen (cut and trimmed to fit the confinement ring and sandwiched by filter papers on its top and bottom) are assembled, the chamber is filled up with water, and a back pressure is applied to fully saturate the specimen. Then, the specimen is deformed axially at a constant strain rate (strictly speaking, a constant deformation rate), with drainage allowed only through its top boundary and excess pore water pressure measured at its base. A standard test comprises a loading phase, a holding phase (to allow the dissipation of base excess pressure), and an unloading phase. The axial deformation, axial load, chamber pressure, and base pressure at any time (t) during the test are measured automatically by the digimatic gauge, load cell and pressure transducers.

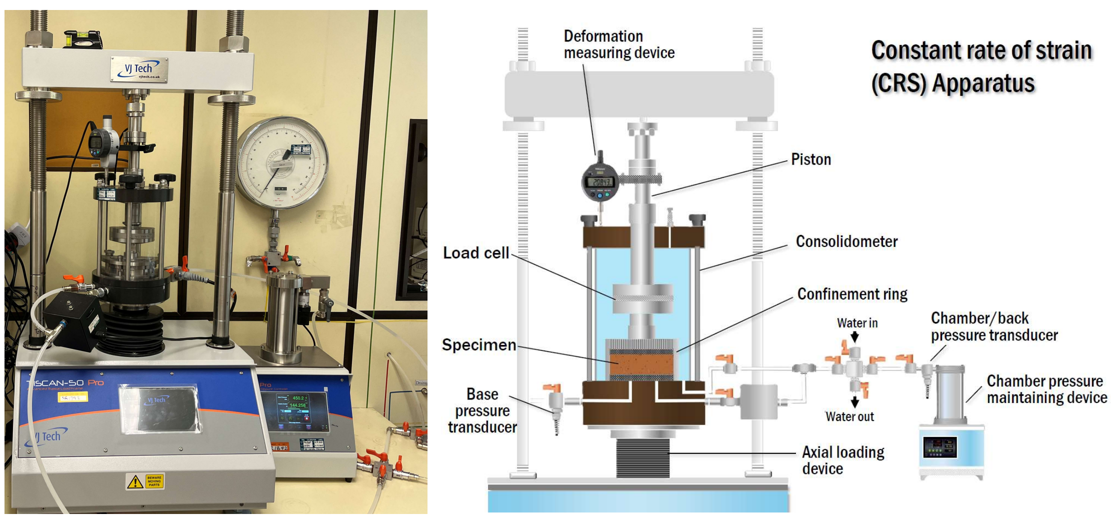

Figure 1: Photo and schematic diagram of the CRS testing apparatus at the Public Works Central Laboratory.

Most of the components of the CRS testing system were properly calibrated to meet the requirements of ASTM D4186 (clauses 6 and 7). In particular, the accuracy and capacity of the pressure transducers and load cell have been checked. In addition, the compressibility of the consolidometer during back pressure saturation and consolidation has been examined, and the magnitude of piston uplift force due to chamber pressure has been calculated to correct the axial force readings. The correctness and reliability of the data acquisition system has been carefully checked. The stability of the strain rate as provided by the system through the axial load device is discussed in Section 4 below. Some checking and calibrations may need to be repeated after a series of trial tests.

2.2 Data reduction

After completing the test, the net axial force, $f_{a,n}$, (kN) is obtained by correcting the system-recorded axial load with the piston uplift force, and the total axial stress, $\sigma_{a,n}$, in kPa is calculated by dividing $f_{a,n}$ with the specimen area. The axial strain rate at each time, $\dot{\varepsilon}_n$, is calculated as follows:

$$\dot{\varepsilon}_n = \frac{\Delta H_{n+1} - \Delta H_{n-1}}{H_0} \cdot \frac{1}{t_{n+1} - t_{n-1}} \tag{1}$$

where ΔH_n is the change in specimen height in cm obtained from the axial deformation records, and H_0 is the initial specimen height in cm.

The base excess pressure that is the difference between the measured base pressure and chamber pressure, in kPa at any given time is obtained as follows:

$$\Delta u_{m,n} = u_{m,n} - \sigma_{c,n} \tag{2}$$

where $u_{m,n}$ is the measured base pressure in kPa, and $\sigma_{c,n}$ is the measured chamber pressure in kPa.

Wissa et al (1971) provide the first complete solution to consolidation under CRS. The solution predicts an initial transient condition generated in the soil as the piston was set in motion and that must be dissipated before steady state conditions exist. They developed more general solutions that consisted of an initial transient portion and a steady-state portion. They also developed a dimensionless steady-state factor to show the degree of transience. The equations based on this modified linear theory for calculating various consolidation properties only apply to steady-state conditions. It can be shown that the Time Factor, T_v, is about 0.5 when the steady state factor is 0.4. The ASTM test method adopts this theory and specifies that the dimensionless steady-state factor F_n at each time is calculated as follows, to evaluate whether the transient strain at the start of a loading or unloading phase is small enough:

$$F_n = \frac{(\sigma_{a,n} - \sigma_{a,l}) - (\Delta u_{m,n} - \Delta u_{m,l})}{\sigma_{a,n} - \sigma_{a,l}} \tag{3}$$

For any line of data with an F value less than 0.4, the calculation results of the steady state equations will be approximate, and the corresponding data is ignored. If F_n is greater than 0.4, the consolidation parameters will be calculated as follows.

The average effective axial stress, $\sigma'_{a,n}$, in kPa is obtained as:

$$\sigma'_{a,n} = \sigma_{a,n} - \frac{2}{3}\Delta u_{m,n} \tag{4}$$

where $\sigma_{a,n}$ is the total axial stress in kPa, and $\Delta u_{m,n}$ is the base excess pressure in kPa. It means that the excess pore water pressure follows a parabolic distribution.

The hydraulic conductivity, k_n, in m/s is calculated using the following equation:

$$k_n = \frac{\dot{\varepsilon}_n \cdot H_n \cdot H_0 \cdot \gamma_w}{2 \cdot \Delta u_{m,n}} \cdot \frac{1}{10000} \tag{5}$$

where γ_w is the unit weight of water at 20 °C, i.e., 9.7891 kN/m^3. H_0 and H_n are the initial and current specimen thicknesses respectively in cm. It may be noted that Equation (5) is a first-order approximation in the calculation of the average thickness of the specimen.

The coefficient of volume compressibility, $m_{v,n}$, in m^2/ kN is calculated as:

$$m_{v,n} = \frac{\varepsilon_{n+1} - \varepsilon_{n-1}}{\sigma'_{a,n+1} - \sigma'_{a,n-1}} \tag{6}$$

Then, the coefficient of consolidation, $c_{v,n}$, is obtained as:

$$c_{v,n} = \frac{k_n}{m_{v,n} \cdot \gamma_w} \tag{7}$$

Finally, the base excess pressure ratio, $R_{u,n}$, (dimensionless) is calculated as:

$$R_{u,n} = \frac{\Delta u_{m,n}}{\sigma_{a,n}} \tag{8}$$

3 TRIAL TESTS PROGRAMME

This study involves selecting two types of soil samples for conducting CRS and IL consolidation tests: kaolin and undisturbed marine deposits obtained near Kau Yi Chau (from a 100 mm Piston sample). The marine deposits consist of soft, dark grey silty clay. The kaolin samples are prepared using various methods, including remoulding, remoulding with applied preconsolidation pressure, and reconstitution. A comprehensive series of tests has been developed for these soils, considering different applied strain rates and back pressure rates. The testing program comprises approximately 20 CRS tests and 10 IL tests. This paper focuses on presenting preliminary test results of the undisturbed marine clay obtained at a depth of 19–20 m below the seabed surface. It includes two CRS consolidation tests conducted under strain rates of 1% and 10%. Additionally, the results of a traditional IL oedometer test are provided for comparison.

4 RESULTS AND DISCUSSION

4.1 Strain Rate

Selecting an appropriate strain rate for the CRS test on a specific soil is a critical step in obtaining reliable and meaningful test data, which is also the main focus of Objective (5) in this research project. For the initial trial, we estimated the strain rate based on the marine clay's liquid limit and the method outlined in Table 1. With the sample's liquid limit at approximately 50%, a suitable strain rate of around 0.6%/hr was determined, leading to the selection of a 1%/hr strain rate in our trial run. Additionally, a higher strain rate of 10% was employed for comparison. Following the CRS test results, we evaluate whether the pressure ratio, $R = u_b/\sigma_v$, falls between 3% and 15% during the normally consolidated stage to assess the suitability of the strain rates (refer to discussions in Figure 7).

Although the accuracy of the applied strain rate has been confirmed through the proper calibration, we take the opportunity to assess the effectiveness of the automated system in providing and maintaining the chosen strain rate during the test. Figure 2 displays the results for the selected strain rates of 1%/hr and 10%/hr.

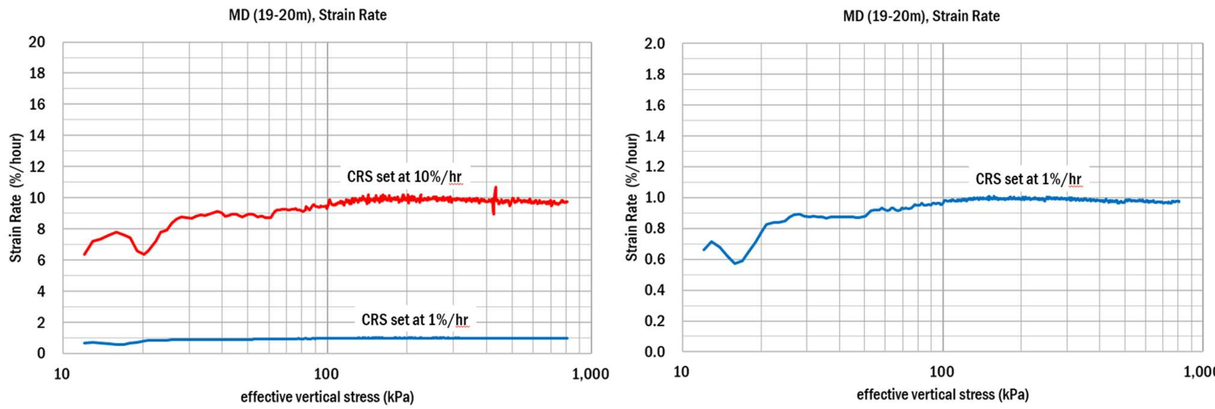

(a) (b)

Figure 2: (a) Strain rates provided by the testing system during the tests; (b) provision of strain rate = 1%/hr.

It can be seen from Figure 2(a) that, for a selected strain rate of 10%/hr, the testing system is capable of providing 90% of the specified strain rate starting at σ′ = 30 kPa. We consider our automated testing system satisfies the ASTM D4186-82 requirement that the rate shall not have more than 10 % cyclic variation. For the selected strain rate of 1%/hr, at a first glance, Figure 2(a) may suggest better performance for a lower strain rate of 1%/hr. However, upon adjusting the vertical axis scale as displayed in Figure 2(b), it becomes apparent that the testing system actually performs similarly in delivering both selected strain rates.

4.2 Steady-state factor, F

As discussed in Section 2.2 above (see also Equation (3)), the equations derived from Wissa's modified linear theory to determine various consolidation properties are applicable only under steady-state conditions. ASTM standard specifies that the calculation of consolidation properties like k, m_v and c_v is considered valid if a minimum F value of 0.4 can be achieved. Figure 3 shows the variation of F with applied effective vertical stresses under two different strain rates. In Figure 3, the variation of F with applied effective vertical stresses is depicted for two distinct strain rates. It is evident that the steady-state factor remains above 0.9 throughout the test for both selected strain rates.

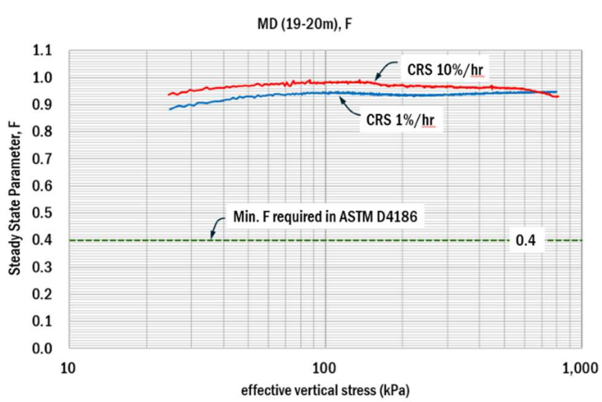

Figure 3: Variation of the steady-state factor, F, during the CRS tests.

4.3 e-log σ' plot and preconsolidation pressure

The void ratio vs effective vertical stress plots for marine clay under three testing scenarios are shown in Figure 4. The CRS tests yield continuous curves, while the IL test results in discrete points that are then manually connected to form a smooth curve. The preconsoldiation pressures, σ'_0, for the three tests are estimated by the Casagrande's construction method and are shown also in the Figure. Given that the current effective vertical stress on the marine clay is around 175 kPa, it is intriguing to observe that Casagrande's method underestimates the preconsolidation pressures based on the test results illustrated in Figure 4. This discrepancy presents a puzzle that warrants further investigation.

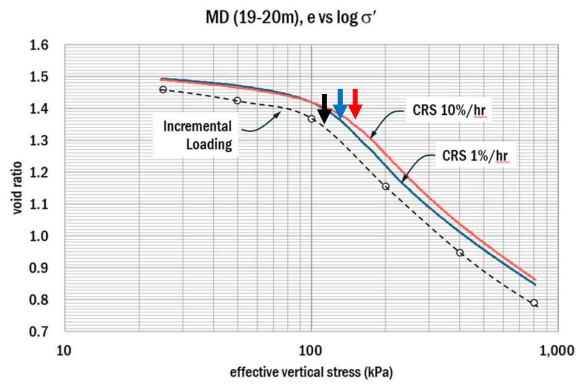

Figure 4: e-log σ' curves for a marine clay obtained by the CRS tests and the IL test.

The range of the preconsolidation pressure may also be seen from the CRS test using the plots as shown in Figures 5 and 6. This provides one of the advantages of the CRS test over the conventional IL test to roughly estimate this parameter by different methods.

As far as the strain rate is concerned, as expected, the CRS test with higher strain rate gives a slightly larger σ'_0. With similar initial void ratio, the position of the curve from the IL test suggests that the average strain rate of this test is somewhat below 1%/hr.

4.4 Coefficient of consolidation

The coefficient of consolidation, c_v, from the IL test is estimated from the square root time plots for each incremental load. For the CRS test, the hydraulic conductivity and coefficient of volume compressibility are first calculated using Equations (5) and (6). Then the c_v values are computed from Equation (7), and the results are plotted in Figure 5. The results for the CRS test with a strain rate of 1%/hr and the IL test are illustrated more clearly in the right panel of the figure by adjusting the vertical axis scale.

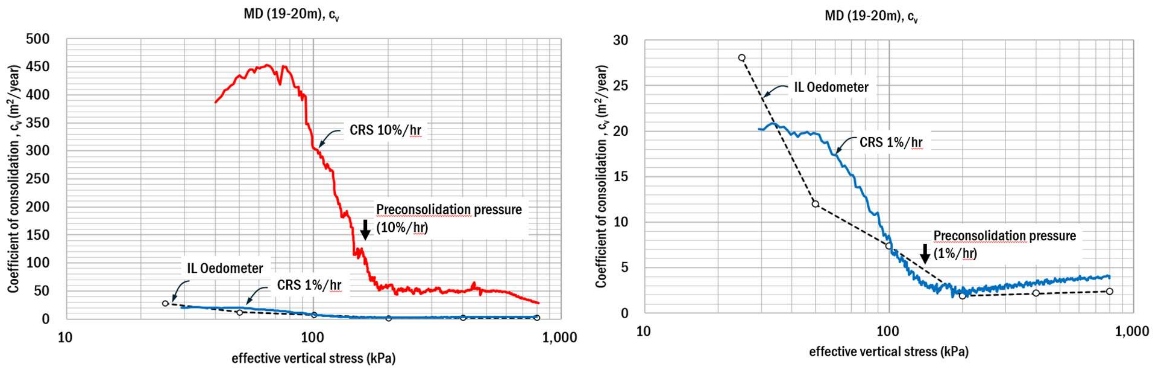

Figure 5: The coefficient of consolidation, c_v, obtained by the CRS tests and the IL test.

The coefficient of consolidation, c_v, values for the normally consolidated sections of the marine deposit, as determined from the CRS 1%/hr and IL tests, are similar, ranging from 2 to 4 m^2/year depending on σ'. However, the c_v values derived from the CRS 10%/hr test might be overestimated when utilizing a high strain rate. These findings underscore the significance of selecting an appropriate strain rate for a CRS test.

The test results presented in Figure 5 also highlight a well-established phenomenon: the coefficient of consolidation for over-consolidated clay are notably higher than those for normally consolidated clay. The drastic shift in c_v values, corresponding to changes in σ', indicates the position of the preconsolidation pressure.

4.5 Base excess pore pressure and base excess pressure ratio

The variation in base excess pore pressure with σ' is illustrated in Figure 6 for the CRS tests carried out at two distinct strain rates. The findings clearly indicate that as the clay sample transitions from the over-consolidated state to the normally consolidated state, the base excess pore pressure begins to rise. This observation aligns with the understanding that the coefficient of consolidation for normally consolidated clay is considerably lower than that for over-consolidated clay. Therefore, the CRS test provides an additional approach to approximately determine the preconsolidation pressure.

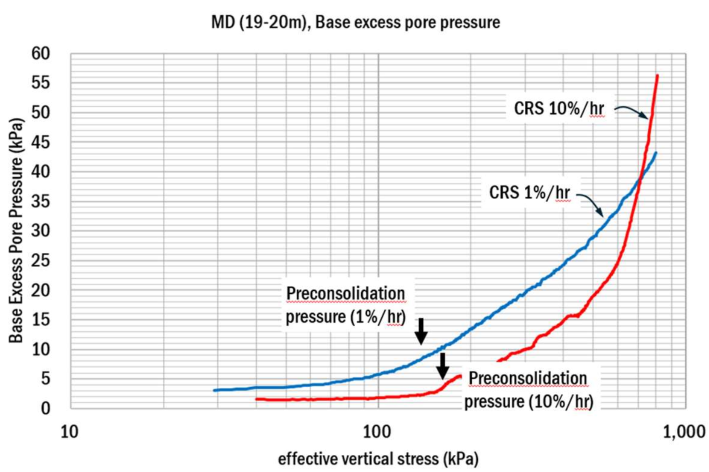

Figure 6: Variation of the base excess pore pressure during the CRS tests.

As discussed in Sections 1.1 and 4.1, the latest ASTM standard suggests selecting a strain rate that maintains the excess base pressure ratio, R (= u_b/σ_v), between 3% and 15% in the normally consolidated range during the test's loading phase. Figure 7 displays the outcomes for the two strain rates employed in the trial experiments.

It is evident that the 1%/hour strain rate meets the ASTM standard, while the 10%/hour strain rate falls marginally within acceptable limits. The test results illustrated in Figures 3 to 7 strongly indicate that the 1%/hour strain rate is a suitable choice for the marine deposits under examination.

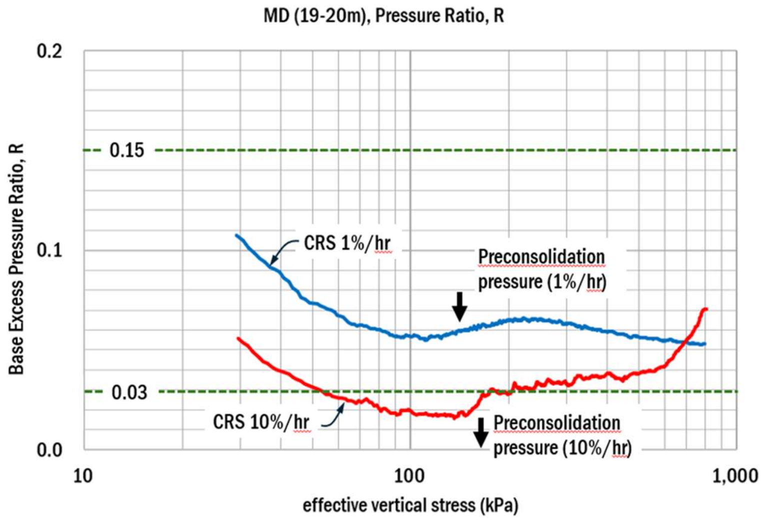

Figure 7: Variation of the base excess pressure ratio, R, during the CRS tests.

5 CONCLUSIONS

A newly automated CRS consolidation testing system has been successfully put together and calibrated. Trial examinations utilizing a marine deposit sample obtained close to Kau Yi Chau have been carried out to showcase that the testing system can be effectively employed for both routine and research-focused tests. A strain rate of 1% per hour has been determined to be suitable for this marine clay. Plots shown in Figures 5 and 6 are utilized to validate the preconsolidation pressures estimated through Casagrande's method. The coefficient of consolidation values, plotted against the effective vertical stress, are presented in Figure 5, along with a comparison to the discrete values obtained from the IL oedometer test.

ACKNOWLEDGEMENTS

We express our appreciation to the technical staff at the Public Works Central Laboratory for their invaluable support in this project. This paper is published with the permission of the Director of Civil Engineering and Development and the Head of the Geotechnical Engineering Office, the Government of the Hong Kong Special Administrative Region.

REFERENCES

ASTM. 1982. Standard test method for one-dimensional consolidation properties of saturated cohesive soils using controlled-strain loading. D4186-82.

ASTM. 1991. Standard test method for one-dimensional consolidation properties of saturated cohesive soils using controlled-strain loading. D4186-89.

ASTM. 2006. Standard test method for one-dimensional consolidation properties of saturated cohesive soils using controlled-strain loading. D4186-06.

ASTM. 2020. Standard test method for one-dimensional consolidation properties of saturated cohesive soils using controlled-strain loading. D4186/D4186M–20$^{\varepsilon 2}$.

Chinese Standard. 2019. GB/T 50123-2019: Standard for geotechnical testing method. Beijing: Standardization Administration of China.

Gorman, C. T., Hopkins, T. C., Deen, R. C., & Drnevich, V. P. 1978. Constant-rate-of-strain and controlled-gradient consolidation testing. *Geotechnical Testing Journal*, 1(1), 3-15.

Gorman, C. T. 1981. Strain-rate selection in the constant-rate-of-strain consolidation test (No. FHWA-KY-81-7 Intrm Rpt.). Lexington, KY, USA: Kentucky Transportation Research Program.

Hamilton, J. J., & Crawford, C. B. 1960. Improved determination of preconsolidation pressure of a sensitive clay. In *Papers on Soils 1959 Meetings* (pp. 254-271). 100 Barr Harbor Drive, PO Box C700, West Conshohocken, PA 19428-2959: ASTM International.

Holm, D. 2016. Influence of strain rate in CRS tests: A laboratory study of three Swedish clays. Master of Science Thesis, Royal Institute of Technology, KTH.

Lee, K. 1981. Consolidation with constant rate of deformation. *Geotechnique*, 31(2), 215-229.

Leroueil, S., Kabbaj, M., Tavenas, F. & Bouchard, R. 1985. Stress-strain rate relation for the compressibility of sensitive natural clays. *Géotechnique*, 35(2): 159-180

Premchitt, J., Ho, K.S. & Evans, N.C. 1996. Conventional and CRS Rowe cell consolidation tests on some Hong Kong clays. (GEO Report No. 55).

Sällfors, G. 1975. Preconsolidation pressure of soft, high-plastic clays. Doctoral thesis, Chalmers University of Technology.

Smith, R. E., & Wahls, H. E. 1969. Consolidation under constant rates of strain. *Journal of the Soil Mechanics and Foundations Division*, 95(2), 519-539.

Stolle, D., & Stolle, J. 2011. Weighted residual approach to constant strain rate test. *Canadian geotechnical journal*, 48(4): 671-675.

Svensk Standard. 1991. SS 02 71 26: Geotekniska provningsmetoder - kompressionsegenskaper - Ödometerförsök - CRS-försök - Kohesionsjord [Geotechnical testing methods - compression properties - Oedometer test - CRS test - Cohesive soil]. Standardiseringskommissionen i Sverige.

Wissa, A. E., Christian, J. T., Davis, E. H., & Heiberg, S. 1971. Consolidation at constant rate of strain. *Journal of the Soil Mechanics and Foundations Division*, 97(10), 1393-1413.

Enhancing Tunnel and Cavern Designs through Seismic Tomography and Numerical Ground Information Modelling (GIM) of Rock Mass Quality Data

Francis Lee, Alexander N. Al-Nuaimi & Michiel Van Der Laarse
AtkinsRéalis Asia Limited, Hong Kong, China

Jim Whiteley, Edward Cox & Samuel Oakley
AtkinsRéalis, GE&T

Richard Hale & Lo Leung
EGS (Asia) Ltd

ABSTRACT

A robust site investigation is pivotal in the design of tunnel and caverns, and collected data often defines the characterization and parameterization of rock mass quality, interpretation of geological features, and understanding of constraints of deep weathering profiles and fault zones. Conventional geotechnical site investigations (SI) for such projects typically rely on intrusive methods, such as drillholes, which provide localized samples and data. However, the isolated nature of these drillhole locations necessitates the extrapolation of geological surfaces, often leading to challenges in accurately estimating the extent, trend, and impact of geological features on adjacent rock mass quality.

To address these challenges, this study discusses how non-intrusive cross-hole seismic tomography can be used to enhance site investigations and as an input for developing integrated numerical modelling applications. This approach allows for more spatially complete evaluation of the lateral and vertical variability of rock mass quality at proposed tunnel and cavern sites. A notable aspect of this work is the exploration of correlations between seismic wave velocities and Rock Mass Quality Q-System as outlined by Grimstad and Barton (1993) and updated by Barton (2002). Additionally, the paper introduces methods for developing confidence intervals and Ground Information Models (GIM) of digital data trends.

The paper also provides a review of the benefits and limitations of these methods, along with suggestions for enhancing the geostatistical prediction of rock mass quality.

1 INTRODUCTION

1.1 Site Investigation for Tunnel and Cavern Studies

Site investigations (SI) are pivotal to characterizing ground conditions for tunnel and cavern projects and ensure designs are well-informed with a robust understanding of subsurface conditions, their constraints, engineering behavior and performability. For tunnel and cavern studies, SI targets the testing and contextualization of rock mass properties—such as strength and geological structure—to derive rock mass quality, identify and interpret geological features, and predict weathering profiles and potential fault zones.

Intrusive techniques such as drillholes are used to inform classification systems such as the Rock Mass Quality Q-System (Grimstad & Barton, 1993). However, the isolated nature of conventional SI sampling often leads to challenges in accurately estimating and extrapolating trends in rock mass quality between drill holes. Moreover, isolated samples may not capture the full extent of geological features, leading to ground risk associated with limited confidence and gaps between data positions.

To reduce uncertainty, additional drillholes are often constructed to close geospatial gaps in data density. Alternatively, non-intrusive geophysical surveying techniques can be prescribed to supplement and optimize drillhole sampling (Whiteley & Cox, 2023) and close gaps between data points, producing continuous profiles. Cross-hole seismic survey is a technique that is used to measure the travel time of seismic waves between drillholes. These waves can be compressional wave (P-wave) or shear wave (S-wave), depending on the type of seismic source. The travel times and wave amplitudes are measured and variations interpreted to derive lithological boundaries, rock density and permeability.

This paper will examine the cross-hole seismic data collected between drillholes, and how it informs the design of two tunnel and cavern studies in Hong Kong, referred to as Cavern A and B. It also discusses the methodology to assess rock mass quality between project-specific drillholes. The results were also used to construct integrated numerically driven Ground Information Models (GIM), that represent data driven 3D representations of the distribution of rock mass quality across the cavern sites.

2 BACKGROUNDS OF THE STUDY

2.1 Site Description and Site Investigation Planning including Cross-hole Seismic Surveys

Cavern A and Cavern B encompass cavern sites spanning more than 20m. A site-specific Ground Information Model (GIM) was developed at the initial stage of the projects. Both locations are situated beneath densely vegetated hillsides with slope angles ranging from 25° to 45°. Geology at both sites is characterized by fine-grained and fine-to-medium-grained granite. Structural geological features such as photolineaments, identified as inferred geological features (GFs), are present at both sites and designated as GFA for Cavern A and GFB for Cavern B.

During SI planning, the geological features represented potential weak zones associated with preferential weathering of in-situ rock. Specifically, weak zones correspond to areas exhibiting continuous occurrences of ‘Grade IV/V Granite’ (GEO, 2017) extending below expected bedrock levels. To validate inferred trends, intrusive drillholes were strategically positioned to intercept and sample ground conditions along these inferred alignments. Rock samples recovered as ‘Grade IV/V Granite’ or where ‘No Recovery’ is recorded represent weak zones. The number of inferred geological features for Cavern A and Cavern B is two and four respectively.

The identification of potential reductions in rock mass quality linked to weak zones and faults is a fundamental aspect of both studies. Drillholes offer isolated windows of observation, however, their limited coverage and scale may lead to the omission of local weak zones and geological features. To address this, both studies conducted cross-hole seismic surveys between vertical drillholes to augment data coverage and elucidate observable trends in weak zones and seismic data related to faults, if present.

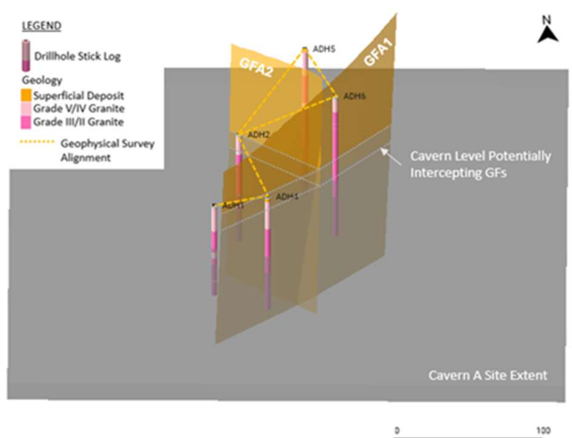

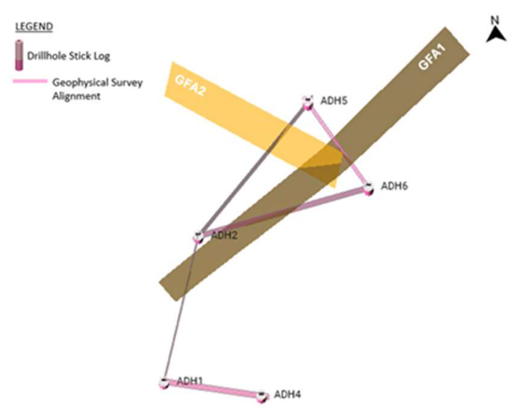

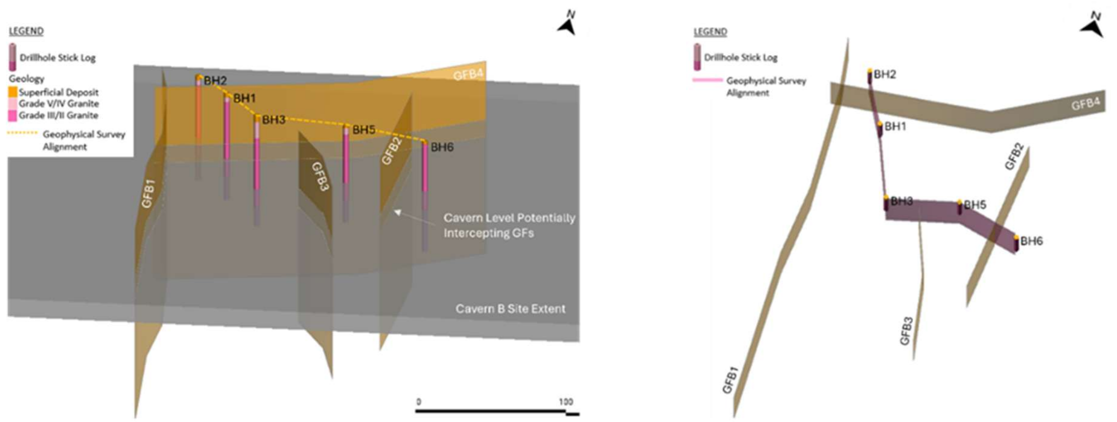

Figure 1: Configuration of Cross-hole seismic survey in relation to inferred geological features and cavern level. Cavern A (upper) and Cavern B (lower).

To ensure adequate sonification across the cavern level, drillholes were drilled to depths below the invert level. The alignment and geometry between the source and receiver drillholes were planned to intercept the potential alignments of GFA and GFB. The spacing between drillholes for the cross-hole seismic surveys was maintained at around 60m. In Cavern B, a triangular configuration was established to create a closed-loop velocity model, which facilitates visualization and interpolation in 3-dimensions (Figure 1).

3 FIELD SETUP

3.1 Site Set Up and Seismic Survey Procedures

To map geological structures between pairs of holes, very tight measurement tolerances are required, including expected accuracy of the seismic traveltime within ±0.25 ms. This ruled out the use of air guns or other low-frequency seismic sound sources. High-frequency sources, such as piezo-electric transducers working above ~10 kHz, would attenuate rapidly with distance and would not provide adequate signal-to-noise ratio over the distance between pairs of holes. A mid-frequency sparker sound source was selected to generate the most power between 1 kHz and 2 kHz.

Helicopter lifts were used to mobilize equipment to the drillhole location. For each pair of holes, the set up included a multi-channel hydrophone string (with 1 m element spacing) lowered down a receiver drillhole and a sparker sound source lowered down the other. Figure 2 (left) shows the seismograph display used on site to check the quality of the seismic records. The sparker sound source was raised to the next level and another set of seismic traveltimes was recorded. This was iterated all the way up to rockhead, until a dense network of seismic rays covered the region between the pair of holes. Figure 2 (right) is a composite seismic record, with sound source at +81 m PD (marked by a red "X"). The hydrophone receivers are from the base of opposite drillhole (+52 m PD) up to just above rockhead (+137 m PD). The seismic traveltime is taken as the onset of the seismic arrival, indicated by a rise above background noise levels. Automatic traveltime picks were made, supplemented by the judgement of the geophysicist on site. The automated process for identifying the first break-peaking was informed by a theoretical range of tolerance. Within each data trace, energy or amplitude changes were detected by applying a gradient threshold. Once the setup was ready, following a strong shot instant pulse record and the seismic traveltimes can be observed clearly.

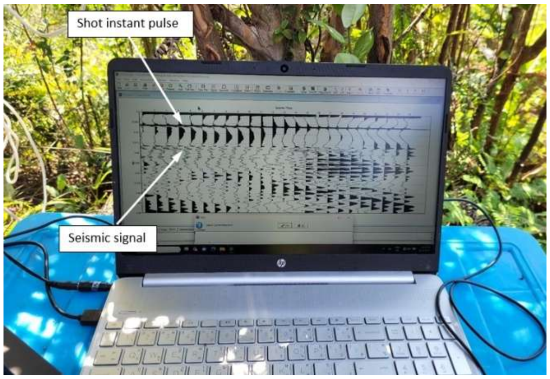

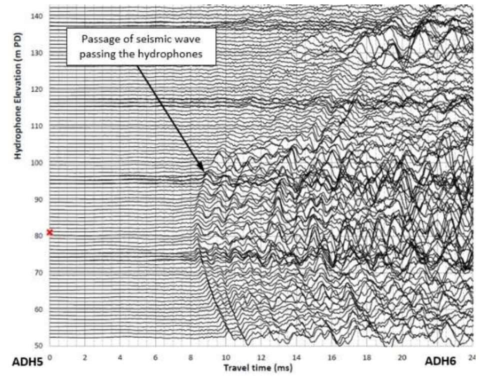

Figure 2: Type of display used by the geophysicist to check the quality of seismic records (left). Example of seismic record, seismic pair from drillholes ADH5 to ADH6 (middle).

4 DATA PROCESSING

4.1 Seismic Processing and Measuring Traveltimes

By design, around 5% of shot-receiver pairs were duplicated to accomplish statistically independent duplicate measurement. The measurements will seldom be identical, but the distribution of the difference in measurements is a robust estimate of the measurement accuracy. During the works of both Cavern A and Cavern B, there were 1447 repeat measurements, in which 96% of the repeat measurements (roughly two standard deviations) were within ±0.10 ms. This was comfortably inside the planned tolerance of ±0.25 ms, validating the survey design.

4.2 Tomographic Inversion

Variations in traveltime can be divided into two components: geometrical effects (the greater the separation between the source and receiver, the greater the traveltime) and the variation of seismic velocities. The algorithm separating these factors to produce an image of seismic velocities is computed in EGS-proprietary in-house Tomographic Inversion software.

The section between source and receiver holes was divided into 5m-by-5m cells. The resulting 5m grid resolution was selected considering the geometry, the distance between the holes and the number of traveltimes measured. A limitation associated with the 5m resolution of seismic survey is that smaller geological features will be 'averaged' over the resolution scale. In future studies, forward-modelling can help to inform the resolution of a given array design, and therefore the size of minimum detectable features. Such forward models can either be from of the assumed ground conditions (informed by pre-existing geological data and desk studies) (Rücker et al., 2017) or using synthetic examples such as checkerboard tests combined with considerations of ray-path coverage (Rawlinson and Spakman, 2016). The outputs of these studies can be used to optimize the cross-hole array design.

For each seismic source, wave fronts were projected through the model of the rock to the receiver positions. A finite difference algorithm was used according to Rawlinson and Sambridge (2005) with bending according to Snell's law of refraction.

For the initial constant-velocity model, the average misfit between measured and calculated traveltimes was ±0.8 ms. This average misfit was considerably greater than the measurement accuracy, ±0.1 ms, indicated by the results of repeated measurements discussed in Section 4.1.

The modelling process adjusts the seismic velocities of each grid cell, with the objective of making the average misfit less than the measurement accuracy. A grid cell was selected at random and its velocity incremented up or down – a trial value. All traveltimes were recalculated in each iteration. If the overall traveltimes were closer to the measured values (reduced discrepancy), the trial value was accepted. Even if the traveltimes were worse using the trial value (increased discrepancy), there was still a finite chance that the change would be accepted. During the initial "fluidisation" phase, all trials were accepted, which increased the misfit to around ±1.0 ms. Over hundreds of thousands of iterations, the chance of accepting a worse value was gradually lowered, a process known as the Monte Carlo annealing schedule. As the number of trials goes on, the selection of seismic velocities becomes less random and converges on the velocities that have given the best calculated traveltimes.

For all iterations for these pairs of holes, after considering 200,000 trial seismic velocities, the final average discrepancy was close to or less than the measurement accuracy of ±0.10 ms. Each iteration finished with a similar, but not identical, final model of seismic velocities. The average of these iterations provides the best unbiased estimate of seismic velocities. The variation between iterations is a fundamental estimate of the accuracy of the results. Examples of inversed velocity models are presented in Figure 3. These models can be visualized using software packages like Oasis Montaj, or in voxel model.

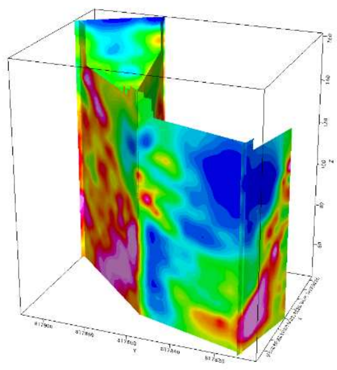

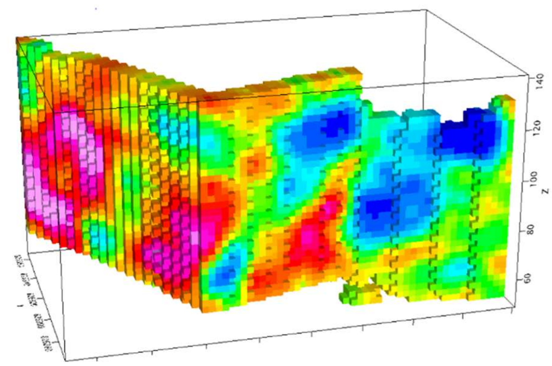

Figure 3: 3D seismic velocity model imported into Oasis Montaj for Cavern A (left) and seismic velocity data voxel model for Cavern B (right).

4.3 Developing Confidence Limits for Results

Presenting the results is of little use to the Engineer without also presenting a quantified assessment of the accuracy and reliability. The following sections describe how the confidence limits were represented and visualized using statistical measurement (standard deviation) and density coverage (raypath coverage model).

4.3.1 Standard Deviation

The uncertainty of seismic velocities is calculated using the statistical measure of standard deviation. The accuracy was calculated by iteration of the tomographic inversion described in Section 4.2, each time using a different random number sequence in the Monte Carlo process. Each iteration has a different random combination of trials, so each will converge on a slightly different result. Although the resulting distribution of seismic velocities is slightly different from one pass to another, all passes gave a similar accuracy in representing the measured seismic traveltimes. The standard deviation of the distribution of the differences between one pass and another equals the standard deviation of the seismic velocities. Figure 4 shows histograms of standard deviations calculated in all cells in the final models for Cavern A (left) and Cavern B (right) projects respectively. In Cavern A, with relatively heterogeneous conditions, around 90% of values were within ±0.6 m/ms. In Cavern B, with more uniform geology, around 90% of values were within ±0.3 m/ms.

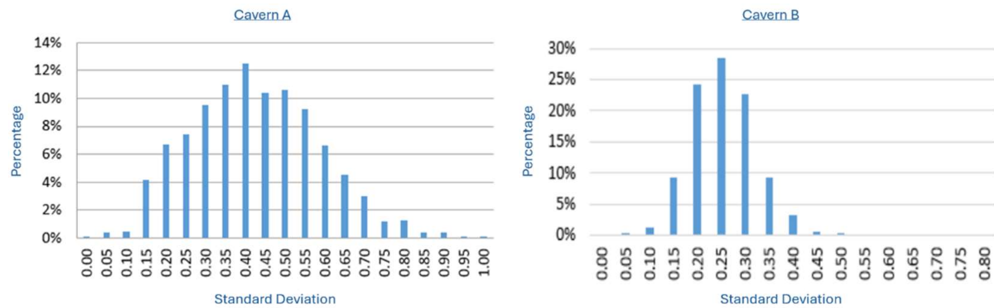

Figure 4: Histograms of standard deviations in seismic velocity. Cavern A (left) and B (right).

4.3.2 Raypath Coverage

While standard deviation describes how well the inversion model fits the data, it does not illustrate the extent of seismic data coverage. At locations where a spatial inversion window model has few or no measured data points available, the inversion process will still generate seismic velocity values and may still output a low standard deviation for the generated seismic velocity values. Therefore, a second phase of processing was undertaken to ascertain a better spatial indication of potential seismic velocity data.

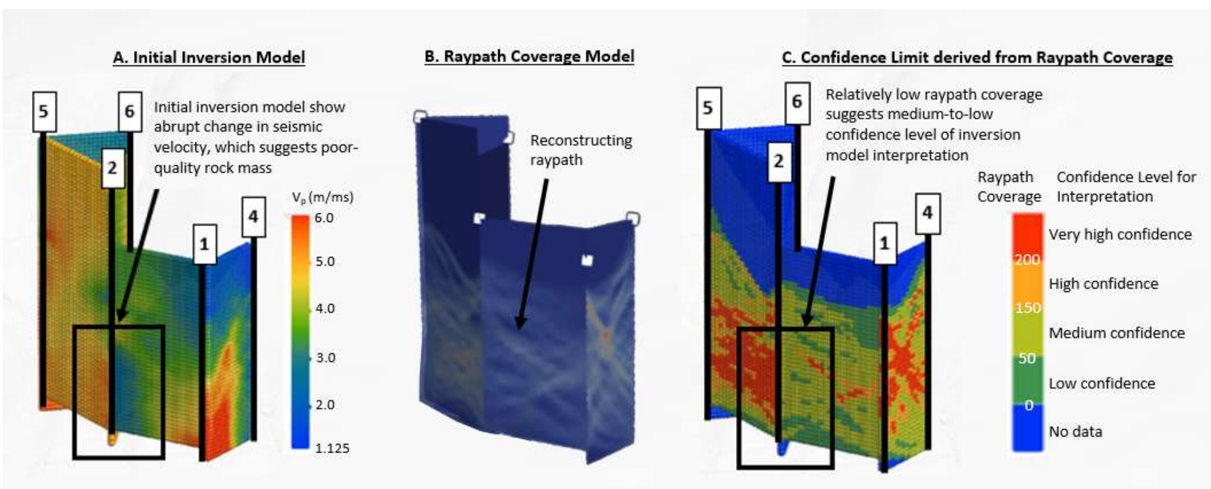

Figure 5: Process of developing confidence limit of seismic inversion model through analysing its raypath coverage.

Additional inversions were run using pyGIMLi (Rücker et al., 2017), which act as independent verification of the Monte Carlo inversion results described in Section 4.2. The ray-path coverage from the pyGIMLi inversion was used to apply confidence limits to the results of the tomographic inversion. The additional inversions also produced models showing the seismic raypath coverage (Figure 5). *Coverage* is the sum of ray lengths having crossed each cell of each model. In Cavern A, the maximum value for coverage was 506 with a lower quartile of 76.64 and an upper quartile of 217.96. Confidence intervals were suggested based on this statistical analysis. Comparison of the initial tomographic inversion described in Section 4.2 and the additional inversions using pyGIMLi showed good agreement in terms of seismic velocity distribution.

The spatial distribution of coverage can be used to qualitatively assess co-located seismic velocity data, areas with low data coverage having a lower confidence of result certainty. For example, an area showing an unusually abrupt change in seismic velocity (Figure 5a) was observed in borehole ADH2 of Cavern A, which possessed relatively lower raypath coverage (Figure 5b), suggesting the seismic velocity inversion should be treated with low-to-medium confidence at this area (Figure 5c). During data integration, data recorded in low confidence zones were generally excluded from ground modelling.

5 INFORMING ROCK MASS QUALITY BY SEISMIC TOMOGRAPHY RESULTS

5.1 Quantitative Seismic Data for Numerical Modelling

Apart from Ground Information Model (GIM) acknowledging the site-specific ground condition, numerically informed, quantitative GIM were also developed to provide data-driven 3D representations of the distribution of rock mass quality Q-value using Leapfrog Works Version 2023.2 (Seequent, 2023). The spheroidal variogram model (interpolant function) was used to model predicted lateral and vertical variability of Q-value distribution at Cavern A and B. The spherical interpolation function has a fixed range beyond which the value transitions into a constant sill. This provided a means for rationalizing the influence of variable data density, in this case, differences in influence of drillholes and geophysical data. Project-specific seismic data was incorporated in GIM as 2D sections and 3D point data source for numerical modelling.

5.2 Rock Mass Quality

Assessment of Q-value along existing and project-specific rock samples was carried out adopting the Norwegian Geotechnical Institute's (NGI) Rock Mass Quality Q-system (Grimstad & Barton, 1993). This assessment considered measurements such as Rock Quality Designation (RQD), condition and number of joints and stress reduction factors associated with rock overburden.

Considering the case study at Cavern A, the sampled bedrock from drillholes is predominantly moderately to slightly weathered granite, with most of the mapped Q-value falling within a range of 0.6 to 15. At locations where weak zones (highly to completely decomposed rock mass) were recorded, mapped Q-value drops to 0.6 (very poor) and occasionally below 0.1 (extremely poor).

Interpretation of the geophysical survey data referred to Reynolds (1997), which suggests that moderately to slightly weathered granite typically corresponds to a seismic velocity range of 4.6m/ms to 6.2m/ms. Project-specific seismic measurements at Cavern A range between 2.5m/ms and 6.5m/ms. This variability indicates patterns/ variation in the occurrence of bedrock weathering grades across the site. An empirical relationship developed by Barton (2002) was employed to correlate seismic velocity with rock mass quality Q-values (Figure 6).

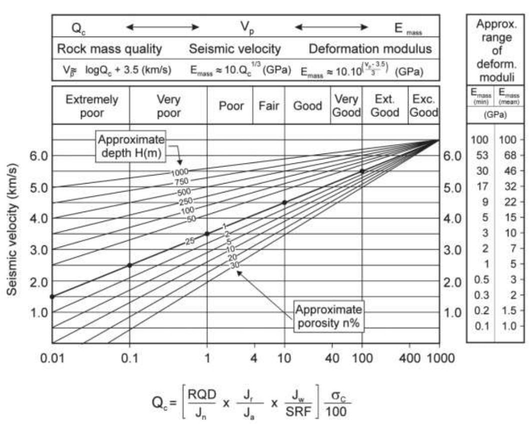

Figure 6: Velocity-depth correlation developed from case records (from Barton, 2002).

This empirical relationship considers the effect of depth, i.e. in-situ stress on rock mass with increasing depth. The presence of overburden and associated stress tends to increase V_p (P-wave velocity) for any given Q-value. Q_c is adopted as the improved correlation to Q-value where θ_c is the uniaxial compressive strength of intact rock mass (MPa) shown in eq.1. It should be noted that laboratory testing such as Uniaxial Compressive Strength (UCS) tests have been performed as part of the site investigation, indicating that a UCS value of θ_c = 70 to 195 MPa is representative of the site-specific rock mass strength for grade III to II granite.

$$Q_c = Q \times \frac{\theta_c}{100} \qquad \text{(eq.1)}$$

Raypath models illustrating data coverage across Cavern A drillholes were reconstructed based on the methodology discussed in Section 4.3.2 (Figure 7a). The raypath coverage depicted in Figure 7b provided essential information regarding seismic data coverage, which was considered as part of the confidence limit assessment of the V_p and rock mass quality Q data models. Areas with a higher percentage of data coverage were interpreted with greater confidence; in this case, a confidence limit was established at not less than 150 of raypath coverage (Figure 7c). The Vp values could then be extracted from regions of high confidence for further interpretation and calculation of rock mass quality Q-values (Figure 7d).

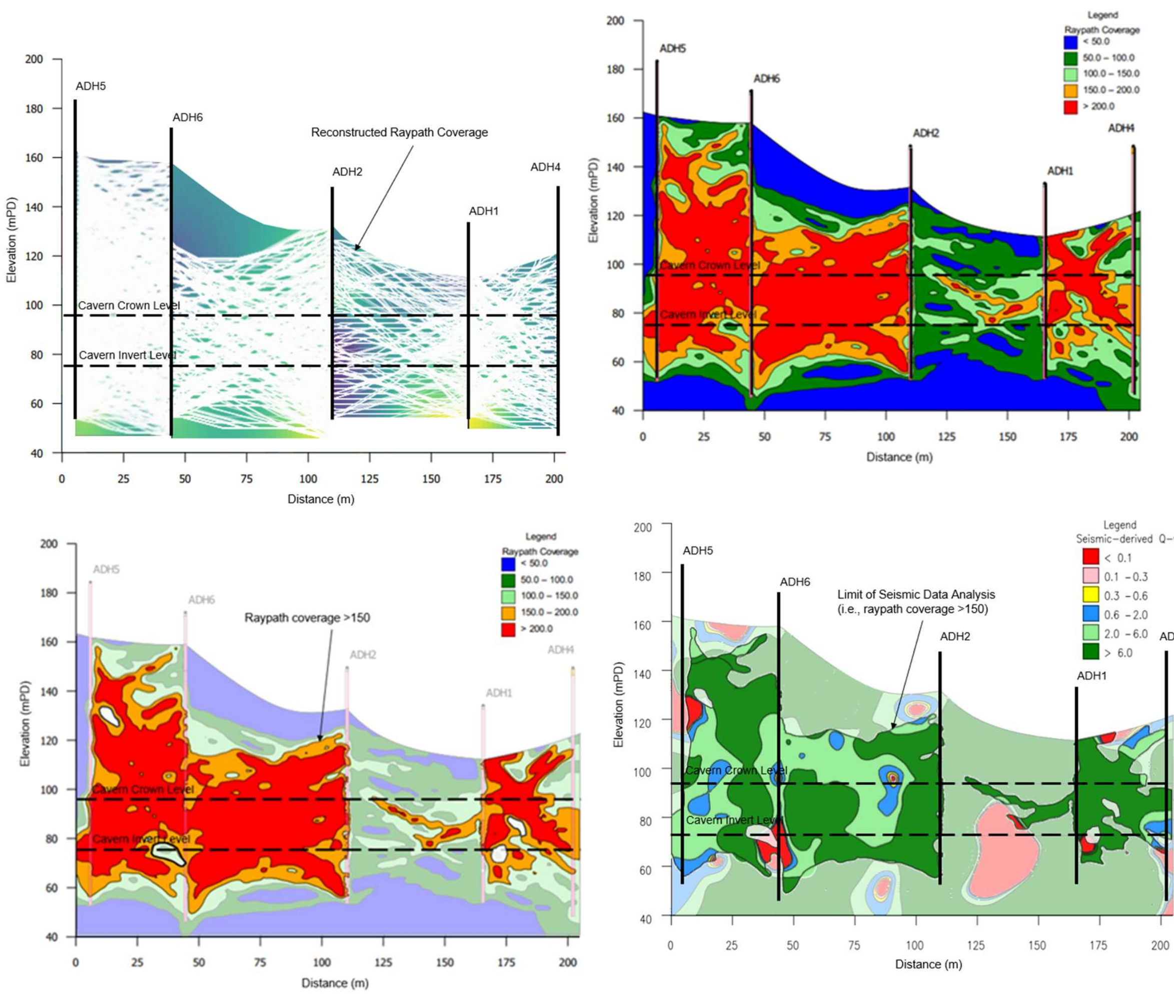

Figure 7: (a) Raypath coverage; (b) Raypath percentage coverage; (c) Raypath coverage higher than 150 is delineated and (d) Limit of seismic data analysis is delineated.

5.3 Geological Features

A key aspect of the studies conducted in Caverns A and B is the verification of the existence, extent and orientation of geological features, as discussed in Section 2. To address the possibility of drillhole locations that could miss these features, cross-hole surveys were utilized to identify seismic velocity patterns indicative of weak zones.

At the Cavern A site, a subvertical geological feature identified as GFA1 was recognized during preliminary studies. The alignment of seismic surveys ADH5-ADH6, ADH6-ADH2 and ADH1-ADH2 intersected GFA1 at three distinct locations (as shown in Figure 1) and the seismic-derived Q-value model are unfolded in Figure 8.

Along the profiles ADH5-ADH6 and ADH6-ADH2 (Figure 8), variations in seismic velocity at cavern level were evident as subvertical pockets of reduced Q-value (0.6-2.0, blue) extending from +100 to +80mPD within a predominantly higher Q-value context of >2.0 (shown in light green to dark green). These subvertical zones signified relatively sharp and confined changes in rock mass quality, correlating with the conceptual alignment of GFA1. Continuous profiling provided information on the apparent depth, immediate thickness (notably confined, as evidenced by sharp contrasts with neighboring rock masses) and the impact of GFA1 on the surrounding rock mass.

Conversely, along the ADH2-ADH1 profile (Figure 8), limited raypath coverage inhibited visualization of the rock mass quality corresponding to GFA1 at this location. Evaluation of GFA1 here necessitated reliance on supplementary site investigation data. This included considering the character of the seismic signals (such as signal-to-noise ratio, attenuation of high seismic frequencies) recorded between holes ADH2-ADH1.

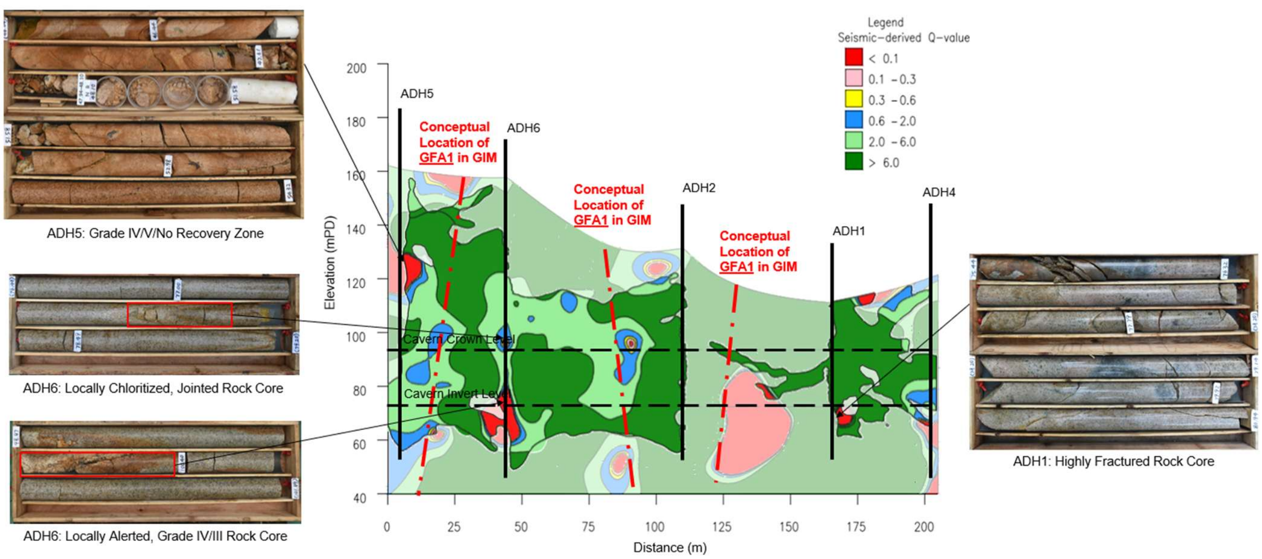

Figure 8: Comparison between seismic survey data, conceptual location of GFA1 and rock core quality along boreholes.
Low seismic-derived Q-values generally consistent with rock core recovery of i) grade IV/V/ No recovery zone; ii) locally chloritized/ altered rock and iii) highly fractured rock.

At the Cavern B site, up to four geological features were recognized during preliminary studies. The alignment of seismic surveys BH2-BH1, BH1-BH3, BH3-BH5 and BH5-BH6 was positioned to intersect the geological features GFB2, GFB3 and GFB4 (as shown in Figure 1). The resulting seismic velocities are profiled in Figure 9.

Along the profiles of BH3-BH5 and BH5-BH6, two significant trends of low velocity (purple to blue) were evident, dipping at an angle of 50° and extending from +125 to +70mPD through the cavern level (Figure 9). The velocity data trends indicated a persistent change of rock mass quality in contrast with the medium to high velocities (green to red) of the neighboring rock mass, coinciding with the conceptual alignments of GFB2 and GFB3. The seismic profiles verified the apparent extent and orientation of GFB2 and GFB3 and provided information on the apparent depth and thickness of the geological features, as well as zone of influence with regard to cavern level.

The seismic result along the BH2-BH1 profile did not indicate trends of low velocity along the conceptual alignment of GFB4. Instead, mostly very high velocities (red) indicating good rock mass quality was recorded at this location. This apparently refuted the existence of GFB4, suggesting better than expected ground conditions.

Additionally, a minor subvertical trend of low velocity was evident along the profile of BH1-BH3, extending from +110 to +70mPD, suggesting the occurrence of a new feature GF? (Figure 9). The identification of GF? allowed the design to accommodate the presence of lower rock mass quality, thereby reducing ground risk and potentially avoiding additional costs at a later stage of the project.

The seismic data visualized trends in 2D tomography cross section and verified the occurrence of geological features, offering a different perspective to conventional SI. The Cavern A study highlights how continuous profiling is useful in validating initial stage results; while Cavern B study highlights how continuous profiling is useful in identifying previously unknown risks.

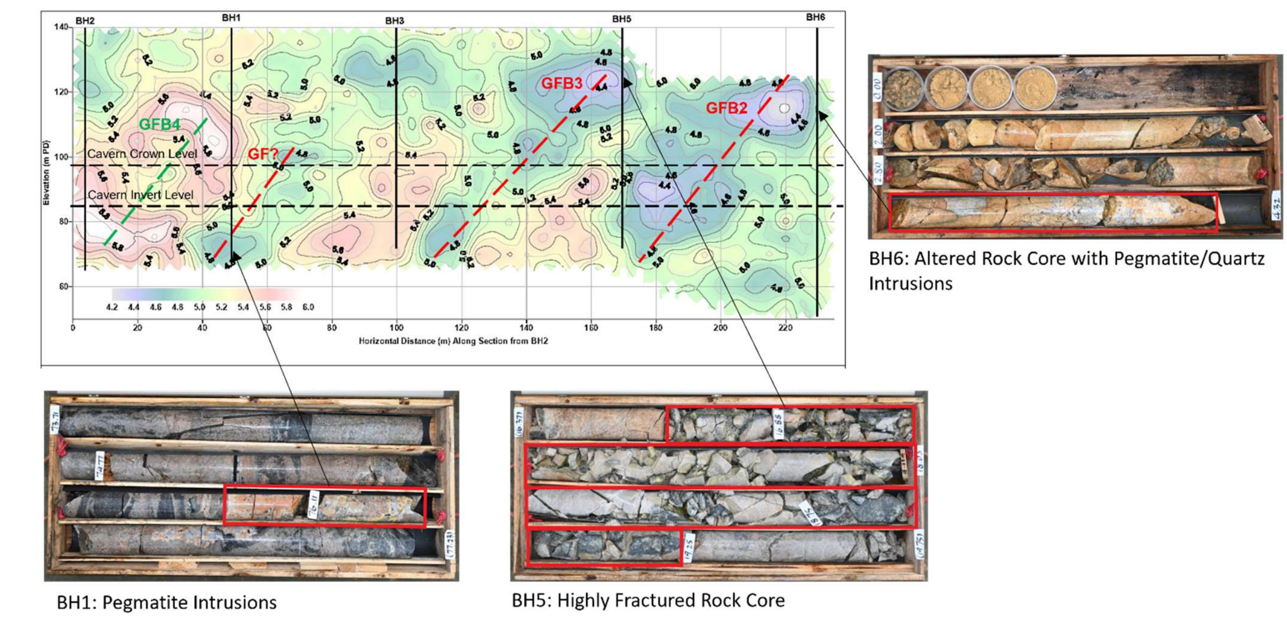

Figure 9: Seismic velocity profiled across BH2-BH1, BH1-BH3, BH3-BH5, and BH5-BH6. Red lines indicate the apparent extent and orientation of GFB2 and GFB3 based on velocity contrast, and newly identified geological feature GF?.

5.4 Informing Geotechnical Designs and Reduce Risk

Processed seismic data provides continuous 2D visualization of subsurface rock mass quality with broad coverage efficiently. This data not only provides insights into the thickness, trend, depth, and consistency of potential geological features but also facilitates informed design decisions regarding 1) cavern/tunnel layout and 2) rock mass support systems.

5.4.1 Informing Cavern/Tunnel Layout

Geological features (GFs) exhibiting varying states of weathering often present complex deformation patterns and variations in rock properties, raising concerns about stability and local stress concentration. Furthermore, these GFs may serve as conduits for groundwater flow, potentially resulting in localized high groundwater inflows during excavation activities. By understanding the orientation, depth and consistency of GFs, the layout and alignment of Cavern A and Cavern B have been optimized. This optimization includes strategies to either avoid intersections with GFs; align parallel to pre-existing weakness planes to exploit these zones of lower strength; or orient perpendicular to minimize interactions with GFs. Additionally, the location and extent of pre-excavation grouting (PEG) were planned to mitigate groundwater inflow into the underground excavations.

5.4.2 Rock Mass Quality

Rock mass quality is one of the major inputs for cavern/tunnel rock mass support system e.g. rock bolt specifications. In contrast to the isolated results obtained from conventional drillhole sampling, seismic data offers continuous measurements that reveal trends in rock mass quality, effectively filling the data gaps between drillhole points. As discussed in Section 5.1, a numerical GIM was constructed using integrated Q-values derived from seismic correlation measurements, as illustrated in Figure 10. The Q-value intervals from rock core samples varied from small (<0.5m in length) to large (>3m in length), together with the seismic derived Q-value (at a 5m grid size) were integrated in the GIM. This integration provides a more comprehensive assessment of both lateral and vertical variability in rock mass quality, thereby informing the design of rock support systems.

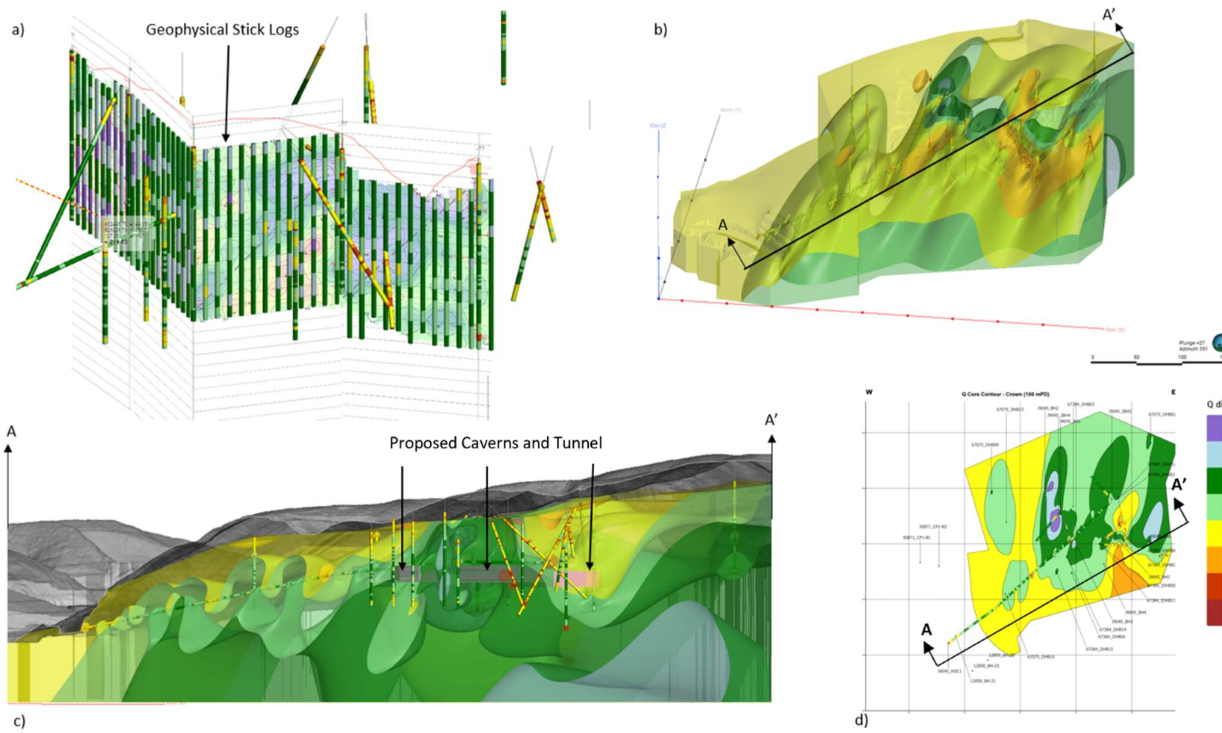

Figure 10: 3D Visualizations of a) Seismic Velocity Derived Q-Value Stick Logs, b) Predictive Q-Value Contour Visualization, c) Profile of Q-Contour along HDC1 and d) Plan View of Q-value.

6 CONCLUSION AND WAY FORWARD

6.1 Conclusion

The studies conducted at Cavern A and B demonstrate how geophysical data can be collected, processed, and utilized to evaluate the characterization and distribution of rock mass quality for tunnel and cavern sites. Although natural terrain hillsides in Hong Kong presents considerable challenges and restrictions in collecting Site Investigation (SI) data, the integration of geophysical surveys significantly enhances the value of these investigations. The resulting continuous, non-intrusive data coverage creates opportunities for apparent ground truth observations, which can be leveraged to inform interpretations of geological structures and weathering patterns, thereby assessing the ground risk associated with geotechnical designs.

This study also emphasizes the importance of implementing quality assurance checks to evaluate the consistency and accuracy of seismic measurements, enabling the isolation of high-confidence data that can be utilized in ground modeling applications. It is essential to quantify the resolution and uncertainties related to the measurements, analyses, and calculated seismic velocities, as these factors must be considered when interpreting the results.

Data-driven ground models were used to assess confidence of collected data, enhance interpretations, and mitigate ground risk along with engineering constraints. The approaches applied in this study demonstrate how geotechnical designs for tunnel and cavern studies can be supported, integrated, and enhanced by incorporating geophysical-informed site investigation efforts.

6.2 Future Opportunities

Conventional methods of interpreting Q-value in tunnel and cavern studies rely heavily on drillhole records, including their spatial positioning, density, and constructability. The ground risk associated with the alignment of infrastructure within a site changes as new geotechnical data becomes available. Increasing the density and spatial distribution of factual data collected during SI using non-intrusive techniques can reduce uncertainty and provide opportunities for time-cost savings associated with design.

The findings in this study show that geophysical surveying techniques combined with numerical modeling applications can expand data coverage and enhance the understanding of subsurface conditions, thereby informing geotechnical designs. Future studies should explore integrating enhanced stochastic/geostatistical methods to facilitate informed decision-making during the planning and construction phases.

REFERENCES

Barton, N. (2002). Some New Q-Value Correlations to Assist in Site Characterisation and Tunnel Design. International Journal of Rock Mechanics and Mining Sciences, 39 185-216.

Grimstad, E. & Barton, N. (1993). Updating of the Q-system for NMT. Proceedings of the International Symposium on Sprayed Concrete – Modern Use of Wet Mix Sprayed Concrete for Underground Support. Norwegian Concrete Association, Fagernes, Oslo.

GEO (2017). Guide to Rock and Soil Descriptions (Geoguide 3) (2017 version). Geotechnical Engineering Office, Civil Engineering and Development Department, HKSAR Government.

Rawlinson, N., & Sambridge, M. (2005). The Fast Marching Method: An Effective Tool for Tomographic Imaging and Tracking Multiple Phases in Complex Layered Media. Exploration Geophysics, 36, 341 - 350.

Rawlinson, N., & Spakman, W. (2016). On the use of sensitivity tests in seismic tomography. Geophysical Journal International, 205(2), 1221-1243.

Rücker, C., Günther, T., & Wagner, F.M. (2017). pyGIMLi: An open-source library for modelling and inversion in geophysics. Comput. Geosci., 109, 106-123.

Whiteley, J. & Cox, E. (2023). Enhancing Site Investigation for Karst Geohazards Using High-Resolution, Quasi-3D Electrical Resistivity Tomography Surveying. NSG2023 29th European Meeting of Environmental and Engineering Geophysics, Vol. 2023, No. 1, pp. 1-5. European Association of Geoscientists & Engineers.

Small-scale Physical Modelling of Geotextile-Reinforced Sand Fill Over Hong Kong Marine Clay Improved by Deep Cement Mixed Soil Columns

P.C. Wu, Q. W. Xie, W.J. Zhao & J.H. Yin
The Hong Kong Polytechnic University, Hong Kong

ABSTRACT

Deep cement mixing (DCM) technology was introduced in Hong Kong for the first time in the reclamation project of the Third Runway System of the Hong Kong International Airport and has been used in many other projects afterwards to improve the soft marine clay. Load transfer platforms (LTP) with or without geotextile reinforcement are often designed to facilitate the load transfer from the reclamation fills to the seabed. In this study, a small-scale physical model test was conducted on a geotextile-reinforced sand fill over Hong Kong Marine Clay (HKMC) improved by DCM columns, aiming to investigate the load transfer mechanism among DCM, HKMD, and geotextile reinforcement. The load transfer mechanism was examined by looking into the vertical stresses measured by earth pressure cells at different locations. The mobilised tensile strain in the geotextile reinforcement was measured using Fibre Bragg Grating sensors. Efficacy was calculated to assess the performances of DCM on load transfer. Furthermore, commonly used design guidelines were reviewed and applied to determine the load taken by DCM and the maximum tensile strain of geotextile reinforcement. It was found that the results offered by Dutch and FHWA methods agreed well with the experimental data.

1 INTRODUCTION

The third runway reclamation project of the Hong Kong International Airport was constructed over a seabed of soft marine clay improved by deep cement mixing (DCM) method. Since then, DCM works have been applied in many other projects involving soft marine clay in Hong Kong. Load transfer platforms (LTP) with or without geosynthetic reinforcement are often designed to facilitate the load transfer from the reclamation fills to the seabed (Lee, 2016). The consideration of the load transfer mechanism and the design of geosynthetic reinforcements in LTP are similar to geosynthetic-reinforced column-supported (GRCS) embankments. The load transfer is normally related to soil arching effect which develops with the settlement of subsoils or the deflection of geosynthetic reinforcements (Iglesia et al., 2014; King et al., 2017; Zhang et al., 2022; Wu et al., 2020 and 2024). Various theories and models for soil arching in column-supported embankments were proposed based on empirical methods or analytical approaches, among which the semi-spherical arches model proposed by Hewlett (1988), multi-shell arches model proposed by Zaesek (2001), and concentric arches (CA) model proposed by van Eekelen et al. (2013) have been adopted in British, German, and Dutch design guidelines. Adopting different design guidelines leads to different considerations of arching effect and predictions of tensile strain in the reinforcement, hence affecting the design and selection of geosynthetic reinforcement.

In this study, a small-scale physical model test was conducted on a geotextile-reinforced sand fill over Hong Kong Marine Clay (HKMC) improved by DCM columns, aiming to investigate the load transfer mechanism among DCM, HKMC, and geotextile reinforcement. The load transfer mechanism was examined by looking into the vertical stresses measured by earth pressure cells at different locations. The mobilised tensile strain in the geotextile reinforcement was measured using Fibre Bragg Grating sensors. Efficacy was calculated to assess the performances of DCM on load transfer. The experimental results were then compared with the predictions according to current design guidelines, such as British standard BS8006, German design recommendation, Dutch CUR design method, and American FHWA design manuals.

2 EXPERIMENT SETUP

2.1 Experiment setup, materials and instrumentation

A small-scale physical model test was conducted in a steel tank with dimensions of 1000 mm (length) × 600 mm (width) × 800 mm (depth), as shown in Figure. 1. Six DCM columns were installed in the subsoil of Hong Kong Marine Clay (HKMC). A geotextile-reinforced sand layer was placed over the DCM-improved HKMC.

Reconstituted HKMC used in this physical model was originally excavated from coastal area of Lantau Island in Hong Kong. HKMC is of high compressibility and notable plasticity. The basics properties of HKMC and sand were listed in Table 1. DCM columns (100 mm in diameter, 400 mm in length) were prepared by mixing ordinary Portland cement with HKMC with the water content of 100%. Cement content (dry mass of cement to dry mass of HKMC) was 20%. Unconfined compressive strength q_u and secant Young's modulus E_{50} were around 0.6 MPa and 70 MPa, respectively, after 28-day curing. A woven geotextile with secant tensile modulus J of 680 kN/m in the longitudinal direction and 150 kN/m in the transversal direction were used as a reinforcement.

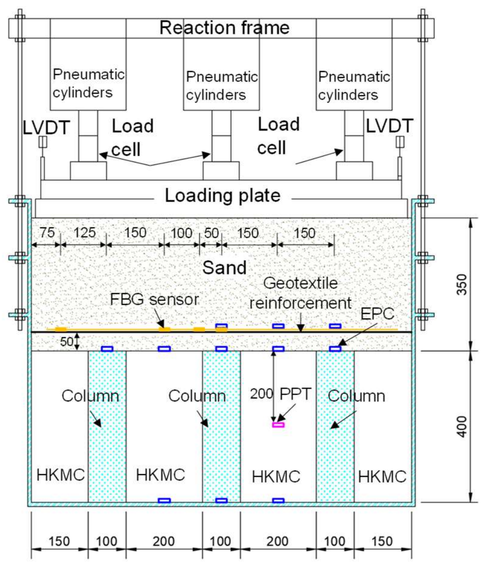

Figure 1: Physical model setup

Table 1: Basic properties of HKMC and sand

Soil	Property	Value
HKMC	G_s	2.65
	LL (%)	43.2
	PL (%)	22.6
	PI (%)	20.6
	w_0 (%)	100
	CR	0.24
	RR	0.03
Sand	G_s	2.56
	$\rho_{d,max}$ (Mg/m^3)	1.742
	$\rho_{d,min}$ (Mg/m^3)	1.536
	w_{opt} (%)	16.5
	φ'	34.6

Earth pressure cells (EPCs) were installed at different locations to measure the vertical stresses. One pore pressure transducer (PPT) was placed at the bottom and one was placed at the middle level of the subsoils to monitor the changes in excess pore pressure. Linear variable differential transformers (LVDTs) were used to measure the surface settlement. Surcharge load was applied using a self-designed loading system consisting of six pneumatic cylinders. The actual loading output of the loading system was monitored by load cells. Fibre

Bragg grating (FBG) sensors were adopted to measure the tensile strength of the geotextile reinforcement. Each FBG sensor covered a sensing zone with a length of 100 mm, with the measured strain from the sensor representing the average strain within the sensing zone.

2.2 Testing program

A multi-stage loading test was performed using the self-designed loading system following a loading sequence of 10, 20, and 40 kPa. Surface settlements were measured during the loading tests. Each loading was conducted until the excess pore pressure was nearly fully dissipated. Figure 2 shows the measured surface settlement and excess pore pressures during the loading test.

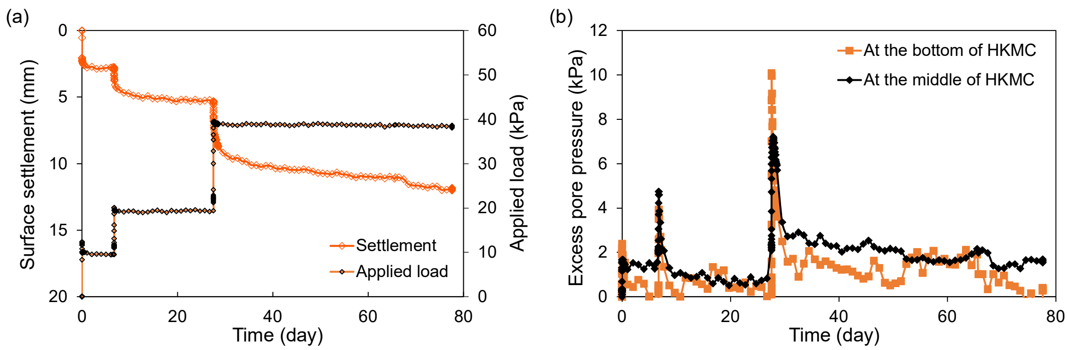

Figure 2: (a) Measured surface settlement and applied load and (b) measured excess pore pressures

3 EXPERIMENT RESULTS

3.1 Vertical stress and load distribution

To better address the mechanism of load transfer, the model test is divided into three zones, namely column, strip, and square zones, as shown in Figure 3(a). The column zone covers the DCM columns and the portion of the sand layer above the columns, the strip zone is the area between two adjacent column zones, and the square zone is the area enclosed by four strip zones. Strip and square zones are similar to those adopted by van Eekelen et al. (2015). It should be noted that the difference between vertical stresses above and beneath the geotextile in the column zone may be significant, depending on the development of the membrane effect of the geotextile. The circular cross section of columns can be converted into a square with an equivalent size of a. The area influenced by each column is illustrated using a column-soil unit, as shown in Figure 3(b).

The load transfer can be divided into load parts A, B, and C, which are the portions of the load acting on columns, transferred to geotextile, and supported by the HKMC subsoil, respectively, as illustrated in Figure 3(c). In this study, the vertical stresses above and beneath the geotextile in the column zone were used to calculate load parts A and $A + B$, respectively, whereas those beneath the geotextile in the strip and square zones were used to determine load part C. The equations for determining load parts A, B, and C are provided as follows.

$$A = \sigma_c^a A_c \quad (1)$$

$$B = \left(\sigma_c^b - \sigma_c^a\right) A_c \quad (2)$$

$$C = \sigma_{strip}^b A_{strip} + \sigma_{square}^b A_{squre} \quad (3)$$

where σ_c^a and σ_c^b are the vertical stresses above and beneath the geotextile in the column zone, respectively, σ_{strip}^b represents the vertical stress beneath the geotextile in the strip zone, σ_{square}^b is the vertical stress beneath the geotextile in the square zones, and A_c, A_{strip}, and A_{square} are the areas of the column, strip , and square zones within each column-soil unit, respectively. σ_{strip}^a and σ_{square}^a are the vertical stresses above the geotextile in the strip and square zones, respectively. σ_c^a, σ_c^b, σ_{strip}^b, σ_{square}^b, σ_{strip}^a, σ_{square}^a, A_c, A_{strip}, and A_{square} are illustrated in Figure 6.

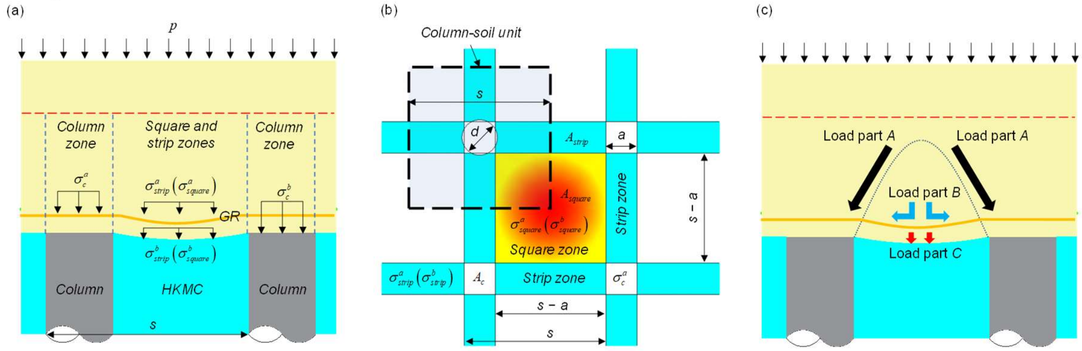

Figure 3: Illustrations of (a) column, square, and strip zones, (b) column-soil unit, and (c) load parts A, B, and C

Figure 4 shows load parts A, B, and C (per column-soil unit) calculated using the vertical stresses measured at different locations and time points. In the first loading stage, there was no significant difference between load parts A and C, and load part B was nearly zero, indicating a slight effect of the geotextile. As the surcharge load increased, load part A became the largest portion among the three load parts. A significant reduction occurred in the load taken by the HKMC subsoil. The increase in load part B indicated that the geotextile started to contribute to the load redistribution.

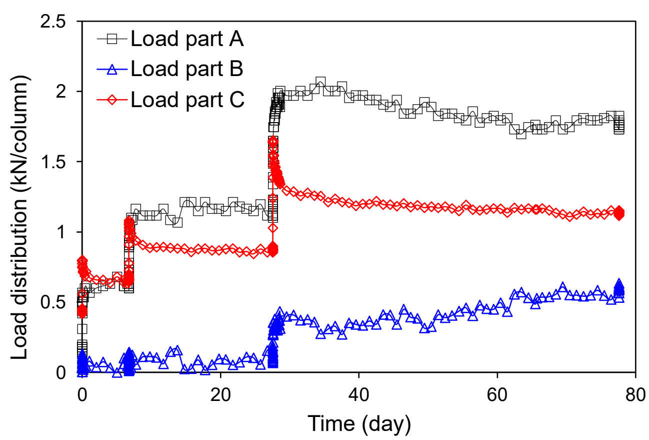

Figure 4: Load distribution in a column-soil unit regarding load parts A, B, and C

3.2 Tensile strain

Tensile strains of the geotextile reinforcement were measured by FBG sensors. The sensing principle of FBG can be expressed by the following equation:

$$\Delta\lambda_B / \lambda_{B0} = c_\varepsilon \Delta\varepsilon + c_T \Delta T \tag{4}$$

where λ_{B0} is the original Bragg wavelength, c_ε and c_T are the coefficients of strain and temperature, respectively. The wavelength change $\Delta\lambda_B$ is sensitive to strain and temperature. By detecting the wavelength changes, changes in strain or temperature can be determined. Figure 5 shows the calibration results between the wavelength change of FBG sensors and global strain of a geotextile with the testing range of 100 mm. It should be noted that the calibration tests and physical model test were performed under the constant temperature. Therefore, the temperature effect on wavelength change of FBG sensors was negligible in this study.

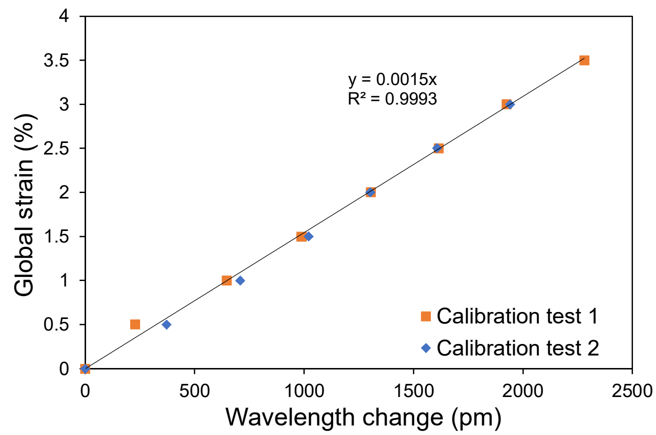

Figure 5: Calibration results of FBG sensors on geotextile

Figure 6 presents the measured maximum strains along the x direction (longitudinal) and y direction (transversal) of the geotextile. It can be seen that the strains in the y direction were greater than those in the x direction, owing to the greater stiffness of the geotextile in the x direction. The strains in both directions saw a significant increase as the surcharge loading reached 40 kPa, indicating that the geotextile started to contribute to the load redistribution. The development of tensile strains agreed reasonably with the load distribution curves presented in Figure 4.

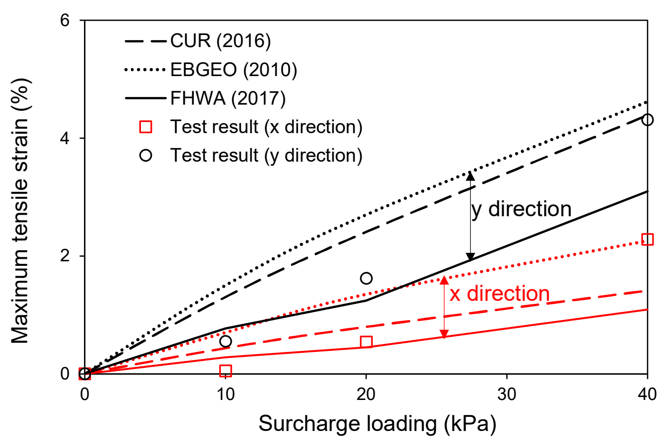

Figure 6: Maximum tensile strains

4 DISCUSSION

4.1 Assessment of arching effect using current design method

In many design guidelines, arching effect can quantify by Efficacy, an index representing the proportion of the load taken by columns, which can be expressed by the following equation:

$$E = A \Big/ \left[\left(\gamma H + p \right) s^2 \right] \tag{5}$$

where p is the surcharge loading, s is the size of the column-soil unit, as indicated in Figure 3(b), γ and H are the unit weight and height of the sand fill, respectively.

The value of Efficacy is in the range of 0 to 1, with the greater value corresponding to greater arching effect. The development of Efficacy with surcharge loading of the small-scale physical model test is plotted in Figure 7.

It was found that Efficacy showed a decrease during the process of increasing the surcharge load. This was attributed to the partially undrained condition of the HKMC subsoil, which delayed the load transfer. The differential settlements between the columns and surrounding soil increased with the consolidation of the subsoil, resulting in an increase in the deflection of the reinforcement, and thus increasing the Efficacy. The Efficacy at the end of the consolidation slightly increased with an increase in surcharge load. A simplified pattern of the development of Efficacy with surcharge loading is also illustrated in Figure 7.

In this study, we reviewed and selected four widely used design guidelines and assessed them with the experimental data of the small-scale physical model test. Those design guidelines are (1) British BS 8006 guidelines, (2) German EBGEO guidelines, (3) American FHWA manuals, and (4) Dutch CUR guidelines. The main theories adopted in this design guidelines are summarised in Table 2.

Table 2: A summary of different design guidelines

Design guidelines	Theories/methods	Remarks
BS8006 guidelines	Hewlett and Randolph (1998) method – Semi-spherical Arching model	A limit-state equilibrium model Ignore the subsoil support Apply to a square arrangement of columns Uniform loading distribution on reinforcements
German EBGEO guidelines	Multi-shell Arches model proposed by Zaeske (2001)	A limit-state equilibrium model The contribution of consolidation of subsoils to arching effect is not considered Consider subsoil support only when calculating tension of reinforcements Apply to a square arrangement of columns/piles. Triangular loading distribution on reinforcements
FHWA manuals	Adapted Terzaghi method (Sloan et al., 2011)	A friction model The results highly depend on the value of K_T (0.5-1). 0.75 is recommended. Can consider multiple layers of fill materials Consider subsoil support and consolidation of subsoil by using load-displacement compatibility (LDC) method (Filz et al., 2019) Uniform loading distribution on reinforcements
Dutch CUR guidelines	Concentric Arches (CA) model (van Eekelen, 2015)	A limit-state equilibrium model Apply to a square arrangement of columns Distinguish square and strip zones Uniform/inversed triangular loading distribution on reinforcements

In BS8006 design guidelines, Hewlett and Randolph's method was adopted to quantify the soil arching effect. German EBGEO adopted the multi-shell arches theory of Zaeske (2001). Adapted Terzaghi model was used in FHWA manuals. A three-dimensional concentric arches (CA) model developed by van Eekelen (2015) was adopted in Dutch CUR guidelines. The main equations used in different guidelines for determining Efficacy were listed in Wu et al. (2024).

Figure 7 presents the Efficacy values determined according to different design guidelines. Generally speaking, EBGEO (2010), CUR (2016) and FHWA (2017) gave Efficacy values similar to those calculated using experimental data. While the BS8006 (2010) overestimated the Efficacy by around 12 %. What leads to different results for various design guidelines is that actual deformations occurring in subsoil or reinforcement are incompatible with the required ones to achieve the arching state assumed by those guidelines.

Among the four design guidelines, the result of the FHWA (2017) agreed well with the trend of Efficacy calculated using the measured data. However, it should be noted that the results calculated by the adapted Terzaghi method are highly dependent on the value of K_T. Higher K_T values result in higher efficacies. Therefore, this method must be used with caution. The Efficacy values calculated according to BS8006 (2010), EBGEO (2010), and CUR (2016) remained constant under the different surcharge loads. This was because these methods are based on limit state equilibrium, which can only determine a constant arching stress value.

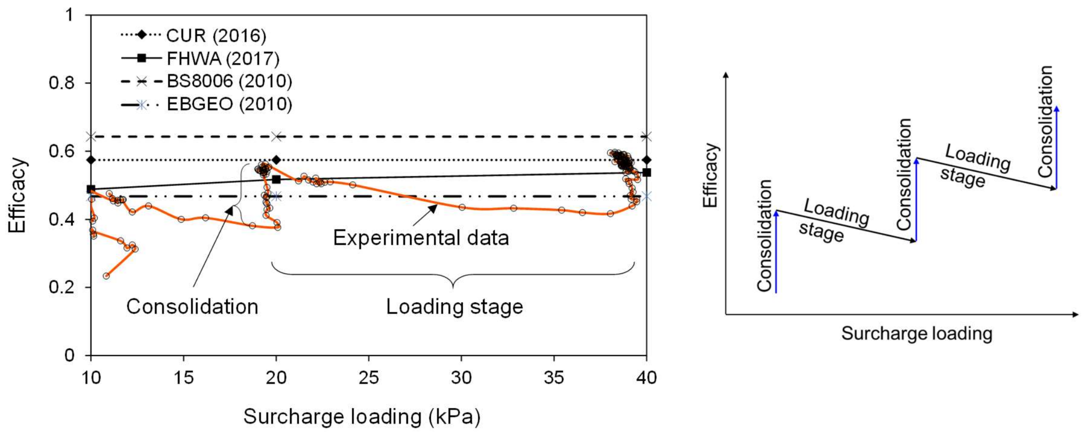

Figure 7: Development of efficacy with surcharge loading

4.2 Tensile strain

Since EBGEO (2010), CUR (2016), and FHWA (2017) provided better results in term of Efficacy, those three design guidelines were selected to further calculate the maximum tensile strains of the geotextile in the physical model.

In EBGEO (2010), design charts were provided to determine the maximum tensile strains of geosynthetic reinforcement. The equations used in Dutch design guidelines for calculating the maximum tensile strains can be referred to CUR (2016). In FHWA (2017), generalised parabolic method was adopted to determine the tension in biaxial geosynthetics placed in alignment with a rectangular array of column:

$$6T^3 + 6T\left(\frac{\sigma_{net}s^2}{p_c}\right)^2 - J\left(\frac{\sigma_{net}s^2}{p_c}\right) = 0 \tag{6}$$

where T is the tension in the geotextile, σ_{net} is the net vertical stress acting on the geotextile, p_c is the perimeter of the column, and J is the stiffness of the geotextile. The maximum tension of the geotextile can be determined by solving Equation (6), and therefore the tensile strain can be calculated as $\varepsilon = T/J$. Figure 6 presents the maximum tensile strains determined according to German, Dutch, and US design guidelines. It can be seen that Dutch CUR (2016) and US FHWA (2017) can predict the maximum tensile strains with reasonable agreement to the experimental data.

5 CONCLUSIONS

A small-scale physical model test on geotextile-reinforced sand layer over HKMC improved by DCM columns has been successfully conducted with the measurement of earth pressures and the tensile strains of the geotextile reinforcement. The load distribution was revealed based on the earth pressure data. It was found that during the loading stage, Efficacy of DCM columns decreased attributed to the partially undrained behaviour of HKMC. As the HKMC consolidated, load was transferred gradually to the column resulting in an increase in Efficacy. Furthermore, the predictions of Dutch design guidelines and FHWA manuals agreed reasonably with the experimental data in terms of Efficacy of DCM columns and the maximum tensile strains of the geotextile.

ACKNOWLEDGEMENTS

The work in this paper is supported by a General Research Fund (GRF) projects (15226722) from Research Grants Council (RGC) of Hong Kong Special Administrative Region Government of China. The authors also acknowledge the financial support from the Start-up fund (BD30) and two research grants from Research Institute for Land and Space (CD82 and CD7A) of The Hong Kong Polytechnic University.

REFERENCES

BS 8006 2010. Code of Practice for Strengthened/Reinforced Soils and Other Fills. British Standard Institution, UK

EBGEO 2010. Empfehlungen für den Entwurf und die Berechnung von Erdkörpern mit Bewehrungen aus Geokunststoffen e EBGEO, vol. 2 German Geotechnical Society, Auflage978-3-433-02950-3 (in German). Also available in English: Recommendations for Design and Analysis of Earth Structures using Geosynthetic Reinforcements e EBGEO, 2011. ISBN: 978-3-433-02983-1 and digital in English ISBN: 978-3-433-60093-1.

Filz, G. M., Sloan, J. A., McGuire, M. P., Smith, M., & Collin, J. (2019). Settlement and vertical load transfer in column-supported embankments. Journal of Geotechnical and Geoenvironmental Engineering, 145(10), 04019083.

Hewlett, W. J. 1988. Analysis of piled embankment. *Ground Engineering*. 21(3): 12-18.

Iglesia, G.R., Einstein, H.H., & Whitman, R.V. 2014. Investigation of soil arching with centrifuge tests. *Journal of Geotechnical and Geoenvironmental Engineering*, 140(2): 04013005.

King, D.J., Bouazza, A., Gniel, J.R., Rowe, R.K., & Bui, H.H. 2017. Load-transfer platform behaviour in embankments supported on semi-rigid columns: implications of the ground reaction curve. *Canadian Geotechnical Journal*, 54(8): 1158-1175.

Lee, D. 2016. Expansion of Hong Kong International Airport into a Three-Runway System, Airport Reclamations – then and now. HKIE YMC Seminar. http://ymc.hkie.org.hk/DocDown.aspx?imgDoc=151_160120+3RS+Reclamation+(20+Jan+2016).pdf

Schaefer, V. R., Berg, R. R., Collin, J. G., Christopher, B. R., DiMaggio, J. A., Filz, G. M., ... & Ayala, D. (2017). Ground modification methods reference manual—Volume II. Washington, DC: Federal Highway Administration.

Sloan, J., Filz, G., & Collin, J. (2011). A generalized formulation of the adapted Terzaghi method of arching in column-supported embankments. In Geo-Frontiers 2011: Advances in Geotechnical Engineering (pp. 798-805).

van Eekelen, S.J.M., Bezuijen, A., & Van Tol, A.F. 2013. An analytical model for arching in piled embankments. *Geotextiles and Geomembranes*, 39: 78-102.

van Eekelen, S. J. M. 2015. Basal reinforced piled embankments: Experiments, field studies and the development and validation of a new analytical design model.

CUR. 2016. Design guideline basal reinforced piled embankments. CRC press.

Wu, P. C., Feng, W. Q., & Yin, J. H. 2020. Numerical study of creep effects on settlements and load trans-fer mechanisms of soft soil improved by deep cement mixed soil columns under embankment load. *Geotextiles and Geomembranes*, 48(3): 331-348.

Wu, P. C., Chen, W. B., Feng, W. Q., Yin, J. H., Ho, T. O., & Huang, S. R. (2024). Load transfer mechanism of geotextile-reinforced sand layer over semirigid column-improved soft soil. *Acta Geotechnica*, 19(5), 2855-2871.

Zaeske, D. 2001. Zur Wirkungsweise von unbewehrten und bewehrten mineralischen Tragschichten über pfahlartigen Gründungselementen. Fachgebiet u. Versuchsanst. Geotechnik, Univ. Gh Kassel.

Zhang, C., Su, L., & Jiang, G. 2022. Full-scale model tests of load transfer in geogrid-reinforced and float-ing pile-supported embankments. *Geotextiles and Geomembranes*, 50(5):896-909.

Geotechnical Insights via Electrical Resistivity Imaging of Fault Zones

M. Akbariforouz
CEE, The Hong Kong PolyU, Hong Kong; EIT, Ningbo

Q. Zhao
CEE, The Hong Kong PolyU, Hong Kong

C. Zheng
EIT, Ningbo; SUSTech, Shenzhen

ABSTRACT

Hong Kong's unique topography, dense population, and lithology necessitate constructing and stabilizing numerous large-scale geoengineering projects, such as tunnels or rock slopes. The rock mass deformation modulus is essential for evaluating the bearing capacity and deformations. Deformation moduli measured through laboratory experiments, empirical equations, or even in situ tests can not present a representative elementary volume (D_{REV}) due to limited test coverage and technical difficulties in harsh geological or topographic conditions, such as near faults. This study utilized electrical resistivity (*ER*) tomography and numerical back-analysis to investigate D_{REV} near faults; we also employed geoelectrical contrasts to detect proper locations for installing extensometers along excavated galleries of rock slopes. The deformations recorded by extensometers were used to back-calculate the D_{REV} values by finite difference numerical modeling. We established a correlation between *ER* and D_{REV}, which was 30 to 80% more accurate than those obtained through conventional approaches. Our methodology provides a systematic approach to assess faulted rock mass behavior for various geoengineering projects, which is also replicable for other geological formations with harsh geology or limited access without exposing an extreme financial burden, technical challenges, or environmental issues.

1 INTRODUCTION

The landscape, high-density population, and geological features of Hong Kong require geoengineering structures like tunnels and slopes. Rock mass behavior for such projects must be investigated at the representative element volume (REV) or the smallest volume representing the whole medium's properties (Hill, 1963).

The rock mass deformation modulus is a scale-dependent parameter controlling the mechanical characteristics; this parameter is different at REV (D_{REV}) from the values obtained by conventional methods, such as empirical equations or laboratory and in situ tests (Aladejare & Idris, 2020; Brady & Brown, 1993), considering the limited coverage and unrepresentative interpretations.

Designing and constructing tunnels or slopes using inaccurate D_{REV} values resulted in extreme financial burdens and devastating impacts on human lives (Peng & Zhang, 2012). D_{REV} controls the bearing capacity and deformations under loading/unloading. The lithological conditions, fracture characteristics, rock strength parameters, water saturation, and the tested volume (i.e., scale impacts) affect D_{REV} (Aksoy et al., 2012; Barnard & Heymann, 2015; Fattahi et al., 2019). Moreover, the excavation or blasting alters D_{REV} (Palmström & Singh, 2001). Therefore, the effects of these parameters on D_{REV} are pivotal.

Numerical back-analysis of deformations recorded by extensometers inside galleries or tunnels is an indirect, promising technique to evaluate D_{REV} (Ghotbi Ravandi et al., 2017; Khodabakhshi & Mortazavi, 2018; Ren et al., 2021); however, performing such a back-analysis is challenging due to the limited in situ data associated with financial concerns or technical difficulties. Moreover, assessing the locations of extensometers is essential for complete coverage of all rock mass conditions. If we can establish a relationship between numerical back analysis and geophysical tomography, it can mitigate such challenges by applying them to other study sites.

Geoelectrical resistivity tomography (*ER*) can cover a representative rock mass (Archie, 1947) as a necessary part of geoengineering projects without exposing the extra financial burden of in situ deformation measurements. The induced electrical current (*I*) between electrodes (K and L in Figure **1a**) causes potential differences (ΔV between voltmeters M and N) for different rock types (Figure **1b-c**) (Telford et al., 1990).

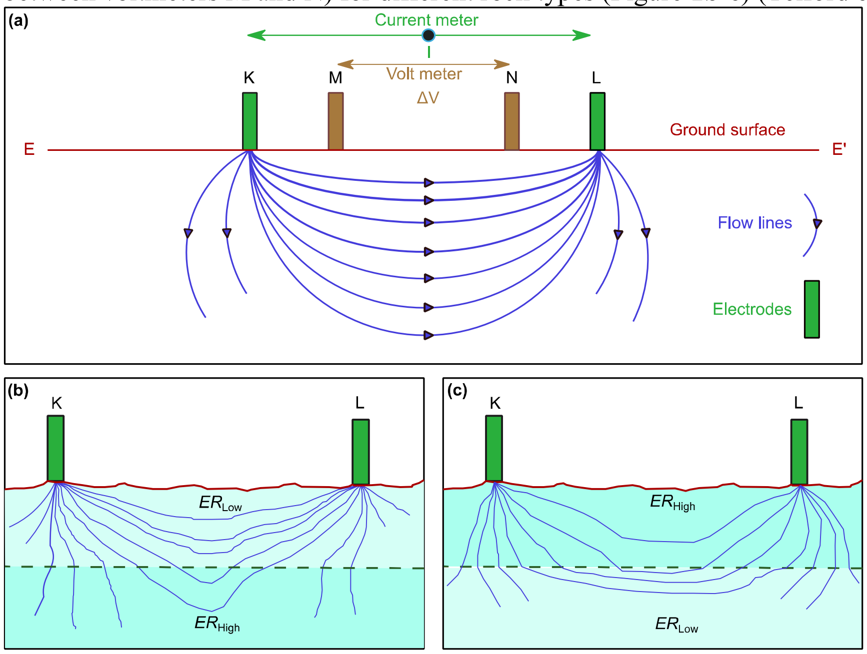

Figure 1: (a) Schematic view for electrical profiles (EE´) with voltmeters M & N and current electrodes K & L. The current is distorted for two rocks (ER_{Low} and ER_{High}) from a lower to higher *ER* (b) and a higher to lower *ER* (c) (modified from (Nia & Mahdavi, 2020)).

The effects of rock discontinuities (Akbariforouz et al., 2023; Carpenter et al., 2011; Li et al., 2015), lithology (Ammar & Kamal, 2018; Pazha et al., 2019), fluid saturation (Ammar & Kamal, 2018; Bhatt & Jain, 2014; Liu et al., 2023), stress regimes (Stavrakas et al., 2003; Triantis et al., 2006), and strength parameters on *ER* and rock mass deformations (Akbariforouz et al., 2022; Kahraman & Yeken, 2010; Ranjbar & Nasab, 2019) were consistent based on laboratory (Kahraman, 2022; Su & Momayez, 2017; Wang & Gelius, 2010) and field evaluations (Li et al., 2015; Pazha et al., 2019; Sandler et al., 2009). Therefore, *ER* variations can be used to assess the faulted rock mass deformations and D_{REV}.

The anomalies, such as cavities, conductive materials, or water-bearing areas, can result in misleading *ER* (Militzer et al., 1979; Rolia & Sutjiningsih, 2018); therefore, additional geophysical techniques must be applied to avoid such misinterpretations. We evaluated D_{REV} for a sedimentary formation by comparing numerical back-analysis of extensometers and *ER* tomography to develop an accurate, environmentally friendly, and financially affordable relationship for D_{REV}.

2 Methods

2.1 Studied Area and ER Tomography

The study site is a slope with 184 m height in the Asmari-Jahrum Formation (AJF) in the Central Plateau of Iran, consisting of thick-bedded carbonate rocks (Amirshahkarami et al., 2007). *ER* measurements were conducted by a Schlumberger array with a maximum length of 3 km and an electrode distance of 30-100. Around 100 electrodes were used along a 3000 m profile for 30 m distances. No igneous masses, conductive minerals, water-bearing structures, or cavities were detected in the study site based on the nuclear magnetic resonance and automated gravity meter up to 250 m depth (Howland-Rose, 1981).

2.2 In situ Tests

Plate-loading (1 m diameter with five extensometers at 0.095, 0.085, 1.79, 2.59, and 3.7 m depths) and dilatometer tests (3 up to 45 m depth and along boreholes with diameter = 10.1 cm) were performed at 2 m × 2 m galleries based on ISRM standards (ISRM, 1998; Ladanyi, 1987). The deformation modulus under loading (D_L) and unloading (D_U) was measured based on these tests. The loading cycles (minimum pressure from 0.5 to maximum 3 and 10 bar) were five for plate-loading and three for dilatometers.

2.3 Back-Analysis of Extensometers

Performing in situ tests at harsh topography or near faults, such as faults F1, F4, and F5 in the study site, is challenging. In galleries, anchor extensometers with an accuracy of ±3μm were installed inside horizontal and vertical boreholes at 0.4-1 m distances from the gallery surface near faults and sharp *ER* variations.

For the numerical models (20 m × 20 m or ten times the gallery size), roller and XY-fixed (pins) boundaries were considered for sides and on the bottom (Figure **2**) with 100 meshes in each direction, ranging from coarse to fine meshes in the middle. Cohesion (C_{rm}) and friction angle (ϕ_{rm}) were assessed by the generalized Hoek-Brown failure criterion (Rocscience, 2007) using rock mass classification index (GIS), overburden (h), density (ρ), and rock index (m_i). The Poisson ratio of rock mass was considered 0.35 based on in situ tests and laboratory experiments.

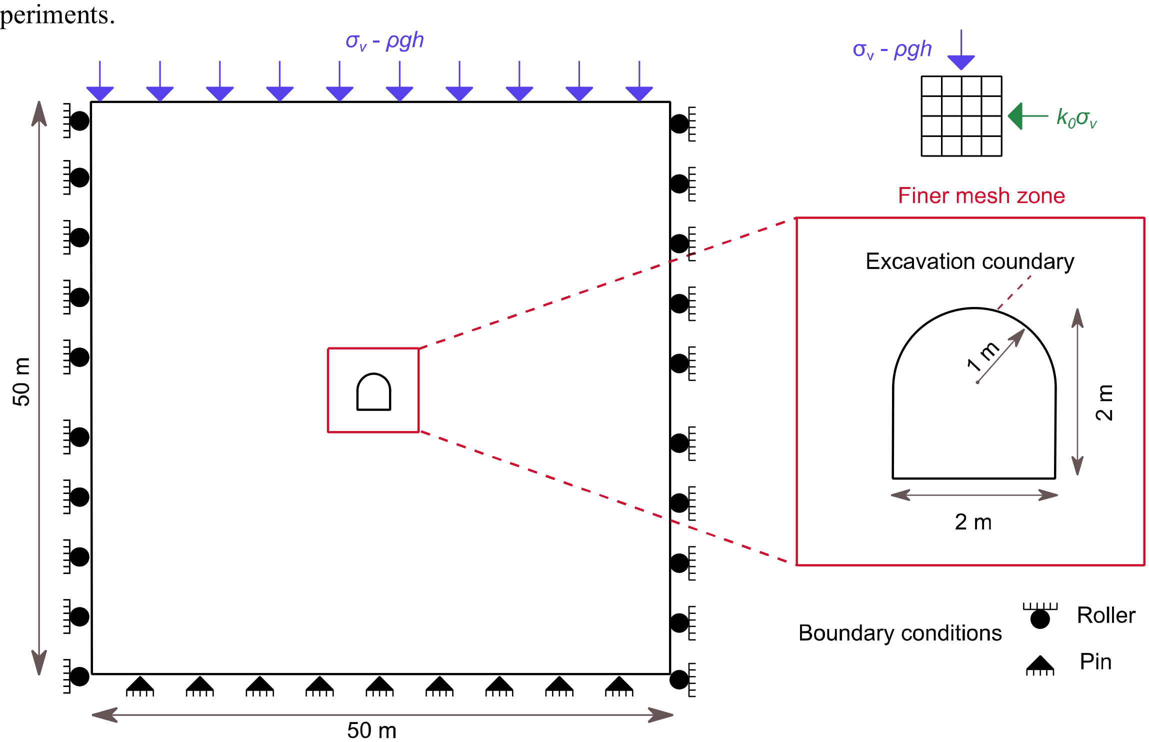

Figure 2. The boundaries, geometry, and parameters of numerical models, where σ_v and $k_0\sigma_v$ are the vertical and horizontal stress components, respectively. ρ, h, and g represent the density, overburden height, and gravity, respectively.

The deformation modulus under unloading at the REV ($D_{UREV} < D_U$ of in situ tests) was evaluated by a numerical back-analysis (FLAC^{2D}) (ITASCA, 2002), starting from D_U up to reaching a modulus that resulted in deformations recorded by the installed extensometer (Δ_{REV}). For D_{REV} under loading (D_{LREV}), the ratio of D_{UREV} by D_U (in situ tests) was used (i.e., $D_{LREV}=(D_{UREV}/D_U)\times D_L$), considering no alternative was available to evaluate D_{LREV}. The flowchart evaluating D_{REV} based on *ER* is shown in Figure **3**.

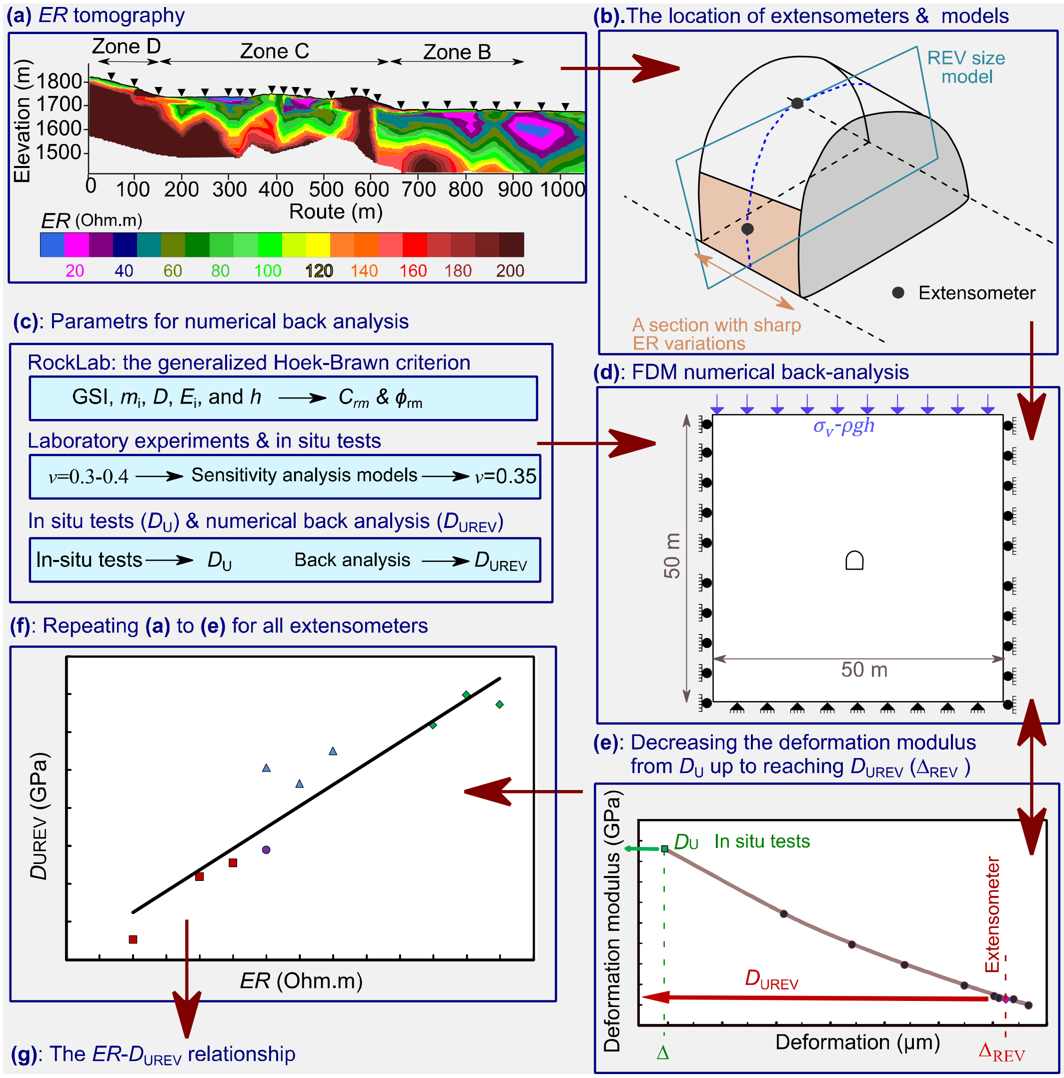

Figure 3. D_{REV} based on *ER*: (a) detecting extensometer locations extensometers based on sharp *ER* changes, (b) the deformations (Δ_{REV}) recorded along borehole extensometers, (c) rock mass parameters for the numerical models, (d) the FDM model, (e) back-analysis from D_L to D_{UREV} (reaching Δ_{REV}), (f) the back-analysis results for all extensometers, and (g) the *ER*-D_{UREV} criterion.

3 Results

The study site was divided into four lithological zones, and *ER* alterations were recorded for the whole study site. *ER* values in Zone A (dolomitic limestone) spanned from 100 to 160 Ω·m, except near F4 and F5 faults (60-100 Ω·m). We divided the excavated gallery (LG3) into five subsections with a 10-20 Ω·m variation and installed borehole extensometers for these subsections. At 15 and 40 distances, *ER* was 160-180 and 120-140 Ω·m, respectively. The *ER* range near Fault F4 (50 m from the gallery) was 100-120, while the range near the intersection of F4 and F5 faults (at 80 and 90 distances) was 80-100 and 60-80 Ω·m, respectively (Figure **4**).
The *ER* range for Gallery LG1 was 20-100 for Zone B (marly limestone) and 100-200 Ω·m for Zone C (dolomitic limestone). The lowest *ER* values for Zone C were recorded near F1 at around 100 Ω·m. Two different layers with *ER* values of 20-60 and 60-100 Ω·m were detected within Zone B. *ER* varies between 120 and 200 Ω·m for Zone D (limestone).

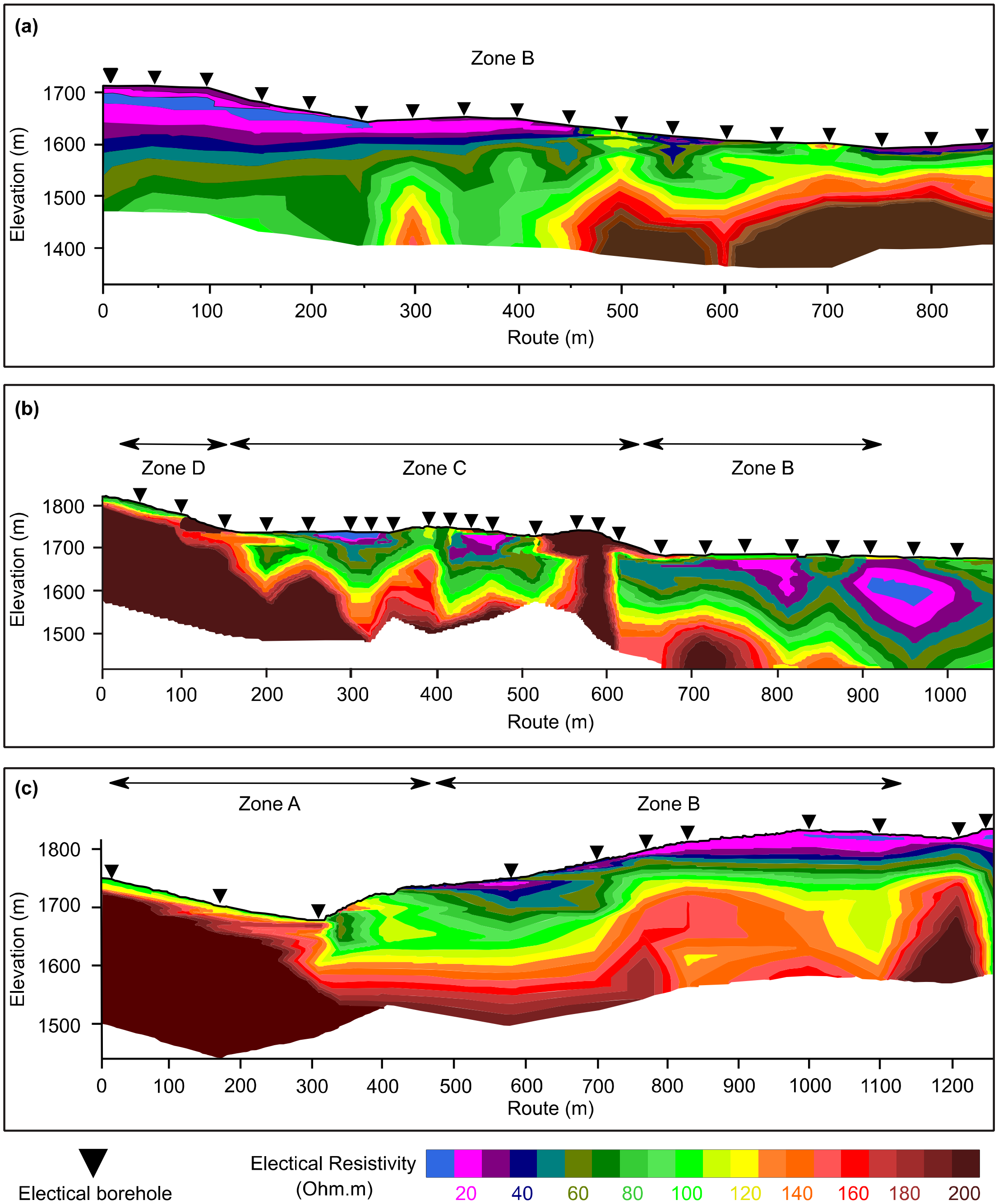

Figure 4. Electrical resistivity tomography for three profiles of the study site

A plastic area (0.25 to 0.5 m) was observed in the numerical models around the galleries for the extensometers; the extensometer deformations also displayed a higher difference between values recorded by equipment inside the plastic area (0.5 m). For example, Δ_{REV} for Zone A was 76 % (1354/1769μm) and 72 % (859/1190μm) of Δ_{REV} outside this zone in horizontal and vertical boreholes, respectively. Therefore, extensometers outside the plastic area (60-100 cm from the gallery inlets) were utilized for measurements.

Figure **5** shows deformations for Extensometer 5 at LG1. First, the deformations based on the minimum D_U values of in situ tests (Δ) were calculated. For example, the minimum modulus was 4.73 GPa based on the plate-loading tests. Subsequently, deformations based on borehole extensometer (Δ_{REV}) were monitored for 120 days until reaching a variation below 10μm for extensometers at 60 cm to 100 cm (outside the plastic deformation zone) distances during the last month. D_{UREV} values were back-calculated based on the recorded Δ_{REV} by decreasing the deformation modulus (D_U) in numerical models until reaching deformations at a ±3μm span from Δ_{REV}.

We also assessed the sensitivity of deformations to Poison ratio (v); maximum deformations enhanced by 3.6 % (from 1989 to 2063μm) for a rise of v from 0.3 to 0.4 (33 %), while a relatively similar deformation modulus change (4.73 to 3.27 GPa) resulted in a deformation increase from 1397 to 2026 μm (31 %). Therefore, the influence of the deformation modulus on deformations was much higher than v, and a Poison ratio equal to 0.35 was employed for all models (same as in situ tests).

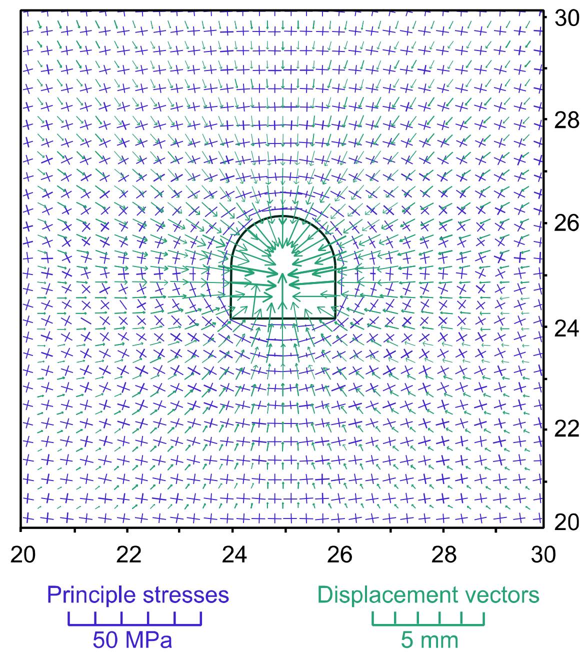

Figure 5. Numerical model (plot: 10 m × 10 m) with Δ_{REV} = 2026μm for the extensometer installed at 80 cm from the gallery span; D_{UREV} back-calculated as 3.27 GPa compared to the in situ tests (4.73 GPa).

We developed a relationship between *ER* and D_{UREV} based on all numerical models and back-calculated values with R^2 = 89.3 % (Equation (**1**)). We utilized this relationship to divide the rock masses at the dam axis into subsections based on sharp *ER* variations for Zones A to D, in addition to faulted rock masses (Figure **6**).

$$D_{UREV} = 0.028\ ER + 0.68 \qquad \textbf{(1)}$$

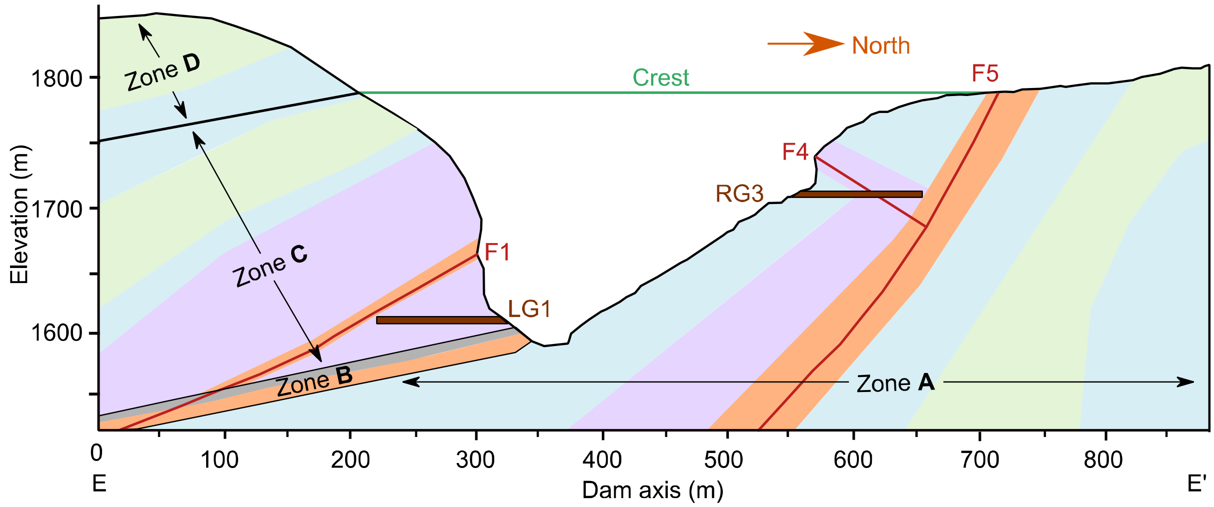

Symbol					
Subsection	I	II	III	IV	V
ER (Ohm.m)	160-200	120-160	100-120	60-100	20-60
D_{UREV} (GPa)	5.13-6.24	4.02-5.13	3.46-4.02	2.35-3.46	1.24-2.35

Figure 6. Ranges of *ER* and D_{UREV} values calculated using the methodology developed in this study for the whole dam axis: Zone A, C, and D are shown by the arrow. D_{UREV} variations within the slope and near faults are shown in the subsections.

4 Discussion

Our approach includes the influence of jointed area, faulted rocks, and weak bedding on the deformation modulus at REV, which is impossible for the in situ tests due to their limited coverage and technical challenges. The *ER*-D_{REV} correlation is proved based on previous laboratory and field-scale studies. Our results also confirm a direct relationship between *ER* and D_{REV}.

Moreover, geophysical prospecting is a common and affordable technique. Therefore, geoelectrical tomography can be a practical solution for evaluating characteristics of faulted rocks without adding extra financial burdens comparing numerous in situ tests. Geophysical methods are also fast, non-destructive, and environmentally friendly.

After elucidating the advantages of the developed technique in this study, explaining the limitations of this study is critical. We evaluate D_{REV} accurately and develop an *ER*-D_{REV} relationship using numerical back-analyses; nonetheless, extensometer data are often unavailable, particularly for small projects. However, Equation (**1**) can predict D_{REV} when no borehole extensometer data is available, particularly for similar sedimentary formations.

The *ER* range, lithology, and fault properties can affect the faulted rock mass conditions. The resolution of electrical data by a 30-50 m electrode distance is enough to detect the 20 m subsections with different D_{REV} values for a maximum depth of 250 m. Nonetheless, the provided *ER*-D_{REV} relationship cannot be used for igneous rocks or other sedimentary formations with *ER* higher than 200 Ω·m. However, this approach can be repeated for different projects by installing borehole extensometers based on *ER* contrasts.

Despite employing low electrode distance and complementary geophysical data, *ER* values can still suffer from variability. We consider a range of *ER* values (10 Ω·m) to control the model results, showing 5-25 % variability for different *ERs*; the effect of *ER* variability of 10 Ω·m is higher for lower *ER* ranges (10-30 Ω·m). A safety factor (e.g., 1.25) or a range of D_{REV} can be considered for lower *ER*. The impossibility of installing borehole extensometers at Subsection B1 (because of the locations of galleries) is another limitation of this study; however, Equation (**1**) is utilized by multiplying the mentioned safety factor.

D_{UREV} is calculated directly from extensometer deformations at REV, but we use the ratio of D_{UREV}/D_U for calculating D_{LREV}. However, this estimated D_{LREV} can be used at the design stage by multiplying a reasonable safety factor, considering the impossibility of evaluating rock mass behavior under loading at REV using alternative methods.

5 Conclusions

The main concerns in the studied slope are Zone B and three faults; we divide Zone B into two sections (B1 and B2). Zone B1 (about 10 m) and faulted rocks are geomechanically weak layers (D_{UREV} of 1.24-2.35 GPa), and reinforcement must be considered. Such D_{UREV} values are up to 80 % lower than the values measured through in situ tests.

Similar ER-D_{REV} relationships can be developed for various rock types, and soft computing methods (such as neural networks) can be employed to analyze the data and present universal equations for a category of rocks (like sedimentary formations). Therefore, removing extreme financial burdens, technical challenges, and environmental issues of in situ tests, in addition to coverage of the rock mass at the representative element volume, are advantages of utilizing *ER* tomography for evaluating the deformation moduli of faulted rock masses.

REFERENCES

Akbariforouz, M., Zhao, Q., Chen, K., Baghbanan, A., Narimani, R., & Zheng, C. (2022). Statistical study of squeezing for soft rocks based on factor and regression analyses of effective parameters. *International Journal of Rock Mechanics and Mining Sciences*, *163*. https://doi.org/https://doi.org/10.1016/j.ijrmms.2022.105306

Akbariforouz, M., Zhao, Q., Taherdangkoo, R., Baghbanan, A., Butscher, C., & Zheng, C. (2023). Prediction of tunnel squeezing in soft sedimentary rocks by geoelectrical data. *Environmental Earth Sciences*, *82*(7). https://doi.org/https://doi.org/10.1007/s12665-023-10835-0

Aksoy, C. O., Ogul, K., Topal, I., Ozer, S. C., Ozacar, V., & Posluk, E. (2012). Numerical modeling of non-deformable support in swelling and squeezing rocks. *International Journal of Rock Mechanics and Mining Sciences 52*, 61-70. https://doi.org/https://doi.org/10.1016/j.ijrmms.2012.02.008

Aladejare, A. E., & Idris, M. A. (2020). Performance analysis of empirical models for predicting rock mass deformation modulus using regression and Bayesian methods. *Journal of Rock Mechanics and Geotechnical Engineering*, *12*(6), 1263-1271. https://doi.org/https://doi.org/10.1016/j.jrmge.2020.03.007

Amirshahkarami, M., Vaziri-Moghaddam, H., & Taheri, A. (2007). Sedimentary facies and sequence stratigraphy of the Asmari Formation at Chaman-Bolbol, Zagros Basin, Iran. *Journal of Asian Earth Sciences*, *29*(5), 947-959. https://doi.org/https://doi.org/10.1016/j.jseaes.2006.06.008

Ammar, A. I., & Kamal, K. A. (2018). Resistivity method contribution in determining fault zone and hydro-geophysical characteristics of carbonate aquifer, eastern desert, Egypt. *Applied Water Science*, *8*(1), 1-27. https://doi.org/https://doi.org/10.1007/s13201-017-0639-9

Archie, G. E. (1947). The electrical resistivity is an aid in determining some reservoir characteristics. *AAPG Bulletin*, *31*(2), 350–366.

Barnard, H., & Heymann, G. (2015). The effect of bedding errors on the accuracy of plate load tests. *Journal of the South African Institution of Civil Engineering*, *57*(1), 67-76. https://doi.org/https://doi.org/10.17159/2309-8775/2015/v57n1a7

Bhatt, S., & Jain, P. K. (2014). Correlation between electrical resistivity and water content of sand-a statistical approach. *American International Journal of Research in Science, Technology, Engineering & Mathematics*, *6*(2), 115-121.

Brady, B. H. G., & Brown, E. T. (1993). *Rock mechanics for underground mining* (2nd ed.). Chapman & Hall.

Carpenter, B. M., Marone, C., & Saffer, D. M. (2011). Weakness of the San Andreas Fault revealed by samples from the active fault zone. *Nature Geoscience*, *4*(4), 251-254. https://doi.org/https://doi.org/10.1038/ngeo1089

Fattahi, H., Varmazyari, Z., & Babanouri, N. (2019). Feasibility of Monte Carlo simulation for predicting the deformation modulus of the rock mass. *Tunneling and Underground Space Technology*, *89*, 151-156. https://doi.org/https://doi.org/10.1016/j.tust.2019.03.024

Ghotbi Ravandi, E., Rahmannejad, R., Karimi-Nasab, S., & Sarrafi, A. (2017). Application of numerical modeling and genetic programming in hydrocarbon seepage prediction and control for crude oil storage unlined rock caverns. *Geofluids*, *2017*, 1-11. https://doi.org/https://doi.org/10.1155/2017/6803294

Hill, R. (1963). Elastic properties of reinforced solids: Some theoretical principles. *Journal of the Mechanics and Physics of Solids*, *11*(5), 357-372. https://doi.org/https://doi.org/10.1016/0022-5096(63)90036-X

Howland-Rose, A. W. (1981). *A report on a rapid reconnaissance magnetic induced polarization survey over a section of the Highland Valley*.

ISRM. (1998). Standard test method for determining the in situ modulus of deformation of rock mass using the rigid plate-loading method. *1.84 (Reapproved)*, 1–9.

ITASCA. (2002). *FLAC^{2D} user guide*. In Itasca Consulting Group, Inc.

Kahraman, S. (2022). Estimating the physicomechanical properties of pyroclastic rocks from electrical resistivity. *Pure and Applied Geophysics*, *179*(1), 301-309. https://doi.org/https://doi.org/10.1007/s00024-021-02898-6

Kahraman, S., & Yeken, T. (2010). Electrical resistivity measurement to predict uniaxial compressive and tensile strength for igneous rocks. *Bulletin of Materials Science*, *33*(6), 731-735. https://doi.org/https://doi.org/10.1007/s12034-011-0137-x

Khodabakhshi, A., & Mortazavi, A. (2018). Numerical modeling of determining in situ rock mass deformation modulus using the plate load test. *International Journal of Geological and Environmental Engineering*, *12*(8), 545–552. https://doi.org/https://doi.org/10.5281/zenodo.1474357

Ladanyi, B. (1987). Suggested method for deformability determination using flexible dilatometers. *International Journal of Rock Mechanics and Mining Sciences & Geomechanics Abstracts*, *24*(2), 123-134. https://doi.org/https://doi.org/10.1016/0148-9062(87)91042-4

Li, K., Pan, B., & Horne, R. (2015). Evaluating fractures in rocks from geothermal reservoirs using resistivity at different frequencies. *Energy*, *93*(P1), 1230-1238. https://doi.org/https://doi.org/10.1016/j.energy.2015.09.084

Liu, X., Beroza, G. C., & Li, H. (2023). Ambient noise differential adjoint tomography reveals fluid-bearing rocks near active faults in Los Angeles. *Nature Communications*, *14*(1), 6873. https://doi.org/https://doi.org/10.1038/s41467-023-42536-4

Militzer, H., Rosler, R., & Losch, W. (1979). Theoretical and experimental investigations for cavity research with geoelectrical resistivity methods. *Geophysical Prospecting*, *27*(3), 640–652. https://doi.org/https://doi.org/10.1111/j.1365-2478.1979.tb00991.x

Nia, H., & Mahdavi, S. A. (2020). Principles of geoelectrical methods. In *Physio-Geo*. https://www.researchgate.net/publication/346969879_principles_of_geoelectrical_methods_8_haifa_raniasari_haifania_2_principles_of_geoelectrical_methods

Palmström, A., & Singh, R. (2001). The deformation modulus of rock masses — comparisons between in situ tests and indirect estimates. *Tunneling and Underground Space Technology*, *16*(2), 115-131. https://doi.org/https://doi.org/10.1016/S0886-7798(01)00038-4

Pazha, H., Nasro, M., & Denya Agustina, R. (2019). Analysis of rock structures based on geoelectrical resistivity data of Wenner-Alpha configuration using Marquardt inversion method. *1st International Conference on Advance and Scientific Innovation*, *1175*(1), 12014. https://doi.org/https://doi.org/10.1088/1742-6596/1175/1/012014 (Journal of Physics Conference Series)

Peng, M., & Zhang, L. M. (2012). Analysis of human risks due to dam-break floods—part 1: a new model based on Bayesian networks. *Natural Hazards*, *64*(1), 903-933. https://doi.org/https://doi.org/10.1007/s11069-012-0275-5

Ranjbar, S., & Nasab, S. K. (2019). Determination of uniaxial compressive strength of granite rock samples using electrical resistivity measurement: NDT. *EAGE-GSM: 2nd Asia Pacific Meeting on Near Surface Geoscience & Engineering*, 22-26. https://doi.org/https://doi.org/10.3997/2214-4609.201900452

Ren, F., Zhang, J., Ouyang, Z., & Hu, H. (2021). Calculating elastic modulus for fractured rock mass using dimensional analysis coupled with numerical simulation. *Mathematical Problems in Engineering*, *2021*, 1-14. https://doi.org/https://doi.org/10.1155/2021/2803837

Rocscience. (2007). *RocLab manual*. In

Rolia, E., & Sutjiningsih, D. (2018). Application of the geoelectric method for groundwater exploration from the surface (A literature study). *AIP Conference Proceedings*, *1977*(1). https://doi.org/https://doi.org/10.1063/1.5042874

Sandler, J., Li, Y., Horne, R. N., & Li, K. (2009). Effects of fracture and frequency on resistivity in different rocks. *EUROPEC/EAGE Conference and Exhibition*. https://doi.org/https://doi.org/10.2118/119872-ms

Stavrakas, I., Anastasiadis, C., Triantis, D., & Vallianatos, F. (2003). Piezo stimulated currents in marble samples: Precursory and concurrent-with-failure signals. *Natural Hazards and Earth System Sciences*, *3*(3-4), 243-247. https://doi.org/https://doi.org/10.5194/nhess-3-243-2003

Su, O., & Momayez, M. (2017). Indirect estimation of electrical resistivity by abrasion and physicomechanical properties of rocks. *Journal of Applied Geophysics*, *143*, 23-30. https://doi.org/https://doi.org/10.1016/j.jappgeo.2017.05.006

Telford, W. M., Geldart, L. P., & Sheriff, R. E. (1990). Applied geophysics. https://doi.org/https://doi.org/10.1017/CBO9781139167932

Triantis, D., Stavrakas, I., Anastasiadis, C., Kyriazopoulos, A., & Vallianatos, F. (2006). An analysis of pressure stimulated currents (PSC) in marble samples under mechanical stress. *Physics and Chemistry of the Earth, Parts*, *47*(4-9), 234-239. https://doi.org/https://doi.org/10.1016/j.pce.2006.02.018

Wang, Z., & Gelius, L.-J. (2010). Electric and elastic properties of rock samples: a unified measurement approach. *Petroleum Geoscience*, *16*(2), 171-183. https://doi.org/https://doi.org/10.1144/1354-079309-013

A Novel Micromechanical Rock-pile Interface Model with Application to Rock-socketed Pile Modeling

Rui LIANG, Zhen-Yu YIN and Jian-Hua YIN
Department of Civil and Environmental Engineering,
The Hong Kong Polytechnic University, Hong Kong, China.

ABSTRACT

The increasing use of rock-socketed piles highlights the importance of developing a suitable design method for their bearing capacity. This study quantifies the shear behavior of the rock-pile interface, which generally dominates the bearing capacity of rock-socketed piles under service load. A micromechanics-based rock-pile interface model with idealized nonuniform profile is proposed with two enhancements: (1) the slip line method together with nonlinear Hoek-Brown failure criteria is integrated to identify the critical shear displacement of rock asperity; and (2) the residual stage of shear behavior is properly considered with the rounding progress of sheared rubbles. Then, the interface model is implemented via user defined FRIC into the finite element code ABAQUS without the need of explicitly building the rock-pile interface profile. Comparison between the predictions and field observed results shows this method can well capture the axial load transfer behavior of pile socket into weak rock. Comparison between the predictions and field observed results shows this method can well capture the axial load transfer behavior of pile socket into weak rock.

1 INTRODUCTION

Rock-socketed bored piles are widely used to support superstructures due to the high axial capacity from both side and toe resistance from the portion of the pile embedded into rock socket (BD (Buildings Department Technical Committee of Hong Kong) 2017). The shaft resistance of drilled rock sockets typically bear a major proportion of working load on the piles, which can account for 80-85% of their total capacity (Chen et al. 2021). This is due to the fact that the mobilized displacement between the shaft and surrounding rock required for the ultimate shaft resistance is smaller than that for the ultimate toe resistance (Carter and Kulhawy 1988). Therefore, predicting pile shaft shear behavior is more critical than predicting toe resistance (Seol et al. 2009, Akgüner and Kirkit 2012). Numerous experimental studies have been conducted to investigate the performance of side resistance on drilled shafts embedded in rocks (Williams 1980, Leung and Ko 1993, O'Neill et al. 1996, Dykeman and Valsangkar 1996, Carrubba 1997, Zhan and Yin 2000, Ng et al. 2001, Omer et al. 2002, Kou et al. 2016, Dai et al. 2017, Xu et al. 2020, Chen et al. 2021). The investigation of influence factors such as test pile details (e.g., pile dimension, socket depth and construction techniques), rock mass characteristics (e.g., rock types and rock stiffness) and rock-pile interface roughness have been reported. However, the lack of detailed information about the constructed socket profile in most of these studies makes it difficult to quantitatively analyze the impact of socket-pile interface roughness on pile side resistance, despite interface roughness being the primary factor influencing shaft friction.

Several interface models (Castelli et al. 1992, O'Neill and Hassan 1994, Seidel and Haberfield 2002, Seol et al. 2009, Tian et al. 2015, Li et al. 2019, Zhao et al. 2022) have been proposed to predict the shear mechanisms between pile shaft and rock joints based on numerous studies and shear tests conducted under constant normal stress (CNS) and constant normal stiffness (CNS) boundary conditions. O'Neill and Hassan (1994) suggested a hyperbolic shear functions that considers the pile diameter and Young's modulus of the rock. Seol et al. (2009) employed a nonlinear triple-curve model to describe the shear load-transfer characteristics of the rock-socketed pile shaft based on the Hoek-Brown failure criterion. Tian et al. (2015) presented an interface model that considers the elastic stage of cohesive bond and the post-peak stage due to the bond failure and increasing friction. Li et al. (2019) proposed an analytical model for rock joint shear behavior consisting of waviness and unevenness asperities separated by wavelet analysis.

The shear mechanism of the rock-socketed pile shaft is of particular interest in this study. The motivation of this paper is to develop a rock-pile interface model and provide a valuable method to calculate the axial bearing capacity of piles socketed into weak rock, since the weathered rock layer is widespread in Hong Kong (Ng et al. 2001). In this paper, a micromechanically based interface model focusing on the shear behavior between the pile shaft and weak rock has been proposed considering rock mass with nonlinear failure criteria with two enhancements: (1) the slip line method together with nonlinear Hoek-Brown failure criteria has been integrated to identify the critical shear displacement of rock asperity; and (2) the residual stage has been elaboratively considered based on the evolution of the rock particle breakage. Then, the proposed interface model is integrated into the ABAQUS finite element (FE) code with no need of explicitly building the rock-pile interface profile. The accuracy of the proposed method is validated through comparisons between the simulation results and the field observed results.

2 ASSUMPTIONS FOR THE PROPOSED MODEL

2.1 Boundary conditions

Two common types of boundary conditions are typically used in direct shear tests, namely constant normal load (CNL) and constant normal stiffness (CNS). The CNL condition is suitable for studying planar and non-reinforced slope stability issues (Johnston and Lam 1989). However, for the analysis of rock-socketed piles under axial loading, the downward motion of the pile reduces the contact area at the interface while the pile undergoes dilation due to the confinement of the socket wall. As a result, normal stress is not constant but increases with the development of dilation, as depicted in Fig. 1. Hence, it is more appropriate to apply the CNS condition to model the shear behavior of the rock-pile interface. To incorporate this condition in the interface model, a spring is employed to represent the CNS boundary condition. The stiffness of the spring can be determined based on the expanding infinite cylinder theory in an elastic half-space, as outlined by Johnston and Lam (1989):

$$K = \frac{\Delta\sigma_n}{\Delta r} = \frac{E}{R(1+v)} \tag{1}$$

where K is the spring stiffness; E is the elastic modulus of the rock; R is the radius of the pile shaft, v is the Poisson's ratio.

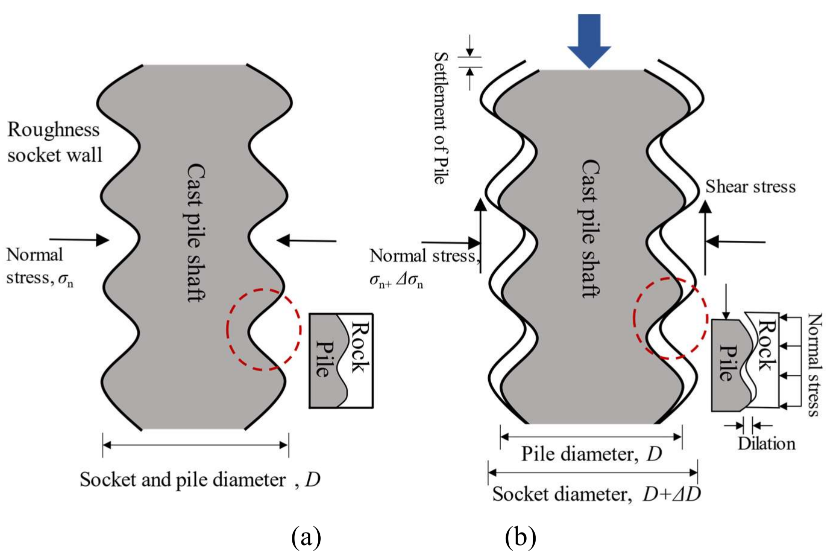

Fig. 1. Bored pile socket into rocks: (a) initial rock-pile interface after casting; (b) pile settlement after axial loading

2.2 Idealized profile of the interface model

It is worth noting that the use of a uniform simplified surface can result in synchronized shear behavior of each asperity, encompassing both the pre-peak and post-peak stages. However, in natural rock boreholes, the shear behavior of individual asperities occurs separately, and each asperity contributes to the overall global shear stress independently (Zhao et al. 2021). To address this limitation, an idealized nonuniform triangular surface with the same inclined angle, θ, is proposed to represent the complex rock profiles, as illustrated in Fig. 2. For instance, considering a pile-rock interface with a nominal length of L, the length of a series of asperities can be determined through linear interpolation in an ascending sequence within the range of the minimum and maximum asperity lengths. The chord length of the i th ($1 \le i \le$ n) asperity can be expressed as follows:

$$2\lambda_i = 2\lambda_1 + \frac{(2\lambda_n - 2\lambda_1)(i-1)}{n-1} \tag{2}$$

where n is the number of the asperities and $n=L/(\lambda_1+\lambda_n)$; $2\lambda_1$ and $2\lambda_n$ denote the minimum and maximum asperity length, respectively, which can be estimated by field-scanned borehole surface.

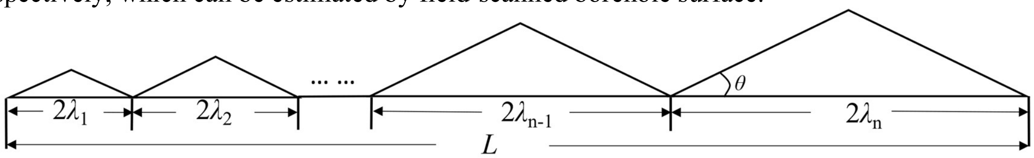

Fig. 2. Sketch of the uniform triangular rock-pile profile

2.3 Single asperity and multi-asperity behavior

The basic friction law can be employed to describe these two stages of shear behavior (Patton 1966):

$$\begin{cases} \tau = \sigma_n \tan(\varphi_i + \theta) \\ \tau_r = \sigma_n \tan(\varphi_r) \end{cases} \tag{3}$$

where τ and τ_r denote the shear stress in the dilation and post-peak stage; φ_i and φ_r are the base friction and residual friction angles; θ is the asperity inclination angle; σ_n represents the normal stress, which is related to the initial normal stress σ_{n0}, dilation displacement, y and spring stiffness, K. The relationship can be expressed as:

$$\sigma_n = \sigma_{n0} + Ky = \sigma_{n0} + Kw\tan\theta \tag{4}$$

where the dilatancy displacement, y, is equal to $w\tan\theta$; w is the relative shear displacement of the interface.

When combining a series of incremental-length asperities at the rock interface, the lift-off behavior needs to be considered. To be specific, as the dilation progresses, the initially closely contacted asperities would be separated, the smaller asperities will lose contact and undertake no more shear stress, as indicated in Fig. 3.

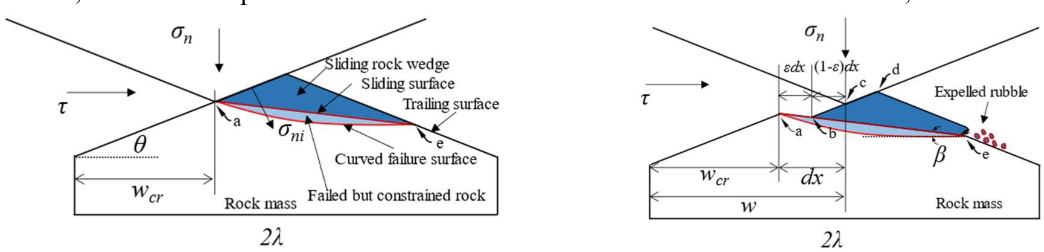

(a) single rock asperity at the critical state (b) newborn wedge slides along the failure surface

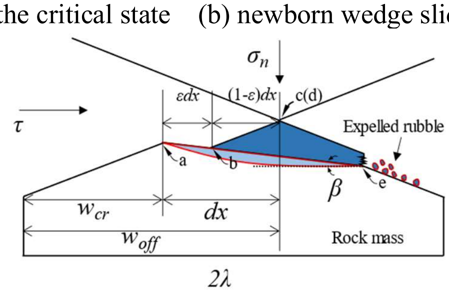

(c) local lift-off of the newly generated wedge

Fig. 3. Shear development of the newborn sliding wedge

3 DERIVATION OF THE MICROMECHANICS-BASED INTERFACE MODEL

3.1 Critical shear displacement with Hoek-Brown model

In this study, the rock mass is regarded as a Hoek-Brown material, the Hoek-Brown failure criterion is defined as follows (Hoek and Brown 2019):

$$\sigma_1' = \sigma_3' + \sigma_{ci}\left(m_b \frac{\sigma_3'}{\sigma_{ci}} + s\right)^a \tag{5}$$

where σ_1' and σ_3' are the major and minor effective principal stresses at failure, respectively; σ_{ci} is the unconfined compressive strength (UCS) of the intact rock mass; m_b is the reduced material parameter derived from m_i for intact rock mass; s and a are the parameters that rely upon the rock mass characteristics. These parameters are functions of the geological strength index (GSI) and can be calculated as follows:

$$\begin{cases} m_b = m_i \exp\left(\dfrac{GSI-100}{28-14D}\right) \\ s = \exp\left(\dfrac{GSI-100}{9-3D}\right) \\ a = \dfrac{1}{2} + \dfrac{1}{6}\left[\exp\left(\dfrac{-GSI}{15}\right) - \exp\left(\dfrac{-20}{3}\right)\right] \end{cases} \tag{6}$$

where D is the disturbance coefficient which varies from 0 for undistributed rock mass to 1 for highly disturbed rock mass; m_i is the constant of the intact rock which counts mainly on lithology and mineralogy of rock and can be obtained from experimental measurements. For intact rock, the constants can be set as s = 1 and a = 0.5.

The ultimate bearing capacity of the weightless rock asperity can be written as (Serrano and Olalla 1994):

$$p_c = \beta\left(N_\beta - \zeta\right) \tag{7}$$

where β and ζ are constants and $\beta = m_b\sigma_c / 8$, $\zeta = 8s / m_b^2$; N_β is the parameter of bearing capacity and $N_\beta = \left(\cot^2 \rho_A\right)/2 + \left(1-\sin\rho_A\right)/\sin\rho_A$; ρ_A is the instantaneous friction angle of zone A.

Following Serrano and Olalla (1994), the stress state associated with the α characteristic line (i.e., Riemann's invariant) can be expressed by Eq. (8) taking into account the Hoek-Brown failure criteria:

$$\frac{1}{2}\left[\cot\rho + \ln\left(\cot\left(\rho/2\right)\right)\right] + \psi = I \tag{8}$$

where ρ is the instantaneous friction angle, defined as ρ=arcsin(dq/dp), where p and q represent the mean stress and deviatoric stress in the plane, respectively; ψ denotes the counterclockwise rotation angle from x-axis to major principal stress; I is the integration constant. Consequently, the stress state in both zone A and zone B can be interconnected by the following relationship:

$$\frac{1}{2}\left[\cot\rho_A + \ln\left(\cot\left(\rho_A/2\right)\right)\right] + \psi_A = \frac{1}{2}\left[\cot\rho_B + \ln\left(\cot\left(\rho_B/2\right)\right)\right] + \psi_B = I \tag{9}$$

where ρ_B is the instantaneous friction angle of zone B and can be calculated as $\rho_B = \sin^{-1}\left(1/\left(1+\sqrt{2\zeta}\right)\right)$. In this analysis, $\psi_B - \psi_A = \delta - \pi/2$. This equation is used to determine the value of ρ_A.

The normal stress on the asperity surface, σ_{ni}, gradually increases with the onward shearing, resulted the dislocation of the asperity and the occurrence of dilation under the CNS boundary condition. When σ_{ni} equals to the ultimate bearing capacity, p_c, the rock asperity enters the critical state. At this point, the asperity undergoes failure and is sheared off, as illustrated in Fig. 3(a) and (b). The value of σ_{ni} at failure can be determined as:

$$\sigma_{ni} = \frac{2\lambda\left(\sigma_n\cos\theta + \tau\sin\theta\right)}{\lambda - w_{cr}} \tag{10}$$

where w_{cr} is the critical shear displacement and can be derived considering $\sigma_{ni} = p_c$ by substituting Eq. (7) and Eq. (10):

$$w_{cr} = \frac{p_c \lambda - 2\lambda \sigma_{n0}\left(\cos\theta + \tan\left(\varphi_i + \theta\right)\sin\theta\right)}{2\lambda K \tan\theta\left(\cos\theta + \tan\left(\varphi_i + \theta\right)\sin\theta\right) + p_c} \tag{11}$$

In the multi-asperity model, the shear-off criterion, $f\left(w_i^{cr}, \lambda_i\right)$, can be given by:

$$f\left(w_i^{cr}, \lambda_i\right) = w - w_i^{cr} = w - \frac{p_c \lambda - 2\lambda \sigma_{n0}\left(\cos\theta + \tan\left(\varphi_i + \theta\right)\sin\theta\right)}{2\lambda K \tan\theta\left(\cos\theta + \tan\left(\varphi_i + \theta\right)\sin\theta\right) + p_c} \tag{12}$$

where the subscript i is the asperity index, when $f\left(w_i^{cr}, \lambda_i\right) = 0$ indicates the failure of i-th asperity.

No sooner had the largest asperity been sheared off than the normal displacement changing from dilation to contraction. A noteworthy aspect of this study is the behavior of the granular material, which is detached from the rock. As depicted in Fig. 4, the separated granular material experiences compression and exhibits translation and rotation at the interfaces with the concrete and rock boundaries.

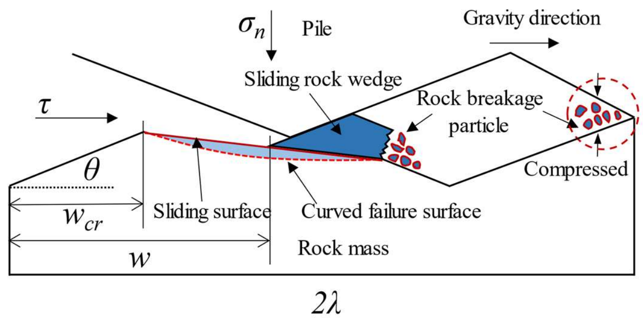

Fig. 4. Local compression after the largest asperity has been sheared off

In order to provide a detailed illustration of this influence on shearing behavior, the red dashed line circle area in Fig. 4 is magnified and shown in Fig. 5. For simplicity, a single rock particle is selected as a representative to analyze the transformation of its morphology. Based on observations from rock compression and sliding tests (Seidel and Haberfield 2002, Gehle and Kutter 2003, Zhu et al. 2010, Xu et al. 2020, Zhao et al. 2023), the hypothetical evolution of particle shape with compression and sliding is depicted in Fig. 5 (a)–(c). The granular material will gradually experience rounding with an increasing shearing displacement, resulting in a lower shear resistance on account of the transition from sliding friction to rolling friction in the global frictional behavior.

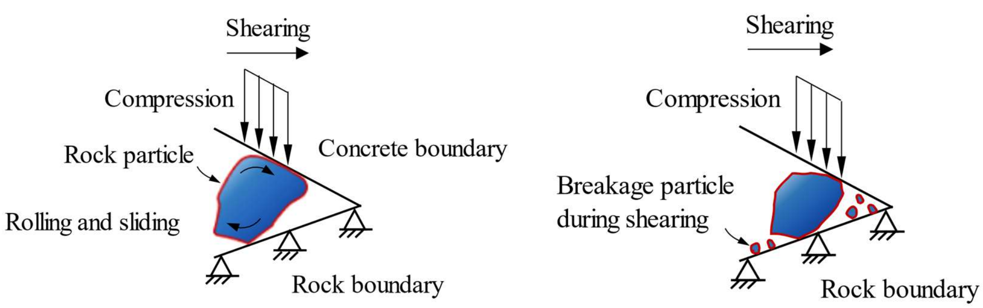

(a) (b)

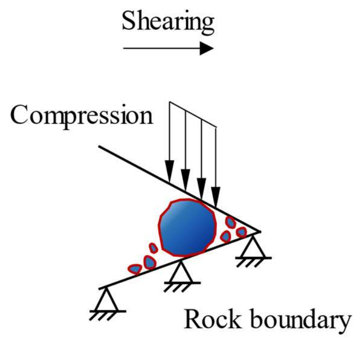

(c)
Fig. 5. Evolution of particle shape with shearing

However, there is currently no established method for quantifying this friction mechanism. Therefore, a novel friction parameter, μ^*, is proposed to describe the shear behavior after the largest asperity has been sheared off, as shown below:

$$\begin{cases} \mu^* = \left(1 - B_r^*\right)\kappa + B_r^* \mu_r \\ B_r^* = \dfrac{w - w_{\max}^{cr}}{b + w - w_{\max}^{cr}} \end{cases} \tag{13}$$

where κ is the friction coefficient after the single asperity has been sheared off; μ_r is the residual friction parameter, $\mu_r = \tan\varphi_r$, φ_r is the residual interface friction angle; B_r^* is the friction degradation factor, which is related to the shear displacement, *w*, the critical displacement of the largest asperity, $w_{\max}^{cr}$ and a constant, *b*, which controls the rate of degradation.

3.2 Schematic representation of calculation result of proposed model

The schematic representation of the calculation results showing the relationship between shear displacement and shear stress using this interface model is presented in Fig. 6. The plot shows the progression of shear in three stages, separated by the two critical displacements. To be specific, in stage 1, the shear stress shows a linear increase with shearing until the minimum asperity is sheared off. In stage 2, as the asperities progressively shear off, there shows an abrupt change in local stress, leading to stress oscillation. After reaching the peak shear stress, a degradation trend is observed on account of the dominance of lift off in the shear behavior. The system enters stage 3 once the shear displacement meets the maximum critical shear displacement, indicating that all the asperities have been sheared off. In stage 3, the shear stress gradually decreases until it stabilizes.

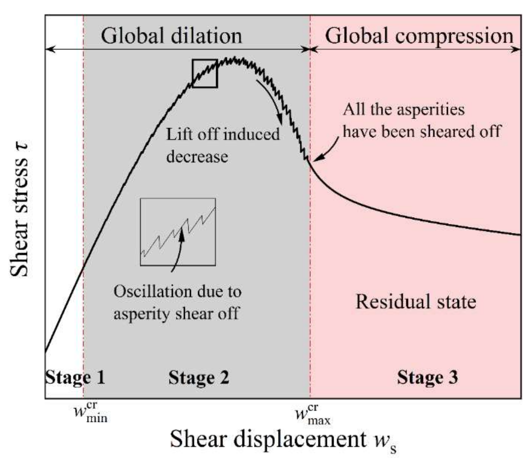

Fig. 6. Schematic representation of calculation result of proposed model

4 FINITE ELEMENT IMPLEMENTATION

4.1 Finite element model of the rock-socketed pile

Fig. 7 shows the schematic and mesh details of the typical axial loaded rock-socketed pile model, incorporating the user-defined interface model. For simplicity, this model is interpreted as 2D axisymmetric. The model has with a width of 20 times the pile diameter, *D*, and a height of 2 times the socket length, *L*, from the socket head to the bottom boundary. The model scale is chosen to be large enough to ignore the boundary effects on pile axial bearing performance (Liang et al. 2021). The tangential behavior between the pile shaft and socket wall is simulated using the user-defined interface model proposed in this study. The pile is assigned an isotropic linear elastic material. The socket and bearing layer are assigned the Hoek-Brown material via using the user material subroutine UMAT following Clausen and Damkilde (2008). The vertical boundary on the left side is an asymmetrical line, while the roller boundary and the fixed boundary are applied on the side and bottom of the model, respectively. A denser mesh is employed near the pile and a coarser mesh is adopted far away from the pile to minimize the influence of the stress concentration and enhance the calculation efficiency. The analysis utilizes four-node bilinear axis-symmetric finite elements (CAX4). In the model verification process, the geostatic step is calculated to establish the initial stress state. After the equilibrium of the geostatic, the equivalent axial pressure is applied with displacement controlled axial loading on the socket head.

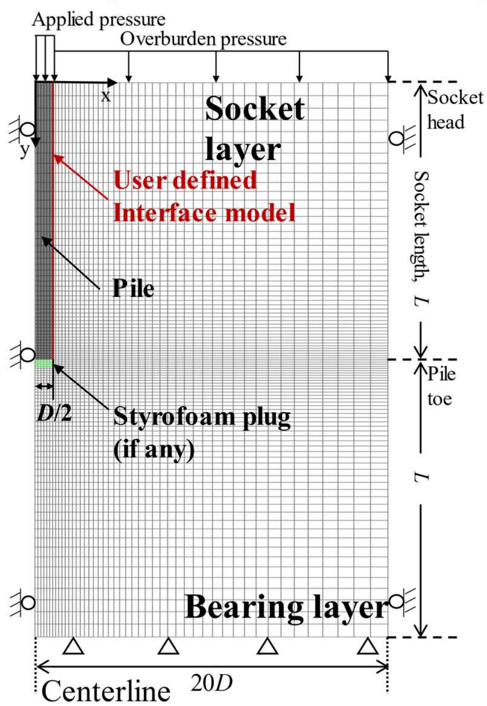

Fig. 7. Schematic representation for the typical 2D axisymmetric axial loaded rock-socketed pile FE model

The flow chart that outlines the user-defined subroutine FRIC for the interface model developed in this study is plotted in Fig. 8. The subroutine takes the constants of the proposed model and the variables computed from ABAQUS as inputs. The subroutine examines the contact pressure (PRESS) and the relative motion flag (LM) to determine the contact status of interface elements and if relative motion is permitted (if the contact point can slip, LM is assigned a value of 0; if the contact point is sticking, LM is equal to 1; if the contact is open, LM is equal to 2). If the conditions are satisfied, the subroutine calculates the shear stress (TAU(1)) and shear stiffness (DDTDDG(1,1)), which are subsequently updated in the main program.

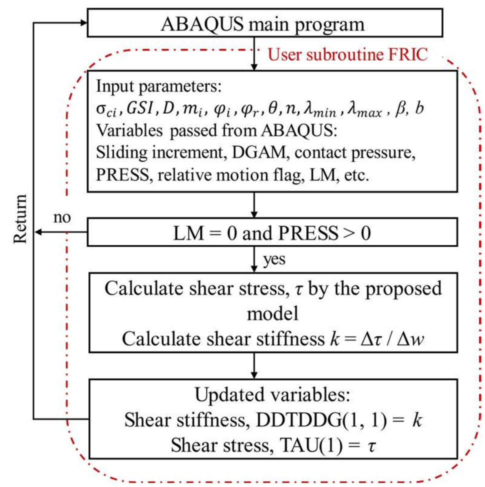

Fig. 8. The flowchart of the user-defined subroutine framework of the proposed analysis

4.2 Application to field cases

4.2.1 Case 1

The shaft under investigation was situated in downtown Dallas, Texas, and the field test was conducted by O'Neill et al. (1996) The sub-soils of the site consisted primarily of a 3 m thick layer of fill, followed by the undisturbed clay-shale with calcareous pockets. The socket was excavated by the soil auger, and the diameter of the tested pile was 0.61 m. The pile was embedded to a depth of 9.44 m, with a socket length of 6.44 m. A Styrofoam plug measuring 0.15 m in thickness was placed beneath the pile toe to exclude base resistance and ensure the complete mobilization of the shaft resistance. Fig. 9(a) provides an illustrative idealized depiction of the cast-in-place pile. The model parameters and interface properties are summarized in Table. 2.

4.2.2 Case 2

The static load test was conducted on bored pile socket into the conglomerate by Skejić et al. (2022) The geotechnical site characterization revealed a layer of sandy gravel and cobbles with a thickness of 4 meters, succeeded by a 7-meter-thick layer of poorly cemented conglomerate, and a transition to well-cemented conglomerate. The combined drilling method, core barrel and casting were utilized to create the borehole. An instrumented pile with a diameter of 0.9 m and an embedded length of 10 m was then constructed. To eliminate any contribution from shaft resistance above the socket level, a steel sleeve with a length of 7 m was installed. Additionally, a 10 cm thick layer of Styrofoam was placed under the pile toe prior to installation, as shown in Fig. 9(b).

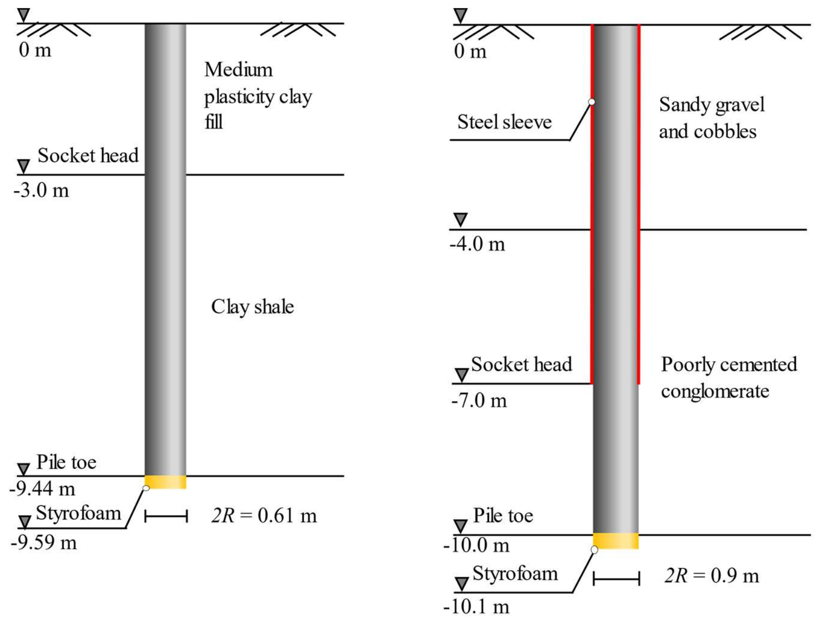

(a) (b)

Fig. 9. Sketch of cast-in-place test pile for different cases: (a) Case 1; (b) Case 2

4.3 Parameters for analysis and comparison results

The material parameters and the interface parameters that are chosen for the finite element analysis based on the field test are summarized in Table 1. The parameters for Hoek-Brown failure criteria, including s_{ci}, GSI, m_i and D are determined following the methods proposed by Hoek and Brown (Hoek and Brown 1997, 2019) and Hoek et al. (2002) The interface profile parameters, such as q , n, l_{min}, and l_{max}, are determined from field-measured borehole roughness. Horvath et al. (1980) defined the roughness factor (*RF*) to quantify the roughness of the rock socket interface, as shown in Eq. (14).

$$RF = \frac{h_m L_t}{R_s L} \tag{14}$$

where R_s is the radius of the socket; h_m, L_t and L represent the average asperity height, travel length and nominal length along the socket side wall, respectively. These parameters can be determined from field scanned roughness data. The calculated *RF* for this idealized nonuniform interface profile can be used to provide additional verification by comparing it to the field-measured *RF*.

Importantly, the laser-based profiling scanning technique estimated the quantitative socket roughness (*RF*) to be 0.0215 in Case 2 (Skejić et al. 2022). Remarkably, the calculated *RF* using the proposed interface model closely matches the site-measured value, with a value of 0.0216. This congruence between the calculated and measured *RF* values provides strong validation for the effectiveness of the proposed profile. Similarly, the calculated *RF* for Case 1 is 0.0076, consistent with the essentially smooth field-measured profile (O'Neill et al. 1996).

Table 1 Material and interface parameters used for finite element analysis

Case	Material type	E MPa	v	σ_{ci} [(b)] MPa	GSI [(b)]	m_i [(b)]	D [(b)]	φ_i °	φ_r °	θ [(c)] °	n [(c)]	λ_{min} [(c)] mm	λ_{max} [(c)] mm	β [(d)] °	b	RF
Case 1																
Socket	Hoek-Brown	232	0.3	1	30	5	0	-	-	-	-	-	-	-	-	-
Pile	Linear elastic	27600	0.3	-	-	-	-	-	-	-	-	-	-	-	-	-
Styrofoam	Linear elastic	10[(a)]	0.3 [(e)]	-	-	-	-	-	-	-	-	-	-	-	-	-
Interface	User-defined	232	0.3	1	30	5	0	30	24	10	100	1	10	-2.4	0.5	0.0076
Case 2																
Socket	Hoek-Brown	1500	0.25	9	50	22	0	-	-	-	-	-	-	-	-	-
Pile	Linear elastic	15000	0.3	-	-	-	-	-	-	-	-	-	-	-	-	-
Styrofoam	Linear elastic	10[(a)]	0.3 [(e)]	-	-	-	-	-	-	-	-	-	-	-	-	-
Interface	User-defined	1500	0.25	9	50	22	0	58	56	30	100	2	25	-5	0.5	0.0216

[(a)] Predicted value by E=0.0097ρ^2−0.014ρ+1.8, ρ is the Styrofoam density (Eriksson and Trank 1991)

[(b)] When field or laboratory tests are unavailable, σ_{ci}, GSI, m_i and D can be estimated from Hoek and Brown (Hoek and Brown 1997, 2019, Hoek et al. 2002)

[(c)] Determined from field measured roughness and verified with roughness factor (RF) (Horvath et al. 1980)

[(d)] Estimated from Seidel and Haberfield (2002)

[(e)] Estimated from Dai et al. (2017)

Fig. 10 presents the measured and simulated axial load distributions with socket depth for the two cases. The FE analysis results predicted by proposed model demonstrates good agreement with the field measurement, capturing the overall load transfer trend accurately. It is clearly observed that as the axial load increases, a substantial portion of the shaft friction is contributed by the upper section of the socket, gradually diminishing towards the pile toe.

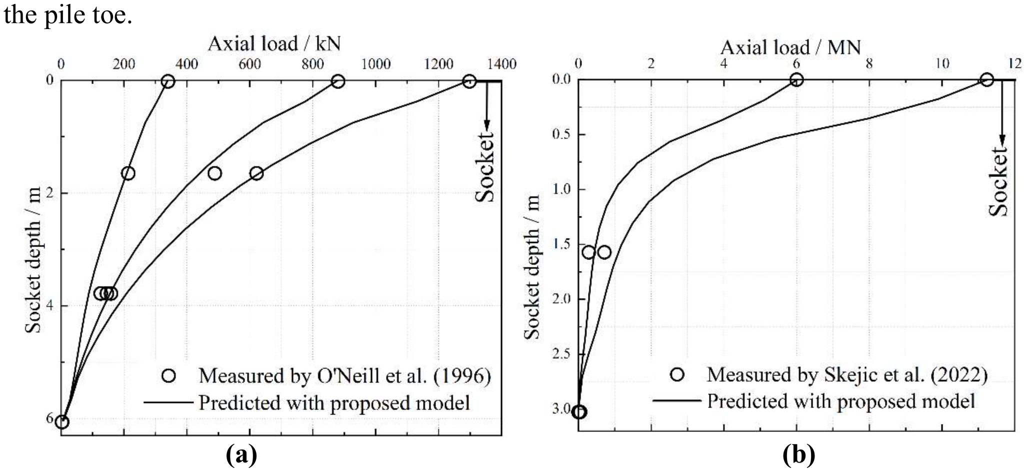

Fig. 10. Simulated and measured axial load distributions with socket depth (a) Case 1; (b) Case 2

5 CONCLUSIONS

This paper provided an enhanced method to estimate the load transfer behavior for the drilled shaft embedded in weak rocks. The micromechanics-based interface model with nonuniform profile was thoughtfully developed with two enhancements. Slip line method combined with nonlinear failure criteria was integrated to derive the critical shear displacement for single rock asperity. The residual state of shearing was well considered based on the evolution of the sheared off debris with the novel friction parameter being proposed. The general shear constitutive function was divided into two scenarios, i.e., global dilation and global compression, to calculate the shear stress. This interface model can be implemented as a user-defined subroutine into the finite element code ABAQUS. This implementation does not require external elaboration to explicitly build the rock-pile interface profile. The applicability of this method was well examined with field-monitored results from literature, in which the axial bearing capacity of the pile was effectively captured.

ACKNOWLEDGEMENTS

The work presented in this paper is supported by the Research Grants Council (RGC) of Hong Kong Special Administrative Region Government (HKSARG) of China (RIF: R5037-18; GRF: 15210020, 15221721, and 15226722).

REFERENCES

Akgüner, C., and Kirkit, M. 2012. Axial bearing capacity of socketed single cast-in-place piles. Soils and Foundations, **52**(1): 59–68. doi:10.1016/j.sandf.2012.01.012.

BD (Buildings Department Technical Committee of Hong Kong). 2017. Code of practice for foundations 2017 of Hong Kong.

Carrubba, P. 1997. Skin friction on large-diameter piles socketed into rock. Canadian Geotechnical Journal, **34**(2): 230–240. doi:10.1139/t96-104.

Carter, J.P., and Kulhawy, F.H. 1988. Analysis and design of drilled shaft foundations socketed into rock.

Castelli, F., Maugeri, M., and Motta, E. 1992. Analisi non lineare del cedimento di un Palo Singolo. RIG, **2**: 92.

Chen, Z.-J., Chen, W.-B., Yin, J.-H., and Malik, N. 2021. Shaft Friction Characteristics of Two FRP Seawater Sea–Sand Concrete Piles in a Rock Socket with or without Debris. International Journal of Geomechanics, **21**(7): 06021015. doi:10.1061/(ASCE)GM.1943-5622.0002059.

Clausen, J., and Damkilde, L. 2008. An exact implementation of the Hoek–Brown criterion for elasto-plastic finite element calculations. International Journal of Rock Mechanics and Mining Sciences, **45**(6): 831–847. doi:10.1016/j.ijrmms.2007.10.004.

Dai, G., Salgado, R., Gong, W., and Zhu, M. 2017. The effect of sidewall roughness on the shaft resistance of rock-socketed piles. Acta Geotechnica, **12**(2): 429–440. doi:10.1007/s11440-016-0470-8.

Dykeman, P., and Valsangkar, A.J. 1996. Model studies of socketed caissons in soft rock. Canadian Geotechnical Journal, **33**(5): 747–759. doi:10.1139/t96-100-321.

Eriksson, L., and Trank, R. 1991. Properties of expanded polystyrene, laboratory experiments. Swedish Geotechnical Institute, Linköping, Sweden,.

Gehle, C., and Kutter, H.K. 2003. Breakage and shear behaviour of intermittent rock joints. International Journal of Rock Mechanics and Mining Sciences, **40**(5): 687–700. doi:doi.org/10.1016/S1365-1609(03)00060-1.

Hoek, E., and Brown, E.T. 1997. Practical estimates of rock mass strength. International Journal of Rock Mechanics and Mining Sciences, **34**(8): 1165–1186. doi:10.1016/S1365-1609(97)80069-X.

Hoek, E., and Brown, E.T. 2019. The Hoek–Brown failure criterion and GSI–2018 edition. Journal of Rock Mechanics and Geotechnical Engineering, **11**(3): 445–463. doi:10.1016/j.jrmge.2018.08.001.

Hoek, E., Carranza-Torres, C., and Corkum, B. 2002. Hoek-Brown failure criterion-2002 edition. Proceedings of 5th North American Rock Mechanics Symposium,: 267–273.

Horvath, R.G., Kenney, T.C., and Trow, W.A. 1980. Results of tests to determine shaft resistance of rock-socketed drilled piers. *In* International Conference on Structural Foundations on Rock.

Johnston, I.W., and Lam, T.S. 1989. Shear behavior of regular triangular concrete/rock joints—analysis. Journal of Geotechnical Engineering, **115**(5): 711–727. doi:10.1061/(ASCE)0733-9410(1989)115:5(711).

Kou, H.-L., Guo, W., Zhang, M.-Y., and Xu, Y.-Q. 2016. Axial resistance of long rock-socketed bored piles in stratified soils. Ocean Engineering, **114**: 58–65. doi:10.1016/j.oceaneng.2016.01.013.

Leung, C.F., and Ko, H.Y. 1993. Centrifuge model study of piles socketed in soft rock. Soils and Foundations, **33**(3): 80–91. doi:10.3208/sandf1972.33.3_80.

Li, Y.-C., Sun, S.-Y., and Tang, C.-A. 2019. Analytical prediction of the shear behaviour of rock joints with quantified waviness and unevenness through wavelet analysis. Rock Mechanics and Rock Engineering, **52**(10): 3645–3657. doi:10.1007/s00603-019-01817-5.

Liang, R., Yuan, Y., Fu, D.-F., and Liu, R. 2021. Cyclic response of monopile-supported offshore wind turbines under wind and wave loading in sand. Marine Georesources & Geotechnology, **39**(10): 1230–1243. doi:10.1080/1064119X.2020.1821848.

Ng, C.W., Yau, T.L., Li, J.H., and Tang, W.H. 2001. Side resistance of large diameter bored piles socketed into decomposed rocks. Journal of Geotechnical and Geoenvironmental Engineering, **127**(8): 642–657. doi:10.1061/(ASCE)1090-0241(2001)127:8(642).

Omer, J.R., Delpak, R., and Robinson, R.B. 2002. Instrumented load tests in mudstone: pile capacity and settlement prediction. Canadian Geotechnical Journal, **39**(6): 1254–1272. doi:10.1139/t02-072.

O'Neill, M.W., and Hassan, K.M. 1994. Drilled shafts: Effects of construction on performance and design criteria. *In* Proc., Int. Conf. Des. Constr. Deep Founds. Orlando, FHWA.

O'Neill, M.W., Townsend, F.C., Hassan, K.M., Buller, A., and Chan, P.S. 1996. Load transfer for drilled shafts in intermediate geomaterials.

Patton, F.D. 1966. Multiple modes of shear failure in rock. *In* 1st ISRM Congress.

Seidel, J.P., and Haberfield, C.M. 2002. A theoretical model for rock joints subjected to constant normal stiffness direct shear. International Journal of Rock Mechanics and Mining Sciences, **39**(5): 539–553. doi:10.1016/S1365-1609(02)00056-4.

Seol, H., Jeong, S., and Cho, S. 2009. Analytical method for load-transfer characteristics of rock-socketed drilled shafts. Journal of Geotechnical and Geoenvironmental Engineering, **135**(6): 778–789. doi:10.1061/(ASCE)1090-0241(2009)135:6(778).

Serrano, A., and Olalla, C. 1994. Ultimate bearing capacity of rock masses. *In* International Journal of Rock Mechanics and Mining Sciences & Geomechanics Abstracts.

Skejić, A., Gavrić, D., Jurišić, M., and Rahimić, Đ. 2022. Experimental and Numerical Analysis of Axially Loaded Bored Piles Socketed in a Conglomerate Rock Mass. Rock Mechanics and Rock Engineering, **55**(10): 6339–6365. doi:10.1007/s00603-022-02932-6.

Tian, H.M., Chen, W.Z., Yang, D.S., and Yang, J.P. 2015. Experimental and numerical analysis of the shear behaviour of cemented concrete–rock joints. Rock Mechanics and Rock Engineering, **48**(1): 213–222. doi:10.1007/s00603-014-0560-6.

Williams, A.F. 1980. The design and performance of piles socketed into weak rock.

Xu, J., Haque, A., Gong, W.M., Gamage, R.P., Dai, G., Zhang, Q., and Xu, F. 2020. Experimental study on the bearing mechanisms of rock-socketed piles in soft rock based on micro X-ray CT analysis. Rock Mechanics and Rock Engineering, **53**(8): 3395–3416. doi:10.1007/s00603-020-02121-3.

Zhan, C.-Z., and Yin, J.-H. 2000. Field static load tests on drilled shaft founded on or socketed into rock. Canadian Geotechnical Journal, **37**(6): 1283–1294. doi:10.1139/t00-048.

Zhao, H., Hou, J.-C., Zhang, L., and Zhao, M. 2021. Towards concrete-rock interface shear containing similar triangular asperities. International Journal of Rock Mechanics and Mining Sciences, **137**: 104547. doi:10.1016/j.ijrmms.2020.104547.

Zhao, H., Hou, J.C., and Zhao, M.-H. 2022. A micromechanics-based model for concrete-rock interface with similar triangular asperities. International Journal of Rock Mechanics and Mining Sciences, **157**: 105183. doi:10.1016/j.ijrmms.2022.105183.

Zhao, L.-Y., Lv, Z.-M., Lai, Y.-M., Zhu, Q.-Z., and Shao, J.-F. 2023. A new micromechanical damage model for quasi-brittle geomaterials with non-associated and state-dependent friction law. International Journal of Plasticity, **165**: 103606. doi:10.1016/j.ijplas.2023.103606.

Zhu, Q.Z., Shao, J.F., and Mainguy, M. 2010. A micromechanics-based elastoplastic damage model for granular materials at low confining pressure. International Journal of Plasticity, **26**(4): 586–602. doi:10.1016/j.ijplas.2009.09.006.

The Redundancy of Systematic Rock Bolts in Cavern Construction

A. K. L. Kwong, Ph.D.
Adjunct Professor, The University of Hong Kong

ABSTRACT

The general design approach for the permanent supporting system of caverns and drained tunnels with more than half a span of rock cover follows a 3-Stages Approach, which is 1) deriving the initial supporting types based on the NGI Q-system (2015), 2) checking of the initial supporting types by Reinforced Rock Arch (RRA, Bischoff and Smart, 1977) theory and 3) verifying the design by finite element analyses to confirm the support requirements arrived from 1) and 2) above.

The development and use of the Q-system for the temporary and permanent design of rock bolts and shotcretes are routinely used in practice, which would not require any deliberations. For the RRA approach, the concept is to form a reinforced rock arch from the systematic rock bolts around the opening by improving the confining pressure to increase the surrounding rock mass strength, which, in theory, provides a better utilization of the rock mass strength than that of the rock bolts.

In this study, 3D and 2D finite element analyses have been carried out to investigate the soil-structure interaction and load transfer mechanism from the rock stress to the rock bolts at each stage of excavation. Typical rock mass properties commonly adopted in Hong Kong are used, and a large cavern span of 32 m and height of 36 m is used. With the use of the same material properties and geometry, finite element simulations are carried out using the 3D software RS3 to generate the ground convergence-support reaction curve and compare it with the longitudinal displacement profile (Vlachopoulos and Diederichs, 2009) for predicting the amount of ground relaxation before the supporting bolts are activated. Based on the ground convergence-support reaction curve from the RS3, another 2D finite element program, RS2, compares the load developed in the systematic rock bolts in a 2D plane strain vs a 3D stress environment.

The paper discusses the stress distribution, plastic zones, convergence in the rock mass and the development of rock bolt loads before, during and after each stage of excavation. With different ranges of Q-value tested, it can be concluded that the ground behaves nearly in an elastic behavior due to the low stress-to-strength ratio of the rock mass, and the load mobilized in the rock bolts has an insignificant contribution to the cavern convergence, stress redistribution due to the free-moving boundary conditions at the cavern walls, as demonstrated by a low mobilized working force less than 20% of the tensile strength of the working forces developed in both the 2D and 3D analyses. The systematic rock bolts in a homogeneous isotropic rock mass can be considered a redundant and prescriptive measure. Its main contribution will only be developed in a jointed rock mass by increasing the confining stresses across the rock joints and mobilizing the shearing resistance of the jointing materials.

1 INTRODUCTION

The general design approach for the permanent supporting system of caverns and drained tunnels with more than half a span of rock cover follows a 3-Stages Approach, which is 1) deriving the initial supporting types based on the NGI Q-system (2015), 2) checking of the initial supporting types by Reinforced Rock Arch (RRA, Bischoff and Smart, 1977) theory and 3) verifying the design by finite element analyses to confirm the support requirements arrived from 1) and 2) above.

The development and use of the Q-system for the temporary and permanent design of rock bolts and shotcretes are routinely used in practice, which would not require any deliberations. For the RRA approach, the concept is to form a reinforced rock arch from the systematic rock bolts around the opening by improving the confining pressure to increase the surrounding rock mass strength, which, in theory, provides a better utilization of the rock mass strength than that of the rock bolts.

Using the RRA approach has become popular in Hong Kong due to increasing cavern developments, with cost savings when a cast in-situ concrete lining is not required after the temporary supports are installed. The concept is illustrated schematically in Figure 1 that a reinforced rock arch can be developed if the rock strength can be mobilized (Points 1 to 2) by increasing the confining stresses (Points A to B) due to introducing the systematic rock bolts within the stress redistributed zone.

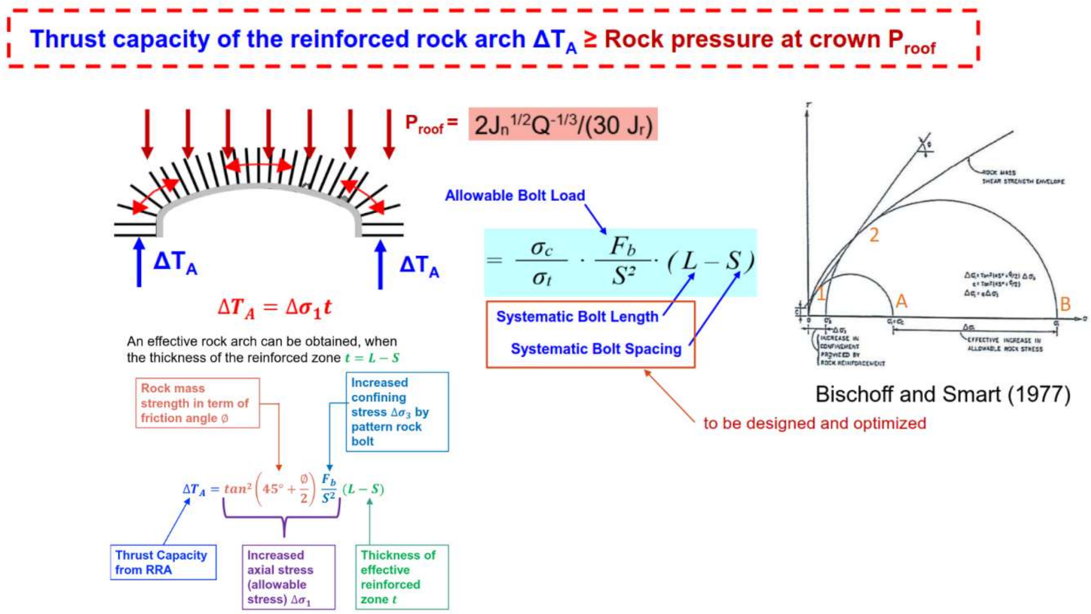

Figure 1: Concept of RRA in a Stress Redistributed Area

The theoretical basis for this concept is sound. Still, it is not evident to the author during the construction stages whether the sequence of excavations followed by bolt installation mimics the assumed boundary conditions in the numerical modeling and whether the bolts can generate a reinforced arch to increase the rock strength. We know that the contribution of the bolts is a stress-path-dependent problem in rock mechanics, which means that the outcome of the redistributed stress depends on the intended construction sequences.

The moving front of the tunnel and cavern excavation is a three-dimensional process where we know stresses and deformation will occur ahead of the tunnel face before the face is reached.

In a typical design, 2D finite element analyses confirm the support requirements from the Q-system and RRA. Due to the limitation of the 2D plane-strain problem, a method was developed by Vlachopoulos and Diederichs (2009) to estimate the amount of convergence occurring before the bolts are installed. The numerical process is referred to as the ground convergence-support reaction approach. As illustrated in Figure 2 for a fictitious case, the Longitudinal Ground Convergence curve (Figure 2B) is predicted based on the equations and calibration works from Vlachopoulos and Diederichs (2009); the supports are installed at a distance behind the face (Point A), and the supports in the 2D finite element program is activated (Point B) to bring into equilibrium for arriving the stress redistributed state (Point C). In the numerical process, the simplified procedure is to reduce the face support pressure (by internal pressure or modulus reduction) from full overburden to zero in multiple stages to represent the tunnel face advance, measure the deformation to generate the ground convergence curve (u in transverse direction in Figure 2A), measure the plastic zone radius, generate the Longitudinal Ground Convergence curve, determine the bolt installing distance from the face (Point A), calculate the amount of movement (Point B) occurring before the tunnel reaches the face, activate the bolts at the stage when the ground has converged some distances (Point B in Figure 2A) and finally let the computer runs until equilibrium is reached (Point C).

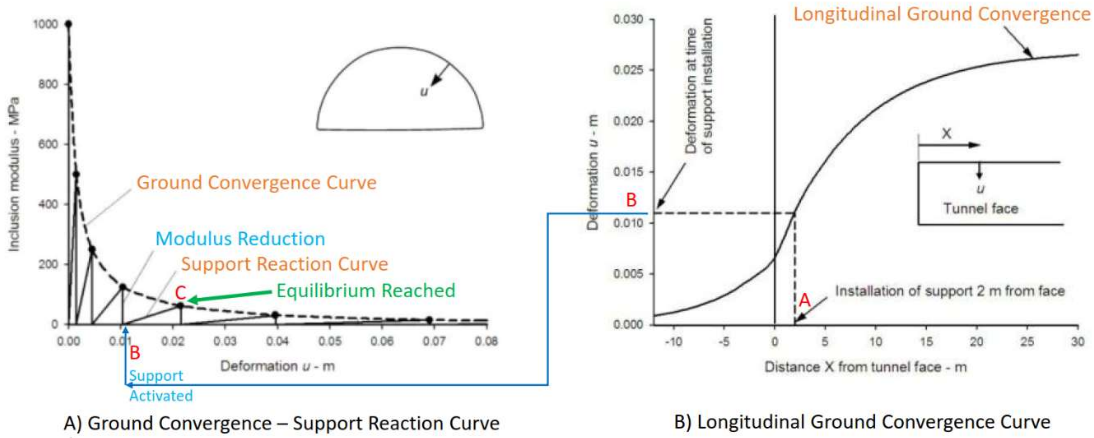

Figure 2: Concept of Convergence-Support Reaction Approach

2 FINTIE ELEMENT MODELLING

2.1 Rock Stress to Strength Ratio

For general purposes, the finite element analysis usually assumes the rock mass to be homogeneous and isotropic, including distinctive weak planes representing rock joints. For a nominal tunnel/cavern depth of 200 m, typically in Hong Kong, with a moderate unconfined compressive strength of 50 MPa of Grade III or better rock where the unit weight is taken as 27 kN/m^3, the stress-to-strength ratio is considered low 0.11. Based on the work by Martin, Kaiser and McCreath (1999), for a low in-situ stress ratio of less than 0.15, linear elastic rock response to falling of rock blocks between weak joint features is expected depending on whether the Rock Mass Rating (RMR) is higher than or lower than 75, essentially stating that it is a kinematic controlled stability problem rather than a stress-yielding problem. With this fundamental principle in mind, the author has worked on a few tunneling and cavern projects in Hong Kong and observed that the ground convergence-support reaction curves obtained from 2D finite element studies are usually linear and that the ground has already significantly moved before the supports are activated in the program. A late activation of support in the convergence curve can be interpreted as most of the stress redistribution due to excavation is taken up by the rock mass instead of the structural capacity of the rock bolts. The above observations triggered the author to analyze the contribution of systematic rock bolts under the RRA approach. With the help of a 3D finite element program, the assumption in Vlachopoulos and Diederichs (2009) can be eliminated for predicting the longitudinal ground convergence curve for use in a 2D finite element program. First, we look at the results from the 3D finite element program (RS3) and then from the 2D finite element program (RS2).

2.2 Geometry and Rock Properties

A hypothetical case is presented in Figure 3, with the geometry set close to some typical caverns in Hong Kong to make the outcome practically near what is usually experienced.

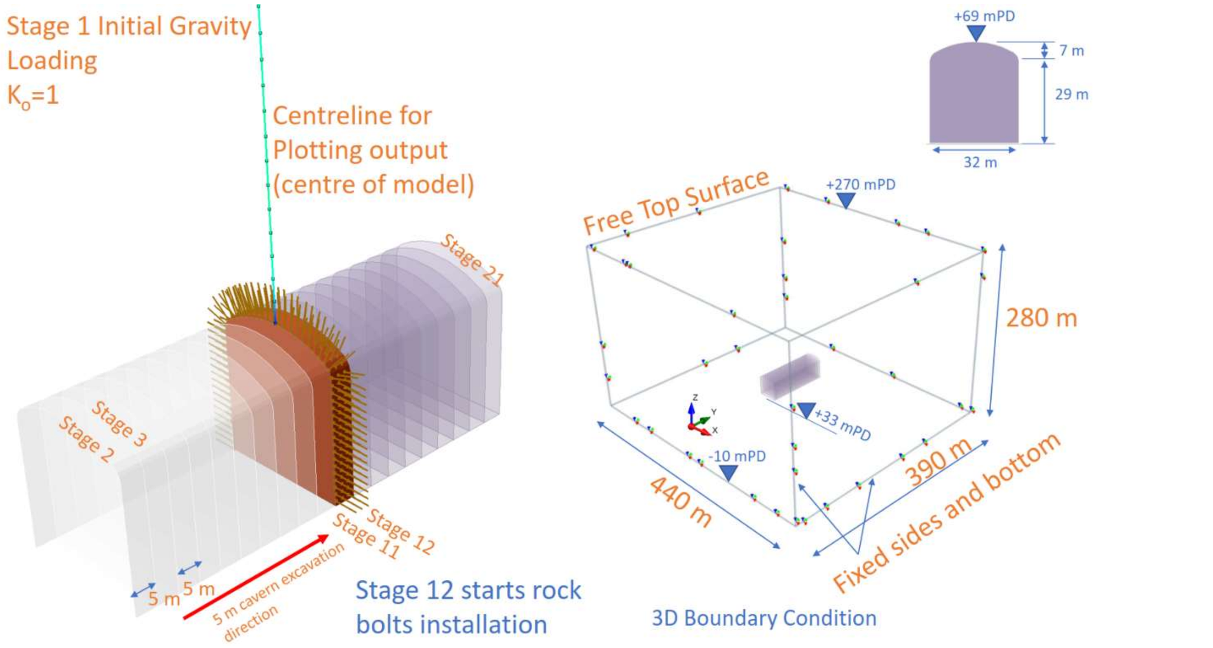

Figure 3: Geometry and Boundary Condition of a 3D Model

The cavern has a span of 32 m and a height of 36 m, situated about 200 m below the ground surface. The model has a free top surface with the bottom fixed in the boundary conditions. Gravity is turned on at Stage 1 for K^0 equal to 1, allowing the side boundary to slide down, and the stresses arrive at equilibrium before the subsequent tunneling stages at 5 m intervals. The boundary surface is set at more than 10 times the geometry to avoid the effects of the boundary constraints. Tunneling is represented by modeling a 5 m full-scale excavation from left to right, as shown in Figure 3, where Stage 11 is just before reaching the center section line of interest and Stage 12 is the stage of excavation and bolt installation in one step. The tunnel continues until it is far from the center section line of interest, essentially modeling from a virgin ground; it passes through the section line of interest and finally away outside the zone of influence.

The rock properties are based on the author's experience and simplified to allow a relatively low Q value of 1.9 in the study, with the key parameters shown in Table 1. Parametric studies to lower the Q value to 0.22 have been carried out. Still, they will not be reported here because the mechanism being developed has not changed. The mechanism discussed in the later section is not sensitive to the assumed parameters but to the modeling sequence.

Table 1: Rock Properties Assumed

Unit weight = 26 kN/m^3	Poisson’s Ratio = 0.3	
Intact Rock UCS = 75000 kPa	Young’s Modulus = 7.7e+06 kPa	
Generalized Hoek-Brown Criterion	Peak Strength	Residual Strength
	GSI=54	GSI=37
	m_i=32	m_i =3.39
	m_b=6.18965	m_b=0.316198
	s=0.006029	s=0.000912
	a=0.504342	a=0.513932
	σ_{cm}=24.7 MPa	σ_{cm}=17.7 MPa
Rock Mass Elastic Modulus EI=2e+07 kPa		
Bolt diameter = 25 mm	Bolt modulus = 2e+08 kPa	Tensile capacity = 125 kN

Bolt type = fully bonded	Bolt spacing = 1.67 m c/c transverse and longitudinal direction	Bolt length = 6 m

2.3 RS3 3D Finite Element Results

The nominal thickness of the plastic zone after all the stages are completed and with systematic bolts added in Stage 12 is about 5.3 m, which is slightly less than the bolt length. Figure 4 shows the change in vertical stresses at the cavern crown centerline as the tunnel advances.

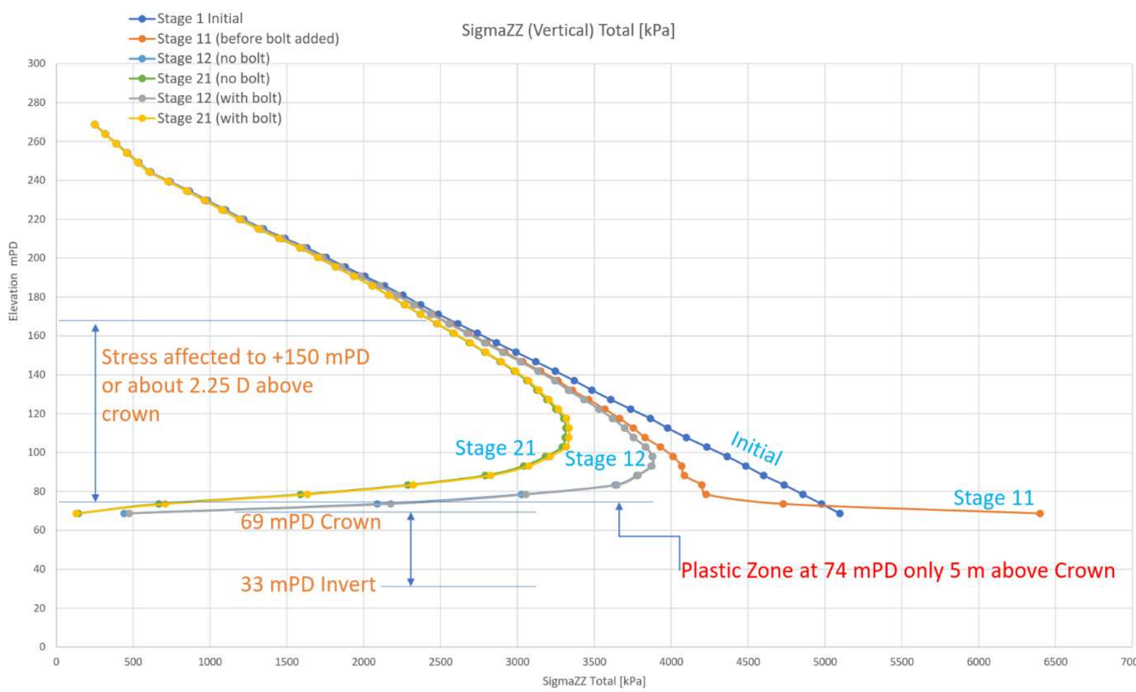

Figure 4: Change of Vertical Stress at the Model Cavern Centerline

1) Some observations can be made. Just before the excavation and without the bolts installed (Stage 11), the vertical stresses increased due to arching developed ahead of the tunnel crown in a longitudinal manner. Immediately after excavation and bolt added (Stage 12), the vertical stresses were reduced below the initial hydrostatic reference due to stress redistribution. Vertical stress was further reduced when the tunnel reached the end (Stage 21). The stresses were affected within a zone of about 2.25 D above the crown, where D is the equivalent diameter of the cavern. What is most interesting and the study's objective is that the stresses are not influenced by whether systematic bolts were added to the cavern.

2) The longitudinal ground convergence curve is depicted in Figure 5A, whereas the normalized displacement (vertical displacement divided by maximum displacement as the tunnel passes through) is shown in Figure 5B. It can be seen from Figure 5A that there is no difference between with or without bolts added to the convergence curve. In Figure 5B (after displacement normalized), the shape of the convergence curve follows closely to that of the 3D model if it is treated as an elastic material without bolts. The observation echoes the concept in Section 2.1 that for a low in-situ stress ratio, a linear elastic rock response may dominate the mechanism.

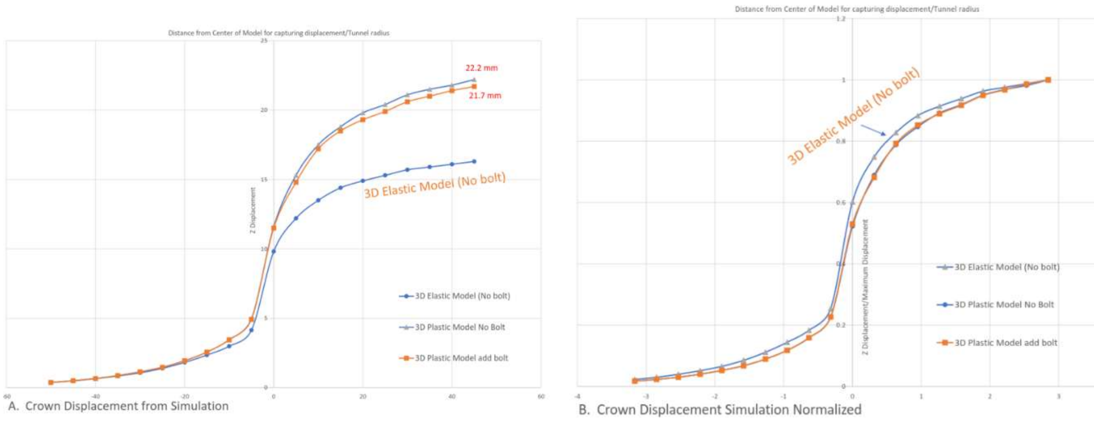

Figure 5: Longitudinal Ground Convergence Curve at the Model Cavern Centerline

3) Figure 5B also suggests that 50% of the convergence occurred before the excavation reached the study centerline of the crown, which may be interpreted as the rock mobilizing its strength earlier than the bolts can be added after excavation.

2.4 RS2 2D Finite Element Results

As discussed in Section 1, the Longitudinal Ground Convergence curves have been developed based on analytical equations by Vlachopoulos and Diederichs (2009) by parametric studies of varying tunnel radii; overburden stresses, in-situ stress to rockmass strength ratio for a 2D problem. The normalized longitudianl displacement profiles from Vlachopoulos and Diederichs (2009) against the normalized plastic radius (R^*) for seven different cases (A_2, B_2, C_2, D_2, E_2, F_2 and G) under a constant unconfined compressive strength for rock mass are reproduced in Table 2 and plotted together in this study for comparison.

Table 2: R* vs maximum displacement after Vlachopoulos and Diederichs (2009)

Constant unconfined compressive strength rock mass 2.8 MPa	A_2	B_2	C_2	D_2	E_2	F_2	G_2
R*	7.5	6.3	5.0	3.3	2.2	1.6	1
u_{max} (m)	2.14	1.25	0.632	0.242	0.0585	0.00167	0.0753

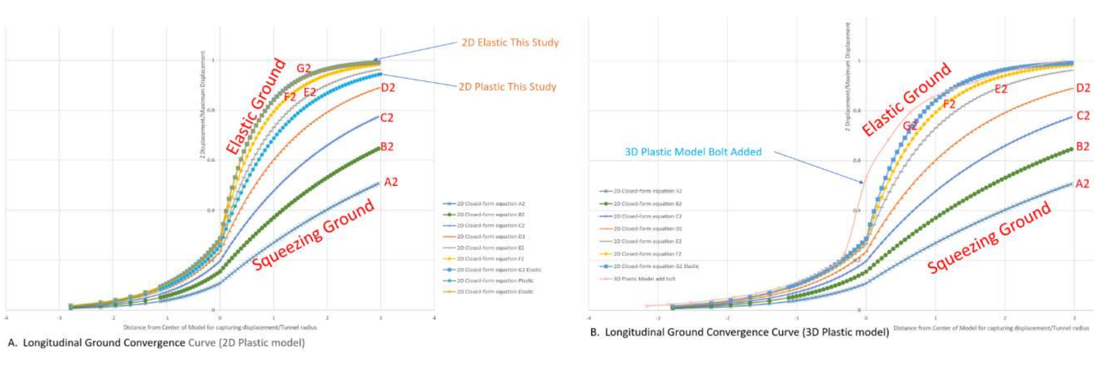

Figure 6: Longitudinal Ground Convergence Curve 2D and 3D Models, Generated after Vlachopoulos and Diederichs (2009)

Figure 6A reveals that under this study for 2D elastic or 2D plastic analysis, the Longitudinal Ground Convergence Curves, when compared to Vlachopoulos and Diederichs (2009), who carried out an extensive range of analysis under varying in-situ stress/rock mass strength ratios, show that our failure mechanisms should more resemble the elastic ground or slightly plastic behavior. The 3D plastic model with bolts added in this study (Figure 6B) shows about 90% of the displacement would behave elastically.

Figure 7 compares the Longitudinal Ground Convergence Curves for the 2D elastic model, 2D plastic model, 3D plastic model without bolts and 3D plastic model with bolts added. Two observations can be made. First, the 3D plastic model is close to the 2D elastic model. Second, there is no difference between whether bolts are added in the 3D analysis.

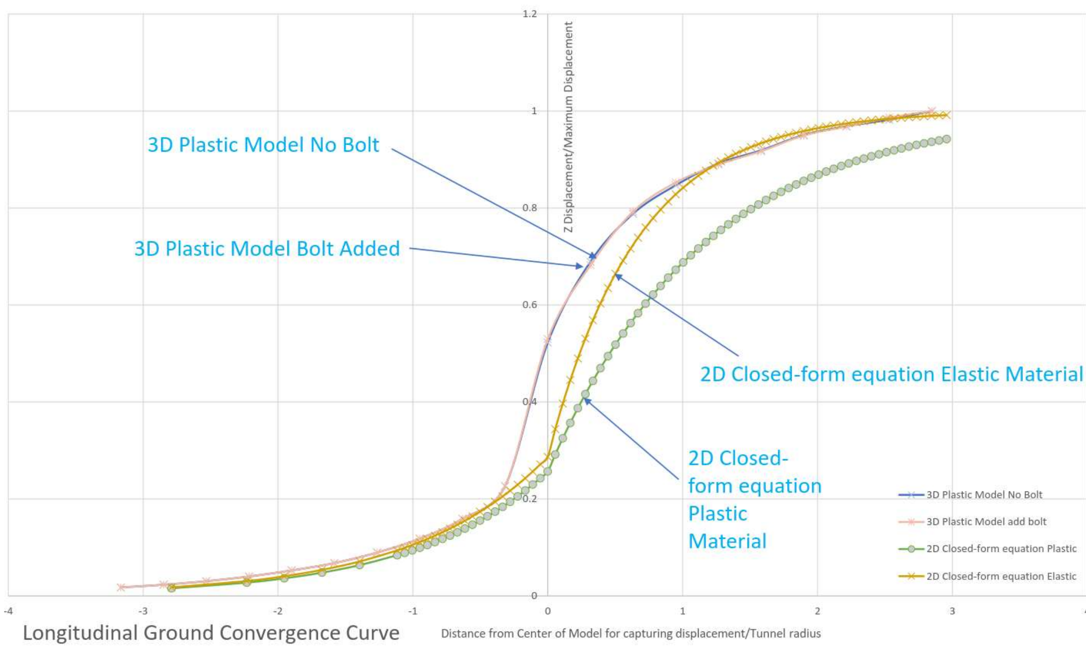

Figure 7: Longitudinal Ground Convergence Curves for 2D and 3D models

The above assessment provides insight into the problem that our failure mechanisms should more resemble the elastic ground or slightly plastic behavior for a low stress-to-strength ratio and that more than 50% of the convergence occurred before the excavation reached, which means that the rock mobilizing its full strength before the bolts can be added after excavation.

All the bolt forces are mobilized due to the movement of the ground, as shown in Figure 8. However, it cannot be seen if there is any contribution to reducing the convergence of a tunnel or stress redistribution. In other words, the concept of forming a reinforced rock arch by increasing the confining stresses due to introducing the systematic rock bolts within the stress redistributed zone is not supported.

Rock bolts can only be installed after the excavation is completed. Whether using a 2D or 3D program, the modeling process and sequencing mimics the construction sequence and controls the outcome more than the material properties. The following section explains why the added bolts do not reduce the convergence and stress state.

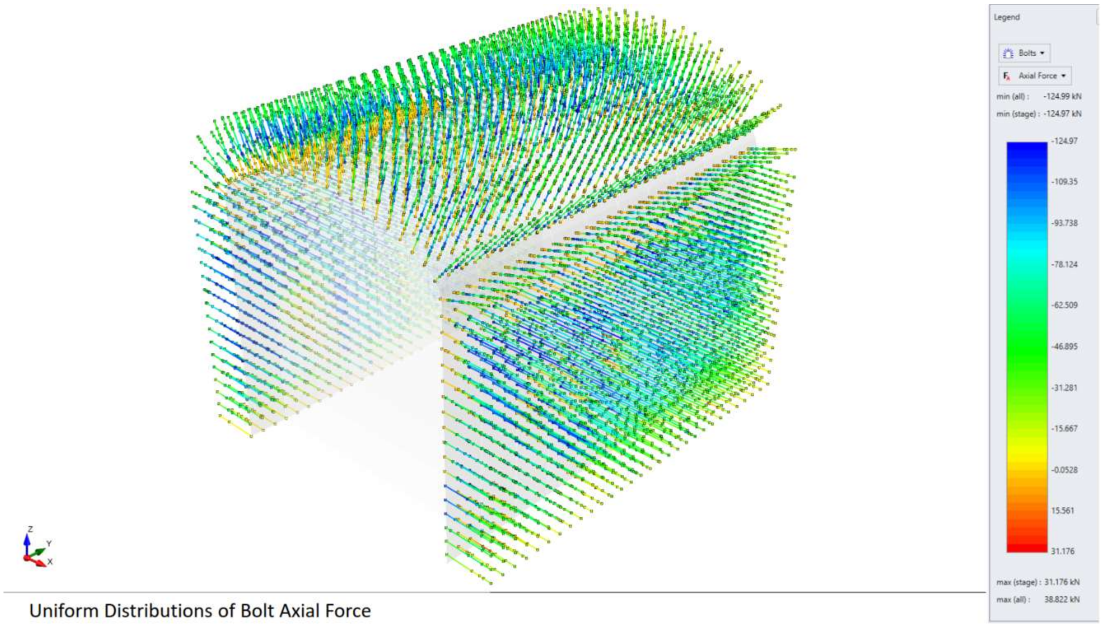

Figure 8: Distribution of Rock Bolt Axial Forces

3 STRESS PATH DEPENDENT PROBLEM

It is well-recognized that geotechnical problems are stress path-dependent, where the outcome depends on the loading sequence far more than the adopted material properties. Figure 9, using an example available from RS2, illustrates that for the same geometry, initial stress state and material properties, the tunnel will behave entirely differently depending on whether the slope is cut first or the tunnel is excavated first.

For the 3D model in this study, Figure 10 shows the extent of the plastic zone and the affected elastic zone based on the plot of stress distribution from Figure 4. It can be seen that the rock bolt length slightly extended beyond the plastic zone into the elastic zone. However, stresses and displacement are affected about 2 times the cavern span, and the cavern boundary perimeter is free to move inward together with the bolts. Unless the bolts are very long and anchored into the undisturbed zone, similar to an analogy of a soil nail grouted outside the slip planes, the bolts and the rock mass will move inward together, stresses in the radial direction are released and confining stresses cannot be built up due to the cavern perimeter has a free moving boundary condition during the unloading excavation sequence.

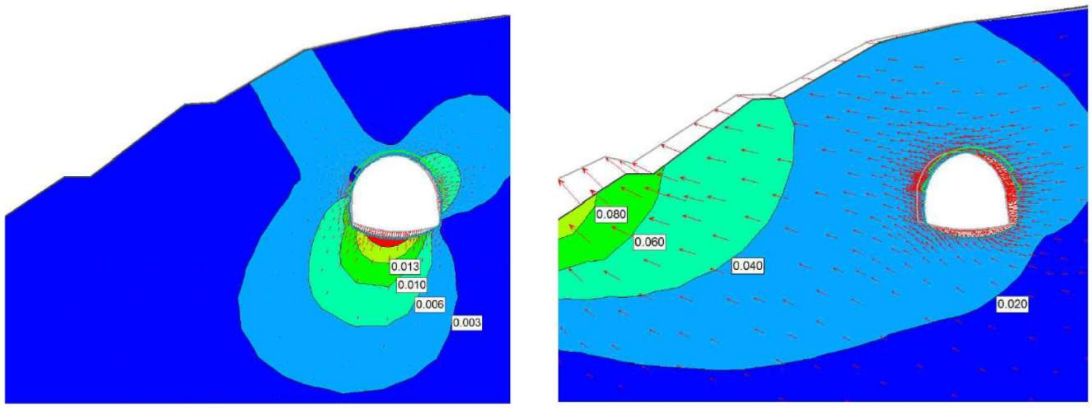

A. The slope is cut first and then tunnel excavated.

B. The tunnel is excavated first, then slope is cut.

The effects of excavation sequence

Figure 9: Illustration of a Stress Path Dependent Problem

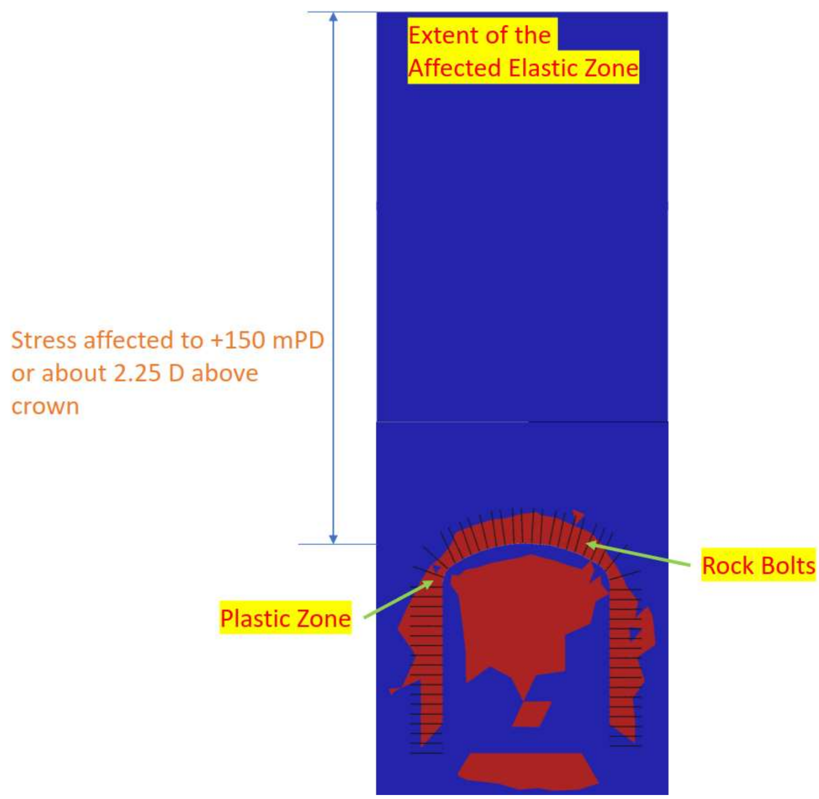

Figure 10: Plastic Zone and Affected Elastic Zone in 3D Model

3.1 Tunnel under a Fixed Boundary and Loading Up.

We can arbitrarily create a boundary condition and loading stage for an opening using the 3D program (RS3) to see if displacement can be reduced and the radial stresses increased due to the contribution of the rock bolts added to the system, as shown in Figure 11. In this example, a small 2 m diameter tunnel in an elastic medium under K_0 equal to 1 is applied with a uniform stress of 10 MPa with the Y longitudinal direction fixed to mimic the plane strain condition. The bolt diameter is 25 mm, the modulus is 116667 MPa, the tensile capacity is 100 MN, 1 m long, and 0.1 m center-to-center is installed. The tunnel is assumed to be formed already, and the load is applied at the far-field boundary. Such boundary and loading conditions do not represent the actual cavern/tunnel excavation sequence; perhaps they represent a reinforced structure with a window opening under some externally applied loads. The results are presented in Figure 12.

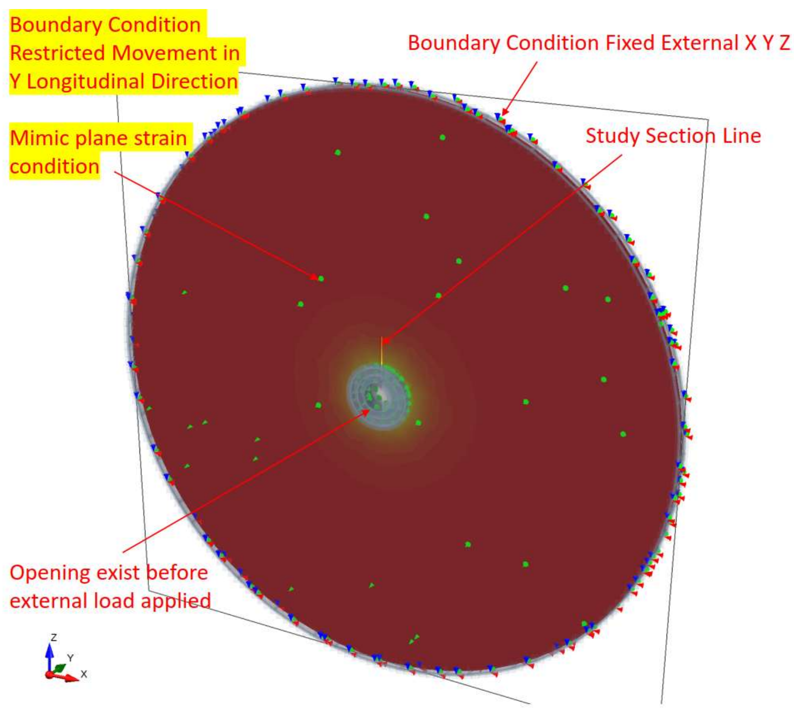

Figure 11: Opening under Axisymmetric Loading with Bolts Added

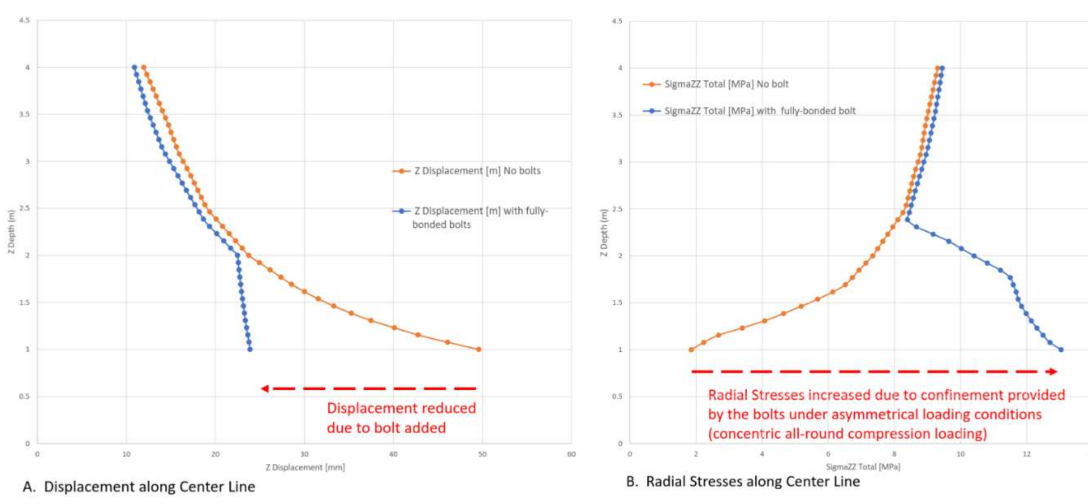

Figure 12: Displacement and Stress Changes under Axisymmetric Loading with Bolts Added

It can be seen from Figure 12A that the displacements are reduced and from Figure 12B that the radial stresses are increased under a very specific boundary condition, which unfortunately does not represent tunneling.

3.2 Benefits of Rock Bolts

The utilization rate (axial bolt force mobilized divided by the bolt tensile capacity) is generally low at less than 5%, as shown in similar studies with different material properties, stress range, and depth. It increases with the decrease of the Q value, which suggests that the rock mass shared the load from redistribution rather than the structural capacity of the bolt.

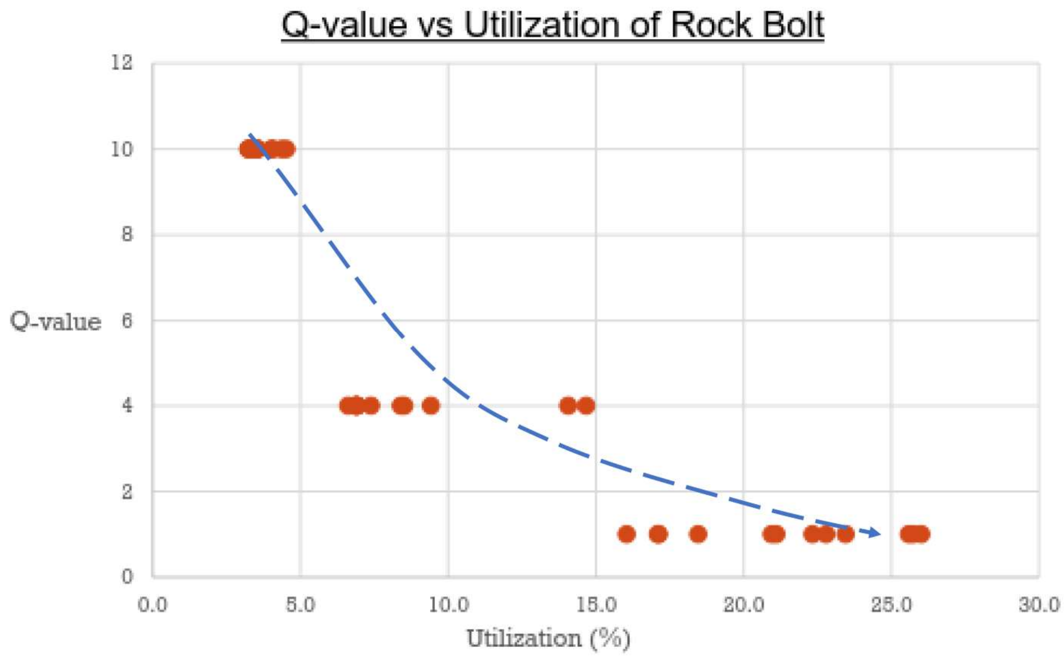

Rock is heterogeneous and anisotropic, a condition different from the assumption made in the 3D finite element studies. The systematic bolts from the ideal homogeneous rock mass study are redundant because they neither reduce the convergence of a cavern/tunnel nor change the stress state during the redistribution process. However, the rock bolts can be considered prescriptive because they lessen the possible kinematic failure of rock blocks formed in adverse joint orientation. They also limit joint slippage, dilation and movement, indirectly increasing the rock joints' strength and maintaining the opening's stability.

4 CONCLUSIONS

Some observations can be made from this study:

Vertical stresses increase ahead of the tunnel crown in a longitudinal manner due to arching developed forward.

There is no difference between with or without bolts for stress redistribution and convergence.

For a cavern excavation, the bolts are situated in the plastic zone and relatively short compared to the cavern perimeter size, where bolts, plastic zone and cavern boundary (crown and two sidewalls) all move inward together, which will not allow the confining stresses to build up, a condition very different from that of an ideal circle under axisymmetric loading.

The 3D model shows that the normalized longitudinal ground convergence curve resembles the elastic ground or slightly plastic ground.

The low in-situ stress-to-strength ratio causes a linear elastic rock response.

The 3D model suggests that 50% of the convergence occurred before reaching the excavation face.

A low utilization rate suggests that the rock mass strength is mobilized, sharing the load from redistribution instead of relying on the structural capacity of the bolt.

The systematic bolts in an ideal homogeneous rock mass study may be redundant. Still, the benefit of its prescriptive uses arises from reducing the kinematic failure of rock blocks formed in adverse joint orientation and maintaining the stability of the opening.

The current research is based entirely on homogenous rock mass, excluding the study of volcanic rock, in which the failure mechanism may be dominated by the degree of fracture relative to the opening size

REFERENCES

Bischoff, J. A. and Smart, J. D. 1977. A method of computing a rock reinforcement system which is structurally equivalent to an internal support system. In Proceedings of the 16th US Symposium on Rock Mechanics, Minneapolis, MN, USA (Fairhurst C and Crouch SL (eds)). ASCE, New York, NY, USA, pp. 279–284.

Martin, C. D., Kaiser, P. K. and McCreath, D. R. 1999. Hoek-Brown parameters for predicting the depth of brittle failure around tunnels. Canadian Geotechnical Journal, Vol. 36, pp. 136-151.

Norwegian Geotechnical Institute. 2015. Handbook Using the Q-system – Rock Mass Classification and Support Design. Norges Geotekniske Institutt, Oslo, Norway.

RS2, 2D Finite Element Analysis Software. 2025. https://www.rocscience.com/software/rs2.

RS3, 3D Finite Element Analysis Software. 2025. https://www.rocscience.com/software/rs3.

Vlachopoulos, N. and Diederichs, M. S. 2009. Improved Longitudinal Displacement Profiles for Convergence Confinement Analysis of Deep Tunnels. Rock Mechanic and Rock Engineering, Vol. 42, pp. 131-146.

Influence of Pile Diameter on Constant of Horizontal Subgrade Reaction n_h

Ming-min WANG & Ting-hao MAO
Ove Arup & Partners Hong Kong Ltd

ABSTRACT

The constant of horizontal subgrade reaction (n_h) is a cornerstone parameter in the Winkler-based subgrade reaction method for analyzing laterally loaded piles. This article re-examines whether n_h is independent of pile diameter. The previous assumption that the deflection of the pile is linearly proportional to the dimension of a pressure bulb does not accurately reflect the real situation. Three-dimensional finite element method was employed to conduct a series of analyses, demonstrating that for the same soil material, n_h increases almost linearly with pile diameter.

By comparing the deflection results of pile obtained from Plaxis3D, with those derived from the subgrade reaction method using n_h, it is evident that when employing the n_h method, the influence of pile diameter should be considered to reduce material costs and carbon emissions in projects involving laterally loaded piles.

1 INTRODUCTION

The analysis of laterally loaded piles is critical for infrastructure such as bridge abutments, pile-supported retaining walls, and high-rise buildings. The subgrade reaction method, first conceptualized by Winkler (1867), models soil-pile interaction using a series of discrete springs along the pile shaft. In this model, the soil resistance per unit length (P_h) is expressed as $P_h = n_h \cdot z \cdot \delta_h$, where z represents the depth below ground level and δ_h represents the lateral deflection. Current standards (HK GEO Publication No.1/2006; HK Code of Practice for Foundations 2017) prescribe n_h as a function of soil type and stress history but treat it to be independent of pile geometry. For granular soils, the value of the constants of horizontal sub-grade reaction (n_h) are provided in Table 5.1 of the HK Code of Practice for Foundations, 2017.

Table 1 Correlation of Constant of Horizontal Subgrade Reaction with SPT N-values for Granular Soil (HK Code of Practice for Foundations 2017)

SPT N-value	n_h for dry or moist sand ($kN/m^2/m$)	n_h for submerged sand ($kN/m^2/m$)
4 to 10	2200	1300
11 to 30	6600	4400
31 to 50	17600	10700

Based on the current method, since n_h is not considered as a function of pile dimensions, a pile with a very large diameter would theoretically exhibit the same soil reaction per unit length as a pile with a very small diameter. In other words, increasing the pile diameter does not enhance the soil reaction acting on the pile. When calculating the deflection of a pile under horizontal loading, the influence of pile diameter (D) on the flexural stiffness of the pile body is taken into account, while the influence of pile diameter (D) on soil resistance per unit length (P_h) is neglected. This discrepancy may lead to an underestimation of deflection for small-diameter piles and an overestimation for large-diameter piles.

2 LITERATURE REVIEW

The Winkler model, despite its simplicity, underpins modern lateral pile analysis due to its computational efficiency. Terzaghi (1955) first adapted it for soils, proposing n_h values for clays and sands. Reese (1974) advanced the method via *p-y* curves, but retained n_h as depth-linear and diameter-agnostic.

Randolph (1981) identified limitations in the Winkler approach, notably its neglect of soil continuity and stress redistribution. Ashour et al. (1998) demonstrated that n_h could vary with pile flexibility (*EI*), but diameter effects remained unexplored. Hong Kong GEO Report No. 21 (1992) hinted that the approach of using n_h for wall analysis has been questioned because the behavior of a pile is governed by its width.

For soil-pile interaction, Dodds (2005) studied the pile behavior in large pile groups under lateral loading, provided insight into the mechanics of large pile group lateral stiffness, various issues such as installation effects, pile, pile head and soil conditions. Wang (2015, 2022 & 2023) studied soil-pile interaction and loads distribution of different kinds of pile; it is found that the diameter influence is significant.

There are many researchers using centrifuge tests or loading test of trial pile to study the behavior of pile taking lateral loads. Russo & Viggiani (2008) reviewed the behavior of piles under lateral loading based on full scale and centrifuge tests results. Nadilla & Prakoso (2019) studied the correlation between the subgrade reaction modulus and the soil N-SPT value is examined by conducting numerical analyses of 34 pile cyclic lateral load tests in Jakarta. Chin, Sew & Chung (2009) presented the results and interpretation of a lateral load test on a fully instrumented spun pile. Li, Wei, Feng & Chen (2019) conducted a series of field tests to examine the behavior of pile foundation subjected to adjacent surcharge loading in deep soft soils.

Sensitive study results are also provided by some scholars. Gebremichael & Berg (2022) used both LPile and Plaxis3D to study horizontally loaded piles. Zhao & Wang (2018) analyzed the pile lateral response from deflection measurement data with a compressive sampling-based method. Tommy, Widjaja & Hutabarat (2023) used three-dimensional finite element method and *P-y* Curve to study the lateral bearing capacity of single bored pile. Law & Cheng (2015) studied the *P-delta* effects of piles embedded in cohesionless soil.

3 METHODOLOGY

3.1 Theoretical adjustment of n_h method

For the traditional subgrade reaction method, Terzaghi assumed that deflection was linearly proportional to the dimension of a pressure bulb and, consequently, linearly proportional to pile width. Hence, for a pile with width d_1 applying a pressure q per unit area and an associated deflection y_1, and another pile of width d_2 (=nd_1) applying the same pressure per unit area with an associated deflection y_2, it is assumed that y_2 should equal ny_1. Based on this assumption, the following relationship applies:

$$(k_h)_2 = \frac{qd_2}{y_2} = \frac{q \cdot nd_1}{ny_1} = \frac{qd_1}{y_1} = (k_h)_1 \qquad (1)$$

Where $(k_h)_1$ = subgrade modulus for pile of width d_1, and
$(k_h)_2$ = subgrade modulus for pile of width d_2.

Thus, the subgrade modulus for a pile has traditionally been considered independent of the pile diameter.

However, the assumption that y_2 equals ny_1 is questionable. Consider a scenario where q_1=1 kPa, d_1=1 m, y_1=10 mm, and d_2=2 m, implying n=2. According to the definition prior to equation (1), $y_2=ny_1$=20mm. Nevertheless, under the same ground conditions and pressure (q_2=1 kPa), the deflection y_2 typically does not reach 20 mm.

Furthermore, the deflection of a pile should not be simplistically assumed to be linearly proportional to the dimension of a pressure bulb, as the size of the pressure bulb cannot quantitatively reflect the stress variation.

To investigate the relationship between the subgrade modulus for a pile and the pile diameter, we employed the three-dimensional finite element method to conduct a series of analyses.

3.2 Decoupling the dimension effects on pile flexural rigidity and soil reaction

Due to the fact that both pile flexural rigidity and soil reaction may be influenced by pile diameter simultaneously, in order to investigate the effect of pile diameter on n_h, it is necessary to maintain the pile stiffness constant. Assuming a pile subjected to a uniformly distributed lateral load along its length, if the pile diameter is increased while keeping the load unchanged, the pile displacement will be affected solely by the variation in soil reaction. This approach effectively eliminates the influence of pile flexural rigidity.

Plaxis3D was employed to preform simulations of a series of piles subjected to uniformly distributed lateral loads. Based on the results from these pile (referred to as pile series A), the soil springs represented by soil resistance per unit length (P_h) were obtained. These soil springs were then incorporated into the GSA model to simulate another series of piles (referred to as pile series B), which are subjected to point loads at the pile head. Additionally, Plaxis3D was also used to simulate pile series B for comparison purpose.

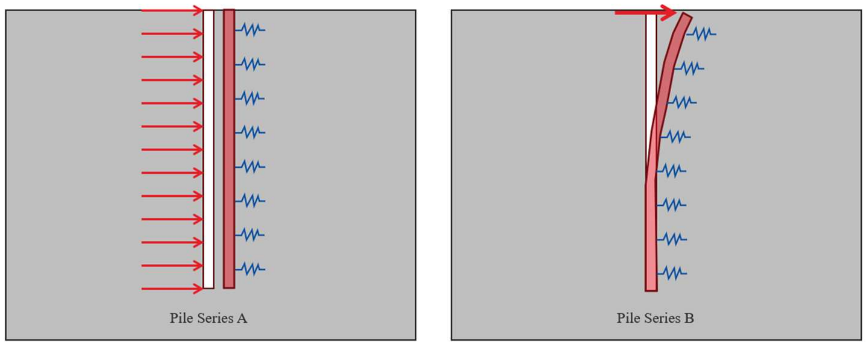

Figure 1: Decoupling the dimension effects on pile flexural rigidity and soil reaction

3.3 Numerical Modeling Framework

Two series of three-dimensional finite element models were developed in Plaxis3D to simulate pile series A and pile series B. These models consisted of 30 m long reinforced concrete piles with diameters ranging from 0.6 m to 3.0 m (in increments of 0.2 m) embedded in homogeneous sand.

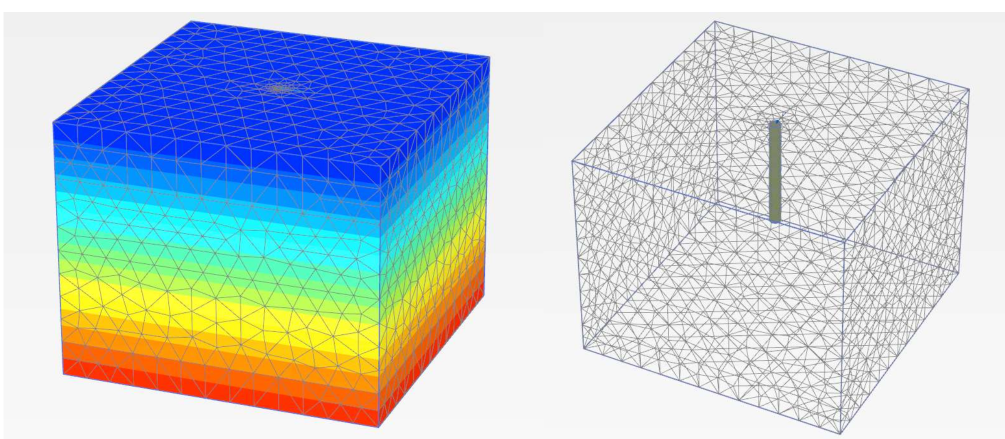

Figure 2: Plaxis3D model of pile series A

The transverse, longitudinal and vertical directions of the models are 75 m, 75 m, and 90 m, respectively. The piles were modeled using an isotropic linear elastic material model with an elastic modulus of 31.5 GPa, a Poisson's ratio of 0.2, and a density of 2500 kg/m^3.

The Mohr-Coulomb criterion was used for the soil. Based on the trial test results reported by Li (2019), the soil has a density of 1939 kg/m^3, an elastic modulus of 78.8 MPa, a Poisson's ratio of 0.25, a cohesion of 0.1 kPa and an internal friction angle of 15.0°. The element sizes were refined to 0.1D near the pile and gradually increased to 0.5D at the domain boundaries. Lateral displacements were constrained at the domain edges, and the base was fully fixed.

A uniformly distributed lateral load of 20 kN/m along the pile length was applied to pile series A. Monotonic lateral point loads of 200 kN were applied at the pile head of pile series B.

Back-calculation was performed to derive n_h from the Plaxis3D results of pile series A. n_h was calculated as follows:

$$n_h = \frac{P_h}{z \cdot \delta_h} \qquad (2)$$

4 INFLUENCE OF PILE DIAMETER ON n_h

4.1 Numerical Results of Pile Series A

Fig. 3 shows the displacement of Pile Series A. As can be observed from Fig.3, for piles with diameters ranging from 0.6 m to 1.4 m, the upper potion (approximately 5 m below the ground surface) exhibits larger deflections than expected. This is due to the reduced confinement and lower yield strength of the soil near the ground surface (Fig. 4). The relatively smaller deflections in the lower portion (approximately 5 m above the pile toe) can be attributed to the three-dimensional confinement at the pile toe and the frictional resistance at the bottom surface of the pile. Wider piles tend to reduce localized yielding by distributing strain over a larger area, thereby preserving more elastic soil behavior.

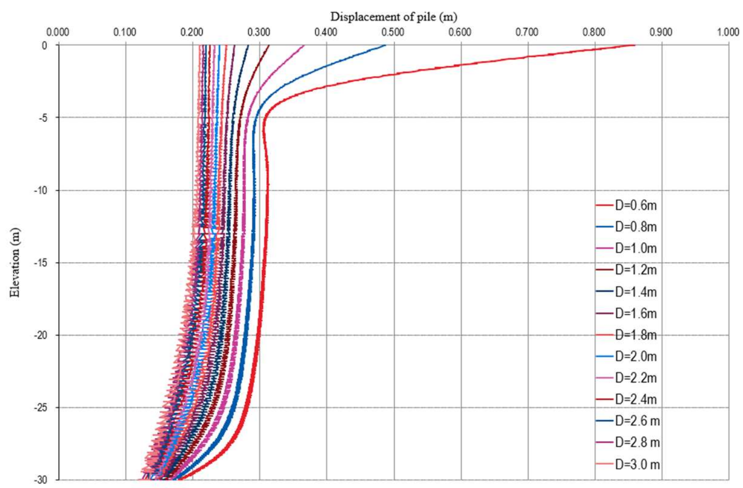

Figure 3: Displacement of pile series A

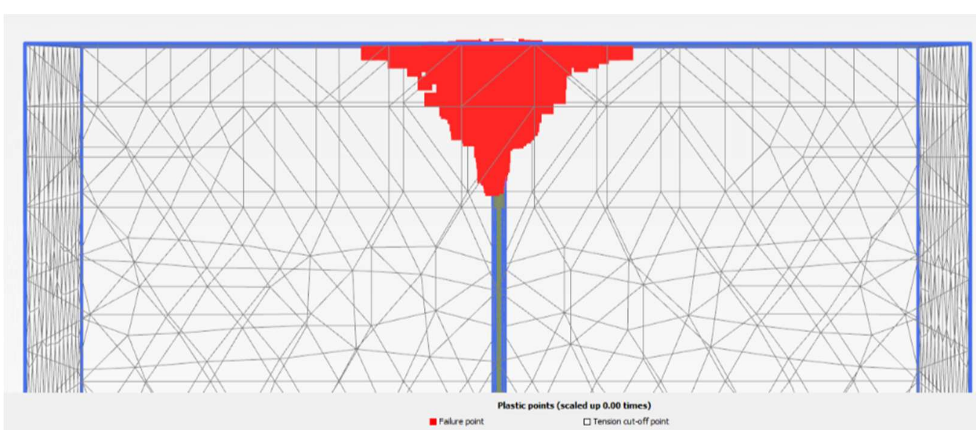

Figure 4: Plastic point of soil in Plaxis3D model

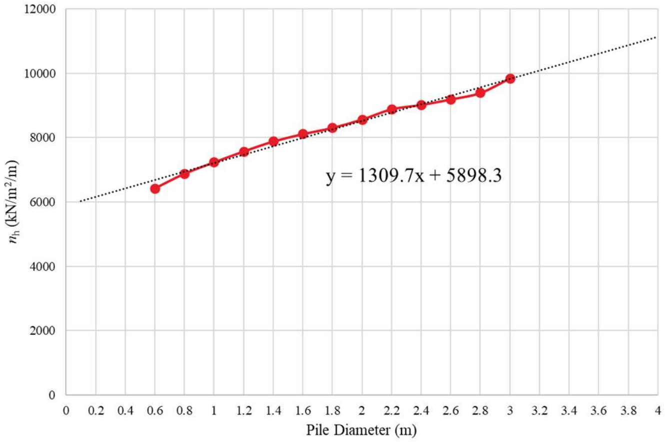

Figure 5: Relation between n_h (10 m below ground surface) and pile diameter D

From Fig. 5 we can observe that for the same soil material, n_h of 10 m below ground surface increased from 6400 kN/m^2/m to 9850 kN/m^2/m when pile diameter D changes from 0.6 m to 3.0 m. The trend followed:

$$n_h = 1309.7D + 5898.3 \quad (3)$$

Larger diameters generated broader passive wedges and deeper shear strain penetration, enhancing confinement and soil stiffness.

4.2 Deflection Results of Pile Series B based on n_h of Code of Practice for Foundations 2017

Since the Young's modulus for the soil in the Plaxis3D model can be converted into SPT N-value, the correlation of constant of horizontal subgrade reaction and SPT N-values for granular soil presented in Table 1 can be utilized to calculate the soil spring. Subsequently, Pile Series B was simulated using both Plaxis3D and GSA (n_h method). A point load of 600 kN was applied to each pile head.

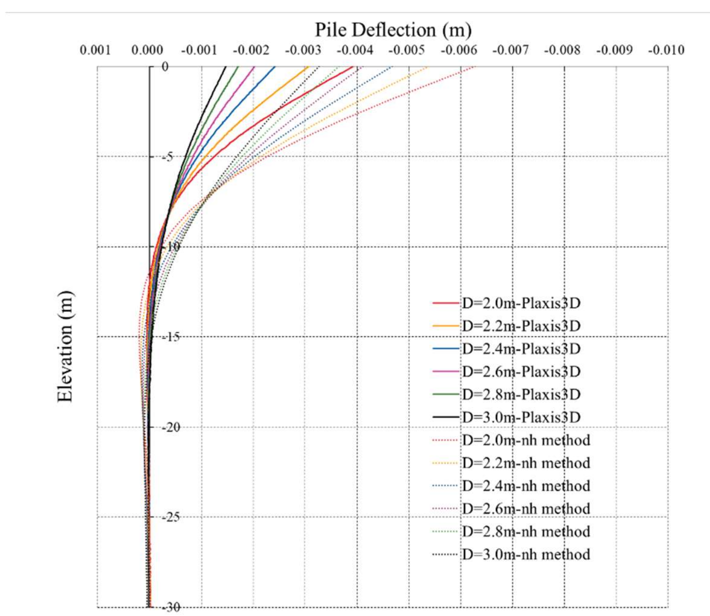

Figure 6: Deflection of Pile Series B (D ranges from 2.0 m to 3.0 m)

From Fig. 6, it can be observed that the pile deflections of Pile Series B calculated by GSA using the n_h method are larger than those calculated by Plaxis3D. However, upon comparing Fig. 5 and Fig. 6, it is evident that when the pile diameter is relatively small, the pile deflections of Pile Series B calculated by GSA using the n_h method are not consistently larger than those calculated by Plaxis3D. This discrepancy arises because the soil in front of the pile has yielded in the Plaxis3D simulations.

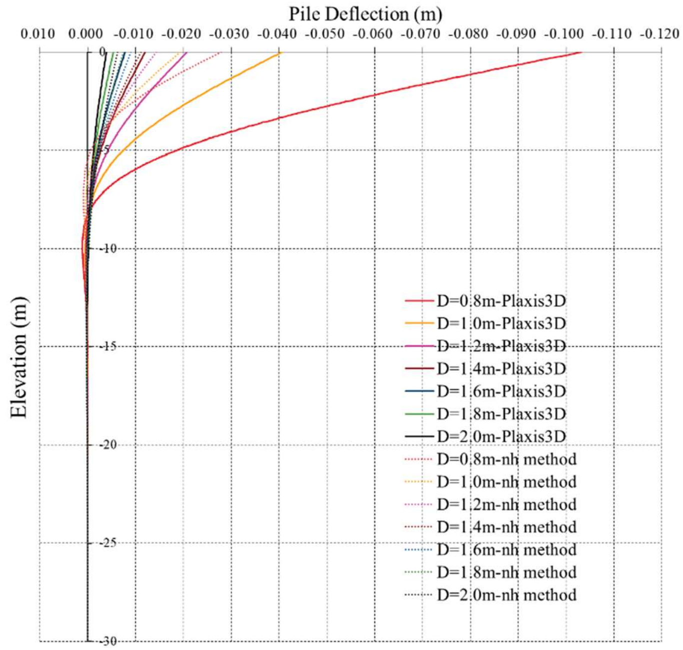

Figure 7: Deflection of Pile Series B (*D* ranges from 0.8 m to 2.0 m)

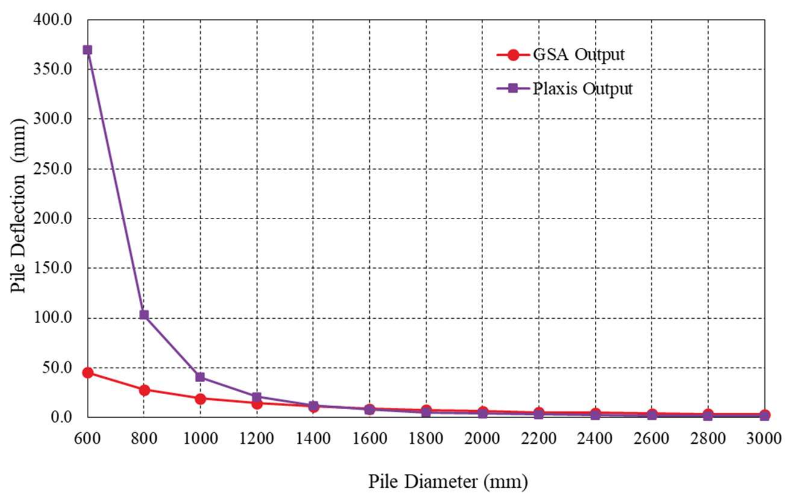

Figure 8: Maximum pile deflection

Table 2 Deflection Results of Pile Series B

Pile Diameter *D (m)*	Plaxis3D Deflection (mm)	n_h method Deflection (mm)	Difference Ratio
0.8	103.2	28.0	-72.9%
1.0	40.7	19.4	-52.4%
1.2	20.8	14.4	-31.0%
1.4	12.1	11.2	-7.5%
1.6	7.9	9.0	14.6%
1.8	5.4	7.4	38.1%
2.0	3.9	6.3	59.9%
2.2	3.1	5.4	75.0%
2.4	2.4	4.7	93.2%
2.6	2.0	4.1	102.6%
2.8	1.7	3.7	113.3%
3.0	1.5	3.3	122.0%

From Fig. 8 and Table 2, it can be observed that when pile diameter is less than 1.4 m, the maximum deflection obtained from Plaxis3D is significantly larger than the pile deflections calculated by GSA using the n_h method. This discrepancy arises because the soil in front of the pile has yielded in the Plaxis3D simulations, whereas the n_h method does not account for the nonlinear behavior of the soil.

When the pile diameter exceeds 1.6m, the difference ratio between the maximum deflection obtained from Plaxis3D and the pile deflections calculated by GSA using the n_h method increases substantially with increasing pile diameter. This occurs because the influence of pile diameter (D) on soil resistance per unit length (P_h) is neglected in the n_h method. Consequently, this leads to inaccuracies in predicting lateral deflections for large-diameter piles.

5 Suitable pile diameters for n_h method

According to the Plaxis3D simulation results, it can be observed that the n_h method is not suitable for all pile diameters.

For piles with small diameters subjected to relatively large lateral loads, the soil in front of the pile will yield. Since the traditional n_h method does not account for the nonlinear behavior of soil springs, when the soil yields, the deflection results based on the n_h method will be significantly underestimated.

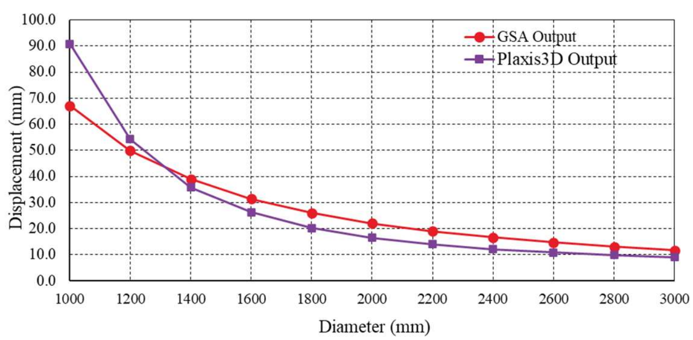

Figure 9: Pile deflection with different diameter when n_h = 1300 kN/m^2/m

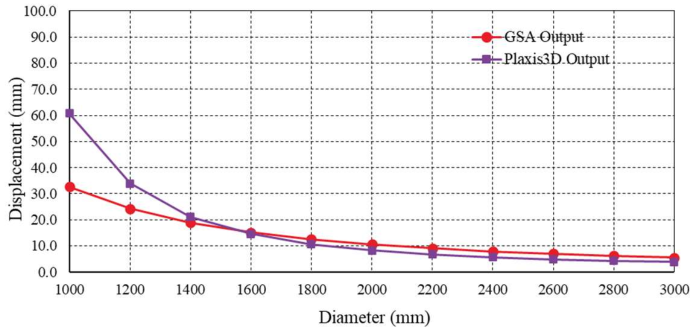

Figure 10: Pile deflection with different diameter when n_h = 4400 kN/m^2/m

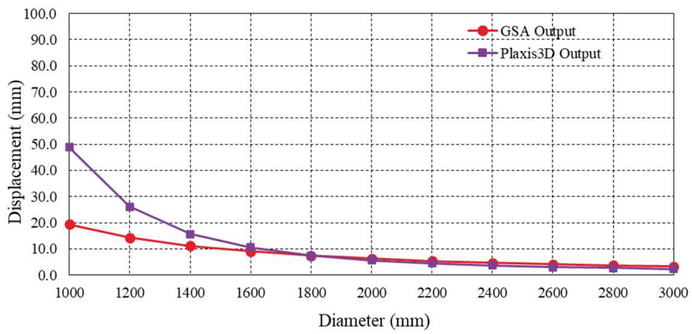

Figure 11: Pile deflection with different diameter when n_h = 10700 kN/m^2/m

Fig. 9 to 11 indicate that there is always a crossover point between the curve of Plaxis3D results and the curve derived from the n_h method. Furthermore, for relatively small pile diameters, the pile deflections obtained from Plaxis3D are larger than those calculated by the n_h method, while for relatively large pile diameters, the pile deflections obtained from Plaxis3D are consistently smaller than those calculated by the n_h method.

Since the pile itself has structural capacity, piles with small diameters typically cannot sustain relatively large lateral loads. However, the limitation imposed by structural capacity may not correspond to the appropriate boundary for the n_h method. Therefore, designers should verify whether the n_h method can be applied based on whether the soil has yielded, rather than whether the pile structure has failed.

6 PRACTICAL RECOMMENDATIONS

Based on the findings in section 5, it can be observed that the n_h method is not suitable for piles with relatively small diameters while taking large lateral loads. When the soil in front of the pile does not yield, the n_h method can be applied but requires adjustment by considering the pile diameter.

To obtain more accurate deflection results for Pile Series B, the value of the constant of horizontal subgrade reaction can be adjusted as follows:

$$n_h' = (D - D_0)n_h \quad (4)$$

Where n_h' is the revised value of the constant of horizontal sub-grade reaction,

D_0 is the baseline diameter for n_h, corresponding to the crossover point in Fig. 8 for this study.

Table 3 and Fig. 11 present the revised deflection results for pile series B. The different ratio between n_h methods and Plaxis3D results are significantly reduced.

Table 3 Revised Deflection Results of Pile Series B

Pile Diameter D (m)	Plaxis3D Deflection (mm)	Revised n_h Method Deflection (mm)	Difference Ratio
0.8	103.2	49.0	——
1	40.7	27.2	——
1.2	20.8	16.8	——
1.4	12.1	11.2	-7.44%
1.6	7.9	7.9	-0.32%
1.8	5.4	5.7	5.06%
2	3.9	4.3	11.46%
2.2	3.1	3.4	9.27%
2.4	2.4	2.7	12.60%
2.6	2.0	2.2	8.81%
2.8	1.7	1.8	7.27%
3	1.5	1.5	1.20%

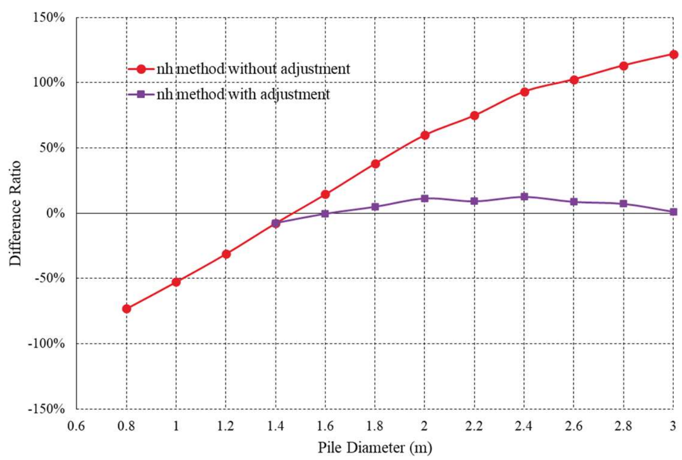

Figure 12: Difference Ratio of nh methods

It can be observed that the subgrade modulus for a pile is dependent on the pile diameter. For large-diameter piles, this adjustment can lead to safe and more economical designs. This finding will help reduce material costs and carbon emissions for projects involving piles subjected to lateral loads.

7 CONCLUSIONS

The constant of horizontal subgrade reaction (n_h) is a cornerstone parameter in the Winkler-based subgrade reaction method for analyzing laterally loaded piles. This article revisits whether the subgrade modulus for a pile is independent of the pile diameter.

Conventional design frameworks assume n_h to be depth-dependent but independent of pile dimensions; however, the author found that the assumption of linearly proportionality between pile deflection and the dimension of a pressure bulb does not reflect the real situation.

To investigate the relationship between the subgrade modulus for a pile and pile diameter, a series of analyses were conducted using the three-dimensional finite element method. By decoupling the dimension effects on pile flexural rigidity and soil reaction, it was observed that for the same soil material, n_h increases almost linearly with pile diameter.

By comparing the deflection results of piles obtained from Plaxis3D and those calculated using subgrade reaction method based on n_h of Hong Kong Code of Practice for Foundations (2017), it can be seen that for different types of sand, the pile deflections obtained from Plaxis3D are larger than those calculated by the n_h method for relatively small pile diameters, while the pile deflections obtained from Plaxis3D are consistenly smaller than those calculated by the n_h method for relatively large pile diameters.

Since the pile possess structural capacity, piles with small diameter typically cannot sustain relatively large lateral loads, meaning most previous projects do not have safety risks. However, the limitation imposed by structural capacity may not the same value of the appropriate boundary of the n_h method. Therefore, designers should verify whether the n_h method can be applied based on whether the soil has yielded, rather than whether the pile structure has failed.

When the soil in front of the pile does not yield, the n_h method can be applied but should ideally be adjusted by considering the influence of pile diameter. For large-diameter piles, this adjustment can provide safe and more economical designs. This finding will help reduce material costs and carbon emissions for projects involving piles subjected to lateral loads.

It should be noted that this study focused on homogeneous ground profiles; layered systems require further analysis. The effectiveness of the n_h method under cyclic or dynamic loads remains unexplored. Since the geological profiles for real projects are far more complex than the Plaxis3D or GSA models mentioned in this article, trial piles and lateral loading tests are recommended to accurately assess the performance of piles subjected to lateral loads.

ACKNOWLEDGEMENTS

The author would like to express sincere gratitude to Ir Mr Jack YIU and Ir Mr Alvin LAM for their valuable suggestions and support in the preparation of this article.

REFERENCES

Ashour, M., Norris, G., & Pilling, P. (1998). *Journal of Geotechnical Engineering*, 124(9), 798–806.

Building Department of Hong Kong. (2017). *Code of Practice for Foundations 2017*.

Chin, T. Y., Sew, G. S., & Chung, F. C. (2009). Interpretation of Subgrade Reaction from Lateral Load Tests on Spun Piles in Soft Ground. *In Association of Consulting Engineers Malaysia (ACEM) Conference and Exhibition on Bridge Engineering*.

de Souza Magnus, T. (2018). The effect of modeling lateral stiffness of pile foundations on numerical analyses of structural frames.

Dodds, A. (2005). A numerical study of pile behavior in large pile groups under lateral loading. University of Southern California.

Gebremichael Mebrahtu, D., & Berg, A. (2022). Design of Horizontally Loaded Piles: FEM and FDM Study on Lilla Lidingö Bridge.

Geotechnical Engineering Office of Hong Kong. (1992). Horizontal Subgrade Reaction for Cantilevered Retaining Wall Analysis. *GEO Report No. 21*.

Geotechnical Engineering Office of Hong Kong. (2006). Foundation Design and Construction. *GEO Publication No. 1/2006*.

Law, C. W., & Cheng, Y. M. (2015). Studies on the P-delta effects of piles embedded in cohesionless soil. *HKIE Transactions*, *22*(3), 134-152.

Li, H. Q., Wei, L. M., Feng, S. Y., & Chen, Z. (2019). Behavior of piles subjected to surcharge loading in deep soft soils: Field tests. *Geotechnical and Geological Engineering*, 37, 4019-4029.

Nadilla, S., & Prakoso, W. A. (2019). Pile lateral subgrade reaction modulus for Jakarta. *In MATEC Web of Conferences* (Vol. 270, p. 02002). EDP Sciences.

Randolph, M. F. (1981). The response of flexible piles to lateral loading. Geotechnique, 31(2), 247-259.

Reese, L. C., Cox, W. R., & Koop, F. D. (1974). Analysis of laterally loaded piles in sand. *In Offshore technology conference* (pp. OTC-2080). OTC.

Reese, L. C., & Van Impe, W. F. (2001). Single Piles and Pile Groups Under Lateral Loading. CRC Press.

Russo, G., & Viggiani, C. (2008). Piles under horizontal load: an overview. *In Foundations: proceedings of the second British Geotechnical Association International Conference on Foundations*, ICOF (Vol. 2008, pp. 24-27).

Terzaghi, K. (1955). Evalution of conefficients of subgrade reaction. *Geotechnique*, 5(4), 297-326.

Tommy, A., Widjaja, B., & Hutabarat, G. M. (2023, October). Py Curve for Estimation Lateral Bearing Capacity of Single Bored Pile in Overconsolidated Soils Using the Three-Dimensional Finite Element Method. In *IOP Conference Series: Earth and Environmental Science* (Vol. 1249, No. 1, p. 012028). IOP Publishing.

Wang, M. M. (2015). Failure Mechanism and Stability Analysis Method of Soil with Vertical Free-face between Supporting Piles. *Chongqing University*.

Wang, M. M., Liu, P., Wang, Y., Zou, J. L & Zhong, C. M. (2022). Action mechanism and loads distribution rule of supplementing non-rock-socketed short piles between rock-socketed piles. *Building Structure*, 52(2), 22-27.

Wang, M. M., Liu, P., Yu G. M., & Zhu, L. G. (2023). Method to obtain load transfer function and non-linear pile stiffness of rock socketed bored pile. *Building Structure*, 53(23), 46-50.

Winkler, Emil. Die Lehre von der Elasticitaet und Festigkeit: mit besonderer Rücksicht auf ihre Anwendung in der Technik, für polytechnische Schulen, Bauakademien, Ingenieure, Maschinenbauer, Architecten, etc. *H. Dominicus*, 1867.

Zhao, T., & Wang, Y. (2018). Interpretation of pile lateral response from deflection measurement data: A compressive sampling-based method. *Soils and foundations*, *58*(4), 957-971.

Multiphysics and Multiscale Modeling of Bouldery Debris Flow Interactions with Baffles and Slit Dam

Terry H. Y. LEUNG† & Jidong ZHAO
Department of Civil and Environmental Engineering, The Hong Kong University of Science and Technology

ABSTRACT

Debris flow is a channelized flow-type landslide that pose significant risks to infrastructures and human life due to its high-velocity slurry and impact forces from entrained boulders. Realistic numerical modeling of debris flow remains challenging, as it involves multiscale interactions between different phases (e.g., boulders, soil, slurry, and water) and multiphysics processes (e.g., fluid-particle and debris-structure interaction). This study introduces two advanced numerical frameworks to unravel the impact mechanism of bouldery debris flows on debris-resisting structures: 1) a fully resolved smoothed particle hydrodynamics-discrete element method (SPH-DEM) coupling model, and 2) a two-level discrete element method (2L-DEM). Both approaches explicitly resolve the multiphase nature of debris flows by treating boulders and fine-grained slurry as distinct interacting phases, enabling previse quantification of momentum transfer, energy dissipation, and structural responses. The SPH-DEM captures fluid-driven boulder dynamics and backflow effects around baffles, while the 2L-DEM captures granular jamming and force redistribution in the impact process on slit dam. The simulation results demonstrate that the formation of bouldery front and viscosity of slurry significantly alter the impact regimes on baffles, whereas the relative size of particle and slit dam aperture critically governs the debris retention efficiency. By bridging microscale particle interactions to macroscale flow-structure behavior, this work provides physics-based insights for optimizing debris-resisting structures, offering geotechnical engineers validated tools to enhanced hazard mitigation strategies on key infrastructure near mountainous region.

1 INTRODUCTION

Debris flow is a rapid, channelized landslide comprising boulders, soil, water, and organic matters that pose severe threats to infrastructure and human life due to its high mobility and destructive impact forces. This event is particularly devastating in urbanized regions, as exemplified by the 2008 Yu Tung Road debris flow in Hong Kong, which damaged critical infrastructure and necessitated a two-month closure of a major transportation artery, incurring substantial economic and social costs. Mitigating such hazards requires a robust understanding of debris flow dynamics and their interaction with protective structures, yet achieving realistic simulations remains a formidable challenge.

Numerical modeling has emerged as a pivotal tool for studying debris flow mechanics. Existing approaches broadly fall into two categories: continuum methods, such as the material point method (MPM) (Li et al. 2020), smoothed particle hydrodynamics (SPH) (Han et al. 2019), and the arbitrary Lagrangian-Eulerian (ALE) method (Kwan et al. 2015), which treat debris flow as a homogenized fluid or solid; and discrete methods, like the discrete element method (DEM) (Choi et al. 2016; Gong et al. 2021), which resolve granular interactions through particle-scale friction and collision. While continuum methods excel at capturing bulk flow behavior, they often oversimplify the multiphase nature of debris. Conversely, DEM provides granular insights but struggles with computational efficiency for large-scale model. Most importantly, these models often neglect critical multiscale phenomena, such as the dynamic interplay between boulders and fine-grained slurry and structures, a gap that limits their predictive capability. Recent advances in computational power have spurred hybrid frameworks (Li & Zhao 2018; Leonardi et al. 2016), coupling continuum and discrete techniques to

† Current Affiliation: Highways Department, Government of HKSAR

capture the multiphysics phenomena while balancing accuracy and scalability.

The inherent complexity of debris flows arises from their multiscale, multiphase composition. Debris materials span orders of magnitude in grain size, from clay particles to meter-scale boulders, which undergo rapid rearrangement during flow, creating spatially heterogeneous rheology (Iverson 2003). A key process is granular segregation (Figure 10), where larger boulders migrate to the flow front and surface of a debris flow (Hungr et al. 2001), amplifying impact force on barriers compared to homogeneous flows (Ng et al. 2021). Conventional models, which homogenize debris into a single phase, fail to resolve this segregation-driven force concentration, leading to underestimations of structural loading. A paradigm shift toward explicit multiphase modeling is essential to advance hazard assessment and structural design.

To address these limitations, this study presents two novel numerical frameworks, 1) fully resolved SPH-DEM coupled model that integrates smoothed particle hydrodynamics (SPH) for fine-grained slurry with discrete element method (DEM) for boulder dynamics, enabling previse simulation of fluid-particle interactions and backflow effects around baffle structures, and 2) a two-level DEM (2L-DEM) approach that efficiently resolve boulder entrained dense granular flows impacting on a slit dam.

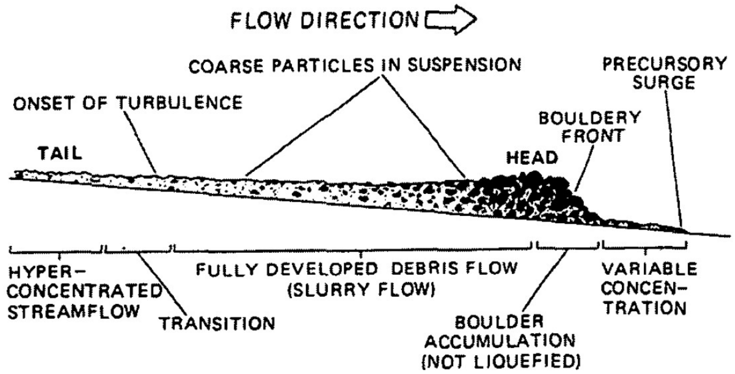

Figure 10 Bouldery front of a debris flow surge (Hungr et al. 2001)

2 RESOLVED SMOOTHED PARTICLE HYDRODYNAMICS – DISCRETE ELEMENT MODEL (SPH-DEM) COUPLING MODEL

The resolved smoothed particle hydrodynamics-discrete element method (SPH-DEM) coupling model bridges fluid dynamics and granular mechanics to explicitly simulate interactions between boulders, slurry and protective baffle structures, with the following features: 1) Boulders are modeled as rigid clumps of SPH “solid particles” to resolve their rigid-body dynamics, collisions, and frictional contacts; 2) Debris slurry (a mixture of water, soil, and fine particles) is represented as a viscous fluid using SPH “fluid particles”, capturing its free-surface behavior, turbulence, and non-Newtonian rheology. The dual-resolution strategy enables precise analysis of momentum transfer between fluid-driven boulders and slurry, critical for evaluating impact forces on baffles.

2.1 Numerical scheme of SPH-DEM

The SPH-DEM framework integrates two open-source solvers: DualSPHysics (Domínguez et al. 2021), employing a weakly compressible smoothed particle hydrodynamics (WCSPH) formulation to simulate free-surface flows, and distributed contact discrete element method (DCDEM) (Canelas et al. 2016), which resolves multi-body interactions between boulders and their contacts with baffles. The surface resolved fluid-particle interaction forces are computed by applying dynamic boundary conditions on SPH “solid particles”. Furthermore, DualSPHysics supports GPU computation, enabling simulations with 786,352 SPH “fluid particles” to be completed within 2 hours.

The WCSPH solves the Navier-Stokes equations governing compressible flow, in terms of the continuity equation (1) and momentum equation (2) in Lagrangian form as follows,

$$\frac{D\rho}{Dt} = -\rho\nabla \cdot \mathbf{v} \tag{1}$$

$$\frac{D\mathbf{v}}{Dt} = -\frac{1}{\rho}\nabla P + \Gamma + \boldsymbol{f} \tag{2}$$

where D/Dt denotes the material rate derivative, $\mathbf{v}$ is the velocity vector, ρ is density, P is pressure, Γ is the dissipation or viscosity term, and $\boldsymbol{f}$ is external acceleration (e.g. gravity).

In SPH, the fluid domain is discretized into particles that serve dual roles: i) Property carriers: each particle holds field properties such as density, velocity, and pressure; ii) Interpolation nodes: Particles act as discrete points for reconstructing continuous field quantities. The SPH interpolation of a flow field quantity $A(\mathbf{r})$ at position $\mathbf{r}$ is defined by the following integral approximation,

$$\langle A(\boldsymbol{r})\rangle = \int_{\Omega} A(\boldsymbol{r}')\, W(\boldsymbol{r} - \boldsymbol{r}', h)\, d\boldsymbol{r}' \tag{3}$$

where $\langle A(r)\rangle$ is the smoothed estimate of A, W is the kernel function, Ω is the domain within the kernel support radius h, $\boldsymbol{r}' \in \Omega$ denotes neighboring particle positions. This formulation approximates field quantities as weighted averages of neighboring particles, with the kernel W ensuring localized interactions with finite number of neighboring particles (see Figure 11). More details can be found in Domínguez et al. (2021).

As for solid phase representation, boulders and walls (including baffles) are modeled as rigid clumps of SPH "solid particles" (see Figure 11). These solid particles serve dual purposes. On one hand, they are applied with dynamic boundary conditions to resolve the fluid-solid interaction forces. On the other hand, each solid particle functions as a DEM particle to compute the solid-solid collisions using the DCDEM. The DCDEM employs a "soft sphere" contact model with 4 parameters: Young's modulus E, Poisson's ratio ν, restitution coefficient e_0 and friction coefficient μ_f. More details can be found in Canelas et al. (2016).

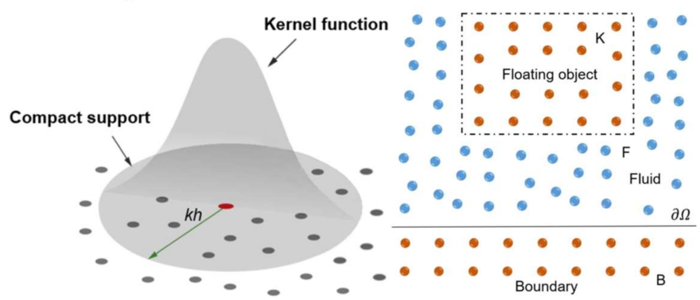

Figure 11 Schematic diagram of kernel function (left) and arrangement of solid/fluid SPH particles (right)

2.2 Numerical model setup

The SPH-DEM model simulates bouldery debris flow impacting staggered baffle arrays (Figure 12) with the following parameters: 102 m^3 of debris slurry modeled as viscous fluid, 5 boulders (1 m diameter) placed initially upstream on a 30° inclined channel of 6 m width and channel length of L_c = 23 m; 3 staggered rows of baffles placed in front of the rigid barrier at the downstream deposition zone. No-slip walls and ground are assumed for the fluid and are prescribed with the same properties for DCDEM particles.

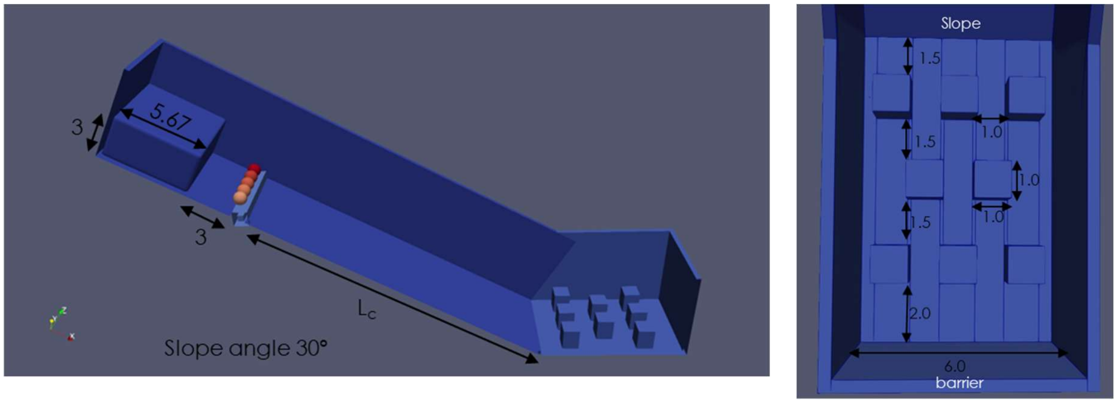

Figure 12 Geometry of SPH-DEM model (unit: m)

2.3 Simulation results

Three debris flow scenarios with different slurry kinematic viscosities (0.1 m^2/s, 1 m^2/s, 5 m^2/s) are simulated and compared in Figure 13. For the low viscosity case (0.1 m^2/s), the slurry overtops and precedes the boulders, forming a fluid-dominated front (Figure 13a). Jet-like run-up is observed during baffle impact with minimal energy dissipation (Figure 14). For the intermediate viscosity case (1 m^2/s), the balanced slurry-boulder coupling produces a coherent bouldery front flow case as shown in Figure 13b. The slurry pushes the boulders forward, showing an intermediate momentum transfer to the boulders. For the high viscosity case (5 m^2/s), slurry rigidity causes boulder detachment and flow stagnation behind motion of boulders (Figure 13c). When impacting baffles, the flow is dominated by pile-up mechanism, forming a hydrodynamic head zone upstream of the baffles (Figure 15).

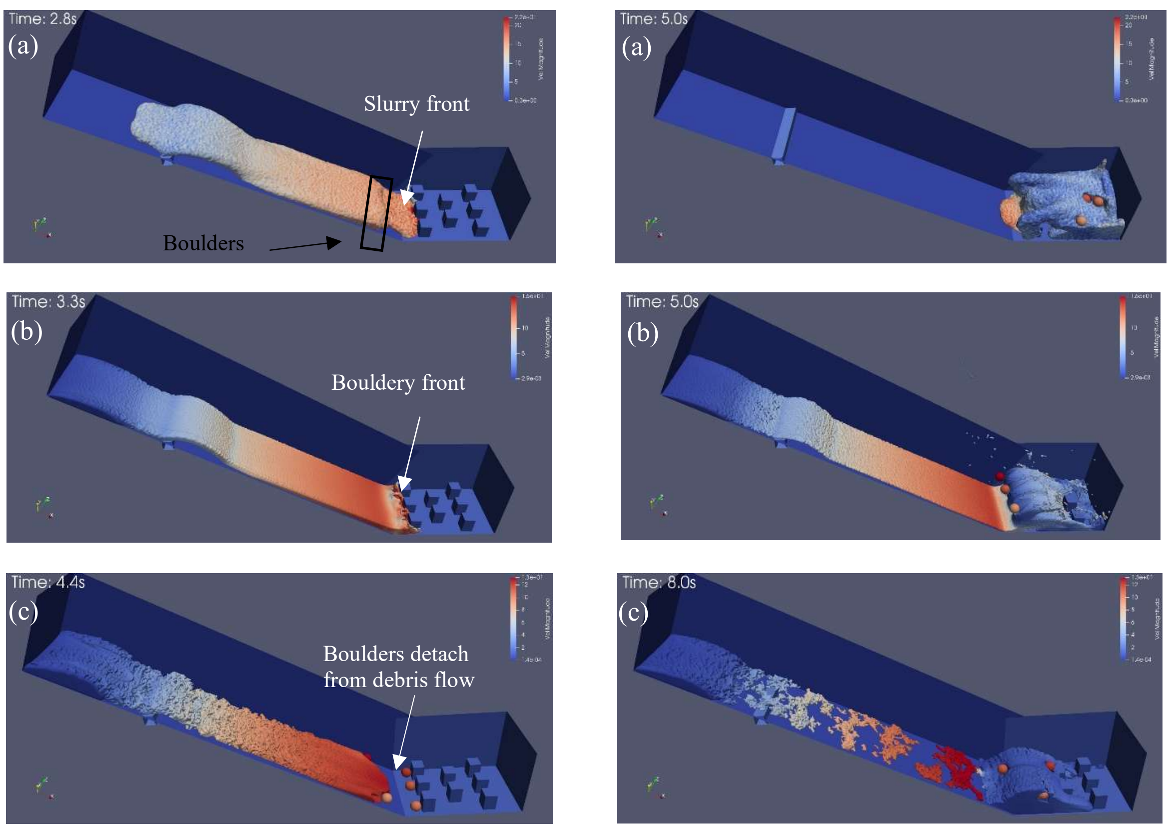

Figure 13 Snapshots of bouldery debris flow impact on baffles (left: impact of flow front; right: after impact) with different slurry viscosity (a) 0.1 m^2/s (b) 1 m^2/s (c) 5 m^2/s

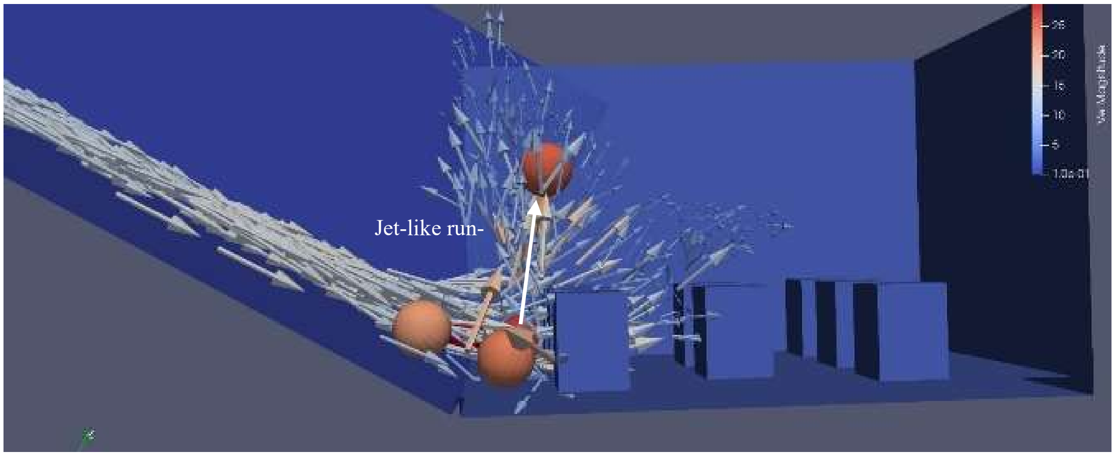

Figure 14 Jet-like run-up mechanism (slurry viscosity 0.1 m^2/s)

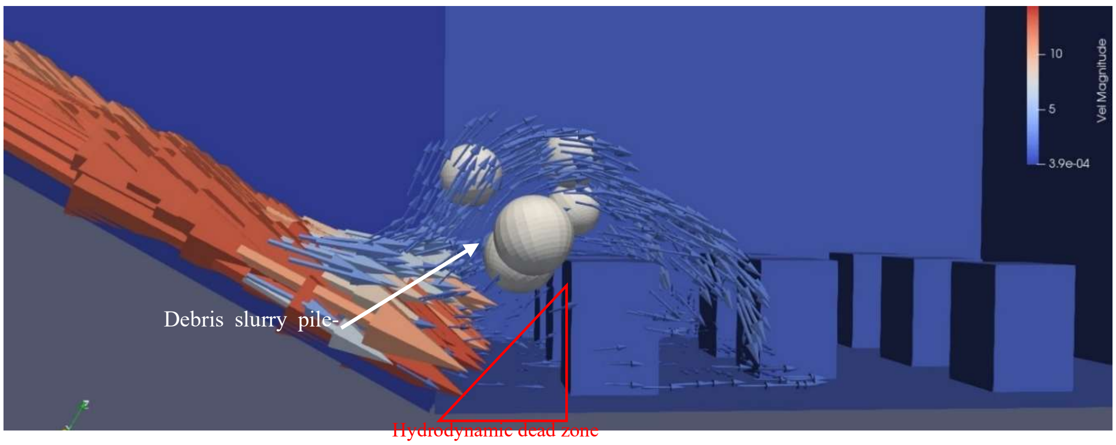

Figure 15 Formation of hydrodynamic dead zone and pile-up mechanism (slurry viscosity 5 m^2/s)

3 TWO-LEVEL DISCRETE ELEMENT METHOD (2L-DEM)

The Two-Level Discrete Element Method (2L-DEM) addresses the multiscale dynamics of bouldery granular flows interacting with slit dam by explicitly resolving two distinct phases: non-spherical boulders and monodisperse fine grains. This framework employs a dual-resolution strategy, where boulders are modeled as non-spherical bodies (constituted by triangular meshes) to capture their rotational and translational motion, while fine grains are represented as spherical particles using conventional DEM for efficient granular flow simulation. By coupling these phases into a co-simulation framework, the 2L-DEM enables detailed analysis of how boulder entrainment influences flow-structure interactions, particularly through slit dam apertures.

3.1 Model framework of 2L-DEM

The 2L-DEM leverages the open-source physics engine Project Chrono (Mazhar et al. 2013), integrating two modules to balance accuracy and computational efficiency. The Chrono Core Module simulates boulder dynamics using method tailored for non-spherical bodies, incorporating Hertzian-Mindlin contact model (for sphere-sphere and sphere-mesh contact) to resolve the force-displacement behavior. In parallel, the Chrono::GPU Module executes on graphics processing units (GPUs) to handle large-scale granular systems, optimizing monodisperse sphere interactions through parallel computing. For instance, a simulation case containing 6,256,544 particles completes in approximately 20 hours—a feat impractical for conventional CPU-based DEM solvers. A synchronization framework facilitates co-simulation between the two modules, enabling bidirectional exchange of contact data to capture coupled boulder-grain interactions.

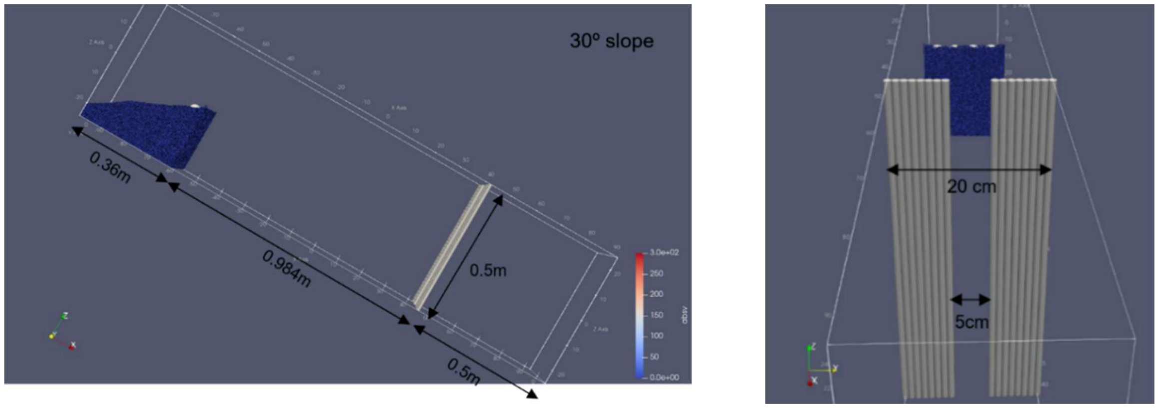

Figure 16 Geometry of 2L-DEM model

3.2 Numerical model setup

The 2L-DEM model replicates a flume experiment featuring a 30° inclined slope and a slit dam with a 5 cm aperture (Figure 16). Two groups of simulations are conducted: Type A, which models fine grains only, and Type B, which incorporates boulders (4 cm diameter) entrained within the granular flow. The slit width-to-particle diameter ratio (s/d) is systematically varied across cases (Table 8), with case IDs such as SD20 denoting a grain diameter d = 5 cm / 20 = 0.25 cm, which is one-twentieth of the slit width. This parameter is critical for understanding how geometric scaling governs discharge and clogging behavior.

3.3 Simulation results

In the Type A simulations, monodisperse granular flows impacting a slit dam are analyzed, with discharge rates (in kg/s) plotted with different particle sizes in Figure 17. All cases exhibited peak discharge at approximately t = 0.85 s, with the slit width-to-particle diameter ratio (s/d) exerting a dominant influence. Specifically, flows with 1 cm particles generated peak discharges 50% lower than those with 0.125 cm or 0.167 cm particles, underscoring the role of interparticle locking in coarser grains. Sensitivity tests on initial mass (e.g., cases A-SD5(1)&(2) and A-SD20(1)&(2)) reveal a marginal increase in discharge magnitude with larger masses, though this effect was secondary to s/d. After impact, a hydrodynamic dead zone forms behind the slit dam, stabilizing flows into quasi-steady regimes (t > 1.6 s) where discharge curves converge irrespective of particle size.

The trapping efficiency of slit dam is governed by distinct mechanisms for inviscid and frictional flows (Goodwin & Choi, 2020; Armanini & Larcher, 2001). While inviscid flows rely on blockage ratios (barrier-to-channel width), frictional granular flows are sensitive to s/d. Prior numerical studies with limited particle counts (typically <100,000) have struggled to resolve s/d-dependent phenomena at scale. This study extends the s/d range significantly, demonstrating that at $s/d \geq 30$ the particle size effects diminish as collisional and frictional forces homogenize within the dense granular packing.

Type B simulations evaluated boulder-laden flows, incorporating 4 cm diameter boulders into the granular matrix. Discharge rates for cases with 4, 16, or 32 boulders (Figure 18) exhibits temporal fluctuations due to transient blockages. Although boulder dimension (4 cm) approaches slit widths (5 cm), the low volumetric concentration ("dilute" distribution) of boulders within the granular packing preclude stable arch formation (Figure 10, 11), ensuring discharge rates never drop to zero.

The entrainment of boulders introduces dual engineering implications. Reduced peak discharge mitigates damage to downstream barriers, while transient boulder trapping could cause increase in both static and dynamic impact forces. In extreme clogging scenarios, the slit dam may behave as a rigid barrier, necessitating limit-state design considerations to account for complete blockage. These findings emphasize the need for balanced slit dam geometries that harmonize discharge reduction with structural integrity.

Table 8 Summary of simulation cases

	Case ID	Grain diameter (cm)	Number of fine grains	Total mass of fine grains (kg)	Number of boulders (4 cm diameter)
Type A	A-SD5(1)	1	12,393	17.20	-
	A-SD5(2)	1	10,697	14.84	-
	A-SD10	0.5	93,747	16.26	-
	A-SD20(1)	0.25	783,801	16.99	-
	A-SD20(2)	0.25	731,774	15.87	-
	A-SD30	0.16667	2,726,619	17.51	-
	A-SD40	0.125	6,256,544	16.96	-
Type B	B-SD10-4B	0.5	93,747	16.26	4
	B-SD20-4B	0.25	783,801	16.99	4
	B-SD10-16B	0.5	93,077	16.14	16
	B-SD20-16B	0.25	773,670	16.77	16
	B-SD30-16B	0.16667	2,608,752	16.67	16
	B-SD10-32B	0.5	93,077	16.14	32
	B-SD20-32B	0.25	773,670	16.77	32
	B-SD30-32B	0.16667	2,618,136	16.82	32

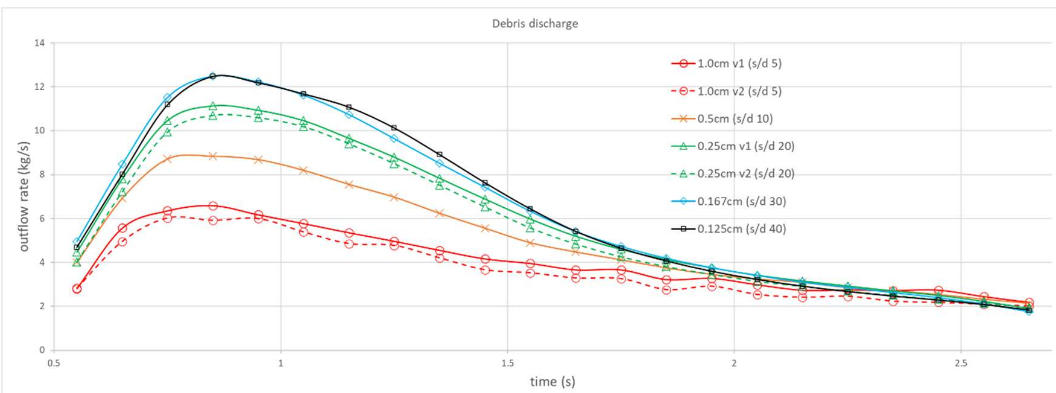

Figure 17 Evolution of granular mass discharge at slit dam for Type A test

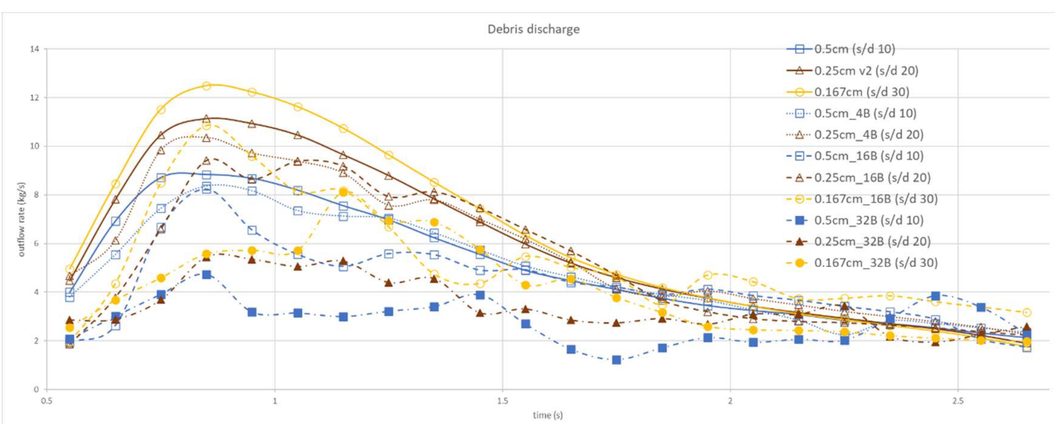

Figure 18 Evolution of granular mass discharge for type B test

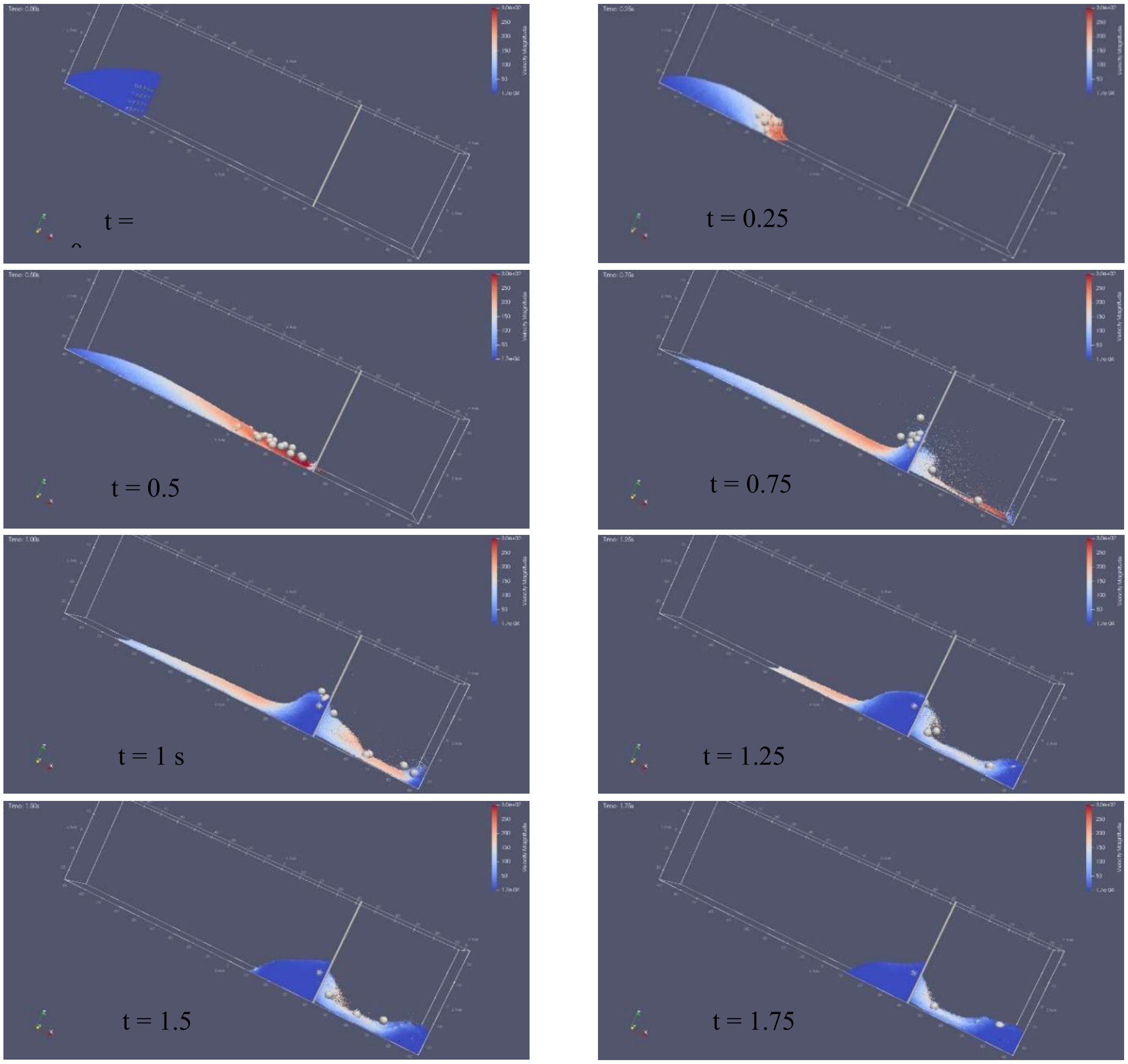

Figure 19 Snapshots of bouldery granular flow of case B-SD10-16B

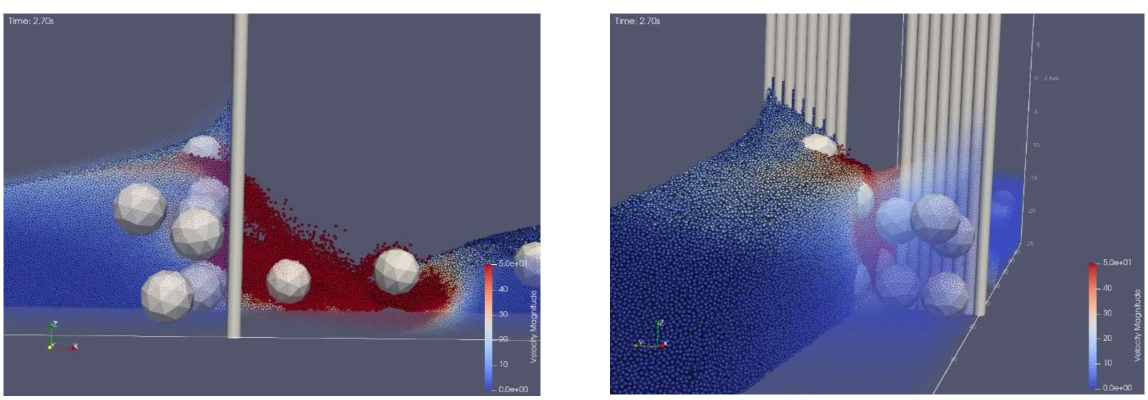

Figure 20 Snapshots of case B-SD20-32B (fine grains at front portion are transparent to reveal the boulders)

4 DISCUSSION AND CONCLUSIONS

This study demonstrates the efficacy of two advanced numerical frameworks, the resolved SPH-DEM coupling and the 2L-DEM for simulating bouldery debris flows and their interactions with debris-resisting structures. By explicitly resolving the multiphase nature of debris flows, these models provide critical insights into the distinct behaviors of boulders and fine-grained phases, which are often homogenized in conventional single-phase approaches. The SPH-DEM model reveals that slurry viscosity plays a pivotal role in governing flow coherence and impact mechanisms. It also underscores the importance of tailoring debris-resisting structures, such as baffle arrays to regional debris flow rheology.

The 2L-DEM framework which leveraged GPU-accelerated computing advances granular flow modeling by resolving the interplay between non-spherical boulders and monodisperse grains. For slit dam, the slit width-to-particle diameter ratio (s/d) emerges as a dominant factor in discharge dynamics. At $s/d \geq 30$, particle size effects diminish, homogenizing collisional and frictional forces within the flow. Boulder entrainment introduces temporal discharge fluctuations due to transient blockages, though permanent clogging is absent under tested conditions. This behavior highlights a critical design trade-off: while boulders reduce peak discharge (protecting downstream barriers), they amplify dynamic loading on slit dams that would require a robust limit-state design to account for potential clogging.

By advancing multiphysics and multiscale modeling capabilities, this study equips geotechnical engineers with predictive tools to enhance the resilience of debris-resisting structure, ultimately safeguarding communities in hazard-prone regions.

ACKNOWLEDGEMENTS

The study was financially supported by National Natural Science Foundation of China (by Project No. 52439001) and Research Grants Council of Hong Kong (by GRF Projects No. 16206322 and No. 16203123, by CRF Project No. C7082-22G, and by TRS Projects No. T22-606/23-R and No. T22-607/24-N).

REFERENCES

Armanini A. & Larcher M. 2001. Rational criterion for designing opening of slit-check dam. *Journal of Hydraulic Engineering* 127 (2): 94-104.

Canelas R.B., Crespo A.J.C., Domínguez J.M., Ferreira R.M.L. & Gómez-Gesteira M. 2016. SPH–DCDEM model for arbitrary geometries in free surface solid–fluid flows. *Computer Physics Communications* 202: 131-140.

Choi C.E., Goodwin G.R., Ng C.W.W., Cheung D.K.H., Kwan J.S.H. & Pun W.K. 2016. Coarse granular flow interaction with slit structures. *Géotechnique Letters* 6: 267-274.

Domínguez J. M., Fourtakas G., Altomare C., Canelas R. B., Tafuni A., García-Feal O., Martínez-Estévez I., Mokos A., Vacondio R., Crespo A.J.C., Rogers B. D., Stansby P. K. & Gómez-Gesteira M. 2021. DualSPHysics: from fluid dynamics to multiphysics problems. *Computational Particle Mechanics.*

Gong S.X., Zhao T., Zhao J.D., Dai F. & Zhou G.G.D. 2021. Discrete element analysis of dry granular flow impact on slit dams. *Landslides* 18: 1143-1152.

Goodwin G.R. & Choi C.E. 2020. Slit structures: Fundamental mechanisms of mechanical trapping of granular flows. *Computers and Geotechnics* 119.

Han Z., Su B., Li Y.G., Wang W., Wang W.D., Huang J.L. & Chen G.Q. 2019. Numerical simulation of debris-flow behavior based on the SPH method incorporating the Herschel-Bulkley-Papanastasiou rheology model. *Engineering Geology* 255: 26-36.

Hungr O., Evans S.G., Bovis M.J. & Hutchinson J.N. 2001. Review of the classification of landslide of the flow type. *Environmental and Engineering Geoscience* VII (3): 221-238.

Kwan J.S.H., Koo R.C.H. & Ng C.W.W. 2015. Landslide mobility analysis for design of multiple debris-resisting barriers. *Canadian Geotechnical Journal* 52: 1345-1359.

Leonardi A., Wittel F.K., Mendoza M., Vetter R. & Herrmann H.J. 2016. Particle–Fluid–Structure Interaction for Debris Flow Impact on Flexible Barriers. *Computer-Aided Civil and Infrastructure Engineering* 31: 323-333.

Li X.P., Yan Q.W., Zhao S.X., Luo Y., Wu Y. & Wang D.P. 2020. Investigation of influence of baffles on landslide debris mobility by 3D material point method. *Landslides* 17: 1129-1143.

Li X.Y. & Zhao J.D. 2018. A unified CFD-DEM approach for modeling of debris flow impacts on flexible barriers. *International Journal for Numerical and Analytical Methods in Geomechanics* 42: 1643– 1670.

Mazhar H., Heyn T., Pazouki A., Melanz D., Seidl A., Bartholomew A., Tasora A. & Negrut D. 2013. Chrono: a parallel multi-physics library for rigid-body, flexible-body, and fluid dynamics. *Mechanical Sciences* 4 (1): 49-64.

Ng C.W.W., Liu H.M., Choi C.E., Kwan J.S.H. & Pun W.K. 2021. Impact Dynamics of Boulder-Enriched Debris Flow on a Rigid Barrier. *Journal of Geotechnical and Geoenvironmental Engineering* 147 (3).

Iverson R.M. 2003. The debris-flow rheology myth. *3rd International Conference on Debris-Flow Hazards Mitigation: Mechanics, Prediction, and Assessment.* Davos.

A Road Map for Urban Planning and Cavern Development in West Hong Kong Island

V. Viniarski
Urban Designer & Planner, MAS., Italy

A. Marcolini
Geotechnical Engineer, MSc Eng., Italy

M. Li
Geotechnical Engineer, MICE C.Eng., Hong Kong

J. Hui
Geotechnical Engineer, MHKIE (GEL), MICE C.Eng., Hong Kong

ABSTRACT

Through an engineering urban planning analysis and considering various aspects of cavern development in West Hong Kong, there is great potential for sports, recreation and rehabilitation facilities. The proof of concept has been presented in the HKIE Think Deep Programme 2024 and was well received by the panelists and participants. By catering to the needs of the public and infusing the cultural elements into the engineering design and development strategy, it is envisaged that the success of the cavern development initiative in Hong Kong is highly probable.

From a macro-perspective, the strive to create “First in Hong Kong Facilities through Cavern Development” can be used as a catalyst to stimulate the economy through the construction and commercial trading of minerals, allowing Hong Kong to retain a competitive edge as well as attract overseas talents through mega-cavern initiatives. From a micro-perspective, the construction of sports, recreation and rehabilitation facilities are means of improving public livelihood whilst catering for the sustainability, environmental and social aspects.

In this paper, the proposed development is fit into the future economic and financial strategy of Hong Kong to understand if the mentioned project is applicable and can have a positive economical outcome for the region.

1 INTRODUCTION

1.1 The Young Professionals’ Think Deep Programme 2024

The HKIE Geotechnical Division Young Professionals’ Think Deep Programme 2024 on Urban Planning and Cavern Development in Hong Kong in October 2024 focused on the future potential of cavern development in Hong Kong as well as tackling various issues faced within Hong Kong. The workshop was intended as an international event to explore opportunities and ideas for developing underground spaces. Gathering participants from all over the world, the event tackles the potential of rock caverns expansion, focusing on Hong Kong’s suitability for underground space uses. This paper highlights the collaborative effort from HKIE (Geotechnical Division of the Hong Kong Institution of Engineers), ISOCARP (International Society of City and Regional Planners), ITACUS (International Tunnelling and Underground Space Association’s Committee on Underground Space) and participants in urban planning, geotechnical engineering, and architectural considerations of cavern potential in Hong Kong and its alignment with the vision of “The Chief Executive’s 2024 Policy Address.”

1.2 Hong Kong case

A key issue in the long-term development of Hong Kong is creating new land; considering all viable options, rock caverns can be a cost-effective solution to relocate "surface" facilities or develop new services for the local population. It is proven that the combination of the hilly terrain and the geological characteristics of rocks in Hong Kong makes the territory a very suitable environment to develop underground structures.

Given the above, the YPTDP workshop focus was on specific Strategic Cavern Areas (defined in the HK Cavern Master Plan) of West Hong Kong island; in particular, the selected areas are Mount Davis and Pok Fu Lam as per the below map (Figure 1).

Figure 1: Boundaries of Cavern Master Plan in West Hong Kong (2017, Civil Engineering and Development Department, Planning Department, Cavern Master Plan Explanatory Statement).

1.3 Background

In 2023, the Outline Zoning Plan (OZP) for Kennedy Town and Mount Davis was updated. Local authorities' target was to delineate further developments within and outside the region to meet social demand. Multiple consultation processes were carried out throughout the Town Planning Boards (TPB), and residents were given the chance to submit suggestions about future developments.

The workshop "Thinking Deep and Enlivening Island West with Rock Cavern Development" was organized thanks to the efforts of professional bodies, academic institutions, and international learned societies. The main goals were to promote cavern development, enhance residents' quality of life, promote sustainable development, and rethink the use of land for regional growth.

1.4 Urban Planning Elements Considerations

Throughout the workshop, the main focus was on delivering an innovative scenario/use of rock caverns on West Hong Kong Island. The following are the key features considered to develop the project:

1. Regional features and urban setting/foreseen developments.
2. Possible SCVAs' location, as well as actual and proposed land use in the surroundings.
3. Assumptions regarding planning principles and purposes of the proposed cavern development.
4. Strengths and constraints of the development.
5. Integrability between the Cavern development and existing/future developments in West Hong Kong Island.
6. Planning at the local and regional level.
7. Sustainability issues in terms of city planning and cultural development.

1.5 Engineering Elements Considerations

From an engineering point of view, the following are the key elements considered for Cavern design and development:

1. Cavern alignment and geometrical feature/cross-section.
2. Preparatory investigation plan for rock cavern design.
3. Construction sequence and rock support strategy.
4. Operational, security, environmental and MEP requirements.
5. Key sustainability and environmental principles
6. Strive for innovation and the application of new technology.
7. Public engagement and communication.

2 LUNG FU ROCKS

2.1 Regional Integrability

The purpose of the first part of the analysis was to comprehend the context, with an emphasis on Hong Kong's vision and objectives for regional integration. From the perspective of Hong Kong Island West, the plan is to enhance development within the Western Islands of Hong Kong and improve connectivity to the harbour front. This aligns with the Harbourfront Commission's initiative for the future development of the Waterfront Promenade and creating a vibrant city with added elements of culture and the arts to represent Hong Kong.

As we expand beyond Hong Kong Island, regional integrability involves synergetic development and connections between the New Territories, Kowloon, and outlying Islands. With the enhanced network between the outlying Islands and Lantau, the strengthened network between Mainland China (Shenzhen) and Hong Kong Island will become possible, thus increasing the social and commercial activities in both regions.

2.2 Planning Principles

Taking into consideration the above mentioned SCVAs, this paper aims to develop a possible scenario for a strategic rock cavern design that attempts to "listen" to the community to be aligned with residents' values and needs.

In 2011, the District Council conducted a survey using a form with inhabitants related to the development planning of promenades in the Central and Western Districts of Hong Kong. The results also included the public esteem related to the Kennedy Town and Mount Davis Planning Study, produced in 2022, which served as a foundation for an analysis. Furthermore, the University of Hong Kong contributed to a related project in the same context, providing a comprehensive approach to the area. The analysis identified the challenges faced by inhabitants of that area and Hong Kong's population. Based on this, the four key problems are listed below:

1. Elderly population and Rising Demand for Health Facilities
2. Craving for Sports Facilities and Green Areas
3. Shortage of Open Spaces and Recreational Areas
4. Lack of Public and Private Parking Lots.

The survey described above points out the key needs of the locals which drove the main strategies for the rock cavern design. The main pillars of the design strategy were inhabitants' assessments, data analysis of residents' needs, consideration of site constraints, existing buildings, and major upcoming projects. The rock caverns' scheme also considers key locations in the area, such as the University of Hong Kong, the new campus and student accommodation, and Queen Mary Hospital.

To fulfil the community's requirements, the proposed layout for the cavern development foresees the creation of a sports facility and a rehabilitation centre. This project aims to reduce the overcapacity of Hong Kong's amenities by providing high-quality health facilities and, considering the dense urban context, improving the surrounding area by adding public spaces, pedestrian zones and leisure centers.

Therefore, four main pillars have been developed: "Short-term" and "Long-term" development scenarios, "Listening" to the community, a Network of "Open Spaces" and "Sports Facilities" and displacing “Parking Lot" to "The Underground" (Figure 2).

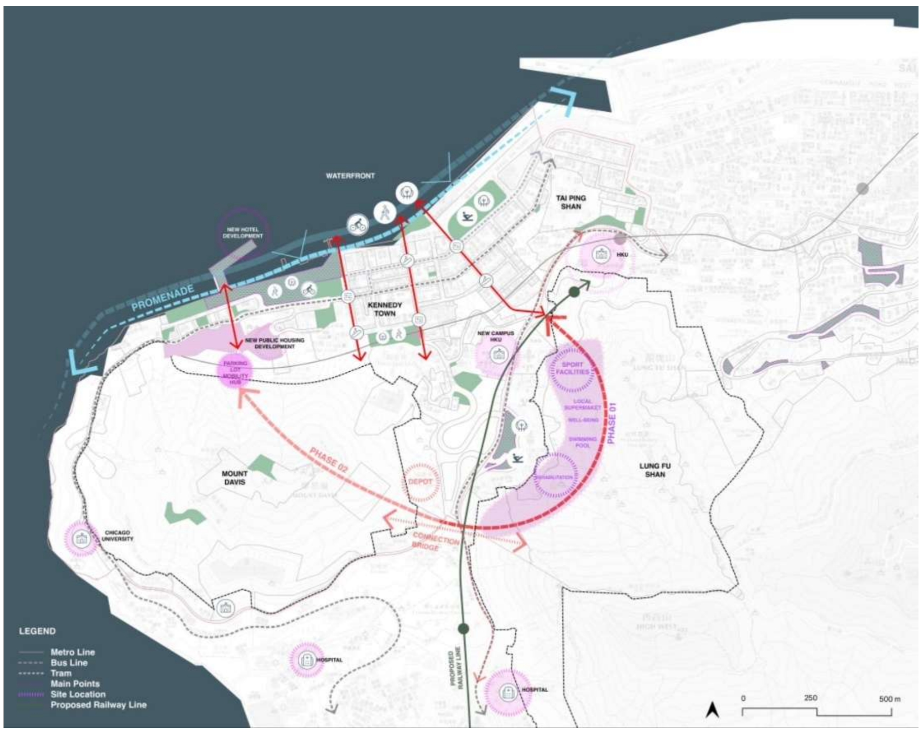

Figure 2: Lung Fu Rocks Vision.

2.3 Cavern Placement

West Hong Kong is heavily populated, so displacing parking lots underground would liberate spaces for recreation areas, walkways, and green areas. Moreover, the connectivity with the railway that intersects Mount Davis and Lung Fu Shan West, Hong Kong, emphasizes the area's relevance. Considering two different time frames, short-term (phase 01) and long-term (phase 02) development stages, the area offers adaptability for enhancements while granting consistent growth.

Lastly, the inclusion of a network of open spaces and sports facilities promotes a comprehensive approach to well-being, which is the bottom line for enhancing quality of life.

Considering the main needs identified for the local population, as per Phase 1, it is foreseen to develop the following: a fully automated car park at Mt.Davis side (SCVAs N.41) to support the new housing plan and move existing car parks underground, and an interconnected series of caverns (at Lung Fu Shan side, SCVAs N.40) that will serve as sports facilities and rehabilitation centers.

The Mt. Davis car park portal/entrance will be located close to the new housing development foreseen in the area, making it easily accessible for locals and the community. Lung Fu Rocks caverns will be served by two different portals: the North portal will be placed near the new HKU campus, while the South portal will be closer to the Queen Mary Hospital to ease the use of the rehabilitation center.

Being the North Portal location close to/at the place of a gas station, as per common practice and regulations an underground utilities identification process will be put in place. These will be assessed via in-situ testing such as "PNAP APP 137 Ground-borne Vibration and Ground Settlement arising from Pile Foundation and Excavation and Lateral Support Works". On top of that, further liaison will be conducted with the gas station provider, Sinopac and Petrol China for a possible diversion of underground utilities if deemed required based on the assessment as stated above.

The existing Pokfield Road Bus Terminus at the proposed North Portal location will also be upgraded and further enhanced to provide connectivity with the public in the Southern part of Hong Kong.

The overall Plan is here under attached for reference (Figure 3).

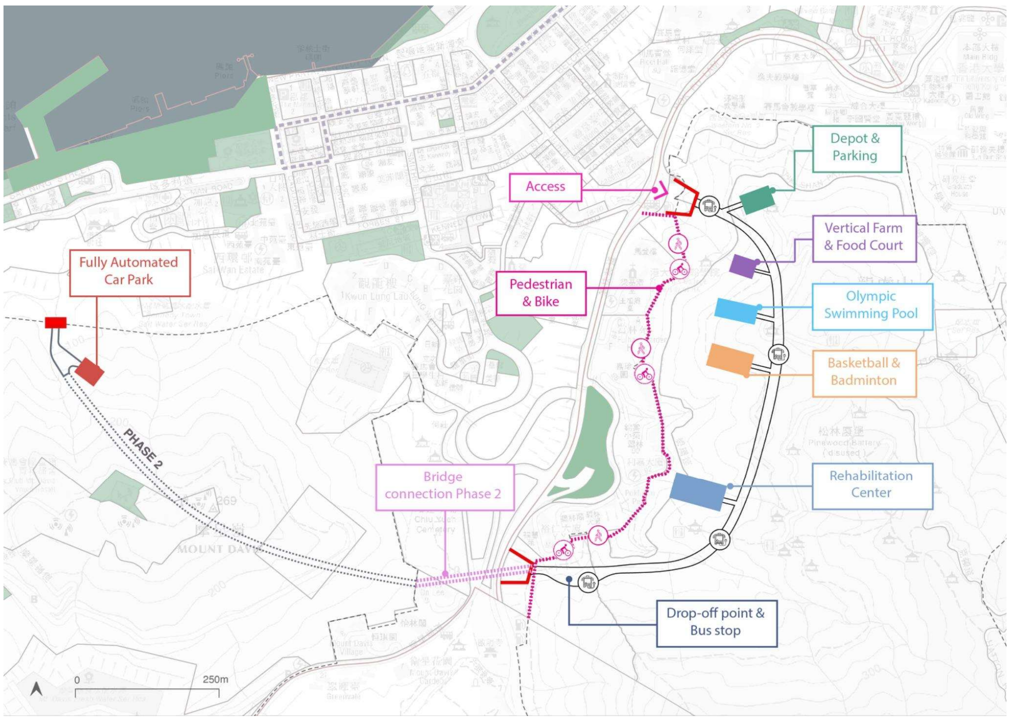

Figure 3: Caverns' plan.

The Lung Fu Rocks cavern complex will also be accessible via a cycle and pedestrian lane excavated all along the hill (reference is to the light purple dotted line in Figure 3). The vision is to have the cycle path run into a gallery, allowing natural light to come into the track through the openings and reducing the need for artificial light.

2.3.1 Mt. Davis - SCVAs 41

A multi-storey parking area will maximize the number of available spots, given the limited space inside the cavern. A fully automated system, with a stacked parking layout, will also allow the population to leave the car at the portal location without entering the underground; a mechanical system will transport the car to and from the car park, completely removing pollution/emissions inside the tunnel and the cavern. Assumes each parking is 3m wide and 5m long, with the height provisioned to stack at least 5 cars, with possibility to further enhance. With a fully automated parking system, the designed cavern will be able to accommodate a maximum of about two hundred car parking spaces, including non-commerical vehicles such as cars and motorcycles, and will be accessed by a tunnel connecting the portal area with the underground area.

Here under are attached the main geometrical properties of the cavern:

- Span: 30 m

- Height: 30 m
- Length: 37.5 m.

2.3.2 Lung Fu Shan - SCVAs 40

This area will accommodate multiple interconnected caverns, each one serving a specific purpose. An internal transportation system via electric self-driven buses will be provided to carry people between the various facilities. In this regard, a 1000 m main tunnel connecting caverns will be excavated at Lung Fu Shan side, while a 200 m main tunnel will be excavated at the Mount Davis portion (being ready for future developments in the long term). A single-lane two-way road will be accommodated in the tunnel. In order to fulfil local regulations for road tunnels and related safety aspects (reference is "Guidance Notes on Design of Road Tunnel Structures and Tunnel Buildings to be Maintained" by the Highway Department, HKSAR), the cross-section of the mentioned tunnel will have a 16 m span and 20 m height. To adhere to local fire safety requirements, during the design phase every possible aspect of the regulations will be taken into consideration. The workflow will be to deliver dedicated plans and analysis for operation, maintenance and fire safety aspects such as CFD Analysis for Smoke Extraction system, Means of Access (MOA) and Escape (MOE), Evacuation Analysis and Fixed Fire Protection systems design. As an example, to ensure safety and timely evacuation in case of fire accident, the staircases inside each cavern will be designed to be connected to pressurized protected corridors, leading to exits of access tunnels, with travel distances to exits limited to ≤36m. Other options such as cross passages would be considered as well if deemed applicable.

Geometrical and functional details regarding each foreseen cavern are listed below.

- Parking spot & Bus depot (Span 30m, Height 20m, Length 40m): The facility will work as a mobility hub for the population enjoying the Lung Fu Rocks complex. It will be located close to the North portal to ease the accessibility of the parking spaces and reduce car traffic inside the main tunnel. Parking (approx. two hundred spots) will be semi-automated, often referred to as puzzle parking, meaning that each car gets parked entirely independently of every other car, allowing access for each car without moving all the other cars around it. The cavern will also accommodate a dedicated bus stop and a depot for the internal mobility transportation system.
- Vertical farm & Coffee shop/event space (Span 20m, Height 20m, Length 30m): The cavern will accommodate a vertical farming system to produce food in spaces that would otherwise be unfit for farming. It will also contain a coffee shop/event space, which will serve as a food court for customers.
- Multipurpose sports hall (Span 32m, Height 20m, Length 60m): The cavern will accommodate N.2 Basketball and N.4 Badminton courts. As two of the most popular sports in Hong Kong, the need for additional courts is one of the most important demands for the community (Figure 4).

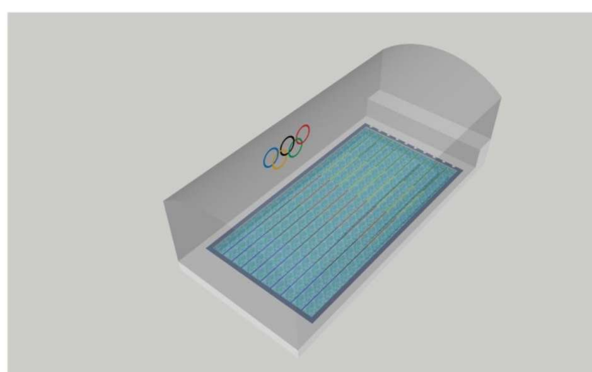

Figure 4: Left: Multipurpose sports hall 3D model (Rex, 2024; Rolie, 2021). Right: Olympic swimming pool 3D model (SDC93, 2014; Olympic rings without rim).

- Olympic grade swimming pool (Span 30m, Height 20m, Length 65m): The Chief Executive's 2024 Policy Address mentioned that the government will continue to foster sports development. One of the proposed measures is the construction of a swimming pool designed to host international competitions. Consequently, the provision of this Olympic swimming pool in the cavern will not only serve as the first Olympic swimming pool in the urban area. However, it will also align with the objectives outlined in the Policy Address (Figure 4).
- Rehabilitation centre (Span 36m, Height 20m, Length 80m): A multi-story building of about 4700 sqm will be erected inside the cavern, providing services such as specialist treatments, radiology, and rehabilitation. The cavern's location is near the South portal, which will bring it closer to Queen Mary Hospital.

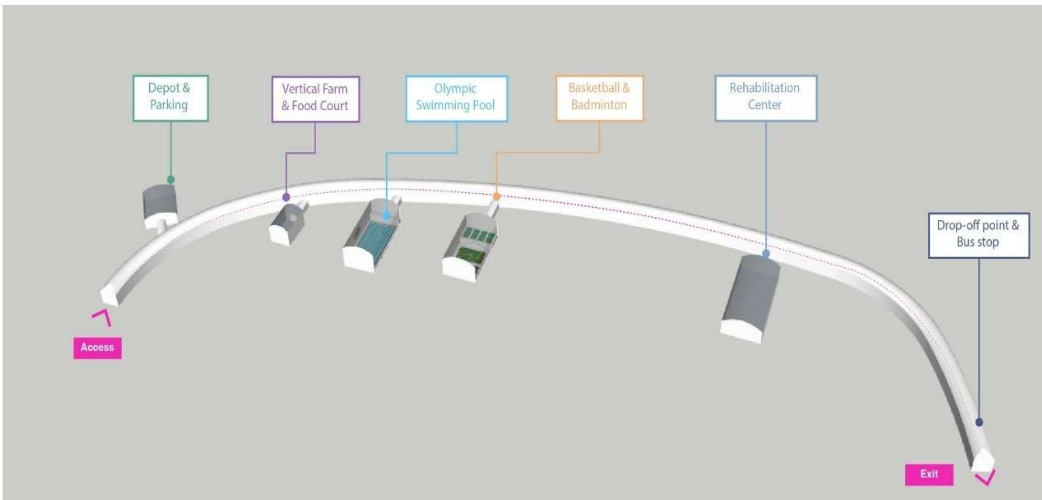

Figure 5: Lung Fu Rocks, Caverns 3D model overview.

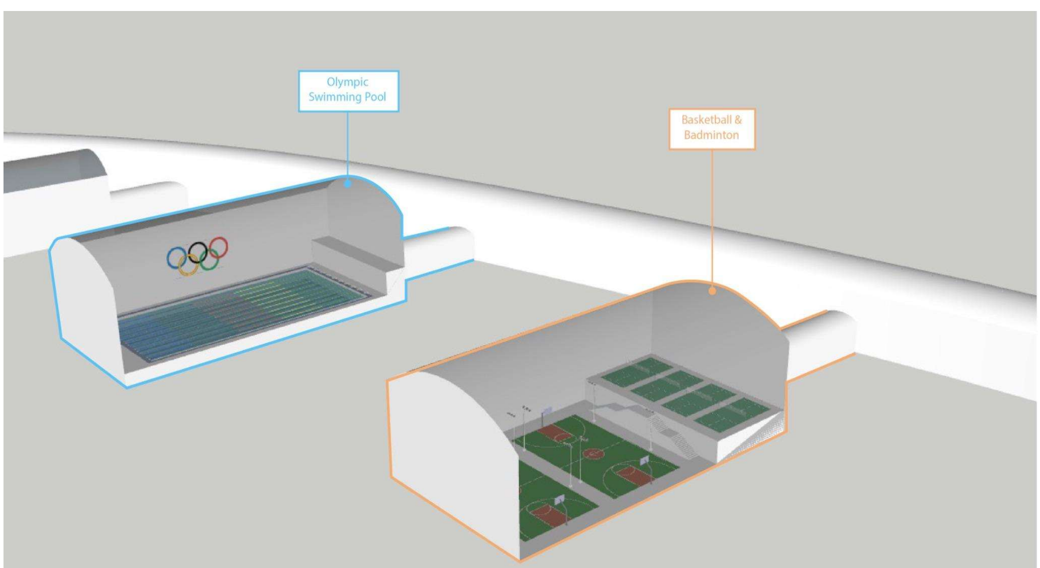

Figure 6: Olympic Pool and Badminton/ Basketball Court (Rex, 2024; Rolie, 2021; SDC93, 2014; Olympic rings without rim).

Every sport-related facility will be furnished with a dedicated area for changing rooms, lavatories and MEP room. It is envisaged that the rooms are to be placed under the 4 badminton courts or in specific areas close to the entrance of each cavern, as shown in the Figure 6 above. Details of each cavern related facilities will be further reviewed and considered in the next detailed design phase.

2.4 Long-Term Vision

Regarding Phase 2, meaning the long-term vision for West Hong Kong development, Lung Fu Shan side and Mt. Davis will be connected through a surface/underground ring road. The main tunnel will be extended to reach the parking spot portal in the Mt. Davis area, and the connection between the two sides of the valley will be achieved thanks to a bridge (reference Figure 3). Having a surface connection between the two underground areas will function as a marking point for the Lung Fu Rocks complex; the bridge will aim to provide the population with accessibility to the underground facilities. Linking the two strategic cavern areas will allow for future developments of the underground system, allowing local authorities to promote new uses and purposes for rock caverns.

2.5 Architectural elements

The proposed cavern design will have its specific architectural vision; the idea is to seamlessly integrate the structure within the mountain, embracing the essence of landscape architecture. The goal is to create a harmonious blend that appears as a natural extension of the terrain. This draft illustration captures the concept: the mountain's fissures function as both entrances and sources of natural light, seamlessly merging with the rocky facade (Figure 7).

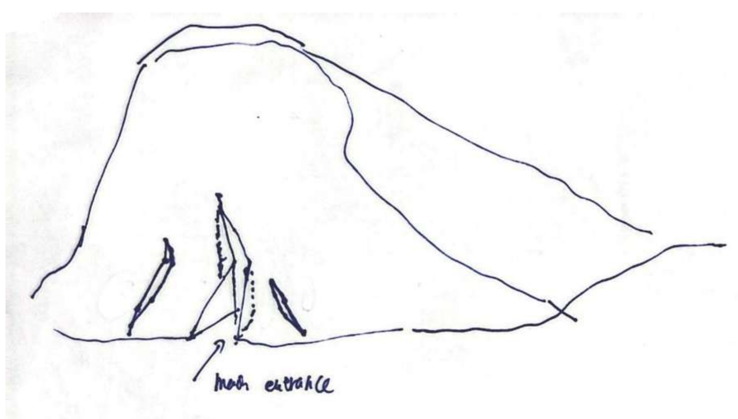

Figure 7: Draft illustration captures the architectural concept.

The concept and the name for "Lung Fu Rocks" were based on the powerful symbols of the Chinese cultural aspects. "Lung" represents the dragon, a figure of majesty and strength, whilst "Fu" signifies the tiger, symbolising bravery and endurance.

For example, the cycle and pedestrian pathways were designed to resemble the sinuous silhouette of a dragon, adapting to the untouched landscape/hills with a fluid shape. The fissures representing the tiger's stripes bring prosperity and fortune. Even though the design honors the mythical symbiosis of the dragon and tiger, it also attempts to invoke abundance and well-being in all users. With a meticulous composition and symbolic depth, "Lung Fu Rocks" is a result and a process of a fruitful collaboration enclosed by nature and human beings.

2.6 Natural Lighting Optimization in Caverns

As explained in the previous section, the core idea in terms of architecture is to optimize the natural lighting entering the complex through the entrance cracks of the cavern design; the use of refracting mirror panels lined along the interior is explored as a possible solution to boost the light coming into the underground.

It is becoming common to enhance the natural lighting in the underground through the concept of a light shaft. The proposed solution protects the natural aesthetic of the mountainous rock facade while reducing the need for lights during the daytime, which also helps to save electricity and reduces the environmental impact of the underground structure.

An existing and reference example is the Reichstag Building in Berlin; the parliament building has an integrated reflecting and refracting mirror system, which serves the conference halls, to focus sunlight and direct it into the underground basement levels. With reference to the mentioned example, a light refraction system is found to be applicable in the proposed cavern design to be integrated into the environment.

2.7 Public engagement

Public engagement is a key aspect of consolidating the concept of Lung Fu Rocks and presenting the underground development to the public. Thus, a well-planned, informative, and interactive public engagement plan will be devised. Through a comprehensive review of past studies from Mount Davis and Kennedy Down Development, public needs and critical aspects will be evaluated and incorporated into the planned design.

Through an interactive public engagement plan, which consists of sports activities at selected venues around Hong Kong Island and community workshops, the goal is to gather public views and propose further development of the design to meet the public's expectations. The vision is to integrate the cultural and geographical aspects of Lung Fu Shan, where "Dragon" and "Tiger" serve as the theme for the cavern development. This theme may be applied to represent Chinese cultural blessings [龍爭虎鬥], meaning competitive spirit, and [龍精虎猛], meaning vitality and growth, which fully aligns with the elements that comprise the foreseen cavern design and development. By infusing these aspects into the project, the public will be much more receptive and appreciative of the development as it creates a recognizable identity in the region.

Concurrently, a series of Value Management Workshops with international Expert reviews and Stakeholder Forums will further enhance the design. Doing so reinforces the Harbourfront Development Initiative and Railway Development Strategy 2014 future SIL(W) project’s constructive collaboration with this new scheme. This will bring additional value to the further development of Hong Kong Island, enhance its connectivity to the Harbourfront, and benefit the public.

3 ECONOMIC PROSPECTS

In the previous sections, the vision for cavern development and urban planning in Hong Kong has been elaborated along with various engineering, cultural & heritage, and sustainability aspects considered, which aligns with the various policies under the Chief Executive’s 2024 Policy Address. Studies from the Policy Address 2024 and Budget Report 2025-2026 have iterated that Hong Kong remains a service-driven economy. Despite the economic instability due to political interferences and financial deficits, it is foreseen that the construction industry, inclusive of geotechnical and infrastructure, will remain a prominent presence and contribute to Hong Kong’s economy.

Although Engineering, Design and Urban Development would not be the solution to resolve the economic constraints faced in Hong Kong, it is common to believe that the construction industry may serve as a catalyst for re-igniting the Hong Kong economy through mega-event constructions. Thus, this Section 3 focuses on the economic viability and financial prospects of the envisaged cavern design / urban development and its potential contribution to add value to the planned projects of Hong Kong.

Based on the policy address, the percentage of the proposed budget was presented, as shown in Figure 8 below. It includes various sectors such as Education, Infrastructure, Social Welfare and various other sectors. Lung Fu Rocks fits well within the share of expenditure. The proposed cavern design falls within the Community & External Affairs, Economic, Education, Health, Infrastructure and Social Welfare. The total coverage accounts for over 65% of the estimated expenditure.

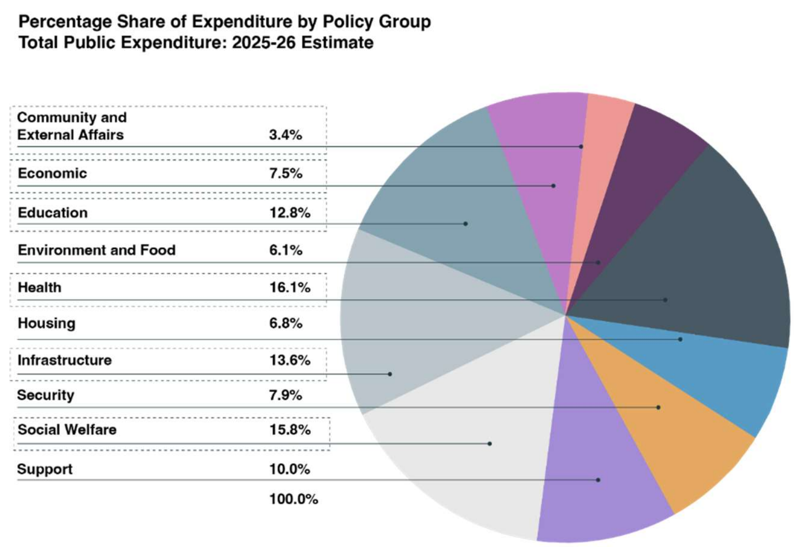

Figure 8: Percentage Share of Expenditure by Policy Group (The 2025-26 Budget. Speech by the Financial Secretary, the Hon Paul MP Chan, moving the Second Reading of the Appropriation Bill 2025).

With the additional Olympic-grade sports facilities and other features, Lung Fu Rocks is believed to help increase local and overseas tourists and thus generate additional economic benefits. Other than that, by moving various infrastructures above ground, the freed-out surface area can be adopted for other usages and generate additional income.

3.1 Value for Sports / Recreation Facilities and Integration with Future Transports

In accordance with the Policy Address 2024, the promotion of Sports Development and building Hong Kong into a Centre for Mega International Sports Events remains one of the long-term goals. It is noted that the current Kai Tak Sports Park can serve as a location for hosting such mega sports events. However, certain restrictions, such as noise restrictions and ease of travel to the Sports Arena, remain a hurdle for fully utilizing the sports facilities.

Whereas by selecting the underground locations of multi-sports facilities, there is greater flexibility in operation time and restrictions on noise, given that the facilities are situated underground. In addition, under the Hong Kong 2025-2026 Budget Report by the Financial Secretary, there are plans to initiate the detailed planning and design of the South Island Line (West) Project. In the proposed strategy for rock caverns, the sports and recreational facilities within the Cavern will add value to the SIL(W) line and serve as a tourist attraction, increasing future MTR patronage.

Furthermore, Kai Tak Sports Park primarily serves as a stadium for non-water-related sports events. It is envisaged that by including into the cavern design an Olympic Grade swimming pool which is a first in Hong Kong, to promote water sports competitions, given the recent success in the 2024 Olympics for Hong Kong and Mainland China. This may bring forth a different sports market in Hong Kong and attract more talent and competition events outside of land-based sports.

In addition, the location of West Hong Kong for housing the various sports facilities in caverns has the potential to stimulate the nightlife economy, which the government is eager to rejuvenate post-COVID. The ideal district to accommodate these desires would be the SOHO and Lan Kwai Fong District, which is near the envisaged Cavern recreation/sport facilities. Thus, this advantageous location has the potential to stimulate the local commercial activities and nightlife economy, giving an edge over Kai Tak Sports Park.

Another advantage of West Hong Kong Cavern Development is the opportunity for expansion. Currently, the above accommodations comprise Phase 1 at Lung Fu Shan. The adjacent Mount Davis is envisaged for future Cavern Development for Phase 2. The possibilities for Phase 2 are vast, with proposals for an underground tunnel network connecting with Mainland China via rail or vehicular access, thus improving the connectivity between the Islands and Mainland China. This has great prospects for linking up the Commercial Business Districts (CBD) of Hong Kong with Mainland China.

3.2 Value for technology

As defined in the Speech by the Financial Secretary-Budget 2025-26, one of the main core areas to further develop Innovation and Technology in Hong Kong is Artificial Intelligence. The goal is to develop Hong Kong into an international exchange and cooperation hub for the AI industry. In the long-term vision, the use of caverns to install research laboratories and/or development institutes may bring together international talents and investors. Moreover, the specific environmental conditions of rock caverns may facilitate the installation of data centers underground; it is becoming common practice to develop this kind of tech-related area underground to reduce the environmental impact of data centers.

3.3 Value for tourism

An additional key aspect mentioned in the Policy Address 2024 is to enhance and revitalize Hong Kong’s tourism through an innovative use of the unique resources of the area. A rock cavern development program such as Lung Fu Rocks may serve as a marking point to promote sports, culture and events in a unique location. It can be a tourist hotspot in an area which is typically not that popular among visitors coming from abroad; coupled with Mt. Davis' historical point of interest, Lung Fu Rocks may become a landmark with a strong appeal in West Hong Kong.

Given the future transportation development in the area, a cavern design such as the one presented in this paper will easily boost the local economy and serve as a reference point for eco-tourism, being presented to the public with its own specific and exclusive characteristics.

4 CONCLUSIONS

In conclusion, based on the various aspects discussed in Sections 2 and 3, it is envisaged that cavern construction and urban development in Hong Kong can still provide added value and contribute to Hong Kong from a social, cultural and economic perspective. Thus, cavern design and urban development provide opportunities to link up with the Mainland, as well as address the 4-key issues that form the basis of the proposed design which coincides with the Policy Address 2024 and the long-term development of Hong Kong

As fellow engineers bearing the “Ir. Title”, and those planning to achieve professional status, the Ir – stands for “*Ingeniour*” and is derived from the Latin term “*ingenium*” (meaning knowledge) and Latin term *“ingeniare*” (meaning to create). These attributes define an engineer the ability to envision the possibilities. Thus, this brings the mentioned vision full circle as this exercise began with the Think Deep Programme 2024 focusing on the possibilities inherent in Hong Kong. Through the strive for knowledge and innovations for establishing the foundations for cavern design, this vision may foster to become a reality.

ACKNOWLEDGEMENTS

Gratitude goes to ISOCARP, ITACUS and the HKIE (Geotechnical Division of the Hong Kong Institution of Engineers) for organizing and hosting the workshop. Having local entities involved in the organization and the progress of the symposium inspired all participants to develop a solid project to be integrated into Hong Kong’s complex urban development.

REFERENCES

Barrett SVL, McCreath DR. 1995. Shotcrete support design in blocky ground: towards a deterministic approach. *Tunneling and Underground Space Technology, incorporating Trenchless Technology Research*. 10(1): 79-89.

Geotechnical Control Office (GCO). 1986. Hong Kong & Kowloon. *Hong Kong Geological Survey Map Sheet 11, Solid and Superficial Geology, 1:20000 Series HGM20 (Edition I)*. Geotechnical Control Office, Hong Kong.

Geotechnical Engineering Office (GEO). 2012. Hong Kong & Kowloon. *Hong Kong Geological Survey Map Sheet 11, Solid and Superficial Geology, 1:20000 Series HGM20 (Edition II)*. Geotechnical Engineering Office, Hong Kong.

Heiniö, M. 1999. *Rock excavation handbook for civil engineering*. Sandvik Group.

Hoek, E. 2023. *Practical rock engineering – 2023 web edition*.

Kong, K. W. K. 2018. Practical shotcrete rock reinforcement for hard rock openings. *HKIE Transactions*. 25(3): 153–164.

The Hong Kong Special Administrative Region of the People's Republic of China. 2024. The Chief Executive's 2024 Policy Address. *Reform for Enhancing Development and Building Our Future Together.*

Financial Secretary, Hong Kong. 2025. *The 2025-2026 Budget speech*.

Town Planning Board (TPB). 7 October 2016. *Study on Long-term Strategy for Cavern Development: Cavern Master Plan (CMP)*. Paper No. 10185

Ho, Y. K., Tsang, W. H., & Chan, C. C. 2019. *Rock cavern development in Hong Kong: past, present and future*. In Proceedings of the Institution of Civil Engineers-Civil Engineering: Vol. 173, No. 5, pp. 25-31.

Hong Kong District Planning Office. 2023. *S/H1/24 Kennedy Town & Mount Davis (HPA 1) Outline Zoning Plan.*

Hong Kong District Planning Office. 2024. *S/H10/22 Pok Fu Lam (HPA 10) Outline Zoning Plan.*

University of Hong Kong (HKU). URBP7008 Strategic & Community Planning Studio. *Final report-Reimagining a Future-ready Strategic Connector for People to Flourish and Enjoy.*

Can the Potential of Hong Kong Rocks be Harnessed for Effective Thermal Energy Storage?

Louis N.Y. Wong[1,2], Zihan Liu[1,2] & Su-Chin Chang[2]
[1] The University of Hong Kong Shenzhen Institute of Research and Innovation (HKU-SIRI), China
[2] Department of Earth Sciences, The University of Hong Kong, Hong Kong

ABSTRACT

Alternative clean energy sources such as solar, nuclear, and geothermal have undergone considerable advancements. Thermal energy storage (TES) can also be employed to directly capture and store waste heat generated from diesel generators' exhaust gases. TES can be classified into three primary categories: sensible heat storage, latent heat storage, and thermochemical heat storage. Sensible heat storage involves storing energy by raising the temperature of a material without changing its phase. No TES systems have been implemented in Hong Kong thus far. This study aims to assess the thermophysical properties of Hong Kong rocks, serving as a foundational reference for future TES site and material selection endeavors. A total of 15 common rock types were selected, comprehensively covering igneous, sedimentary, and metamorphic lithologies. These rock samples were tested for four physical or petrology and five thermophysical parameters under continuous real-time heating up to 1000 °C. Through multidimensional evaluation, the suitability of these rocks from Hong Kong to serve as thermal energy storage media was assessed. The results obtained indicated that Hong Kong basalt is the optimal candidate for high-temperature TES material, with 850°C identified as the suitable maximum working temperature. Other igneous rocks from Hong Kong can be utilized for mid-to-low temperature range (100–500 °C) TES engineering.

1 INTRODUCTION

With the continuous depletion of fossil energy resources and the escalating importance for environmental protection, alternative clean energy sources such as solar, nuclear, and geothermal have undergone considerable advancements. Specific low-carbon technologies, including concentrating solar power, have emerged to address this prevailing issue. However, the intermittency inherent in these energy sources poses a challenge to the security of energy supply. Consequently, energy storage has been identified as a viable solution for managing fluctuations and intermittencies in renewable energy sources. For instance, solar energy harvested during periods of sunlight can be utilized to provide heat or electricity during nighttime or peak demand periods. Thermal energy storage (TES) can also be employed to directly capture and store waste heat generated from diesel generators' exhaust gases.

TES can be classified into three primary categories: sensible heat storage, latent heat storage, and thermochemical heat storage (Park et al., 2014). The classification is based on the underlying mechanisms by which energy is stored and released. Sensible heat storage involves storing energy by raising the temperature of a material without changing its phase. Insulating materials are used around the storage medium to minimize heat loss to the surrounding environment. These insulation barriers can consist of natural materials, such as clay, or engineered solutions designed to limit thermal conductivity. Additionally, implementing heat exchangers optimizes heat transfer when needed while minimizing losses during storage. During the charging phase (heat input), the exchangers facilitate efficient heat transfer; during discharging, they help extract heat with minimal loss. There are a few studies on the suitability of various rocks for high-temperature packed-bed TES systems. Grirate et al. (2014) investigated the thermogravimetry and heat capacity changes of granite, basalt, quartzite, marble, and hornfels within the temperature range of 25 – 400 °C. They concluded that these rocks are good candidates for thermal energy storage by sensible heat up to 350 °C (Grirate et al., 2014). Tiskatine et al. (2016) examined the changes in Vickers hardness and porosity of limestone, granite, rhyolite, and marble from

Morocco when heated between 20 °C and 650 °C. They found that rhyolite showed excellent potential for high-temperature TES (Tiskatine et al., 2016). Becattini et al. (2017) selected six types of rocks of Alpine origin, and tested the changes in specific heat capacity, porosity, and degree of cracking under temperatures ranging from 100 to 600 °C. They concluded that thermal treatment led to decreases in specific heat capacity and increases in porosity (Becattini et al., 2017).

The principle of localization holds significant importance in terms of both economic considerations and practical convenience. Besides, Allen et al. (2014) emphasize the necessity for site-specific studies of rock properties (Allen et al., 2014). In Hong Kong, there is an increasing government-led initiative toward adopting clean energy practices, making large concentrated solar power stations a feasible option. Additionally, data center operations typically produce large amounts of waste heat, presenting a considerable potential for the application of sensible heat storage in the region. However, to date, no TES systems have been implemented in Hong Kong thus far, and systematic research on the thermophysical properties of common rocks in the region remains limited. This study aims to identify typical and prevalent rock types and assess their thermophysical properties, serving as a foundational reference for future TES sites and material selection endeavors. In this work, a total of 15 common rock types were selected, comprehensively covering igneous, sedimentary, and metamorphic lithologies. These rock samples were tested for four physical or petrology tests (density, P-wave velocity, X-ray diffraction, and X-ray Fluorescence) and five thermophysical parameters (thermogravimetry, thermal expansion coefficient, heat capacity, thermal diffusivity, and thermal conductivity) under continuous real-time heating up to 1000 °C, a temperature that is sufficiently high for most TES systems. Besides, in the characterization process, the heterogeneity and anisotropy of typical rock types were considered and analyzed. To the best of our knowledge, this study provides a relatively comprehensive characterization of rocks for sensible thermal energy storage medium, making it a valuable reference for future research in the field. Additionally, the thermal properties of rocks are crucial considerations for environmentally sensitive projects such as the design and installation of buried high-voltage power cables and oil and gas pipelines. The findings of this study are beneficial not only for selecting appropriate rock types for TES medium but also for current and prospective high-temperature rock engineering endeavors in Hong Kong and the world.

2 Materials and methods

2.1 Sample preparation

Fifteen rock types (Table 1) were selected based on their prevalence and representativeness in the geological makeup of Hong Kong. Encompassing granitic, volcanic, sedimentary, and metamorphic varieties, these chosen rocks collectively offer a representative overview of the geological diversity found within Hong Kong. Besides, to consider the effects of heterogeneity or rocks, we collected rocks with different mineral grain sizes, such as fine-grained, medium-grained, and coarse-grained granite, metasiltstone, and fine metasandstone. The fine metasandstone and metasandstone have the same mineral composition (slightly different mineral proportion), but their grain size and texture appear slightly different. Their differences are likely due to different depositional environment and metamorphism histories, which we believe may affect their thermodynamic properties.

Table 1: General properties of testing rock samples

No.	Rock type	Acronym	Weathering degree	Sampling location	Density (kg/cm^3)	V_p (km/s)
1	Fine-grained Granite	GF	Fresh	Braemar Hill, North Point	2587	3.935
2	Medium-grained Granite	GM	Fresh	Elevated Road, Kai Yuen Street, North Point	2593	4.300
3	Coarse-grained Granite	GC	Fresh	Black Point, Tuen Mun West, New Territories	2616	5.063
4	Granodiorite	GD	Fresh	Tai Po	2648	4.900
5	Tuff-Tai Mo Shan Formation	TT	SD	Tai Mo Shan	2589	5.000
6	Tuff-High Island Formation	TH	SD	East Dam	2604	5.441
7	Basalt	BS	SD	Cheung Chau Ferry Pier	2742	5.568
8	Feldsparphyric rhyodacite	FRD	Fresh	Cheung Chau Ferry Pier	2631	5.833
9	Feldsparphyric rhyolite	FRL	Fresh	North Lantau	2722	6.279
10	Marble	MB	Fresh	Yuen Long	2703	5.909
11	Metasandstone	MSD	SD	Ma Cho Lung	2543	2.016
12	Sandstone	SD	Fresh	Kong Nga Po Road and Ping Che Road	2687	4.868
13	Siltstone	ST	Fresh	Sandy Ridge Cemetery, Sandy Ridge	2724	5.214

14	Metasiltstone	MST	SD	Tai O	2683	4.904
15	Fine Metasandstone	FMSD	SD	Tai O	2684	5.263

2.2 Characterization techniques

XRD analyses were conducted using a Rigaku MiniFlex 600 powder X-ray diffractometer (Rigaku, Tokyo, Japan) equipped with Cu Kα radiation. Thermogravimetric analysis (TGA) was conducted using a TGA 55 instrument (TA Instruments, New Castle, DE, USA) to determine the weight loss of the samples at elevated temperatures. The analysis involved heating the samples from room temperature (25 °C) to 1000 °C at a rate of 10 °C/min under a nitrogen atmosphere. The Laser Flash Analysis (LFA) technique, performed using the Netzsch LFA 427 instrument, was employed to determine the thermal diffusivity of the samples. Subsequently, thermal conductivity is computed based on thermal diffusivity. The thermal conductivity (k) of the rocks under investigation was determined by multiplying their density (ρ), specific heat capacity (C_p), and thermal diffusivity (λ) as a function of temperature (T) (Nahhas et al., 2019). The specific heat capacity was determined using a comparison method with sapphire serving as the calibration standard. The linear thermal expansion of Hong Kong rocks was assessed to establish the suitable maximum operational temperature. This evaluation utilized the NETZSCH DIL 402 Expedis Supreme pushrod dilatometer, heating samples to 1000 °C at a rate of 2.5 °C/min.

3 Results

3.1 Mineralogical compositions

Table 2 presents the mineralogical compositions of the tested rocks. Quartz minerals are prevalent in nearly all the examined samples. Metasandstone, fine metasandstone, and metasiltstone consist primarily of muscovite (a hydrated mineral from the mica group) and quartz. Quartz is renowned for its high thermal conductivity, 7.7 W/m·°C. This property facilitates thermal stratification within the bed and accelerates the rate of heating and cooling during thermal cycling. Additionally, rocks abundant in quartz are known for their hardness (Özkahraman et al., 2004) and tend to exhibit higher thermal conductivities at room temperature (Allen et al., 2014).

On the other hand, the high quartz content could lead to the degradation of rocks abundant in this mineral, such as metasandstones and metasiltstones, during thermal cycling. The anisotropic expansion of quartz during its α-β phase transition at 573 °C significantly compromises the integrity of granite samples (Chaki et al., 2008). Additionally, Allen et al. (2014) and Tiskatine et al. (2016) demonstrated that rocks with elevated quartz content are ill-suited for thermal cycling at high temperatures due to the disparate expansion rates of quartz (Allen et al., 2014), which exhibits a substantially larger volumetric coefficient of expansion compared to other minerals, thereby predisposing them to cracking and disintegration (Tiskatine et al., 2016). However, it has also been noted that the mechanical strength of rocks typically increases with quartz content (Allen et al., 2014). Therefore, rocks containing quartz as a binding agent may be better suited for the lower and middle sections of the storage facility, where temperatures are lower and greater mechanical resilience is required.

Marble, consisting predominantly of calcite, is characterized by interlocking calcium carbonate crystals, resulting from the metamorphism of limestone subjected to heat and pressure. Additionally, Fredrich and Wong (1986) observe that in calcitic rocks, the unusual thermal expansion anisotropy of calcite can induce thermal cracking, suggesting that these rocks may undergo permanent alterations prior to the onset of calcination reactions (Fredrich and Wong, 1986).

Table 2: Mineralogical compositions of the rocks

Mineralogical composition (vol%)	A	B	C	D	E	F	G	H	I	J	K	L	M	N	O	P
Fine–grained Granite	19.36	66.62		6.45	6.57											
Medium–grained Granite	20.62	72.98		5.41												
Coarse–grained Granite	36.53	51.77	10.70													
Granodiorite	29.07	31.49	7.18	31.26												
Tuff-Tai Mo Shan Formation	29.20						30.46	39.35								
Tuff-High Island Formation	21.34	46.85		4.46		20.48			5.88							
Basalt	18.8	29.8		46.6	3.8											
Feldsparphyric rhyodacite	10.17	45.97								1.05	32.90	8.91				
Feldsparphyric rhyolite	11.3	33.9			6.9								46.9			
Marble														99.00		
Metasandstone	65.63														33.37	
Sandstone	21.85	45.45			9.13										22.57	
Siltstone	19.27				36.53											43.21
Metasiltstone	63.36														35.64	
Fine Metasandstone	72.40														26.60	

Notes: A-Quartz; B-Albite ; C-Biotite; D-Anorthite; E-Clinochlore; F-Microline; G-Berlinite; H-Graphite; I-Orthoclase; J-Sodalite; K-Microperthite; L-Epidote; M- Microcline; N-Calcite; O-Muscovite; P-Pargasite

3.2 Thermogravimetric Analysis

Thermal stability analysis holds significant importance in evaluating the resistance of TES materials to high temperatures. TGA curves illustrate the mass loss of the sample as a function of temperature during thermal degradation. The differentiation of the TGA curve results in the Derivative Thermogravimetric (DTG) curve, which provides insights into the relationship between the rate of mass change of the sample and temperature. Figure 1 illustrates the relationship between sample weight and temperature. TGA was utilized to estimate the total volatile content within the rocks, including carbon dioxide and water. The findings suggest that most of the rocks exhibit minimal organic matter and consequently experience limited weight loss during heating. Notably, all samples displayed weight loss occurring in three distinct stages.

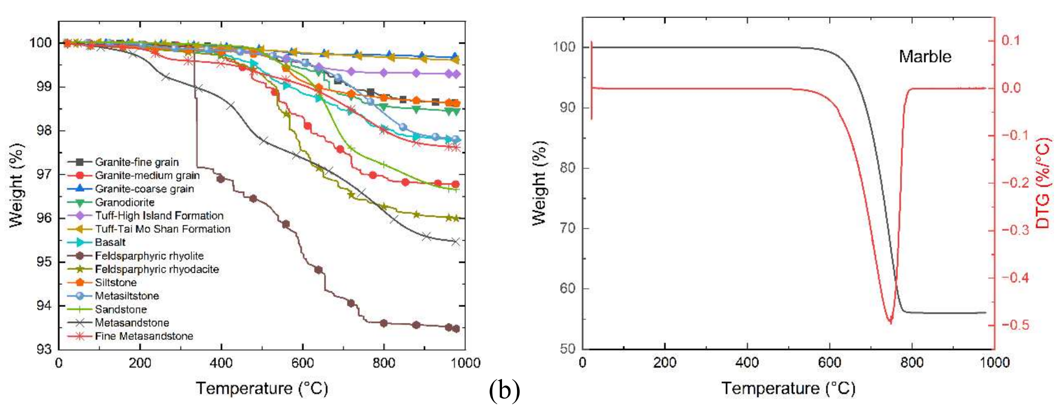

(a) (b)

Figure 1: Thermogravimetric analysis curves of major Hong Kong rocks. (a) most rock types except marble; (b) marble

The initial stage occurs from room temperature up to approximately 300 °C, with minimal mass variation observed. Within this temperature range, the weight loss is approximately 1% for metasandstone and nearly 0.5% for fine metasandstone, while for other samples, the weight loss is negligible. In this stage, weight loss in most rocks can be attributed to the evaporation of absorbed water and bonded water. During the second stage (300 – 800 °C), the rate of mass loss escalates and varies among different rock types. Within this temperature range, weight loss primarily arises from mineral decomposition, notably clay minerals. For most rocks, beyond 550 °C, all the tested rock samples exhibit oxidation of organic matter, contributing to the increased mass loss observed in the TGA curve. In addition, the mass loss at temperatures up to 600 °C can be attributed to the dehydration phenomenon due to water evaporation and the decomposition of hydrated minerals containing hydroxyl bonds that broke at high temperatures, such as muscovite and biotite, as observed in the petrographic examination at temperature up to 760 °C (Hrifech et al., 2020). In the third stage (800 – 1000 °C), the mass loss gradually approaches a stable state. For most rocks, including carbonates, those containing clay minerals, or hydrates, significant reactions such as dehydration, dehydroxylation (i.e., the removal of water from hydroxyl compounds), and decomposition of carbonates typically conclude by 800 °C.

Overall, within a moderate temperature range of 100 °C to 300 °C, all examined rocks exhibit minimal mass loss, measuring less than 1%. Thus, they can be deemed thermally stable within this temperature range. In summary, the moderate temperature range (100 to 300 °C) effectively prevents the transformation of mineral phases, such as calcite and quartz, thereby ensuring the thermal stability of the rocks. Consequently, rocks like marble, granite, and sandstone, which are typically unsuitable for high-temperature applications due to transformations in calcite and quartz, demonstrate potential as energy storage materials for moderate temperatures (Hrifech et al., 2020; Mugi et al., 2022; Li et al., 2024). Conversely, mafic rocks such as basalt, along with felsic rocks like granodiorite and feldsparphyric rhyodacite, are identified as suitable candidates for high-temperature thermal energy storage at this stage.

3.3 Thermal expansion coefficient

To determine the appropriate maximum working temperature for rocks in Hong Kong, thermal expansion coefficient measurements were conducted to evaluate the temperature range within which the material can be utilized without significant alteration of its mechanical properties. For the labels of anisotropic rocks, "//" denotes that the direction of heat source aligns with the bedding direction of the rock sample, while "⊥" indicates a perpendicular orientation. Figure 2 illustrates that granites, tuff-High Island Formation, tuff-Tai Mo Shan Formation, feldsparphyric rhyodacite, and sedimentary rocks exhibit a notable increase in thermal expansion around 573 °C. This phenomenon is attributed to the presence of quartz minerals, which undergo a 5% volume expansion as a result of the α-β phase transition (Chen et al., 2017). Hence, the maximum temperature at which these rocks can effectively store energy should not exceed 550 °C, to mitigate the substantial volume changes that occur during the cyclic heating-cooling processes encountered during their service life. Granodiorites (Figure 2b) experience a surge in thermal expansion at around 656 °C, which may be due to their high feldspar content compared to their low quartz content, in addition to the high content of total iron oxide that is represented by a high content of normative mafic minerals (Rashwan et al., 2023).

Basalt exhibits a relatively gradual increase in thermal expansion behavior from room temperature up to 850 °C. No significant discontinuities are observed in the expansion behavior throughout the entire temperature range from room temperature up to 850 °C, indicating stability. This stability aligns with the high-temperature origins of basalt rocks, suggesting they are already stabilized at this temperature range.

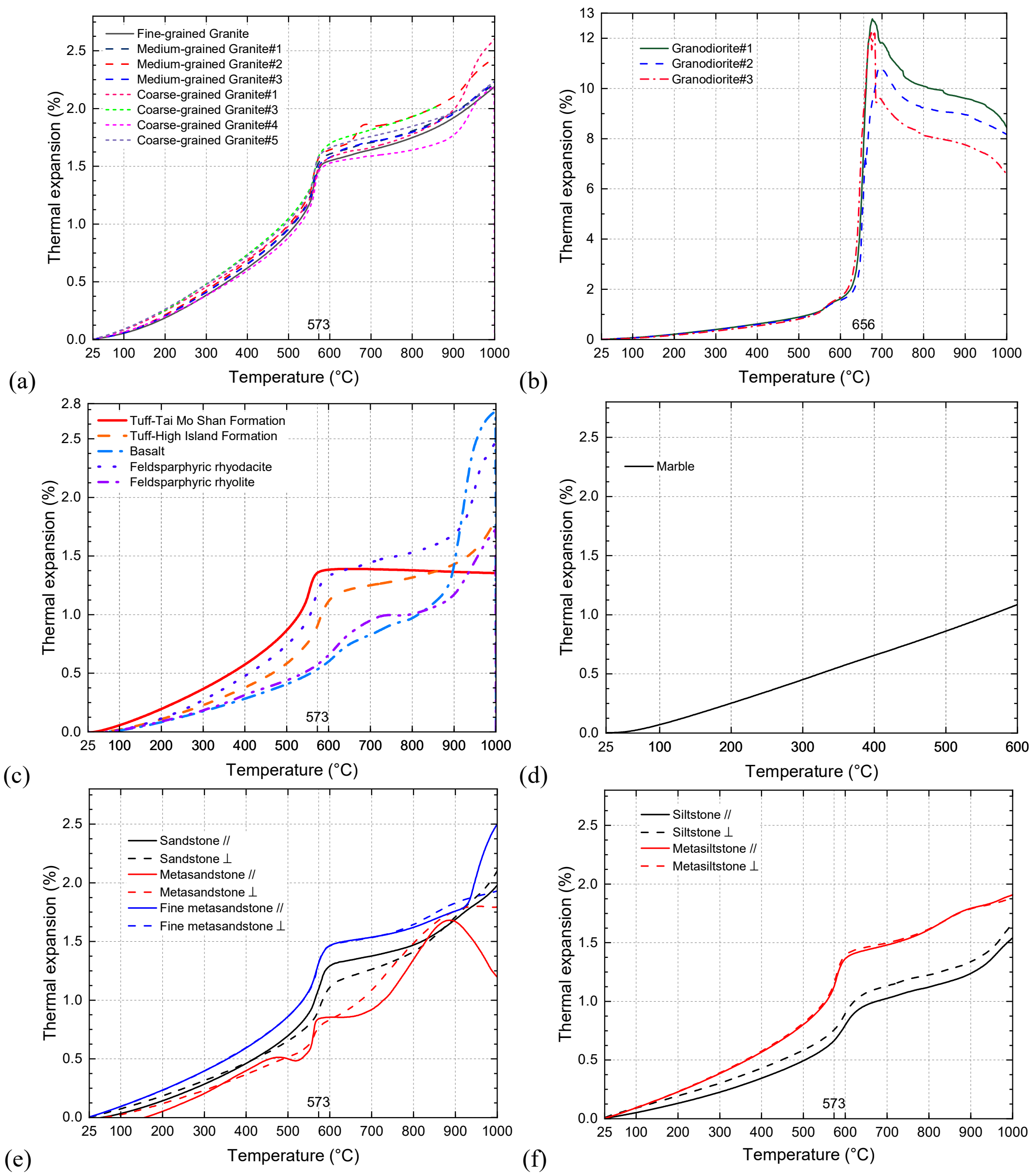

Figure 2: Thermal expansion of Hong Kong rocks. (a) Granites; (b) Granodiorites; (c) Other igneous rocks; (d) Marble; (e) Sandstones; (f) Siltstones

3.4 Heat capacity

The characterization of heat capacity is essential when selecting a sensible heat storage material because an increase in this property enhances the energy stored and reduces the volume of material required, thereby making the storage system more cost-effective. For all these tested samples, the specific heat capacity increases significantly with temperature. In the higher temperature range (700 - 1000 °C), the thermal expansion values gradually converge. This behavior aligns with the Dulong-Petit law, indicating that the heat capacity of solids reaches a constant value at high temperatures (Sutera and Skalak, 1993).

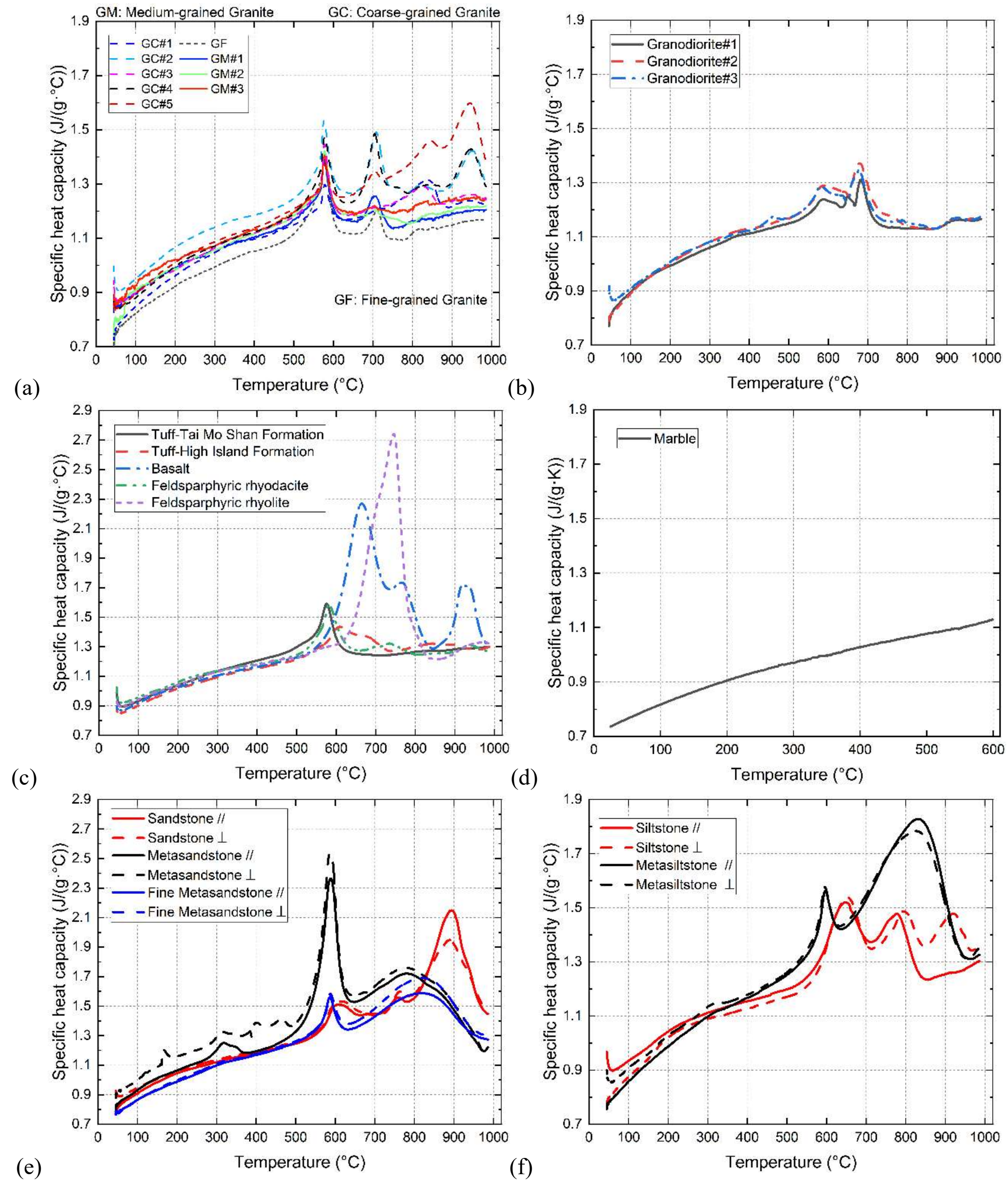

Figure 3: Specific heat capacity of Hong Kong rocks. (a) Granites; (b) Granodiorites; (c) Other igneous rocks; (d) Marble (600 °C); (e) Sandstones; (f) Siltstones

Among igneous rocks, basalt (Figure 3c) notably exhibits relatively high specific heat capacity values, particularly within the temperature range of 600-800 °C. Some minerals in basalt, such as chlorite and clinochlore, may undergo dehydration reactions at around 650 °C (Steudel et al., 2016). The dehydration process requires a large amount of heat absorption, resulting in spikes in the specific heat capacity curve. n granites, multi-peaks can be observed in the specific heat capacity curve. The first peak is associated with the quartz α-β-transition at 573 °C. The second peak, around 700 °C, may result from the decomposition and dehydration of biotite (Hrifech et al., 2020).

The specific heat capacity of the marble sample (Figure 3d) demonstrated a linear increase from 0.74 J/(g·°C) at room temperature to 1.13 J/(g·°C) at 600 °C. Previous research by Vosteen et al. (2003) has reported that sedimentary rocks, such as sandstone and siltstone, generally exhibit higher specific heat capacities compared to metamorphic rocks like marble (Vosteen and Schellschmidt, 2003). Our experimental findings validate this trend.

3.5 Thermal diffusivity and conductivity

Thermal diffusivity, along with the derived thermal conductivity, plays a crucial role in determining the rate at which heat can be released and extracted (Gil et al., 2010). During the discharge phase, rocks can transfer the energy accumulated to the heat transfer fluid (HTF). Optimal material for storage should possess high thermal diffusivity/conductivity, enhancing transient heat transfer and consequently reducing the duration of charging and discharging processes.

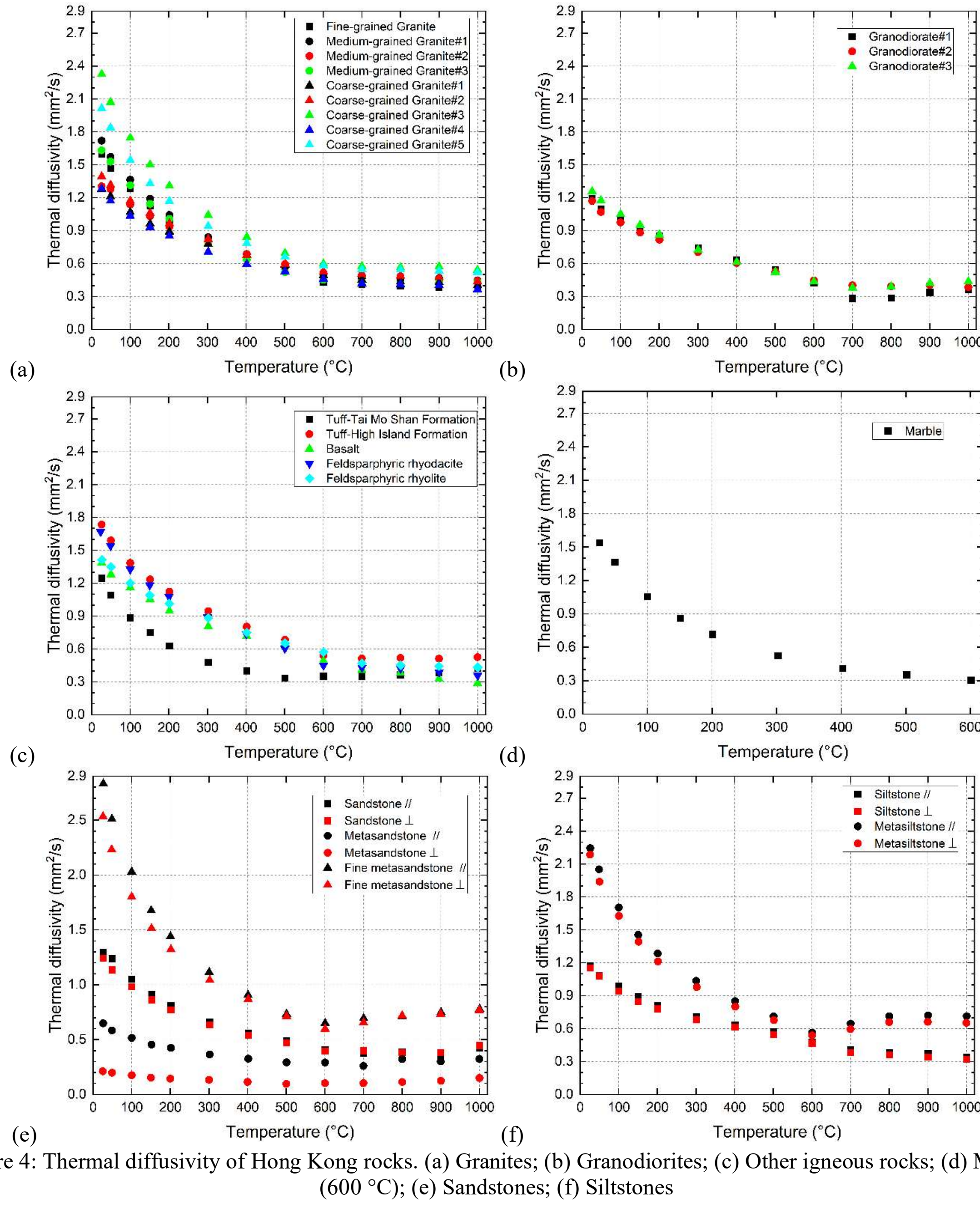

Figure 4: Thermal diffusivity of Hong Kong rocks. (a) Granites; (b) Granodiorites; (c) Other igneous rocks; (d) Marble (600 °C); (e) Sandstones; (f) Siltstones

Overall, there is an exponential decrease in thermal diffusivity across the temperature range of 25 to 1000 °C. At elevated temperatures, approximately 600 °C, thermal conductivity tends towards constant values. Among the tested igneous rocks, granites (Figure 4a), tuff-High Island Formation (Figure 4c), and feldsparphyric rhyodacite (Figure 4c) exhibit the highest thermal diffusivities, while basalt and feldsparphyric rhyolite in Figure 4c fall into the intermediate range. In igneous rocks, thermal diffusivity correlates with quartz and feldspar content, with higher feldspar content (a poor conductor) associated with reduced diffusivity, and higher quartz content associated with higher thermal diffusivities. Despite calcite's superior heat conductivity compared to feldspars, rocks with high calcite content, such as marble (Figure 4d), exhibit low thermal diffusivities due to the absence of quartz. (Hanley et al., 1978).

Thermal conductivity stands as a pivotal criterion in identifying the optimal storage materials (Ismail and Stuginsky Jr, 1999). Theoretical calculations of thermal conductivity were conducted based on thermal diffusivity and heat capacity data (Figure 5).

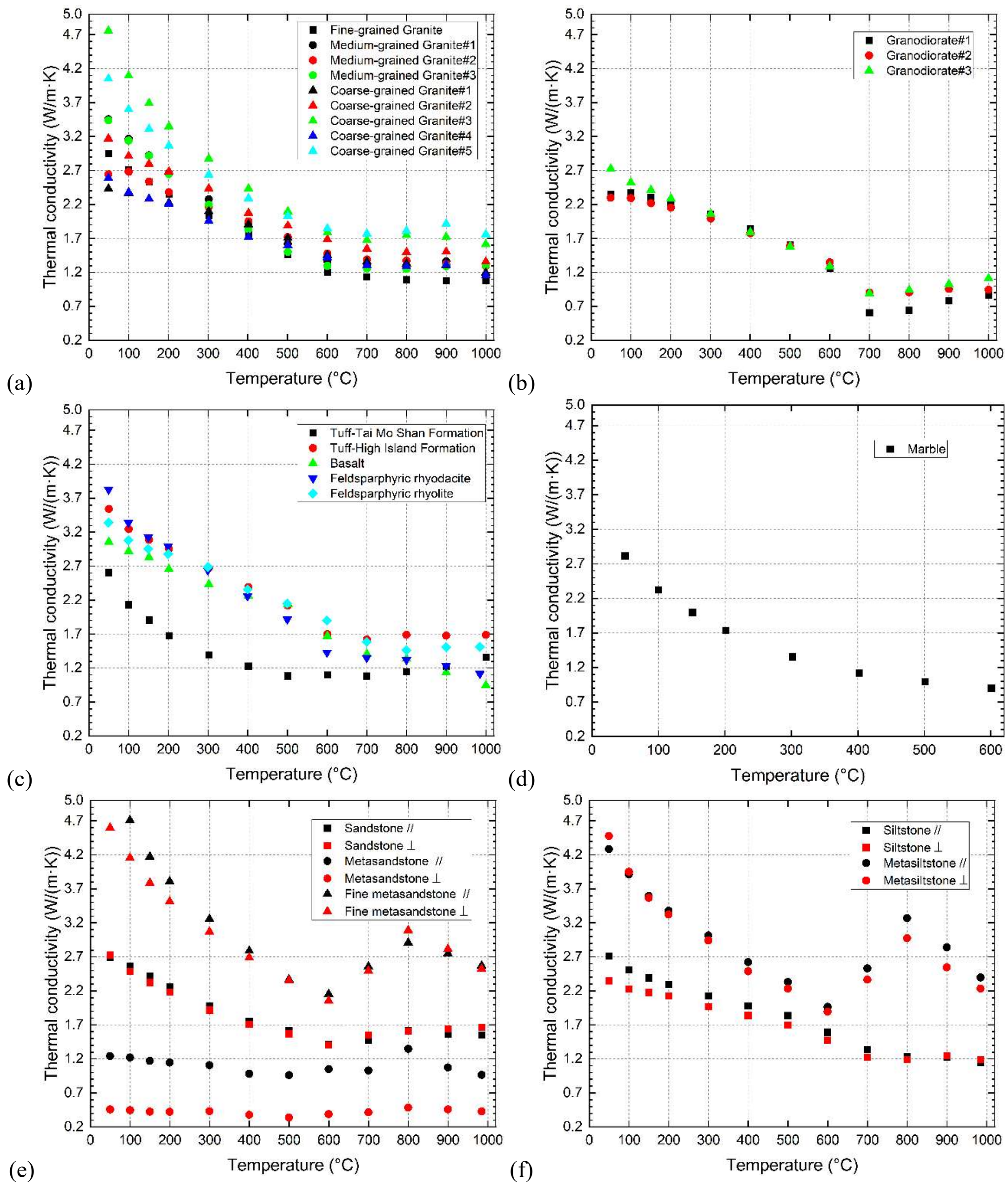

Figure 5: Thermal conductivity of Hong Kong rocks. (a) Granites; (b) Granodiorites; (c) Other igneous rocks; (d) Marble; (e) Sandstones; (f) Siltstones

Generally, the thermal conductivity of crystalline rocks decreases as temperature rises, unlike amorphous materials, which exhibit an increase in thermal conductivity with temperature. This phenomenon can be attributed to the reduction in the mean free path of phonons as temperature increases (Hu et al., 2017). Moreover, rocks with higher initial thermal conductivity experience a more pronounced decrease as temperature increases (Labus and Labus, 2018). The integrity of the rock diminishes as microcracks and micropores develop, impeding the heat transfer process (Liu and Wong, 2024).

The examined rocks exhibit relatively high thermal conductivities when compared to other solid sensible heat storage materials. Specifically, the analyzed basalts demonstrate elevated thermal conductivity values at high temperatures in contrast to concrete. For instance, at 200 °C, concrete exhibits a thermal conductivity of 1 W/m·°C, whereas basalts (Figure 5c) display higher values, reaching 1.1 W/m·°C at 332.5 °C. Additionally, basalts significantly outperform molten salts in terms of thermal conductivity. Molten salts, on average, exhibit a thermal conductivity of 0.52 W/m·°C within the temperature range of 265–565 °C (Herrmann and Kearney, 2002; Tamme et al., 2005; Meffre, 2013; Bouvry et al., 2017).

4 Discussion

The conducted tests provide a comprehensive evaluation of various major rock types in Hong Kong as potential candidates for sensible TES based on experimental data. The assessment criteria for an ideal high-temperature TES medium encompass several aspects, each associated with specific parameters: 1. Durability (Strength); 2. Thermal stability (TGA); 3. Energy density (Specific heat capacity); 4. Efficiency (Thermal diffusivity /conductivity); 5. Availability (Distribution density).

Developing an evaluation function can be intuitive for selecting the optimal TES medium. Overall, the five aspects (durability, thermal stability, energy density, efficiency, and availability) must have varying degrees of importance according to different situations. Here, for simplicity and universality, we have assigned them equal weight. The three levels of suitability (optimal, average, poor) can be quantified as scores 3, 2, and 1. Then, a basic evaluation function can be expressed below:

$$\begin{cases} S = w_D s_D + w_T s_T + w_E s_E + w_{EF} s_{EF} + w_A s_A \\ w_D + w_T + w_E + w_{EF} + w_A = 1 \\ w_D, w_T, w_E, w_{EF}, w_A \in [0,1] \end{cases} \tag{1}$$

where, s_D, s_T, s_E, s_{EF}, and s_A are the scores of suitability in terms of durability, thermal stability, energy density, efficiency, and availability, respectively. w_D, w_T, w_E, w_{EF}, and w_A are the weights of durability, thermal stability, energy density, efficiency, and availability, respectively.

Figure 6 provides a preliminary overall evaluation of Hong Kong rocks' suitability for TES medium. Among all the 15 rocks, basalt possesses the highest total score, followed by coarse-grained granite and feldsparphyric rhyolite, making these three types of optimal candidates. According to the 50-30-20 budget rule, we select the top 20%, i.e. 3, of the total rock types as the optimal, and determine 2.4 as the threshold score. It should be noted that, in this case, the weights of the five assessment factors are equal. In a specific TES system engineering, the weights can be determined according to an expert grading system or other methods, which warrants further site-specific research.

Rock type \ Assessment factors	Durability $w_D = 0.2$	Thermal stability $w_T = 0.2$	Energy density $w_E = 0.2$	Efficiency $w_{EF} = 0.2$	Availability $w_A = 0.2$	Total score S
Fine-grained Granite	3	2	1	2	3	2.2
Medium-grained Granite	3	2	1	2	3	2.2
Coarse-grained Granite	3	2	1	3	3	2.4
Granodiorite	3	1	1	1	3	1.8
Tuff-Tai Mo Shan Formation	1	3	2	1	2	1.8
Tuff-High Island Formation	1	3	2	3	2	2.2
Basalt	3	3	3	2	2	2.6
Feldsparphyric rhyodacite	3	2	2	3	2	2.4
Feldsparphyric rhyolite	3	1	3	2	2	2.2
Marble	2	1	1	2	1	1.4
Metasandstone	2	1	2	1	1	1.4
Sandstone	1	2	2	2	1	1.6
Siltstone	1	2	2	1	1	1.4
Metasiltstone	2	2	1	3	1	1.8
Fine metasandstone	2	2	2	3	1	2.0

Notes: **Green** = Optimal (3); **Yellow** = Average (2); **Red** = Poor (1)

Figure 6: Evaluation of fifteen Hong Kong rocks over multiple assessment factors

Several igneous rock types, including granite, granodiorite, tuff-Tai Mo Shan Formation, tuff-High Island Formation, and feldsparphyric rhyodacite, exhibit a noticeable increase in thermal expansion at 573°C due to the quartz phase transition. This characteristic poses a significant risk to long-term **durability** as the cyclic expansion and shrinkage induced by heating and loading will generate numerous microcracks, compromising material strength. Additionally, the increased porosity can lower thermal diffusivity/conductivity, impacting the **efficiency** of these rocks as TES medium. Consequently, these igneous rocks are deemed unsuitable for exposure to temperatures exceeding 573 °C. However, some scholars propose their potential use in mid-low temperature range (100–500 °C) TES engineering (Tiskatine et al., 2017; Hrifech et al., 2020; Mugi et al., 2022). Besides, some of them still have other weaknesses. For example, granites contain a considerable proportion of hydrous minerals (e.g., biotite), which are not **stable** under hydrothermal conditions and alter to numerous minerals. Feldsparphyric rhyolite exhibits significant mass loss starting from 300 °C, indicating inadequate **thermal stability**. Granodiorites and tuff-Tai Mo Shan Formation exhibit low thermal diffusivity and conductivity, which could decrease the **efficiency** of the charging and discharging processes in TES engineering.

Basalt exhibits relatively high volumetric heat capacity and thermal diffusivity/conductivity, particularly at elevated temperatures ranging from 600 to 800 °C. It demonstrates stable thermal dilation behavior and the lowest thermal expansion coefficient recorded at 850 °C (0.011/°C), accompanied by negligible mass loss up to 1000 °C. Therefore, basalt appears to be well-suited for applications within this temperature range, or even higher, following thermal treatment. Experimental investigations indicate that basalt did not manifest any macroscopically visible damage after undergoing multiple thermal cycles (Geiger, 1984). The findings indicate that basalt stands out as the most suitable candidate for high-temperature TES material, meeting the required performance criteria for storage materials. This assertion is corroborated by previous studies (Grirate et al., 2016; Becattini et al., 2017; Nahhas et al., 2019). It is important to note, however, that basalt is not compatible with thermal oil, making it more suitable for alternative HTFs such as air (Grirate et al., 2016).

Solar tower systems can reach operating temperatures up to 600 °C, while conventional nuclear plants typically produce waste heat around 300 °C. Microsoft's Project Natick, an underwater data center, features cooling systems that efficiently manage heat, often exceeding 50 °C in some areas. Based on this analysis, if Hong Kong plans to build a TES system for different purposes, different rock types can be chosen according to their optimal operating temperature ranges.

5 Conclusions

The prosperity of Hong Kong's economy is accompanied by significant energy consumption. To alleviate potential future energy shortages, the development of clean energy and energy storage projects will be imperative. In this study, we examine the potential of fifteen rock types found in Hong Kong to serve as environmentally friendly and cost-effective materials for solid sensible thermal energy storage systems. Thermo-physical and mechanical properties of the selected Hong Kong rocks were analyzed, alongside their chemical and structural compositions. A comprehensive evaluation was conducted to assess the suitability of these rocks for thermal energy storage applications. Based on our findings, the following conclusions can be drawn:

- Thermogravimetric analysis revealed significant mass losses in marble and feldsparphyric rhyolite, necessitating their exclusion from the list of candidates under study to prevent any potential damage during thermal energy storage operations.
- Thermal dilatometry tests reveal that the majority of selected rocks in Hong Kong undergo a notable increase in thermal expansion around 573 °C due to the α-β phase transition of quartz. Granodiorite exhibits a distinctive surge in thermal expansion around 650 °C followed by a rapid decrease. Marble demonstrates a sudden decrease in expansion at 600 °C.
- Sandstone and siltstone exhibit high heat capacities, although they may fluctuate at elevated temperatures. Among the igneous rocks sampled in Hong Kong, basalt and feldsparphyric rhyodacite demonstrate relatively high heat capacities. Marble, on the other hand, exhibits the lowest but consistent heat capacity compared to all tested rocks.
- Fine metasandstone, metasiltstone, granites, tuff-High Island Formation, and feldsparphyric rhyodacite exhibited the highest thermal diffusivity/conductivity among the tested rocks from Hong Kong. Sandstone, basalt, and feldsparphyric rhyolite showed moderate levels of thermal diffusivity/conductivity. Siltstone,

metasandstone, granodiorites, and tuff-Tai Mo Shan Formation displayed the lowest thermal diffusivity/conductivity.

- Hong Kong basalt is considered an ideal candidate for high-temperature thermal energy storage material, with 850 °C identified as the appropriate maximum working temperature. Other igneous rocks found in Hong Kong can be utilized for TES engineering applications within the mid-to-low temperature range (100 – 500 °C). However, sedimentary and metamorphic rocks in Hong Kong do not appear to be suitable.

The testing results presented herein contribute to our comprehension of the alterations in the thermophysical properties of Hong Kong rocks under heating conditions. Additionally, they offer valuable insights into parameter configurations for numerical simulations aimed at the future design of storage systems and the prediction of their operational efficacy.

ACKNOWLEDGEMENTS

The work is supported by the Research Grants Council of Hong Kong (General Research Fund Project Nos. 17200721 and 17202423), the National Natural Science Foundation of China (Grant No. 42377149) and Dr. Stephen S.F. Hui Trust Fund 2022-23 (No. 263820871). The second author acknowledges the Postgraduate Scholarship from the University of Hong Kong (HKU).

REFERENCES

Allen, K.G., Von Backström, T.W., Kröger, D.G. & Kisters, A. 2014. Rock bed storage for solar thermal power plants: Rock characteristics, suitability, and availability. *Solar Energy Materials and Solar Cells*, 126: 170-183.

Becattini, V., Motmans, T., Zappone, A., Madonna, C., Haselbacher, A. & Steinfeld, A. 2017. Experimental investigation of the thermal and mechanical stability of rocks for high-temperature thermal-energy storage. *Applied Energy*, 203: 373-389.

Bouvry, B., Carrión, A.J.F., Andújar, J., Veron, E., Ory, S., Brassamin, S., Echegut, P., Escape, C., Nahhas, T. & Py, X. 2017. Mediterranean basin basalts as potential materials for thermal energy storage in concentrated solar plants. *Solar Energy Materials and Solar Cells*, 171: 50-59.

Chaki, S., Takarli, M. & Agbodjan, W.P. 2008. Influence of thermal damage on physical properties of a granite rock: porosity, permeability and ultrasonic wave evolutions. *Construction and Building Materials*, 22(7): 1456-1461.

Chen, S., Yang, C. & Wang, G. 2017. Evolution of thermal damage and permeability of Beishan granite. *Applied Thermal Engineering*, 110: 1533-1542.

Fredrich, J.T. & Wong, T.F. 1986. Micromechanics of thermally induced cracking in three crustal rocks. *Journal of Geophysical Research: Solid Earth*, 91(B12): 12743-12764.

Geiger, T., 1984. Diverse gesteine als mögliche speichermaterialien. Sulzer Winterthur, Switzerland.

Gil, A., Medrano, M., Martorell, I., Lázaro, A., Dolado, P., Zalba, B. & Cabeza, L.F. 2010. State of the art on high temperature thermal energy storage for power generation. Part 1—Concepts, materials and modellization. *Renewable and Sustainable Energy Reviews*, 14(1): 31-55.

Grirate, H., Agalit, H., Zari, N., Elmchaouri, A., Molina, S. & Couturier, R. 2016. Experimental and numerical investigation of potential filler materials for thermal oil thermocline storage. *Solar Energy*, 131: 260-274.

Grirate, H., Zari, N., Elamrani, I., Couturier, R., Elmchaouri, A., Belcadi, S. & Tochon, P. 2014. Characterization of Several Moroccan Rocks Used as Filler Material for Thermal Energy Storage in CSP Power Plants. *Energy Procedia*, 49: 810-819.

Hanley, E.J., Dewitt, D.P. & Roy, R.F. 1978. The thermal diffusivity of eight well-characterized rocks for the temperature range 300 – 1000 K. *Engineering Geology*, 12: 31-47.

Herrmann, U. & Kearney, D.W. 2002. Survey of thermal energy storage for parabolic trough power plants. *Journal of Solar Energy Engineering-Transactions of the Asme*, 124(2): 145-152.

Hrifech, S., Agalit, H., Jarni, A., Mouguina, E.M., Grosu, Y., Faik, A., Bennouna, E.G. & Mimet, A. 2020. Characterization of natural rocks as filler materials for medium-temperature packed bed thermal energy storage system. *Journal of Energy Storage*, 32: 101822.

Hu, N., Khan, M., Wang, Y., Song, X., Lin, C., Chang, C. & Zeng, Y. 2017. Effect of microstructure on the thermal conductivity of plasma sprayed Y2O3 stabilized zirconia (8% YSZ). *Coatings*, 7(11): 198.

Ismail, K.A. & Stuginsky Jr, R. 1999. A parametric study on possible fixed bed models for pcm and sensible heat storage. *Applied Thermal Engineering*, 19(7): 757-788.

Labus, M. & Labus, K. 2018. Thermal conductivity and diffusivity of fine-grained sedimentary rocks. *Journal of Thermal Analysis and Calorimetry*, 132: 1669-1676.

Li, H., Ma, H., Zhao, K., Zhu, S., Yang, K., Zeng, Z., Zheng, Z. & Yang, C. 2024. Parameter design of the compressed air

energy storage salt cavern in highly impure rock salt formations. *Energy*, 286: 129520.
Liu, Z. & Wong, L.N.Y. 2024. A new thermomechanical coupled FDEM model for geomaterials considering continuum-discontinuum transitions. *Journal of Rock Mechanics and Geotechnical Engineering*, 16(11): 4654-4668.
Meffre, A., 2013. Matériaux de stockage thermique haute température issus de la valorisation de matières premières secondaires inorganiques. Perpignan.
Mugi, V.R., Das, P., Balijepalli, R. & Chandramohan, V.P. 2022. A review of natural energy storage materials used in solar dryers for food drying applications. *Journal of Energy Storage*, 49: 104198.
Nahhas, T., Py, X. & Sadiki, N. 2019. Experimental investigation of basalt rocks as storage material for high-temperature concentrated solar power plants. *Renewable and Sustainable Energy Reviews*, 110: 226-235.
Özkahraman, H.T., Selver, R. & Işık, E.C. 2004. Determination of the thermal conductivity of rock from P-wave velocity. *International Journal of Rock Mechanics and Mining Sciences*, 41(4): 703-708.
Park, J., Park, D., Ryu, D., Choi, B. & Park, E. 2014. Analysis on heat transfer and heat loss characteristics of rock cavern thermal energy storage. *Engineering Geology*, 181: 142-156.
Rashwan, M.A., Lasheen, E.S.R. & Azer, M.K. 2023. Thermal and physico-mechanical evaluation of some magmatic rocks at Homrit Waggat Area, Eastern Desert, Egypt: petrography and geochemistry. *Bulletin of Engineering Geology and the Environment*, 82(6).
Steudel, A., Kleeberg, R., Koch, C.B., Friedrich, F. & Emmerich, K. 2016. Thermal behavior of chlorites of the clinochlore-chamosite solid solution series: Oxidation of structural iron, hydrogen release and dehydroxylation. *Applied Clay Science*, 132: 626-634.
Sutera, S.P. & Skalak, R. 1993. The history of Poiseuille's law. *Annual Review of Fluid Mechanics*, 25(1): 1-20.
Tamme, R., Steinmann, W. & Laing, D., 2005. Thermal energy storage technology for industrial process heat applications, pp. 417-422.
Tiskatine, R., Eddemani, A., Gourdo, L., Abnay, B., Ihlal, A., Aharoune, A. & Bouirden, L. 2016. Experimental evaluation of thermo-mechanical performances of candidate rocks for use in high temperature thermal storage. *Applied Energy*, 171: 243-255.
Tiskatine, R., Oaddi, R., El Cadi, R.A., Bazgaou, A., Bouirden, L., Aharoune, A. & Ihlal, A. 2017. Suitability and characteristics of rocks for sensible heat storage in CSP plants. *Solar Energy Materials and Solar Cells*, 169: 245-257.
Vosteen, H. & Schellschmidt, R. 2003. Influence of temperature on thermal conductivity, thermal capacity and thermal diffusivity for different types of rock. *Physics and Chemistry of the Earth, Parts a/B/C*, 28(9-11): 499-509.

Trial Piles and Foundation Design in Meta-sedimentary Rocks

Sylvia S.W. Chik, Kian Y.K. Chiu, Rachel W.Y. Lau, Alan Y.L. Chau,
Eric H.Y. Sze, Patrick P.C. Wong & Thomas H.H. Hui
Geotechnical Engineering Office,
Civil Engineering and Development Department,
Government of the Hong Kong Special Administrative Region,
Hong Kong SAR, China

ABSTRACT

The rapidly developing Northern Metropolis (NM) is situated in a geologically complex region in Hong Kong where clastic sedimentary rocks being affected by metamorphism are present. Due to extensive folding, faulting and weathering, meta-sedimentary (MS) rocks in the NM are found to be highly variable in nature. However, there is a general lack of geotechnical information for those MS rocks mainly because of minimal urban development in the region so far. As there will be a surge of development works within the region in the coming few decades, the Geotechnical Engineering Office (GEO) recently initiated a large-scale pile loading test programme with a view to collecting extensive field data on end-bearing capacity and rock socket shaft resistance of various types of MS rocks in the region. The key objective is to explore room for enhancing the prevailing foundation design guidelines for MS rocks, thereby facilitating material and cost saving of the associated foundation works. As part of the study, some trial piles are strategically designed to investigate the constructability and performance of using eco-friendly Ground Granulated Blastfurnace Slag (GGBS) and high-strength S690 steel section in piling works. The study outcome would facilitate the wider application of these new and green materials for the benefit of advancing sustainable and cost-effective geotechnical solutions. While the pile loading tests are actively on-going, this paper reports the preliminary findings of the trial piling works, including bi-directional loading tests on instrumented piles, the applications of high-percentage GGBS concrete and grout as well as S690 steel section in pile foundations.

1 INTRODUCTION

The Northern Metropolis (NM), located in the northwestern and northern parts of Hong Kong, has many planned mega-scale infrastructural developments in the coming few decades. This region is situated in a geologically complex sedimentary basin with intense faulting and deep weathering profile, and in particular complicated metamorphism. The presence of MS rocks has been posing challenges to the foundation design of some actively developing areas such as Yuen Long South, Kwu Tung North and San Tin Technopole. Due to the lack of geotechnical information for MS rocks, the prevailing foundation design guideline remains relatively conservative. With a view to reviewing the foundation design parameters of MS rocks, including the end-bearing capacity and the rock socket shaft resistance of piles, it is considered desirable to conduct trial piling works with full-scale instrumented pile loading tests at different sites underlain by meta-sedimentary rocks. Since 2024, the GEO initiated a large-scale pile loading test programme to collect essential information and test data with a view to exploring the feasibility to enhance the foundation design guidelines for MS rocks. In addition, the results of the pile load tests would directly be used in the foundation designs of site-specific projects, thus achieving productivity and saving in cost, time and sustainability.

In cognisance of recent successful applications of low-carbon GGBS concrete and high-strength S690 steel in building and infrastructural works, there is an opportunity to apply these new construction materials in foundation works. However, recent communications with relevant departments and practitioners revealed that there was generally a short of site operation and quality control experience with these new materials in piling works. It renders their applications in the construction of pile foundations not common in Hong Kong. As such, two large-diameter bored piles with high-percentage GGBS concrete (75% and 80% GGBS replacement of the total cementitious content) and two rock-socketed steel H-piles with high-strength S690 steel sections as well as high-percentage GGBS grout (75% GGBS replacement of the total cementitious content) are strategically designed in this study to address these concerns.

While the trial piling works are still actively on-going, this paper reports the preliminary findings of the above-mentioned study, highlighting the potential of enhancing the foundation design guidelines for MS rocks as well as the wider application of GGBS concrete/grout and S690 steel in piling works.

2 META-SEDIMENTARY ROCKS IN NORTHERN METROPOLIS

A considerable extent of the NM is underlain by MS rocks belonging to Lok Ma Chau Formation (Csl), with a minority belonging to Tuen Mun Formation (Ju) and Tai O Formation (Jo) (**Figure 2.1**). Both Lok Ma Chau Formation and Tuen Mun Formation are rather prominent at the northwest of New Territories. The rocks of Lok Ma Chau Formation occur as a northeast-trending outcrop and subcrop stretching from Tuen Mun to Lo Wu, comprising metamorphosed sandstone and carbonaceous siltstone with graphitic interbeds and calcareous content. While rocks of Tuen Mun Formation at NM are relatively confined to the area at the west and north of Tuen Mun, predominated by fine-grained, cross-bedded, well-graded quartzitic sandstone, metasiltstone and phyllite, the Tai O Formation at NM is exposed near the Ma Tso Lung area, including metasandstone, metasiltstone with graphite interbeds (Tse & Tang, 2024).

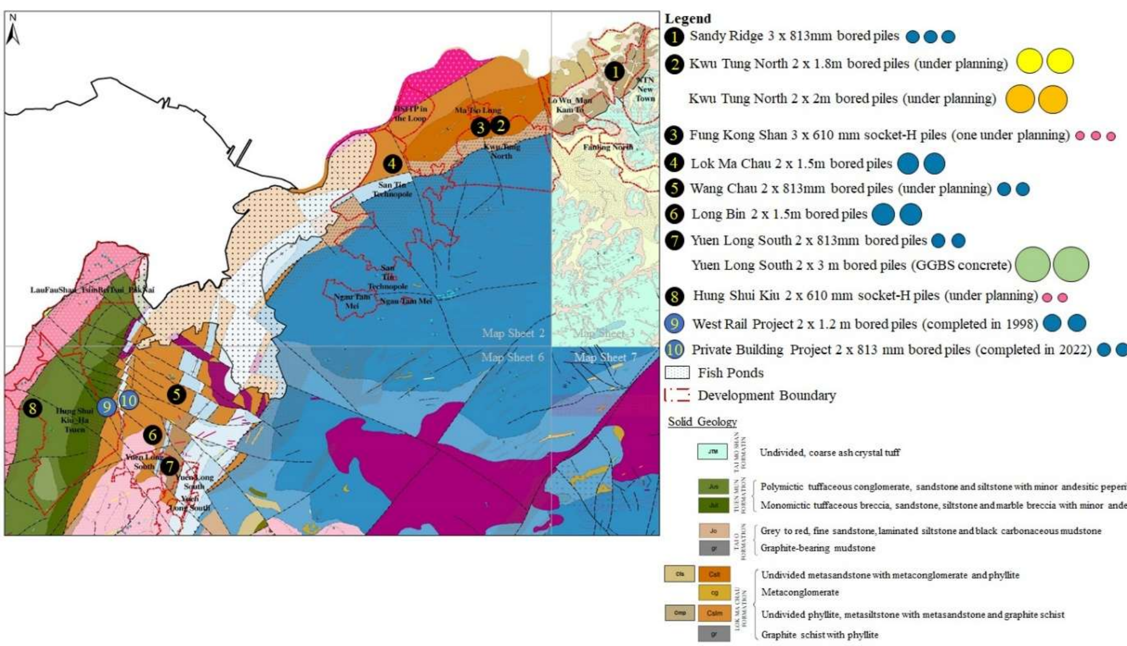

Figure 2.1: Overview of Geology at Northern Metropolis (Simplified from Tse & Tang, 2024) with locations of trial piles in this study

The engineering geological characteristic of MS rocks is complicated as the rock is sedimentary in nature and may have been subjected to different degree of metamorphism. The parent nature of MS rocks at NM is due to sedimentary process. The rock is mostly clastic, of which, the material strength and durability are largely controlled by the composition and property of the constituent grains as well as the degree of compaction and cementation. The bedding planes may also act as planes of weakness where weathering is more intense. As such, MS rocks could be consisting of various properties in lateral and vertical extent, and may change over short distances.

The sedimentary rocks subsequently subjected to dynamic metamorphism due to intense fault movements in the region. Langford et al. (1989) proposed that the structural framework of the northeast New Territories was dominated by the NE-trending Lo Wu-Tuen Mun Fold Belt (fault zone). The major structures have been updated as: the Deep Bay Fault, Yuen Tau Shan Fault, Mai Po Fault and the San Tin Fault in 2024 (**Figure 2.2**) (Tse & Tang, 2024).

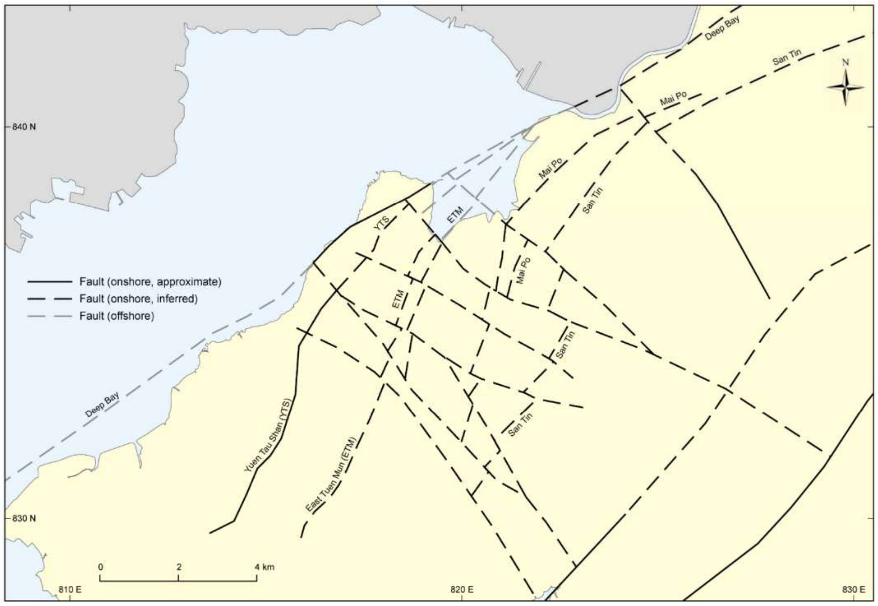

Figure 2.2: Major Faults in the Northwest New Territories
(Modified from Tse & Tang 2024 from So & Sewell 2019)

The tectonic movements may result in brecciated and brittled rocks, introducing further structures (i.e. joints and fractures) to the bedding planes originated from the sedimentary process. As a result, the engineering rockhead may not be as easily defined as compared to igneous rocks in Hong Kong. On the other hand, dynamic metamorphism is prominent in the northern and northwest of New Territories, particularly near San Tin Fault, by way of north or northwest inclined foliation (Sewell et al., 2000.). Foliation is favourable for weathering along the preferred alignment of minerals, leading to rapid disintegration of rock cores. Besides, local variations of foliation orientation will introduce anisotropic material properties relative to the alignment of the fabrics. In addition, other metamorphic processes such as recrystallization and hydrothermal alteration would lead to the rock strength varying across the rock mass depending on the type and distribution of the resulting minerals remain in the rock. For instance, if silicification takes place at bands intercalated with the metasedimentary rock, the rock strength may differ across the intercalated layers, with those layers possessing high concentration of silica may have a relatively higher strength than the adjacent layers.

For shallow foundation near the ground surface, the complicated engineering geological characteristic of MS rocks may have more pronounced effects to engineering works if they are exposed to air with time (e.g. Greenway et al., 1988). For deep pile foundations, the high confinement may have beneficial effects in minimising the adverse impacts of closely-spaced joints on end-bearing capacity of MS rocks. This aspect will be further reviewed based on the pile loading tests conducted in this study.

3 FOUNDATION DESIGN IN META-SEDIMENTARY ROCKS

In Hong Kong, pile foundation design in MS rocks primarily follows the Code of Practice for Foundation 2017 (2024 Edition) published by Buildings Department (BD) (BD, 2024) with the presumed design values summarized in **Table 3.1**. It should be noted that the design provision for Category 2 rock (i.e. MS rocks) first appeared in the 2017 Code. With the lack of geotechnical information for MS rocks at that time, a presumed allowable bearing pressure of 3,000 kPa was conservatively set. This design value is akin to that used for

Category 1(d) rock i.e. Grade III or better granite or volcanic rock with not less than 50% Total Core Recovery of the designated grade. Before 2017, some housing projects might adopt a presumed allowable bearing pressure of 5,000 kPa in their foundation designs i.e. akin to Category 1(c) rock.

Table 3.1: Presumed allowable vertical bearing pressure extracted from BD (2024)

Category	Description of rock or soil	Presumed allowable bearing pressure (kPa)	Presumed allowable bond or friction (kPa)
2	*Meta-Sedimentary rock:* Moderately decomposed, moderately strong to moderately weak meta-sedimentary rock of material weathering grade III or better, and with not less than 85% TCR of the designated grade.	3,000	300 (under compression or transient tension) 150 (under permanent tension)

Instead of adopting the presumed value for foundation design in MS rocks, there are several projects involving the use of Rock Mass Rating (RMR) (GEO, 2006), coupled with site-specific pile loading tests, to determine the allowable bearing pressures of MS rocks for the projects. For example, Yau & Lau (2024) carried out two pile loading tests on MS rocks at Kiu Cheong Road, Tin Shui Wai and by using the RMR method, they obtained the consent from BD to adopt an allowable bearing capacity of 5,000 kPa in the foundation design leading to cost and time saving of the piling works for a building project.

The use of pile loading tests to enhance foundation design was also reported by Littlechild et al. (2000). They carried out two pile loading tests on MS rocks and found that the mobilised bearing pressure could be up to 26,500 kPa and 24,000 kPa respectively. Together with a series of pile loading tests on other rock types, the local railway project adopted an allowable bearing capacity of at least 7,500 kPa for MS rocks and others.

4 PLANNING OF TRIAL PILING WORKS IN THIS STUDY

Based on a review of the local foundation design experience in MS rocks, there is room for enhancing the prevailing design guideline for MS rocks. The use of full-scale pile loading tests appears to be a promising approach to investigate the actual pile-rock behavior under pressure (e.g. Littlechild et al., 2000). As the MS rocks in the NM may have varying properties in terms of rock strength, fractureness, presence of foliation or bedding plane, etc., it is planned to carry out a systematic pile load test programme targeting on MS rocks of different characteristics in the NM. **Table 4.1** summarises the pile loading tests conducted in this study as well as the brief details of trial piles, testing systems and ground conditions. The locations of test sites are shown in **Figure 2.1**.

Table 4.1: Summary of trial piles conducted in this study

Site	Pile No.	Pile Diameter (mm)	Rock Socket Diameter (mm)	Pile Length (m)	Rock Socket Length (m)	Pile Founding Material *	Pile Type / Loading System
Yuen Long South	YLS-P1	813	750	47.17	1.61	SD Meta-siltstone / SD Meta-sandstone	Bored Pile / 10MN O-cell with kentledge
Yuen Long South	YLS-P2	813	750	46.92	0.9	SD Calcareous Meta-siltstone	Bored Pile / 10MN O-cell with kentledge
Yuen Long South	GGBS-YLS-P1	3000	2850	63	0.3	-	For studying GGBS, not pile loading test
Yuen Long South	GGBS-YLS-P2	3000	2850	52	0.3	-	For studying GGBS, not pile loading test
Long Bin	LB-P1	1500	1350	90.86	1.5	SD / MD Meta-siltstone	Bored Pile / 32MN O-cell with kentledge

Site	Pile No.	Pile Diameter (mm)	Rock Socket Diameter (mm)	Pile Length (m)	Rock Socket Length (m)	Pile Founding Material *	Pile Type / Loading System
Long Bin	LB-P2	1500	1350	74.07	1.5	SD/ MD / HD Meta-siltstone	Bored Pile / 32MN O-cell with kentledge
Sandy Ridge	SR-P01	813	750	28.09	3.8	SD/ MD Meta-siltstone	Bored Pile / 10MN O-cell without kentledge
Sandy Ridge	SR-P02	813	750	25.57	3.1	SD/ MD Meta-siltstone	Bored Pile / 10MN O-cell without kentledge
Sandy Ridge	SR-P03	813	750	40.1	4.17	SD/ MD Meta-sandstone	Bored Pile / 10MN O-cell without kentledge
Lok Ma Chau	LMC-P1	1500	1350	39.6	1.8	SD Calcareous Meta-siltstone	Bored Pile / 32MN O-cell with kentledge
Lok Ma Chau	LMC-P2	1500	1350	43.94	1.59	SD Calcareous Meta-siltstone	Bored Pile / 32MN O-cell with kentledge
Fung Kong Shan	FKS-P1	610	550	54.21	2.2	MD Meta-siltstone	Socketed-H with S690 steel section / 6MN O-cell without kentledge
Fung Kong Shan	FKS-P2	610	550	36.95	6.4	SD Meta-siltstone (along rock socket)	Socketed-H with S690 steel section / top load with kentledge

* SD stands for slightly decomposed, MD stands for moderately decomposed, HD stands for highly decomposed, CD stands for completely decomposed according to the rock descriptions in Geoguide 3

So far, loading tests on 11 trial piles at five sites straddling across NM have been completed. Data interpretation and analysis are on-going. Amongst them, nine are rock-socketed bored piles (813 mm or 1.5 m in diameter) whilst two are rock-socketed H-piles (610 mm in diameter) aiming also for studying the use of S690 steel section and high-percentage GGBS grout. Two additional trial piles are rock-socketed bored piles (3 m in diameter) constructed using high-percentage GGBS concrete without any loading tests. The founding level of piles are determined by predrills. In general, for tests with both O-cell and kentledge, shorter rock socket length (i.e. 0.9 m to 1.8 m) is adopted, which targeted to test the ultimate rock socket friction. For tests with O-cell but without kentledge, as the reaction to the O-cell is solely provided by rock socket and the soil shaft above, longer rock socket length (i.e. 2.2 m to 4.17 m) is adopted to ensure sufficient reaction is provided to the O-cell for applying load to the bearing stratum.

Apart from the pile loading tests, a series of pre-drilling works, post-drilling works, field tests in boreholes, laboratory tests on rock specimens and geophysical survey have been carefully planned to obtain information to support the study. For example, in view that MS rocks are usually highly fractured, rendering conventional uniaxial compressive strength test and diametric point load test difficult to carry out, it is planned to study the feasibility of using irregular lump point load tests to replace point load test to determine the strength of MS rocks. This will require an establishment of the correlation between uniaxial compression tests and irregular lump point load tests. In addition, in-situ Goodman Jack test and laboratory tests will be carried out, where applicable, to assess the rock modulus, which is an important property dictating the pile settlement behavior. These ground investigation works and laboratory tests are being conducted and the results will be reported later.

5 PILE LOADING TEST SETUP AND PRELIMINARY FINDINGS

5.1 Pile Loading Test Setup and Instrumentations

Figure 5.1 shows the schematic sectional views for all the trial piles conducted in this study. As illustrated, a majority of the pile loading tests is conducted using the bi-directional loading system, namely the Osterberg cell (O-cell) installed at the pile base. Comparing to conventional top loaded pile loading tests with kentledge, O-cell directly exerts loading on the bearing rock and measured the actual pressure applied to the bearing strata. Another benefit of loading at the pile base is to allow measurement of rock socket friction together with the end bearing pressure at the same time. This setup well overcomes the limitation of the conventional top loading system using kentledge of which the load applied at the top of pile will dissipate along the soil portion (even with sleeving) and the forces being mobilised along the rock sockets and on the pile bases have to be back-calculated (i.e. indirectly) from strain gauges readings. In this study, all piles above the tested rock socket sections are sleeved by permanent casing with bituminous coating. Kentledge on the ground surface would be added if additional reaction force is required for the sake of maximising the end-bearing pressure on rock.

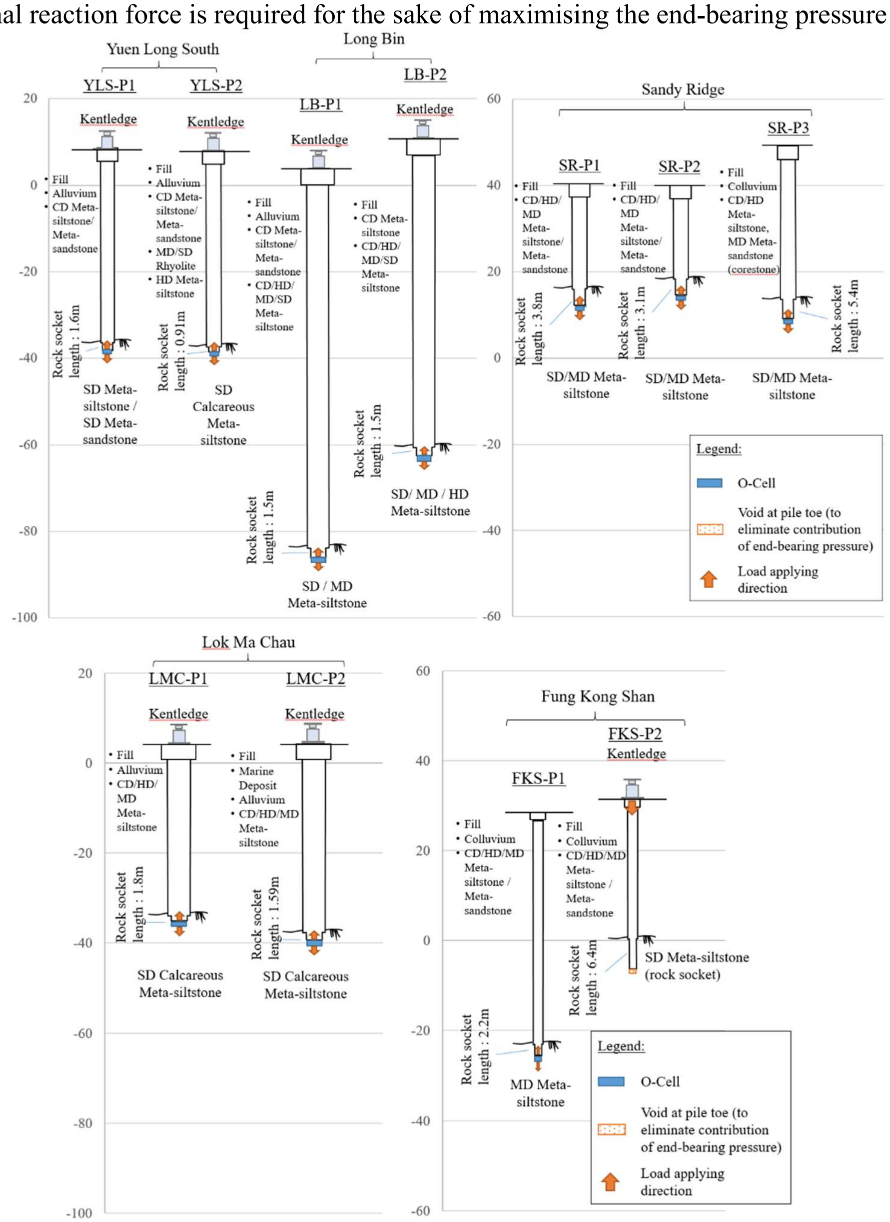

Figure 5.1: Schematic sectional views of trial piles

All trial piles are heavily instrumented (see **Figure 5.2**). The measurement of movement at different parts of the pile is critical. A series of extensometers are installed at the top and bottom plates of O-cell, rockhead level and pile top, aiming to measure the gross movement and shortening of the pile. A set of linear vibrating wire displacement transducers (LVWDT) is installed between the top and bottom plates of the O-cell, aiming to measure the stroke of O-cell thereby cross-checking whether its opening has reached the limit.

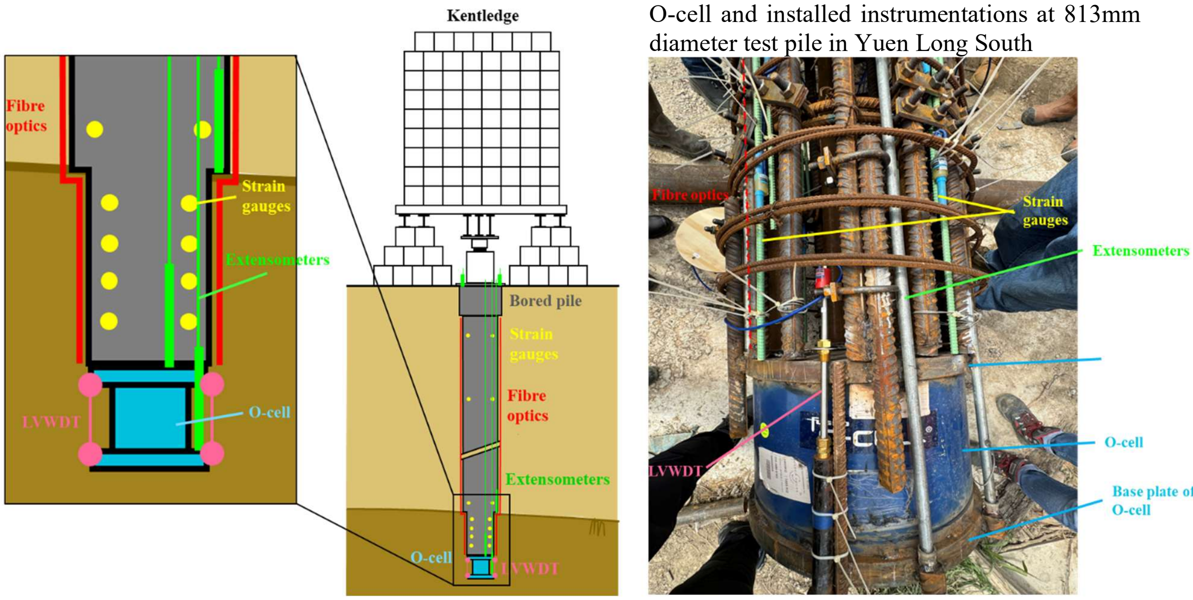

Figure 5.2: Illustration of bi-directional loading system with O-cell and instrumentation arrangement

For force measurement, an innovative dual strain measurement scheme is adopted where the forces mobilised along the pile shaft are concurrently captured by both strain gauges and fibre optics. The measured strain (ε) along the piles can be converted to pile axial force (Q) at the strain gauge level by multiplying the axial pile stiffness EA, where E is the pile modulus and A is the pile cross-section area. Apart from point-wise measurements by the strain gauges, fibre optics provide a continuous profile of strain measurement results making up the missing data between individual strain gauges. Fibre optic, which gives a continuous load distribution profile, is particularly useful in small diameter piles as there is limitation on the number of strain gauges that could be installed under a congested environment. For more details about the test setup, instrumentation arrangement and loading schedules adopted in this study, please refer to Lam et al. (2025).

5.2 Preliminary Results

While the analysis of test data is ongoing, preliminary results of two selected trial piles from test sites at Yuen Long South and Long Bin in this study are presented in **Table 5.1**, together with four existing pile loading tests for MS rocks available from the literature. Echoing from section 2 above, MS rock has much affected by foliation and possibly preserved bedding, which makes the rock generally more fractured than granitic rock and volcanic rock. Therefore, the 'Fracture State' of the founding rock mass is also summarised in the table, in terms of Total Core Recovery (TCR), Rock Quality Designation (RQD) and Fracture Index (FI) (Geoguide 3). In addition, Rock Mass Rating (RMR) (Bieniawski, 1989) for each test pile is interpreted from the respective borehole log in accordance with GEO Publication No. 1/2006. RMR, which includes parameters on rock strength, RQD, conditions of joints, etc., is also a widely used index to classify rock mass. It could be used for estimating the in-situ deformability of rock mass (Bieniawski, 1993), which is useful for estimating the settlement of the foundation.

From **Table 5.1**, albeit involving only two out of five sites under this study and two sites from the literature, all piles have achieved the designed test load with a settlement at pile toe less than 1.2% pile base diameter, mobilising end-bearing pressure of about 16,000 kPa to 27,000 kPa. It is noteworthy that the maximum test load was capped by the testing equipment's capacity.

Table 5.1: Preliminary results of selected pile loading tests in this study and other results of MS rocks in Hong Kong

Site	Pile No.	Pile Type	Pile Diameter (mm)	Rock Socket Diameter (mm)	Mobilised End Bearing Pressure (kPa)	Pile Base Settlement (mm)	Pile Founding Material	TCR / RQD / FI (within 1B) #	RMR At Bearing Stratum
Yuen Long South **(this study)**	YLS-P1	Bored Pile	813	750	~27,000	~4 (0.5% dia.)	SD Meta-siltstone / SD Meta-sandstone	100/ 100/ 0	84
Long Bin **(this study)**	LB-P1	Bored Pile	1500	1350	~25,000	~12 (0.9% dia.)	SD / MD Meta-siltstone	100/ 0-16/ 14.1 - >20	47
West Rail [1]	TSW1	Bored Pile	1200	1200	26,530	14 (1.2% dia.)	SD meta-sandstone	-/ 43-77/ -	59 [3]
West Rail [1]	TSW2	Bored Pile	1200	1200	24,000	2 (0.17% dia.)	SD meta-siltstone	-/ 86-88/ -	58 [3]
Kiu Cheong Road [2]	BTP-01	Bored Pile	813	813	16,254	9.4 (1.2% dia.)	Meta-sandstone	93 (min)/ 13/ >20 [4]	53 [4]
Kiu Cheong Road [2]	BTP-02	Bored Pile	813	813	16,989	9.4 (1.2% dia.)	Meta-sandstone	90 (min)/ 35/ >20 [4]	52 [4]

1. Data from Littlechild et al. (2000) ; 2. Data from Yau & Lau (2024); 3. RMR value from GEO (2006); 4. Value interpreted from ground investigation results
'-' information not available

The mobilised end-bearing pressure of each test is plotted against the pile toe settlement in **Figure 5.3**. As can be seen, the load-settlement behaviour of the two trial piles in this study, under test loads of ~23,000 kPa to ~27,000 kPa, is well within the virtually linear elastic portion, showing no evidence of plastic behaviour. While detailed data analysis is on-going, the test results from this study are found similar to those reported in the literature for MS rocks, granite and tuff (Yau & Lau, 2024; Littlechild et al., 2000).

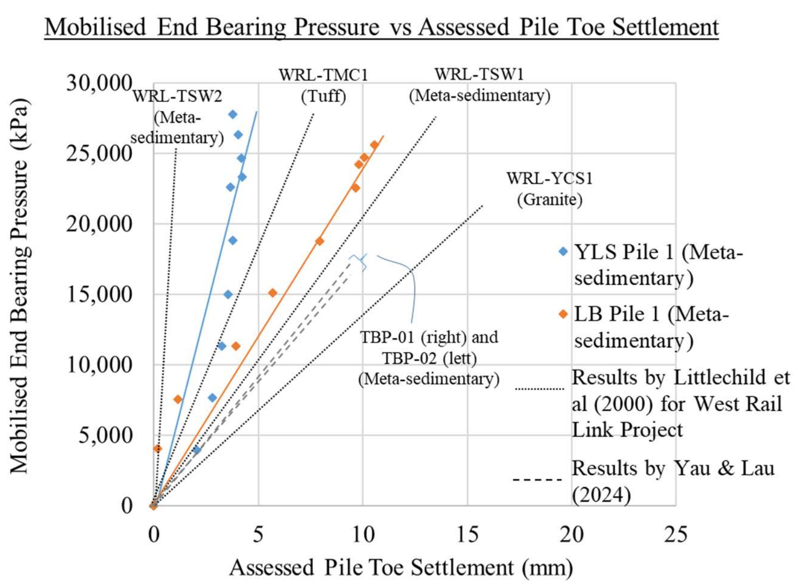

Figure 5.3: Comparison of preliminary results in MS rock and results in Tuff, Granite

The mobilised end-bearing pressure of the MS rocks is also plotted against the Uniaxial Compressive Strength (UCS) of the intact rock obtained from predrilling in **Figure 5.4**, and the RMR at the bearing stratum in **Figure 5.5**. It is worth to note that the preliminary results of proven bearing capacity are at least 5 times higher than presumed allowable vertical bearing pressure of 3,000 kPa for MS rock.

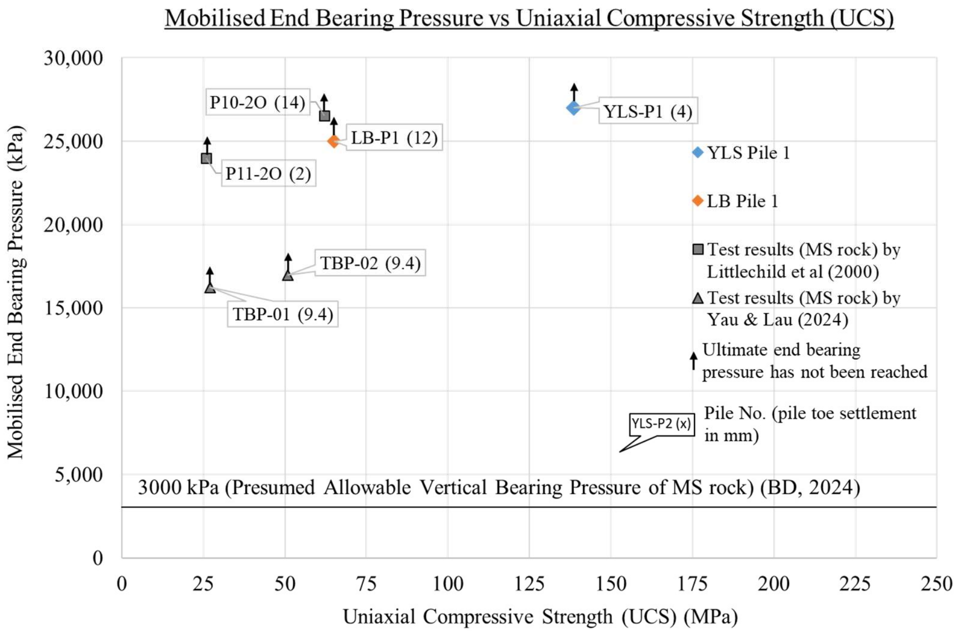

Figure 5.4: Preliminary results – mobilised end bearing pressure and UCS

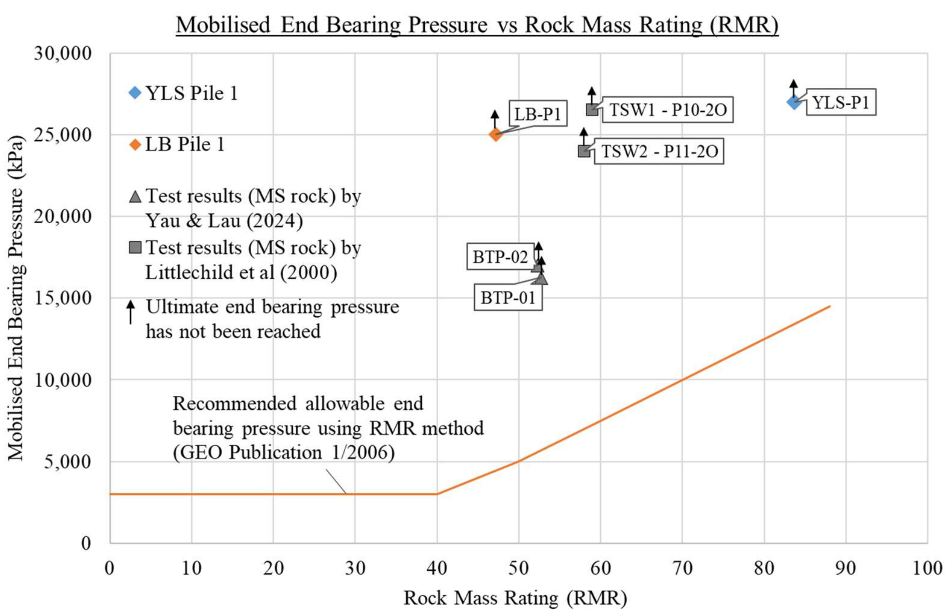

Figure 5.5: Preliminary results – mobilised end bearing pressure and RMR (based on Figure 6.7 in GEO (2006)

Since the ground investigation and laboratory tests associated with the pile loading tests are still underway, the test results with different rock mass properties (e.g. fracture state, RMR, rock strength, etc.) will be further studied and reported later.

6 APPLICATIONS OF NEW AND GREEN MATERIALS IN PILING WORKS

With a view to advancing sustainable and cost-effective geotechnical solutions, there is a pressing need to promote wider application of new and green materials, as well as advanced and efficient design in construction works. While the use of eco-friendly GGBS and efficient high strength steel in pile construction in Hong Kong is still at the early stage, technical design considerations and industry's concerns on constructability remain challenges to be addressed. In connection with the systematic pile load tests conducted by the GEO in the Northern New Territories, concrete with high replacement level of GGBS as the supplementary cementitious material (SCM) and high strength S690 steel H-sections were used in some selected piles. These results will not only optimise the foundation design for MS rocks in the Northern Metropolis areas, but will also provide technical evidence to support broader adoption of GGBS concrete and high strength S690 steel in foundation projects.

6.1 Trial Piles with High Percentage GGBS at Yuen Long South

Benefits and Challenges

The use of GGBS, a by-product of the iron manufacturing industry and has been used as a SCM in concrete, has been proven effective in reducing the total carbon emission of the concrete production process by lowering the content of Ordinary Portland Cement (OPC). Since the publication of the General Specification for Civil Engineering Works (GS) in 2012, GGBS concrete (with a replacement level between 35% and 75% allowed for normal concrete) has been used in the construction of superstructure and precast facades, but rarely seen in the construction of piles in Hong Kong. It is probably because of various practical concerns from the stakeholders, including piling contractors and concrete suppliers, of adopting GGBS concrete with a high replacement level (i.e. ≥ 50%) in piling works, such as potential high cohesiveness of the concrete due to the fineness of GGBS, which could pose challenges to the tremie concreting process and the pile casing extraction process. Other concerns include workability, retention of slump, temperature evolution in the pile, and the long-term strength development.

Technical Details, Testing and Monitoring of the Trial Piles

In order to collect more field data and site operation observations of using high percentage GGBS concrete in the actual construction operation and quality control of piling works with large concreting volume and long concreting time on site, two full-scale trial bored piles of 3 m in diameter, namely GGBS-YLS-P1 and GGBS-YLS-P2 with 75% and 80% (i.e. exceeded the recommended replacement % in the GS) of GGBS replacement level respectively, were constructed at a site in Yuen Long South (see **Figure 6.1**).

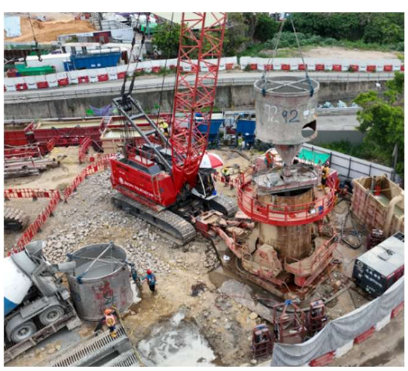

Technical details	**GGBS-YLS-P1**	**GGBS-YLS-P2**
Pile shaft diameter	3.0 m (2.85 m in rock)	3.0 m (2.85 m in rock)
Pile shaft length	63 m (300 mm toe-in into rock)	52 m (300 mm toe-in into rock)
Steel reinforcement ratio	1.8% to 2.6%	1.8% to 2.6%
Proportion of GGBS to total cementitious content in concrete	75%	80%
Concrete grade strength	60D/20	60D/20
Designed slump value	200 mm	200 mm

Figure 6.1: Overview of the trial piling works

To properly identify any potential construction issues during site operation and quality control, the entire construction process, including tremie concreting and pile casing extraction, was carefully monitored and recorded. Typical testing and monitoring procedures for bored piles, including slump retention test for the workability, sonic logging test and interface core drilling were applied. In addition, concrete cubes for compressive strength tests at the age from 3 days to 90 days were sampled, together with full-length core drilling for UCS tests at the age from 58 days to 120 days were carried out for capturing the strength development from early age to long term. To address the industry's concern about the temperature evolution in the pile, beside conventional thermal couples, fibre optic sensors (for continuous temperature-change profile) were also installed along the pile shaft and across pile diameter.

Results and Observations

One of the major concerns of using GGBS concrete in piling works is the high cohesiveness of the GGBS concrete with a high replacement level. In comparing with typical concreting time of a bored pile with Pulverised Fly Ash (PFA) concrete, a longer pouring time of concrete from the concrete bucket to the tremie pipe was observed when a high percentage of GGBS was adopted. As reflected by the contractors and the concrete supplier, other concreting stages (e.g. concrete pouring from the mixing plant to the agitator of trucks at the plant, and the transfer from the agitator of trucks to the concrete bucket at the site) could have also taken a slightly longer time due to the cohesiveness of GGBS concrete, especially at the early stage of the construction works due to a lack of experience with the new concrete mix. As experience accrued in optimising the concrete design mix and concreting procedure, the situation was found to be improved.

Other aspects of the construction process for both trial piles were found to be normal. Despite the relatively higher cohesiveness of the GGBS concrete, no clogging of the tremie pipe was observed. There was also no difficulty during pile casing extraction. As reported by the piling contractor, comparing with the typical operation when OPC or PFA concrete was used, no extra power was required to extract the casing, and no up-dragging of the steel cage was observed throughout the process. For workability, the measured average slumps for both trial piles fulfilled the design requirements. Strength development was observed slower at the early stage with increasing replacement level of GGBS. However, the 28-day strength for both 75% and 80% GGBS concrete met the design requirements. The UCS tests on concrete cores extracted from the test piles at the age from 58 days to 120 days indicated that there was a continuous strength gain of GGBS concrete with time. More technical details about these trial piles can be referred to Chiu & Sze (2024).

6.2 Trial Piles with High Strength S690 Steel H-section at Fung Kong Shan

Benefits and Challenges

Due to its higher design structural capacity, high strength steel attracts industrial attention due to benefits of reduction in steel tonnages and structural weights, and saving in cost. Following the successful application of high strength S690 steel in the construction of the Cross Bay Link, the industry has been exploring to extend its application to other construction disciplines, including piling construction. Under the current foundation design standard, however, effective adoption of high strength S690 steel could also be governed by geotechnical capacity which errs on the conservative side. Long socket length (over 10 m) for achieving the currently required shaft friction leads to heavy machinery and high construction cost. Limited experience for welding high strength S690 steel on site in Hong Kong also imposes hurdle for wider application.

Technical Details and Observations during the Construction of the Trial Piles

Two full scale trial socketed H-pile of 610 mm in diameter, namely SHP-FK-P1 and SHP-FS-P2, using high strength S690 steel H-section and 75% GGBS grout were constructed at one of the test sites in this study, namely Fung Kong Shan near Kwu Tung North. In order to verify the end-bearing capacity and the rock socket shaft resistance of piles in meta-sedimentary rocks beneath the site, an O-cell was installed at the bottom of SHP-FK-P1 and a kentledge system was constructed at the top of SHP-FK-P2 for pile loading test. The technical details of these two trial piles are summarised in **Table 6.2**.

Table 6.2: Technical details of trial piles with S690 steel and GGBS grout

	SHP-FK-P1 (with Osterberg cell)	**SHP-FK -P2 (with kentledge)**
Pile shaft diameter	610 mm (550 mm in rock)	610 mm (550 mm in rock)
Steel H-section	305×305×219 JBP (S690)	305×305×219 JBP (S690)
Pile shaft length	54 m (2.2 m socket into rock)	37 m (6.4 m socket into rock)
Proportion of GGBS to total cementitious content in grout	75%	75%
Grout strength	30 MPa	30 MPa

Figure 6.2 shows some photos during the construction of the trial piles. The high strength S690 steel H-sections were fabricated by welding three steel plates in factory. Shear studs were installed along the H-sections to maximise the bonding at the steel-grout interface. Fibre optic sensors and strain gauges were also installed along the H-sections for monitoring the strain development and pile movement throughout the load test. While strain gauges provide point-wise strain measurements at the installation levels, the fibre optic sensors adopting Optical Frequency-domain Reflectometry (OFDR) technique pick up high spatial resolution of continuous strain data which facilitates determination the shaft friction along the pile.

(a) (b) (c)

Figure 6.2: Construction details of trial piles with high strength S690 steel H-section: (a) Instrumentation with fibre optic sensors; (b) on-site welding; and (c) testing of weld.

These trial piles also aim to demonstrate the constructability of high strength S690 steel in piling construction, including the installation of steel H-sections and on-site welding operation. Qualified high strength S690 steel welders were trained in advance and engaged in the welding process. Hold time before weld tests and inspection procedures using non-destructive testing methods (including Magnetic Particle Inspection and Ultrasonic Examination), in accordance with the current steel design standard, were strictly followed to identify any potential challenge in the construction and quality control. The welding process was reported smooth during the construction and no prolongation was recorded comparing to construction using typical steel H-section. While the detailed interpretation of the pile load test results was still undergoing, preliminary results revealed that the end-bearing capacity and the rock socket shaft resistance tested were well above the values in the current foundation standard.

7 CONCLUSING REMARKS AND WAY FORWARD

A comprehensive trial piling works programme is being implemented at different sites within NM. All trial piles are founded on MS rocks with varying characteristics (e.g. different RMR values). Based on the preliminary results of pile loading tests conducted at Yuen Long South and Long Bin together with some existing local test data, there is a room for enhancing the prevailing foundation design guideline for MS rocks i.e. the presumed allowable bearing pressure and the presumed allowable bond or friction in rock socket for MS rocks in the Northern New Territories. Taking cognisance of the variable nature of MS rocks, and subject to the findings of other pile loading tests and the associated field and laboratory testing results of which the data interpretation and analysis are underway, it is considered promising that the foundation design guidelines for MS rocks could be improved. Such improvement could bring about substantial saving in cost and time of the foundation works whilst benefiting material saving and sustainability in general. In fact, results of some pile loading tests conducted in this study have been adopted by the site-specific housing development projects for improving their foundation designs. It signifies the immediate benefits brought about by this study.

The successful application of high-percentage GGBS in both concrete (75% and 80% replacement) and grout (75% replacement) in the trial piles have addressed the industry concerns regarding constructability and operational challenges of this eco-friendly materials in piling works. In a similar fashion, the trial piles using high-strength S690 steel H-sections in socketed piles have well demonstrated viable constructability, including welding and installation processes, while achieving robust shaft resistance and end-bearing performance. These innovations align with sustainability goals by reducing carbon emissions and material usage.

ACKNOWLEDGEMENTS

This paper is published with the permission of the Head of the Geotechnical Engineering Office and the Director of Civil Engineering and Development, the Government of the Hong Kong Special Administrative Region of the People's Republic of China.

REFERENCES

BD 2024. *Code of Practice for Foundation 2017 (2024 Edition).* Buildings Department, HKSAR Government, pp 11-13.

Bieniawski, Z.T. 1989. *Engineering Rock Mass Classification*. John Wiley, New York, 251 p.

Bieniawski, Z.T. 1993. *Classification of Rock Masses for Engineering: The RMR System and Future Trends*.

Chiu, K.Y.K. & Sze, E.H.Y. 2024. *Trial Piles with High Percentage GGBS*. *Proceedings of the HKIE Geotechnical Division Annual Seminar 2024*.

GEO 2017. *Guide to Rock and Soil Descriptions (Geoguide 3) (Continuously Updated E-Version released on 29 August 2017)*. Geotechnical Engineering Office, Civil Engineering and Development Department, HKSAR Government, 171 p.

GEO 2000. *The Pre-Quaternary Geology of Hong Kong*. Geotechnical Engineering Office, Civil Engineering and Development Department, HKSAR Government, 181 p.

GEO 2006. *Foundation Design and Construction (GEO Publication No. 1/2006)*. Geotechnical Engineering Office, Civil Engineering and Development Department, HKSAR Government, pp 105-111.

GEO 2007. *Engineering Geological Practice in Hong Kong (GEO Publication No. 1/2007).* Geotechnical Engineering Office, Civil Engineering and Development Department, HKSAR Government, 278 p.

Greenway, D.R., Powell, G.E. & Irfan T.Y. 1988. A case history of slope design in complex weathered lowgrade metamorphic rock. *Geotechnical Engineer, Vol. 18*, pp 145-166.

HKSAR 2006. *General Specification for Civil Engineering Works (GS 2006), 3 volumes*. Government Logistics Department, HKSAR Government.

Irfan, T.Y. & Powell, G.E. 1991. *Foundation Design of Caissons on Granitic and Volcanic Rocks (GEO Report No. 8)*. Geotechnical Engineering Office, Civil Engineering and Development Department, HKSAR Government.

Lam, A.K.M., Wong A.T.F., Chik, S.S.W, Chiu, K.Y.K., Sze, E.H.Y., Wong, P.P.C., Hui, T.H.H. 2025. Full-scale Pile Load Tests using Osterberg Cells in Meta-sedimentary Rock. *Proceedings of the HKIE Geotechnical Division Annual Seminar 2025*.

Langford, R.L., Lai, K.W., Arthurton, R.S. & Shaw, R. 1989. *Geology of the Western New Territories (Hong Kong Geological Memoir No. 3)*, Geotechnical Engineering Office, Civil Engineering and Development Department, HKSAR Government, 140 p.

Littlechild, B.D., Hill, S.J., Plumbridge, G.D. & Lee, S.C. 2000. Load Capacity of Foundations on Rock. *Proceedings of Sessions of Geo-Denver 2000 - New Technological and Design Developments in Deep Foundations*, ASCE Geotechnical Special Publication, Issue 100, pp 140-157.

Sewell, R.J., Campbell, S.D.G., Fletcher, C.J.N., Lai, K.W. & Kirk, P.A. 2000. *The Pre-quaternary Geology of Hong Kong*. Geotechnical Engineering Office, Civil Engineering and Development Department, HKSAR Government, 181 p.

So, K.W.F. & Sewell, R.J. 2019. *Updating of Hong Kong Geological Survey 1:20,000-scale Maps Major Findings and Revisions Map Sheet 6 – Yuen Long (Geological Report No. GR 4/2019*). Geotechnical Engineering Office, Civil Engineering and Development Department, HKSAR Government, 58 p.

Suen, M.H.Y., Chow, C.C.F., Lau, R.W.Y., Chau, A.Y.L., Wong, P.P.C., Hui, T.H.H. 2025. Evaluation of RMR for Meta-Sedimentary Rocks in Hong Kong: Challenges and Potential Solutions. *Proceedings of the HKIE Geotechnical Division Annual Seminar 2025*.

Tse, T.K. & Tang, D.L.K. 2024. *Updating of Hong Kong Geological Survey 1:20,000-scale Maps Major Findings and Revisions Map Sheet 2 – San Tin (GEO Report No. 371)*. Geotechnical Engineering Office, Civil Engineering and Development Department, HKSAR Government, 40 p.

Yau, T.L.Y. & Lau, C.K. 2024. Review on the End Bearing Capacity of Large Diameter Bored Piles founded on Meta-sedimentary Rock in Hong Kong. *Proceedings of the HKIE Geotechnical Division Annual Seminar 2024*, pp 374-385.

Yim, N.M.C., Tse, T.K. & Tang, D.L.K. 2024. *Updating of Hong Kong Geological Survey 1:20,000-scale Maps Major Findings and Revisions Map Sheet 5 – Tsing Shan (Castle Peak) (GEO Report No. 375)*. Geotechnical Engineering Office, Civil Engineering and Development Department, HKSAR Government, 35 p.

Advancing Geotechnical Practice with Design for Manufacture and Assembly (DfMA) Retaining Wall Construction

Simon C.M. Leung, Matthew M.K. Chan
AECOM Asia Company Ltd., Hong Kong, China

Michael W.K. Choi
Drainage Services Department, HKSAR, Hong Kong, China

Joel Y.F. Wong, Elton M.Y. Ko
Civil Engineering and Development Department, HKSAR, Hong Kong, China

Ryan Wong
Sheung Ying Construction Limited

ABSTRACT

This paper presents the application of Design for Manufacture and Assembly (DfMA) in the construction of a 52m long L-shaped retaining wall with a maximum height of 4.8m, founded on Completely Decomposed Granite, as part of the Relocation of Sha Tin Sewage Treatment Works into Caverns project. This initiative not only enhances sewage infrastructure but also mitigates environmental impact and frees up valuable land for sustainable urban development. The retaining wall supports a 500m access road to the Site Explosives Magazine, strategically designed for the supply of explosives for multiple blasts daily. By favoring DfMA over conventional in-situ methods, the project implemented an innovative design featuring precast steel beams encased in concrete, which were assembled on-site. This approach dramatically reduced construction time from 147 days to approximate 10 days, streamlined on-site activities from 70 to 21, and completely eliminated working-at-height risks, significantly enhancing safety and efficiency. A key to this success was collaboration among the RSS, contractors, subcontractors, and strong client support. Active engagement enabled the collective development of the DfMA strategy, leveraging on-site experience in design optimization and risk management. This approach facilitated early risk identification, ensuring DfMA strategies were well-resourced and successfully implemented.

1 INTRODUCTION

The construction industry is undergoing a transformative shift toward innovative methodologies that not only enhance efficiency but also deliver improvements in safety and sustainability. In an era where rapid urban development and environmental stewardship are paramount, DfMA emerges as a pioneering approach. While traditionally leveraged in building construction and bridge engineering, DfMA is now breaking into geotechnical applications, promising substantial benefits in complex site conditions. This paper presents a case study of the DfMA retaining wall implemented in the project 'Relocation of Shatin Sewage Treatment Works to Caverns' (STC).

Urban environments, particularly high-density metropolises like Hong Kong, pose a unique set of challenges. Geotechnical projects here encounter constraints such as steep or irregular terrain, in close proximity to the site boundary, limited working space, and heightened safety concerns. The STC project exemplifies these challenges. It demands a solution that minimized on-site activities while delivering structural robustness. By integrating DfMA into the retaining wall designthe project team was able to transition key construction activities from congested and risky site environments to controlled, off-site manufacturing settings. The integration of DfMA into retaining wall construction is the first of its kind being adopted in Hong Kong. This shift not only streamlined operations but also opened the door to enhanced precision and quality control. This paper will discuss the DfMA considerations involved in the design and construction of the retaining wall, including casting yard, transportation, and lifting strategies. Additionally, it will highlight the benefits of DfMA in addressing common challenges faced in geotechnical projects, ultimately contributing to improved project outcomes. Through this case study, we aim to demonstrate the effectiveness of DfMA in modern geotechnical practice and encourage its adoption in future projects within Hong Kong and beyond.

1.1 Design of DfMA

DfMA is often misperceived by some contractors and subcontractors as merely an enhanced form of precast construction. However, its philosophy extends well beyond off-site fabrication. Boothroyd (2005) noted that DfMA evaluate and improve product design by considering the downstream manufacturing and assembly processes – a view of that, while partly accurate, does not reveal the full scope of the approach. At its core, DfMA embodies the principle of "starting with the end in mind," meaning every design decision is intrinsically linked to the entire DfMA cycle. This cycle encompasses ensuring adequate space for a casting yard and storage area of the precast unit, transportation of precast unit from precast yard to the installation location, the maximum capacity of lifting cranes. Designers must also address external constraints, including steep or narrow access roads that could impede delivery and installation. Collectively, these factors dictate the maximum dimensions of precast units, compelling designers to thoughtfully divide the structure into sensible, manageable segments that not only optimize assembly but also enhance overall efficiency. In addition, ensuing that the design units are repetitive and standardized is crucial. If units are not designed to be uniform for ease of manufacture, contractors will face increased costs due to the necessity of developing additional types of molds during fabrication. In the case of retaining walls, which often exhibit variations in retaining height, it is advisable to incorporate at least two identical units in terms of dimensions or to design the molds with the flexibility to accommodate minor adjustments for slight variations. Finally, the design of the connections between units is paramount. Standardized, robust connections ensure proper alignment, structural integrity, and efficient on-site assembly while minimizing the need for custom joint solutions that could further inflate costs.

In order to achieve such a comprehensive DfMA approach, RSS can no longer rely solely on approving contractor proposals under the New Engineering Contract (NEC) and assume that the construction method is exclusively the contractor's responsibility. Instead, RSS must engage actively with both contractors and subcontractors to collectively develop and refine the DfMA construction strategy. This integrated approach leverages the invaluable on-site experience and resources of contractors while capitalizing on RSS's expertise in design optimization, risk management, and regulatory compliance. Lu (2020) suggests that the early collaboration of all contracting parties brings more detailed information to light compared to traditional design processes. This integrative approach, anchored in DfMA principles, not only enhances the understanding of project requirements from the onset but also facilitates the early identification of potential risks during manufacturing and construction. Perhaps most importantly, robust support from the client is critical to ensure that effective DfMA strategies are adequately resourced and successfully implemented.

1.2 Consideration of Casting Yard

Determination of the casting yard location and the associated logistics is critical. Ideally, if a project site can accommodate it, establishing an onsite casting yard is advantageous because it simplifies logistics and improves site supervision through direct oversight of fabrication activities. In such cases, the facility may either be provided as part of the contract or rented at the contractor's expense, each carrying its own implications. Conversely, when an offsite casting yard is used, which is often the case in Mainland China, additional factors come into play. Designers must carefully review the dimensional limitations imposed by border crossing facilities to ensure that oversized precast units can be transported without issue. Offsite production also demands that experienced engineers or supervisors be deployed to remotely manage fabrication, ensuring quality control and adherence to project specifications. Furthermore, a temporary stock area is essential for storing precast elements prior to installation. For smaller projects with limited onsite storage, renting additional space may further complicate the process and increase costs. All these factors form an interconnected mind map that must be carefully considered and balanced to optimize the DfMA approach and ensure successful project outcomes.

1.3 Consideration of Transportation

In Hong Kong's bustling urban landscape, transportation is the lifeblood of successful DfMA projects. Narrow streets, strict regulations, and precise load limits demand innovative planning and flawless execution. Designers must carefully consider truck capacity and traffic routing intricacies, such as road gradients, available turning space, and the challenges posed by steep terrain. Particularly, DfMA solutions for retaining walls often involve construction on steep terrain with narrow access roads, where accessibility is limited and U-turns can be extremely difficult. Moreover, all trailers and loads must comply with the local road traffic ordinance, which stipulates a maximum width of 2.5 meters, a maximum height of 4.6 meters, and a maximum length of 12 meters for rigid vehicles or 16 meters for articulated vehicles. Should any load exceed these dimensions, a special permit for wide or long loads becomes mandatory.

1.4 Consideration of Lifting

One of the key benefits of DfMA is mitigating the hazards associated with working at height by transferring the risk to controlled lifting operations. When implementing DfMA, the design of precast units should be optimized not only for their structural roles in a retaining wall but also for their weight, size, and lifting requirements. Typically, precast units weigh between 30 tonnes and 40 tonnes, based on the typical lifting capacity of the crane. Geotechnical engineers play a critical role in assessing the ground conditions at the site, particularly the bearing capacity of soil, to ensure that it can support both the lifting crane and the temporary loads imposed by the precast units during placement. This is especially important in areas near the edge of natural terrain, where soil stabilization or additional support may be necessary. In addition, the lifting capacity of the crane must be meticulously assessed to ensure that the maximum lifting radius for the intended load is not exceeded.

1.5 Effective Cost Assessment

The benefits of DfMA are widely promoted in Hong Kong for their potential to reduce costs, boost productivity, and enhance safety, quality, and sustainability (Devb, 2018). These outcomes however are not universal across all projects. Therefore, RSS and the contractors must conduct a thorough cost-effectiveness analysis to evaluate the financial viability of adopting DfMA principles. This analysis should consider key factors such as labor expenses, stockpiling area rentals, transportation, and lifting costs. Importantly, it must also assess whether any temporary works will be required, as these additional works can significantly increase overall project expenses. Regional cost differences further influence the cost-benefit equation. For instance, off-site casting yards in mainland China benefit from substantially lower labor costs and stockpiling rentals. Such variations can markedly affect the overall economics of DfMA implementation. In addition, not all project scopes are equally suited to DfMA. For example, water retaining structure designs are often irregular and non-uniform, leading to elevated labor costs and expensive manufacturing cost that may negate the expected cost savings and watertightness concern. In contrast, projects such as retaining walls, with construction divided into uniform, repetitive units, tend to offer clearer cost incentives due to streamlined manufacturing and assembly processes. Ultimately, a comprehensive cost-effectiveness analysis is vital in determining whether DfMA will deliver genuine cost savings and enhanced efficiency for a specific project. By systematically evaluating these factors, contractors can make informed decisions regarding the adoption of DfMA.

2 CASE STUDY – RELOCATION OF SHATIN SEWAGE TREATMENT TO CAVERNS

2.1 Project Background and DfMA Retaining Wall

The Relocation of the Sha Tin Sewage Treatment Works to caverns is a groundbreaking initiative aimed at addressing urban development challenges while prioritizing environmental sustainability. This ambitious project not only seeks to modernize existing sewage treatment facilities but also aims to free up valuable land for alternative uses, such as public infrastructure, residential development, and green spaces. Additionally, the relocation mitigates adverse impacts on the surrounding community, fostering a more sustainable and harmonious urban ecosystem. The overview of project scope is shown in Figure 1.

The project involves a wide array of complex geotechnical engineering and construction challenges, one of which is the excavation and construction of a cavern to house the sewage treatment works. Crucial to the success of this undertaking is the development of a 500-meter-long access road to the Site Explosives Magazine (SEM), a facility essential for the timely completion of cavern excavation. This road, engineered to ascend steep natural terrain while adhering to strict spatial and logistical constraints, is supported by an L-shaped retaining wall. We have selected a portion of the retaining wall RMZ3, as shown in Figure 2, located on the steepest natural terrain near the site boundary for DfMA construction. Conventional cast in-situ methods would be especially challenging in this area due to its close proximity to the site boundary, which complicates scaffolding and formwork erection, and the elevated safety risks associated with steep slopes

Figure 1: Overview of project scope

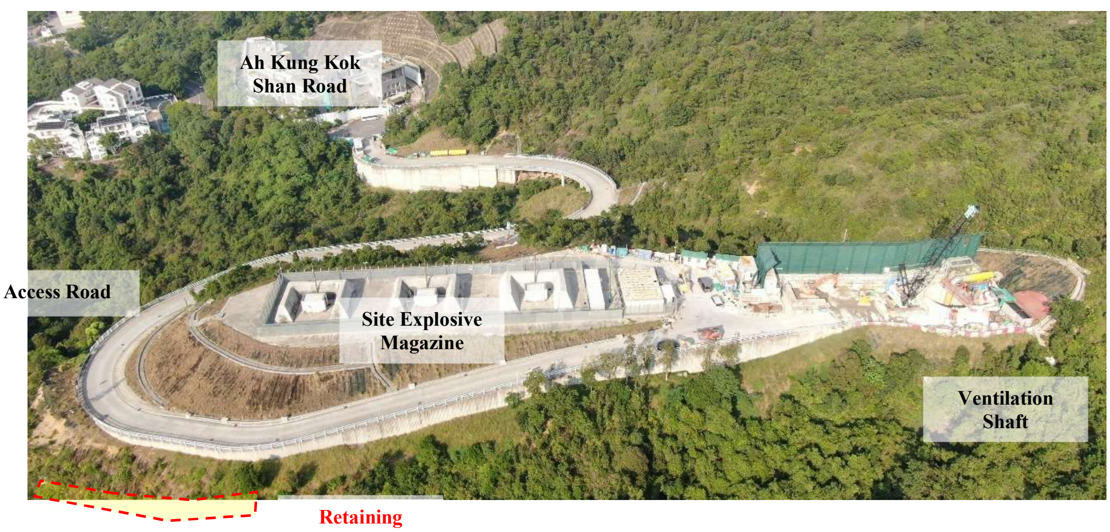

Figure 2: DfMA for retaining wall RMZ3

2.2 Conceptual Design

Retaining wall RMZ3, spanning bay 1 to bay 7 with a total length of 53 m and a maximum retaining height of 4.8 m, was selected for construction using the DFMA method. The wall is designed to be founded on completely decomposed granite with designed strength parameters (g'=19kN/m3, c'=3kPa, f'=39°). The design conservatively assumes a groundwater level located at one-third of the retaining height based on available groundwater monitoring records. The overall stability of the retaining wall against sliding, overturning, and bearing failures were evaluated under a 20 kPa surcharge under normal conditions, while another loading condition, including seismic, blasting, vehicle impact, and wind loads, were also considered.

2.3 Evaluation of Design Scheme

According to Tan (2020), "the emerging technological advancements, such as Building Information Modelling (BIM), 3D printing, the Internet of Things (IoTs), and robotics provide the construction industry, DfMA in particular, new entry points for manufacturing knowledge and efficiency improvement". Our project team employs these manufacturing technologies and computer software–based engineering tools in developing the DfMA design scheme. Traditionally, the precast retaining wall is regarded as an idea only because of the difficulty in aligning connection joints. This issue could be solved with the aid of BIM, as shown in Figure 3. Several schemes are designed for different splicing methods of the retaining wall units. The details of the segments, such as the shape, dimensions and connection details, are considered. The reinforcement details are also modelled to justify the best option for the project. Different design options are printed using a 3D printer, as shown in Figure 4, for easier visualization and evaluation of their structural properties. After rounds of evaluation, the retaining wall is split into two segments with structural steel beams as a connection and major reinforcement. Two separate precast elements, each incorporating an encased steel I-beam, which are connected on site to form the complete structure. For ease of assembly, the base slab has been designed to interconnect with a minor portion of the wall stem, with this connection being welded during the prefabrication process. The remaining segment of the stem includes approximately 300 mm of exposed steel that is intentionally left un-encased in concrete to facilitate bolt installation during on-site assembly. Once all connections are established, the exposed steel section is concreted to ensure full structural integration.

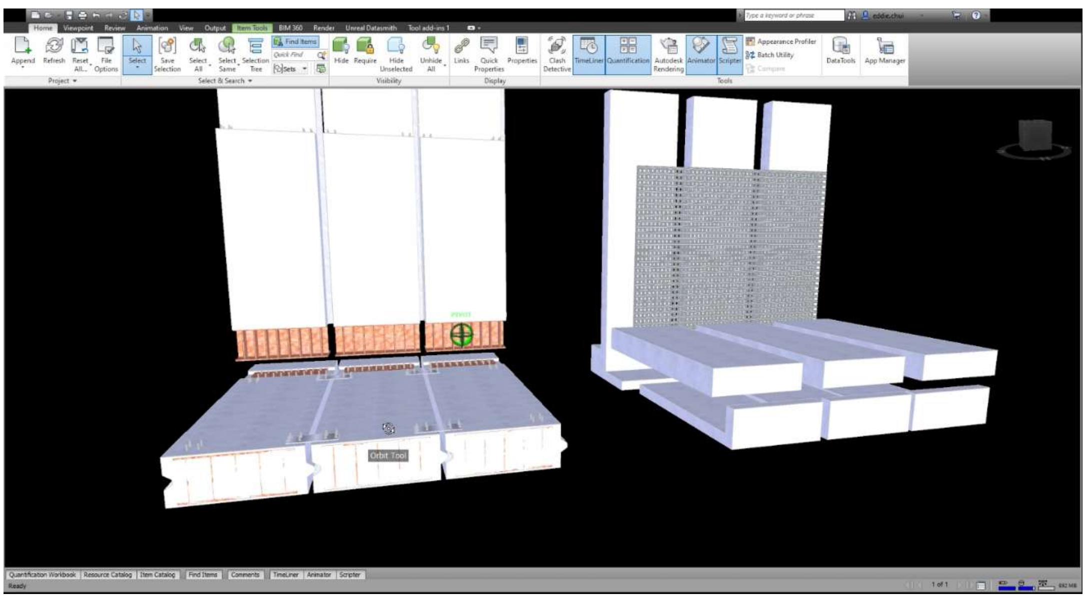

Figure 3: Evaluation of different design schemes

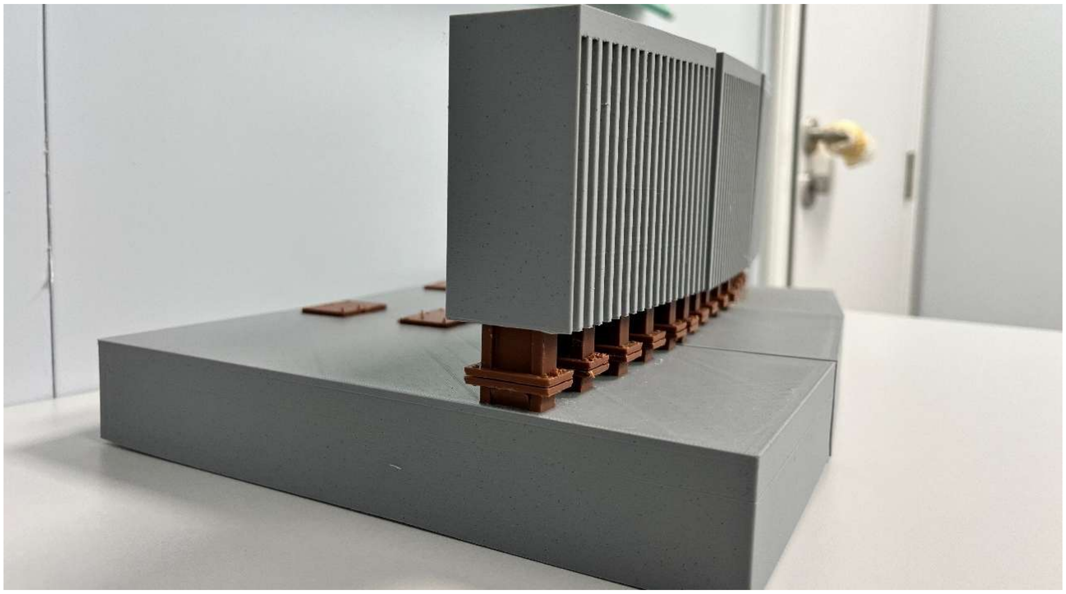

Figure 4: 3D printing model of RMZ3

2.3.1 Connections between Precast Units

This design scheme, which uses structural steel beams, is more efficient for both design and construction than a scheme that uses rebar. Only the connection portion is cast in situ, thereby minimizing on-site construction work. The connection between the wall base and the stem is achieved via a base plate secured with four bolts. These bolts are fixed during assembly to ensure the stability of the wall elements throughout the temporary construction stage. Since the bolts provide robust support for the wall stem, no additional temporary support is necessary during the concreting of the 300-mm un-encased concrete portion. In contrast, if conventional rebar were used, the numerous connections between the wall stem and the base would be difficult to manage. Such a design would require extra supports to hold the wall stem upright and in position during the concreting of the 300-mm un-encased concrete portion. Moreover, these temporary supports would need to remain in place until the concrete gain sufficient strength, thereby introducing higher risks during construction.

2.3.2 Division of Precast Units

The retaining wall is constructed with a uniform base and stem, incorporating only minor height variations to support the ascending access road. Each bay of the wall spans approximately 7.5 meters in both width and length. Several schemes for dividing the structure into manageable units were explored with the aid of BIM, as shown in Figure 5. For ease of transportation and to avoid the need for special wide and long load permits, each bay is divided into three modular precast units. Each unit measures roughly 2.5 meters in width and 7.5 meters in length. At least two of these modular units per bay are designed with identical widths, while the third unit may have a slight deviation, which is accommodated by an adjustable mold design. This strategy minimizes the number of different molds required, thereby streamlining construction and reducing costs. The division of the precast units also needs to consider lifting operations, as the crane must operate near the edge of the natural terrain. Consequently, stringent limits on the weight of both the crane and the lifting load must be strictly enforced. Thanks to BIM, the precise weight of the precast units, which is composed of steel members, steel reinforcement, and concrete, can be quickly determined, facilitating an efficient evaluation of different division schemes.

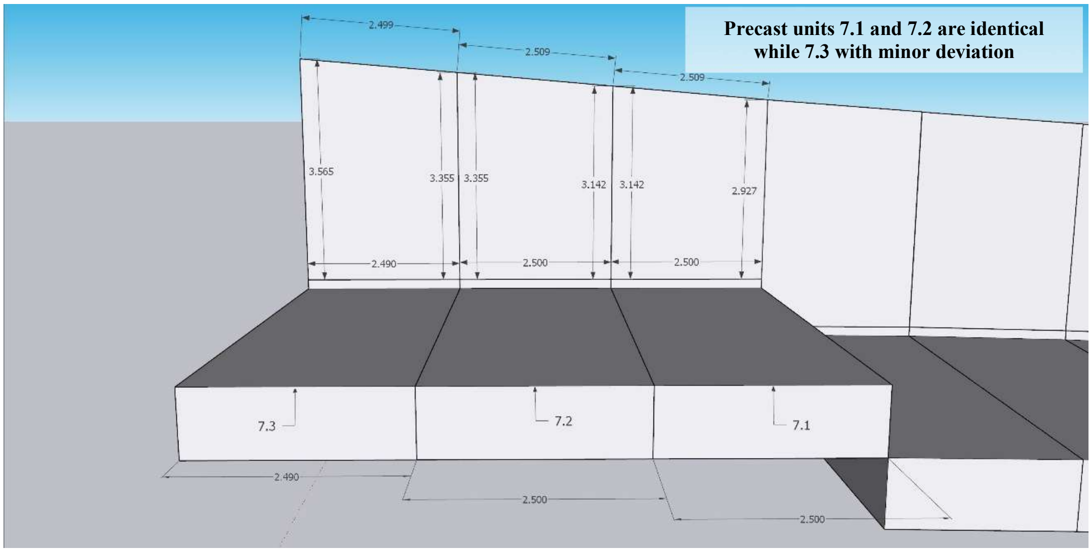

Figure 5: Division of the precast unit by BIM

2.3 On-site Casting Yard

The on-site casting yard, as shown in Figure 6, minimizes long-distance hauling, thereby reducing transportation costs and streamlining overall project logistics, a compelling incentive for adopting DfMA principles throughout construction. Although a 150 mm sub-base must be laid at the contractor's expense to establish a stable, level foundation for the casting yard, its benefits extend well beyond casting. The on-site casting yard enables workers to cast precast units from ground level rather than working at heights, as required with conventional cast-in-situ methods, significantly enhancing safety and improving overall construction quality. A detailed digital simulation of the precast process, developed using software Fuzor, enhances project efficiency by providing clear, on-site demonstrations for staff and serving as a crucial tool during client meetings to secure approvals.

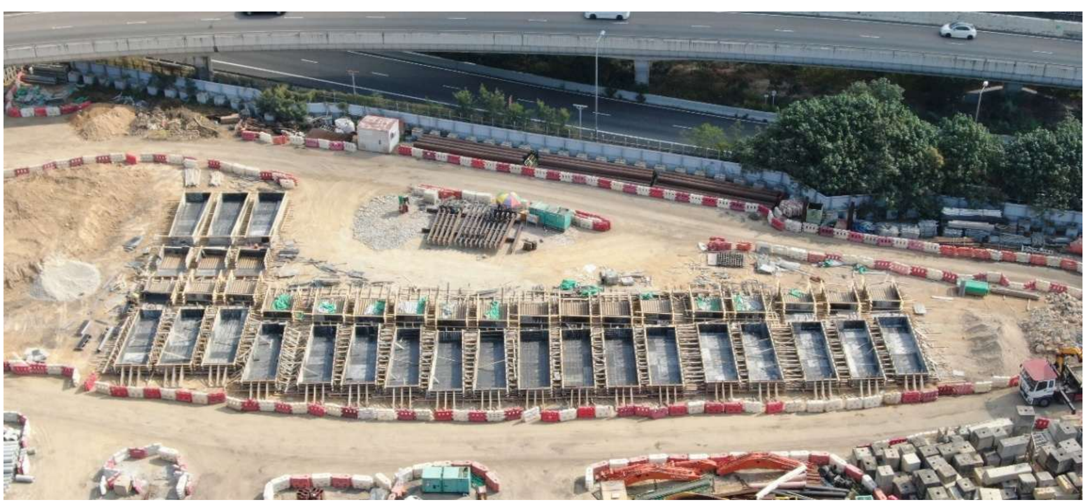

Figure 6: On-site casting yard

2.4 Transportation

The dimensions of the precast segments were carefully optimized to meet transportation requirements, following a comprehensive survey from the on-site precast yard to the designated installation area. Based on the design loads of the precast units, the project deployed two types of trailers: one with a maximum gross combined weight of 44 tonnes and a total length of 15.8 meters for wall base units, and another with a maximum gross combined weight of 38 tonnes and a total length of 11.2 meters for wall stem units. Two potential routes were identified and evaluated using Autodesk Vehicle Tracking software to conduct a swap path analysis for assessing the feasibility of turning. Although the shorter route was initially considered, it was ultimately rejected due to its abrupt junctions and a highway bridge with low headroom that restricted the passage of precast units. Instead, a slightly longer route featuring gentler turns and no height restrictions was finally adopted. In addition, since the proposed installation location is within natural terrain, a haul road is required to access it. A photogrammetric model of the site haul road was developed, and its gradient was assessed using Vehicle Tracking software to ensure that the maximum allowable load can be transported. Re-levelling a portion of the haul road, which is at the contractor's expense, was required to ensure smooth transportation of the precast units. In a related logistical challenge, the delivery truck was unable to execute a U-turn on the limited space available on the haul road. To resolve this, the project team deployed a crawler crane to assist the truck in turning around safely. A detailed simulation was prepared and presented as a safety demonstration to the site staff, ensuring that all personnel were aware of and prepared for the new manoeuvring procedures

2.5 Lifting

The BIM model serves as a critical tool during the planning of lifting operations by providing an integrated, data-rich digital representation of each segment's weight, dimensions, and assembly details. This detailed model enables engineers to accurately calculate the load of each precast segment and simulate the lifting sequences, ensuring that every step from crane positioning to the safe placement of wall components is well coordinated. By integrating the crawler crane's specifications, including its safe working load and allowable working radius, the BIM model allows engineers to assess various lifting scenarios, optimize operational pathways, and identify potential hazards before they occur on site. In addition, the clear visualization provided by the BIM model facilitates effective communication among the project team, thereby enhancing overall operational efficiency and risk management during the construction process. Lifting of precast unit is shown in Figure 7.

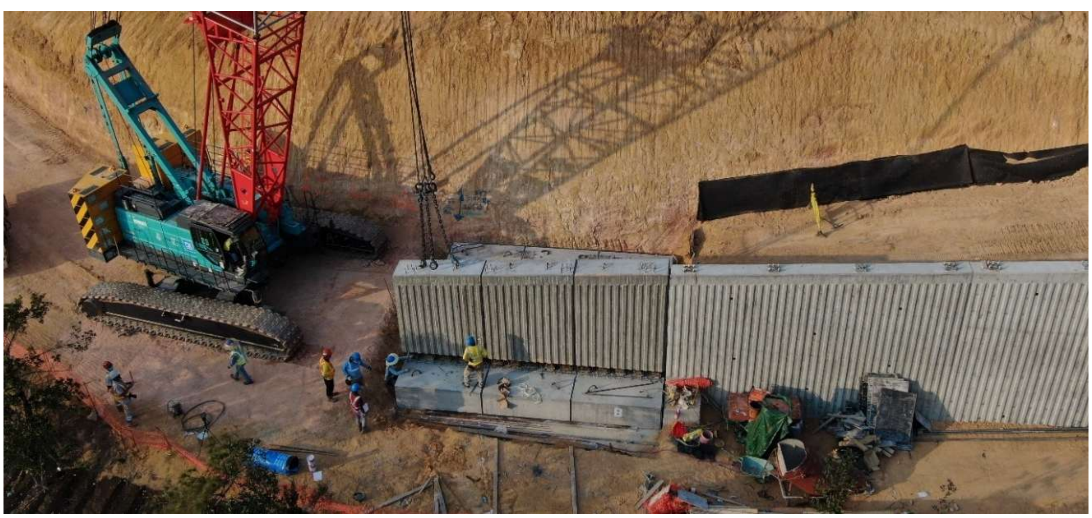

Figure 7: Lifting of precast unit

2.6 Match Cast

The success of DfMA construction heavily relies on high-quality workmanship during the connection process. Numerous factors—such as an uneven blinding layer, movement between the wall base and the wall stem during concreting, or deviations even in the controlled environment of the casting yard—can compromise alignment. Since the wall base and wall stem connect via five I-beams per bay, precise alignment is essential. Any deviation in one of the I-beams, whether due to levelling issues or discrepancies in length, can hinder the connection and cause the wall stem to tilt, thereby raising both safety and structural integrity concerns. To ensure a secure and accurate connection, a detailed survey was conducted to scan the blinding layer and verify its levelness, as shown in Figure 8. After positioning the wall base, a pre-assembly check was performed to ensure a seamless connection and to verify the leveling of the base plate relative to the I-beams, as shown in Figure 9. The resulting point cloud is first imported into Autodesk Recap Pro for a preliminary review and then into Autodesk Civil 3D. In addition, a match cast is performed for the wall stem's I-beams to guarantee a gap-free fit and symmetry, with minor adjustments made to the length of un-encased I-beams as necessary. These meticulous measures collectively uphold both safety and structural integrity throughout the construction process.


Figure 8: Scanning the segments (left) ; Figure 9: Check the alignments with point cloud

2.7 Design Review

A scan-to-BIM process was employed after connecting the base plates of the I-beams between the wall base and wall stem, and before concreting the 300 mm un-encased length. Using the integrated Autodesk Revit plugin, the Revit BIM model was seamlessly exported to Autodesk Robot Structural Analysis for a detailed design review, automatically transferring the alignment and properties of as-structure without requiring additional manual input. The key reinforcement members were then evaluated against both ultimate and serviceability limit states under various load cases, with axial, shear, bending, stress, and deflection parameters computed to verify capacity of each component. Additionally, internal forces at the connections were extracted to inform the design of connection details, ensuring that real-world deviations are incorporated into the analysis. Autodesk Robot Structural Analysis further accounts for stress concentrations by applying a workmanship factor that captures the effects of slight misalignments, details often oversimplified or overlooked in hand calculations or conventional analysis software that assume ideal, perfectly upright members. This integrated approach aligns all digital models and data inputs, ensuring that the design review accurately reflects the true conditions of the construction and meets the required design standards. The output of Robot Structural Analysis is shown in Figure 10.

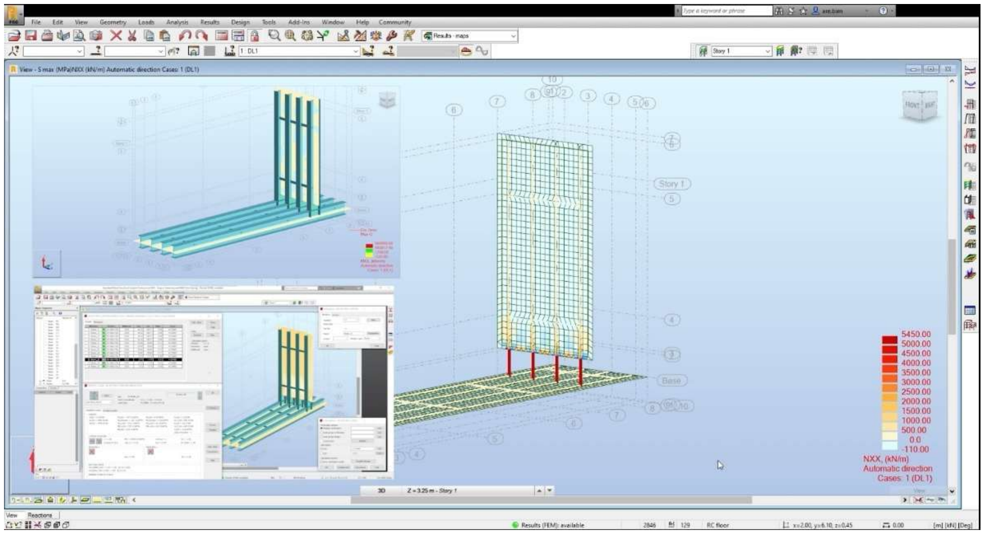

Figure 10: Structural load analysis with Autodesk Robot Structure Analysis

2.8 Operational and Maintenance

Since this is the first time DfMA has been applied to retaining wall construction in Hong Kong, sensors with real-time monitoring capabilities have been installed to record the strain induced in the wall's structural elements, addressing concerns regarding structural performance. The collected data is transmitted to an IoT platform, where engineers can access real-time strain values and receive alerts if those values exceed set limits. Additionally, ground settlement caused by wall deflection can be monitored, providing comprehensive data for engineers to assess performance. This combined monitoring approach ensures structural integrity during construction and offers valuable insights for future projects. The IoT platform is shown in Figure 10.

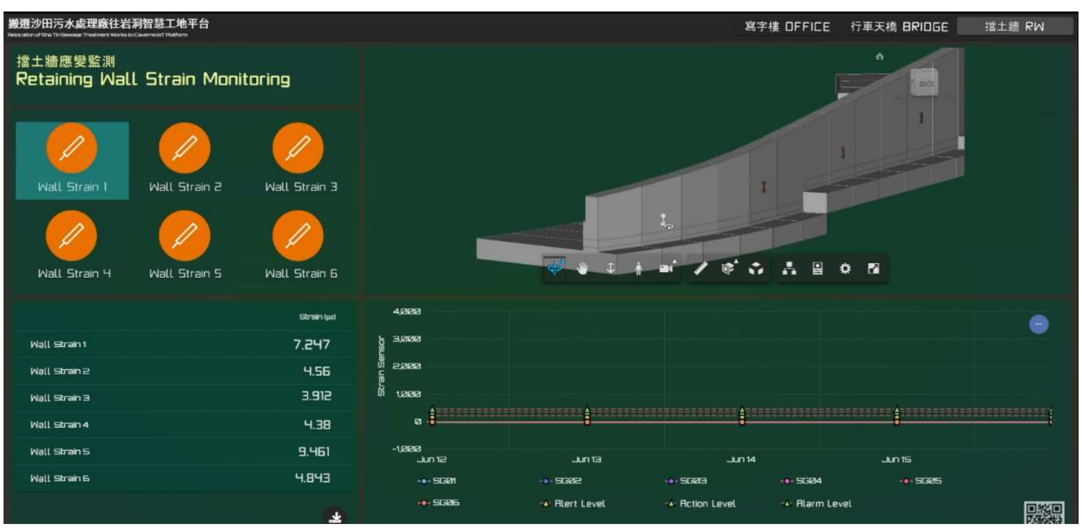

Figure 10: Lifting of precast unit

2.9 Superior Outcome Achieved by DfMA

The adoption of DfMA for the retaining wall in the Sha Tin Cavern project has delivered exceptional results, with substantial improvements over the conventional cast in-situ method. Table 3 illustrates these comparative outcomes, emphasizing the remarkable efficiency achieved through DfMA principles in geotechnical works. It is particularly noteworthy that the conventional cast in-situ method required 21 days per bay, resulting in a total construction time of 147 days for seven bays of retaining wall. the detailed breakdown of the construction programme is shown in Figure 11. In contrast, DfMA completed each bay in approximately one day, with a conservative buffer accounting for a total of around 10 days for all seven bays.

Table 1: Comparison between DfMA and cast in-situ method for retaining wall RMZ3

	Cast In-situ Method	DfMA	Comparison
Duration for On-site activities (days)	147	~10	~137 days saved
On-site activities (Categories)	70	21	49 categories reduced
Working at height activities (nos.)	42	0	42 nos. eliminated

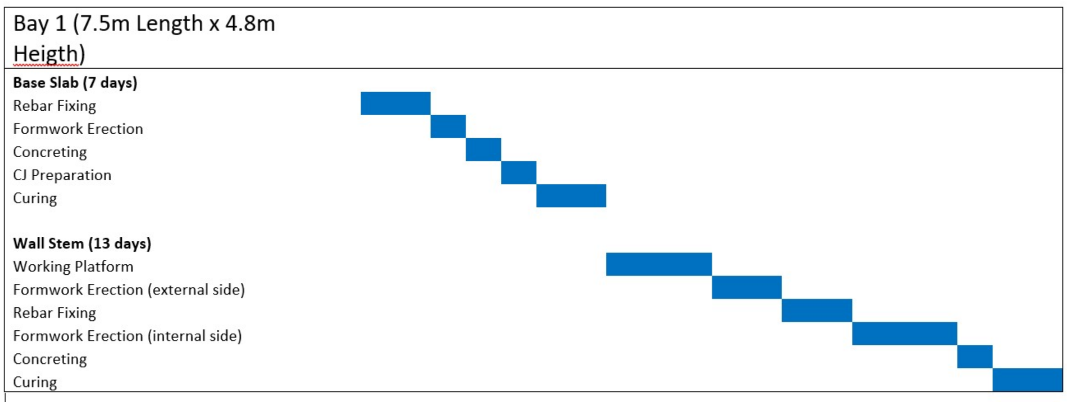

Figure 11: Breakdown of programme for conventional cast in-situ method

3 DISCUSSIONS

Given the diverse factors influencing the cost-effectiveness of DfMA across projects, there is a critical need to develop a standardized evaluation protocol. This protocol would empower engineers with a reliable framework to assess whether DfMA offers genuine benefits compared to conventional construction methods. By integrating key parameters—such as labor costs, transportation and lifting expenses, stockpiling requirements, temporary works, and regional cost differences—into a systematic assessment tool, the decision-making process becomes more streamlined. Furthermore, the protocol would account for project-specific conditions, such as the uniformity and repetitiveness of construction units, ensuring that the advantages of DfMA are accurately measured. Ultimately, such a standardized approach would enable engineers to make informed judgments and optimize construction strategies for safety, efficiency, quality, and sustainability.

4 CONCLUSIONS

The principle of "starting with the process in mind" is a foundational element of DfMA, guiding the design process by fostering a comprehensive understanding of the entire project lifecycle from initial design through manufacturing, transportation, lifting, and final assembly. This approach ensures that each phase is optimized, risks are minimized, and the project aligns with its ultimate goals from the outset.

The Sha Tin Cavern project serves as a compelling example of DfMA's transformative potential in geotechnical engineering. By leveraging early collaboration among stakeholders and robust client support, the project successfully addressed the challenges of urban construction, delivering impressive results:

- 93% reduction in on-site construction time: Off-site fabrication and streamlined processes drastically shortened the construction schedule.

- Enhanced safety: The elimination of working-at-height activities reduced risks to workers.
- Improved quality: Controlled off-site fabrication ensured higher precision and consistency.
- Digital integration: Effective use of digital tools enhanced planning, monitoring, and execution.

However, these outcomes are not guaranteed across all projects. The success of DfMA hinges on project-specific factors such as scope, site conditions, and regional cost variations. As a result, Resident Site Staff (RSS) and contractors must undertake a thorough cost-effectiveness analysis to assess the financial viability of adopting DfMA. This analysis should account for variables like labor costs, transportation expenses, lifting requirements, and the need for temporary works, ensuring that the benefits justify the investment. The achievements of the STC project highlight the importance of developing standardized evaluation protocols to systematically evaluate DfMA's cost-effectiveness. Such protocols would provide engineers with a consistent framework to assess whether DfMA is suitable for a given project, enabling data-driven decisions that optimize safety, efficiency, quality, and sustainability. By establishing this foundation, the geotechnical engineering industry can encourage the wider adoption of DfMA, unlocking its benefits for a broader range of applications.

ACKNOWLEDGEMENTS

The authors would like to extend their sincere appreciation to the Drainage Services Department of the Government of Hong Kong SAR for granting permission to publish this paper. Special recognition is also extended to China State Joint Venture, Sheung Ying Construction Limited for their invaluable assistance and hands-on experience in implementing DfMA practices in the construction of retaining walls.

REFERENCES

Boothroyd, G. (2005). *Assembly automation and product design*. CRC Press.

Lu, W., Tan, T., Xu, J., Wang, J., Chen, K., Gao, S. & Xue, F. (2020). Design for Manufacture and Assembly (DfMA) in construction: The old and the new. *Architectural Engineering and Design Management*, in press. Doi: 10.1080/17452007.2020.1768505

Devb. (2018). *Construction 2.0 Time to change*. P.28. Development Bureau.

Tan, T., Lu, W., Tan, G., Xue, F., Chen, K., Xu, J., Wang, J. & Gao, S. (2020). Construction-Oriented Design for Manufacture and Assembly (DfMA) Guidelines. *Journal of Construction Engineering and Management*, in press.

Engineering Geological and Geotechnical Challenges of Lin Ma Hang Mine Revitalization – A Unique Community-based Educational Mining Heritage Project

Xavier Tang, Geoffrey Pook, Samson Leung, Elvina Tam, Kevin Styles
Meinhardt Infrastructure and Environment Ltd.

K L Lo
Geotechnical Engineering Office, Civil Engineering and Development Department

ABSTRACT

The revitalization of the 19th-century Lin Ma Hang Lead Mine cavern and surrounds provides a unique demonstration of innovative geotechnical investigation and design for conservation and educational purposes in country park. The restoration of the cavern complex and nearby area aimed to improve the safety of the old heritage mining complex for the public, whilst enhancing the recreational value of the newly designated Robin's Nest Country Park. The project is a unique example of historical and scientific preservation and safety-based enhancement for the public and community. From the outset, assessment of the engineering geological and geotechnical conditions of the natural terrain, drainage, anthropogenic influences and the rock mass related to the ore body were key for prioritizing the geotechnical works. Insights gained from the challenges encountered during the background study, investigations, design and construction phases will contribute valuable experience for future projects with similar sensitivity in Hong Kong and elsewhere.

The design balanced safety and stakeholder issues with the goal of promoting the outstanding mining heritage and associated scientific value as a unique user-based educational facility showcasing the splendour of the remote environment, the outstanding mine geology and geomorphological setting within a palimpsestic framework of old anthropogenic activity ranging from several phases of mine activity, war intervention, and cycles of land management over many centuries. Technical challenges included: (1) methodology for assessment with limited access to the rock face; and (2) balancing robust geotechnical works with resultant visual impact. The NGI Q-system was utilized for rock stabilization along with analytical design through kinematic analysis. Enhanced access afforded by the construction stage refined geotechnical works for rock pillars and blocks formed as part of the historical and geological context of the mine, potentially blast-induced open apertures, a fault zone, and a galena vein found in association with highly decomposed materials.

Construction challenges were numerous due to the remoteness of the site. Advanced techniques such as 3D point cloud model from laser scanning of the cavern complex helped develop an authentic record of the mining heritage in parallel with the works. Comprehensive planning was important to ensure timely project delivery with helicopter-lifts as the major means of material and machinery delivery. To ensure safety during drilling works, tensioned safety nets were used to protect workers from potential rock fall. Grouting the mostly vertical rock dowels in highly jointed / fractured rock required a multi-stage approach with control of grout viscosity. Coring was utilised to reduce vibration and noise impacts to minimize disturbance to the Site of Special Scientific Interest (SSSI) bat roosts nearby. Artificial rock cladding was employed for pillar buttresses and waste rock features, together with heritage-style brown finishes for dowel heads and wire meshes. All essential elements in helping establish a balance between making “safe for purpose” without compromising the integrity of the heritage and scientific character of the site. From an industrial mining perspective, the finished cavern works resemble features commonly associated with active mine environments and some original rusted steel structures.

1 INTRODUCTION

The revitalization for the Lin Ma Hang Lead Mine was completed and open to the public on 31 December 2024. It provides a unique demonstration of innovative geotechnical investigation and design for conservation and educational purposes. The restoration was aimed at upgrading the cavern for public access by providing a safe environment through engineering geological and geotechnical assessment. The cavern now serves as a focus to enhance the recreational value of the new Robin's Nest Country Park.

For some context, other successful cavern examples for tourism purposes in the world, include The Mammoth Cave System in Kentucky, USA (Palmer, 2016), and other karstic caves in Jenolan Caves in NSW, Vietnam and Guizhou, China. Many of the cavern examples are formed in carbonate rock due to natural dissolution of the rock with some later human influence. While for the underground city in Cappodocia in Central Anatolia of Turkey, caverns were developed in soft pumice of volcanic tuff through carving with simple hand tools (Erguvanli & Yüzer, 1978). The host rock in Lin Ma Hang Lead Mine cavern is mainly ash tuff, which shares some similarities with Cappodocia despite the mineralogical differences. The tuffs in Cappodocia, in spite of having lower UCS (5-13 MPa, vs 80 MPa in Lin Ma Hang), modelled with Finite Element Modelling (FEM) method, shows that the rock mass is self-supporting while kinematically driven rockfall risk is sufficiently mitigated by light protective measures including bolts, mesh and scaling (Sari, 2022). As with all heritage sites, protective measures need to maintain aesthetic appearance and zonation may be considered an alternative method (Tunusluoglu & Zorlu, 2008). The balance between heritage protection and geotechnical safety is paramount for such sites globally, and was a significant driver for the cavern revitalization works at Lin Ma Hang.

The Project Team was appointed by the Civil Engineering and Development Department (CEDD) of the Government of the Hong Kong Special Administrative Region (HKSAR) to provide professional services to revitalize the existing Lin Ma Hang Lead Mine cavern and turning into an open museum as proposed by the Agriculture, Fisheries and Conservation Department and complete natural terrain hazard studies to make the accessible area safer for the public. This included revitalization works for the main cavern and nearby adits, as well as provision of recreational space for scenic points, covering geotechnical, civil & structure, drainage, electrical and mechanical, landscape among other disciplines. Table 1 details the key items under the Project scope. This paper summarizes some of the challenges associated with the engineering geological and geotechnical aspects of project delivery and documents the strategies to ensure the successful completion of this unique community-based educational mining heritage project.

Table 1: Major items - Project Scope of Lin Ma Hang Lead Mine Revitalisation

Location	Typical Measures
Main Cavern	• Rock Dowels, Wire Mesh, Buttress • Additional gravel layers on cavern floor • Concrete structures covered by Artificial Rock Claddings
Adit A6B	• Shotcreting, Dentition, Wire Mesh • Additional Lighting
Slope at the Atrium	• Rock Dowels, Shotcreting, Wire Mesh
Shafts	• Fencing off with chain link fence
Scenic Point	• Viewing point with a pavilion and footpath with handrailing

2 SITE DESCRIPTION & GEOLOGY

The Lin Ma Hang Lead Mine is an abandoned mine site operated intermittently from the 1860s until 1962 (Mellor, 2021). Uncovered after the retreat of the frontier closed area in 2016, it remains an important and intact cultural heritage contributing to the mining history of Hong Kong. Galena, and the associated lead and silver, was the major targeted mineral of the mine operation (Chu & Chan, 2015; Williams, 1991). The mine had produced an estimated 16,000 tonnes of lead metal and 360,000 ounces of silver over its life. The mineralization is associated with an NW-SE striking fissure vein deposit which dips between 15° and 60° (Davis & Snelgrove, 1956 & 1964). From an engineering geological perspective, these mineralization veins often occur along weak zones that could contribute to crown instability, posing geotechnical risks of rockfall to visitors. Therefore, unlike other underground engineering projects, the revitalization of this site requires more in-depth engineering geological understanding before analysis on the rock mass and kinematic conditions. The rock is dark grey to brownish grey, strong to moderately strong, slightly to moderately weathered, Grade II/III, coarse ash tuff, associated with localized white quartz veins up to 20-60mm thick and light grey galena occurring in patches up to 100mm in thickness (GEO, 1991; GEO, 1996; Unpublished Site Observation). Locally, a highly to moderately decomposed tuff belt striking 020-200 was observed at the crown in association with veining in the southern portion of the cavern. The rock in proximity is highly fractured moderately decomposed tuff. In general, the rock mass is PW90/100 at the crown around the cavern. Joints are persistent (up to >10m), medium- to very widely-spaced, tight to narrow with surface roughness ranging from rough undulating to slickensided planar. The joints are generally clean and occasionally stained with iron oxide. Persistent seepage and groundwater flow from the cavern crown was observed during inspections in January 2024 (dry season) which implies that infiltration along the rock mass discontinuities occurs throughout the year. It also indicates that the rock mass is likely drained with little development of water pressure.

3 PROJECT DELIVERY

The Project commenced in early 2021 with a literature review of the history of Lin Ma Hang Lead Mine, together with desk study and site reconnaissance to gain understanding of extent of development. The project team adopted various innovative approaches for site inspection and analysis. Firstly, a hand-held LiDAR scanner was used to acquire point cloud data during site reconnaissance, enabling a fast and efficient means to form models for 2D and 3D engineering geological assessments of rock pillars and cavern crown and adits (Leung et al., 2022). Preliminary kinematic assessment was also made through use of the point cloud data by CloudCompare for joint facet dip and dip orientation (Dewez et al., 2016; Idrees & Pradhan, 2018). For natural terrain hazard assessment, aerial photograph interpretation (API) integrated with digital classification of anthropogenic features was applied using ArcGIS to assess the Quasi-natural Heritage Landscape of the Lin Ma Hang Lead Mine area by utilizing territory-wide LiDAR data (Lai et al, 2012; Styles & Law, 2012; Lee et al., 2022; Wong, 2021). These approaches were implemented to overcome technical challenges due to the remote location of the mine and to ultimately accelerate the Design Stage. Construction commenced in November 2023. Scaffolding platforms erected during construction allowed closer verification of joint conditions as well as verification of rock mass classification data. Rock dowel locations and wire mesh extent inside the cavern were finalized in February 2024. Buttress extents were confirmed in August 2024 and effectively communicated with the Contractor to preserve and maintain the landscape and authenticity of the site. By November 2024, all major geotechnical items were completed. The Lin Ma Hang Lead Mine was officially opened to the public on 31 December 2024.

a)

b)

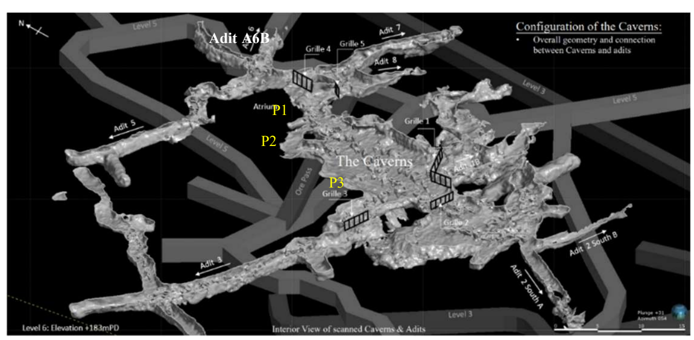

Figure 1: (a) The main cavern after completion; (b) 3D configuration of the cavern, atrium and Adit A6B, the main scope of the rehabilitation works - the atrium was formed during the mine operation before 1924; three major pillars in the main cavern are labelled as P1, P2 & P3.

4 DESIGN

4.1 Commitment

The team was committed to provide geotechnical design balancing safety issues and other stakeholder issues on maintaining the authenticity of the mining heritage. The design approach of the main cavern roof (Figure 1b for the configuration) was to use the room and pillar concept and rock pillar strength to model the crown stability and reduce concrete reinforcement from adversely affecting the natural heritage / appearance of the cavern. The design approach demonstrated that the dominant failure mode within the cavern was governed by structurally controlled instability due to the relatively low overburden (average 4.5m) with stress induced spalling identified as a localized risk. The overburden pressure was assumed to be distributed proportionally over the rock pillars. Figure 2 shows the main cavern during the rock dowel installation and works to the atrium.

a) b)

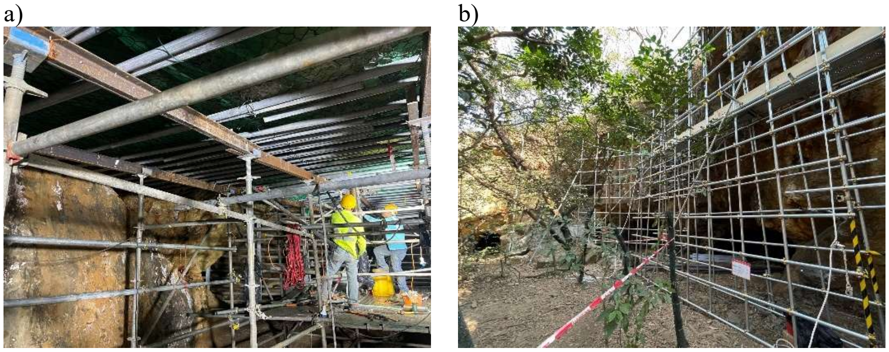

Figure 2: (a) Works in the main cavern; (b) Works in the atrium area

4.2 Technical Challenges

Two key technical challenges were encountered during design: (1) methodology for assessment with limited access to the rock face; and (2) balancing robust geotechnical works with resultant visual impact. The main cavern is about 8m high and 19m wide with limited access to rock face during initial investigations, and therefore initial assessments were from ground level. To maintain the authenticity of the mine appearance, it was decided that the site should be dealt with as a rare case with neither concrete or shotcrete lining to be utilized. Minor rock fall was considered the residual risk due to the rock mass discontinuities. Empirical and observational methods were adopted for initial rock mass assessment for tendering purposes by using the NGI Q System (NGI, 2022), with spot dowel verification during construction to cater for local instability. The innovative use of hand-held laser scanner technology was particularly well suited in capturing the geometry required for stability assessment by empirical means together with analytical methods including limit equilibrium method and kinematic analysis. A coloured point cloud model enabled better visualization of the main cavern and facilitated early development of design options for holistic stabilization measures, for example, the colour requirements for dowel heads and artificial cladding for concrete surfacing works.

4.3 Design Stage - Initial Geotechnical Assessment

i. Crown Stability

Vertical stress above the main cavern was based on average overburden of soil and rock. The ground cover ranged from 9m in the southern part of the gallery, to 4m at the rock arch entrance, implying vertical stress above the cavern between 91.25 kN/m^2 and 166 kN/m^2. This geometry was confirmed in 3D models of the surface LiDAR and the geo-rectified scanning data from inside the cavern. Given this low confining stress environment, stability issues were governed by adverse joint controlled failure or gravity driven fallout of wedges and blocks from the roof. Evidence of instability, such as roof collapse and fallen blocks were identified in some of the nearby adits but not within the main cavern.

ii. *Rock Mass Assessment – the Main Cavern*

Discontinuity mapping and rock mass survey of RMR_{89} / GSI / Q-system were completed for the main cavern roof and pillars. The four major joint sets are presented in **Table 2**. The lead mineralization containing Galena occurred in veins oriented similar to Major Joint Set J2, which gave insight on the multiple lineated ore distribution, in spite of minor striking variations in lower working levels northward to the main cavern.

Table 2: Major Joint Sets in the Main Cavern

Major Joint Set	Manual Discontinuity Survey	
	Dip Angle	Dip Direction
J1	43	117
J2	76	023
J3	42	044
J4	79	183

The following Q and RMR parameters are typical. (**Tables 3 & 4**)

Table 3: Q-system Rock Mass Classification - Estimated Q-value range: 0.32 – 2.67

Parameter	Wall (East)	Wall (South)	Roof
RQD	75	75	80
Jn	9	12	9
Jr	1.5	0.5	1.5
Ja	2	4	2
Jw	0.66	1	1
SRF	2.5	2.5	2.5
Calculated Q	1.65	0.32	2.67

Table 4: Rock Mass Rating - Estimated RMR_{89}: 58

Parameter	Value	Rating
UCS	Estimated 50 MPa	7
RQD	50 – 75%	13
Joint Spacing	0.6 – 2m	15
Joint Condition - Persistence	Most joints are 3 – 10m long	2
Joint Condition – Separation	Most joints have 1 – 5mm aperture	1
Joint Condition – Roughness	Most joints have slightly rough to smooth surface	1
Joint Condition – Infilling	Most joints are clean	6
Joint Condition – Weathering	Most joints are moderately weathered with stained surface	3
Groundwater	Damp	10

The estimated GSI range indicates the rock is moderately weathered with interlocked undisturbed blocky rock mass with two intersecting joint sets. GSI values ranging from 50 to 60 are estimated for the rock mass based on the empirical relationship between Bieniawski Rock Mass Rating (RMR89) and GSI. FEM software RS2 was used to develop a numerical model and three rows of pattern dowels were proposed based on the cavern geometry and the above parameters utilizing the Q-system for systematic support spacing.

iii. *Rock Mass Assessment – Adit A6B*

Adit A6B stability assessment was also examined by empirical Q-system rock mass quality and rock support chart. A Q-vale of 1.25 is assigned to the rock mass within the adit based on the mapped parameters shown in **Table 5**:

Table 5: Q-system Rock Mass Classification of Adit A6B

Parameter	Value
RQD	50
Jn	12
Jr	1.5
Ja	2
Jw	1
SRF	2.5
Calculated Q	1.25

Dentition was proposed to support a localized rock block on the western wall of the adit to mitigate risk of structural controlled minor rock block failure. For a 12m portion, 100mm shotcrete with 2 layers of A252 mesh (Figure 3) was proposed to mitigate the stress due to shallow rock cover and localized fractured rock.

Figure 3: Paving wire mesh prior to shotcreting in Adit A6B (Left);
Lighting on the shotcrete lining added after works (Right)

iv. Pillar Stability

Adverse joints were identified at rock pillar P1 and P3 with the risk of structurally controlled failure at these pillars necessitating stabilization measures. The fractured southern face at rock pillar P1 may undermine the remaining portion of the pillar, while open sub-horizontal joints were identified near Pillar 3 and the adjacent crown. Therefore, two concrete buttress, B1 & B2, were proposed as a measure to maintain roof stability caused by the potentially sliding rock block exerted. Checking of the buttress against sliding, overturning and bearing capacity utilized the point cloud geometric data and the results are summarized in Table 6.

Table 6: Factor-of-Safety for Concrete Buttresses

Concrete Buttress	**Sliding**		**Overturning**		**Bearing Pressure**	
	Required FoS	**Designed FoS**	**Required FoS**	**Designed FoS**	**Required FoS**	**Designed FoS**
B1 (for Pillar P1)	1.5	1.88	1.5	1.72	3	14
B2 (for Pillar P3)	1.5	4.81	1.5	1.55	3	20.69

Limit Equilibrium analysis adopted rock joint shear strength derived from Barton-Bandis empirical criteria to check structurally controlled failure induced by adverse joints at rock pillar P2 (Matin & Maybee, 2000). No stabilization works were required at this pillar. Conventional concrete surfacing of buttresses is totally different from the exposed rock in the cavern. To integrate this structure with the environment, artificial rock-like cladding was adopted to address the aesthetic requirement of mine heritage.

4.3 Design Verification

The initial geotechnical assessment was based on visual inspection during site reconnaissance and point cloud data obtained from handheld laser scanning. The permanent nature of the works and the lack of a concrete lining meant that verification of the design was required for confirmation of the geological model and groundwater conditions. The assumptions made on rock weathering grade, joint conditions, seepage and instability was reviewed and assessed. Construction commenced in November 2023, with verification works conducted in January 2024, followed by design amendments regarding localized instability identified on site. Open joints were observed during inspection at heights that were previously obscured during mapping from the cavern floor. These open joints presented potential rockfall hazards and either related to fractures resulting from blasting of the cavern during mining or stress release of the major joint sets after excavation. A locally persistent joint was observed near the southern portion of the main cavern in which no rock wall contact was recorded, and infill was >50mm in thickness. To address these issues spot dowels and wire mesh were recommended as part of design amendments to mitigate the local risk of instability.

4.4 Design Outcomes

The cavern provided unique engineering geological, geotechnical and technical challenges that were overcome through adopting innovative technology and collaborative union of all the stakeholder. The use of hand-held laser scanning was particularly useful in developing point cloud data of the geometry for analysis, accelerating the design programme and works progress, as well as providing early insight of the design from an aesthetic perspective.

5 CONSTRUCTION CHALLENGES

5.1 Logistical Difficulties

The remote and undeveloped nature of the site resulted in logistical challenges. The site is at +181mPD with access limited to a hiking trail of "998 steps" without vehicular access. This posed enormous difficulties for manual lifting methods as a means to transport material to the site. Therefore, material delivery was limited to airlift, requiring advanced planning and coordination between the site supervision team and the contractor (Figure 4).

Figure 4: Helicopter Lift in Operation

5.2 Dowel Installation in SSSI

i. Coring for Rock Dowels

The majority of the geotechnical works are confined to the main cavern and atrium area, situated in proximity to a SSSI for one of the most important bat roosts in Hong Kong (Wong et al., 2004). The Site Team planned and conducted works to minimize disturbance to bats, particularly during the breeding season, through control of work procedures and programming of work fronts. Typical coring works present noise and dust issues.

Therefore, an electrical coring machine with water flushing was utilized within the operational area enclosed by tarpaulin sheeting to reduce noise reflection and spread of dust. Noise enclosure was used at the front of the coring machine to reduce dust emission. As the main cavern remained unsupported during construction, a safety net and lifting jet were deployed to prevent rock falling triggered by the coring works. Handheld tools were used to scale loose material and unstable rock fragments to reduce the risk of falls. Figure 5 illustrates the set up during the coring works.

ii. Grouting for Rock Dowels

The challenges of grouting works for rock dowels were revealed during Construction Stage due to presence of interconnected joint networks and blast-induced open apertures. Grout leakage led to requirement of more stringent grouting procedures.

Figure 5: Coring Works - Scaffolding platform with safety net to prevent rockfall

Innovative method using multi-stage grouting was preferred by first developing a grout fan above the crown, utilizing more diluted grout because of better penetration capability in the rock mass. As the cracks and joints were sealed, more viscous grout was used to fully grout the dowels. Figure 6 illustrates the setup for grouting. All the grouting works utilized the cored hole for the rock dowels and any leakage was immediately cleaned to avoid damage to the adjacent mine area. To check integrity of the grout inside the drillhole, the set up illustrated in Figure 6 was used. When the dowel was fully grouted, the grout pressure would drive the grout up along the pipe and reach the end for verification. Grouting terminated only when the inflow rate was equivalent to the outflow rate of the grout, allowing grout leakage to be checked indirectly.

Figure 6: Details of grouting works (Left); Site photos of grouting of dowels (Right)

5.3 Finishing and Landscaping for Heritage Preservation

i. Natural Finishing

From an industrial mining perspective, suitably rock coloured pigments were applied to dowel heads and PVC coating of wire meshes, so that the finish resembled original rusted steel structures consistent with the mine heritage.

ii. Artificial Rock Cladding

To integrate concrete structures within the mine context, artificial rock cladding resembling the weathered tuff was applied to the concrete surface. The cladding is cement, sand and ST-C01, mixed with water. ST-C01 is dry packed proprietary pre-mix and polymerized cementitious plaster, commonly adopted as a topcoat on relatively coarse exterior environments. Table 7 summarizes product performance from the product catalogue. Resistant to alkali and acid attack, and along with its strength performance, the cladding was as a durable material that requires reduced maintenance and routine inspection. This is a benefit given the remoteness of the site.

Figure 7: An example of a rusted steel structure in Ma On Shan Iron Mine (from online source) (Left); Dowel heads and wire mesh recently installed for the main cavern during the works (Right)

Table 7: Properties of ST-C01, a dry packed proprietary pre-mix and polymerized cementitious plaster

Colour	Grey/White
Density	Dry: $1650 \pm 200kg/m^3$ Wet: $1750 \pm 200kg/m^3$
Compressive Strength (at 28 days)	$\geq 6MPa$
Flexural Strength (at 28 days)	$\geq 3MPa$

The cladding was sculpted and coloured on site. As illustrated in Figure 8, the cladding is fixed to a steel frame and mesh. An initial scratch coat made of cement, sand and water is applied. The carve coat is established on top of the scratch coat and allows for decorative and sacrificial surfacing and can be easily profiled to achieve the required appearance. To blend in the mine heritage environment, the coat was carved to assimilate natural block shape of rock mass with joint traces, then coloured with brush, sponge and airless spray.

a) b)

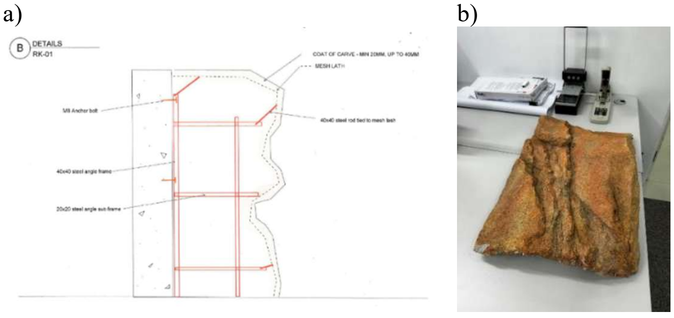

Figure 8: (a) Details of artificial rock cladding – interior consists of steel frame, with mesh lath paving as supporting material for the carving, which forms the final decorative surface covering the buttresses; (b) Sample of a piece of rock cladding

Figure 9a-9c shows a buttress before and after cladding. This is a unique example in Hong Kong demonstrating integration of mitigation measures to mimic the original landscape with a goal of heritage preservation and geotechnical safety both achieved.

a) b)

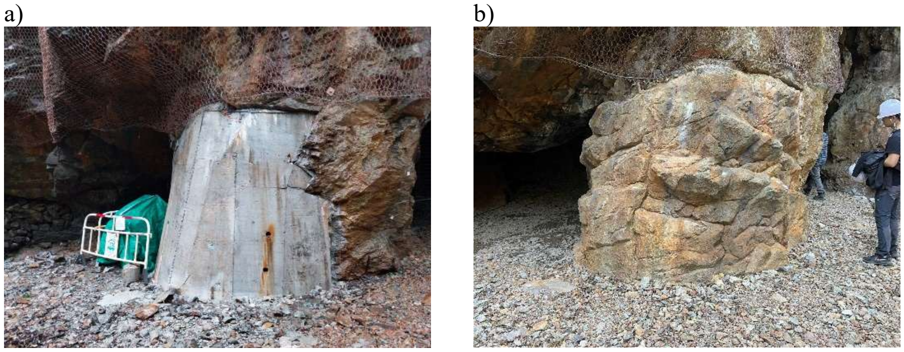

Figure 9a: Buttress B1 - (a) before artificial rock cladding fixed on concrete surface;
(b) after artificial rock cladding over concrete surface

a) b) c)

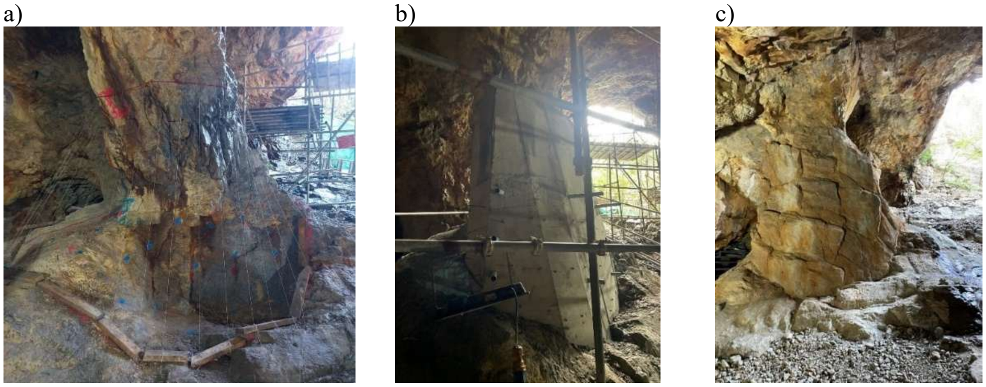

Figure 9b: Buttress B2 (Pillar P3) – (a) rock spalling as recorded during setting out the buttress extent; (b) before artificial rock cladding fixed on concrete surface; (c) after artificial rock cladding

a) b)

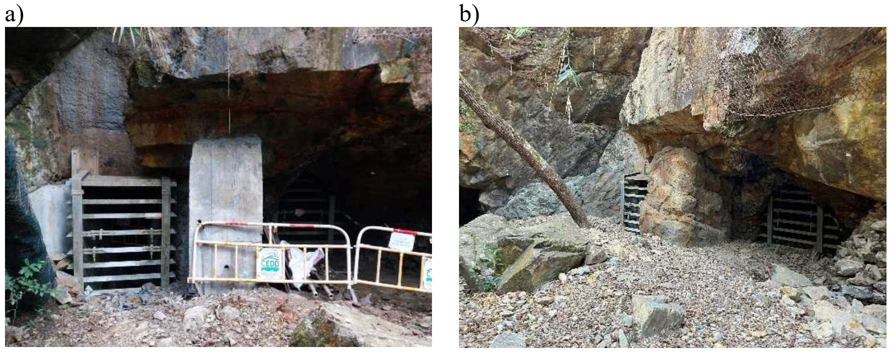

Figure 9c: Buttress B3 - (a) before artificial rock cladding fixed on concrete surface;
(b) after artificial rock cladding

iii. Preservation of Geological Features of Special Interest – Mylonite Zone

The eastern end of the atrium at the entrance to Adit A6B exhibits a unique example of a geological feature of special interest – mylonitized fault zone striking into the atrium and main cavern. Whilst it was necessary to apply some protection measures to the fault zone, the design tried to retain the unique nature of the original geological feature without full shotcreting or wire meshing that a section of the mylonitized fault breccia was preserved without facing (Figure 10a & 10b).

Figure 10: Geological Features of Special Interest in the atrium - (a) Fault Zone exposed in the atrium; (b) mylonitized fault breccia preserved at Entrance to Adit A6B as a geological feature of special interest showing results of crushing in a fault zone

5 CONCLUSIONS

As a community-based educational mining heritage site, it was essential to consider the final finish from the country park users' perspective. As demonstrated, a balance between preserving authenticity of the mine heritage while maintaining geotechnical safety, through utilizing analytical methods to model rock pillar strength as supporting the cavern, resulted in reduced use of concrete reinforcement.

To achieve the stakeholder shared revitalization "vision", the project team overcame various technical challenges to validate the design, including (1) methodology for assessment with limited access to the rock face; and (2) balancing robust geotechnical works with resultant visual impact. Adoption of innovative technology, such as the hand-held LiDAR scanner, was a part of achieving success in design due to the accuracy in obtaining geometry and kinematic data and ability to model. The construction team encountered multiple challenges caused by the unique nature of the site: (1) logistical difficulties in remote terrain, (2) dowel installation near SSSI, and (3) finishing and landscaping to preserve the geological and mining heritage. These challenges were addressed through efforts of site supervision team, the Contractor and other stakeholders. With the revitalization works completed and open to the public since end December 2024, we hope the experience in delivering this project will contribute valuable insight for future projects with similar sensitivity in Hong Kong and elsewhere.

ACKNOWLEDGEMENTS

This paper is published with the permission of the Director of Civil Engineering and Development and the Head of the Geotechnical Engineering Office, the Government of the Hong Kong Special Administrative Region.

The authors acknowledge Ir. Michael Wright, Mr. Ming Kwok, Mr. Cloud Lo and Mr. Cheuk Fung Lam for their effort in design and investigation phrases and liaison with relevant parties, Ir. Ivan Kwok Wai Lo for supervising the whole construction phrase, and continuous support from the Agriculture, Fisheries and Conservation Department and the Geotechnical Engineering Office of the Civil Engineering and Development Department, the Government of the Hong Kong Special Administrative Region for successful completion of the project.

REFERENCES

Williams, T. 1991. The Story of Lin Ma Hang Lead Mine, 1915-1962, *Geological Society of Hong Kong Newsletter Vol 9*: 3-27.

Wong, C., Lau, M., Ades, G., Chan, B. & Ng, S. C. (Eds.). 2004. A Pilot Biodiversity Study of the eastern Frontier Closed Area and North East New Territories, Hong Kong, June-December 2003.

Chu, J., & Chan, J. 2015. *Hong Kong Mining History:* 19–41. ProjecTerrae.

Davis, S. G., & Snelgrove, A. K. 1956. *Geology of the Lin Ma Hang lead mine, New Territories, Hong Kong*. [Publisher not specified].

Davis, S. G., & Snelgrove, A. K. 1964. The geology of the Lin Ma Hang lead mine, New Territories, Hong Kong. In *Symposium on land use and mineral deposits in Hong Kong, Southern China and South East Asia: Proceedings* (pp. 263). HKU Press.

Dewez, T. J., Girardeau-Montaut, D., Allanic, C., & Rohmer, J. 2016. Facets: A Cloudcompare plugin to extract geological planes from unstructured 3D point clouds. *International Archives of the Photogrammetry, Remote Sensing & Spatial Information Sciences, 41*.

Erguvanli, A. K., & Yüzer, A. E. 1978. Past and Present Use of Underground Openings Excavated in Volcanic Tuffs at Cappodocia Area. In *Storage in Excavated Rock Caverns: Rockstore 77:* 31-36. Pergamon.

Geotechnical Engineering Office. 1991. *Hong Kong geological survey (HKGS) map sheet 3, solid and superficial geology, Sheung Shui, 1:20,000 - scale, HGM20 series*. Geotechnical Engineering Office, Civil Engineering Department, Hong Kong.

Geotechnical Engineering Office. 1996. *Hong Kong geological survey memoir No. 5 - Geology of the Northeastern New Territories* (pp. 28, 99–100, 119, 122). Government of Hong Kong.

Geotechnical Engineering Office. 2018. *Guide to Cavern Engineering. Geoguide 4*. Geotechnical Engineering Office, Civil Engineering and Development Department, HKSAR Government.

Grimstad, E. 1993. Updating the Q-system for NMT. In *Proceedings of the international symposium on sprayed concrete - Modern use of wet mix sprayed concrete for underground support, Fagernes, Oslo*. Norwegian Concrete Association.

Idrees, M. O., & Pradhan, B. 2018. Geostructural stability assessment of cave using rock surface discontinuity extracted from terrestrial laser scanning point cloud. *Journal of Rock Mechanics and Geotechnical Engineering, 10*(3), 534–544. https://doi.org/10.1016/j.jrmge.2017.11.007

Lai, A. C. S., So, A. C. T., Ng, S. K. C., & Jonas, D. 2012. The territory-wide airborne light detection and ranging survey for the Hong Kong Special Administrative Region. Paper presented at the 33rd Asian Conference on Remote Sensing, Pattaya, Thailand.

Lee, P., Tse, C., Lee, F., Pook, G., & Styles, K. 2022. Digital classification of anthropogenic features for natural terrain hazard assessment in the quasi-natural heritage landscape of the Lin Ma Hang lead mine. In *Proceedings of The HKIE Geotechnical Division 42nd Annual Seminar: A new era of metropolis and infrastructure developments in Hong Kong, challenges and opportunities to geotechnical engineering*. Hong Kong Institution of Engineers (HKIE).

Leung, S., Pook, G., Kwok, M., Lo, C., & Wright, M. 2022. Engineering geological assessment of Lin Ma Hang mine caverns using handheld LiDAR scanner. In *Proceedings of The HKIE Geotechnical Division 42nd Annual Seminar: A new era of metropolis and infrastructure developments in Hong Kong, challenges and opportunities to geotechnical engineering*. Hong Kong Institution of Engineers (HKIE).

Martin, C. D., & Maybee, W. G. 2000. The strength of hard rock pillars. *International Journal of Rock Mechanics and Mining Sciences, 37*(8), 1239–1246. https://doi.org/10.1016/S1365-1609(00)00032-0

Mellor, T. 2021. *Lin Ma Hang mine part 1 - The early years*. The Industrial History of Hong Kong Group. https://industrialhistoryhk.org/lin-ma-hang-mine-part-1-the-early-years/

Norwegian Geotechnical Institute. 2022. *Using the Q-system: Rock mass classification and support design*. Norwegian Geotechnical Institute.

Palmer, A. N. 2016. The Mammoth Cave system, Kentucky, USA. *Boletín geológico y minero*, *127*(1), 131-145.

Sari, M. 2022. Evaluating rockfalls at a historical settlement in the Ihlara Valley (Cappadocia, Turkey) using kinematic, numerical, 2D trajectory, and risk rating methods. *Journal of Mountain Science*, *19*(12), 3346-3369.

Styles, K. A., & Hansen, A. 1989. *Geotechnical area studies programme - Territory of Hong Kong (GASP report XII)*. Geotechnical Control Office, Hong Kong.

Sturfer, K. A., &Law, M. H. 2012. Some Observations about man-made features on natural terrain in Hong Kong. Quaternary Journal of Engineering Geology and Hydrogeology 2012, v4s, p131-138.

Tunusluoglu, M. C., & Zorlu, K. 2009. Rockfall hazard assessment in a cultural and natural heritage (Ortahisar Castle, Cappadocia, Turkey). *Environmental geology*, *56*, 963-972.

Wong, J. 2021. *Detector in the air - 2020 airborne LiDAR survey*. Paper presented at the Joint Technical Symposium on Digital Geosciences & Geotechnology, Hong Kong, China.

An Overview of Mined Tunnel Design in the Kingdom of Saudi Arabia: Constraints and Optimizations

Yang Gao, Elva Mao, Anupama Augustine, Sammy Ng & Roger Lee
Meinhardt Infrastructure and Environment Limited, Hong Kong

ABSTRACT

In recent years, Saudi Arabia has experienced a significant increase in civil engineering projects, driven by the government's Vision 2030 initiative to diversify the economy and improve national infrastructure. The paper highlights key considerations addressed the authors in the project practices that distinguish tunnel designs in the Kingdom of Saudi Arabia (KSA) from typical tunnel projects in Hong Kong. These include unique geological, geotechnical and seismic considerations. Additionally, it explores the use of different rock mass classification approaches in local tunnel design, and section geometry optimization strategies. The study also addresses environmental and aesthetic considerations in KSA tunnel design projects, emphasizing the importance of balancing technical requirements with broader social and environmental impacts. This paper underscores how international consultants contribute to advancing best practices in tunnel design and construction within KSA's dynamic engineering landscape.

distinguish them from typical tunnel designs elsewhere. Such considerations include the challenging and unique geological and geotechnical features and constrains, the site-specific seismic considerations, the rock mass classification methodology comparison, the tunnel cross section geometry design and optimization options, as well as a discussion of the environmental and aesthetics considerations.

1 INTRODUCTION

The Kingdom of Saudi Arabia (KSA) is currently experiencing a transformative phase of rapid infrastructure development, driven by its Vision 2030 initiative, which aims to diversify the economy and improve national infrastructure. As part of this ambitious plan, the construction of tunnels has become a critical component in supporting the nation's transportation networks and utility systems.

As Hong Kong consultants increasingly participate in infrastructure projects in the KSA region, this paper provides an overview of distinctive considerations in tunnel design within the KSA context relative to practices in Hong Kong. The study is based on our mined tunnel design practices in KSA's mountainous and low-lying coastal areas, predominantly utilizing the Drill and Blast technique for excavation purposes, with a primary function of accommodating transportation and utility transitions.

This paper first discusses geological characteristics, geotechnical constraints and rock mass classification methodologies pertinent to tunnel design in the KSA (Chapters 2-4). Chapter 5 investigates key elements of tunnel cross-sectional geometry and methodologies for optimizing design parameters to ensure a holistic approach that balances functionality, safety, and economic viability. Finally, Chapters 6 and 7 address environmental and aesthetic considerations of tunnel design in the KSA, emphasizing region-specific constraints and solutions.

2 GEOLOGICAL AND GEOTECHNICAL CONDITION

The geological condition in KSA is diverse and complex, significantly influencing the design and construction of infrastructure projects, including tunnels. The western region, dominated by the igneous rock of the Arabian Shield, is well-suited for mined tunnelling due to the high rock strength yet pose issues related to fracturing and jointing. The central and eastern regions predominantly consist of sedimentary rocks like limestone and sandstone, which pose issues related to aquifers and the presence of karst features. Coastal areas, particularly along the Red Sea, feature sabkha soils and high groundwater levels, posing challenges such as soil compressibility and seawater intrusion. In each case, treatment and support types will vary based on the prevailing site conditions.

2.1 Regional Geology

The northwestern corner of the Arabian Peninsula called Midyan Peninsula is part of the crystalline shield of the Arabian plate. The structural style of this region appears to be controlled by the evolution of active faulting, with three recognized systems N-S, NW-SE, and E-W, respectively. These regional fault systems, actively control the sedimentary history of the basin. The Precambrian basement rocks consist mainly of granitic rocks intruded by basalt, rhyolite, and andesite dykes trending to the N and the NE. The Miocene and Pliocene rocks are mainly represented by a thick-sedimentary succession. Quaternary deposits are mainly represented by raised reefal limestones (Pleistocene), terraces of gravels and sands, gravel sheets, sabkha, eolian sand dunes, alluvial outwash (Holocene), and fringing reefs with saline sands (Recent).

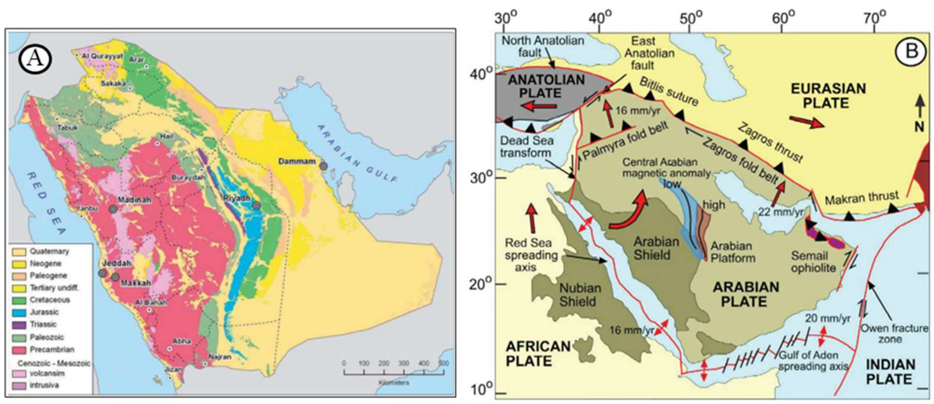

Figure 21 - (A) Simplified geological map of KSA (Al Saud & Rausch, 2012); (B) Tectonic map of the Arabian and East African plates (Stern and Johnson, 2010).

2.2 Topography

The study area is contrasted by topographic highs and flat lands. The elevated terrain, at around 600m above sea level, comprises of Precambrian (>400 Ma) basement rocks; whilst the lower-lying flat land, around 10m above sea level, is composed mainly of Quaternary deposits (<10 Ma). The existing rugged mountains altitude ranges from 50 to 600m above sea level. Broad and narrow dry desert wadis intersect mountainous areas. Along the coast, steep mountains are either separated from the shoreline by a narrow littoral fringe or plunge directly into the sea. Raised Quaternary limestones occur at the mouths of the wadis draining into the sea. They range in elevation from several meters to about 20 meters. The wadis themselves are filled with alluvial deposits characterized by large boulders derived from the Precambrian bedrock.

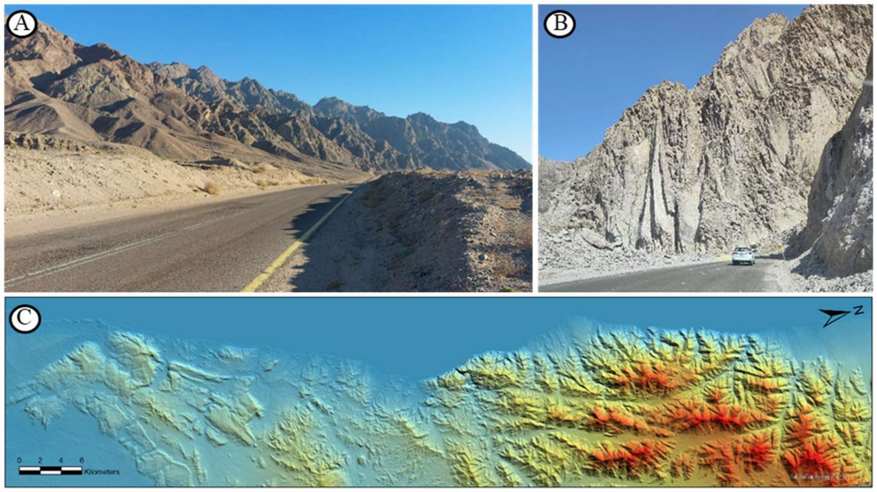

Figure 22 - (A) General topography of the study area; (B) Steep hillslope along the road; (C) Hillshade map of the study area

2.3 Geotechnical Constraints

Slope works for mined tunnel portals in this region required careful consideration of various geological hazards and their unique characteristics. Natural steep rock slopes are often characterized by fracturing and jointing of strong rock, exacerbated by erosion and seismic processes, where failure is controlled by discontinuities. Footslopes, formed of taluvium, present instability challenges due to the low shear strength of the of the unconsolidated rocky soil. Coastal areas are prone to Quaternary raised reefal limestones formed as shelves reef-building coral exposed during sea level regression or as a result of tectonic uplift. This irregular, porous and relatively weak structure is not controlled by jointing and will instead have issues related to bearing capacity or rotational / sliding failure in the mass. These varied conditions mean that both natural or cut slopes require different systems to assess and analyze as part of tunnel portal design works. The Q-system, GSI, RMR and Hoek-Brown failure criterion were used to assess the stability and mechanical behaviour of jointed, intact rock and heavily jointed rock masses.

The northeastern coastal region is prone to earthquakes, with magnitudes ranging from 5.5 to 6.0 on the Richter scale. The NNE-SSW trending Aqaba fault system and its branching faults represent one of the most tectonically active faults with the highest concentration of earthquakes in the Middle East.

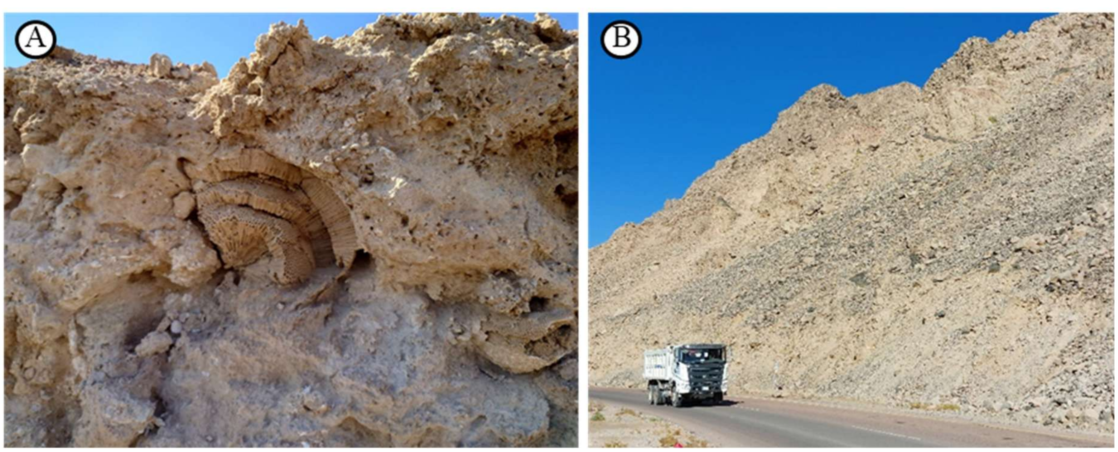

Figure 23 - (A) Reefal limestone; (B) Taluvium slope

Table 9 : Geotechnical Constraints

Identified Geohazard	Potential Impact
Quaternary reefal limestones	• Collapse associated with dissolution infill of cavities by weak material • Settlement and low bearing capacity due to the low shear resistance and high porosity
Taluvium / hillside accumulation / transported accumulation at slope toe (including lateral spread or flow slides)	• Increased foundation depths or robust stabilization measures • Difficulties in infrastructure construction on the strata • More challenging to reuse poorly sorted excavated material
Rock fall or debris flow	• High-cost remedial measures required due to highly fractured rock / taluvium on portal slopes
Liquefaction / dry sand settlement	• Increased foundation depths and/or footprint
Seismicity	• Liquefaction of soft / loose material • Affect previously stable rocks • Structural damage to infrastructure and services • Loss of life

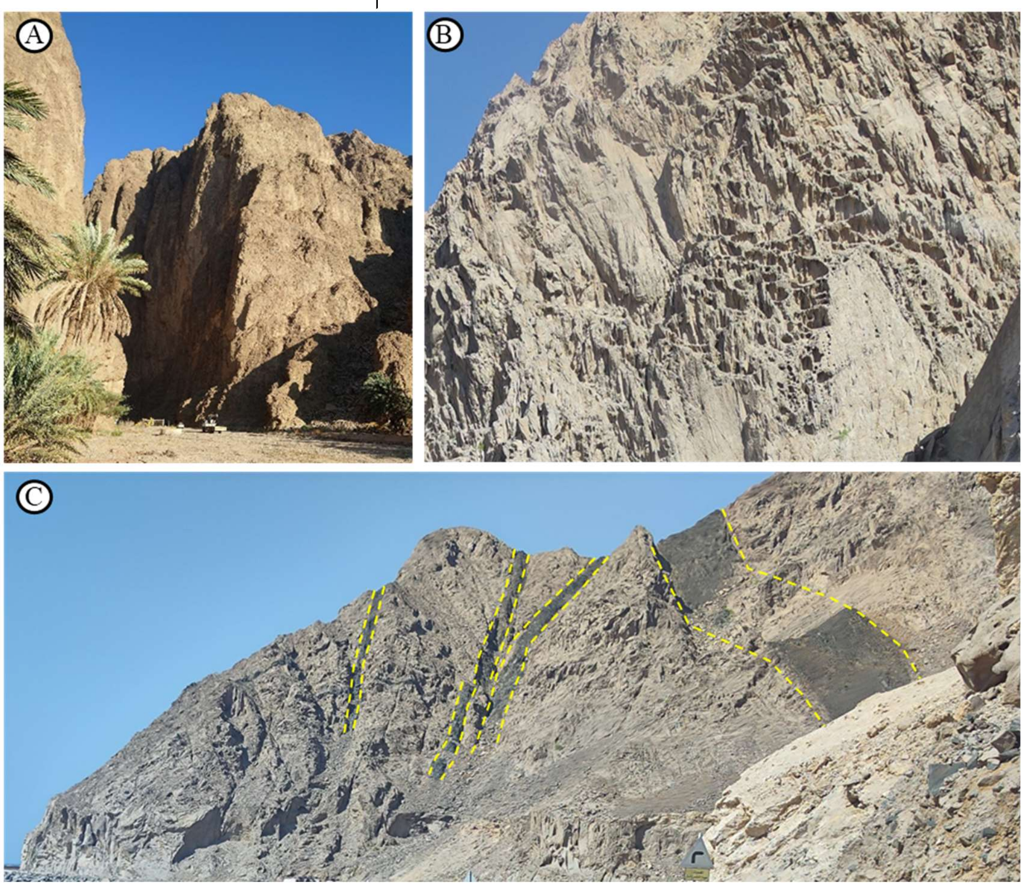

Figure 24 - (A) Wadi channel cutting through steep mountainous terrain; (B) Tafoni weathering pattern observed on a rocky cliff face showcasing intricate honeycomb-like structures; (C) Dykes cross cutting the granitic terrain

3 SEISMIC CONSIDERATION

Seismic design considerations for tunnels and infrastructure in KSA and Hong Kong (HK) differ significantly due to contrasting geological and tectonic settings. KSA, located on the stable Arabian Plate, experiences low to moderate seismic conditions, with risks concentrated near the Red Sea Rift Zone. As a result, seismic design in KSA is typically site-specific for most infrastructure, except in high-risk zones where localized fault activity and liquefaction risks may necessitate detailed analyses. KSA's codes (e.g., Saudi Building Code SBC-301-CR) apply seismic measures selectively based on localized tectonic risk.
Tunnel structures, in general, are subject to less impact from earthquake effects compared to above-ground structures. The procedure for seismic design and analysis for underground tunnel structures is recommended to be based on the ground deformation approach (FHWA, 2009). In contrast, the surface tunnel facilities such as the tunnel portal, earth retaining structures and portal slopes are designed based on the inertial force approach. For underground tunnel structure seismic analysis, at least three response-spectrum-compatible time histories were used for each component of motion (horizontal, longitudinal, and vertical) in representing the seismic design. The motion components in three directions are considered respectively. Dynamic time history analysis is performed in computer software MIDAS GTS NX to calculate the maximum response of the structure, which is adopted in LRFD load combination.

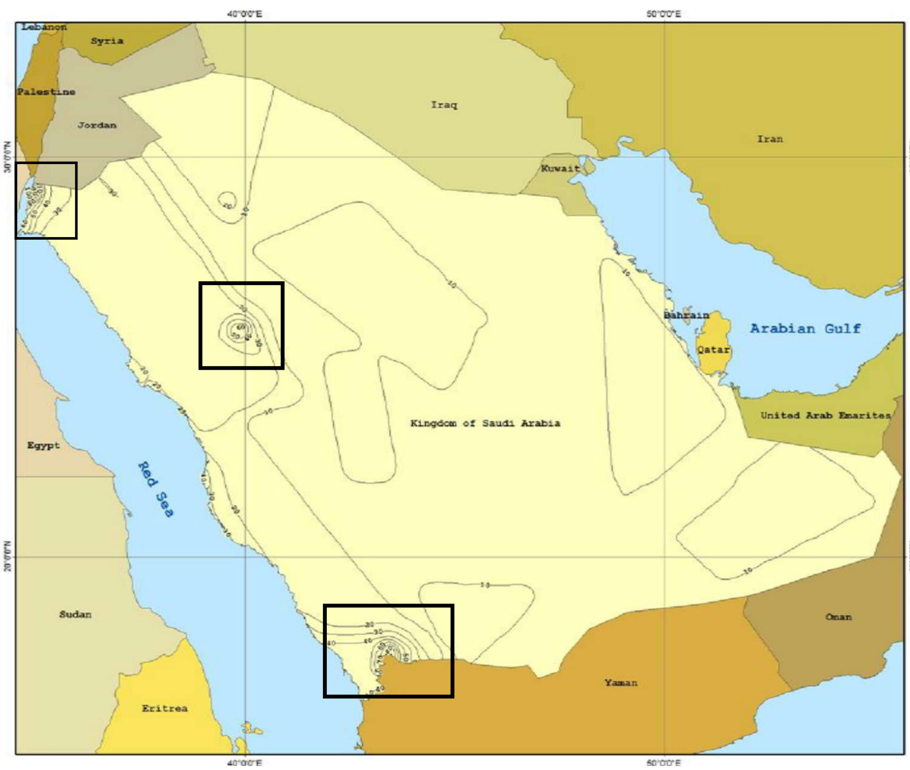

Figure 25 - Maximum Considered Earthquake Ground Motion for the Kingdom of 0.2 sec. Spectral Response Acceleration (Ss in %g) (5 percent of Critical Damping), Site Class B (MOMRA, 2013)

4 ROCK MASS CLASSIFICATION

The ground conditions of a tunnel case study were characterized by a strong rock mass intersected by a series of discontinuities, including faults, joints and dykes. These discontinuities meant the rock mass behaved as heterogeneous and discontinuous, in which the geotechnical properties and hydraulic conductivity were greatly impacted by spacing, continuity, orientation, aperture, and infilling of the discontinuities and must be defined for the rock mass as a whole based on zones apportioned along the tunnel alignment.

Field mapping records provided a foundational dataset for the area of this tunnel. RQD values were obtained from GI, whilst Q (NGI, 2022), GSI (Hoek & Brown, 1997) and RMR (Bieniawski, 1973) were recorded during geological mapping on site, see Table 2. Q-values for the tunnel alignment were derived from horizontal drillholes, nearby tunnel mapping, and field mapping integrated with satellite image interpretation. Additionally, high-resolution drone images were utilized to delineate faults and joints, enhancing the accuracy and extent of the analysis and the consistency with field mapping records. GSI values were obtained as an intermediate step in the design process for rock mass characterization through mapping or the well-established correlation with RMR.

Table 10 : Rock Mass Classification of a Case Study Tunnel

Area	Rock Type	RQD	Q-value	GSI	RMR
Mountainous	Granite	50-90	1.0-4.0	55	60
	Limestone	25-90	0.4-1.0	37	42
Coastal Low-lying	Sandstone	50-90	N/A	40	45
	Limestone	25-90	0.4-1.0	37	42
	Conglomerate	75-90	N/A	40	45

In Hong Kong, the Q-system (NGI, 2022) is the preferred classification method (Geoguide 4, 2018) and is extensively used in mined tunnel projects. In KSA, however, local codes (MOMRA, 2013) do not favor a specific empirical method, allowing for the use of Rock Loads (Terzaghi, 1946) & RQD (Deere, 1964), RSR (Wickham et al., 1972), RMR (Bieniawski, 1973) and the Q-system (NGI, 2022). Although historically more reliant on the RMR system, KSA's mined tunneling practices are now converging toward a hybrid approach that integrates both RMR and Q-system methods.

In our tunnel design practice for the KSA region, the Q-system was considered more applicable for tunnels with massive or variable spans compared to the RMR method. Therefore, the Q-system has been more applied during detailed and developed design stages, as well as for real-time support adjustments during construction. In a local mined tunnel project, the RMR method was employed in the conceptual design stage for the tunnel initial support design, particularly when the target tunnel span was around 10 meters. In this project, the RMR method was deemed applicable and intuitive for the earliest design phase. The adopted approach consisted of RMR values calculated directly from its principles rather than relying on Q-system correlations.

5 TUNNEL SECTION GEOMETRY OPTIMIZATION

5.1 Introduction

The geometric design of a mined tunnel section is an important aspect of tunnel design. This design decision not only affects the tunnel's structural stability, serviceability, inspectability, maintainability, and Fire-Life-Safety (FLS) performance but also impacts its economic viability and constructability (SHC 301 and 310, 2023). Furthermore, the tunnel span is often directly linked to support design parameters, with empirical methods like the Q-system and RMR method commonly used for this purpose. As a result, optimizing tunnel section geometry becomes a key consideration, offering significant advantages during the design phase.

The typical mined tunnel cross section elements are shown in the Figure 26. Tunnel span typically is affected by travel lane, shoulder, barrier, sidewalk and other elements. The summary of various codes' requirement regarding these elements and the optimization of tunnel geometry in KSA tunnel design practices is shown in Section 5.2.

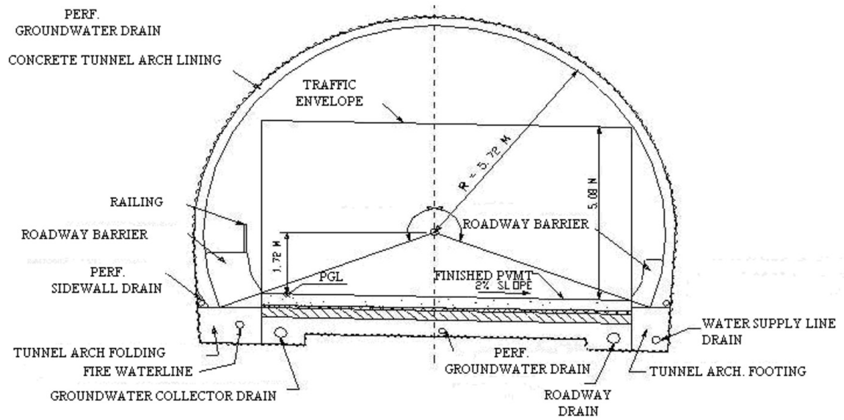

Figure 26 - Typical Two-Land Road Tunnel Cross Section and Elements (FHWA, 2009)

In KSA, the recent design of tunnels has focused on integration with new infrastructure assets, requiring meticulous planning for utility arrangements. Beyond the elements discussed above, the tunnel cross-section design also takes into account for the accommodation of utility systems, such as dry utilities (e.g., telecommunications and power cables), wet utilities (e.g., water and sewage systems), ICT infrastructure, and MEP & FLS (Mechanical, Electrical, Plumbing, and Fire Life Safety systems). Achieving a balance among these utilities is essential to ensure that tunnels fulfill both their primary transportation function and efficiently supports ancillary services. The design development of tunnel geometry through utility arrangement is presented in Section 5.3.

5.2 Tunnel Section Geometric Parameter

Comparing to Hong Kong infrastructure design which mostly take reference from European and British codes, KSA tends to reference American codes for infrastructure projects. However, European or British standards may be used in projects with European consultants or contractor involvement. Saudi Building Code (SBC) acts as an overarching framework for guiding the infrastructure design, mostly refers to American codes for tunnel-specific designs (e.g., AASHTO, ACI, NFPA 502, ASCE, and FHWA). In contrast, the Saudi Highway Code (SHC) integrates American codes, the European Union's Tunnel Directive 2004/54/EG, and German guidelines such as FGSV in tunnel geometric design requirements (SHC, 2023). It is therefore recommended to prioritize a hierarchy of applicable codes as an initial step in KSA tunnel design projects.

The standards and design manuals summarized in Table 11 are commonly referenced in KSA tunnel projects. They outline variations in recommendations for vertical clearance, shoulder width, sidewalk dimensions, and means of egress in a two-lane highway tunnel. It is important to acknowledge the cross-referencing and evolution of these design standards in tunnel design practices. For instance, FHWA (2009), the earliest design manual in Table 11, relies on outdated references such as the AASHTO Green Book (2004), necessitating alignment with its updated version in 2018. The latter has introduced stricter geometric recommendations (see Table 11, Column 3). Similarly, MOMRA (2013) draws heavily on the FHWA, AASHTO, and NFPA standards. Given the progressive revisions among these documents, the latest three: AASHTO (2018), SHC (2023) and NFPA 502 (2023) are considered more applicable for contemporary KSA tunnel design. Notably, NFPA 502 primarily provides guidelines for tunnel fire safety and ventilation design, while AASHTO and SHC are referenced for tunnel geometry requirements.

Table 11 : Geometric parameter requirements for a 2-lane tunnel in different codes

Reference Code	FHWA (2009)	MOMRA (2013)	AASHTO (2018)	NFPA (2023)	SHC (2023)
Vertical Clearance (m)	4.3-4.9	5.5	4.9	-	5.5
Horizontal Curb-Curb Clearance (m)	7.8	refers to FHWA and AASHTO	(26 ft) 7.9m	-	7.6
Shoulder Width (m)	0.6-3.0	refers to FHWA and AASHTO	0.6-3.0	-	-
Sidewalk Width (m)	0.5-0.7	0.9	1.1-1.5	1.12	1.0-2.2
Means of Egress (MOE)	Per NFPA502 (2023), Means of Egress (MOE) distance shall not be more than 300m (1000 ft), and most typical exit separations are between 30m and 200m, with minimum clear width of 1.12m..				Per SHC (2023), MOE distance is 300m.

Most codes typically do not impose strict or uniform regulations on geometric dimensions, but provide desirable guidelines (e.g., the AASHTO Green Book in 2018, for tunnels exceeding 60m in length), granting designers flexibility to optimize cost-effectiveness. For instance, some codes suggest that, considering additional construction cost, the inside shoulder can be eliminated, while the outside shoulder dimension is subject to a cost-benefit analysis and tunnel risk analysis (SHC, 2023). With appropriate design of road curbs and barriers aligned to the design speed, it is also acceptable to further reduce the shoulder width. This allows designers to optimize tunnel geometry based on project-specific factors like tunnel function (cable or road tunnel), design speed, location (urban or rural), traffic direction (unidirectional or bidirectional), lane count, and other parameters, ensuring functionality, safety, and economic efficiency.

Both the KSA standard (MOMRA, 2013) and American code (AASHTO, 2020) have indicated that the proper selection of road barriers can effectively absorb collision loads in tunnels (Table 12). As previously noted, the AASHTO (2020) is considered more applicable for KSA modern tunnel design. Given that tunnel sidewalk widths typically range from 1.0m to 1.5m, by implementing the AASHTO's requirement for a 1.07m high barrier, this can eliminate the need to incorporate a 2668kN collision load, thereby optimizing the tunnel cross-section. Conversely, omitting the barrier necessitates integrating collision loads into LRFD load combinations, significantly increasing structural demands (e.g., concrete volume and reinforcement). Additionally, the tunnel design life, serviceability and maintenance costs without the barrier should also be taken into considerations, and designers should compare these options and select the most applicable code and the proper design case to case.

Table 12 : Road barrier requirement for road tunnels within different codes

Reference Code	MOMRA Bridges, Tunnels, Culverts and Pedestrian Bridges Specifications in Urban Areas (2013)	AASHTO LRFD Bridge Design Specifications (2020)
Collision Load	1800kN	2668kN
Protection Measures	1.37m high crash tested TL-5 barrier when distance from barrier to component being protected is within 3.0m	1.07m high MASH crash tested rigid TL-5 barrier when distance from barrier to component being protected is greater than 1.0m

5.3. Utility Integration and Tunnel Section Design Development

The integration of utilities within tunnels depends on site-specific constraints and infrastructure priorities. In scenarios where no alternative diversion routes are available, utilities are fully integrated into the tunnel structure. While this centralizes maintenance access, it requires an enlarged cross-section to accommodate all utility systems. Conversely, external utility corridors can divert non-critical systems outside the tunnel, allowing the cross-section to prioritize essential operational utilities. This reduces the tunnel's geometry but demands coordination with external stakeholders and additional land allocation.

A hybrid approach—partial integration—aligns certain utilities with existing road infrastructure by partially embedding them within the tunnel and routing others externally. This balances spatial efficiency with flexibility for future upgrades. Table 13 provides a comparative analysis of the three utility arrangement strategies.

However, the design of the appropriate utility integration approach should consider project requirements, client expectations, site conditions, and other relevant factors.

Table 13 : Pros and Cons by Utility Integration Considerations

Type	Pros	Cons
Type 1:Fully Integrated Utilities Inside Tunnel	• Centralized maintenance access. • Faster construction. • Enhanced utility security.	• Limited future adaptability. • Waterproofing challenges. • High risk of cascading failures.
Type 2: Fully External Utilities	• Isolates operational risks (e.g., leaks, fires). • Easy upgrades. • Long-term cost efficiency.	• High upfront costs. • Coordination complexity across stakeholders. • Requires external space.
Type 3: Partially Integrated Utilities	• Balances safety and flexibility. • Moderate costs. • Protects critical systems.	• Complex hybrid design. • Dual maintenance requirements. • Risk of utility misclassification.

Consolidating utilities within the tunnel footprint necessitates strategic planning to balance operational sustainability and maintenance efficiency. Firstly, maintenance accessibility is critical: utilities are required to be conveniently accessible through optimally located access points and corridors, enabling repairs without disrupting traffic. Secondly, seamless integration of external and internal networks demands precise alignment of pipelines and robust connections to prevent leakage. Thirdly, modular designs and phased maintenance minimize road closures by isolating tunnel sections for repairs. Finally, redundancy measures ensure tunnel operability during maintenance, avoiding full shutdowns. This holistic approach prioritizes functionality, maintenance efficiency, and minimal public disruption.

The arrangement of utility corridors significantly influences tunnel geometry, spatial efficiency, and operational functionality. Figure 27 below provides a design development by considering utility corridors at different locations. As shown in Figure 27(A), a complex utility corridor layout with densely clustered pipelines and equipment occupies a significant amount of tunnel space, reducing the effective cross-sectional area available for other purposes and increased construction costs. Such congestion also impedes maintenance workflows, as technicians encounter limited accessibility to critical systems. In contrast, Figure 27(b) illustrates a developed design where utilities are streamlined into consolidated, modular pathways. This approach minimizes redundant space and simplifies routing. The reduction of approximately 10% in the tunnel area in Figure 27(A) compared to Figure 27(B), achieved through the rearrangement of the utility corridor, offers significant advantages including reduced excavation volumes, less temporary work quantities, reduced construction cost, reduced construction time and associated risks.

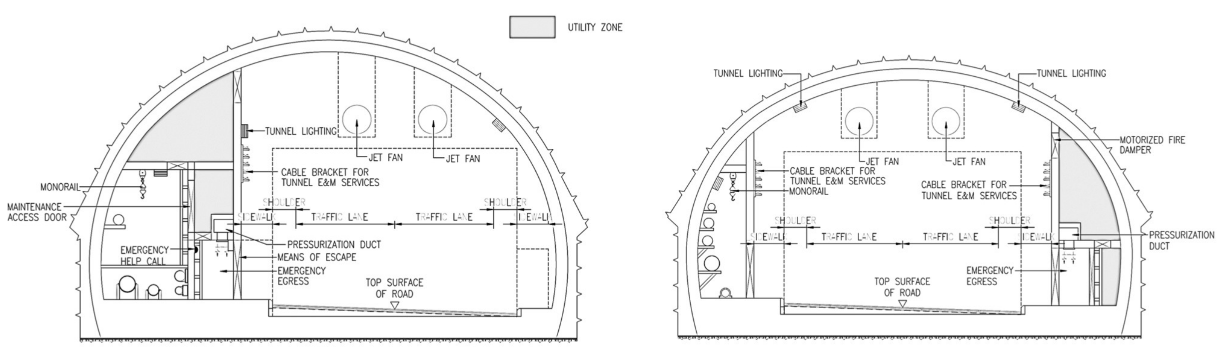

Figure 27 – (A) Utility Corridor Positioned on One Side (B) Utility Corridors Positioned on Both Sides

6 TUNNEL PORTAL SLOPE COSMETIC ENHANCEMENTS

Mined tunnel portals require site formation and cut slopes. In the KSA tunnel projects, the challenges are amplified by the need to balance geotechnical requirements with stringent contextual and aesthetic objectives.

Therefore, the context-sensitive tunnel portal design becomes one of the key constraints the designer may face in KSA design projects.
Conventional cut slope designs often produce visually intrusive "engineered" landscapes that disrupt the natural surroundings. To better understand the scope of the aesthetic improvement works of the portal cut slopes, classification is conducted to determine the extent and type of typical tunnel portal slopes as shown in Table 14.

Table 14 : Tunnel Portal Slope Zone

Category	Definition	Requirement
A	Direct Exposure	For locations where individuals have direct access and proximity, such as near driveways, walkways, or parking spaces adjacent to tunnel portals, a high level of detailing is required to camouflage man-made structures. Solutions such as natural stone facades, vegetated retaining walls, or bespoke gabion systems filled with local materials is possible.
B	Vehicular Exposure	For slopes above the portal structures that are visible to road users at enter or exit tunnels, or on the driveways, the stabilization structures will require an intermediate level of detailing. Retaining elements would harmonize with the landscape and can afford to have a smaller degree of detail whilst blending into the natural surroundings, softening the visual impact.
C	Aerial or Elevated Exposure	For slopes where stabilization structures are visible from an elevated perspective, such as aerial viewpoints, from hillsides, or low-flying aircraft, camouflage solutions that integrate into the larger visual landscape are critical. Options such as vegetative covers, natural stone, and earth-coloured materials will be prioritized to create a seamless visual transition from above.

The following are recommended measures for enhancing the aesthetics of the tunnel portal slopes (

Table 15, **Error! Reference source not found.**, Figure 29 and Figure 30).

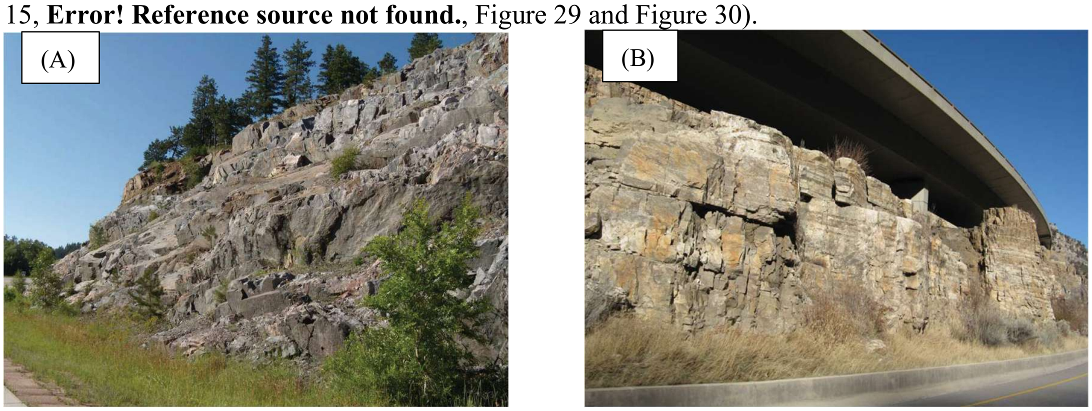

Figure 28 - (A) Rock slope excavated using slope variation and sculpting techniques (Andrew et al., 2011); (B) Staining on the completed slope to create a natural-looking rock face (Glenwood Canyon, Colorado).

Table 15 : Tunnel Portal Slope Aesthetics Improvement Measures

Slope Profile	Reinforcement	Mitigation
• Slope warping: Rounds the ends of the cut to smooth the transition between the rock cut and the natural terrain. • Slope rounding: Rounds the crest of the cut slope to smooth the transition to the natural terrain. • Slope angle variation: Varies the slope angle laterally along the slope to accentuate prominent geological features or differences in weathering rates.	• Spot or systematic bolting with hidden heads (recessed heads, headless dowels) • Fiberglass or carbon fibre reinforced polymers (GFRP, FRP, or CFRP): Strong, lightweight alternatives to steel; can be colored. • Textured or colored shotcrete: Adds both texture and color for environmental blending.	• Bio-engineering: Prevents erosion and maintains a natural appearance with suitable vegetation for site conditions, and is suitable for the local temperature and moisture. • Rock staining and artificial rock cladding: Alters the appearance of rocks to blend naturally. • Rockfall barrier offset at crest: Reduces visibility for road users. • Catch ditch at slope toe where space allows: Manages potential hazards like erosion or debris flow. • Steel element painting: Painting steel elements (e.g., rockfall barriers, dowels) to match surroundings.

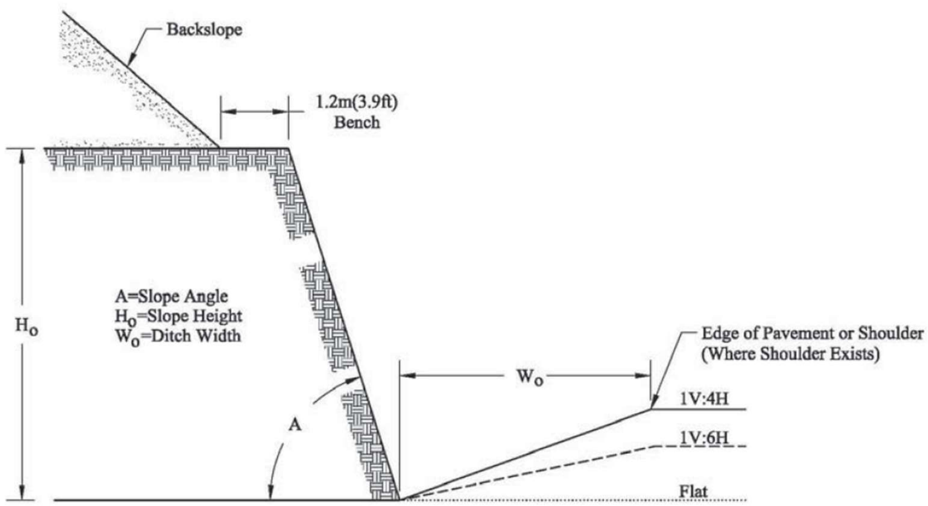

Figure 29 - A Typical Oregon ditch design, is aesthetically acceptable measures (modified from Pierson, Gullixson, and Chassie 2002).

Figure 30 - (A) Rock cladding in glass fiber or aluminum with a textured and coloured finish (Lin Ma Hang, Hong Kong); (B) Completed structural shotcrete, ready for staining (Andrew et al., 2011); (C) Recessed head bolt which may be covered with facing brick or stone works.

7 ENVIRONMENTAL CONSIDERATIONS

Environmental considerations during mined tunnel construction in KSA are critical due to the region's unique ecological and climatic conditions. One of the primary concerns is groundwater management, as tunnelling activities can disrupt local aquifers, leading to water table depletion and affecting ecosystems and communities that rely on these resources. Grouting is often used to control groundwater ingress, but excessive extraction can harm vegetation and water supplies. To mitigate these impacts, careful monitoring of groundwater levels is essential. For instance, monitoring data can confirm that no significant drawdown occurs, ensuring that the design avoids disruption to local aquifers. Stabilizing the slope at the tunnel portal often required measures such as shotcrete, anchor bots, or gentler slope gradient. These measures can enhance slope stability although inherits potential environmental impacts. To address these concerns, mitigation strategies should be incorporated into the design, such as minimizing land disturbance and implementing erosion control measures.
Air and noise pollution from blasting and drilling operations and cut slope was minimized to protect nearby communities and wildlife. Dust suppression techniques and noise barriers were essential to mitigate these impacts. The disruption of natural habitats during construction, particularly in ecologically sensitive areas, required careful planning to avoid impact to biodiversity. Finally, sustainable practices, such as recycling excavated materials and using energy-efficient equipment, would reduce the environmental footprint of tunnelling projects. By addressing these considerations, tunnel construction in KSA, construction is carried out in an environmentally responsible manner, balancing infrastructure development with ecological preservation.

8 CONCLUSIONS

This study examines tunnel design practices in KSA, and highlights the region's unique geological and geotechnical characteristics. By evaluating local codes against international standards, and implementing utility integration strategies, engineers can ensure structural integrity, safety, serviceability, sustainability and cost-effectiveness in tunnel projects. The research also addresses the importance of context-sensitive design requirements for KSA projects, proposing solutions to achieve both functional and aesthetic objectives.
In conclusion, this study provides a valuable resource for professionals involved in KSA tunnel projects, offering practical insights into tunnel design in one of the world's most dynamic regions. Future research would focus on the application of innovative technologies and materials to further enhance and optimize tunnel design and performance in a safe and constructable method.

ACKNOWLEDGEMENTS

The author would like to thank Mr. Xavier Tang and Mr. Geoffrey Pook for their valuable support and expertise during this research. Their assistance, especially in providing important technical documents and insights was crucial to the progress of this work. Their knowledge and guidance greatly improved the quality and accuracy of this study. The author is truly grateful for their help and collaboration.

REFERENCE

Al Saud, M., & Rausch, R. 2012. *Integrated groundwater management in the Kingdom of Saudi Arabia*. Proceedings "Hydrogeology of Arid Environments, 1-6.

American Association of State Highway and Transportation Officials. 2017. *LRFD Road Tunnel Design and Construction Guide Specifications*. Washington, DC, USA. AASHTO.

American Association of State Highway and Transportation Officials. 2018. *Green Book - A policy on geometric design of highways and streets*. Washington, DC, USA. AASHTO.

American Association of State Highway and Transportation Officials. 2020. *LRFD Bridge Design Specifications 9th Edition*. Washington, DC, USA. AASHTO.

Andrew, R. D., Bartingale, R., & Hume, H. 2011. *Context sensitive rock slope design solutions (No. FHWA-CFL/TD-11-002)*. United States. Department of Transportation. Federal Highway Administration.

Bieniawski, Z. T. 1973. *Engineering classification of jointed rock masses*. Civil Engineer in South Africa, 15(12), 335-343

Brown, G. F., Schmidt, D. L., & Huffman Jr, A. C. 1989. *Geology of the Arabian Peninsula; shield area of western Saudi Arabia (No. 560-A)*. US Geological Survey.
Deere, D.U. 1964. *Technical description of rock cores for engineering purpose*. Rock Mechanics and Engineering Geology 1(1):16–22.
Geotechnical Engineering Office. 2018. *Guide to cavern engineering. Geoguide 4*. Geotechnical Engineering Office, Civil Engineering and Development Department, HKSAR Government.
Hoek, E. & Brown, E. T. 1997. *Practical estimates of rock mass strength*. International Journal of Rock Mechanics and Mining Sciences, 34(8), 1165-1186.
K.S.A. Ministry of Municipal & Rural Affairs, Deputy Ministry for Technical Affairs. 2013. *Bridges, Tunnels, Culverts and Pedestrian Bridges Specifications in Urban Areas. Design Specifications. MA 100-D-V1/2.* Ministry of Municipal & Rural Affairs, Deputy Ministry for Technical Affairs.
K.S.A. Ministry of Municipal & Rural Affairs, Deputy Ministry for Technical Affairs. 2013. *Bridges, Tunnels, Culverts and Pedestrian Bridges Specifications in Urban Areas. Design Specifications. MA 100-D-V2/2.* Ministry of Municipal & Rural Affairs, Deputy Ministry for Technical Affairs.
Kahal, A. Y. 2020. *Geological assessment of the NEOM mega-project area, northwestern Saudi Arabia: an integrated approach*. Arabian Journal of Geosciences, 13(10), 345.
National Fire Protection Association, G. 2023. *NFPA 502: Standard for road tunnels, bridges, and other limited* access *highways.* USA. NFPA.
Norwegian Geotechnical Institute. 2022. *Using the Q-system: Rock mass classification and support design.* Norwegian Geotechnical Institute.
Roads General Authority. 2023. *Saudi Highway Code. Design of Highways, Bridges and Tunnels. SHC 301 – Highway Geometric Design*. Road General Authority.
Roads General Authority. 2023. *Saudi Highway Code. Design of Highways, Bridges and Tunnels. SHC 310 – Bridges and Tunnels Design*. Road General Authority.
Şenalp, M., & Tetiker, S. 2021. *Stratigraphic evolution of the Midyan Basin and its hydrocarbon potential (NW Saudi Arabia)*. Türkiye Jeoloji Bülteni, 64(1), 1-40.
Terzaghi, K. 1946. *Rock defects and loads on tunnel supports*. Rock tunneling with steel supports.
The Saudi Building Code National Committee. 2018. *Saudi Building Code. SBC 301-CR*. SBCNC.
U.S. Department of Transportation Federal Highway Administration. 2009. *Technical Manual for Design and Construction of Road Tunnels-Civil Elements (No. FHWA-NHI-10-034)*. National Highway Institute (US).
Wickham, G. E., Tiedemann, H. R., & Skinner, E. H. 1972. *Support determinations based on geologic predictions*. In N Am Rapid Excav & Tunnelling Conf Proc (Vol. 1).

Design of Temporary Construction Adit and Tunnel Plug for Nenggiri Hydroelectric Project

G. Ravindran & J.F. Chung
Aurecon Perunding Sendirian Berhad, Malaysia
J.T.Y. Chin
Aurecon Hong Kong Limited, Hong Kong
Y. Ali
Protext Construction (M) Sendirian Berhad, Malaysia

ABSTRACT

The Nenggiri Hydroelectric Power Plant Project, located in the state of Kelantan, Malaysia, is among the largest renewable energy initiatives in the country. The main dam structure is 88.1m in height and can hold 1.239 billion m^3 of water. A twin main diversion tunnel (DT) is required to divert existing river flow to enable construction of the cofferdam and the main dam structures. The horseshoe-shaped temporary construction adit (TCA) with a 6m span and approximately 146m long, excavated using drill and blast method, aims to expedite construction progress by providing access at the middle of the proposed DT thus allowing additional excavation faces for the DTs. Key design approach involves NGI-Q System for initial tunnel support design, followed by the Convergence-Confinement Method to establish relationship between stress relaxation and advance length, forming the basis for subsequent temporary support design using finite element RS2 program. This paper presents an optimized design and construction approach for the TCA and the tunnel plug located at the TCA-DT junction. Innovative design was adopted that results in significant reduction of plug length compared to conventional design. Despite various major challenges the TCA and DTs were able to be completed one month ahead of schedule.

1 INTRODUCTION

1.1 Background and significance

Malaysia is a small open economy which is currently experiencing rapid urbanization and growing population, with population expected to grow from 32,700,000 to 40,000,000 people from 2022 to 2050, the energy demand is expected to rise by 2% annually until 2050 (Ministry of Economy, 2023). As of 2020, a large portion of Malaysia’s energy supply still rely heavily on fossil fuels such as natural gas, crude oil and petroleum products and coal. To achieve sustainable development, the government has taken proactive steps in driving the energy transition process to reshape its energy landscape towards renewable energy.

The Nenggiri Hydroelectric Project in Malaysia is a key initiative aimed at increasing renewable energy (RE) capacity, enhancing energy security, and promoting regional growth. It supports Malaysia's goal of achieving RE capacity mix target of 40% by 2035, and 70% by 2050. Beyond power generation, the project also helps with flood mitigation by managing rainwater during the monsoon season, and the re-regulating dam ensures a steady river flow. It will benefit the State of Kelantan by providing clean water and improving irrigation for agriculture.

The project includes essential components such as a roller-compacted concrete (RCC) dam, saddle dam, re-regulating dam, and a surface power station with two 150 MW generators that can transmit power to the main 275kV Switchyard. These generators will supply an average of 599.5 GWh annually. The dam, standing 88.1m high, can store 1.239 billion m^3 of water, supporting regional energy needs. A critical aspect of the project is the twin main diversion tunnels (DT), necessary to redirect river flow and facilitate the construction of the cofferdam, which enables subsequent works on the main dam structures. To optimize construction timelines, a

Temporary Construction Adit (TCA) and temporary cross passage (TCP) was designed and implemented, allowing access to the middle section of the tunnel alignment and enabling simultaneous excavation from both ends. Refer to Figure 1(a) which shows the project site layout plan.

This paper presents an optimized design and construction approach for the TCA, highlighting innovative solutions to address structural and site constraints, and evaluating the overall project outcomes and performance.

1.2 Project overview

The Nenggiri Hydroelectric Project (HEP) site is located within the Sungai Nenggiri catchment in Jajahan Gua Musang, approximately 30 km from Gua Musang town (Figure 2(a)). As mentioned in the background, the project requires the twin main diversion tunnels (DT) to facilitate the construction of the cofferdam and subsequent main dam structures. To optimize the construction schedule of the DTs, a TCA was added. The horseshoe-shaped TCA, approximately 145.9m in length and 6m in span, plays a crucial role in expediting the excavation of the diversion tunnels. By providing access to the middle section of the tunnel alignment, it enables simultaneous excavation from multiple headings, significantly reducing the overall construction timeline. Upon completion of the DTs, tunnel plugs were constructed to seal off the TCA prior to the commissioning of the DT for river diversion works. The typical sections of TCA and DT are shown in Figure 31(b) and 1(c).

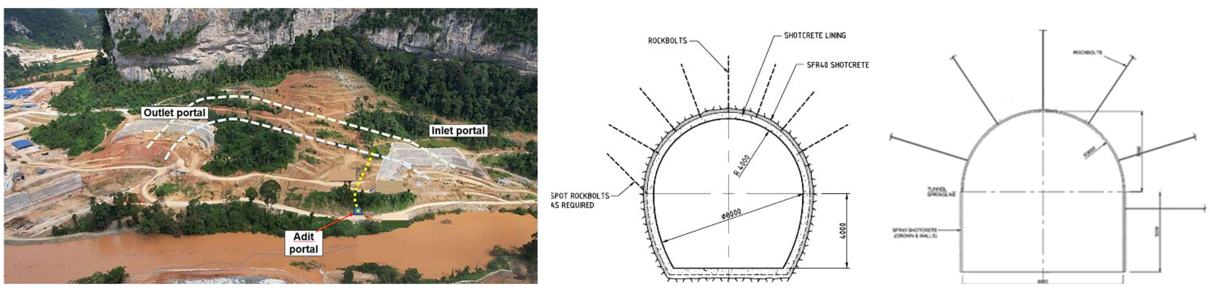

(a) (b) (c)

Figure 31: (a) Site layout plan (b) Typical section DT (c) Typical section of TCA

2 SITE CONDITIONS

2.1 Geology

According to the Geological Map of Peninsular Malaysia, 9th Edition, 2014 (Geological Map of Peninsular Malaysia, 2014), the project site is located on the Gua Musang Formation, which dates to the Middle Permian to Late Triassic period. This formation includes a range of geological materials, such as limestone, slate, phyllite, sandstone, minor conglomerates, and volcanic rocks like andesite and granite. The geological map of the site area, along with the corresponding legends, is provided in Figure 2(b) and 2(c). Limestone hills are prominently exposed in several locations within the Nenggiri area. The limestone here is characterized by low to high hills with very steep faces and pinnacles. The depositional environment of the site is a shallow marine shelf, with active volcanic activity, which has resulted in much of the local limestone being metamorphosed into marble. The nearest major fault, the Galas Fault, is located approximately 28 km to the north of the project site, and it is surrounded by minor fault zones.

2.2 Site investigation & laboratory testing

Two boreholes were drilled close to the alignment of the temporary adit tunnel. The borehole locations were selected based on site accessibility and to allow safe operation of the SI machinery. As the area is hilly with no proper berms or platforms during the early stage, the initial SI locations had to be shifted to location with safe access. The final borehole positions, as shown in Figure 5(a) were kept as close as possible to the TCA alignment to ensure the ground conditions were still representative. Standard Penetration Tests (SPT) were conducted at 1.5m intervals in all boreholes where soil was present to assess the soil profile and determine soil parameters using the SPT-N values. Rock coring was also performed to obtain rock samples as shown in Figure 33, and measure the Rock Quality Designation (RQD) and core recovery. One standpipe piezometer was installed at one of the boreholes to monitor the groundwater level.

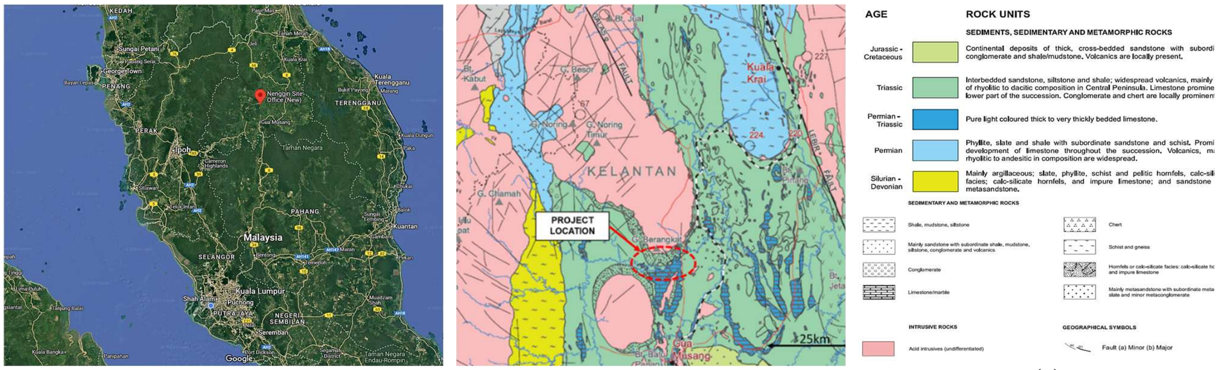

(a) (b) (c)

Figure 32: (a) Site location (b) Geological map of the site area and the surroundings (c) Geological map legend

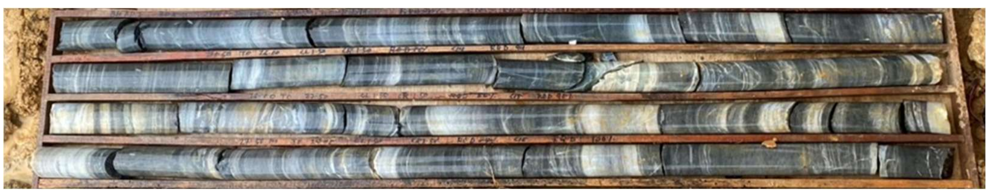

Figure 33: Rock samples from coring

Based on data from two boreholes, the site consists of a 3m thick hard sandy silt in one location, and in another, a 3m thick medium stiff silty sand overlying 2m of hard silty sand. The ground parameters were determined based on experience and engineering judgment. The elastic modulus for soft ground was calculated using local practices and SPT-N correlations, where E = 1N for SPT-N > 30, and E = 1.5N for 30 > SPT-N > 10. Unconfined Compression Tests were carried out on the rock core samples from the two boreholes. The results showed significant variation in strength, with up to a 50% difference in fracture load between samples. The rocks were identified as mixed rock types consisting of metasedimentary and meta-volcanic (metamorphic) rock types, with unconfined compressive strength (UCS) ranging from 30.4 to 168.4 MPa. The adopted parameters for the design are listed in Table 16.

Table 16: Design parameters for portal slope

Soil/Rock Type	Effective Cohesion, c' (kPa)	Effective Angle of Friction, φ'	Bulk Density, γ (kN/m^3)	Elastic Modulus (MPa)
Silty Sand, SM (Layer 1)	7	31	19	30
Sandy Silt, MS (Layer 2)	10	35	20	50
Moderately Weathered Rock (Layer 3)	10	38	20	-
Fresh to Slightly Weathered Rock (Layer 4)	15	45	24	-

The geotechnical design parameters for intact rock were determined by reviewing site-specific geotechnical information, including laboratory UCS test results on rock core samples. The modulus ratio (MR) was based on rock type using the MR recommendation table from “RS2” software by Rocscience, with a typical MR value of

400 adopted for design. The parameters for the intact metasedimentary and meta-volcanic rock, classified by weathering condition, are summarized in Table 17.

Table 17: Design parameters for rock tunnel

Rock Type	Bulk Density (kN/m^3)	Uniaxial Compressive Strength, UCS (MPa)	Elastic Modulus (GPa) [(2)]	Mi	Ko
Moderately Weathered	26	10[(1)]	3	9	1.5
Fresh to Slightly Weathered	26	50 – 80	20 – 32	9	3

Note 1: Estimated conservatively for moderately weathered metasedimentary and meta-volcanic rock.
Note 2: Calculated using the modulus ratio, MR, ratio between elastic modulus and UCS.

2.3 Geological Features from Face Mapping

During the excavation of the TCA, face mapping was carried out to determine the prescribed support system needed. Two main rock types were encountered, meta-sedimentary rock and meta-volcanic rock, both showing consistent geological features and engineering-relevance to tunnel design.

The meta-sedimentary rock was mostly good to very good quality, black to grey with white stripes, fine-grained, interbedded, and massive. The rock was strong, with UCS between 50 to 100 MPa, and appeared fresh to slightly weathered (Grade I to II). The meta-volcanic rock, found near the end of the tunnel, had similar strength and weathering grades but darker in color, fine-grained, and massive. Overall, the rock mass quality was suitable for tunnelling, with most sections requiring only 50 mm thick safety shotcrete with spot bolts as the support.

Several joint sets were observed during mapping. The joints were close to moderately spaced, with joint roughness observed as rough undulated and rough planar. Localized open apertures were also encountered, some of which contained quartz infilling. Weathering and infill were generally minimal. Some areas had intersecting joints, which created wedge-prone zones. Joint density was observed to be approximately 15 per cubic metre.

The rock mass quality was classified according to Q-System (NGI, 2015). Q-values ranged from 0.6 in weak zones to as high as 13 in strong sections. The average Q-value was about 7, with most values above 8, indicating generally good rock mass quality. Higher Q-values (10 to 13) were observed in fresh, massive rock, while lower values (0.6 to 1.0) were limited to localized sections near the portal and isolated weak zones.

3 DESIGN & ANALYSIS

3.1 Portal slope

The formation of portal slope involves strengthening of new soil cut slope using the soil nailing technique, the requirement of the design factor of safety is assessed by referring to the Hong Kong Geoguide 7: Guide to Soil Nail Design and Construction (GEO, 2023). In view of the portal slope is located inside construction site with controlled access and low heavy traffic volume, the consequence-to-life and economic consequence from a slope failure is categorized as category 3 and category C respectively, which a minimum factor of safety of greater than 1.0 is recommended considering 10 years return period rainfall.

The portal slope comprises 3 tiers, with 3 slope faces and 2 berms; the height and gradient of the bottom slope, middle slope and top slope is 9m (4V:1H), 6m (2V:1H) and 5m (2V:1H) respectively, as shown in Figure 4(a). Galvanized T25 steel bars were used for corrosion protection and shotcrete slope facing were proposed. Slope stability computation was carried out using limit equilibrium method following Morgenstern-Price method. With ground water level anticipated to be at 3m below the existing slope crest, a series of 12m long subsoil drain with 4.5m center-to-center spacing was proposed to be constructed on the second slope face to manage the ground water level. The design of portal slope has been optimized by incorporating various soil nail spacings and length for different slope face, the details and photo of designed portal slope are presented in Table 3 and Figure 4 respectively.

Table 3: Details of reinforced soil cut slope

Slope Details	Slope Height (m)	Slope Gradient (m)	Soil Nails Spacing (m)		Factor of Safety (Local)	Factor of Safety (Global)
			Vertical	Horizontal		
Bottom Slope	9	4V:1H	1.2	1.5	2.655	
Middle Slope	6	2V:1H	1.5	1.5	2.669	1.495
Top Slope	5	2V:1H	1.2	1.5	2.246	

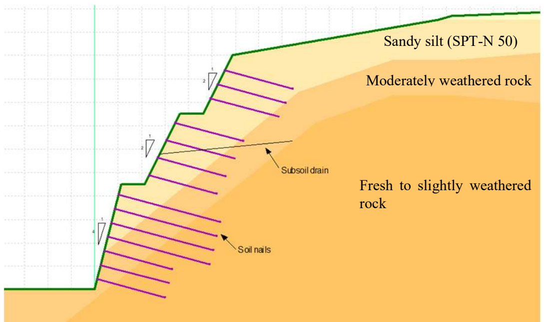

(a)

(b)

Figure 4: (a) Cross section of portal slope (b) Close-up view of portal slope

3.2 Temporary construction adit (TCA)

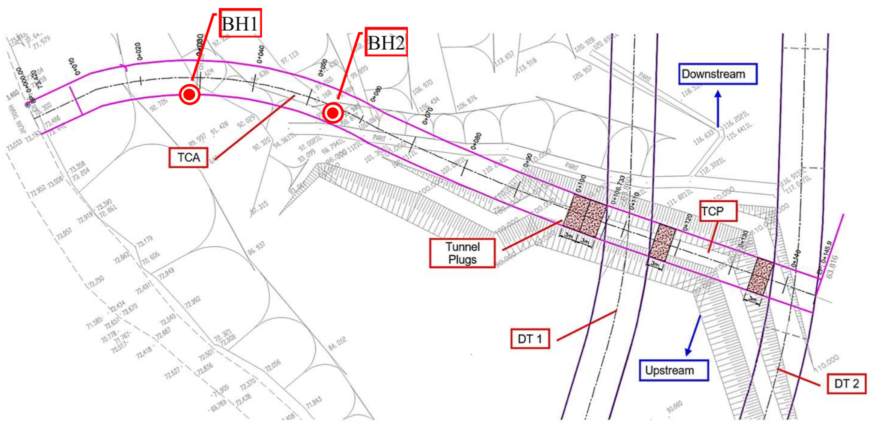

Figure 5(a): General layout plan

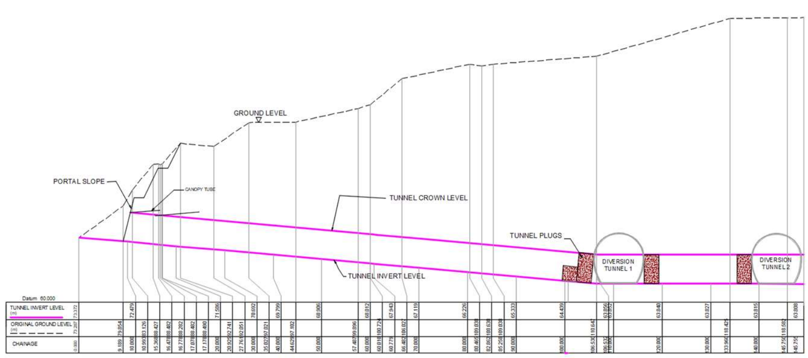

Figure 5(b): Vertical Profile of TCA

The design of temporary support systems for the construction adit adopted a multi-faceted approach, integrating empirical, numerical, and analytical techniques. Figure 5(a) and 5(b) illustrates the layout and profile of the TCA and its associated structures. The design steps of TCA, in general, follows that as described in Chin (2024) where empirical, analytical, and numerical design approaches are being adopted for the successful design and construction of TCA.

For empirical approach, the NGI Q-System (NGI, 2015) has been adopted to determine the temporary support requirements for the construction adit, as shown in Figure 6(a). Analytical approach is then deployed to assess the structural performance of the proposed supports such as steel ribs and canopy tubes. The designs are further validated by numerical modelling to assess the movements and the forces in the proposed support members.

In terms of numerical analysis, the Longitudinal Displacement Profile (LDP), established through Vlachopoulos and Diederichs' analytical method (Vlachopoulos & Diederichs, 2009), was used to determine the convergence behavior of an unsupported tunnel due to a specified tunnel advance length. The Ground Reaction Curve (GRC) analyzes the convergence behavior of an unsupported tunnel under progressive stress relaxation as excavation progresses, assessed through numerical analysis under varying ground conditions. By integrating these curves, as shown in Figure 6(b), the relationship between stress relaxation within the tunnel and tunnel advance length was determined. This general design approach adopted for TCA is being described in detail with example in Chin (2024).

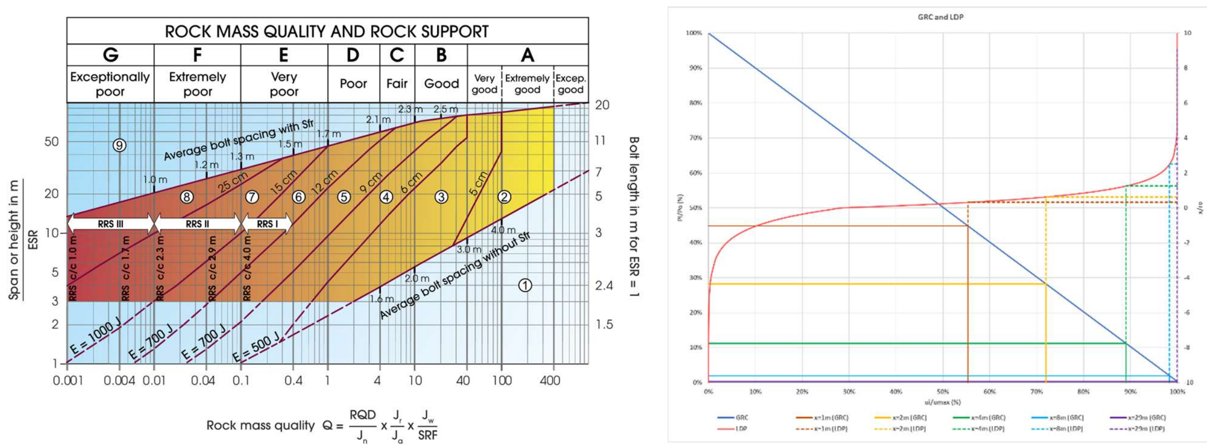

(a) (b)

Figure 6: (a) Rock Support Design Chart (NGI, 2015) (b) Graph of LDP & GRC

Numerical analysis was carried out using RS2 finite element software, with the model adopted stratified ground conditions according to borehole logs. The Mohr-Coulomb model was applied to the soil and weak rock near the portal, while the Hoek-Brown failure criterion was adopted for the mixed metasedimentary and meta-volcanic rock. Parameters such as joint spacing, orientation, surface condition, and weathering were considered through the use of the Geological Strength Index (GSI), which was derived primarily based on the Q-value ranges assessed. These GSI values were then used to calculate the rock mass strength parameters for the Hoek-Brown model.

Joints were not explicitly modelled, but their influence was accounted for through the adjustment of rock mass properties using the GSI approach. The numerical analysis, combined with empirical design using the Q-System and analytical checks, provided a reliable and conservative basis for designing the temporary support system across the varying ground conditions encountered along the TCA (Chin, 2024). Design parameters adopted for the RS2 model are summarized in Table 4. The design of tunnel face support for soft and mixed ground conditions was conducted using Slope/W, a two-dimensional numerical analysis tool that calculates the factor of safety of slip surface considering the loading conditions, porewater pressure, and failure plane shapes.

For forepoling design, canopy tubes was installed above the tunnel crown in soft/mixed ground and/or low rock cover conditions as pre-excavation support measure. These tubes serve to stabilize the unsupported ground that will be exposed right after excavation but before installation of prescribed support, and provide load transfer ahead of the face in the longitudinal direction in conjunction with steel arches. Excavation round length was 1.5m, with temporary lining installed before next cycle excavation. The vertical stresses acting on the canopy tubes are assessed using silo theory John & Mattle (2002) as recommended by Geoguide 4: Guide to Cavern Engineering (GEO, 2008).

Table 4: Design parameters adopted in RS2

Soil / Rock Type	c' (kPa)	φ' (°)	γ (kN/m^3)	Elastic Modulus (MPa)	UCS (MPa)	GSI	mi	D
Sandy silt	10	34	20	50	-	-	-	-
Q = 0.1 - 1	-	-	-	182.7	10	20	9	0
Q = 1 - 40	-	-	-	4186.1	50	44	9	0

3.2.1 Typical tunnel section and portal section

The TCA is a horseshoe-shaped tunnel with 6m wide by 6m height were constructed, since the tunnel is a temporary structure, a factor of 5.0 is applied to the design Q-value obtained using Barton et al (1974). The primary support design includes three support classes for typical tunnel sections and two support classes for tunnel portals. The Q-ranges for typical tunnel sections were categorized as $0.1 \leq Q < 0.4$, $0.4 \leq Q < 1.0$, and $Q \geq 1.0$. The NGI Q-System is applicable when the rockhead cover exceeds 1 × span of the adit (i.e. rockhead at least 6m above tunnel crown), accounting for the relatively small tunnel size. However, for portal design, where ground condition is predominantly soil and highly fractured rock mass, the Q-System was not applicable due to insufficient anchoring of systematic dowels. Instead, finite element analysis using RS2 software was employed to assess ground stability and propose suitable support measures.

The adopted support system for typical tunnel section comprises steel fibers reinforced concrete (SFRC) with characteristic strength of 30MPa. T25 dowel bars ranging from 1.5 to 3.0m with spacing ranging from 1.5 to 1.8m grid were adopted to provide rock arching surrounding the tunnel opening. For tunnel portal area where soft mixed ground was encountered, temporary supports comprising steel ribs of 125 x 125 x 23.8kg UC at 1.0m spacing with 150mm thick SFRC were adopted. Canopy tubes of 114.3 x 5mm CHS with spacing ranging from 0.30m to 0.45m center-to-center and 3m overlap were proposed as pre-excavation support for soft mixed ground near the portal.

To ensure excavation stability, advance lengths were set based on ground conditions. In soft mixed ground and areas with shallow rock cover, the advance length was limited to 1m per round, while in hard rock conditions, an advance length of 3m per round was implemented. These selected advance lengths were further verified through numerical methods, incorporating longitudinal displacement profiles and ground reaction curves to ensure structural integrity during excavation.

3.2.2 Junction section at TCA and main diversion tunnels

The junction section design addresses the intersection between the TCA and Diversion Tunnels, following a staged excavation sequence to ensure stability. Excavation proceeds along the TCA alignment until reaching the boundary of Diversion Tunnel 2. Upon completion of the TCA and cross passage (CP) excavations, Diversion Tunnel 1 was excavated upstream towards the portal, while Diversion Tunnel 2 advanced downstream in the opposite direction along the tunnel alignment. The main Diversion Tunnels are 8m in width and 8m in height. To accommodate the transition from a smaller TCA to larger Diversion Tunnels, the excavation profile of Diversion Tunnel 1 from junction gradually expands from 6m to 8.6m, increasing by 0.5m per round until the final design profile is achieved. Support measures were installed incrementally at each excavation stage, following the prescribed junction support requirements. Once the design profile is reached, the remaining rock cover in the main diversion tunnel was removed to establish the final tunnel geometry. This sequential approach ensures controlled excavation and structural integrity throughout the process.

The overall design methodology for the junction follows the same approach as the TCA design, incorporating empirical, analytical and numerical techniques to ensure structural stability. The NGI Q-System (2015) is used to determine temporary support requirements, analytical methods further evaluate the structural performance of elements such as steel ribs and canopy tubes. while numerical modeling validates the proposed support system by assessing ground movements and forces in support members (Chin, 2024).

For the junction, numerical analysis focuses on critical sections, specifically at the TCA tunnel side and the Main Diversion Tunnel side. Due to the structural complexities at the intersection, an adjustment factor of 3 × Jn was applied to the design Q-value to determine the support requirements, extending one tunnel span from the junction to account for additional exposed rock wedges and 3D stress redistribution surrounding the junction openings. This comprehensive approach ensures that the support system effectively addresses the challenges associated with tunnel intersections.

Similar to typical tunnel section, the adopted support system for junction section comprises SFRC with characteristic strength of 30MPa, and T25 dowel bars ranging from 1.5 to 3.0m with spacing ranging from 1.0 to 1.8m grid were adopted as the rock bolt to stabilize the surrounding rock mass. For ground with Q-value less than 0.4 but greater than 0.1, steel ribs of 125 x 125 x 23.8kg UC with spacing ranging from 1.0 to 2.0m coupled with 150mm-thick SFRC were proposed. However, during actual construction, the ground condition was better than expected, predominantly Q-value greater than 1.0, with occasional localized weak zone with Q-value between 0.4 to 1.0, therefore no steel ribs were installed in the junction area.

3.3 Tunnel Concrete Plug

Constructed to expedite the excavation of the twin main DTs, both the TCA and CP were to be sealed upon the completion of and before utilizing the DTs for diversion of river water for the construction of the dam. It has been decided that instead of fully backfilling the entire TCA and CP, several concrete plugs will be installed at specific locations to seal off both TCA and CP from the main diversion tunnels (DT). A total of 3 tunnel plugs were planned and constructed. These plugs are located at (1) the opening of TCA – DT1 Junction, (2) DT1 – TCP Junction, and (3) TCP – DT2 Junction. Figure 5(a) and 5(b) show the location of the concrete plugs along TCA and CP.

The tunnel plugs design has adopted an innovative design approach, differing from the conventional friction-based design. The tunnel plugs are subject to maximum hydrostatic pressure of approximately 650kPa imposed by the water head at the upstream of the river, conventional friction-based design approach, which relies on frictional resistance between the concrete and rock, would result in up to 20m concrete plug length. The rock plug design adopted for this project included T40 galvanized rebar as shear anchorage at interface of the plug and surrounding rock mass, leveraging the strength of the rock mass in addition to the frictional force to withstand the design water pressure. Using concrete grade of G40 with characteristic strength of 40MPa, the design plug length is reduced from 20m to 3m, enabling massive saving in concrete volume and construction program, and subsequently reducing the carbon footprint.

The design procedures involve performing structural analysis of the concrete plug using SAP2000 program where the concrete plug was modelled as a plate subject to lateral hydrostatic pressure applied linearly and increasing with increasing depth. Boundary conditions of the plate element was modelled as pinned in the x- and y-axis along the periphery of the concrete plug, while pinned at x, y and z-axis along the invert as shown in Figure 7. This results in zero bending moment at the peripheral while maximum bending moment near center of the plug. The structural capacity of the concrete plug was assessed by means of plotting a M-N interaction capacity envelop and comparing against the state of stress (axial force and bending moment) of the plug. Instead of adding reinforcement bars for flexural capacity like a conventional slab design, the thickness of the plug is increased such that the entire section without rebar is structurally sufficient. The design bending moment has also considered the effect of twisting moment.

The anchorage design of tunnel plug consists of equally spaced T40 rebar distributed along the tunnel plug's periphery to transfer the hydrostatic load and anchor the plug to the surrounding rock mass. The sliding action of the plug under the hydrostatic pressure was designed to be counteracted by the shear capacity of T40 rebar. Friction resistance at the base of the plug, which is favourable, has been ignored in the design. The shear capacity, V_c, of rebar was calculated using Equation (1).

$$V_c = \frac{p_y \times A_v}{\sqrt{3}} \qquad (1)$$

Where p_y = design yield strength of rebar = $\frac{1}{\gamma s} \times f_{yk}$, γs is partial factor for anchor rebar = 1.15, f_{yk} is characteristic yield strength of rebar = 500MPa, and A_v = shear area = 0.9A (for solid bars), where A is steel bar nominal cross sectional area.

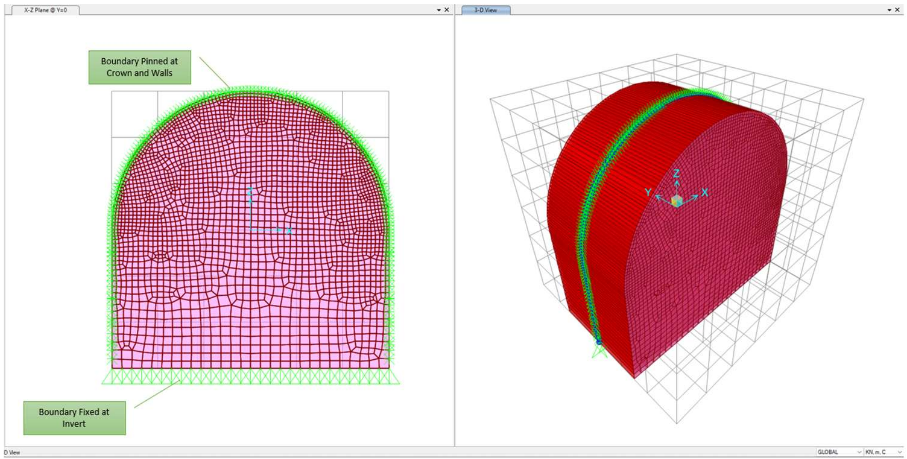

Figure 7: Model set-up for concrete plug in SAP2000

The required shear force was extracted directly from the structural model as boundary reaction force and compared against the shear capacity of rebar. The number of rebars required to resist the shear force is calculated accordingly. A load factor of 1.05 is applied to the maximum hydrostatic pressure for safe design. Load factors of 1.35 or 1.4 are usually adopted for hydrostatic pressure due to uncertainty, however it was considered overly conservative here because the maximum height of the dam is known, and it is physically impossible for the plug to consider hydrostatic pressure that is higher than the crest of the dam.

The required embedment depth of anchoring rebar was calculated according to EOTA, TR 029, Section 5.2.3 (EOTA, 2010) resistance to shear loads. Various failure mechanisms such as steel failure, concrete pry-out and concrete edge failure were assessed. Sufficient embedment depth is vital to ensure the full allowable shear capacity of rebars is mobilized.

The final design concluded with T40 rebar embedded minimum 900mm each side i.e. into rock and concrete plug, with in- and out-of-plane spacings of 0.70m and 0.75m respectively. The minimum achieved Factor of Safety for against steel failure, concrete pry-out and concrete edge failure is 1.1, 2.7 and 1.2 respectively. Figure 8 below shows the site photo of the drill hole for the T40 dowel bars.

(a) (b)

Figure 8: Site Arrangement of Rebar Along Tunnel Profile for Tunnel Plug (a) Left Side Wall, (b) Right Side Wall

4 INSTRUMENTATION & MONITORING

A comprehensive Instrumentation and Monitoring (I&M) system was implemented, consisting of three key components which are convergence monitoring, vibrating wire rock bolts, and vibrating wire shotcrete cells. These instruments were installed and monitored throughout the construction period. Leveraging the extensive experience of the contractor and the systematic installation of temporary support measures such as SFRC and rock bolts following each excavation cycle, the I&M and support system effectively mitigated any potential displacements and prevented any exceedance of alert thresholds (Yasir Ali, n.d.).

Figure 9 illustrates the three convergence monitoring points, which were assessed using optical prisms. Monitoring was conducted daily before the commencement of work and after the completion of each blast cycle at the TCA. The instrumentation data indicated no significant displacement, with measurements remaining well below the alert threshold throughout the monitoring period.

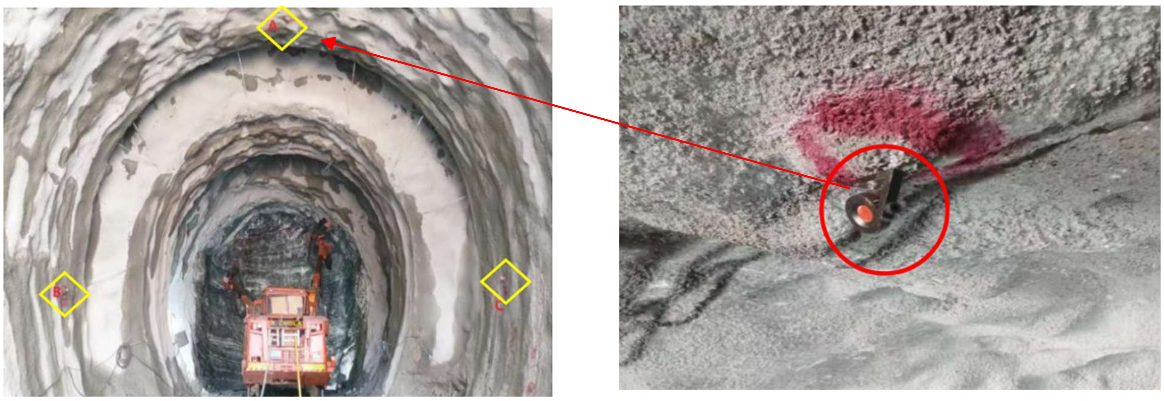

Figure 9: Instrumentation installed in TCA

5 CHALLENGES AND MITIGATION STRATEGIES IN TCA EXCAVATION

The excavation of the Temporary Construction Adit (TCA) at the Nenggiri Hydroelectric Power Project presented significant engineering and logistical challenges. The need for precise planning and innovative solutions was critical to ensuring safety and progress, particularly given the constraints posed by simultaneous excavation of twin diversion tunnels (DT1 and DT2).

5.1 Logistical challenges and traffic management

The excavation of DT1 and DT2 from a single access point via the TCA resulted in congestion and machinery movement constraints at ingress and egress. To mitigate delays and streamline excavation operations, a comprehensive traffic management plan was implemented to regulate machinery movement, ensuring smooth transitions between excavation, mucking, and support works. The main contractor Protext Construction (M) Sendirian Berhad developed detail excavation sequence to coordinate four active excavation faces concurrently, reducing idle time and maximizing efficiency. Additionally, an optimized haulage strategy was introduced, deploying designated pathways for muck disposal and material transport, which significantly enhanced overall workflow.

5.2 Tunnel gradient related challenges and stability measures

The TCA's steep vertical gradient (approximately 9 degrees) presented operational challenges such as increased risk of machinery skidding and water accumulation. To mitigate these potential risks, an efficient dewatering system was implemented to prevent water ponding and maintain continuous excavation progress. The invert was reinforced with BRC A6 mesh and G30 concrete to enhance durability, and groove lines were introduced at concrete surface to facilitate smoother vehicle maneuverability and improve safety. Additionally, a pump sump was strategically located at the TCA-DT junction, with a dedicated operator (bankman) on standby to manage water control operations, ensuring uninterrupted site functionality. As shown in Figure 10, the dry surface inside the tunnel demonstrates the effectiveness of the bund system in mitigating water entry.

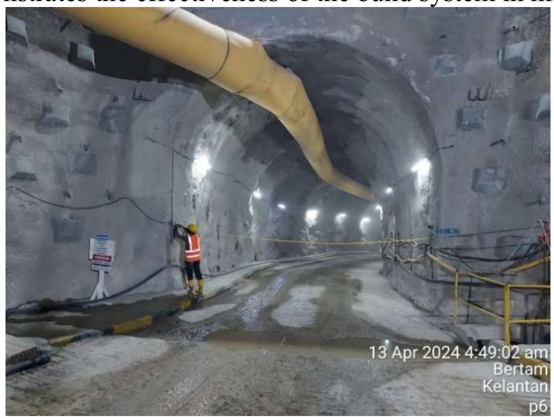

Figure 10: Reinforced Invert of the TCA

5.3 Machinery safety & equipment optimization

Given the steep gradient and continuous heavy-duty operations, safety concerns, particularly the risk of brake failures, were proactively reviewed and addressed. To mitigate such risk, advanced construction machinery was deployed, including 10-wheel tipper trucks and brand-new equipment, ensuring reliability and adherence to safety protocols. These measures collectively minimized risks and enhanced productivity throughout the TCA excavation process.

6 SUSTAINABILITY CONSIDERATIONS IN DESIGN & CONSTRUCTIO

Sustainability plays a key role in optimizing both environmental and economic performance throughout the design and construction of the portal slope, temporary construction adit, and associated tunnel systems. Efforts have been made to minimize resource consumption and reduce the carbon footprint.

For the portal slope, the design incorporated corrosion-resistant galvanized T25 steel bars and SFRC to enhance durability. This, alongside with optimized soil nail design spacing and groundwater management strategies, ensures long-term slope stability with reduced maintenance needs. The proposed subsoil drainage system, designed to control groundwater, was strategically placed to reduce the risk of slope failure due to water accumulation.

In tunnel construction, the design of concrete plugs at critical junctions was innovatively adapted to reduce material usage. By anchoring the plug to the surrounding rock mass instead of relying solely on friction at the interface of plug and surrounding rock, the required length of the concrete plug was reduced from 20m to 3m. This optimization significantly reduced concrete volume, reducing both material cost and the associated carbon emissions. Additionally, the use of higher-strength concrete (G40) further contributed to a more efficient, sustainable design.

The use of advanced structural program such as SAP2000 and finite element analysis ensured the most efficient and sustainable solutions for structural integrity, minimizing unnecessary material use and energy consumption during construction.

7 CONCLUSIONS

The Nenggiri Hydroelectric Project is a key step in Malaysia's shift towards renewable energy, showcasing innovative design and construction solutions. The project design, particularly portal slope, temporary construction adit (TCA), and tunnel plug, was optimized to address difficult site constraints, reduce construction time, while ensure safety and overall stability.

To stabilize the portal slope, soil nailing was used with calculated spacing, considering ground conditions, slope height, and gradient. This created a safe and stable structure with a high safety factor. The use of galvanized T25 steel and shotcrete facing further improved durability and long-term performance.

For the TCA, a combination of empirical, analytical, and numerical design approach was adopted. The design included the Q-System (NGI, 2015), analytical methods such as Longitudinal Displacement Profile (LDP) and Ground Reaction Curve (GRC) , and numerical modelling which resulted in a support system that fit the varying ground conditions of the project. Canopy tubes and steel arches provided essential support in soft and mixed ground during excavation. And finite element analysis using RS2 software helped assess tunnel stability and support measures for fractured rock, while validating the support system from empirical method, demonstrating the project's commitment to advanced design technologies.

These design choices reflect a comprehensive approach to geotechnical engineering, focusing on safety, efficiency, and resource optimization. The strategies not only support the project's timely completion but also contribute to Malaysia's energy goals and sustainable development. By integrating detailed planning, innovative engineering solutions, and advanced equipment, the project successfully overcame obstacles, setting a benchmark for managing complex excavation works in hydroelectric power projects.

REFERENCES

Barton, N., Lien, R. & Lunde, J., 1974. Engineering Classification of Rock Masses for The Design of Tunnel Support. Rock Mechanics, 6(4): 189-236.

Chin, J. T. Y., 2024. Design of Tunnels and Caverns in Rock. Hong Kong, Hong Kong Institute of Engineers.

Economy, M. o., 2023. National Energy Transition Map: Part 1. Ministry of Economy.

EOTA, E. O. f. T. A., 2010. EOTA TR029 Design of Bonded Anchors. European Organisation for Technical Assessment.

GEO, G. E. O., 2008. Geoguide 4: Guide to Cavern Engineering. Civil Engineering and Development Department (CEDD).

GEO, G. E. O., 2023. Geoguide 7: Guide to Soil Nail Design and Construction. Civil Engineering and Development Department (CEDD).

John, M. & Mattle, B., 2002. Design of Tube Umbrellas. Magazine of the Czech Tunnelling Committee and the Slovak Tunnelling Association ITA/AITES, 11: 4-11.

Malaysia, M. a. G. D., 2014. Geological Map of Peninsular Malaysia. 9 ed. The Director General of Minerals and Geoscience Malaysia.

NGI, 2015. Handbook of Using the Q-System. The Norwegian Geotechnical Institute.

Vlachopoulos, N. & Diederichs, M. S., 2009. Improved Longitudinal Displacement Profiles for Convergence Confinement Analysis of Deep Tunnel. Rock Mechanics and Rock Engineering, 42(2): 131-146.

Yasir Ali, n.d. Statement on construction methodology, practices and overall construction works. Protext Construction (M) Sdn Bhd, unpublished document.

High-Resolution Shallow Structure Constrained by Ambient Noise S-wave Tomography using Dense Linear Arrays—a case study in Northern Hong Kong

Guoxu Chen, Tao Xie, Zhiqian Liu, Liang Lyu, Hansong Pang, Boyang Su, Shupeng Chai, Andy Y. F. Leung, Yiqing Ni & Qi Zhao
The Hong Kong Polytechnic University, Hong Kong

Dennis C.S. Lau
AtkinsRéalis Asia Limited, Hong Kong

ABSTRACT

Conducting shallow structure tomography in Hong Kong is of great significance for engineering construction, urban underground space utilization, and geological disaster prevention. In this study, we deployed a linear array of 48 node seismometers at a construction site in northern Hong Kong and collected ambient noise data for about 2 days. The effects of different stacking durations and stacking methods on the noise cross-correlation function (NCF) were tested, indicating that the signal-to-noise ratio of NCF can be effectively improved by considering weighted methods during short-time stacking. We used the passive source-based multi-channel analysis of surface wave method (MASW) to extract the Rayleigh wave dispersion curve and inverted it to obtain the two-dimensional S-wave profile of the test site. Our results demonstrate that shallow S-wave tomography based on ambient noise data can quickly, safely and non-invasively constrain shallow structures, showing great potential for underground engineering applications.

1 INTRODUCTION

Reliable detection of shallow surface structures can provide important priori guidance for practical applications such as urban underground space development, geological disaster prevention, and engineering construction. Especially in Hong Kong, the vigorous promotion of the Northern Metropolis Development Strategy requires effective investigation of shallow structures in northern Hong Kong to ensure safe and efficient construction. In addition to the igneous rocks（including granite and volcanic rocks) formed during the large-scale volcanic eruptions of the Mesozoic era, the northeastern New Territories also feature extensive sedimentary rocks, which account for approximately 15% of land surface of Hong Kong (Sewell, 2000). This contributes to the complex geological settings of the Northern Metropolis, distinguishing it from other regions of Hong Kong. The presence of sedimentary rocks provides the necessary geological conditions for the development of karst cavity, and significant karst morphology has already been discovered in the Yuen Long area (Chan et al., 1994). Therefore, it is necessary to investigate and assess the shallow geological conditions of the Northern Metropolis using appropriate methods.

Seismic tomography is an effective method for multi-scale detection of underground structures (Aki et al., 1977; Park et al., 1999; Shapiro et al., 2005; Virieux & Operto, 2009). Seismic wave signals generated by natural earthquakes or artificial sources carry valuable information about the medium through which they pass. Through appropriate mathematical and physical modeling, the physical parameters of the underground medium (such as P-wave/S-wave velocity, attenuation, etc.) can be constrained by inversion to image two-dimensional or three-dimensional imaging of underground structures. At the engineering scale, shallow structures tens to hundreds of meters underground are particularly important because they are closely related to human activities and urban development. Commonly used shallow structure detection methods can be divided into body wave-based and surface wave-based methods. The body wave data collected based on active sources can be used for seismic reflection/refraction imaging and is widely used in geological surveys. On the other hand, the surface wave method is based on the inversion of surface wave signals collected by active or passive sources. The lateral resolution in shallow layers is relatively high. Besides, the tomographic S-wave velocity can be used to effectively evaluate site characterization (Foti et al., 2011). Therefore, it has been widely used in engineering practice. The traditional active source high-frequency surface wave method uses hammer, vibroseis truck, etc. to stimulate active sources to collect surface wave signals, and extracts the phase velocity dispersion curve for inversion through methods such as multi-channel analysis surface wave (MASW). This type of active source method offers high resolution in shallow part due to the high frequency of the data used (several Hz to tens of Hz), but it also faces the limitations of high equipment and labour costs and limited imaging depth.

Ambient noise tomography has developed rapidly in the past 20 years and has been successfully applied in the imaging of crust-mantle structures and shallow surface structures (Nakata & Snieder, 2012; Shapiro et al., 2005). Under the assumption that the noise source is uniformly distributed and the interior of the study area is homogeneous, previous studies have shown that the Green's function of the wave field can be generated from the cross-correlation function of the station pair (Kästle et al., 2016; Lobkis & Weaver, 2008). Therefore, by long-term stacking of ambient noise data segments, the empirical Green's function (EGF) with one seismometer station as a virtual source and the other station as a receiver can be obtained and used for surface wave tomography. The primary noise source in urban environments is traffic noise (with frequency bands ranging from a few to several tens of Hz). In specific areas, it also includes construction noise (such as from construction sites). Therefore, it is effective to utilize the ambient noise continuously generated by these urban noise sources to conduct shallow subsurface structure tomography. Compared to active source surface wave methods, this approach offers advantages such as lower cost, safety, and greater detection depth, considering that the noise source is generally lower in frequency than the active source. Combining ambient noise tomography with MASW allows for the effective extraction of phase velocity dispersion curves and S-wave imaging without relying on active sources (Cheng et al., 2016; Cheng et al., 2015).

In this study, we investigated the effects of different stacking durations and stacking methods on noise cross-correlation functions (NCFs) based on ambient noise data collected at a construction site. Based on the stacked NCFs, we extracted phase velocity dispersion curves through passive source MASW and inverted them to obtain a 2D S-wave profile of the test site. Our results demonstrate that this method can safely and effectively estimate the S-wave structure of the site, showing great potential for application in engineering construction in Hong Kong.

2 TEST SITE AND DATA COLLECTION

The test field is located at a construction site in Fanling, in the northern region of Hong Kong. For ambient noise data collection in this experiment, we utilized the ANT-1C (5 Hz) vertical component node seismometer manufactured by Earth Pulse Technologies (Wuxi) Co., Ltd. This equipment features an effective frequency range of 0.2 to 1000 Hz, fully covering the surface wave frequency band of interest (1-50 Hz). We deployed a nearly linear array consisting of 48 nodes (labelled sta01 to sta48, increasing from south to north along the survey line) with 2-meter spacing, forming a survey line approximately 94 meters in length (Figure 1b). Each node was set to a sampling rate of 1000 Hz. Besides, alongside the linear array of node seismometers, we have deployed a distributed acoustic sensing (DAS) cable to collect axial strain data (Figure 1c), which will be combined with the data from node seismometers in future studies. Data collection spanned approximately 42 hours, from 6:00 p.m. on March 22, 2025, to 12:00 a.m. on March 24, 2025 (Hong Kong time). There is a nearly parallel road (Ma Tak Road) on the east side of the survey line, where construction vehicles often travel back and forth on weekdays (Figure 1b). Approximately 1.2 km southwest of the survey line lies the East Rail Line (Figure 1a), contributing to the stable ambient noise sources we are aware of. In addition, vibrations that can be sensed by instruments, such as building construction and human activities, will also be recorded.

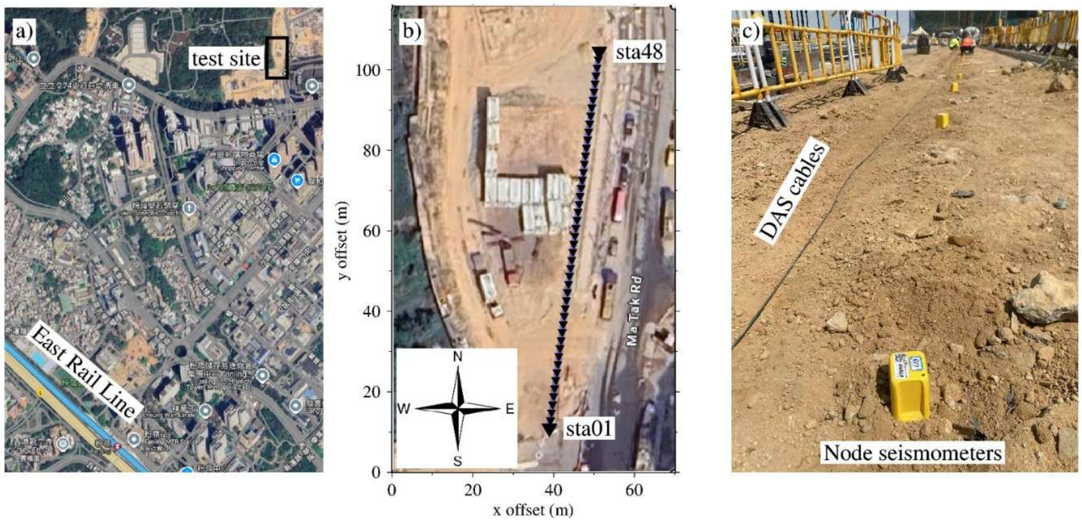

Figure 34: Test site and node seismometers used for data collection.

We can roughly divide the data collection periods into the following three types: daytime on rest days, nighttime on rest days, and daytime on working days. The collected data reveals a distinct day-night pattern in ambient noise signals, closely linked to human activities. Using sta01 as an example, we extracted one-hour segments of data for Power Spectral Density (PSD) analysis for each of these periods (Peterson, 1993). The specific durations are: 0:00 a.m. to 1:00 a.m. on March 23, 2025 for nighttime on rest days (Sunday), 12:00 a.m. to 1:00 p.m. on March 23, 2025 for daytime on rest days, and 9:00 a.m. to 10:00 a.m. on March 24, 2025 for daytime on working days (Monday). Next, we use PSD to estimate the energy distribution of different frequency components of the recorded ambient noise. For each ambient noise time series $s(t)$, the PSD can be calculated by

$$p(\omega) = \frac{1}{T}|U(\omega)|^2, \quad (1)$$

where T is the signal duration and $U(\omega)$ is the Fourier spectrum of $s(t)$, defined by $U(\omega) = \int_{-T/2}^{T/2} s(t)e^{-i\omega t}\mathrm{d}t$.

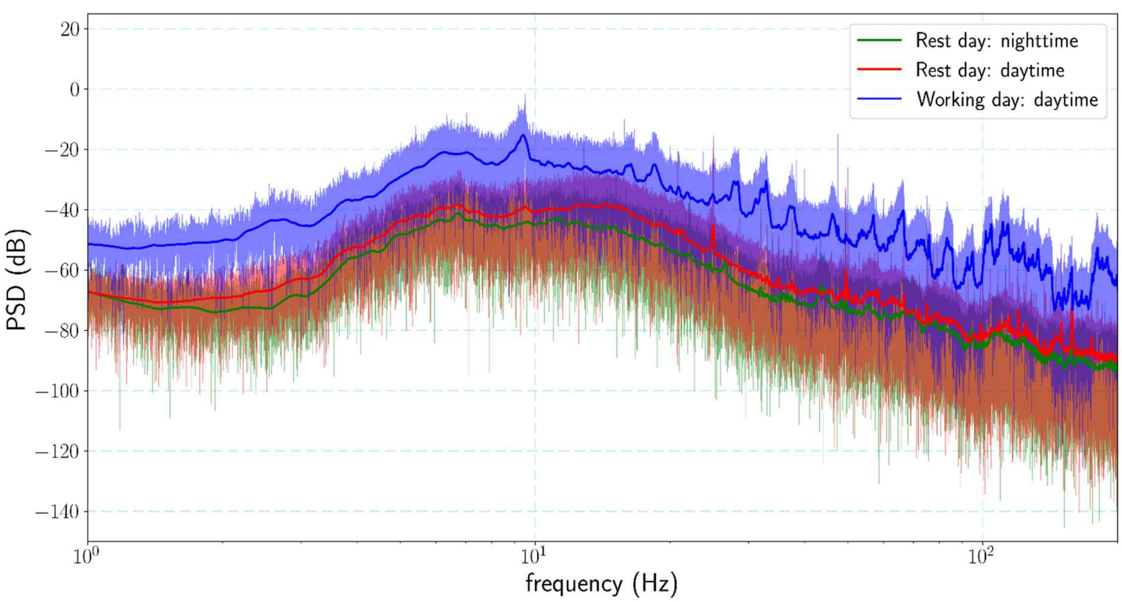

Figure 35: Power spectral density (PSD) of ambient noise signal at different periods.

Figure 2 illustrates the PSD estimates for three time periods. It can be found that in any frequency band, the noise energy during the daytime on working days is significantly higher than that on rest days, indicating that human activities such as traffic transportation and construction substantially enhance the signal energy. Additionally, the noise energy during the daytime is slightly higher than that at nighttime. In the traffic noise frequency band (a few to tens of Hz), the ambient noise records for all three time periods exhibit stronger energy.

3 DATA PROCESSING

3.1 Cross-correlation stacking

The extraction of cross-correlation functions (CCFs) from ambient noise data has advanced significantly over the past two decades, leading to the development of a well-established data processing workflow. For data preprocessing, we primarily follow the methodology outlined by Bensen et al. (2007), which is essential for subsequent cross-correlation stacking to obtain NCFs. For the raw data collected by each node seismometer, the following steps are executed sequentially to prepare the waveform for cross-correlation. Using the one-hour data recorded by sta01 as an example, we first remove the instrument response, mean, and linear trend to obtain the ground motion. The signal is then downsampled to 200 Hz, and a zero-phase second-order Butterworth band-pass filter with corner frequencies of 1-30 Hz is applied to produce the preprocessed waveform (Figure 3a). Next, time domain normalization is applied to the preprocessed waveform to mitigate the influence of irregular instrument noise and non-stationary noise sources near the station. Common time domain normalization techniques include running absolute mean normalization and one-bit normalization. We adopt the latter, which uses a sign function to normalize the time domain signal, due to its simplicity and effectiveness (Figure 3b). Finally, spectral whitening is performed, that is, normalization in the frequency domain, to smooth the noise spectrum and broaden the frequency band of the signal (Figure 3c-d). Figure 3e illustrates the time domain signal obtained by inverse Fourier transform after spectral whitening, which is ready for the next step of time domain cross-correlation.

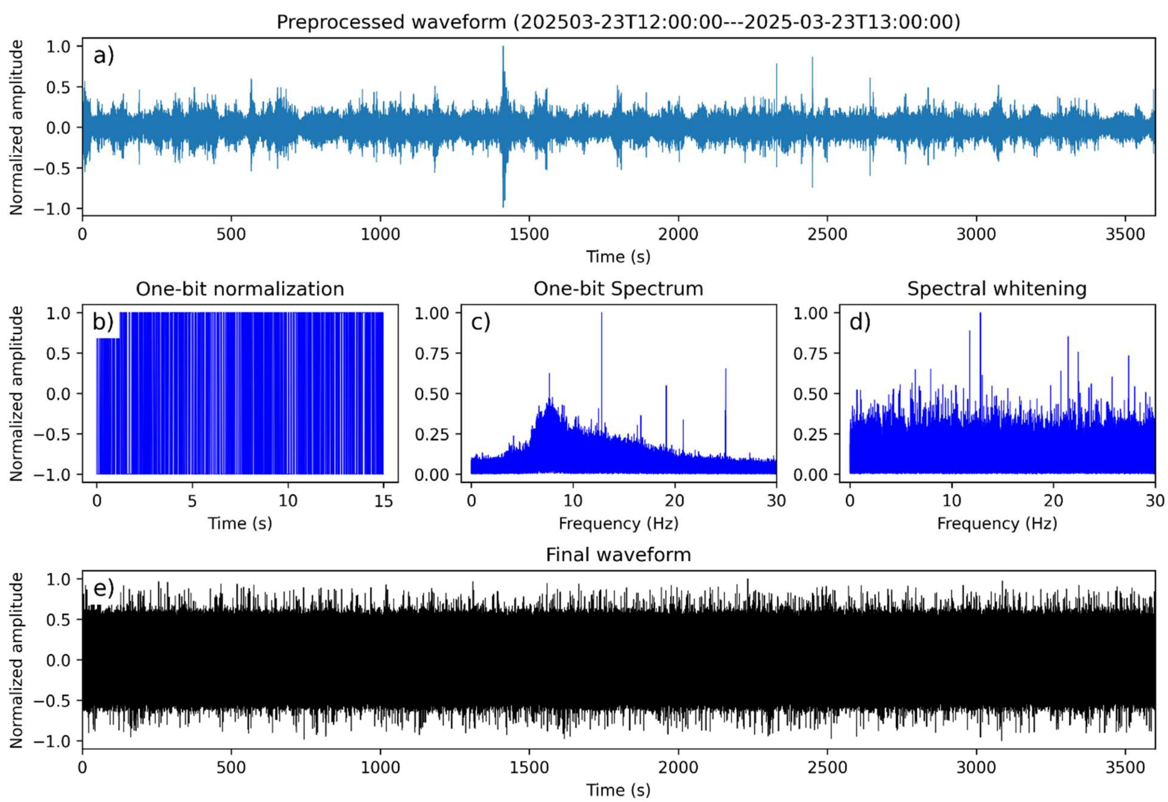

Figure 36: Data processing workflow for a single station.

NCFs are derived by stacking the CCFs of pre-processed waveform segments between station pairs. We evaluated the effects of different stacking durations and stacking methods on NCFs. For each station, we prepared signal lengths of 1 hour (from 2024-03-22T18:00:00Z to 2024-03-22T19:00:00Z) and 42 hours (from 2024-03-22T18:00:00Z to 2024-03-24T12:00:00Z) to test short-time stacking and long-time stacking, respectively. All signals are cut into segments of 2 seconds, resulting in 1,800 segments for short-term stacking and 75,600 segments for long-term stacking to obtain NCFs. We employed four different stacking methods: linear stacking, SNR-weighted stacking, phase-weighted stacking (PWS), and time-frequency domain phase-weighted stacking (tf-PWS), to evaluate the SNR of the generated NCFs. Linear stacking is a traditional approach that obtains NCFs by directly stacking all CCFs together. Typically, surface wave signals with high SNR can generally be obtained through long-time signal stacking. SNR-weighted stacking pre-screens CCFs by setting a threshold, retaining only those CCFs with SNR greater than the given threshold for stacking and rejecting CCFs below the threshold, and using the SNR of CCFs as a weight for signal stacking, thereby effectively improving the signal quality of the NCF (Cheng et al., 2015). PWS is a nonlinear stacking method based on the instantaneous phase. We first calculate the analytical signal $S(t)$ of the seismic signal $s(t)$ by Hilbert transform $S(t) = s(t) + iH\big(s(t)\big) = A(t)e^{i\Phi(t)}$, here $A(t)$ and $\Phi(t)$ are the amplitude and instantaneous phase of the signal, respectively. Then, by calculating the phase coherence of the signal, different weights are assigned to the original linear stacking to improve the SNR of the final signals (Schimmel & Paulssen, 1997). In detail, PWS stacked signals is formulated as

$$g(t) = \frac{1}{N}\sum_{j=1}^{N} s_j(t)\left(\frac{1}{N}\sum_{k=1}^{N} e^{i\Phi_k(t)}\right)^{v}, \qquad (1)$$

where N represents the total number of stacked segments, and v is the weight factor. PWS is equivalent to linear stacking if we take $v = 0$. Increasing v enhances the suppression of random noise but may lead to waveform distortion. Here, we follow the common practice of setting $v = 1$. tf-PWS is an extension of PWS (Schimmel et al., 2011) by transforming the signal into the time-frequency domain using the S transform, stacking the waveforms, and then applying the inverse S transform to obtain the final tf-PWS waveform (Schimmel et al., 2011).

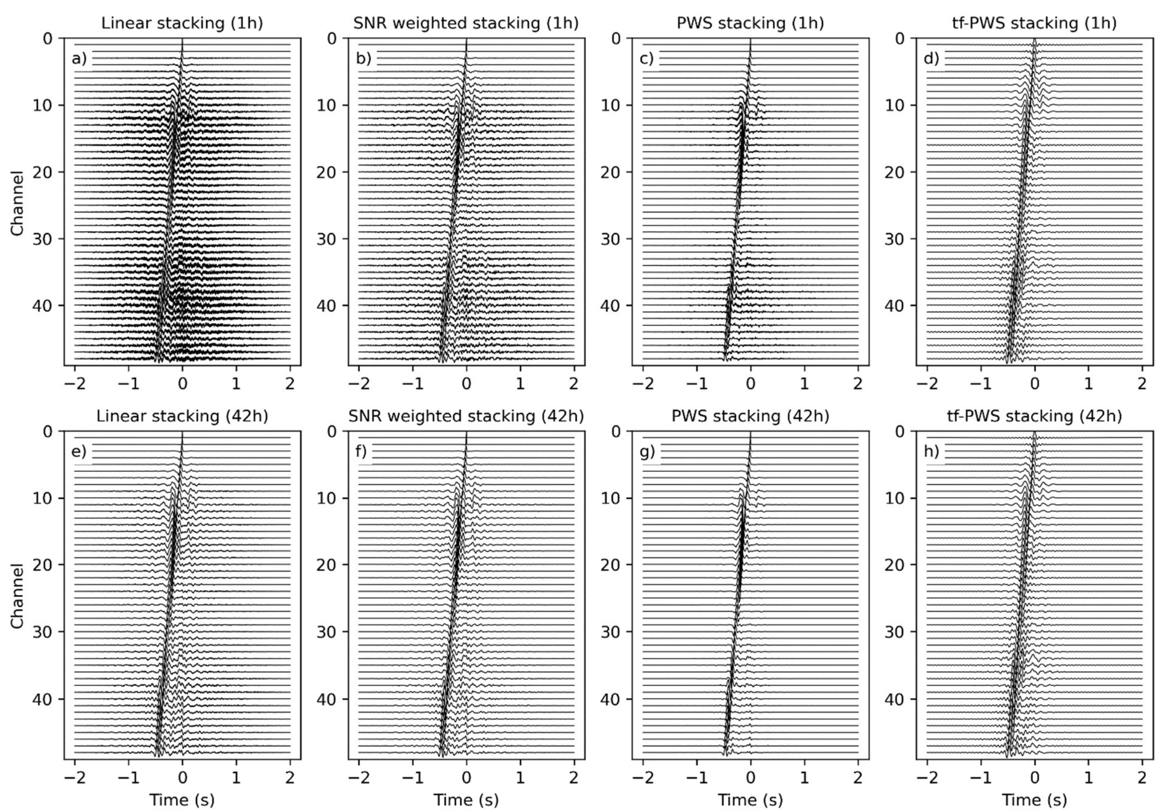

Figure 37: Comparison of the effects of stacking duration and method on NCFs.

Figure 4 illustrates the effects of stacking duration and method on NCFs, obtained by cross-correlating sta01 with all other stations using different stacking methods. We can clearly observe surface wave signals in nearly all stacking results. For short-time stacking (1h), the SNR of NCFs obtained based on linear stacking is slightly lower. Above mentioned weighting methods can all enhance the SNR of NCFs, with the PWS method showing the best improvement (Figure 4a-d). For long-time stacking (42h), almost all stacking methods reveal surface wave signals with high SNR considering that the data collection is long enough (Figure 4e-h). Therefore, SNR weighted method and tf-PWS method have limited improvement in signal quality. However, the improvement of waveform SNR by PWS can still be observed. This illustrates the necessity of weighted stacking when long-term acquisition is difficult to achieve (such as regulatory restrictions on experimental sites). It is worth mentioning that in an ideal situation (noise sources are evenly distributed), stacked NCFs should be symmetric about the origin. Here, regardless of stacking duration, signal energy is predominantly concentrated in the non-causal branch (negative half-axis in the time domain), indicating the presence of stable and uneven noise sources near the test site, particularly in the southern part of the survey line. We speculate that this may be the influence of the East Rail Line. In future studies, waveform beamforming analysis may be used to more accurately study the distribution of regional ambient noise sources.

3.2 Dispersion curve extraction

We employ the multi-channel analysis of surface wave (MASW) method based on the phase shift method (Park et al., 1999; Xia et al., 1999) to extract the Rayleigh surface wave dispersion. In the frequency domain, the phase difference of each channel is calculated according to the phase velocity and distance. The phase-corrected signals from each channel are then stacked to obtain the stacking energy corresponding to a specific frequency and phase velocity. The maximum value of the stacking energy of each frequency in the frequency-phase velocity map is taken as the corresponding phase velocity, thereby forming a dispersion curve. It reflects the S-wave velocity structure below the midpoint of the linear channels used (Cheng et al., 2015).

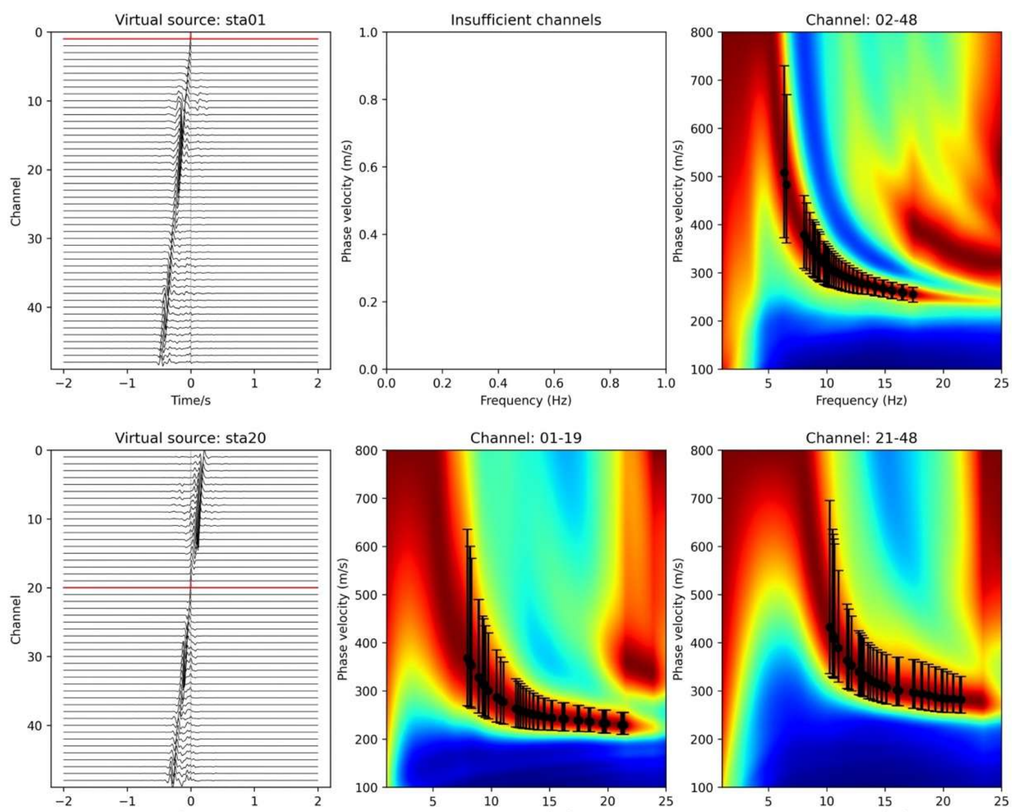

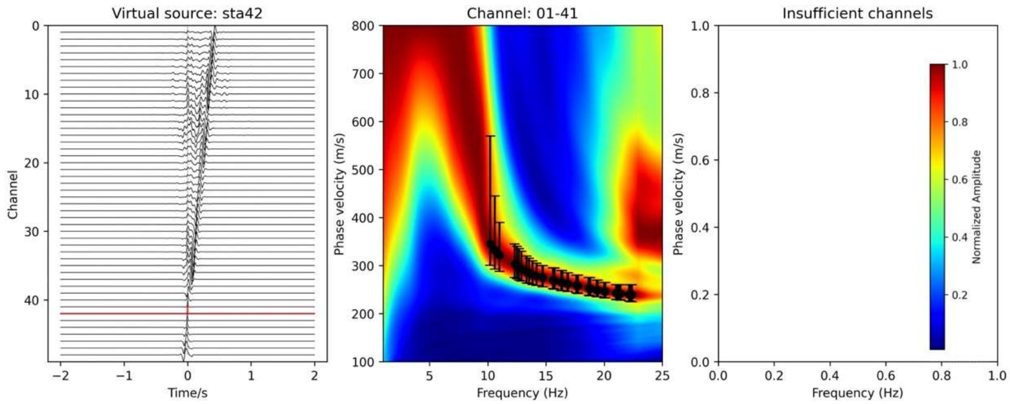

Figure 38：NCFs and corresponding surface wave dispersion spectrum imaging obtained using sta01, sta20, and sta41 as virtual sources

We use bidirectional shot mode to determine the subset of linear arrays used for dispersion curve extraction (Cheng et al., 2015). Specifically, except for sta01 and sta48, each station (virtual source) can be regarded as a bidirectional shot, allowing each virtual source to generate two common virtual source gathers (CVSGs) in addition to those at the two ends. For example, with sta20, the CVSG composed of sta01-sta19 on the left can be used for imaging the midpoint of this subarray, and the CVSG composed of sta21-sta48 on the right is similar. The resolution of the frequency-phase velocity map generally increases with the number of channels. Here, we empirically set the minimum number of channels that a CVSG should contain to 12, meaning that sta13-sta46 are used as bidirectional shots. The remaining stations serve as unidirectional virtual sources. Figure 5 displays the NCFs of the three stations as virtual sources and the dispersion curves extracted based on the phase shift method. Note that sta01 and sta41 are unidirectional virtual sources, which means they can only extract one dispersion curve each. In contrast, sta20 is considered a bidirectional shot, allowing its two subarrays on the left and right sides to be used for extracting dispersion curves separately.

4 SHEAR WAVE VELOCITY INVERSION

For each CVSG, the corresponding surface wave dispersion curve data can be inverted to characterize the one-dimensional S-wave structure at the array midpoint of the CVSG. Considering the total survey line length of about 94 m and the 2 m station spacing, we can approximately determine the structure of the middle part of the total survey line from 14 to 85m. By combining all the one-dimensional velocity models, we can construct a two-dimensional velocity profile, providing a more comprehensive analysis of the subsurface structure.

The inversion of dispersion curves is a typical ill-posed problem with strong nonlinearity and non-uniqueness. The target is to find a locally optimal S-wave velocity model that best fits the observed dispersion data. To achieve this, we utilize the Cooperative Particle Swarm Optimizer (CPSO) heuristic algorithm (Van den Bergh & Engelbrecht, 2004) to search for the best model. The objective function is considered as the root mean square error (RMSE) between the observed data and the synthetic data. Here the synthetic dispersion data is forward-modeled based on the fast delta matrix algorithms developed by Buchen and Ben-Hador (1996) , which can be implemented with open source software packages such as Computer Programs in Seismology (Herrmann, 2013) or disba (Luu, 2021). In addition to being mainly affected by the S-wave velocity, layer thickness, density and P-wave velocity also have an impact on dispersion data. Given the limited length of the linear array, the uncertainty associated with low-frequency data is relatively high (Figure 5). Therefore, we focus on using dispersion data with frequencies greater than 7.5 Hz for inversion, if available. Based on the extracted dispersion curve data, the phase velocity for 7.5 Hz is estimated to be approximately 400-500 m/s, corresponding to a wavelength of about 60 m. According to previous research, the detection depth for surface waves in shallow structure is typically about 0.5-0.67 times its wavelength, which limits the reliable inversion depth to 32 meters. The layer thickness is set to 4 m, which is twice the station spacing. The P-wave velocity and density are estimated by empirical formulas (Brocher, 2005) and are adjusted simultaneously with the update of the S-wave velocity model during the inversion.

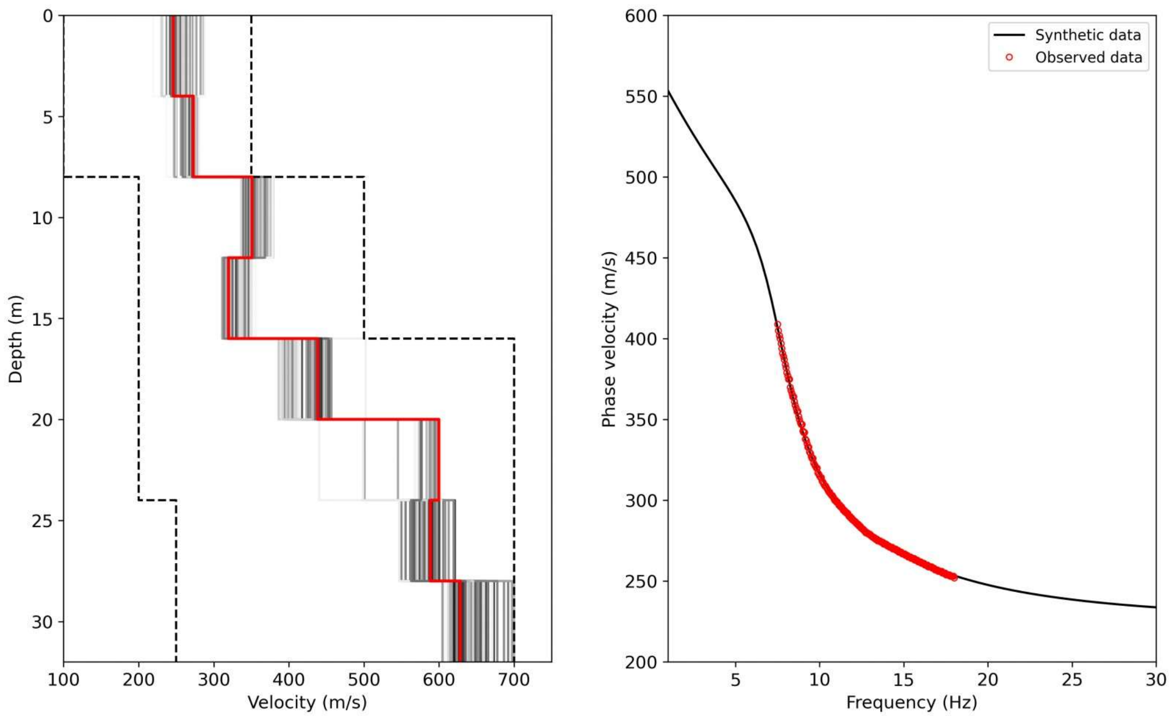

Figure 39: Dispersion curve inversion using sta01 as a virtual source

Figure 6 presents the inversion results of CVSG data (sta02-sta48) using sta01 as the virtual source. As previously mentioned, it reflects the midpoint of CVSG, that is, the one-dimensional S-wave structure located 50 meters from the start of the survey line. The black dashed lines give the upper and lower bounds of the search range for model parameters. Gray lines depict 500 models with the smallest objective function values, while the red line represents the final inversion result. Based on the obtained velocity model, we can calculate the synthetic dispersion curve, and find that it corresponds well to our observed data, which to some extent illustrates the reliability of the inversion. We apply similar processing to all CVSGs to obtain the corresponding one-dimensional S-wave models. The final 2D velocity profile is constructed by the combination of all 1D models (Figure 7). The final model shows significant lateral heterogeneity, especially in the left half of the section, where the dispersion data covers lower frequencies and thus has better constraints on the deeper structure. For the right part, the dispersion data coverage is generally above 10 Hz, and the dispersion data at different inversion points have similar distributions, thus showing a similar structure. In subsequent studies, we will combine core data and active source data for joint analysis to enhance the reliability of the results.

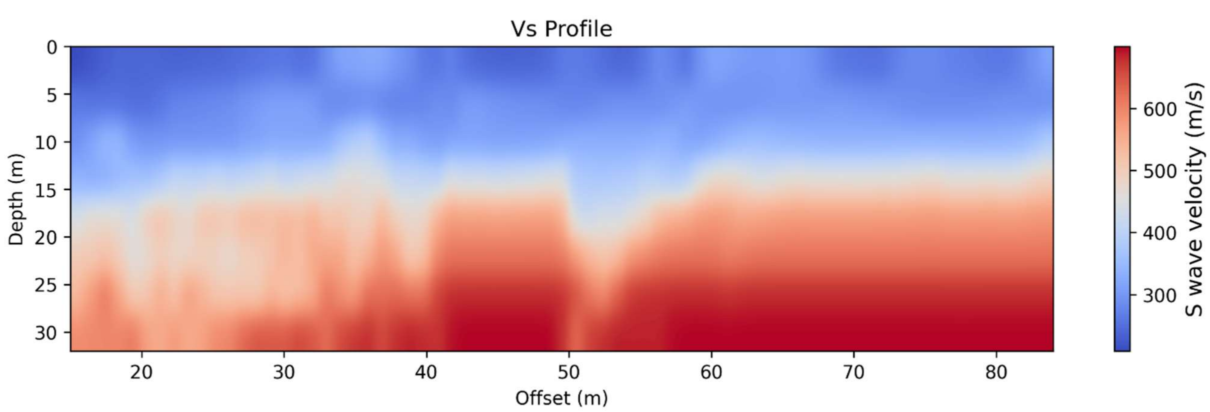

Figure 40: 2D S-wave velocity profile obtained based on one-dimensional inversion results

5 CONCLUSIONS AND FUTURE WORKS

5.1 Conclusions

We deployed a linear array of 48 seismic nodes at a construction site in northern Hong Kong to collect and analyze ambient noise data for nearly two days. The noise energy exhibited a marked difference between working days and rest days, demonstrating that the presence of local traffic noise and construction noise has a significant positive effect on data collection. Additionally, noise energy was slightly higher during the daytime compared to nighttime, reflecting variations in human activity across different time periods.

We investigated the effects of different stacking durations and stacking methods on the noise cross-correlation functions (NCFs). For short-term stacking (1h), employing different weighted stacking methods (SNR-weighted, PWS, tf-PWS) can effectively improve the signal-to-noise ratio of NCFs, among which PWS seems to have the best effect. For long-time stacking, even using conventional linear stacking can obtain high signal-to-noise ratio surface wave signals.

Utilizing the stacked NCFs, we extracted the dispersion curve using the phase shift method and employed the bidirectional shot mode to determine the inversion point for one-dimensional S-wave imaging. By integrating all the one-dimensional S-wave structures obtained through inversion, we built a 2D S-wave velocity profile at a depth of 30 meters in the middle part of the survey line. The velocity profile given by tomography can be combined with other engineering geophysical prospecting results such as drilling data and core data to provide useful support for engineering applications. Our results demonstrate the feasibility of shallow S-wave structural tomography based on ambient noise data in Hong Kong. It has a good application prospect in geotechnical engineering of Hong Kong and can provide reliable prior information for engineering construction and urban underground space utilization, especially considering its low cost, safety and non-intrusiveness.

5.2 Future works

In this field test, the site conditions allowed us to deploy a survey line of approximately 94 m, which posed challenges for low-frequency data acquisition and consequently limited the depth of tomography. In subsequent field tests, we will try to lay out longer survey lines in order to detect deep structural information (such as bedrock surface). In S-wave velocity structure inversion, we currently only use the fundamental mode of dispersion curve. However, some higher-order modes are visible in the surface wave dispersion spectrum (Figure 5), and we intend to incorporate them in subsequent studies to better constrain the velocity structure and enhance imaging depth. In addition, this research uses a linear node seismometer array with a station spacing of 2 m for data collection. Previous studies suggest that the inversion resolution is empirically comparable to the station spacing. By combining the current rapidly developing dense data acquisition technology (such as distributed acoustic sensing, DAS), the imaging resolution can be greatly improved. In future studies, we aim to combine node seismometers with data collected by DAS to improve the resolution of tomography.

ACKNOWLEDGEMENTS

We are very grateful to Civil Engineering and Development Department (CEDD) for providing the construction site for experiments. We thank Dr. Zhengyang Li from the Southern University of Science and Technology for helpful discussions.

REFERENCES

Aki, K., Christoffersson, A., & Husebye, E. S. (1977). Determination of the three-dimensional seismic structure of the lithosphere. *Journal of Geophysical Research*, *82*(2), 277-296.

Bensen, G. D., Ritzwoller, M. H., Barmin, M. P., Levshin, A. L., Lin, F., Moschetti, M. P., Shapiro, N. M., & Yang, Y. (2007). Processing seismic ambient noise data to obtain reliable broad-band surface wave dispersion measurements. *Geophysical Journal International*, *169*(3), 1239-1260. https://doi.org/10.1111/j.1365-246X.2007.03374.x

Brocher, T. M. (2005). Empirical relations between elastic wavespeeds and density in the Earth's crust. *Bulletin of the Seismological Society of America*, *95*(6), 2081-2092.
Buchen, P. W., & Ben-Hador, R. (1996). Free-mode surface-wave computations. *Geophysical Journal International*, *124*(3), 869-887. https://doi.org/10.1111/j.1365-246X.1996.tb05642.x
Chan, Y., Ho, K., & Pun, W. (1994). A new marble rock mass classification system for the interpretation of karst morphology in Hong Kong. *HKIE Transactions*, *1*(2), 1-12.
Cheng, F., Xia, J., Luo, Y., Xu, Z., Wang, L., Shen, C., Liu, R., Pan, Y., Mi, B., & Hu, Y. (2016). Multichannel analysis of passive surface waves based on crosscorrelations. *Geophysics*, *81*(5), EN57-EN66.
Cheng, F., Xia, J., Xu, Y., Xu, Z., & Pan, Y. (2015). A new passive seismic method based on seismic interferometry and multichannel analysis of surface waves. *Journal of Applied Geophysics*, *117*, 126-135. https://doi.org/https://doi.org/10.1016/j.jappgeo.2015.04.005
Foti, S., Parolai, S., Albarello, D., & Picozzi, M. (2011). Application of surface-wave methods for seismic site characterization. *Surveys in Geophysics*, *32*, 777-825.
Herrmann, R. B. (2013). Computer programs in seismology: An evolving tool for instruction and research. *Seismological Research Letters*, *84*(6), 1081-1088.
Kästle, E. D., Soomro, R., Weemstra, C., Boschi, L., & Meier, T. (2016). Two-receiver measurements of phase velocity: cross-validation of ambient-noise and earthquake-based observations. *Geophysical Journal International*, *207*(3), 1493-1512. https://doi.org/10.1093/gji/ggw341
Lobkis, O. I., & Weaver, R. L. (2008). On the emergence of the Green's function in the correlations of a diffuse field.
Luu, K. (2021). disba: Numba-accelerated computation of surface wave dispersion. *Zenodo, Dec*.
Nakata, N., & Snieder, R. (2012). Estimating near-surface shear wave velocities in Japan by applying seismic interferometry to KiK-net data. *Journal of Geophysical Research: Solid Earth*, *117*(B1). https://doi.org/https://doi.org/10.1029/2011JB008595
Park, C. B., Miller, R. D., & Xia, J. (1999). Multichannel analysis of surface waves. *Geophysics*, *64*(3), 800-808.
Peterson, J. R. (1993). *Observations and modeling of seismic background noise* (2331-1258).
Schimmel, M., & Paulssen, H. (1997). Noise reduction and detection of weak, coherent signals through phase-weighted stacks. *Geophysical Journal International*, *130*(2), 497-505. https://doi.org/10.1111/j.1365-246X.1997.tb05664.x
Schimmel, M., Stutzmann, E., & Gallart, J. (2011). Using instantaneous phase coherence for signal extraction from ambient noise data at a local to a global scale. *Geophysical Journal International*, *184*(1), 494-506. https://doi.org/10.1111/j.1365-246X.2010.04861.x
Sewell, R. (2000). *The pre-quaternary geology of Hong Kong*. Hong Kong Geological Survey, Geotechnical Engineering Office, Civil ….
Shapiro, N. M., Campillo, M., Stehly, L., & Ritzwoller, M. H. (2005). High-resolution surface-wave tomography from ambient seismic noise. *Science*, *307*(5715), 1615-1618. https://doi.org/10.1126/science.1108339
Van den Bergh, F., & Engelbrecht, A. P. (2004). A cooperative approach to particle swarm optimization. *IEEE transactions on evolutionary computation*, *8*(3), 225-239.
Virieux, J., & Operto, S. (2009). An overview of full-waveform inversion in exploration geophysics. *Geophysics*, *74*(6), WCC1-WCC26.
Xia, J., Miller, R. D., & Park, C. B. (1999). Estimation of near-surface shear-wave velocity by inversion of Rayleigh waves. *Geophysics*, *64*(3), 691-700.

Application of Precast SFRC Tunnel Segment Lining in HK and its Benefit

Clayton Y. K. Chan, Brian K.L. Ieong, Terry C.W. Ma & Joe F.K. Kun
AECOM Asia Company Limited
Keith K.F. Wong, Johnny S.C. Lau, Sebastien L. Chen,
Ruby S. P. Chan & Harry H.C. Wong
Dragages Hong Kong Limited & Bouygues Travaux Publics
Albert K.H. Kwan & Alex W. K.Wong
Independent Reviewers

ABSTRACT

Precast concrete tunnel segment lining reinforced with conventional steel rebar have been generally used with the Tunnel Boring Machine (TBM) since 1950s. As ample concrete cover needs to be provided to protect the steel reinforcement tunnel lining against corrosion and fire, concrete cover would be easily damaged during the segment handling, erection and TBM thrusting. This will induce different degrees of damaging to the precast tunnel segment lining which affects the long-term durability performance of the permanent lining and involves substantial maintenance to the tunnel structure. To tackle the subjected problems, steel fibres are adopted to replace the conventional steel reinforcement in precast concrete segment. The adoption of precast steel fibres reinforced concrete (SFRC) tunnel segment lining increased significantly in tunnel industry since 2000 with the increase on the understanding of SFRC behavior and enhancement on the quality assurance on production.

Until now there is no precedent case project using precast SFRC segments as the permanent tunnel lining in Hong Kong, but Dragages Hong Kong (DHK) has stepped forward as a pioneer contractor to promote the adoption of precast SFRC segment as the temporary tunnel lining for pilot tunnel in two highway tunnel projects which can provide the foundation on expanding the usage of precast SFRC segment to the permanent tunnel lining in the near future.

This paper is to present the general mechanical behavior and design principles on SFRC and discuss in detail for the appropriateness and benefit on the adoption of SFRC for the permanent precast concrete tunnel segment lining in Hong Kong. This paper also shares the local experience on using precast SFRC segments in HK.

1 INTRODUCTION

In the construction industry, people are understanding plain concrete has inherent deficiencies such as low tensile strength, low post cracking capacity, and brittleness. The weakness in tension can be overcome by the use of conventional steel reinforcement and to some extent by the inclusion of a sufficient dosage of certain fibres. The concept of using fibres in order to reinforce the concrete matrices weak in tension is more than 4500 years old. Steel fibres mixed into the concrete can provide an alternative to the provision of conventional steel bars or welded fabric in some applications. The concept has been in existence for many years (the first patent was applied for in 1874) and it has been used in a limited range of applications: among the first major uses was the patching of bomb craters in runways during World War II. However, it was during the 1970s that commercial use of this material began to gather momentum, particularly in Europe, Japan and the USA. Today, major applications for fibre-reinforced concrete include ground-supported and pile-supported floors, external paved areas, sprayed concrete, composite slabs on steel decking and precast elements, industrial floor slabs, shotcrete and prefabricated concrete products and full replacement of the conventional reinforcing cages for precast tunnel segments.

Depending upon the use and the strength requirement to achieve, steel fibres have different shape and size as shown in Plate 1.

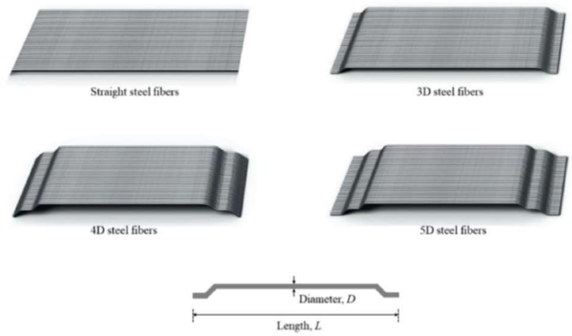

Fig. 1—Steel fibers with different end hooks.

Plate 1: Steel fibres with different end hooks and straight end (courtesy of Kwan et al. (2024))

End hooks of steel fibres provide a stronger bridging force across the concrete matrix in SFRC. Previous research findings including Kwan et al. (2024) confirmed that the improvement of the concrete flexural behavior (toughness and flexural strength) exhibited by hooked end steel fibres was better than that of straight steel fibres because the end hooks of steel fibres provide a better anchorage at the fibre ends and hence stronger bridging force across the concrete matrix in SFRC. A properly designed concrete mix is essential for avoiding fiber balling. To prevent the potential of fiber balling formed before mixing with concrete which will affect the fibre distribution in concrete, so glued fibres technology has been developed by blinding the fibres into bundles with the glue. Then the glue will be dissolved in water during concrete mixing, so the fibre can spread evenly throughout the concrete matrix. With this arrangement, balling of fibres can effectively be avoided and a homogenously mix of high performing steel fiber reinforced concrete can be achieved.

Table 1 below shows the essential characteristics and properties of a commonly-used glued hooked-end steel fibres:

Type	Hard-drawn wire and ungalvanized	BS EN 14889-1: 2006
Length	60 mm +/- 10%	BS EN 14889-1: 2006
Diameter	0.75 mm +/- 10%	BS EN 14889-1: 2006
Aspect ratio (length/dia.)	80 +/- 15%	BS EN 14889-1: 2006
Nominal Tensile strength	2,200 MPa +/- 15%	BS EN 14889-1: 2006
Bending	Withstand 3.2 mm diameter pin to an angle of 90° at temperatures not less than 16°C without breaking	ASTM A820

Table 1: Essential characteristics and properties of a commonly-used glued hooked-end steel fibres

2 GENERAL MECHANICAL BEHAVIOUR OF STEEL FIBRES IN CONCRETE

SFRC is a composite material that incorporates steel fibres well distributing into the concrete matrix (see Plate 2) to enhance its mechanical properties such as the flexural tensile strength and toughness of concrete (see Plate 3) thus creating the necessitate flexural bending capacity and also minimizing the potential damage to the concrete covers. Moreover, the inclusion of steel fibres could help reducing early-age thermal cracking, dry shrinkage cracking and the risk of spalling when exposing to fire incident.

Plate 2 - Steel fibres in wet concrete

Plate 3 - Steel fibres exposed in a cut concrete section

The general mechanical behavior of SFRC is influenced by the type, shape, size, dosage and distribution of steel fibres within the concrete matrix. The key aspects of its mechanical behavior include the following enhanced characteristics: tensile strength, flexural tensile strength, crack resistance, ductility and post-crack tensile strength. Even after the initial cracking, SFRC maintains its load-carrying capacity due to the bridging action of the steel fibres (see Plate 4). This post-crack behavior is characterized by a gradual reduction in load rather than a sudden failure, providing a safer and more predictable performance.

Plate 4:Post-crack behaviour of SFRC

3 ADVANTAGES OF USING SFRC

3.1 General advantages of using SFRC

The general advantages of using SFRC are summarized in Table 2 below:

Homogeneous distribution	Steel fibres spread close to the surface, ensure excellent reinforcement at the joints of segments
Multidirectional reinforcement	Steel fibres provide resistance to stress in all directions
Increased load bearing capacity	Steel fibres provide substantial increase in load capacity to the first crack and ultimate load at the joints
High impact resistance	The absorbed energy by the steel fibre reinforced concrete during impact is many times greater than the energy absorption of plain concrete
Excellent control of shrinkage cracks	Large number of steel fibres in the concrete ensure good control of shrinkage cracks
Best durability solution available	Several research investigations have shown that the durability of SFRC under chloride exposure is superior to RC

Table 2: Advantages of using SFRC (BEKAERT)

3.2 Advantages of using SFRC on precast segmental tunnel linings

During the installation of precast segmental tunnel lining through TBM tunnelling advancement, the TBM thrusting rams in the tail shield exert a longitudinal force on the circumferential joint of precast segments to ensure them be stayed in contact with the previous ring to ensure the water gasket still in compression before the annulus grouting is applied to the gap between the ground and segment. Since the hydraulic rams impose loads concentrated over small bearing surfaces, these loads in turn redistributed within the segment body. This concentrated load redistribution leads to transverse tensile stress, also known as bursting or splitting stress at the segment joint. Furthermore, spalling tensile stresses are generated between the adjacent jack pads along the circumferential joint. As ample concrete cover needs to protect the steel reinforcement of conventional reinforced concrete tunnel lining against corrosion and fire, concrete cover would be easily damaged during the TBM tunnel construction (Plate 5) and be deteriorate in long-term durability. The thrust loads acting in the cross section of the tunnel induce spalling and bursting stresses in the circumferential joints of the tunnel segments (see Plate 6).

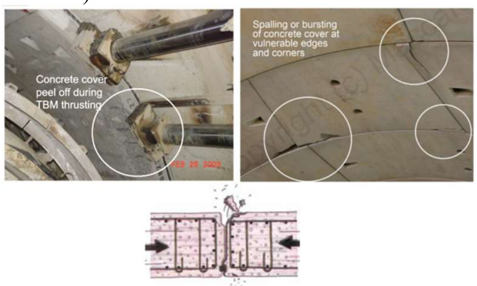

Plate 5: Damage of concrete caused by jacking

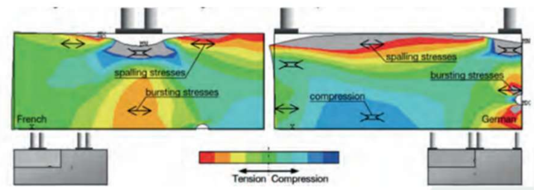

Plate 6: Bursting stresses due to jacking (ITA)

Compared to conventional reinforced concrete tunnel segments, no concrete cover is required for SFRC tunnel segments. The use of steel fibres instead of steel bar reinforcement can be an advantageous alternative. Steel fibres are uniformly dispersed through the segment and the minimum concrete cover required to prevent corrosion is irrelevant. This bursting stress due to thrusting force on segment is resisted by the tensile strength of SFRC which can help to prevent damages to the concrete and minimize the cracks due to bursting or splitting stresses.

Even though steel fibres can be exposed on the surface of tunnel linings (see Plate 7), concrete spalling is not anticipated to occur since the fibres are small in diameter and discrete, and so the expansion force due to corrosion causing concrete spalling is negligible. In addition, the steel fibres are surrounded by the concrete matrix which is alkaline basis, so the steel fibres are not easy to be corroded and spread to other fibres. On the other hand, concrete spalling due to corrosion of steel reinforcement was commonly observed on the surface of conventional precast R.C. tunnel segments (see Plate 8).

Plate 7:Steel fibres exposed on surface of tunnel linings

Plate 8:Concrete spalling caused by corrosion

When spalling occurs, a conventional R.C. tunnel segment has to be repaired or even replaced for obvious reasons of durability. This however delays the tunnel construction progress and leads to a high long term maintenance cost.

In addition, steel fiber reinforcement is present in the cover zone where having the tensile resistance in resisting the impact loads during segment handling and erection. This will significantly reduce the potential on the tunnel segment damage when comparing with the conventional reinforced segment.

The permanent loading situation under normal circumstances (including self-weight, surcharge, vertical and horizontal ground pressure and water pressure, see Figure 1) of circular, segmental tunnel linings is typically characterized by the dominance of hoop forces combined with relatively small bending moments due to the confined pressure from the ground, surcharge and water around the tunnel.

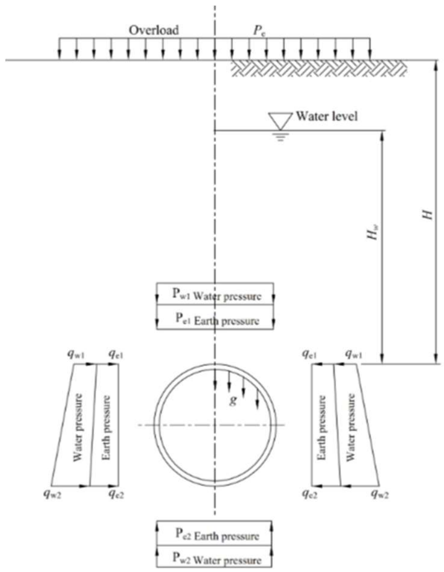

Figure 1: Permanent loadings of designing tunnels

If high bending moment is generated by high accidental loadings (e.g. earthquake) or insufficient hoop force due to lacking of confinement pressure under shallow ground condition, the use of steel fibres alone may not be sufficient and a hybrid of conventional steel reinforcement and SFRC is required. However, the seismic hazard in Hong Kong is much lower than places like Japan, Taiwan and the western USA where lie close or within the Earth's more seismically active zones along crustal plate boundaries, and the seismicity of Hong Kong is low to moderate. Therefore, in Hong Kong, the bending moment acting on tunnel linings induced by earthquake loading is not high and so SFRC to replace steel reinforcement cage (Plate 9) may represent a cost-effective alternative to the precast concrete tunnel segments.

Plate 9: Steel reinforcement cage of tunnel segment

4 DESIGN PRINCIPLE OF SFRC FOR PRECAST CONCRETE TUNNEL LININGS

The fundamental design principle of SFRC structural elements is based on its residual flexural tensile strength after cracking (see Figure 2). The steel fibres control the crack by transmitting stress through the bond at the deformed anchors at both fibre ends to the concrete matrix, thereby providing resistance to the crack widening and fracturing process. Once the maximum bond strength with the concrete is reached, the pull-out action takes full effect.

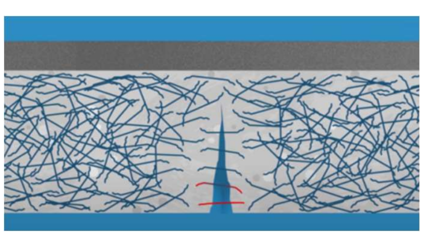

Figure 2: Steel fibres can prevent crack widening

RILEM TC162-TDF "Test and Design Method for SFRC" published by the International Union of Laboratories and Experts in Construction Materials, Systems and Structures **(RILEM)** has been widely used for the design of tunnel linings. AECOM and Dragages had experience in the design and construction of SFRC tunnel lining in number of oversea projects based on RILEM which provides comprehensive guidelines for testing and designing SFRC to ensure its effective use in construction. RILEM recommends determining the flexural tensile strength of SFRC section through three-point beam (550 mm x 150 mm x 150 mm) bending test in accordance with BS EN 14651 (see Plate 10). The flexural tensile behaviour of SFRC is evaluated in terms of residual flexural tensile strength values, determined from the load-crack mouth opening displacement (CMOD) curve (see Figure 2), obtained by applying a centre-point load on a simply supported notched beam. Typical result of three-point beam bending test is shown in Figure 3.

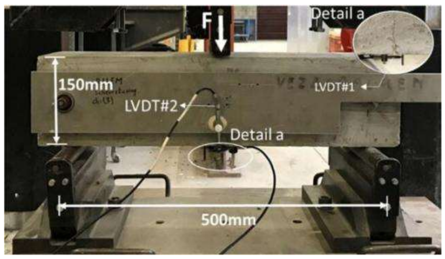

Plate 10: Set-up of three-point beam bending test

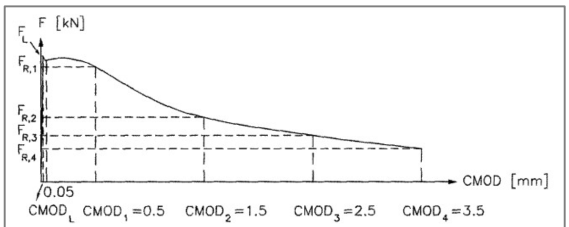

Fig. 1 - Load – CMOD diagram.

Figure 2: Load-CMOD diagram (RILEM)

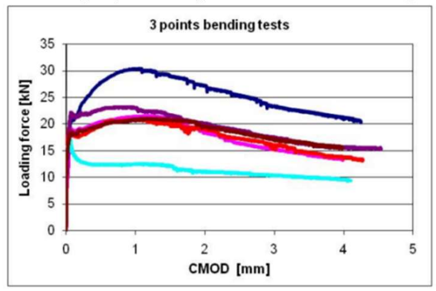

Figure 3: Typical results of beam bending test

The forces F_L, $F_{R,1}$ and $F_{R,4}$ are recorded respectively at defined Limit of Proportionality (LOP) andCMOD values of 0.5 mm and 3.5 mm. Based on the obtained force values, the residual flexural tensile strengths, $f_{R,1}$ and $f_{R,4}$, are calculated based on the following equation of RILEM (Figure 4).

$$f_{R,i} = \frac{3\,F_{R,i}\,L}{2\,b\,h_{sp}^2} \quad (N/mm^2) \qquad (7)$$

where:
b = width of the specimen (mm)
h_{sp} = distance between tip of the notch and top of cross section (mm)
L = span of the specimen (mm)

Figure 4: Calculation for residual flexural tensile strength (RILEM)

Hardened SFRC is classified by using two parameters that are determined by the residual flexural strengths $f_{R,1}$ and $f_{R,4}$. The first parameter $FL_{0.5}$ is given by the value of $f_{R,1}$ reduced to the nearest multiple of 0.5 MPa, and can vary between 1 and 6 MPa. The second parameter $FL_{3.5}$ is given by the value of $f_{R,4}$ reduced to the nearest multiple of 0.5 MPa, and can vary between 0 and 4 MPa. These two parameters denote the minimum guaranteed characteristic residual strengths at CMOD values of 0.5 and 3.5 mm, respectively. Subsequent to the tensile stress block developed in the stress distribution along the section, stress parameters σ_1, σ_2, and σ_3 can be derived as per RILEM (Figure 5).

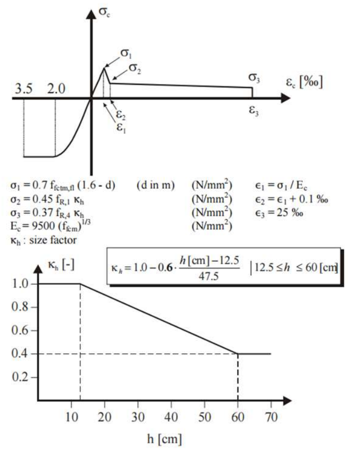

Figure 5: Stress-strain diagram (*RILEM)*

The compression and tension resistance of SFRC following the moment thrust interaction (M-N) diagram for SFRC (see Figure 6) can be derived in accordance with the simplified rectangular stress-strain curve and the HK Concrete Code. The calculation of moment capacity in SFRC uses the same principles as conventional reinforced concrete. The partial material factor, γc, adopted in SFRC is 1.5 for both flexural and tensile failures. The simplified rectangular stress-strain curve is shown in Figure 7 below:

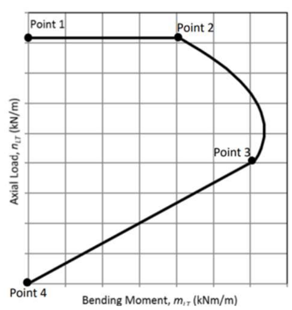

Figure 6: M-N curve for SFRC design

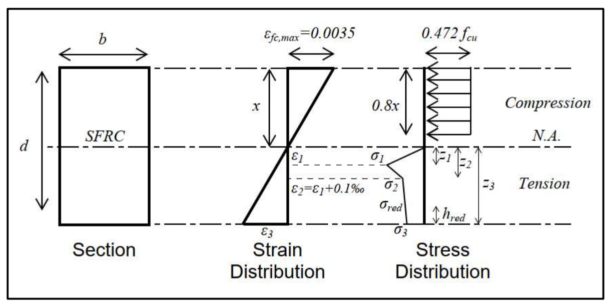

Figure 7: Simplified stress block for SFRC design

Comparison of the stress-strain behaviour (i.e. stress block) between conventional reinforced concrete and SFRC sections is given in Figure 8 below:

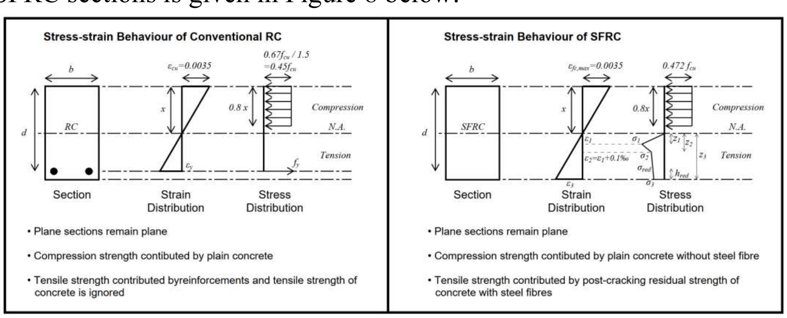

Figure 8: Comparison of stress block between RC and SFRC

For SFRC, the tensile stress block is developed using data obtained from a 3-point bending test for the tensile performance, while the tensile stress block of conventional reinforced concrete is solely based on the tensile strength of the main reinforcing bars.

5 OVERSEAS PROJECTS USING PRECAST SFRC SEGMENTAL TUNNEL LINING

Traditionally, tunnel segments for shield excavated tunnels have utilized conventional steel reinforcement. Since early 2000s, there has been a growing tendency to consider steel fibres to replace steel reinforcement in precast concrete tunnel linings. Therefore SFRC was used for segmental linings on a range of tunnelling projects. They mostly related to tunnels with smaller profiles (water, gas or heat supply tunnels) and, in some cases, to metro sections (London, Barcelona, Napoli). The most extensive application of SFRC segments was experienced at tunnels for the high speed rail link between Paris and London (the Channel Tunnel Rail Link - CTRL), where 2 x 24 km of single-track tunnels with the lining consisting of precast SFRC segments without using conventional steel reinforcement cage were constructed by means of full-face TBM.

The latest completed SFRC tunnel was the Grand Paris Express subway in France that supporting the capital hosting the 2024 Summer Olympic Games (https://www.tunnel-online.info). In that tunnel project, Olympic Village and the Press Village were set up. Saint Denis, both have an underground railway station for metro Line 16.1 of the Grand Paris Express, including segments made of SFRC over a length of 12 km. 6000 tunnel rings with a diameters of 8700/9500mm were installed. The achievements in using SFRC for the project included the following:

- Firstly, comparing the 40 kg/m^3 steel fibres against the 85 kg/m^3 of steel reinforcement yielded a potential material saving of more than 50% (ITATech Report No. 7 recommends a steel fibre dosage of 30 to 50 kg/m^3, a range commonly used in SFRC tunnel projects worldwide).
- Secondly, the reduction of steel quantity required also provided a corresponding reduction in transport-related CO_2 emissions. One truckload delivery of fibres to the manufacturing plant allows the production of nearly 185 precast concrete tunnel segments, compared with 60 equivalent segments per truckload of conventional steel bar reinforcement; &
- Furthermore, SFRC reduced the quantities of concrete by 2 cm to 3 cm in segment thickness

Past research found that, in a typical metro tunnel of 10 km length, SFRC tunnel segments can save up to 5000 tonnes of steel reinforcement and 10,000 tonnes of CO_2 can be reduced.

6 SHARING OF LOCAL EXPERIENCE IN SFRC TUNNEL LININGS

SFRC precast tunnel linings were installed by Dragages in Liantang/Heung Yuen Wai Boundary Control Point Site Formation and Infrastructure Works Contract 2 and Central Kowloon Route projects of Highways Department in Hong Kong. These were installed in medium to large diameter pilot bored tunnels section for approx. 1 km in total through faulted, mixed and rock conditions. In both projects, SFRC was adopted as temporary lining as part of an early initiative to evaluate its suitability under Hong Kong's underground construction environment. These pilot applications aimed to address common issues observed in conventional RC segments, particularly spalling and cracking under handling and TBM thrust jacking.

Detailed information of the 2 SFRC temporary tunnels is summarized in Table 2 below.

	Liantang Project	***Central Kowloon Route Project***
Tunnel length with SFRC segment	*Approx. 314 m*	*Approx. 710 m*
Tunnel Internal Diameter	*12600 mm*	*6170 mm*
Lining Thickness	*500 mm*	*330 mm*
Nominal Ring Width	*1600 mm*	*1500 mm*
Concrete Grade	*Grade 50*	*Grade 50*
Steel Fibre Content	*35 kg/m3*	*45 kg/m3*
Characteristic Residual Flexural Strength, f_{R4}	*2.5 MPa*	*3.4 MPa*
Characteristic Tensile Splitting Strength	*3.8 MPa*	*4.8 MPa*
Encountered Ground Conditions	*Rock and mixed ground with fault zone*	*Rock with fault zone*

Table 2: Summary table of SFRC tunnel lining constructed in Liantang and Central Kowloon Route projects

Geological profile of the 2 tunnels is shown in Plates 11 and 12 below.

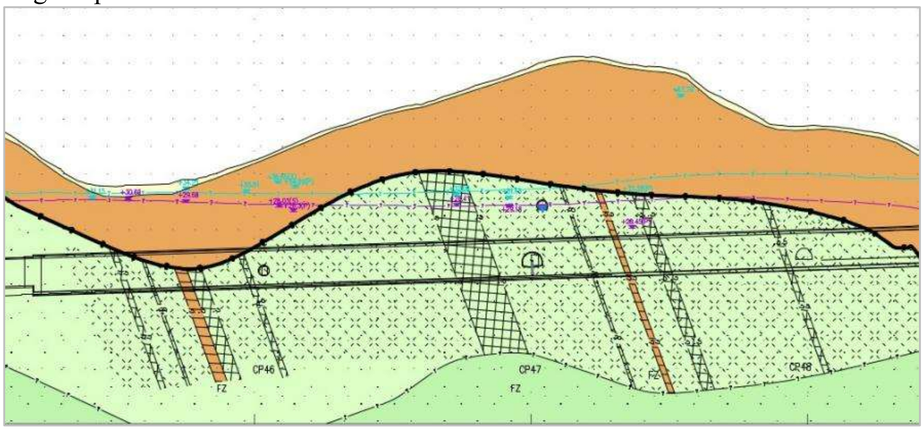

Plate 11: Geological profile of SFRC tunnel lining section in Liantang Project

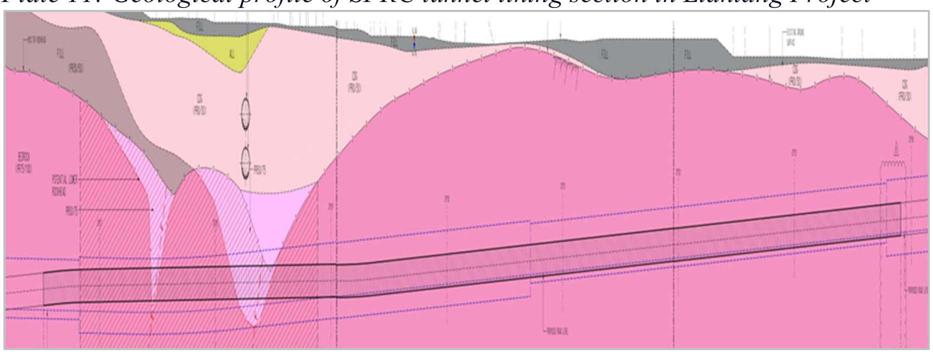

Plate 12: Geological profile of SFRC tunnel lining section in Central Kowloon Route Project

Segment performance was benchmarked against RC segments. key findings included reduced cracking, improved handling resilience and no spalling observed under TBM thrusting force (X. Monin. et al.). The adoption of steel fibre reinforcement in replacing steel rebar reinforcement accelerated segment production, and reduced labour intensity and optimized steel consumption. This full-scale application served as a technical validation step to assess SFRC performance under real TBM tunnelling conditions in Hong Kong. The experience and performance data collected from these two tunnelling projects provided confidence in the use of SFRC for tunnel linings and established a robust local reference to support further investigation into its permanent application.

While these pilots demonstrated technical feasibility, several challenges must be addressed for broader adoption in permanent tunnel linings:

- Code Compliance: Local construction standards do not yet fully address SFRC design based on residual flexural tensile strength and associated test methods.
- Industry familiarity: Wider understanding of SFRC's characteristics, performance behaviour, and quality assurance requirements are required across approval authorities, clients, designer and precast subcontractors.
- Fire and long-term performance: Further validation is required to confirm SFRC behaviour under fire exposure, and to assess long-term durability under local groundwater, load and environmental conditions.

7 CONCLUSION

In this paper, the benefits of adopting SFRC for precast tunnel segments are discussed. The experience gained in using SFRC for overseas tunnel projects and two pilot local tunnels of short sections with temporary SFRC tunnel linings were shared.

SFRC offers significant potential for tunnel construction in Hong Kong. Its enhanced tensile strength, crack resistance, and ductility are particularly beneficial make it ideal for the city's geotechnically challenging conditions. SFRC minimizes maintenance needs, reduce carbon emission, increases structural resilience, and effectively accommodates dynamic loads, ensuring safer, long-lasting tunnel infrastructure. Additionally, SFRC can effectively withstand dynamic loads and seismic activities, ensuring long-lasting and safer tunnel structures. Also, the use of SFRC can significantly reduce the material and labour cost of producing precast tunnel segments, and speed up the casting process. By incorporating SFRC, Hong Kong can achieve more efficient and sustainable tunnel construction, meeting the city's growing transportation and infrastructure demands.

AECOM and Dragages are collaborating together to implement the adoption of SFRC permanent precast segments for the first time in a tunnelling project of Hong Kong and hopefully that project will be completed successfully and have a review on the performance which we can share the experience gained later.

REFERENCES

S. H. Chu, L. Sneed, D. Y. Yoo & A. K. H. Kwan (2024) - Hooking Effect on Flexural Strength and Toughness of Steel Fiber-Reinforced Concrete Beams, *ACI Materials Journal*, November 2024

“Tunnelling Applications: Concrete Segment Reinforcement” published by BEKAERT

RILEM TC 162-TDF (2003):’Test and design methods for steel fibre and reinforced concrete’

ITAtech Report No. 7 (APRIL 2016): ITATECH GUIDANCE FOR PRECAST FIBRE REINFORCED CONCRETE SEGMENTS: VOL. 1: DESIGN ASPSECTS, published by The International Tunnelling and Underground Space Association

https://www.tunnel-online.info :Grand Paris Express: Steel Fibre Reinforced Concrete Tunnel Segments for the Metro Line 16 - tunnel

X. Monin, R.B. Storry, G. Steiner, A. Maxwell, J. Zhu & S. Sparrow (2019) - Full scale testing of rebar and SFRC segmental lining using independent and wireless instrumentation systems, *The HKIE Geotechnical Division Annual Seminar 2019*

Jet Grout Slab to Reduce Wall Movements Caused by Excavation

L.W. Wong
SMEC Asia Limited, Hong Kong

ABSTRACT

Two-dimensional numerical analysis has been conducted on an excavation case in soft ground using jet grout slab to reduce wall deflections. The Young's moduli of the jet grout slab were assessed from the uniaxial compression tests with the axial strains ranging from 0.4 % to 1.4 %. The lower bound secant moduli and uniaxial compressive strengths for the jet grout slab have been adopted in the numerical analysis. The computed wall deflections and ground movements match with those observed in the inclinometers installed in wall and in ground. The analyzed results show that the jet grout slab is an effective measure that could reduce the wall deflections by 36 %. By using the wall deflection path concept, the effects of the jet grout slab and adjacent piles on the wall movements have been assessed in a convenient way.

Keywords: Jet grout slab, Hardening-Soil Model, Small Strain, Wall deflection path

1 INTRODUCTION

Jet grouting has been one of the strengthening measures for reducing wall deflections of deep excavations in soft clay. Buried struts by means of jet grout slabs are often installed below the final excavation level aiming to reduce the maximum wall deflections occurring at that level. In numerical analysis, estimation of the stiffnesses of the jet grouted soil has been one of the challenges to the professional. The uniaxial compressive strengths of the jet grouted soil scatter in wide range. Secondly, like the soil materials, the cement grouted soil mass is non-linear and exhibits strain-softening at the post-peak strain levels. The post-peaks uniaxial compressive strengths would be as low as 10 % of the peak values. The performance of excavations supported by the jet grout slab shall be closely monitored to check if the wall movements would encroach to the post-peak range.

In this paper numerical analysis has been conducted on an excavation case history on City Hall Station supported with jet grout slab. The Hardening-Soil with Small Strain stiffness (HSS) model has been adopted for the soft clay. For the jet grout slab, the Hardened-soil (HS) model has been adopted. The wall deflection path concept has been adopted to assess the effects of the jet grout slab and the adjacent piles on reduction in wall deflections. Further than that, the abrupt change in the rate of wall deflection indicating the nonlinear performance of the jet grout slab could be readily identified in the wall deflection paths. The result of analysis is presented herein to provide a rational approach for design and assessment on the effects of the jet grout slab in reducing wall deflections.

2 CASE HISTORY ON JET GROUTING

2.1 Excavation case at City Hall Station

City Hall Station of the Nankang Line, Taipei MRT, is located in the K1 Geological Zone (MAA, 1987) at the eastern portion of the Taipei Basin. The excavation case history was presented by Chen et al. (1997). As depicted in Figure 1 and Figure 6, the station is 278 m in length and 24 m in width. The subsoil is mainly composed of a clay stratum of 43 m in thickness. The excavation was carried out to a depth of 18.8 m.

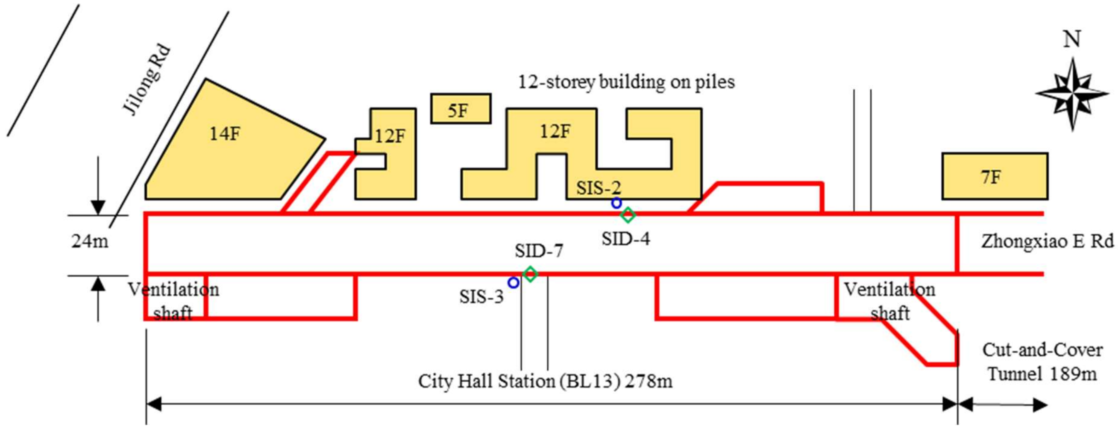

Figure 1: Instrumentation layout of the City Hall Station

The pit was retained by diaphragm wall of 1.2 m in thickness and 45 m in length. The excavation in 6 stages was supported by 5 levels of steel struts. Inclinometers SID4, SID7, SIS2 and SIS3 were deployed on both sides of the station. According to Chen at al. (1997), it was estimated that the wall deflections for the excavation in soft clay supporting with the diaphragm wall of 1.2 m in thickness would be as large as 75 mm. The ground settlements would then exceed the allowable limits. As there were existing buildings of 7-storey to 14-storey located on the north side of the station, jet grout slab of 4 m in thickness was installed beneath the final excavation level to reduce the wall deflections and the ground movements. The jet grout slab was installed during the period between April 1994 and November 1994. Excavation commenced in January 1995. The final excavation depth of 18.8 m was reached in June 1995 and the base slab was cast in September 1995.

2.2 Groundwater conditions

The piezometric level in the Jingmei Formation, a gravel (GM) layer, was lowered to a level near the bottom of the Songshan Formation in the 1970s due to excessive extraction of groundwater to supply water to the city, leading to significant reductions in water pressures in the Songshan Formation and substantial ground settlements as a result. The piezometric level in the Jingmei Formation did not recover till 1974 although pumping had been banned since 1968. The subsoils in the Songshan Formation in the Taipei Basin are thus substantially over-consolidated. Based on monitoring records at the deep well at Sun Yet Sin Memorial Hall, located at 0.5 km west of City Hall Station, Hwang & Moh (2022) reported that the piezometric level in the Jingmei Formation in the eastern portion of the Taipei Basin was around El. -10.0 m in 1995. In the central portion of the Taipei Basin, the piezometric level in the Jingmei Formation recovered to El. 0 m in 2017.

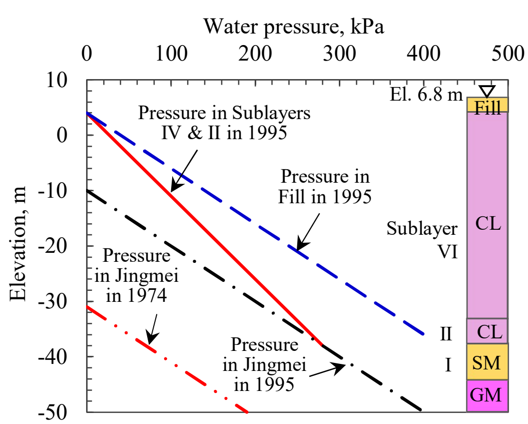

Figure 2: Groundwater pressures on the outer face of the diaphragm walls

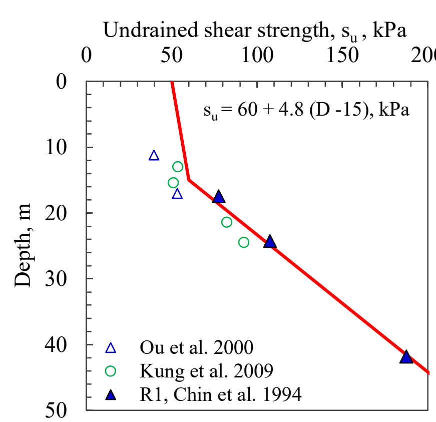

Figure 3: Undrained shear strengths of clays obtained by CK_0UC triaxial tests (after Wong 2024a)

The distributions of the water pressures outside the diaphragm wall at City Hall Station in 1995 are presented in Figure 2. For the Sublayer I and the Jingmei Formation, the piezometric level of El. -10.0 m in 1995 is adopted. The water pressures for Sublayers II to IV clay (CL) are interpolated between the fill layer and Sublayer I sand (SM). Inside the pit, the piezometric levels maintaining at a depth of 1 m below the excavation levels in each stage have been adopted in the analysis.

2.3 Undrained shears strengths for clay sublayers

The undrained shear strengths of the clayey Songshan Formation obtained by the Ko consolidated compression undrained tests were reported by Chin et al. (1994), Ou et al. (2000) and Kung et al. (2009). The undrained shear strength profile is presented in Figure 3. Based on these test results, Wong (2024a) determined that the undrained shear strengths of the Sublayers IV and II clayey soils at the depths below 15 m in the K1 Geological Zone of the Songshan Formation could be expressed by the empirical Equation 1:

$$s_u = 60 + 4.8\,(D - 15) \text{ in kPa} \tag{1}$$

where D is the depth in metre and s_u is the undrained shear strength in kPa.

3 CHARACTERISTICS OF JET GROUTED SOIL

3.1 Peak strength and secant modulus

The properties of the jet grout slab installed at City Hall Station was reported by Wong & Hwang (1997). The jet grout slab was installed by Jumbo Special Grout, the double-fluid JSG method. The jet grout piles were 2.55 m in diameter spacing at 2.2 m in triangular pattern. As presented in Figure 4, the uniaxial compressive strengths, σ_p, of the core specimens taken from the jet grout slab ranged from 1.8 MPa to 9.4 MPa, with an average of 3.8 MPa. The secant moduli, the E_{50} values interpreted at 50 % σ_p, ranged from 0.11 GPa to 0.38 GPa.

In-situ pressuremeter (PMT) tests were performed in the jet grout slabs. The PMT tests indicated that the σ_p values ranged from 0.8 MPa to 4.8 MPa, with an average of 2.4 MPa. It is noted that two of the PMT tests had the undrained shear strength $s_{u\text{-}pmt}$ values of 30 kPa and 90 kPa, which are virtually the untreated soil strength.

The E_{50} values are commonly normalized with the σ_p values of the jet grouted soil. Figure 5 shows the relationship between the E_{50}/σ_p ratios and the axial strains occurring at 50 % σ_p, the ε_{50} values. Based on the 60 number of the uniaxial compression tests reported by Wong & Hwang (1997), regression analysis gives the relationship that expressed in Equation 2:

$$E_{50} / \sigma_p = 0.5 / \varepsilon_{50} \tag{2}$$

Equation 2 is exactly the definition of the secant modulus of the jet grouted soil. The E_{50}/σ_p ratios are inversely proportional to the axial strains, the ε_{50} values.

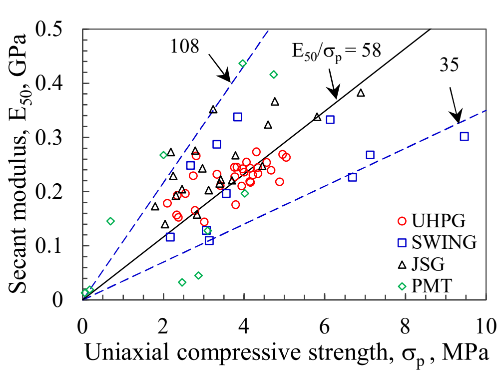

Figure 4: Uniaxial compressive strengths versus secant moduli of jet grouted soil (after Wong & Hwang 1997)

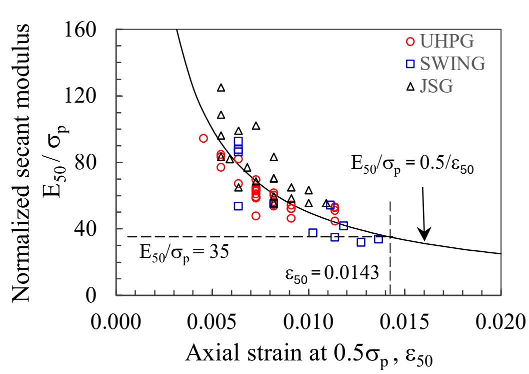

Figure 5: Variation of secant moduli with axial strains for jet grouted specimens

Figure 4 shows that the E_{50}/σ_p ratios of the jet grouted soil ranged from 35 to 108, with an average of 58. According to Equation 2, the ε_{50} values for the UCS tests ranged from 0.4 % to 1.4 % with an average of 0.86 %. The widely scattering in the E_{50}/σ_p ratios in Figure 4 are caused by the variation in ε_{50} values mobilizing the 50 % σ_p.

3.2 Modeling of the jet grout slab

Based on the results of uniaxial compression tests conducted on 90 core specimen of jet grouted soil, Wong (2024b) reported that the stress-strain relationship of the jet grouted soil is nonlinear. The moduli defined at the peak strengths, E_p, are lower than those for the secant moduli, E_{50}. The E_{50}/E_p ratio is around 1.4. In this numerical analysis, the Hardening-soil (HS) model is adopted for simulating the nonlinearity of the jet grouted soil. The stiffness parameters for inputting the HS model are given in Equations (3) and (4):

$$E^{ref}_{50} = E^{ref}_{oed} = E_{50} \tag{3}$$
$$E^{ref}_{ur} = 2.8\, E^{ref}_{50} \tag{4}$$

where E^{ref}_{ur} , E^{ref}_{50} and E^{ref}_{oed} are the reference stiffness parameters for the HS model and E_{50} is the secant moduli for the jet grouted soil obtained by the UCS tests. In this analysis, the lower bound E_{50}/σ_p ratio of 35 presented in Figure 5 is adopted. Using a σ_p value of 1 MPa, the E^{ref}_{ur} value of 100 MPa computed by Equations (3) and (4) is adopted in the numerical analysis.

4 NUMERICAL SIMULATIONS

4.1 Finite element mesh

The 2-Dimensional finite element model for the numerical analysis is depicted in Figure 6. The width of the excavation is 24 m. The excavation is carried out to a depth of 18.8 m in the analysis. The lateral extent of the finite element model reaches a distance of 100 m from the central axis of the excavation trench. The ground model is 60 m in depth. The diaphragm wall of 45 m in length is located at a distance of 12 m from the axis of the trench. The Jingmei Formation is a competent formation with very high stiffness. However, the base of the finite element model in this study is placed at a depth of 60 m to include a 9 m layer of the Jingmei Formation to ensure that the contribution of this formation to ground movements is accounted for.

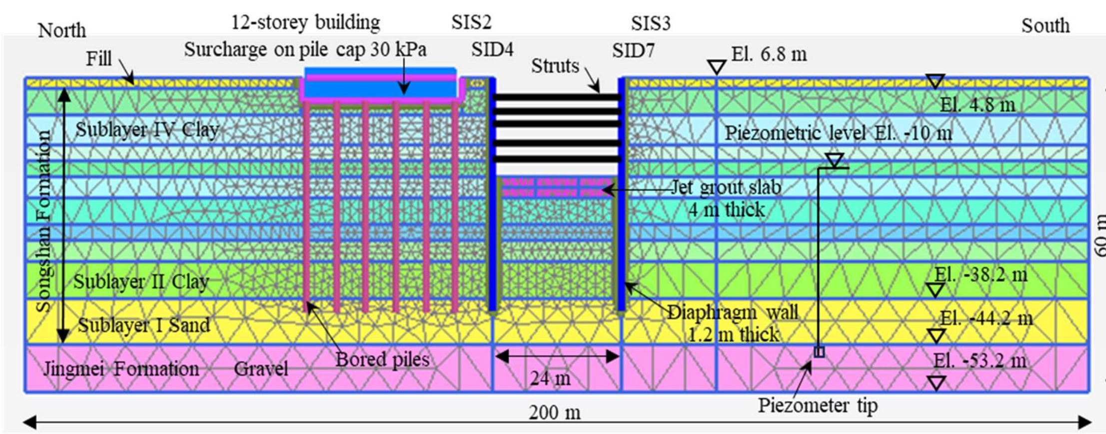

Figure 6: Finite element mesh for the analytical section for 6 stages of excavation

4.2 Hardening-soil with small-strain stiffness model for the surrounding ground

The PLAXIS-2D finite element software developed by PLAXIS BV (2013) has become a very popular tool in geotechnical analysis and design. The Hardening-Soil with Small-strain stiffness (HSS) constitutive soil model is an extension of the Hardening-Soil (HS) model (Benz 2006, Schanz & Vermeer 1998; Schanz et al. 1999) introduced in the PLAXIS program and is adopted herein to simulate the non-linear stress-strain relationship of soils under loading and unloading conditions.

Wong (2024a) adopted the HSS soil model in the study for the effect of diaphragm wall installation to ground movements for City Hall Station. The stiffness parameters adopted for the various soil layers are presented in Table 1. The Readers can refer to that reference for the relationship of the stiffness parameters with the undrained shear strengths and with the N values. The effective shear strength parameters, i.e., the c' and ϕ' values, for the silty sand strata, are determined from laboratory tests conducted on thin-wall tube specimens.

It is noted that for the clayey layers, c' = s_u and $\phi' = 0^o$ is assumed in the analyses. The dilation angle, ψ', of 2^o, 0^o, and 3^o are adopted for the sandy, the clayey, and the gravelly soils respectively. The R_f equals 0.9 is adopted. The unload-reload Poisson's ratio, υ_{ur}, of 0.2 is used as suggested by Benz (2006) and Schanz et al. (1999). Although the HSS soil model is an effective stress model and adopting the $\phi' = 0^o$ for the clayey soils loses its compression hardening function and stress-dependent stiffness, parametric studies using both the effective and the total stress models show that the computed wall deflections and settlements are essentially the same. The total stress model for clay is adopted in this study.

In the PLAXIS software, an elastic-plastic model following the Mohr-Coulomb criterion is used to describe the interfaces for the soil-structure interaction. The R_{inter} value of 1 is the rigid mode and represents the rough interface. In this study, the R_{inter} value of 0.7 has been adopted for the soil-wall interface and along the interface between the wall and the jet grout slab.

Table 1: Soil parameters for the HSS model adopted in the PLAXIS analyses

Mid depth m	Soil type	Unit weight γ' kN/m^3	N value	Undrained shear strength s_u, kPa	Effective cohesion c' kPa	Effective friction angle ϕ', deg	Dilation angle ψ' deg	Reference stiffness, MPa		Initial shear moduli G^{ref}_0, MPa
								Secant stiffness E^{ref}_{50}	Unload-reload stiffness E^{ref}_{ur}, MPa	
1	SM	18.5	8	-		30	0	16	80	80
4.5	CL	18.4	2	54	0			8.1	41	41
10	CL	18.4	3	57				8.6	43	43
14.5	CL	18.4	4	60				9	45	45
17.5	CL	18.4	5	72				10.7	54	54
20.5	CL	18.4	6	88				13.2	66	66
25.5	CL	19	7	110				16.5	82	82
29.5	CL	19	9	130				19.5	97	97
33	CL	19.5	10	146	0			22	110	110
38.55	CL	19.5	20	173				26	130	130
46.5	SM	19.5	26	-	0	32	2	52	260	260
55.5	GM	21.9	>100	-	0	35	3	200	1000	1000

4.3 Determination of small-strain stiffness of soil

The parameters for the small-strain stiffness, i.e., the G^{ref}_0 and the $\gamma_{0.7}$, have been determined from the laboratory tests. Based on the results of the bender element tests, Kung et al. (2009) obtained the G_{max}/s_u ratios ranging from 738 to 788, with an average ratio of 759 for the axial compression tests, where G_{max} is the initial shear modulus. For the axial extension tests, the G_{max}/s_u ratios ranged from 614 to 751, with an average of 671. In this study, the $G^{ref}_0 = 750\ s_u$ is adopted.

Chin et al. (2007) presented the CK_0UDSS test results that depicted in Figure 7. Santos & Correia (2001) recommended that the stress-strain curve for small-strains can be described in Equation 5 as:

$$G / G_0 = 1 / (1+ 0.385\ \gamma / \gamma_{0.7}) \tag{5}$$

where G_0 is the maximum small-strain shear modulus. The moduli degradation curves with the threshold $\gamma_{0.7}$ values ranging from 0.8 x 10^{-4} to 10^{-3} are shown in Figure 8. The degradation of the shear moduli with shear strain interpreted from the direct simple shear test is presented Figure 8, showing that the Taipei clay would have the $\gamma_{0.7}$ value of 5 x 10^{-4}. This $\gamma_{0.7}$ value has been adopted in this study.

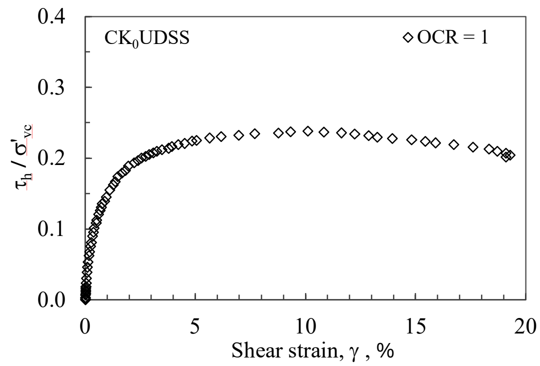

Figure 7: Stress-strain curve of Taipei clay under CK_0UDSS test (After Chin et al. 2007)

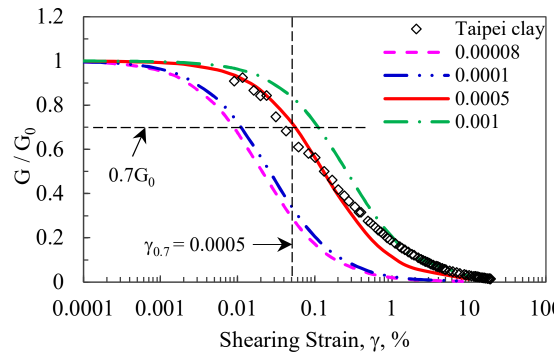

Figure 8: Degradation of shear moduli with shearing strain (after Wong 2024a)

4.4 Modeling of the retaining structures and piles

The excavation scheme and the retaining structures for City Hall Station are depicted in Figure 6. The diaphragm wall is simulated by plate element and an E_c value of 25,000 MPa is adopted for concrete with a characteristic compressive strength of 28 MPa. The estimated flexural rigidity (denoted as E_cI_c where I_c is the moment of inertia) and the axial stiffness (denoted as E_cA_c where A_c is the sectional area) of the diaphragm wall of 1.2 m in thickness are 2,520 MN-m and 21,000 MN/m respectively. These values have already been reduced from their original values by 30 % to account for tensile cracks and creeping of concrete during excavation.

The excavation was supported by 5 levels of steel struts, which are represented by the node-to-node anchors. The properties for the steel struts are presented in Table 2. The Young's modulus (E_s) for steel of 210 GPa has been adopted. The struts had the horizontal spacing, s, of 4.5 m. The 50 % design preloads have been adopted to cater for releasing of the strut loads caused by loading of the adjacent struts.

As shown in Figures 1 and 6, there is a 12-storey building supported on bored piles on the north side of City Hall Station. Chen et al. (1999) reported that the concrete bored piles were 0.8 m to 1.2 m in diameter and 45 m in depth. There was one basement floor at 4.5 m depth. The building load of 30 kPa acting at the basement level has been adopted in the analysis.

The embedded beam model available in the PLAXIS software is adopted to simulate the piles. The embedded beam is a 2.5-Dimensional model taking the stiffnesses of the pile and the surrounding soil into account. In this study the pile diameter of 0.85 m spacing at 5.5 m along the east-west direction have been adopted. The Young's modulus of 18,000 MPa for the concrete piles is used. Sensitivity analysis on the effect of the pile stiffness using one-half of the AE value found that the effects to wall movements are insignificant.

Table 2: Strut properties

Excavation stage	Strut level	Depth of strut, m	Strut type	Area A_s, cm^2	Stiffness E_sA_s/s, MN/m	Design preload, kN/m
1	S1	3.8	1H300x300x10x15	138.5	645	120
2	S2	6.4	1H400x400x13x21	218.7	1,021	150
3	S3	9.0	1H350x350x12x19	347.8	1,623	250
4	S4	12.2	2H400x400x13x21	437.4	2,041	255
5	S5	15.4	2H400x400x13x21	437.4	2,041	255

4.5 Analysis cases

Three cases have been analyzed to assess the performance of the jet grout slab and its effectiveness on reducing wall deflections. Case 1 considered the jet grout slab of 4 m in thickness. Case 2 assessed the performance of the jet grout slab of 2 m in thickness. The jet grout slab is located at the depths between 18.8 m and 20.8 m. Case 3 analyzed the conditions without the jet grout slab. Table 3 summarizes the features for these analytical cases.

5 RESULTS OF NUMERICAL ANALYSIS

5.1 Computed versus observed wall deflections

The computed wall deflection profiles for Case 1 with the 4 m thick jet grout slab are presented in Figure 9 and Figure 10. The analysis results are compared with those observed in the inclinometers installed on the north and the south sides of the station. Inclinometers SIS4 and SID7 were installed in the diaphragm wall. Inclinometers SIS-2 and SIS-3 were installed in ground at the distance of 2 m behind the diaphragm walls. The toe levels of the diaphragm walls were at 45 m depth. The toe levels of the inclinometers on the north side, SID4 and SIS2, were at 49.5 m depth. For SID7 and SIS4 installed on the south side, their toe levels were at 48.0 m depth.

As shown in Figure 9 and Figure 10, the computed wall deflection profiles in the final stage fall between those observed in wall and in ground. The deviation between the computed and the observed profiles have been less than 1 mm. In the intermediate Stage 4, Figures 9b and 10b show that the computed maximum deflections deviate by 6 mm at the north wall and by 9 mm at the south wall. The discrepancies could be attributable to various conditions and are discussed in Section 6.3.

Comparison of the wall deflections between the north and the south sides shows that with the presence of the piles, the maximum computed wall deflections of 32.4 mm for the north wall have been less than the 42.3 mm that computed for the south wall.

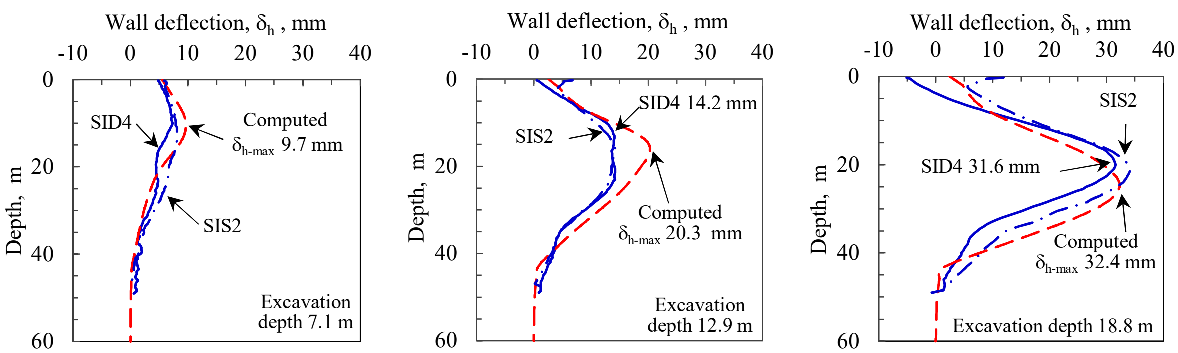

(a) Stage 2 (b) Stage 4 (c) Final stage

Figure 9: Computed and observed wall deflections at north wall with piles nearby - Case 1

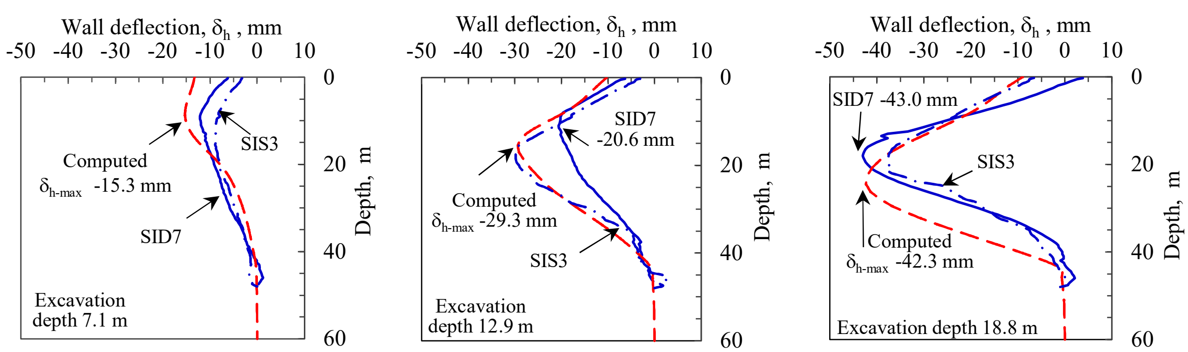

(a) Stage 2 (b) Stage 4 (c) Final stage

Figure 10: Computed and observed wall deflections at south wall with no pile - Case 1

5.2 Effects of jet grout slab and piles

The computed wall deflection profiles for Case 1 to Case 3 in the final stage are presented in Figure 11. As summarized in Table 3, the deflections were affected by the jet grout slab and by the piles. For the south wall with no pile, the maximum wall deflections in Case 1 with 4 m thick jet grout slab could be reduced by 36 %, from 66.3 mm to 42.3 mm. For Case 2 with 2 m thick jet grout slab, the wall deflections could be reduced by

22 %, from 66.3 mm to 51.6 mm. Comparing the deflections between the north and the south walls, the presence of the piles next to the north wall could reduce the wall deflections by around 23 % in Case 1 to Case 3.

Prakasa & Hsiung (2023) reported the results of numerical analysis on the jet grout slab conducted at Yung Chun Station (BL14), which is located at 1 km east of City Hall Station (BL13). The excavation of 16.7 m in depth and 19.5 m in width was supported with diaphragm wall of 38 m in length and 1.2 m in thickness. With the jet grout slab of 3 m in thickness, the maximum wall deflection could be reduced by 33 %, from 39 mm to 26 mm. That 33 % reduction is similar to the 36 % reduction computed at the south wall of City Hall Station.

Table 3: Effects of piles and jet grout slab to wall deflections in the final stage

Case	Feature	Computed maximum wall deflection		Effects of piles	Effects of jet grout slab	
		North side with piles, δ_{h-N}, mm	South side with no pile, δ_{h-S}, mm	$\delta_{h-N}/\delta_{h-S}$	North	South
Case 1	Jet grout slab 4 m thick	32.4	-42.3	0.77	0.62	0.64
Case 2	Jet grout slab 2 m thick	39.5	-51.9	0.76	0.76	0.78
Case 3	No jet grout slab	51.9	-66.3	0.78	1	1

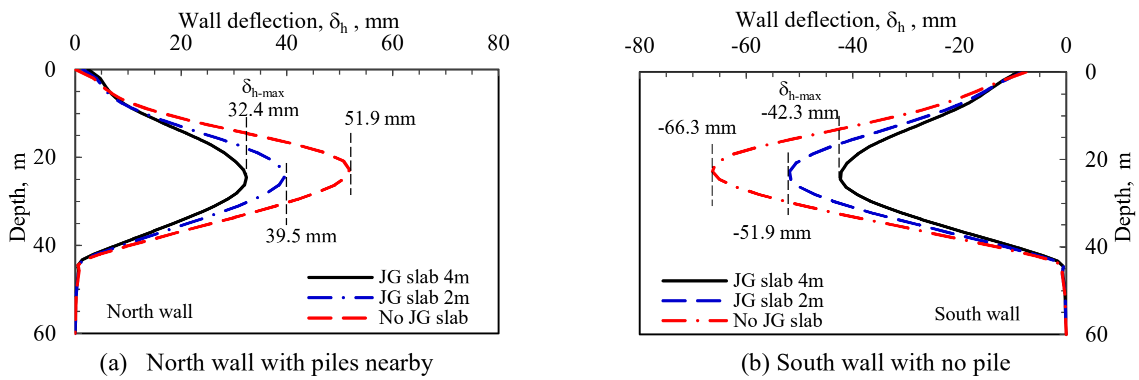

Figure 11: Computed wall deflections in the final stage with and without jet grout slab - Case 1 to Case 3

5.3 Axial strains in the jet grout slab

The computed axial strains along the top, the middle and the bottom levels, or at the depths of 18.8 m, 20.8 m and at 22.8 m, of the jet grout slab in the final stage for Case 1 are presented in Figure 12a. Along the middle level the jet grout slab would have the horizontal strains, ε_h, ranging from -0.09 % to -0.36%, with an average of -0.29 %. The largest ε_h value of -1.20 % occurred at the top corners, at the interface between the walls and the jet grout slab. The localized strains concentration is compatible with the upper range of axial strain of 1.4 % for the jet grout slab that shown in Figure 5. It is noted that the negative value denotes compressive strain.

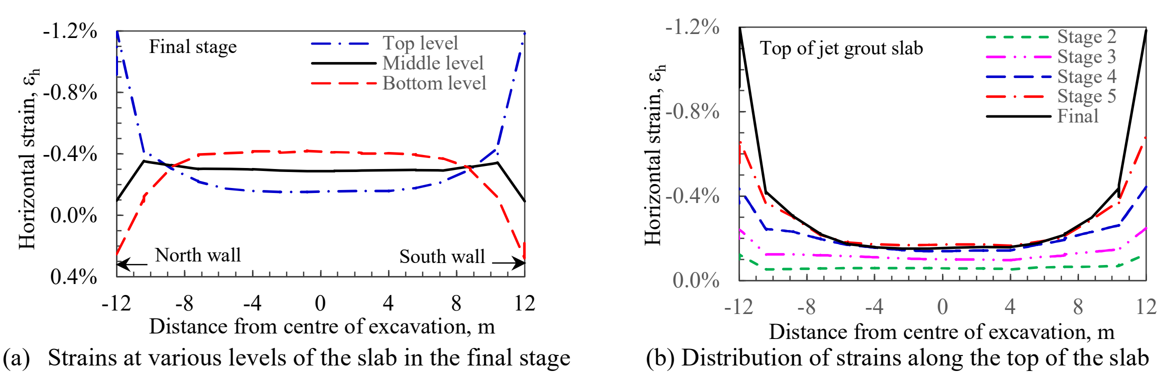

Figure 12: Computed horizontal strains along the jet grout slab in various stages - Case 1

Figure 12b shows the development of the ε_h values at the upper corners of the jet grout slab. The computed maximum ε_h values in Stages 3, 4, 5 and in the final stage have been -0.25 %, -0.44 %, -0.68 % and -1.20 %

respectively. The abrupt increase in the ε_h values from -0.68 % to -1.2 % between Stage 5 and the final stage is likely due to the nonlinear response of the jet grout slab in the final stage.

Figure 12a shows that the axial strains along the central portion of the jet grout slab in the final stage range from -0.2 % to -0.4 %. As these axial strains are less than the lower bound strain of 0.4 % shown in Figure 5, majority of the jet grout slab has not encroached to the post-peak range. The use of the HS model for simulating the jet grout slab is applicable in this study.

5.4 Back-analyzed stiffnesses for the jet grout slab

The parameters of E^{ref}_{ur} of 100 MPa, E^{ref}_{50} of 35 MPa and the σ_p value of 1 MPa for the jet grout slab have been obtained by back-estimation in this study. According to Chen et al. (1997), the minimum σ_p value of 1.2 MPa was specified for the jet grout slab at City Hall Station. The back-calculated σ_p value of 1 MPa is close to the specified minimum value. It is noted that the UCS tests were conducted on good quality core specimens and inferior specimens could not be taken for testing. As the in-situ tests could detect weak seams in the jet grouted soil mass, it would be prudent to conduct more pressuremeter tests to determine the σ_p values to be adopted for future jet grout slabs design and analysis.

6 ASSESSMENTS ON THE PERFORMANCE BY WALL DEFLECTION PATHS

6.1 Effects of piles

The assessment on the effects of the jet grout slab to wall deflections in Table 3 compared only the results in the final stage. The wall deflections in all stage are also useful information for assessing the performance. Moh & Hwang (2005) adopted the wall deflection path concept to assess the performance of the excavation cases. The deflection path is basically plotting of the maximum wall deflections against the excavation depths in various stages. Expressed in log-log scale, the wall deflection path falls into a common straight line under the similar hydro-geological conditions. The wall deflection path is defined by Δ_4 and Δ_{100}, where Δ_4 is the maximum wall deflections occurring at the excavation depth within 4 m and Δ_{100} is the projection of the maximum wall deflection values from the 4 m depth to the excavation depth of 100 m.

The application of the wall deflection path is demonstrated in Figure 13. The computed maximum wall deflections versus the excavation depths for Case 3 with no jet grout slab from Stage 1 to the final stage are plotted up in Figure 13. The Δ_4 values of 6 mm and 10 mm respectively are interpreted for the north and the south walls. The Δ_{100} value 500 mm is interpreted both for the north and the south walls. The presence of the piles on the north side only affects the wall deflections at shallow depths. As excavation goes deeper, the effects of piles diminish so that the Δ_{100} value is unaffected. The piles next to the wall had the effects of reducing the Δ_4 values by 40 %, from 10 mm to 6 mm.

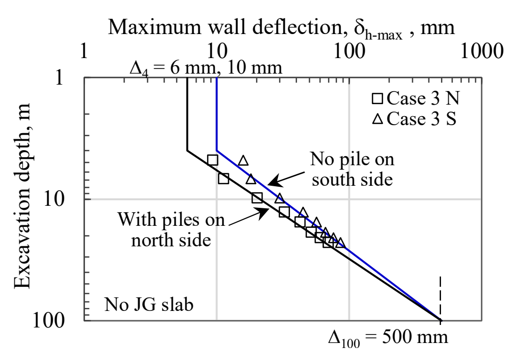

Figure 13: Effects of piles assessed by wall deflection paths - Case 3

The set of the Δ_4 and the Δ_{100} values of 10 mm and 500 mm respectively for the south wall with no jet grout slab and no pile nearby is consistent with that for the excavation cases in the K1 Geological Zone of the Taipei Basin, which is dominant with thick deposits of soft clay. Hwang et al. (2016) proposed that the reference deflection path for the diaphragm wall of 1.0 m in thickness and 15 m to 25 m in excavation width could be defined with the Δ_4 and the Δ_{100} values of 10 mm and 500 mm respectively.

6.2 Effects of jet grout slab

Figure 14 shows the wall deflection paths for the cases with and without the jet grout slab, Case 1 and Case 3. For the north wall next to the piles, the deflection path with the Δ_4 and Δ_{100} values of 6 mm and 200 mm respectively is interpreted for Case 1 in Figure 14a. For the south wall with no pile nearby, the deflection path with the Δ_4 and the Δ_{100} values of 10 mm and 200 mm respectively is interpreted for Case 1 in Figure 14b.

The wall deflection paths for Case 3 presented in Figure 13 are reproduced in Figure 14 for comparison with those for Case 1. The effects of the jet grout slab to the north and the south walls are discernable. Figure 14 shows that for the walls on both sides, the presence of the jet grout slab reduces the Δ_{100} values from 500 mm to 200 mm. As the excavation goes deeper, the effectiveness of the jet grout slab increases. Figure 14 also shows that the jet grout slab has minimal influence on shallow excavation so that the Δ_4 value is unaffected.

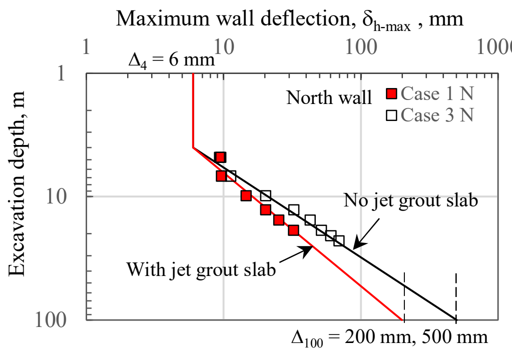

(a) North wall with piles

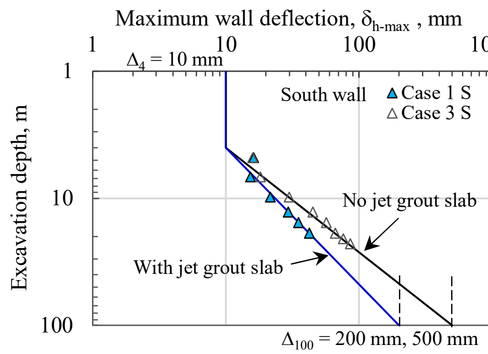

(b) South wall with no piles

Figure 14: Effect of jet grout slab assessed by wall deflection paths - Case 1 & Case 3

6.3 Comparison between observed and computed deflection paths

The computed wall deflection paths for Case 1 are compared with those observed in the inclinometers in Figure 15. The deflection path with the set of Δ_4 and Δ_{100} values of 6 mm and 200 mm for the north side is applicable to those deflections observed in inclinometers SID4 and SIS2. For the deflections observed in inclinometers SID7 and SIS3, the set of Δ_4 and the Δ_{100} values of 10 mm and 100 mm is applicable.

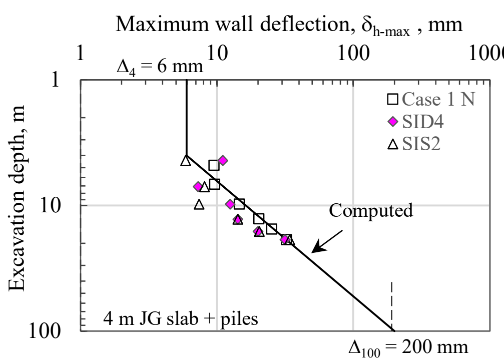

(a) North side

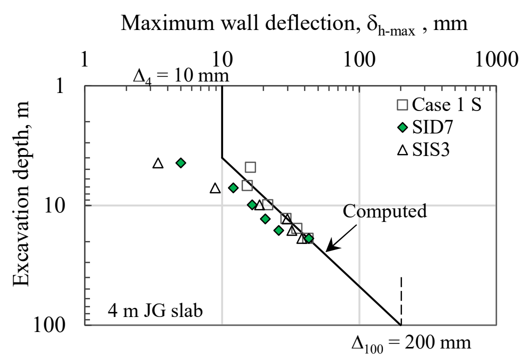

(b) South side

Figure 15: Comparison of computed wall deflection profiles with observation - Case 1

There has been deviation on the wall deflections between the computed and the observed in the intermediate stages. In Stage 4, the observed maximum deflections deviate from the computed by 6 mm and 9 mm in the north and the south walls respectively. Such discrepancies would be due to various conditions. First of all, Chen et al. (1997) reported that traffic decks were erected along the road and jet grouting was conducted below the decks at the depth of 2.5 m. It is noted that the inclinometer readings were initialized after jet grouting at the commencement of the main excavation. The wall deflections occurred prior to the commencement of excavation were excluded. The observed wall deflection values for Stages 1 and 2 were therefore under-reported. Secondly, the utilities along the busy road were diverted on trenches of around 2 m in depth on the south side of City Hall Station. As less earth pressures acting on the south side, less wall deflections would occur. Thirdly, while drilling groutholes would disturb the soil, cement grout left in the groutholes would have some strengthening effects on the soil above the jet grout slab. Such strengthening effects have been ignored in the numerical analysis. Finally, as the excavation was conducted in thick clay layer, the consolidation effects cause delaying of the ground movements. While these various conditions have not been simulated in the analysis, discrepancies between the observed and the computed wall deflections would be inevitable.

Figure 15 shows that the observed deflections increased abruptly between Stage 5 and the final stage. The deflections in SID4 increased from 20.0 mm to 31.6 mm. In SID7, the deflections increased from 25.9 mm to 43.0 mm. As shown in Figure 12b, the horizontal strains at the interface between the north wall and the top of the jet grout slab increased from 0.68 % to 1.20 %. Such abrupt change in the rate of wall deflections is due to reaching the peak strain around 1.2 % at the top corners between the walls and the jet grout slab. Figure 15 demonstrates that the wall deflection paths is a convenient criterion that abnormal deflections such as the onset of the mobilization of the post-peak range of the jet grout slab can be identified.

7 CONCLUSIONS

Two-dimensional numerical analysis on an excavation in soft ground strengthened with jet grout slab has been conducted. The nonlinear Hardening-soil with small-strain stiffness (HSS) soil model is adopted for the soil materials. The Hardened-soil (HS) model has been adopted to simulate the nonlinear behaviour of the jet grout slab. The following conclusions could be drawn:

(1) In the estimation for the stiffness parameters for the jet grout slab, the lower bound uniaxial compressive strength and the lower bound secant modulus shall be adopted.
(2) The jet grout slab proves to be an effective method for reducing ground movements. The reduction factor could be 36 % of the excavation without jet grout slab in the final stage.
(3) The presence of the piles reduces the wall deflections by around 23 % of those without piles.
(4) The wall deflection paths interpreted from the observed and the computed wall deflections are useful criterion for assessing the performance of the wall deflections of the excavation cases. The effects of the jet grout slab and the presence of piles on the reduction in wall deflections can be readily differentiated. The wall deflection paths can identify abnormal deflections such as the mobilization of the post-peak range of the jet grout slab.

The close agreement between the computed and the observed wall deflections demonstrates that the nonlinear constitutive models for the jet grout slab and for the surrounding ground are reliable tools for analyzing the excavation works.

ACKNOWLEDGEMENTS

The Author wishes to expressed his sincere thanks to Dr R. N. Hwang of Moh and Associates, Inc. for his invaluable comments on the manuscript and in particular his advices on the assessment on the performance of the jet grout slab using the wall deflection paths.

REFERENCES

Bentley. 2022. *PLAXIS 2D-Reference Manual*. CONNECT Edition V22.02, Bentley Advancing Infrastructure, August 2022.

Benz, T. 2006. Small-strain stiffness of soils and its numerical consequence. *Dissertation of thesis*, the Institute of Geotechnics, University Stuttgart.

Chen, Y.K., Huang, C.C & Wang, F.K. 1997. Grouted raft for building protection in excavation in soft clay. *Proceedings of 7th Conference on Current Researches in Geotechnical Engineering*. Pintung, Taiwan, August, 1999: 1425-1432. (in Chinese)

Chen, Y.W., Duann, S.W., Hwang, R.N. & Kong S.K. 1999. Influence of excavation on adjacent piles. *Proceedings of 8th Conference on Current Researches in Geotechnical Engineering*. Chishan, Taiwan, August, 1997: 593-600. (in Chinese)

Chin, C.T., Chen, J.R., Hu, I.C., Yao, D.H.C. & Chao, H.C. 2007. Engineering characteristics of Taipei clay. In T.S. Tan, K.K. Phoon, D.W. Hight & S. Leroueil (Eds), entitled*: Characterization and Engineering Properties of Natural Soils,* Taylor & Francis Group, v3:1755-1803.

Chin, C.T., Crooks, A.J.H. & Moh, Z.C. 1994. Geotechnical properties of the cohesive Sungshan deposits. *Geotechnical Engineering, J. Southeast Asian Geotechnical Society*, Taipei, Taiwan 25(2): 77-103. (in Chinese)

Hwang, R. & Moh, Z.C. 2022. Groundwater drawdown and subsidence in the Taipei Basin. *Sino-Geotechnics,* No. 173/2022.9: 99-110. (in Chinese)

Hwang, R.N., Wang, C.H., Chou C.R. & Wong, L.W. 2016. Deep excavations in Taipei Basin and performance of diaphragm walls, *Geotechnical Engineering Journal of the SEAGS & AGSSEA Vol. 47, No. 2*, June 2016. ISSN 0046-5828: 34-40.

Hu. I.C., Chin, C.T. & Liu, C.J. 1996. Review of the geotechnical characteristics of the soil deposits in Taipei, *Sino-Geotechnics*, No. 54: 5-14. (in Chinese)

Kung, G.T.C, Ou, C.Y. & Juang C.H. 2009. Modelling small-strain behavior of Taipei clays for finite element analysis of braced excavations. *Computers and Geotechnics* 36 (2009): 304-319.

MAA 1987. *Engineering properties of the soil deposits in the Taipei Basin*, Report No. 85043, Ret-Ser Engineering Agency and Taipei Public Works Department, Taipei. (in Chinese)

Moh, Z.C. & Hwang, R.N. 2005. Geotechnical considerations in the design and construction of subways in urban areas. *Seminar on Recent Development om Mitigation of Natural Disasters, Urban Transportation and Construction Industry*, 30 Novmeber-2 December.

Ou, C.Y., Liao, J.T. & Cheng, W.L. 2000, Building response and ground movements induced by a deep excavation, *Geotechnique*, Vol. 50, No. 3: 209-220.

PLAXIS B.V. 2013. *PLAXIS Reference Manual*. PLAXIS, BV, Delft, the Netherlands.

Prakasa, M.D.A & Hsiung, B.C.B, 2023. Effectiveness of jet-grouted soil on excavation: A case study. *IOP Conf. Series: Earth and environmental Science*, 1249 (2023) 012022.

Santos J.A. & Correia, A.G. 2001. Reference threshold shear strain of soil. Its application to obtain a unique strain-dependent shear modulus curve for soil. *In 15th Int. Conf. SMGE*, Volume 1, Istanbul, A.A. Balkema: 267-270.

Schanz, T. & Vermeer, P.A. 1998. On the Stiffness of Sands. *Geotechnique,* 46, No. 1: 145-151.

Schanz, T., Vermeer, P.A. & Bonnier, P.G. 1999. The hardening soil model: formulation and verification. *Beyond 2000 in Computational Geotechnics*. Rotterdam, the Netherlands. 281-290.

Wong, L.W. 2024a. Ground movements caused by diaphragm wall installation. *Proceedings of the 44th HKIE Geotechnical Division Annual Seminar 2024*, May: 321-332.

Wong, L.W. 2024b. The strain-softening behaviour of jet grouted soil. *Proceedings of the HKIE-CIE-IEM Tripartite Seminar*, Hong Kong, 28 November, 2024.

Wong, L.W. & Hwang, R.N. 1997. Evaluation of Jet Grouting by In-situ Tests, *Proceedings of the International Conference on GROUND IMPROVEMENT TECHNIQUES*, May, Macau: 641-647.

An Improved Limit Equilibrium Method for Stability Analysis of Unsaturated Soil Slopes

Kai Liu
Department of Civil and Environmental Engineering, The Hong Kong Polytechnic University, Kowloon, Hong Kong, China; College of Civil and Transportation Engineering, Shenzhen University, Shenzhen, China
Weihang Ouyang & Si-wei Liu
Department of Civil and Environmental Engineering, The Hong Kong Polytechnic University, Kowloon, Hong Kong, China
Jian-hua Yin
Department of Civil and Environmental Engineering, The Hong Kong Polytechnic University, Kowloon, Hong Kong, China; College of Civil and Transportation Engineering, Shenzhen University, Shenzhen, China

ABSTRACT

Unsaturated soil is widely distributed around the world but less considered in design due to the absence of a convenient analysis method in practice. The Morgenstern-Price (MP) method incorporating the extended Mohr–Coulomb shear strength equation provides a reliable approach to evaluating slope stability in such conditions. However, this method is time-consuming due to the need for a tedious trial-and-error process in determining the scaling factor, which involves complex iterations during each trial. Furthermore, since the relatively complicated nature of unsaturated soil, a dense slice division is necessary to obtain reliable results, making the analysis even more cumbersome. In this paper, an improved MP method for unsaturated soil slope stability analysis is presented, which eliminates the need for a dense slice mesh by employing only a few strategically placed Gauss points along the slip surface. Moreover, the trial-and-error process for determining the scaling factor with the corresponding complex iterations is replaced by an efficient search algorithm with a more concise iteration process, resulting in a more convenient implementation of the proposed method. Extensive examples are provided to validate the effectiveness of the proposed improved MP method, indicating its potential as an accurate and efficient analysis method for unsaturated soil slopes in practical application and relative study involving repetitive analyses.

1 INTRODUCTION

Unsaturated soil slopes present a critical concern in geotechnical engineering due to the significant reduction in soil shear strength caused by water infiltration (Cai & Ugai 2004). Such strength reduction can cause severe failures in both natural and man-made slopes, especially for those in reservoir areas, such as more than 60 landslides occurred in the Three Gorges Reservoir region since 2003 (Xiong et al. 2019). The primary triggers for these landslides are repeated water infiltration due to rainfall and fluctuating reservoir water levels, leading to significant damage to both human life and engineering structures. Although analyzing slope stability based on saturated soil mechanics might appear as an approach to prevent such catastrophic events, it sometimes results in excessively conservative and inefficient design outcomes, imposing substantial construction costs for large-scale geotechnical projects (Houston 2019). Thus, the feature of unsaturated soil slope must be appropriately evaluated for a safe and economical design result. In practice, however, slope stability analyses commonly neglect suction effects, not only due to a lack of suitable analysis methods but also because conservative design practices intentionally omit these beneficial effects to ensure safety margins.

Various methods have been developed for slope stability analysis over the past few decades, including limit analysis method (LAM) (Sun et al. 2019), finite element method (FEM) (Griffiths & Lu 2005), and limit equilibrium method (LEM) (Duncan 1996; Ouyang et al. 2022). The LAM is usually used in simple geotechnical problems but less suitable for complicated geological conditions in engineering practice. For more general slope stability analysis methods, the FEM has been employed to evaluate the slope stability by incorporating the strength reduction technique. This method is robust; however, it requires solid knowledge of constitutive models, linear and nonlinear failure criteria, and plasticity flow rules for determining critical slip surfaces. In addition, the effort and cost of FEM are sometimes unbearable in design practice. Consequently, the LEM is still the predominant slope stability analysis method in current design practice and recommended by various specifications.

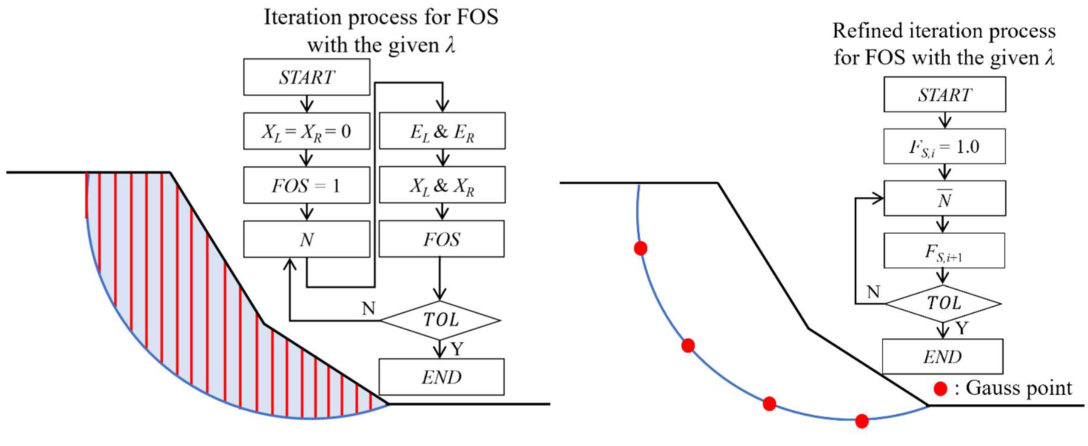

(a) The traditional MP method (b) Present study

Figure 1: Comparison between the traditional MP method and the present study

In the conventional LEM, the potential sliding soil mass is required to be discretized as vertical slices. The factor of safety (FOS) is calculated based on the force and moment equilibrium of the potential sliding soil mass. Different methods have been proposed based on various assumptions of interslice forces and satisfied conditions for force and moment equilibrium (Cheng & Lau 2014), including Bishop method, Morgenstern-Price (MP) method, Spencer method, Sarma method, and Janbu method. Among these methods, the MP method is the most widely used approach since it satisfies stricter equilibrium conditions. Subsequently, various shear strength equations, such as the extended Mohr–Coulomb shear strength equation (Fredlund et al. 1978), have been introduced in this method to extend it from only saturated/dry soil slopes to those unsaturated. However, this MP method is still less employed for the unsaturated slope stability analysis in design practices since it is relatively time-consuming and complicated in implementation.

In this study, an efficient numerical implementation of the LEM for stability analysis of unsaturated soil slopes is presented. An improved MP method proposed by Ouyang et al. (2022) for dry slopes is extended to evaluate the stability of unsaturated soil slopes, where the dense division of slice is replaced by the alignment of only several Gauss points. To improve the searching efficiency of the scaling factor, a linear search method is introduced to replace the best-fit method. Moreover, this paper firstly proposes a refined iteration process for the FOS with the given scaling factor (as shown in Fig. 1b), making the implementation process of the improved MP method for unsaturated slopes more convenient and efficient. To validate the robustness and efficiency of the proposed method, two benchmark examples are provided, including homogeneous and nonhomogeneous unsaturated soil slopes. Finally, one case study of unsaturated residual soil slope in Hong Kong is illustrated for future applications in engineering practice. It is believed that this improved MP method for unsaturated slopes will be a useful tool for investigating the unsaturated feature of slope stability in design practice.

2 THE IMPROVED MORGENSTERN-PRICE METHOD

2.1 The factors of safety F_m and F_f

In the traditional MP method, the slice division must be dense enough by increasing the slice number to achieve the reliable results. When the slice of width, b_i, trends to be infinitesimally small and the slice number, n, is infinite, the FOSs when considering the moment equilibrium and lateral force conditions (Fredlund 2006) can be written as follows:

$$F_m = \lim_{b_i \to 0} \frac{\sum_{i=1}^{\infty} \left\{ c'_i l_i R_i + \left[N_i - u_{w,i} l_i \frac{\tan\varphi_i^b}{\tan\varphi_i'} - u_{a,i} l_i \left(1 - \frac{\tan\varphi_i^b}{\tan\varphi_i'} \right) \right] R_i \tan\varphi_i' \right\}}{\sum_{i=1}^{\infty} W_i d_i - \sum_{i=1}^{\infty} N_i f_i}$$

$$= \lim_{b_i \to 0} \frac{\sum_{i=1}^{\infty} \left\{ c'_i \frac{b_i}{\cos\alpha_i} R_i + \left[N_i - u_{w,i} \frac{b_i}{\cos\alpha_i} \frac{\tan\varphi_i^b}{\tan\varphi_i'} - u_{a,i} \frac{b_i}{\cos\alpha_i} \left(1 - \frac{\tan\varphi_i^b}{\tan\varphi_i'} \right) \right] R_i \tan\varphi_i' \right\}}{\sum_{i=1}^{\infty} b_i \rho_i d_i - \sum_{i=1}^{\infty} \frac{N_i}{b_i} b_i f_i} \tag{2}$$

$$= \frac{\int \left\{ c' \frac{R}{\cos\alpha} + \left[\frac{dN}{dx} - \frac{u_w}{\cos\alpha} \frac{\tan\varphi^b}{\tan\varphi'} - \frac{u_a}{\cos\alpha} \left(1 - \frac{\tan\varphi^b}{\tan\varphi'} \right) \right] R \tan\varphi' \right\} dx}{\int (\rho d)\, dx - \int \left(\frac{dN}{dx} f \right) dx}$$

$$F_f = \lim_{b_i \to 0} \frac{\sum_{i=1}^{\infty} \left\{ c'_i l_i \cos\alpha_i + \left[N_i - u_{w,i} l_i \frac{\tan\varphi_i^b}{\tan\varphi_i'} - u_{a,i} l_i \left(1 - \frac{\tan\varphi_i^b}{\tan\varphi_i'} \right) \right] \cos\alpha_i \tan\varphi_i' \right\}}{\sum_{i=1}^{\infty} N_i \sin\alpha_i}$$

$$= \lim_{b_i \to 0} \frac{\sum_{i=1}^{\infty} \left\{ c'_i \frac{b_i}{\cos\alpha_i} \cos\alpha_i + \left[N_i \cos\alpha_i - u_{w,i} b_i \frac{\tan\varphi_i^b}{\tan\varphi_i'} - u_{a,i} b_i \left(1 - \frac{\tan\varphi_i^b}{\tan\varphi_i'} \right) \right] \tan\varphi_i' \right\}}{\sum_{i=1}^{\infty} N_i \sin\alpha_i} \tag{3}$$

$$= \frac{\int \left\{ c' + \left[\frac{dN}{dx} \cos\alpha - u_w \frac{\tan\varphi^b}{\tan\varphi'} - u_a \left(1 - \frac{\tan\varphi^b}{\tan\varphi'} \right) \right] \tan\varphi' \right\} dx}{\int \left(\frac{dN}{dx} \sin\alpha \right) dx}$$

where dx denotes width of an infinitesimal soil slice; ρ is the weight of the slice per unit width; and dN/dx is normal force at the base of the slice per unit width.

The interslice force and the normal force acting on the infinitesimally thin slice can be expressed as:

$$dN = \frac{\rho dx - dX - \frac{c'}{F_S} \tan\alpha dx + u_a \frac{\tan\alpha}{F_S} \left(\tan\varphi' - \tan\varphi^b \right) dx + u_w \frac{\tan\varphi^b}{F_S} \tan\alpha dx}{m_\alpha} \tag{3}$$

$$dX = \lambda f(x) dE \tag{4}$$

$$dE = \left(\rho \tan\alpha \right) dx - \tan\alpha dX - \frac{1}{\cos\alpha} dS_m \tag{5}$$

where,

$$dS_m = \frac{1}{F_s} \left\{ \frac{c'}{\cos\alpha} dx + \tan\varphi' dN + \left[\frac{u_a}{\cos\alpha} \left(\tan\varphi^b - \tan\varphi' \right) - \frac{u_w}{\cos\alpha} \tan\varphi^b \right] dx \right\} \tag{6}$$

Only four unknown variables, including dN, dX, dE, and dS_m, within the above linear equation group. Thus, by rearranging Eqs. (11) to (14), dN can be obtained as:

$$dN = \frac{1}{\overline{m}_\alpha}\left[\rho - \frac{c'}{F_S}\tan\alpha + u_a\frac{\tan\alpha}{F_S}\left(\tan\varphi' - \tan\varphi^b\right) + u_w\frac{\tan\alpha}{F_S}\tan\varphi^b\right]dx + \frac{1}{\overline{m}_\alpha \lambda f(x) F_S}\left[c' + u_a\left(\tan\varphi^b - \tan\varphi'\right) - u_w\tan\varphi^b\right]dx \tag{7}$$

where,

$$\overline{m}_\alpha = m_\alpha + \lambda f(x)\left(\sin\alpha - \cos\alpha\frac{\tan\varphi'}{F_S}\right) \tag{8}$$

But even the expression of dN is obtained, the analytical solutions for Eqs. (1) and (2) are still hard to be derived. Thus, a numerical integral technique, named the Gaussian integral, is introduced for simplifying the expression of FOSs. Using the Gaussian integral, Eqs. (1) and (2) can be rewritten as:

$$F_m = \frac{\sum_{j=1}^{NG}\omega_j\left\{c_j'\frac{R_j}{\cos\alpha_j} + \left[\overline{N}_j - \frac{u_{w,j}}{\cos\alpha_j}\frac{\tan\varphi_j^b}{\tan\varphi_j'} - \frac{1}{\cos\alpha_j}u_{a,j}\left(1 - \frac{\tan\varphi_j^b}{\tan\varphi_j'}\right)\right]R_j\tan\varphi_j'\right\}}{\sum_{j=1}^{NG}\omega_j\left(\rho_j d_j\right) - \sum_{j=1}^{NG}\omega_j\left(\overline{N}_j f_j\right)} \tag{9}$$

$$F_f = \frac{\sum_{j=1}^{NG}\omega_j\left\{c_j' + \left[\overline{N}_j\cos\alpha_j - u_{w,j}\frac{\tan\varphi_j^b}{\tan\varphi_j'} - u_{a,j}\left(1 - \frac{\tan\varphi_j^b}{\tan\varphi_j'}\right)\right]\tan\varphi_j'\right\}}{\sum_{j=1}^{NG}\omega_j\left(\overline{N}_j\sin\alpha_j\right)} \tag{10}$$

where,

$$\overline{N} = \frac{1}{\overline{m}_\alpha}\left[\rho - \frac{c'}{F_S}\tan\alpha + u_a\frac{\tan\alpha}{F_S}\left(\tan\varphi' - \tan\varphi^b\right) + u_w\frac{\tan\alpha}{F_S}\tan\varphi^b\right] + \frac{1}{\overline{m}_\alpha \lambda f(x) F_S}\left[c' + u_a\left(\tan\varphi^b - \tan\varphi'\right) - u_w\tan\varphi^b\right] \tag{11}$$

in which, NG is the number of Gauss points; the subscript $_j$ denotes the number of Gauss point; and ω is the weight coefficient of Gauss point.

To maintain the function's continuity within the domain, the slip surface should be divided into several integration intervals when the present study is employed for some slip surfaces with gradient-discontinuity points or passing through interfaces of soil layers. Therefore, the FOS expressions can be further rewritten for generality as:

$$F_m = \frac{\sum_{k=1}^{NI}\left(x^k - x^{k-1}\right)\sum_{j=1}^{NG}\omega_{kj}\left\{c_{kj}'\frac{R_{kj}}{\cos\alpha_{kj}} + \left[\overline{N}_{kj} - \frac{u_{w,kj}}{\cos\alpha_{kj}}\frac{\tan\varphi_{kj}^b}{\tan\varphi_{kj}'} - \frac{1}{\cos\alpha_{kj}}u_{a,kj}\left(1 - \frac{\tan\varphi_{kj}^b}{\tan\varphi_{kj}'}\right)\right]R_{kj}\tan\varphi_{kj}'\right\}}{\sum_{k=1}^{NI}\left(x^k - x^{k-1}\right)\sum_{j=1}^{NG}\omega_{kj}\left(\rho_{kj}d_{kj}\right) - \sum_{k=1}^{NI}\left(x^k - x^{k-1}\right)\sum_{j=1}^{NG}\omega_{kj}\left(\overline{N}_{kj}f_{kj}\right)} \tag{12}$$

$$F_f = \frac{\sum_{k=1}^{NI}\left(x^k - x^{k-1}\right)\sum_{j=1}^{NG}\omega_{kj}\left\{c_{kj}' + \left[\overline{N}_{kj}\cos\alpha_{kj} - u_{w,kj}\frac{\tan\varphi_{kj}^b}{\tan\varphi_{kj}'} - u_{a,kj}\left(1 - \frac{\tan\varphi_{kj}^b}{\tan\varphi_{kj}'}\right)\right]\tan\varphi_{kj}'\right\}}{\sum_{k=1}^{NI}\left(x^k - x^{k-1}\right)\sum_{j=1}^{NG}\omega_{kj}\left(\overline{N}_{kj}\sin\alpha_{kj}\right)} \tag{13}$$

where NI denotes the number of intervals of integration; the subscript $_k$ is the number of the interval of integration; and x^{k-1} and x^k are two end points of the interval of integration, which should be the intersection point between the slip surface or the gradient-discontinuity point of the slip surface (as demonstrated in Fig. 2).

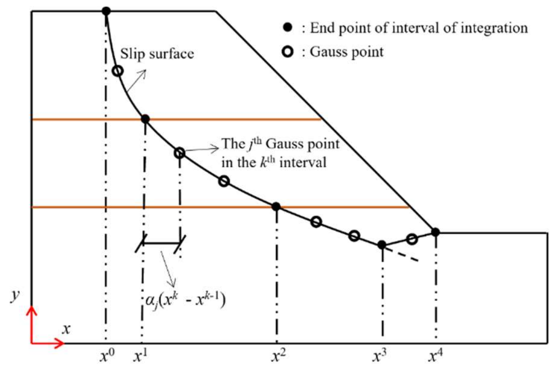

Figure 2: Alignment of Gauss points in the proposed method

The location of the adopted Gauss point, (x_{kj}, y_{ky}), can be calculated as follows:

$$x_{kj} = \alpha_j (x^k - x^{k-1}) + x^{k-1} \tag{14}$$

$$y_{kj} = S(x_{kj}) \tag{15}$$

where α is the dimensionless coefficient of Gauss point; and $S(x)$ is the shape function of the slip surface. It is recommended to use 3-5 Gauss points in one integral region to achieve reliable results. More Gauss points can also be defined based on the specific situation.

2.2 Refined procedures for solving FOS

The solving procedures for the FOS in the present study include two parts: (1) solving the FOS with the selected scaling factor; (2) obtaining the scaling factor satisfying the total equilibrium conditions.

When solving factor of safety equations in the traditional MP method, the interslice force distribution must be assumed to be zero initially. Then, in each iterative step, the interslice force should be updated separately, leading to a tedious computational procedure. In the present study, a set of more concise iteration procedures (see Fig. 3) can be described as follows:

(i) Input slope conditions and λ.
(ii) Align Gauss points.
(iii) Set $F_{s,i}$ = 1.0.
(iv) Get the normal force at each Gauss point.
(v) Calculate $F_{s,i+1}$ according to Eq. (12) or Eq.(13).
(vi) Set $F_{s,i} = F_{s,i+1}$ and return to Step (iv) until the differences in values of F_s between two consecutive iterations are within specified limits of tolerance, *TOL*.

It is convenient to implement the best-fit regression method for searching the scaling factor for the total equilibrium condition. However, the data points must be distributed densely enough to searching the accurate results of the joining between F_m and F_f, implying the relatively large computational effort is taken in the analysis. For efficiently searching the scaling factor satisfying both moment and force equilibrium conditions, a linear searching method is employed in the present study. The linear searching method (as illustrated in Fig. 4) can be described as follows:

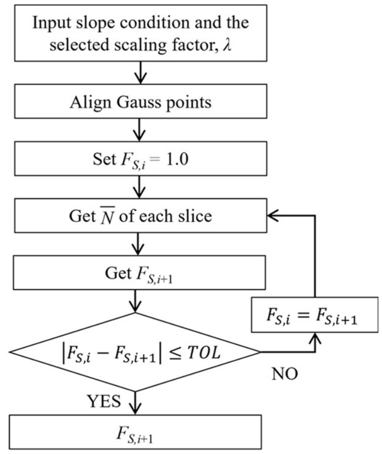

Figure 3: Solving FOS with the selected scaling factor in the present study

(i) Input the searching range [λ_L, λ_R].
(ii) Obtain $\Delta F(\lambda_L)$ and $\Delta F(\lambda_R)$, where $\Delta F(\lambda) = F_m(\lambda) - F_f(\lambda)$.
(iii) Calculate λ_M using the secant relation as:

$$\lambda_M = \frac{\lambda_L \Delta F(\lambda_R) + \lambda_R \Delta F(\lambda_L)}{\Delta F(\lambda_R) - \Delta F(\lambda_L)}$$

(iv) Check whether $\Delta F(\lambda_M)$ achieves the convergence criterion. If the convergence tolerance is satisfied, output λ_M as the result. Otherwise, return to Step (iv) and update the searching range according to:

$$\lambda_L = \begin{cases} \lambda_L & if \quad \Delta F(\lambda_L)\Delta F(\lambda_M) < 0 \\ \lambda_M & if \quad \Delta F(\lambda_L)\Delta F(\lambda_M) \geq 0 \end{cases} \quad AND \quad \lambda_R = \begin{cases} \lambda_R & if \quad \Delta F(\lambda_R)\Delta F(\lambda_M) < 0 \\ \lambda_M & if \quad \Delta F(\lambda_R)\Delta F(\lambda_M) \geq 0 \end{cases}$$

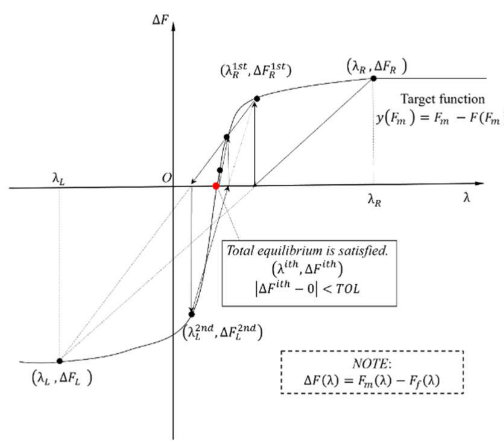

Figure 4: Schematic diagram of linear search algorithm for determining the scaling factor

3 VERIFICATION EXAMPLES

In this section, two typical types of slopes are studied to validate the present method based on Gaussian integral for assessing the stability of unsaturated soil slopes, including homogeneous and nonhomogeneous slopes.

3.1 Example 1: Stability analysis of a homogeneous unsaturated soil slope

In this example, a steep and homogeneous slope with a height of 30 m and a slope angle of 50° is re-analysed (Zhang et al. 2014). Fig. 5 illustrates the geometry of this homogenous steep slope and prescribed critical slip surface. The unit weight of the soil is γ = 18 kN/m^3. The cohesion and effective internal friction angle of the soil are c' = 10 kPa and φ' = 34°, respectively. The average depth of piezometric line is more than 10 m below the surface of slope.

A specific slip surface is selected for evaluating the stability of this unsaturated soil slope (see Fig. 5). Table 1 lists the values of FOS of the slope with the prescribed slip surface under different φ^b-values. The FOS-values of the unsaturated soil slope in this study are generally consistent with those calculated by Zhang et al. (2014). The FOS of slope increases gradually with the increase of φ^b. This increasing trend is because the increasing φ^b has enhanced the shear strength listed in Eq. (1), and thus, the enhancing mobilized shear force shown in Eq. (8) at the slice base increases. The error is also evaluated, which is defined by ratio of difference between the previous value of FOS and FOS in the present study to the FOS in the present study. The error decreases with the increasing φ^b.

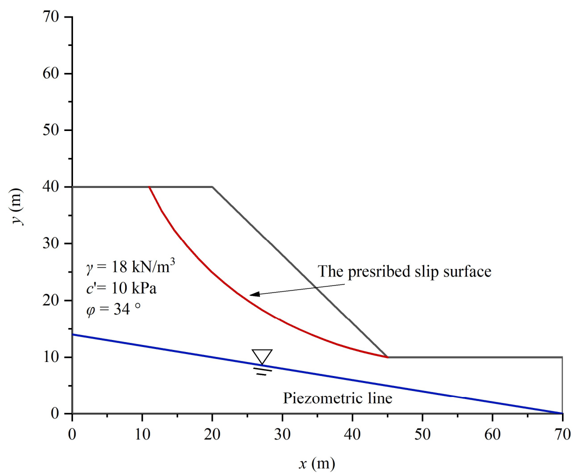

Figure 5: Geometry and prescribed critical slip surface of a homogenous unsaturated soil slope

Table 1: FOS under different values of φb for the example of a homogenous unsaturated soil slope

φ^b (°)	FOS in Zhang et al. (2014)	FOS in present study	Error
0	1.005	1.001	0.39 %
15°	1.430	1.426	0.28 %
34°	2.118	2.121	0.14 %

The traditional MP method has also been used to validate the new method. The numbers of soil slices for traditional MP method and gauss points for present study are 32 and 5, respectively. Table 2 summarises the FOS and computational cost in the present proposed and traditional MP methods for this example. The improved MP method using Gaussian integral with only 5 Gauss points shows much higher efficiency than the traditional MP method with 32 slices, no matter which value of φ^b is assumed. In general, for different values of φ^b, the time used in the present study is approximately only one tenth of that used in the traditional MP method. Fig. 6 shows comparisons of critical slip surfaces based on the present study and traditional MP method for the homogenous slope. The critical slip surfaces obtained from the present study agree well with those surfaces suggested by Zhang et al. (2014) . The depth of critical slip surface increases with the rising φ^b. Compared with the other two critical slip surfaces, the critical slip surface for $\varphi^b = \varphi'$ is much deeper. This example demonstrates the accuracy and efficiency of this improved MP method in evaluating the stability of unsaturated and homogenous soil slope. In addition, Table 2 also demonstrates that ignoring unsaturated characteristic of soil by taking φ^b = 0° will lead to significant underestimation of slope stability, underscoring the critical need to accurately account for the unsaturated properties of soil in slope stability assessment.

Table 2: FOS and computational cost in different methods for the example of a homogenous slope

Analysis method	n_{SP}	φ^b (°)	FOS	Computational time (s)
Traditional MP	32 slices	0	0.887	1202
		15	1.420	1532
		34	1.908	1598
Present study	5 Gauss points	0	0.895	113
		15	1.399	122

	34	1.879	185

Notes: n_{SP} denotes the number of sampling points in different methods

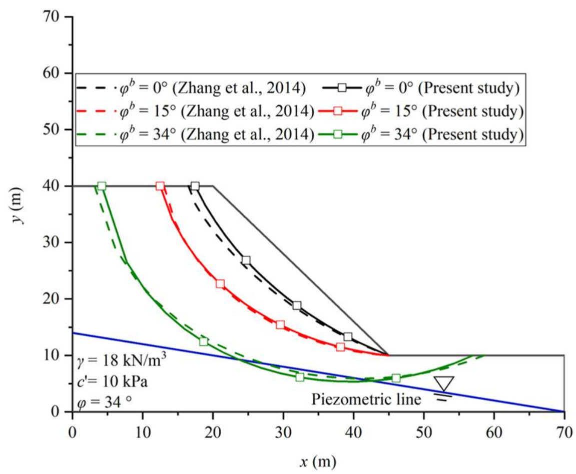

Figure 6: Critical slip surfaces based on present study and traditional MP method for a homogenous unsaturated soil slope

3.2 Example 2: Stability analysis of a nonhomogeneous unsaturated soil slope

Example 2 was originally presented by Fredlund et al. (2006). The example is a nonhomogeneous slope with three layers, in which there is a weak layer between medium and hard layers. The geometry, soil properties of different layers, and piezometric line are shown in Fig. 7. Fredlund et al. (2006) compared the values of FOS based on dynamic programming method and MP method and found that FOS of dynamic programming method was around 14% lower than that of MP method. The critical slip surface is highly irregular and influenced by the position of weak layer.

Here, the example is reanalysed using the proposed method and traditional MP method. In this example, 3-4 Gauss points are aligned at each soil layer in the proposed method. The different values of FOS for different values of φ^b based on these two methods are shown in Fig. 7. In general, with the rise of φ^b, the critical slip surface gets shallower for the two methods. The shape of critical slip surfaces changes from a typical circular arc to an irregular shape. It seems that the position of weak layer affects the shape of critical slip surfaces and leads to the irregular shape of critical slip surfaces. This phenomenon agrees well with those observed by Fredlund et al. (2006). For both two methods, the FOS decreases with the increase of φ^b. The declining trend of FOS with increasing φ^b for the nonhomogeneous slope is different from the increasing trend observed in a homogeneous slope since the FOS is influenced by the combination of factors, such as soil layers, soil properties, and piezometric line. The FOS results based on proposed method are generally consistent with those based on the traditional MP method. This example shows the effectiveness and accuracy of this proposed method in evaluation of stability of nonhomogeneous slope.

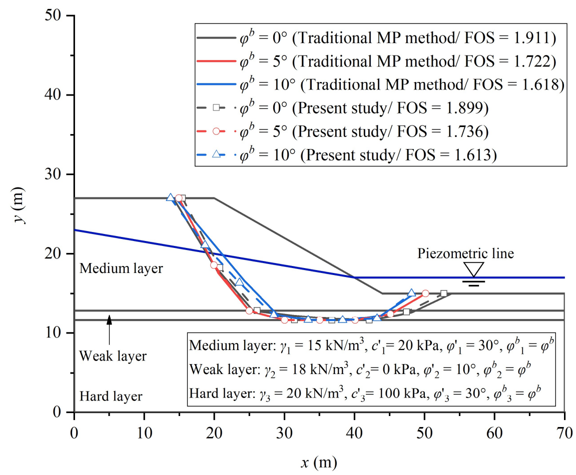

Figure 7: Critical slip surfaces based on present study and traditional MP method for a nonhomogeneous unsaturated soil slope

4 CASE STUDY: STABILITY ANALYSIS OF A CUT SLOPE OF WEATHERED GRANITE

As shown in Fig. 8, a steep cut slope of weathered granite behind a hospital and residential buildings in Hong Kong is investigated. There have been dangerous small periodic failures at the crest of slope, which require a comprehensive investigation. The average inclination of the slope is 60°. The slope surface is a layer of soil cement and lime plaster which can protects the slope from water infiltration. The soil stratigraphy is broadly distributed in Hong Kong especially for the colluvial slopes in the mountain area, including granitic colluvium, completely weathered granite, and highly weathered granite. The weathered granite is one of the most common residual soils in Hong Kong. The depth of bedrock is 20 to 30m below the ground surface. The approximate position of water table is located in the bedrock. Table 3 lists the soil properties of different layers in the case study. The average value of φ^b is 15.0° based on the results of triaxial tests (Ho & Fredlund 1982). The measured soil suction ranges from approximately 0 to 80 kPa due to different elevations. With the increasing elevation, the soil suction gets greater.

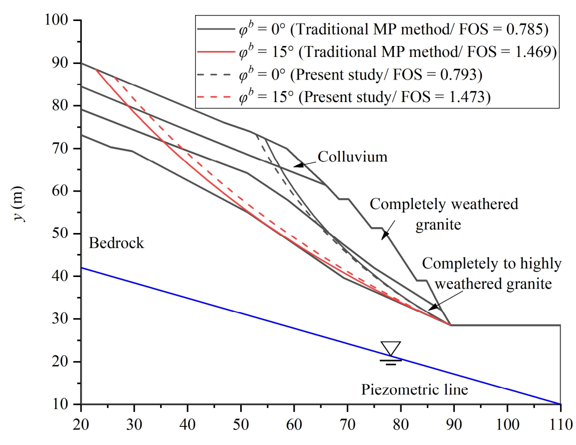

Figure 8: Critical slip surfaces based on present study and traditional MP method for an unsaturated soil slope of weathered granite

Table 3: Soil properties in the case study

Soil type	γ (kN/m³)	c' (kPa)	φ' (°)	φ^b (°)
Colluvium	19.6	10.0	35.0	15.0
Completely weathered granite	19.6	15.1	35.2	15.0
Completely to highly weathered granite	19.6	23.5	41.5	15.0

This case study has been re-analysed by comparing the slope-stability evaluation using the efficient LEM based on Gaussian integral and the traditional MP method (see Fig. 8). 3-4 Gauss points are placed in each soil layer in this case study. In the analysis, the suction was ignored (φ^b = 0°) firstly. The FOS-values based on the traditional MP method and present method are 0.785 and 0.793, respectively. These results can generally agree well with the FOS of 0.864 based on the Bishop simplified method. These slight differences might be due to the different assumptions in these methods, such as different force equilibrium conditions and soil discretization methods, etc. Nevertheless, it seems that the slope is still stable. This might be attributed to the enhanced shearing strength due to suction has strengthened the slope stability, reflecting the significant role of suction in soil slope stability. Secondly, the average value of φ^b which is equal to 15.0° was adopted in the analysis. The values of FOS for the traditional MP method and present method are 1.469 and 1.473, respectively. It shows that the consideration of suction has greatly enhanced the slope stability. In addition, the critical slip surfaces based on these two methods are consistent with each other no matter whether the suction is considered or not. With the increase of φ^b, the depth of critical slip surface gets deeper. These results of FOS-values and critical slip surfaces agree well with those observed by Zhang et al. (2014). Moreover, the computational cost with different methods on the same device are also given in Table 4 to illustrate the computational efficiency of the proposed method.

Table 4: Computational cost of different methods in case study

Analysis method	Average computational time
Traditional MP method	15 min
Present study	3 min

5 CONCLUSIONS

This study presents an efficient numerical implementation of limit equilibrium method (LEM) based on the Morgenstern-Price method using Gaussian integral for stability analysis of unsaturated soil slopes. This new method is an extension of the improved Morgenstern-Price method proposed by Ouyang et al. (2022). Compared with the other methods, this method may be a useful attempt and might provide a new solution to evaluate the stability of unsaturated soil slopes. Conclusions are mainly summarized as follows:

(1) The extended Mohr–Coulomb shear strength equation is adopted to be the governing shearing strength equation in the analysis of slope stability. In traditional LEM, the slice division shall be dense enough by increasing the slice number to achieve reliable results. However, in the new method, a numerical integral technique named Gaussian integral, is introduced for simplifying the expressions and calculations of FOS values. In addition, the solving procedures for the FOS in the present study mainly include two parts, including solving the FOS with the selected scaling factor and determining the scaling factor satisfying the total equilibrium conditions. Based on the developed formula, the iteration process for calculating the FOS with the given scaling factor is refined where the step of assuming the initial force distribution is eliminated. Besides, the linear search method is used in searching the scaling factor to fulfil the total equilibrium conditions.

(2) This new method is validated based on two typical benchmark examples such as homogeneous and nonhomogeneous unsaturated soil slopes and one case study of unsaturated residual soil slope in Hong Kong. Overall, compared with the traditional MP method, the newly proposed method with a few Gauss points is reliable, accurate, and efficient in evaluating the stability of unsaturated soil slopes.

ACKNOWLEDGEMENTS

The Start-up Fund for RAPs under the Strategic Hiring Scheme from PolyU (UGC) (Project ID: P0045938) is acknowledged. The authors also acknowledge the supports by a RIF project (Grant No.: R5037-18) and GRF projects (Grant No.: 15217918, 15213019, 15210020, 15231122) from Research Grants Council (RGC) of Hong Kong Special Administrative Region Government of China. The authors also acknowledge the financial support from grants (CD7A and CD82) from the Research Institute for Land and Space of Hong Kong Polytechnic University, and financial support (W23L, ZDBS) from The Hong Kong Polytechnic University. This financial support is gratefully acknowledged. This work is also partially supported by grants from the Research Grants Council of the Hong Kong Special Administrative Regain, China (Grant No.: 15203121).

REFERENCES

Cai, F., Ugai, K. 2004. Numerical analysis of rainfall effects on slope stability. *Int J Geomech*, 4(2): 69–78.

Xiong, X., Shi, Z., Xiong, Y., Peng, M., Ma, X. & Zhang, F. 2019. Unsaturated slope stability around the Three Gorges Reservoir under various combinations of rainfall and water level fluctuation. *Eng Geol*, 261(December 2018): 105231.

Houston, S.L. 2019. It is time to use unsaturated soil mechanics in routine geotechnical engineering practice. *J Geotech Geoenviron Eng*, 145(5): 02519001.

Sun, D., Wang, L., Li, L. 2019. Stability of unsaturated soil slopes with cracks under steady-infiltration conditions. *Int J Geomech*, 19(6): 04019044.

Griffiths, D.V., Lu, N. 2005. Unsaturated slope stability analysis with steady infiltration or evaporation using elasto-plastic finite elements. *Int J Numer Anal Methods Geomech*, 29(3): 249–267.

Duncan, M.J. 1996. State of the art: limit equilibrium and finite- element analysis of slopes. *J Geotech Eng*, 122(7): 577–596.

Ouyang, W., Liu, S.W., Yang, Y. 2022. An improved morgenstern- price method using gaussian quadrature. *Comput Geotech*, 148: 104754.

Cheng, Y.M., Lau, C. 2014. Slope stability analysis and stabiliza- tion: new methods and insight. CRC Press, Boca Raton.

Fredlund, D.G., Morgenstern NR, Widger RA 1978. The shear strength of unsaturated soils. *Can Geotech J*, 15(3): 313–321

Fredlund, D.G. 2006. Unsaturated soil mechanics in engineering practice. *J Geotech Geoenviron Eng*, 132(3): 286–321.

Zhang, L.L., Fredlund, D.G., Fredlund, M.D., Ward, Wilson G. 2014. Modeling the unsaturated soil zone in slope stability analysis. *Can Geotech J*, 51(12): 1384–1398.

Ho, D.Y., Fredlund, D.G. 1982. Increase in strength due to suction for two Hong Kong soils. *Proceedings of the ASCE specialty conference on engineering and construction in tropical and residual soils*, Hawaii. p. 263-96.

Development of Three-Dimensional Geotechnical Models for Territorial and Infrastructural Development in Hong Kong

Lawrence KW SHUM, Sammy PY CHEUNG,
Richard CM HO, Charles CL CHAN & James ZJ RUAN
Geotechnical Engineering Office, Civil Engineering and Development Department
The Government of the HKSAR, Hong Kong, China

ABSTRACT

With an aim to support the Smart City Blueprint for Hong Kong, the Geotechnical Engineering Office (GEO) of Civil Engineering and Development Department (CEDD) has been taking a steering role in developing 3D geotechnical models (3DGM) for supporting territorial and infrastructural development in Hong Kong. In parallel to the recent revamp of the centralised data repository Geotechnical Information Infrastructure into a three-dimensional mapping system (namely 3DGInfo), the GEO has initiated a pilot study to develop territory-wide 3DGM utilising existing ground investigation (GI) records collected from public and private projects. Unlike conventional geological maps, the 3DGM is designed for practical engineering applications, such as giving reference to the optimal foundation depths for various types of deep foundations. By providing detailed insights into subsurface conditions, the 3DGM enables planners and engineers to efficiently assess site-specific geology and streamline decision-making during the early stages of development projects. A customised workflow was proved successful in generating 3DGM blocks in Wan Chai, Tung Chung East reclaimed land and a marble site in Yuen Long. Riding on the success of the pilot study, the GEO is working to further enhance the 3DGM generation methodology using state-of-the-art technologies and has prioritised a new phase of 3DGM block creation in the Northern Metropolis Development areas. This paper discusses the innovative solutions adopted and the GEO's vision and roadmap for developing territory-wide 3DGM to enhance GEO services and benefit practitioners.

1 INTRODUCTION

The GEO is always taking a steering role in the application of innovation and technology (I&T) for advancing geotechnical practice in Hong Kong (Cheung, 2006; Cheung, 2021; Shum et al., 2024). As part of the Government's mission to digitally transform the construction industry, including private development and public works, one of the initiatives is to convert raw data into actionable insights, i.e. moving from being data-rich to information-rich structure, to enhance the efficiency in the delivery of engineering projects.

In parallel to the evolution of the Geotechnical Information Infrastructure to a three-dimensional mapping system (3DGInfo), the GEO has initiated a pilot study to develop territory-wide subsurface ground models, namely the 3D Geotechnical Models (3DGM). This initiative aligns with the Hong Kong Smart City Blueprint, which will equip practitioners to rapidly assess subsurface conditions and streamline the decision-making on engineering applications for future projects. By harnessing decades of ground investigation (GI) records collected by the GEO, a subsurface spatial data inventory in a truly three-dimensional space is being established. The GEO envisions that the 3DGM will be the fundamental step to advance digitalisation and automation in the engineering sector, fostering widespread adoption of digital models and enabling the industry to unlock the full potential of modernised digital workflows.

2 PILOT THREE-DIMENSIONAL GEOTECHNICAL MODEL

To facilitate the understanding of the ground conditions in the early stages of engineering projects, the GEO developed 3DGM in designated pilot areas for trial uses in foundation studies. Unlike conventional geological maps, the 3DGM emphasises its relevance to engineering applications. In the pilot study, stratigraphic interfaces are delineated with reference to typical foundation design practices in Hong Kong. For instance, steel-H piles are usually driven to refusal in soil stratum with Standard Penetration Test (SPT) N-value greater than 200, whereas end-bearing piles are founded on Category 1(d) and Category 1(c) rocks with specific presumed allowable bearing pressure. Figure 1 illustrates the stratigraphic interfaces adopted in the pilot 3DGM.

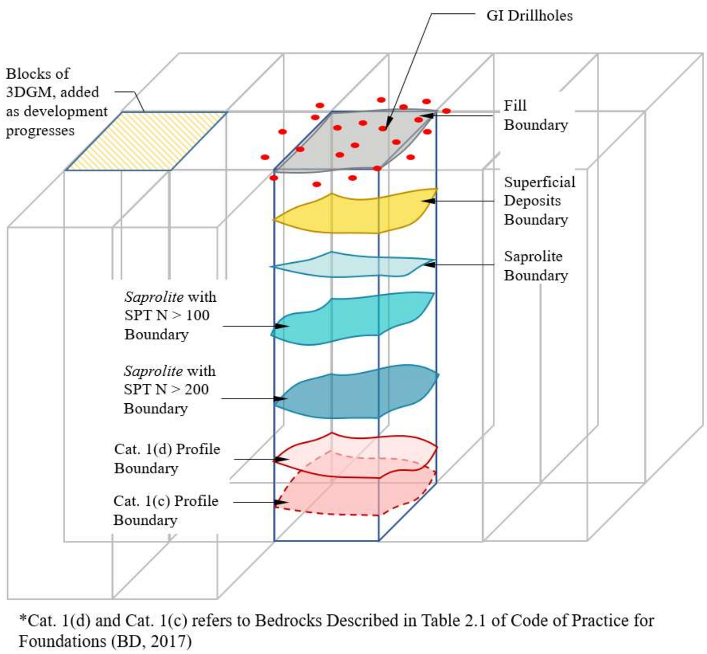

Figure 1: Stratigraphic interfaces in pilot 3DGM for typical foundation design in igneous rock

2.1 The Pilot 3DGM generation methodology

The pilot 3DGM generation methodology is developed based on the prevailing engineering practice to support foundation design in Hong Kong. The key procedures are shown in Figure 2 and summarised below:

1. **Data Collection:** Territory-wide air-borne LiDAR survey (for ground profile), borehole records.
2. **Data Extraction:** Extract relevant information (e.g., soil/rock type, SPT N-value, total core recovery and weathering grade of bedrock) and determine levels of relevant stratigraphic interfaces for foundation design (e.g. Cat. 1(c) level).
3. **Interpolation:** Generate contours of different stratigraphic interfaces using the linear triangulation method in commercial software.
4. **3D Model Generation:** Populate the volume between the contoured surfaces and the ground profile with voxels (3D pixels) in the network common data form (netCDF) format by using customised Python scripts and GIS software.

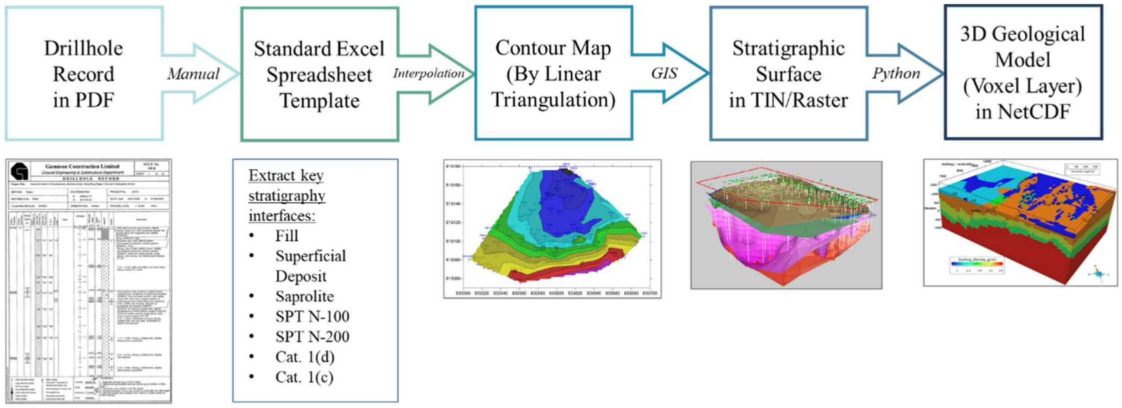

Figure 2: Existing pilot 3DGM generation methodology

By using the above generation methodology, the GEO created four pilot 3DGM blocks in Hopewell Centre II, Wan Chai urban area (Map Sheet No. 11SW-14B), Tung Chung East reclaimed land (Map Sheet No. 9SE-4B) and a marble site in Yuen Long. These pilot 3DGM blocks comprise voxel cells (each of 1 m cubic dimension) in grids (Figure 3). Voxels are small, cube-shaped units of volume that can be arranged in 3D space to represent objects of any size and shape. In recent years, voxel-based 3D modelling has gained popularity for representing complex and discrete volumetric objects. They are particularly well-suited for representing irregular and fragmented structures, such as terrain and geological formations.

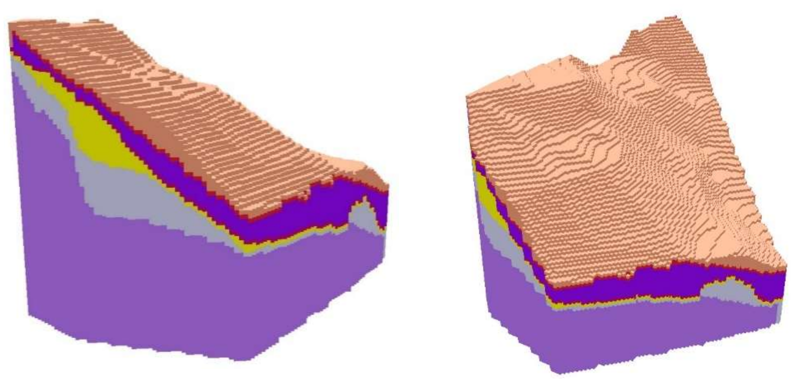

Figure 3: Pilot 3DGM in voxel format

Besides representing the 3DGM blocks in voxel format, the corresponding boreholes can be generated concurrently together as 3D sticks under the same process. Practitioners can display the 3D borehole sticks on top of the 3DGM blocks in 3DGInfo (Figure 4). The spatial distribution of the boreholes used could indicate the density of source data and qualitatively give a measure of reliability for the 3DGM generated. Practitioners should be cautious when using the pilot 3DGM in areas with limited borehole data. However, they can focus on adding GI boreholes in those areas with a lower density of existing boreholes to supplement the insufficiency of subsurface data.

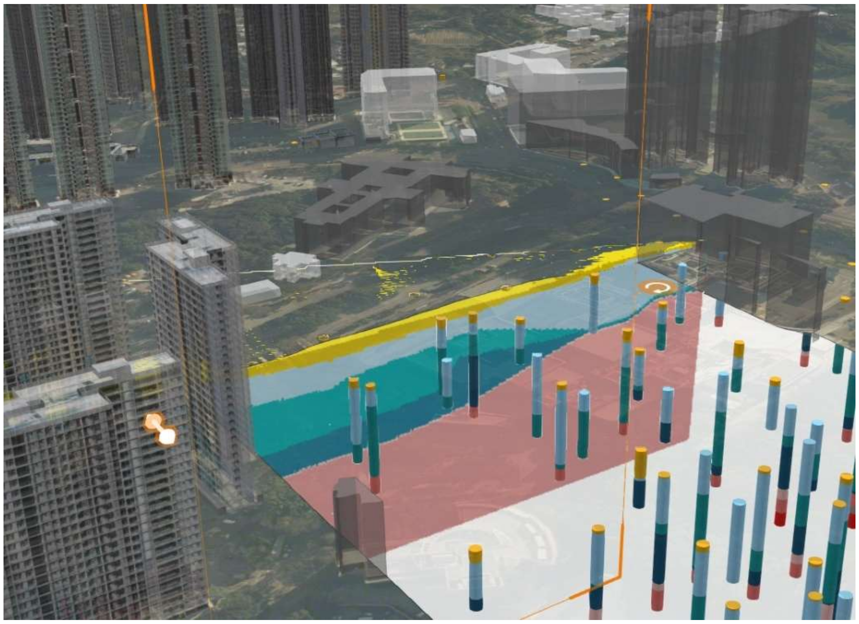

Figure 4: 3DGM overlaying with GI in 3DGInfo

2.2 Pilot 3DGM currently available in 3DGInfo

The first batch of pilot 3DGM blocks confirmed the feasibility of transforming conventional 2D contour maps into 3D models, which enable a rapid visualisation of regional subsurface conditions for foundation studies. Instead of creating project-specific models, the GEO targeted to progressively build up a city-scale subsurface spatial dataset by linking up multiple 3DGM blocks built in standard 1:5000 survey map sheet scale, i.e. a plan area of 750 m × 600 m for each block. This delineation method allows flexibility in phased development and future updating of individual blocks on a modular basis. Figure 5 shows the pilot 3DGM block in Wan Chai.

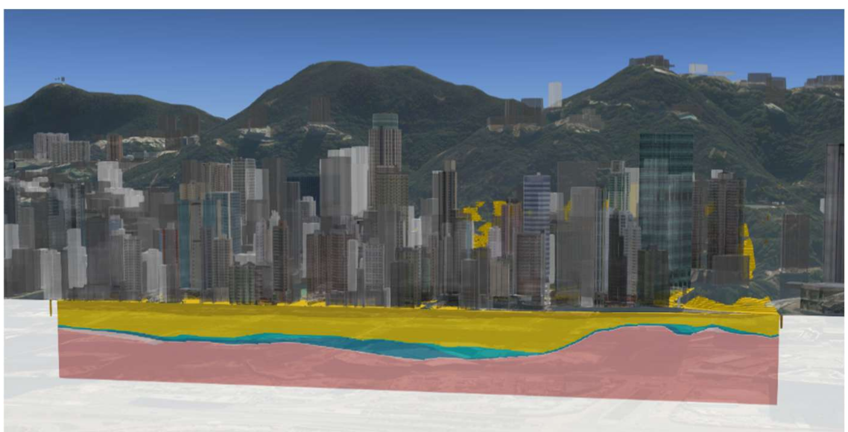

Figure 5: Pilot 3DGM block in Wan Chai (Map Sheet No. 11SW-14B)

2.3 Pilot 3DGM blocks facilitating Northern Metropolis Development

Building on the success of the in-house pilot study, the GEO engaged consultants with the objectives of tapping their expertise and knowledge to enhance the 3DGM generation methodology in ground modelling and accelerating the construction of the 3DGM to support upcoming new town developments in the Northern Metropolis Development Areas (NMDAs).

Study areas with different geological settings were selected to evaluate the applicability of the existing 3DGM workflow and identify areas for improvement. The enhanced generation methodology can now modify the ground profile based on 2020 LiDAR survey results (Figure 6), incorporate inferred rock contact and sub-vertical boundary change interpreted by experienced geologists (Figures 7 & 8) and attach in-situ field test results (such as SPT-N values and total core recovery) on 3D borehole sticks (Figure 9).

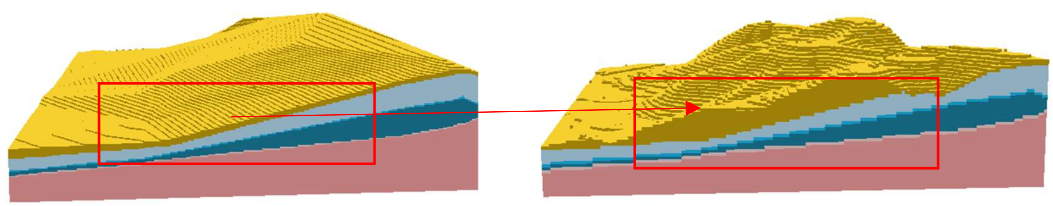

(a) Ground surface based on GI data (b) Ground surface based on 2020 LiDAR results

Figure 6: Modification of 3DGM ground profile based on 2020 LiDAR survey results (AECOM, 2024)

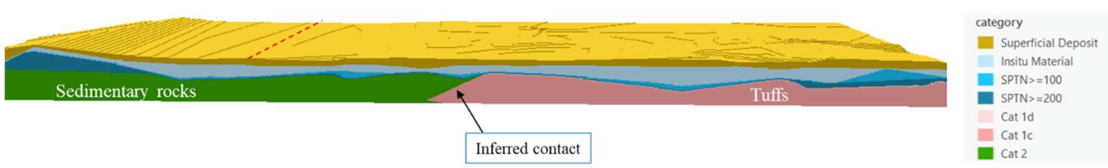

Figure 7: Modelling of inferred rock contact and sub-vertical boundary change (AECOM, 2024)

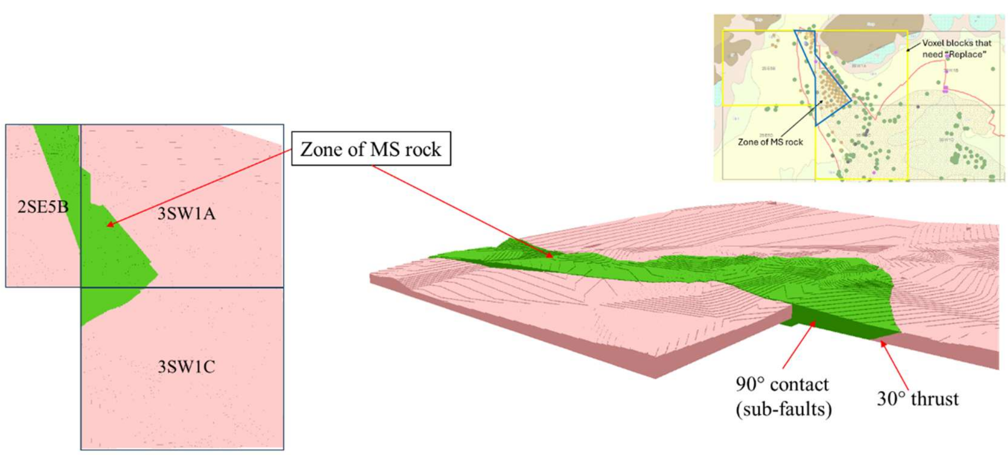

Plan View *Side View*

Figure 8: Modelling of different rock types within and across different 3DGM blocks (AECOM, 2024)

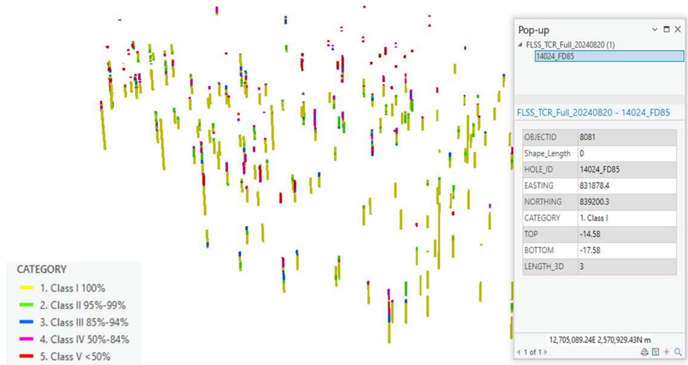

Figure 9: Total core recovery attached to 3D Borehole Sticks (AECOM, 2024)

Currently, thirty-nine 3DGM blocks have been assembled for the proposed new towns in Fanling, Sheung Shui and Yuen Long using available GI data. All pilot 3DGM blocks have been uploaded to the 3DGInfo and are available for practitioners to use. To support the NMDAs, the GEO has accorded priority to expand the 3DGM blocks to cover these future development areas, such as the High-end Professional Services and Logistics Hub (i.e. Tin Shiu Wai, Hung Shui Kui, Ha Tsuen, Tsim Bei Tsui, Lau Fau Shan, Pak Nai and Yuen Long), Innovation and Technology Zone (i.e. San Tin, Lok Ma Chua and Ngua Tam Mei) and the Boundary Commerce and Industry Zone (i.e. Kwu Tung North, Man Kam To, Fanling, Sheung Shui and other northern districts).

3 ENGINEERING APPLICATIONS OF 3DGM

The pilot 3DGM enables instant assessment of ground conditions within a project boundary, significantly accelerating the creation of preliminary geotechnical models for better-informed decisions by planners and practitioners. This is particularly useful in preliminary planning, budgeting and schematic design of substructure works in projects. For example, practitioners can determine the spatial distribution of competent strata and the approximate founding levels of deep foundations. This facilitates a more efficient assessment of foundation options, as well as improving the estimations on the cost and time for the substructure works. The benefits and engineering applications of 3DGM are elaborated in the following sections.

3.1 Utilisation of valuable ground investigation records

The establishment of a territory-wide 3DGM is one of the best options to utilise and visually present comprehensive GI and laboratory testing inventory currently stored in the Digital Geotechnical Information Unit (DGIU). The GEO has collected over 370,000 GI records and associated laboratory test reports from various public and private projects since the 1980s. Despite the availability of some digital data in AGS file format, the majority of GI records in the DGIU are disseminated as scanned documents. This format is inconvenient for users who want to quickly appreciate the subsurface geology and ground conditions. Currently, practitioners have to download and review individual scanned reports from the DGIU, and extract data for subsequent use. The data are often manually entered into spreadsheets for processing in computer-aided design (e.g. CAD and BIM) and other engineering software. This manual extraction process can be error-prone and require laborious cross-checking that can take days. Furthermore, many practitioners usually lack a quick and efficient tool to visualise ground conditions before undertaking this time-consuming data extraction and CAD/BIM visualisation process. In essence, the 3DGM under 3DGInfo would provide practitioners a quick reference to readily visualise and understand subsurface conditions in a 3D perspective.

3.2 Efficient planning for site investigation

The 3DGM serves as an efficient tool for practitioners to systematically study regional geological conditions, identify potential constraints, and strategically plan site-specific GI works to mitigate uncertainties in ground conditions. Traditionally, during desk studies, GI planners should assess the relevance and spatial distribution of existing GI records and construct preliminary ground models or geological profiles for initial geotechnical assessments. In contrast, the 3DGM already integrates all available GI records and provides a reference model, significantly reducing the time and resources spent on repeating these processes across projects in the same region (Figure 10). Instead of building preliminary models from scratch, practitioners can explore the 3DGM to understand the subsurface conditions and extract relevant data for further analysis. Additionally, by overlaying geological maps within the 3DGInfo, practitioners can swiftly pinpoint areas with complex geological features, and plan targeted GI works as needed. The 3DGM further optimises GI planning by enabling simultaneous evaluation of stratigraphy and existing GI data locations, fostering data-driven decision-making during preliminary studies and site-specific GI design.

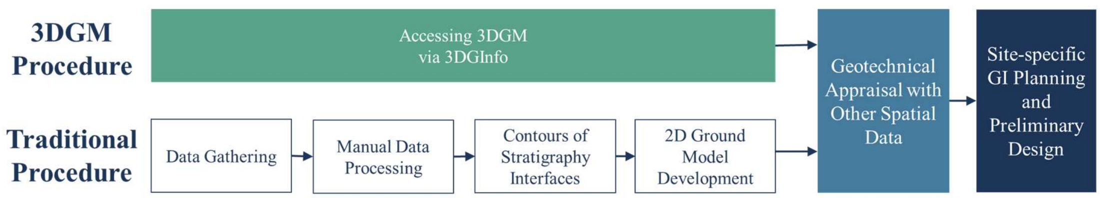

Figure 10: Prevailing engineering practice subsumed in 3DGM generation methodology

3.3 Interaction with different spatial data facilitating informed decision-making

The 3DGInfo integrates diverse datasets, enabling practitioners to visualise ground conditions alongside other spatial information and leverage synergies for project planning and risk assessment. For example, users can overlay geological maps, aerial photographs, tunnel protection zones, sensitive receivers (e.g., buildings, slopes), and topography with subsurface data within a unified 3DGInfo interface. This integrated approach extends beyond basic ground condition analysis, offering practical advantages for construction planning. Instant access to critical parameters, such as fill thickness, superficial deposit distribution, and groundwater conditions, streamlines the rapid evaluation of excavation and lateral support systems. For projects near sensitive structures (e.g., residential buildings, historical masonry walls, or underground tunnels), the 3DGInfo and 3DGM empower practitioners to assess potential impacts like ground movements, subsidence, and piling-induced vibrations/noise. These insights facilitate informed decisions on pile types and construction methodologies (Figure 11). Additionally, the system identifies risks such as structural loading on adjacent slopes or infrastructure, ensuring proactive mitigation strategies.

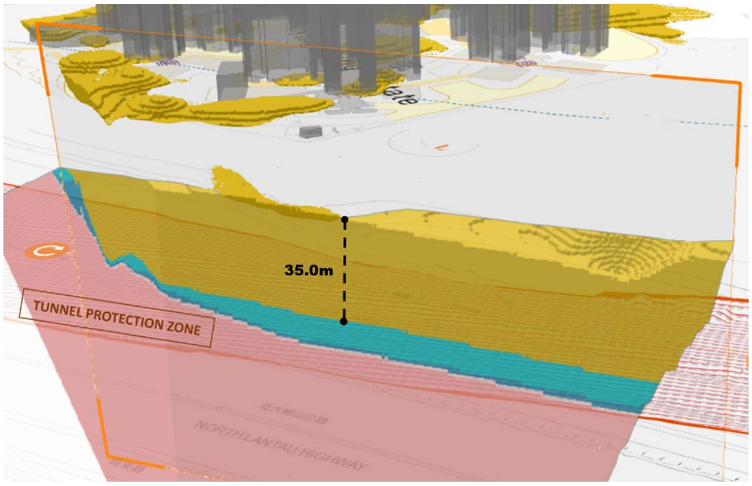

Figure 11: 3DGM overlaying with tunnel protection zone in 3DGInfo

3.4 Available geo-processing tools for 3DGM

In addition to visualisation in 3DGInfo, the interpreted stratigraphy (e.g. contours) and voxel data can be downloaded from the 3DGInfo in formats that could be used in other engineering software for contouring and GIS/BIM applications. This allows practitioners to integrate the data into their design workflows and GIS/BIM platforms. Several geo-processing tools are also available in the 3DGInfo to facilitate the use of the 3DGM, such as slicing tools for visualising the ground conditions in cross-sections. Figures 12 and 13 illustrate the available geo-processing tools for utilising the 3DGM within the 3DGInfo.

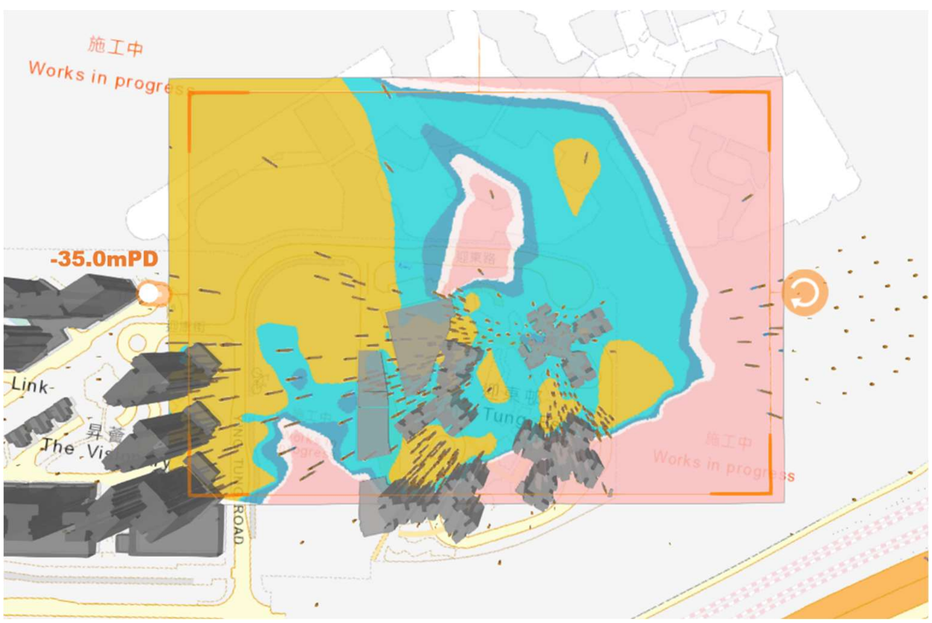

Figure 12: Geo-processing tools showing spatial distribution of ground materials at -35.0mPD

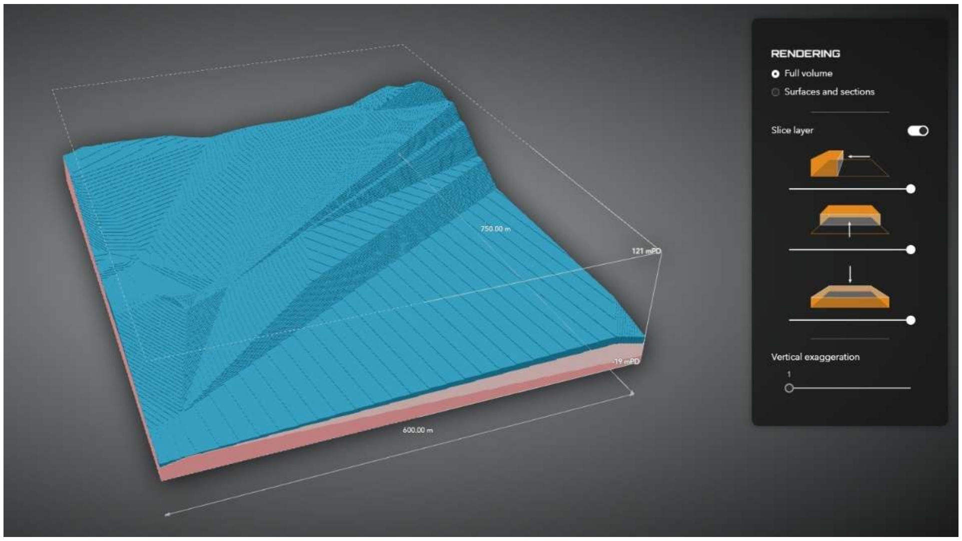

Figure 13: Geo-processing tools displaying selected stratigraphy

4 CHALLENGES AND LIMITATIONS

Despite the successful implementation of the pilot 3DGM and its benefits for engineering applications, the current 3DGM generation methodology inevitably has limitations and definitely room for further enhancements. For example, the current workflow still relies heavily on manual processing when handling complex geological conditions, such as marble area, rock contacts, etc. The reliability of each 3DGM block is currently represented qualitatively by the superposition of 3D borehole sticks, but the reliability arising from different interpolation methods and geological variations cannot be properly quantified statistically.

4.1 Challenges in modelling complex geological conditions

In an attempt to model complex geology, the GEO created a pilot 3DGM in a marble site in Yuen Long (Figure 14). The modelling method of this pilot 3DGM is based on the karst geomorphology model (GEO, 1994). The presentation of the subsurface conditions with karst features suitable for founding deep foundations is fundamentally different from the conventional approach of representing other rock formations.

The karst geomorphology model employs a marble class system to categorise complex geological conditions in marble formations into a structured and abstracted framework. A key challenge in constructing deep foundations in marble formations is their highly variable nature and the presence of karstic features, such as overhangs, underground channels, cavities, and irregular rock surfaces. To streamline foundation design in such subsurface conditions, marble rock masses are classified into six distinct classes based on the percentage of the Marble Quality Designation (MQD) achieved in boreholes within predefined elevation levels. The MQD is computed from the core samples in boreholes and is a useful index to indicate the presence of dissolution cavities. Amalgamating zones of similar MQD will give the physical and mechanical implications of karstic features in the marble formation that can have a profound influence on the foundation stability.

In this system, Marble Classes I and II represent very good to good quality marble masses with MQD greater than 50%, and with no or minimal karstic features, making them ideal for foundation purposes. Class III defines fair to marginal quality marble mass influenced by karstic features, requiring detailed assessment to evaluate their impact on foundation stability. Conversely, Classes IV and V classify poor to very poor quality marble masses, heavily compromised by karstic features with MQD less than 25% and are typically unsuitable for foundations. Class VI, the final class, refers to non-marble rock types (e.g., interbedded layers) within the marble formation. This systematic approach enables practitioners to efficiently evaluate risks and tailor foundation solutions to site-specific conditions.

In the process of building the karst geomorphology model, the MQD of each borehole is calculated for the entire rock cores to derive the corresponding marble classes at every 5 m interval in the vertical elevation. The marble masses are then broadly grouped into competent marble classes (i.e. Classes I and II) and non-competent (i.e. Classes III to V) marble classes. Due to its inherent complexity, sound professional judgement is needed to develop a formidable geotechnical framework. The pilot 3DGM block digitised the categorised marble zone, similar to stacking Legos at 5 m intervals. This enables a 3D visualisation of karstic features within the marble rock formation (Figure 14). With the pilot 3DGM in such complex ground conditions, practitioners can now quickly identify possible zones of non-competent marble, for example, buried underground channels, and carefully assess its effect on the foundation design of high-rise buildings. For example, significant cost and programme advantages can be achieved by relocating building blocks to avoid installing piles in non-competent marble zones, thereby minimising costly construction and potential risk in foundation works. The 3DGM built for sites underlain by marble may be used for preliminary cost estimates and construction programmes.

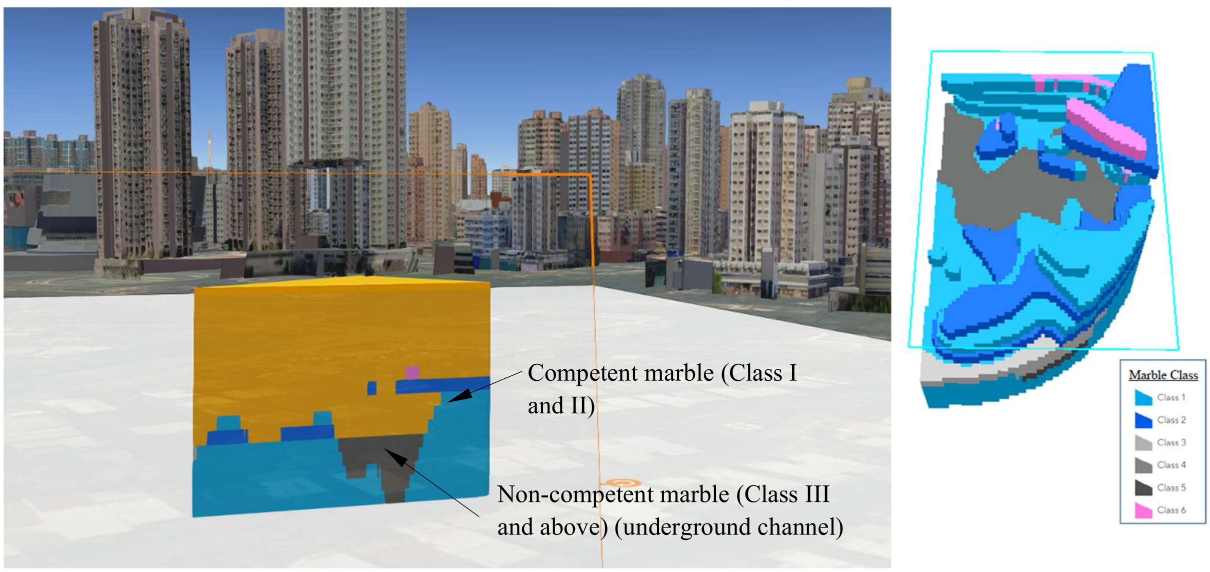

Figure 14: Pilot 3DGM block showing the karst geomorphology in a Yuen Long site

The current 3DGM generation methodology for marble sites relies heavily on manual scrutiny and professional judgement. For instance, decisions about the spatial distribution of marble classes across varying elevations often require expert interpretation. While the workflow outlined in Section 2 permits modifications to 3DGM by incorporating inferred rock contacts and adjusting sub-vertical boundaries, manual intervention is still required to delineate zones of abrupt geological change. More complex geological conditions, such as severe karstic features in fault zones between contacts of marble and intrusive rocks, are expected to require advanced modelling processes (Chan & Pun, 1994) to produce representative models for engineering assessments.

4.2 Ensuring reliability in the 3DGM

Communicating the reliability of the 3DGM to practitioners is crucial for their effective and safe applications. Since the generation of the 3DGM often involves interpretation and interpolation between GI data, it is essential to ensure transparency and provide flexibility in selecting the 3DGM generated using different modelling approaches. The GEO would implement several measures to assist practitioners in understanding the limitations of the data and modelling method.

The GEO is developing visual reliability indicators to guide practitioners in applying the 3DGM outputs appropriately. The reliability of stratigraphic interpretations depends on two key factors: the quantity and quality of GI data and the spatial variability of stratigraphy, such as the rate at which geological unit boundaries shift. To quantify this reliability, the GEO is leveraging machine learning technology to analyse stratigraphic variability in regions with similar geological settings. Additionally, the GEO is creating a reliability map based on the geospatial distribution of borehole data. Areas with dense borehole coverage typically exhibit higher reliability, while zones with sparse data reflect lower reliability due to greater reliance on interpolation. These visual indicators (Figure 15) will help practitioners assess confidence levels across different blocks of 3DGM, enabling more informed decisions in geotechnical planning.

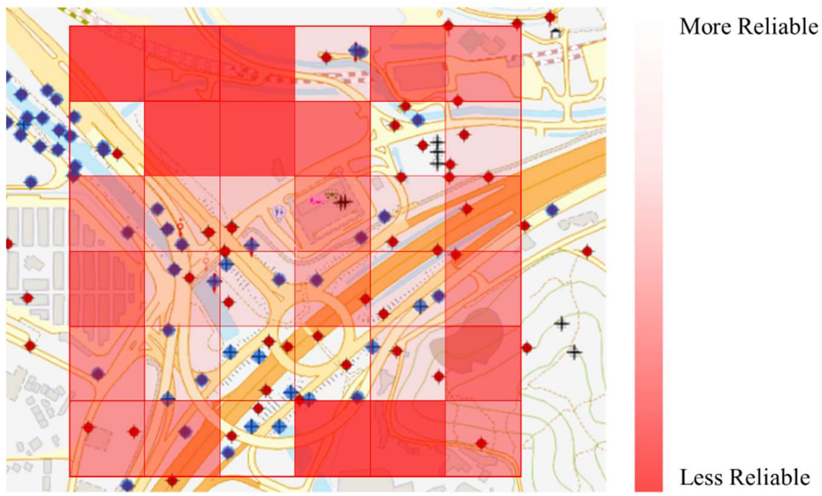

Figure 15: Conceptual graphical representation of reliability of stratigraphic interpretation based on borehole density

To ensure transparency, the GEO would provide clear and comprehensive information about each 3DGM, including descriptions of data sources, interpretation methods, model generation methods, resolution, etc. While attempting to include more advanced techniques to generate the 3DGM, the practitioners would be given the adopted interpolation methods for assessing its reliability. Cautionary remarks would also be attached to each 3DGM highlighting the limitations of the modelling technique and the need for expert verification on critical components, such as major unit boundaries or areas with highly variable material properties.

4.3 Other limitations

The accuracy of the 3DGM is inherently limited by the completeness and quality of available GI records in the target area. It is emphasised that the 3DGM should not be considered a substitute for thorough desk studies and site-specific ground investigation works. Instead, the 3DGM should be regarded as a supplementary reference tool for practitioners. Ultimately, practitioners remain responsible for developing project-specific geotechnical models coupled with site-specific GI data tailored to their unique project requirements. They should manage geotechnical risks in accordance with their professional judgement and the specific conditions of the site.

5 WAY FORWARD

The current 3DGM generation methodology still heavily relies on manual data processing, which severely hindered the timely development and update of 3DGM on a city scale. The GEO recognised the urgency of automating the existing 3DGM generation method in a more efficient manner.

5.1 Automation of 3DGM generation methodology

The GEO has been collaborating with local IT firms in developing a series of automated tools that will incorporate data validation and quality control processes for generating new 3DGM. Latest digital technologies would be adopted to streamline the complex design processes and replace repetitive manual procedures.

The automation process would begin by establishing a centralised digital GI database containing machine-readable data. While the DGIU holds a vast volume of GI records, most are scanned PDFs lacking digitised data in a consistent data specification, e.g. the AGS format. To address this issue, an automation tool would be developed to extract data from existing GI records (e.g., PDFs) and convert it into standardised digital GI data structure and format (e.g., MS Excel, CSV, AGS, JSON). This transformation would leverage machine learning techniques and advanced generative AI algorithms to ensure accuracy and consistency in extracting the data. The next phase involves creating a customisable 3DGM generator that allows users to select from various interpolation methods or algorithms. This tool would enable the generation of project-specific 3DGM tailored to unique engineering design requirements, ensuring alignment with technical and risk management objectives.

By leveraging the digital GI data, practitioners can unlock the full potential of the 3DGM generator by customising the 3DGM for diverse applications and seamlessly integrating them with numerical tools and CAD/BIM software. It is contemplated that the establishment of digital geotechnical models would pave the way for more design automation, enhanced efficiency, optimised geotechnical designs and cost reductions in engineering projects.

5.2 AI-enabled 3DGM generation methodology

In urban areas, existing GI data is often densely distributed, allowing simple interpolation methods to generate sufficiently accurate 3DGM. However, this is less viable in new development areas where existing GI data is sparse. In such data-scarce environments, traditional interpolation methods may become ineffective or impractical, leaving practitioners to rely heavily on professional judgement, and even speculative interpolation and extrapolation, to infer critical geological interfaces (e.g., rockhead levels) during preliminary project assessments. This may introduce significant variability in the accuracy of geotechnical assessment, as outcomes depend on the experience of the practitioner.

The GEO has collaborated with local universities to investigate the application of AI algorithms for interpreting subsurface conditions. This is achieved by analysing stratigraphic patterns in geologically similar settings. A fine-tuned AI model is being developed to identify and learn these patterns from analogous sites. By combining the AI-derived and trained stratigraphic patterns with available borehole data, an enhanced 3DGM can be generated. Unlike the conventional linear triangulation method, the AI model provides a systematic, controlled prediction of geological interfaces between widely spaced boreholes. It is anticipated that this will significantly outperform simplistic approaches like straight-line interpolation or speculative guesswork. Lyu et *al*. (2025) used this methodology in a study predicting stratigraphy at a reclamation site in Tung Chung, highlighting the advantages of a machine-learned, data-driven approach. The resulting AI-generated ground model serves as a preliminary reference for practitioners interpreting stratigraphy in data-scarce conditions (Figure 16).

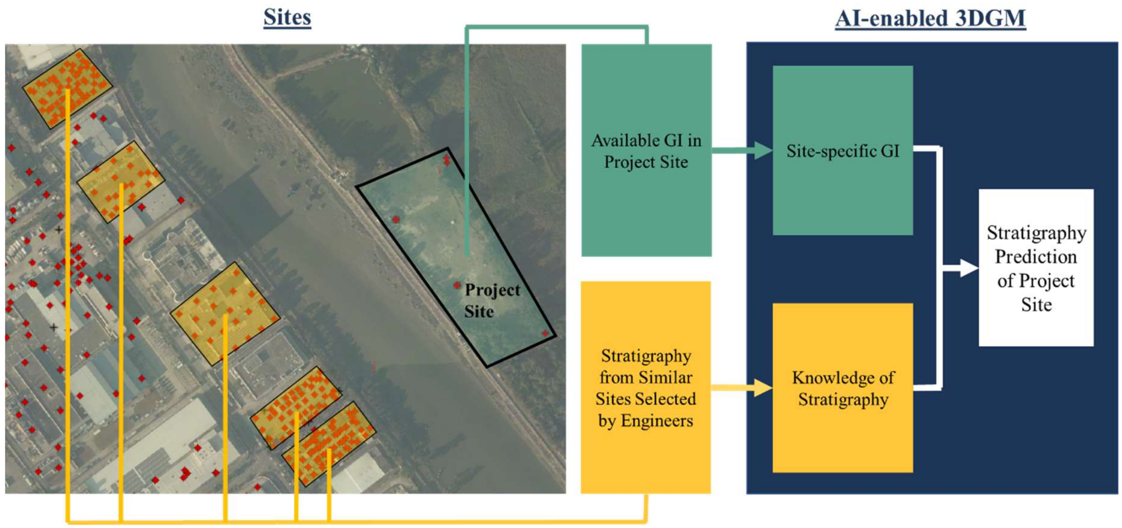

Figure 16: Conceptual diagram of AI-enabled 3DGM

5.3 Wider engineering application of 3DGM

The voxel-based 3DGM framework offers additional advantages, as each voxel cell can store multidimensional geotechnical variables (e.g., SPT-N values, shear strength, uniaxial compressive strength, unit weight, pore water pressure history). A centralised 3DGM inventory, acting as a laboratory and field test data repository, can unlock significant value. By aggregating geotechnical monitoring data from individual projects in the voxel cells, practitioners can design safer and more cost-effective engineering works, as historical data provide valuable information for future projects in adjacent areas or redevelopment of the same site.

Furthermore, integrating 3DGM with digital twins, incorporating data on foundations, excavation and lateral support systems, and underground utilities, can empower practitioners with enhanced insights into soil-structure interaction, enabling improved assessment of geotechnical risks and, consequently, the design of efficient engineering works.

6 CONCLUSIONS

Geotechnical engineering inherently involves postulating the subsurface ground conditions and applying engineering solutions to overcome construction challenges below ground. Whereas the current development of spatial data and 3D digital maps intuitively focused on ground level, such as the land topography and building blocks, the GEO recognised the need to drive the development of subsurface spatial data that would benefit the practitioners of Hong Kong at large. The GEO would continue to embrace the opportunity of rapid technological advancement and apply the latest machine learning and AI technology to promote smart and digital geotechnology.

ACKNOWLEDGEMENTS

The authors are grateful to Prof. Wang Yu of the Hong Kong University of Science and Technology for providing technical advice on utilising artificial intelligence to generate 3D geotechnical models. This paper is published with the permission of the Head of Geotechnical Engineering Office and the Director of Civil Engineering and Development, Government of the Hong Kong Special Administrative Region, China.

REFERENCES

AECOM 2024. *Review Report for the 3D Geotechnical Model Developed by GEO*, an unpublished report on Regional Geological Study of Northern New Territories (North) – Feasibility Study.

BD 2017. *Code of Practice for Foundation*. Buildings Department, Hong Kong Government, Hong Kong, 104 p.

Chan, Y.C. 1994. *Classification and Zoning of Marble Sites. GEO Report No. 29*. Geotechnical Engineering Office, Civil Engineering and Development Department, Hong Kong Government, Hong Kong, 37 p.

Chan, Y.C. & Pun, W.K. 2004. *Karst Morphology for Foundation Design. GEO Report No. 32 (Second Edition)*. Geotechnical Engineering Office, Civil Engineering and Development Department, Hong Kong Government, Hong Kong, 90 p.

Cheung, R.W.M. 2021. Landslide risk management in Hong Kong. *Landslides*, 18 (10), 3457-3473.

Cheung, S.P.Y. 2006. The application of information technology in managing landslide risk. *Symposium of the Science in Public Services*, Hong Kong, 12 p.

GEO 2006. GEO Publication No. 1/2006. *Foundation Design and Construction*. Geotechnical Engineering Office, Civil Engineering and Development Department, Hong Kong Government, Hong Kong, 376 p.

Lyu, B., Wang, Y., Miao, C., Yao, J., Shum, L.K.W., Wong, A.L., and Ho, R.C.M. 2025. "Fusion of limited site-specific borehole Logs and geophysical data from a different site for three-dimensional subsurface geological modelling using Multi-Scale Generative Adversarial Network." *Journal of Geotechnical and Geoenvironmental Engineering,* accepted.

Shum, L.K.W., Cheung, S.P.Y., Tang, C.S.C., Ho, R.C.M., and Koo, R.C.H. 2024. Evolution of Three-Dimensional Geotechnical Information Infrastructure. *Proceeding of the HKIE Geotechnical Division 44th Annual Seminar*, 31 May 2024, Geotechnical Division, The Hong Kong Institute of Engineers.

Steel Fibre Reinforced Concrete Tunnel Lining Segments: Design, Construction and Sustainability Aspects

P.L. Ng & A.K.H. Kwan
The University of Hong Kong, Hong Kong, China

ABSTRACT

In contrast to conventional reinforcing bars that form directional reinforcement in concrete elements, steel fibres form distributed reinforcement to effectively bridge across cracks at all locations and orientations. This improves the resistance to crack proliferation and propagation, ductility, energy absorption capability, and durability performance. Steel fibre reinforced concrete (SFRC) are particularly advantageous for the crack control of concrete elements under complex stress conditions, such as tunnel lining segments. In this paper, an account of the structural design, materials design, construction and sustainability aspects of precast SFRC tunnel lining segments is presented. It is remarked that regarding the fire resistance, polypropylene fibres can be incorporated in conjunction with steel fibres to form a hybrid fibre system for mitigating the risk of concrete spalling under elevated temperature.

1 INTRODUCTION

Steel fibres have offered an alternative way of reinforcement provision for reinforced concrete construction. Conventionally, reinforcing bars are installed as directional reinforcement to resist tensile stresses and control cracking. In contrast, steel fibres act as distributed reinforcement to bridge across cracks in concrete. Depending on the structural configuration and requirement, the steel fibres could be adopted solely or in combination with reinforcing bars as hybrid reinforcement. The crack-bridging capability of steel fibres enhances the resistance to crack proliferation and propagation, ductility, and toughness of concrete elements (Kovács and Balázs 2004; Singh 2017). Therefore, the post-crack flexural and shear resistances, splitting resistance, localized bearing and concentrated stress resistances, bond-slip resistance, as well as energy dissipation capacity could be improved. Moreover, being non-continuous and discrete, the fibres do not provide any mechanism for propagation of corrosion as conventional reinforcing bars do. Any chloride penetration via micro-cracks would not lead to widespread corrosion of discontinuous reinforcement, and hence the durability performance would be improved. Furthermore, in precast construction, unlike conventional reinforced concrete where there is no reinforcement in the concrete covers, the fibres would distribute themselves into the surface, edge and corner regions of the precast elements so as to prevent or reduce damages due to handling and thus minimize the subsequent concrete repair works for rectification.

In view of the above advantages, steel fibre reinforced concrete (SFRC) has been adopted for various applications such as railway sleepers (Parvez and Foster 2017), industrial flooring (Destrée and Mobasher 2022), and tunnel linings (Song and Breitenbücher 2014; Johnson et al. 2017; Kallan 2023), etc. In particular, SFRC is considered highly suitable for precast tunnel lining segments, where crack control under complex stress states during construction and long-term durability are key issues. With reference to the prevailing design practice in Hong Kong, this paper presents an account on the structural design, materials design, construction and sustainability aspects of SFRC tunnel lining segments. One additional aspect is the combined use of polypropylene and steel fibres to form a hybrid fibre system for fire spalling resistance.

2 STRUCTURAL DESIGN

Several structural design approaches for SFRC elements have been promulgated in a number of design codes and standards, including the *fib* Model Code 2010 (Fédération Internationale du Béton 2013), ACI Committee

Report 544-18 (American Concrete Institute 2018), Singapore Standard SS 674 (Singapore Standards Council 2021), and European Standard EN 1992-1-1 (CEN 2023), etc. Furthermore, the methodologies for determination of engineering properties of SFRC have been specified in a number of testing standards, including the RILEM TC 162-TDF (RILEM 2000, 2001, 2002, 2003), European Standard EN 14651 (CEN 2005), and German DAfStb Guideline (German Committee for Structural Concrete 2012).

2.1 Flexural behaviour

It should be noted that for flexural testing of SFRC, RILEM TC 162-TDF and European Standard EN 14651 adopt the three-point bending test of SFRC notched prismatic specimens, whereas the German DAfStb Guideline recommends to use the four-point bending test of SFRC un-notched prismatic specimens.

For the three-point bending test, the crack mouth opening displacement (CMOD) across the tip of the notch is measured. The highest load level up to CMOD of 0.05 mm is denoted F_L for determining the flexural tensile strength (limit of proportionality). The load levels at other given values of CMOD are also measured (Figure 1) for determining the residual flexural tensile strength, which characterize the flexural toughness.

For the four-point bending test, the loading is exerted at third points of the specimen span, amidst of which the central portion of specimen is subjected to pure bending. The residual tensile stress-strain relationship is obtained from the load-deflection diagram of the specimen.

In general, depending on the fibre content by volume (also called fibre volume or fibre dosage), fibre length, and anchorage resistance, the post-crack regime could exhibit strain softening or strain hardening behaviour. Strain hardening is not a must but would give better ductility and toughness.

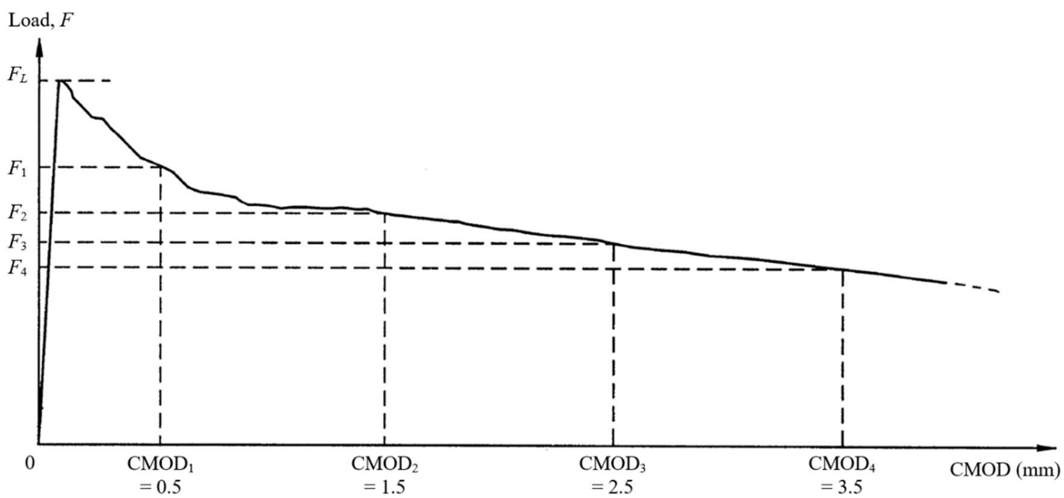

Figure 1: Load versus crack mouth opening displacement in three-point bending test

2.2 Uniaxial behaviour

Regarding uniaxial compression, the compressive strength is only little influenced by the addition of steel fibres, while it is mainly dependent on the concrete mix design parameters such as the water to cementitious ratio and incorporation of condensed silica fume. In structural design, the compressive stress block could be derived in the same manner as for conventional concrete without steel fibres.

Regarding uniaxial tension, direct tension test of SFRC specimens is seldom conducted due to the practical difficulties in performing the test. Therefore, the flexural tensile behaviour is usually referred to. In structural design, the tensile stress block could be derived from the flexural tensile strength and residual values, as further explained later.

2.3 Other mechanical behaviour

According to literature, the steel fibres would only marginally increase the elastic modulus of SFRC (Shadafza and Saleh 2016). As the effect on the elastic modulus is not significant, the elastic modulus of SFRC may be considered the same as the corresponding concrete with no steel fibres in structural design practice.

The shrinkage characteristics as well as the heat generation and thermal expansion/contraction characteristics are not affected by the provision of steel fibres. But, instead of forming a small number of shrinkage and/or thermal cracks with relatively wide crack width, the presence of steel fibres would lead to the formation of a larger number of cracks with finer crack width. Since it is the wide cracks that allow the ingress of deleterious ions and dilapidate the structural conditions, SFRC can alleviate both the shrinkage cracking and thermal cracking problems, with the degree dependent on the fibre volume.

It has been proven that steel fibres could remarkably enhance the impact resistance, fatigue resistance, and abrasion resistance of concrete (Lok and Pei 1996; Liu et al. 2020), and for this reason SFRC is desirable for use in industrial flooring and even in military applications (Zircher et al. 2017).

In particular, when applied to precast concrete tunnel lining segments, SFRC demonstrates a multitude of properties enhancement in comparison with conventional reinforced concrete tunnel lining segments, as summarized in Table 1, which provides the rationale for using SFRC.

Table 1: Properties enhancement by SFRC in precast tunnel lining segments

Property	Performance of SFRC compared to conventional reinforced concrete
Compressive strength	Unchanged
Strength to onset of cracking	Unchanged
Tensile splitting strength	Increased
Workability*	Reduced
Plastic shrinkage cracking	Unchanged
Early thermal cracking	Reduced
Drying shrinkage cracking	Reduced
Resistance to chloride attack	Increased
Resistance to spalling under fire	Slightly increased
Water permeability	Unchanged
Abrasion resistance	Increased
Fatigue resistance	Increased
Impact resistance	Largely increased
Stray current corrosion	Largely reduced

* The reduction in workability could be (partly) compensated by adopting a higher superplasticizer dosage

2.4 Structural analysis and design

The analysis of stresses in SFRC tunnel lining segments under different load combinations during the construction stage and the working stage follows the same procedures as in the structural analysis and design of conventional reinforced concrete tunnel lining segments. The loading in the construction stage encompasses loads arisen from handling, lifting, stacking, bursting, TBM (tunnel boring machine) thrust load, grouting pressure load, etc. As usual, the structural design could be an iterative procedure, depending on whether there is any previous similar design for reference. First, given a (trial) section of lining segment, the structural actions due to different load combinations are evaluated. Then, the axial force-bending moment (N-M) interaction diagram is derived from the lining section properties and the compressive and tensile stress blocks. Figure 2 illustrates the strain diagram and stress blocks of SFRC lining section. The choice between adopting SFRC lining and combining SFRC with reinforcing bars to form hybrid reinforcement lining is primarily affected by the segment sizing and has to be assessed on a case-by-case basis.

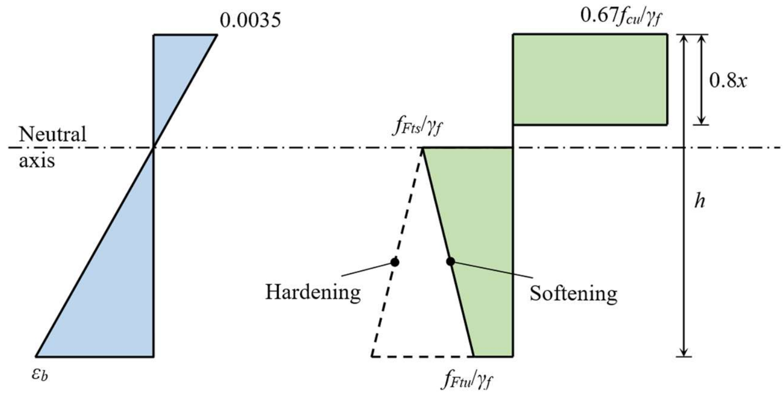

Figure 2: Strain diagram and stress blocks of SFRC

From force and moment equilibria, the following equations of axial force and bending moment can be derived:

$$N = \left[\frac{0.67 f_{cu}}{\gamma_f} \cdot 0.8x + \frac{f_{Ftu}(h-x)}{\gamma_f} + \frac{0.5(f_{Fts} - f_{Ftu})(h-x)}{\gamma_f} \right] b \qquad (1)$$

$$M = \left[\frac{0.67 f_{cu}}{\gamma_f} \cdot \frac{0.8x(h-0.8x)}{2} - \frac{f_{Ftu}(h-x)x}{2} + \frac{(f_{Fts} - f_{Ftu})(h-x)}{2} \cdot \left(\frac{2(h-x)}{3} - \frac{h}{2} \right) \right] b \qquad (2)$$

where h = depth of section, x = depth of neutral axis, b = breadth of section, f_{cu} = characteristic cube compressive strength, γ_f = concrete material factor which can be taken as 1.5, f_{Fts} and f_{Ftu} = reference values defining the tensile stress block which can be computed from the equations below:

$$f_{Fts} = 0.45 f_{R1} \qquad (3)$$

$$f_{Ftu} = f_{Fts} - \frac{w_u}{\mathrm{CMOD}_3}\left(f_{Fts} - 0.5 f_{R3} + 0.2 f_{R1}\right) \geq 0 \qquad (4)$$

in which w_u = maximum crack opening acceptable in structural design and is dependent on the required ductility (w_u could be taken as CMOD_2 or 1.5 mm), $f_{R1} = 3F_1L/2b_ph_{sp}^2$ and $f_{R3} = 3F_3L/2b_ph_{sp}^2$, where F_1 and F_3 are as defined in Figure 1, L = span length of notched prism specimen which is equal to 500 mm, b_p = width of notched prism specimen which is equal to 150 mm, and h_{sp} = distance between the notch tip and top of specimen which is equal to 125 mm.

By varying the neutral axis depth x in Equations (1) and (2), the N-M interaction curve can be obtained. This provides the basis for checking the structural adequacy of the assumed lining section, through verifying the computed structural actions being within the envelop of the N-M interaction curve.

3 MATERIALS DESIGN

3.1 Concrete materials

The concrete mix design for SFRC and conventional reinforced concrete basically follows the same principles, and the ingredients should comply with the same materials standards (except the fibres which are absent in conventional reinforced concrete). The mix proportioning parameters of water to cementitious ratio, paste volume, fine to total aggregate ratio, and replacement ratios of supplementary cementitious materials, such as pulverized fuel ash (PFA), ground granulated blastfurnace slag (GGBS) and condensed silica fume (CSF) are common to both SFRC and conventional reinforced concrete. However, appropriate adjustments of the contents of ingredients, aggregate grading, and superplasticizer dosage are necessary to accommodate the fibres in the concrete volume and to compensate the workability loss due to fibre addition. Some typical requirements on the concrete mix design of SFRC are listed in Table 2 as an indicative example.

Table 2: Typical requirements on concrete mix design of SFRC

Parameter	Requirement
Characteristic 28-day cube strength (grade strength)	50 MPa
Characteristic tensile splitting strength	3.8 MPa
Characteristic residual flexural strength	2.7 MPa
Characteristic limit of proportionality	4.2 MPa
Maximum nominal aggregate size	20 mm
Supplementary cementitious materials	min. 30% PFA or min. 60% GGBS or min. 25% PFA + 5% CSF
Total cementitious content	min. 400 kg/m^3 and max. 450 kg/m^3
Volumetric ratio of steel fibres	min. 0.5%
Volumetric ratio of polypropylene fibres	Min. 0.1%

3.2 Fibre materials

The requirements of the fibre materials vary with the project specification. Basically, the steel fibres shall comply with European Standard EN 14889-1 (CEN 2006a). They are produced from cold-drawn wire and are un-galvanised. They may have hooked ends for better anchorage in concrete compared to straight fibres. The minimum steel fibre content recommended by some manufacturers is 30 kg/m^3. Besides, polypropylene fibres that possess a relatively low melting point are required to be added to the concrete, in order to provide channels for release of vapour pressure in case of fire. The addition of polypropylene fibres is a proven method to avoid or minimize risk of concrete spalling under fire, especially in high-strength concrete with dense microstructure (Shihada 2011; Lee et al. 2012), and is preferentially adopted for tunnel lining where post-fire repair is in general difficult. The polypropylene fibres shall comply with European Standard EN 14889-2 (CEN 2006b). It is of fine monofilament type with straight geometry and is alkali resistant. Table 3 and Table 4 summarize the typical properties of commonly used steel fibres and polypropylene fibres, respectively. The co-addition of steel fibres and polypropylene fibres forms a hybrid fibre system (Qian and Stroeven 2000; Tawfik et al. 2022).

Table 3: Properties of steel fibres

Parameter	Requirement
Fibre length	60 mm
Fibre diameter	0.75 mm
Aspect ratio	80
Minimum tensile strength	1550 MPa
Elastic modulus	210 GPa

Table 4: Properties of polypropylene fibres

Parameter	Requirement
Fibre length	12 mm
Fibre diameter	0.032 mm
Aspect ratio	375
Melting point	162°C
Ignition point	593°C

3.3 SFRC concrete mix design and testing

Depending on the performance standard set in the project specification, the actual requirements on the concrete mix design of SFRC could be more stringent than those listed in Table 2. In Hong Kong, the performance standard is often set very high and much higher than in other places, and for this reason, the concrete mix design of SFRC in Hong Kong is particularly difficult. Expert advice may be needed, but first of all, we have to sort out the additional requirements on durability (such as RCPT (Rapid chloride penetration testing) and NTB (NT Build) limits (Tang et al. 2012)) and fire resistance (in terms of fire rating, polypropylene fibre content and fire tests to be carried out). The durability and fire resistance requirements are sometimes conflicting with each other and it is not easy to comply with both. For instance, the addition of CSF would improve the durability in terms of RCPT performance but would reduce the fire spalling resistance. At the end, we may have to add more polypropylene fibres than originally planned and thus increase the difficulty of concrete mixing and the cost of SFRC production.

Trial concrete mixing in a laboratory is required to determine the content of each ingredient material and the optimum concrete mix proportions. Trial concrete mixing in the production plant is also required because the mixing method, time of adding fibres and total mixing time could affect the performance of the SFRC produced. Generally, excessively rigorous mixing in a high rotation speed stirrer type mixer should be avoided because this could cause kinking of the steel fibres and/or balling of the polypropylene fibres. Moreover, a somewhat longer mixing time may be needed to achieve thorough and uniform mixing especially when high dosages of steel fibres, polypropylene fibres and CSF are added. For precast concrete construction, a high slump is not needed and in fact not preferred because a high slump achieved by adding a high dosage of superplasticizer may cause bleeding and segregation.

Lastly, due to the presence of rigid steel fibres up to 60 mm long, the concrete cube specimens for testing the cube strength of the SFRC produced should be 150 mm in size instead of 100 mm in size because the use of small cube moulds would affect the fibre distribution and orientation in the concrete cube specimen. And, when carrying out the RCPT for checking compliance with the durability requirement in terms of RCPT total coulomb passed, the SFRC should have the steel fibres removed because the steel fibres are electrically conductive and thus would affect the total coulomb passed (an alternative is to produce the concrete mix without steel fibres added solely for the RCPT test).

4 CONSTRUCTION ASPECT

Fibre entanglement of the steel fibres hampers the uniform dispersion of steel fibres throughout the concrete matrix and thus could adversely affect the performance of the SFRC produced. Fibre entanglement is sometimes described as fibre balling but actually the fibre entanglement of rigid fibres is not the same as the fibre balling of flexible fibres. To reduce fibre entanglement of the steel fibres, the 20 mm coarse aggregate content should be reduced because the steel fibres also entangle with the coarse aggregate particles, and the paste volume of the SFRC may need to be increased so as to provide more paste to wrap around the steel fibres and fill into the space between the steel fibres. In addition, it is recommended to first add all the ingredients except the steel fibres into the mixer for mixing until the mixture becomes uniform and then add the steel fibres in an uncollated manner into the plain concrete mixture without steel fibres in the mixer for mixing.

The steel fibres may be added using an automatic motorized fibre doser equipped with feeder coil and mesh screen (Figure 3) as well as conveyor belt (Figure 4). Basically, the steel fibres are initially filled into the feeder coil, the motor of the fibre doser operates at a controlled fibre feed rate which is synchronized with the conveyor belt by an automatic feedback control system. The steel fibres are then added to the mixer for thorough mixing with the plain concrete mixture in the mixer. This would help to disperse the steel fibres while dosing into the mixer to avoid the formation of clumps due to fibre entanglement.

More recently, it has become quite popular to add the steel fibres to the concrete mixture in the form of glued bundles (Figure 5). The glued bundles each has a fixed weight and a fixed number of steel fibres, and thus no weighing is needed for batching. What is needed is just to add the required number of bundles according to the concrete mix design. The glue would dissolve in the concrete mixture for the steel fibres to get free and disperse in the concrete mixture during mixing. Experience indicates that such method of adding and mixing steel fibres would ensure homogeneous distribution of the steel fibres throughout the concrete mixture to avoid fibre entanglement and formation of clumps, provided of course the mixing time is sufficiently long for the steel fibres to disperse throughout the concrete mixture.

Figure 3: Automatic fibre doser

Figure 4: Conveyor belt for steel fibres

Figure 5: Steel fibres in the form of glued bundles

5 SUSTAINABILITY

The use of SFRC would significantly improve the durability of precast tunnel lining segments by mitigating steel corrosion of continuous reinforcement and by reducing shock damages during installation which could adversely affect the durability of the installed lining segments. With the improved durability and extended service life taken into account, the carbon footprint per year of service would be dramatically reduced. In fact, depending on the structural design, the use of SFRC may help to reduce the thickness of the tunnel lining segments for further reduction of the carbon footprint.

Moreover, the use of recycled steel fibres could provide a great potential of low-carbon construction for circular economy (Soltanzadeh et al. 2022; Shahzad et al. 2023).

6 CONCLUSIONS

SFRC has already been used in many parts of the world for diverse applications. It is particularly advantageous when used in precast tunnel lining segments. It may take time to learn the structural design, materials design, construction and sustainability aspects of SFRC but Hong Kong engineers are smart and fast learners and perhaps in a few years of time, we shall become a world leader in SFRC construction.

REFERENCES

ACI Committee 544. 2018. ACI 544.4R-18. *Guide to Design with Fiber-Reinforced Concrete*, American Concrete Institute, Michigan.

CEN 2005. EN 14651: 2005. *Test Method for Metallic Fibered Concrete - Measuring the Flexural Tensile Strength (Limit of Proportionality (LOP), Residual)*, European Committee for Standardization, Brussels.

CEN 2006a. EN 14889-1: 2006. *Fibres for Concrete - Part 1: Steel Fibres - Definitions, Specifications and Conformity*, European Committee for Standardization, Brussels.

CEN 2006b. EN 14889-2: 2006. *Fibres for Concrete - Part 2: Polymer Fibres - Definitions, Specifications and Conformity*, European Committee for Standardization, Brussels.

CEN 2023. EN 1992-1-1: 2023. *Eurocode 2 - Design of Concrete Structures - Part 1-1: General Rules and Rules for Building, Bridges and Civil Engineering Structures*, European Committee for Standardization, Brussels.

DAfStb (Deutscher Ausschuss für Stahlbeton) 2012. *DAfStb Guideline: Steel Fibre Reinforced Concrete*. German Committee for Structural Concrete, Berlin.

Destrée, X. & Mobasher, B. 2022. Industrial floors with fiber-reinforced concrete: a review of knowledge and experience. *Concrete International*, 44(7): 28-33.

Fédération Internationale du Béton (fib) 2013. *fib Model Code for Concrete Structures 2010*. Ernst & Sohn, Berlin.

Johnson, R.P., Psomas, S. & Eddie, C.M. 2017. Design of steel fibre reinforced concrete tunnel linings. *Structures and Buildings, ICE Proceedings*, 170(2): 115-130.

Kallan, D. 2023. *Steel Fiber Reinforced Concrete for Tunnel Linings*. MSc Thesis, Delft University of Technology, Delft.

Kovács, I. & Balázs, G.L. 2004. *Structural Performance of Steel Fiber Reinforced Concrete*. Budapest University of Technology and Economics, Budapest.

Lee, J.H., Sohn, Y.S. & Lee, S.H. 2012. Fire resistance of hybrid fibre-reinforced, ultra-high-strength concrete columns with compressive strength from 120 to 200 MPa. *Magazine of Concrete Research*, 64(6): 539-550.

Liu, Y.-W., Lin, Y.-Y. & Cho, S.-W. 2020. Abrasion behavior of steel-fiber-reinforced concrete in hydraulic structures. *Applied Sciences*, 10(16): 5562.

Lok, T.S. & Pei, J.S. 1996. Impact resistance and ductility of steel fibre reinforced concrete panels. *HKIE Transactions*, 3(3): 7-16.

Parvez, A. & Foster, S.J. 2017. Fatigue of steel-fibre-reinforced concrete prestressed railway sleepers. *Engineering Structures*, 141: 241-250.

Qian, C.X. & Stroeven, P. 2000. Development of hybrid polypropylene-steel fibre-reinforced concrete. *Cement and Concrete Research*, 30(1): 63-69.

RILEM TC 162-TDF 2000. Test and design methods for steel fibre reinforced concrete: recommendations. *Materials and Structures*, 33: 3-5.

RILEM TC 162-TDF 2001. Test and design methods for steel fibre reinforced concrete: uniaxial tension test for steel fibre reinforced concrete. *Materials and Structures*, 34: 3-6.

RILEM TC 162-TDF 2002. Test and design methods for steel fibre reinforced concrete: design of steel fibre reinforced concrete using the σ-ε method: principles and applications. *Materials and Structures*, 35: 262-278.

RILEM TC 162-TDF 2003. Test and design methods for steel fibre reinforced concrete: σ-ε design method: final recommendation. *Materials and Structures*, 36: 560-567.

Shadafza, E. & Saleh, J.R. 2016. The elastic modulus of steel fiber reinforced concrete (SFRC) with random distribution of aggregate and fiber. *Civil Engineering Infrastructures Journal*, 49(1): 21-32.

Shahzad, S., Pirttikoski, K. & Wolf, S. 2023. Steel fibre reinforced concrete for sustainable construction. In *IABSE Congress Report: Engineering for Sustainable Development*. New Delhi, India, 20-22 September 2023. International Association for Bridge and Structural Engineering.

Shihada, S. 2011. Effect of polypropylene fibers on concrete fire resistance. *Journal of Civil Engineering and Management*, 17(2): 259-264.

Singapore Standards Council 2021. SS 674: 2021. *Fibre Concrete - Design of Fibre Concrete Structures*, Singapore Standards Council, Singapore.

Singh, H. 2017. *Steel Fiber Reinforced Concrete: Behavior, Modelling and Design*. Springer Nature, Singapore.

Soltanzadeh, F., Behbahani, A.E., Hosseinmostofi, K. & Teixeira, C.A. 2022. Assessment of the sustainability of fibre-reinforced concrete by considering both environmental and mechanical properties. *Sustainability*, 14(10): 6347.

Song, F.B. & Breitenbücher, R. 2014. Load-bearing behavior of steel fiber-reinforced concrete for precast tunnel lining segments under partial-area loading. In W.Q. Ding, L.Y. Zhang, X.J. Li & X. Zhang (ed.), *Tunneling and Underground Construction, Proceedings of the Geo-Shanghai 2014 International Conference*. Shanghai, China, 26-28 May 2014. American Society of Civil Engineers.

Tang, L.P., Nilsson, L.-O. & Muhammed Basheer, P.A. 2012. *Resistance of Concrete to Chloride Ingress: Testing and Modelling*. Spon Press, Boca Raton.

Tawfik, M., El-said, A., Deifalla, A. & Awad, A. 2022. Mechanical properties of hybrid steel-polypropylene fiber reinforced high strength concrete exposed to various temperatures. *Fibers*, 10(6): 53.

Zircher, T., Keuser, M., Burbach, A. & Lehmann, S. 2017. Protective components made of steel fiber reinforced concrete under contact detonation. *Procedia Engineering*, 199: 2525-2530.

Overcoming Limitations in Raft Footing Design: Alternative Approaches to Uniform Modulus of Subgrade Reaction Analysis

Ted Tse, Ka-Ming Lee and Jeffrey Lam
Binnies Hong Kong Limited

ABSTRACT

Raft footing is a cost and time effective foundation solution for building and infrastructure development. By eliminating the need for deep piling, raft foundation significantly reduces embodied carbon, construction time, capital expenditure and disturbances to surroundings. In current industry practice, the Winkler Spring Model is commonly employed for shallow foundation design. This approach simulates the founding soil as a series of independent spring supports defined by the modulus of subgrade reaction (k_s) for analysis using structural software such as SAFE.
However, the simplified method for estimating k_s and the assumption of uniform subgrade support across the entire raft footing have limitations, often producing unrealistic settlement and differential results. Misinterpreted subgrade values may lead to the rejection of the raft footing option and necessitating to opt for a more costly and time-consuming piling foundations.
This paper explores an alternative approach to estimate the modulus of subgrade reaction (k_s) in a more comprehensive manner using geotechnical finite element software PLAXIS 3D. This method can capture complex subsurface conditions and soil-structure interaction effects, allowing the distribution of k_s to vary spatially across the raft. The outcome provides a more accurate and realistic k_s estimation, ensuring better decision-making in the design of raft footings.

1 INTRODUCTION

Foundation works in Hong Kong are often expensive, time-consuming, and fraught with uncertainty due to the city's complex and varying geological conditions, including deep bedrock, hilly terrain, and extensive reclaimed land. On average, foundation works account for approximately 15% to 25% of the total construction cost, 10% to 25% of the total embodied carbon footprint, and 20% to 25% of the total construction period. Therefore, pursuing sustainable foundation solutions can have a significant impact on the overall efficiency, cost, and environmental footprint of land and infrastructure developments.

To achieve more sustainable outcomes in foundation design, the following strategies are crucial:
- Conducting thorough information search and detailed desktop studies;
- Undertaking sufficient site investigations and laboratory testing;
- Developing a comprehensive geological model;
- Considering alternative foundation systems;
- Applying value engineering to optimize foundation design.

Minimizing subsurface uncertainties is essential to avoid conservative, over-engineered solutions. Selecting an appropriate foundation system tailored to site conditions is equally important.

Raft foundations are often more cost-effective, time-efficient, and environmentally sustainable than piled foundations. They can reduce foundation costs by approximately 50%, embodied carbon footprint by up to 75%, and construction time by around 50%. Furthermore, the minimization of piling activities helps to reduce disturbances such as vibration, noise, and dust, thereby lowering the impact on adjacent structures and communities and to alleviate the potential workplace risk associated with plant maneuvering and heavy lifting operation for piling construction.

Given these substantial benefits, it is essential to adopt an appropriate and accurate design approach for raft foundations. Inaccurate or simplified modeling may lead to over-design, causing unnecessary rejection of raft options in favor of piling systems, or under-design, which can compromise structural safety and serviceability.

According to GEO Publication No. 1/2006, raft foundations, being relatively large in size, are typically governed by total and differential settlements rather than bearing capacity. A common design method involves modeling ground support using the Winkler Model, which simulates the soil as a series of independent springs defined by the modulus of subgrade reaction (k_s). As noted by BSI (2004), subgrade reaction models are generally inadequate for estimating total or differential settlements in raft foundations. Finite element analysis or elastic continuum models are recommended to capture the soil-structure interaction in a realistic and reliable manner (French, 1999; Poulos, 2000).

2 CURRENT DESIGN PRACTICE FOR RAFT FOOTING DESIGN

2.1 Determination of Modulus Subgrade Reaction (k_s)

The current practice for raft footing design analysis typically involves the Winkler Model, implemented using structural software such as SAFE. In this approach, the interaction between the foundation and the soil is represented by a series of independent linear elastic springs, each characterized by the modulus of subgrade reaction (k_s). This parameter is crucial for determining foundation performance and is typically linked to the soil's Young's modulus (E_s), Poisson's ratio (υ), and the width of the footing (B).

The most widely adopted formulation for estimating the modulus of subgrade reaction (k_s) is based on Vesic (1961) equation that k_s could be computed using the stress-strain modulus E_s as

$$k_s = \frac{E_s}{B(1-\upsilon^2)} \qquad \text{(Eq. 1)}$$

where E_s = Young's modulus of soil, B = width of footing and υ = Poisson's ratio of soil.

While Vesic's equation is simple and widely applied, it often falls short in addressing more complex soil behaviors. For such cases, modified approaches have been proposed. For example, Tse (2024) introduced a refined method that incorporates a conceptual relationship between soil pressure and deformation to better estimate k_s under varying ground conditions.

The estimated k_s values are input into SAFE to model the raft footing. The software then analyzes the structural responses under Ultimate Limit State (ULS) conditions, such as bending moments and shear forces, as well as settlement behavior under Serviceability Limit State (SLS) loading.

Settlement assessment in raft footing design is conducted through deformation analysis using SAFE modeling under Serviceability Limit State (SLS) loading combinations. The deformation results are influenced by the modulus of subgrade reaction (k_s) and the stiffness of the footing. The k_s is inversely proportional to the width of the footing, resulting in lower k_s values for wider a raft footing. Consequently, it results in larger predicted settlements and differential settlements, which may exceed the allowable design criteria of 30mm total settlement and 1 in 500 differential settlement, as specified in the Code of Practice for Foundations 2017.

2.2 Drawbacks of the Current Practice on Winkler Model with Uniform Modulus of Subgrade Reaction (k_s)

The Winkler Model (WM), which acts soil support as discrete, uniform springs with constant stiffness (k_s), has several critical limitations when applied to raft footing design:

- **Non-intrinsic Property:** The subgrade modulus is not a fundamental soil parameter. Its value depends not only on soil stiffness but also on the foundation dimensions (Poulos, 2000). As footing width increases, k_s decreases, potentially leading to exaggerated settlement predictions, particularly near edges and corners.
- **Lack of Soil Continuum Behavior:** The Winkler Model treats soil as isolated springs with no interaction and the spring only deflects if a pressure is applied to it. Thus unloaded areas in a Winkler soil model do not deflect, and hence there is no stress transmission or interaction within the soil (Poulos, 2000). In reality, soil behavior involves stress redistribution and interaction between adjacent zones. The absence of these effects leads to inaccurate predictions of soil pressure and structural response, especially under non-uniform loads.
- **Neglect of Shear or Lateral Resistance:** The springs in the Winkler Model only resist vertical displacements and so the vertical loading will produce only vertical displacements, and no horizontal displacements, and vice-versa (Poulos, 2000). Shear interactions and edge effects, which are significant in raft foundations, are ignored. This results in overestimation of settlement at corners and underestimation of structural forces.
- **Oversimplified Elastic Medium:** Treating the founding soil as a discrete elastic medium fails to capture complex behaviors such as bulging, arching, or differential stiffness across the foundation. This is particularly problematic in heterogeneous or layered soils which commonly encountered in Hong Kong.
- **Neglect of Time-Dependent Effects:** The Winkler Model does not account for long-term settlement due to consolidation or creep. This can lead to underestimation of differential settlements over time, especially in clayey soils or newly reclaimed land.
- **Incompatibility with Irregular Geometries:** Uniform k_s values do not accurately represent complex raft geometries or varying load conditions. This over-simplification can result in misleading predictions for bending moments, shear forces, and settlement profiles.

Given these limitations, there is a clear need for more advanced and representative modeling approaches, such as finite element methods, that can more accurately simulate soil-structure interaction and the spatial variability of subgrade reactions across the raft footprint.

3 COMPARISON OF WINKLER MODEL (WM) AND FINITE ELEMENT METHOD (FEM)

3.1 Parametric Studies for Raft Footing Design

Two sets of parametric studies were carried out to compare raft footing analyses between the Winkler Model (WM) with a uniform modulus of subgrade reaction using structural software (SAFE) and Finite Element Method (FEM) by using the geotechnical software (PLAXIS 3D). The objectives of these parametric studies were to evaluate the accuracy and limitations of the WM with uniform k_s against FEM in predicting settlement, pressure distribution and structural responses under varying design parameters as follows, refer to Table 1 and Table 2:

1) Loading pattern – Uniform Distributed Load (UDL) vs Point Load (PL), refer to Set A
2) Footing thickness – from 0.5m to 1m, refer to Set B
3) Founding materials – Elastic Modulus from 15,000kN/m^2 to 30,000kN/m^2, refer to Set B
4) Footing sizes – from 5m x 5m to 30m x 30m, refer to Set B

Table 1: Inputs and Results for Set A Parametric Study

Model No.	Footing Size (B x L x D) (m)	Load Pattern	Equ. Pressure$^{(4)}$ (kPa)	Founding E_s (kPa)	Max. Settlement (mm)			Max. Pressure (kPa)		
					WM$^{(1)}$	FEM$^{(2)}$	% Diff$^{(3)}$	WM$^{(1)}$	FEM$^{(2)}$	% Diff$^{(3)}$
Model A1	10 x 10 x 1	1 No. PL	25	15,000	31	25	-21	51	92	45
Model A1a	10 x 10 x 1	3 Nos. PL	25	15,000	30	25	-22	50	87	42
Model A1b	10 x 10 x 1	UDL	25	15,000	30	24	-23	50	89	44

Remark: (1) WM = Winkler Model by SAFE with Uniform k_s
(2) FEM = Finite Element Method by PLAXIS 3D
(3) % Diff = Percentage Difference between WM and FEM results = (FEM -WM)/FEM x 100%
(4) Applied Equivalent Pressure = Total Column Loads / Footing Area

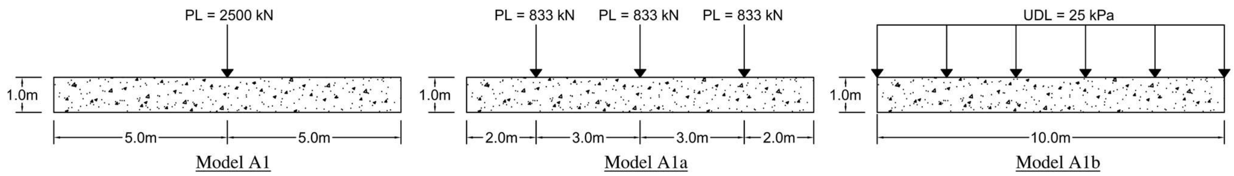

Table 2: Inputs for Set B Parametric Study

Model No.	Footing Size (B x L) (m x m)	Thk. (D) (m)	No. of PL	Equ Pressure(4) (kPa)	Founding E_s (kPa)	Max. Settlement (mm)			Max. Pressure (kPa)		
						WM(1)	FEM(2)	% Diff(3)	WM(1)	FEM (2)	% Diff(3)
Model B1	5 x 5	1	1	100	15,000	38.0	40.3	5.7	125.1	204.0	38.7
Model B1a	5 x 5	0.5	1	100	15,000	35.6	36.2	1.7	117.2	160.4	26.9
Model B1b	5 x 5	1	1	100	30,000	19.1	20.1	5.0	125.8	199.2	36.8
Model B2	10 x 10	1	4	100	15,000	76.0	68.5	-10.9	125.2	242.5	48.4
Model B2a	10 x 10	0.5	4	100	15,000	71.2	61	-16.7	117.4	206.9	43.3
Model B2b	10 x 10	1	4	100	30,000	38.2	34.2	-11.7	125.9	239.9	47.5
Model B3	15 x 15	1	9	100	15,000	114.7	92.3	-24.3	126.0	292.5	56.9
Model B3a	15 x 15	0.5	9	100	15,000	110.8	87	-27.4	121.8	325.0	62.5
Model B3b	15 x 15	1	9	100	30,000	58.0	46.8	-23.9	127.5	279.8	54.4
Model B4	20 x 20	1	16	100	15,000	156.0	116.0	-34.5	128.5	321.8	60.1
Model B5	25 x 25	1	25	100	15,000	208.1	141.8	-46.8	130.1	329.4	60.5
Model B6	30 x 30	1	36	100	15,000	242.3	164.5	-47.3	133.0	355.7	62.6

Remark: (1) to (4) are same as Table 1 above, refer to sketch as shown below for load patterns.

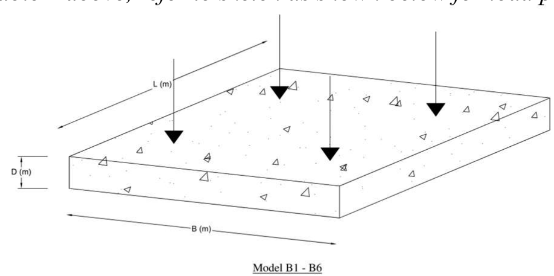

3.2 Findings from the Parametric Studies

- **Load Pattern Effect:** Set A parametric study investigated the effect of varying load pattern on the accuracy of WM. The study transitioned from a single point load to a uniformly distributed load (UDL), maintaining constant equivalent pressure. As shown in Table 1, the load pattern had minimal influence on the estimated maximum settlement and bearing pressure using WM.

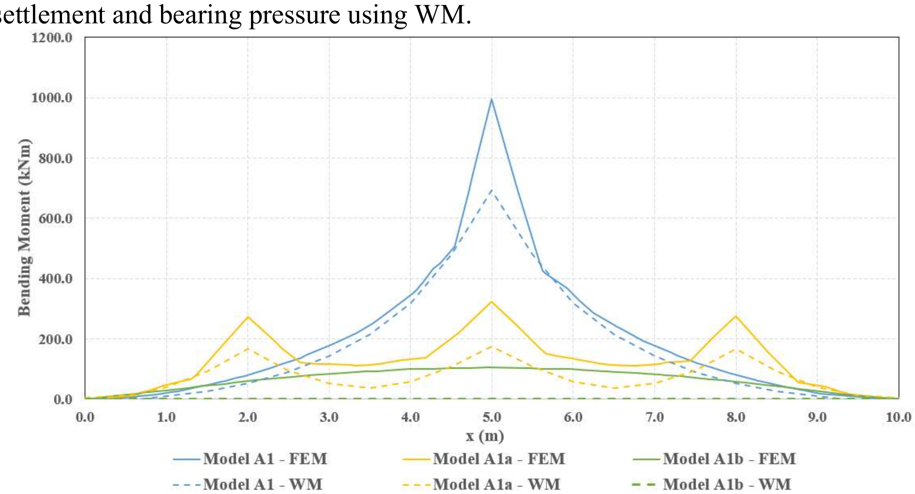

Figure 1: Bending Moment Diagram of Raft Footing under Different Load Patterns

However, significant discrepancies were observed in the estimation of bending moments. Figure 1 demonstrates that as loading became more distributed, the divergence between FEM and WM predictions increased. Notably, under the UDL, the WM predicted zero bending moment, underscoring its limitations in modelling structural response under distributed loads.

- **Footing Thickness and Founding Material Effect:** Comparative analysis was conducted on Models B1, B1a, B1b, B2, B2a, B2b, B3, B3a, and B3b to explore the influence of footing thickness and founding material stiffness. As illustrated in Figure 2, varying the modulus of elasticity (E_s) of the founding material had a limited effect on WM accuracy. Even when the E_s was doubled from 15MPa to 30MPa, the differences in the estimated maximum settlement and pressure remained relatively consistent.

On the other hand, the study highlighted that the effect of footing thickness was more pronounced. The thickness of the footing demonstrated a more significant impact on the accuracy of the Winkler Models. This indicates that WM sensitivity is more influenced by the rigidity of the raft than the stiffness of the supporting soil.

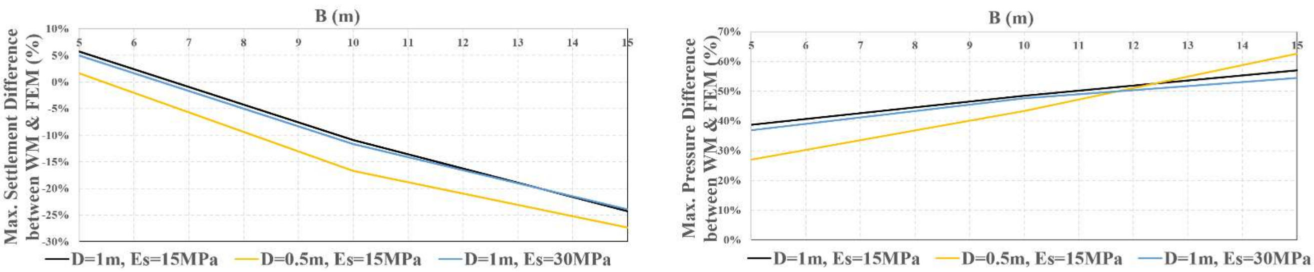

Figure 2: Difference between WM and FEM under Different Footing Thickness and Founding Material

- **Footing Size Effect:** As shown on Figure 5 below, it is evident that there is an inverse proportionality between the accuracy of the WM and the sizes of footing. The accuracy of the WM decreases as the footing size increases, leading to significant impacts on settlement and pressure estimations. The study revealed that as the footing size reaches 10m, the differences in maximum settlement and pressure estimations exceed 10% and 50%, respectively, highlighting the substantial impact of footing size on the suitability for application of Winkle Model on footing design.

Furthermore, the comparative study on Model B2, B4, and B6 examined the profiles of parameter concerning settlement, pressure, and bending moment diagrams. The findings indicate that for footings wider than 10m, the WM tends to overestimate settlement, with decreasing accuracy as the footing size increases. A notable discrepancy was also observed in settlement profiles by WM and FEM, where WM predicted greater settlement at the edge compared to the center portion, showcasing an opposite trend to FEM as the footing size increased.

Regarding pressure estimations, significant differences were noted between WM and FEM profiles. WM returned a uniform pressure profile due to its simple assumption of a uniform soil subgrade, leading to pressure under-estimation at the edge compared to the hogging pressure profile of FEM.

In terms of bending moment diagrams, discrepancies between WM and FEM increased with larger footing sizes as well as the number of column loads. While WM initially showed reasonable agreement with FEM for a 10m x 10m footing, this agreement diminished as the footing size increased to 30m x 30m, resulting in an underestimation of sagging moment by WM.

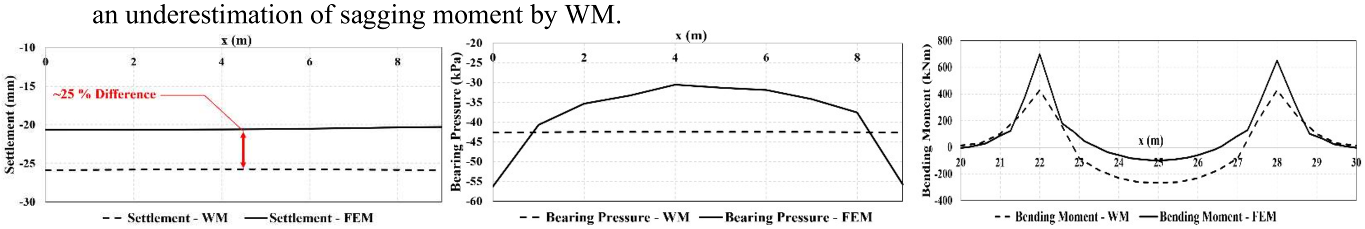

Model B2 – 10m x 10m x 1m Raft Footing

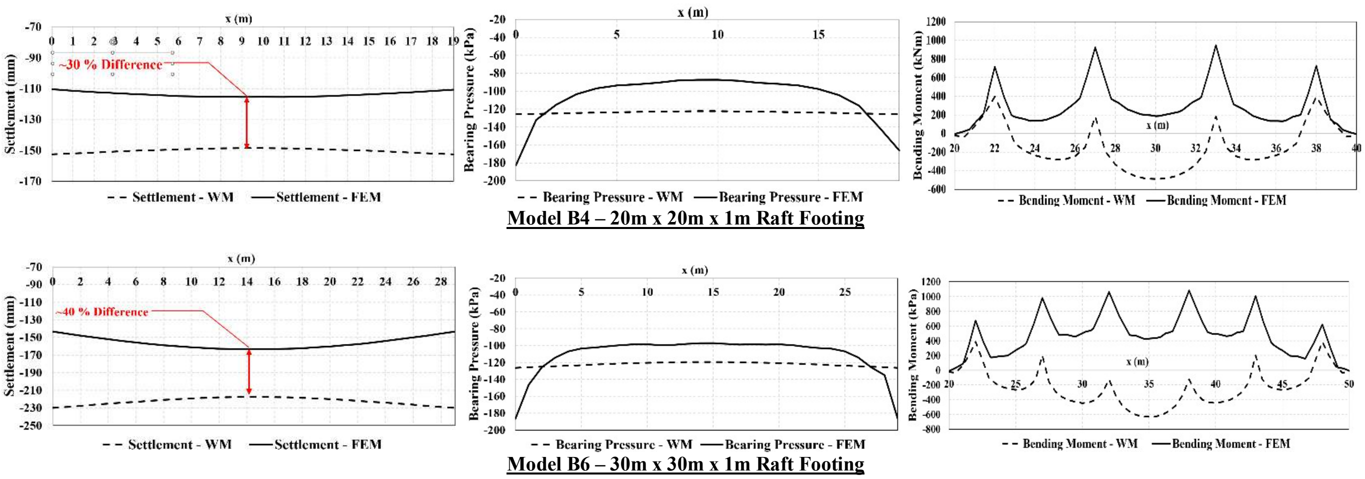

Figure 3: Comparison of WM and FEM results - Settlement Profiles (Left Graphs), Bearing Pressure Profiles (Middle Graphs) and Bending Moment Profiles (Right Graphs) under Different Footing Sizes

- **Spatial Location Effect:** The relationship between the position of a footing (center, edge, and corner) and the accuracy of settlement estimation using WM was also examined, the percentage difference in settlement estimated by WM and FEM was analyzed grid by grid. The findings, illustrated in Figure 4, revealed that the difference in settlement by WM and FEM increased radially from the center towards the edge of the raft footing, reaching peak values at the corners. Moreover, as presented in Figure 5, results from Model B1 – B6 were compared to also take footing size effect into account. The accuracy difference between the center, edge, and corner progressively increases as the size of the footing expands. The trend suggests that while the footing size increases, the discrepancy in settlement estimation between the different spatial locations (center, edge, and corner) becomes more pronounced.

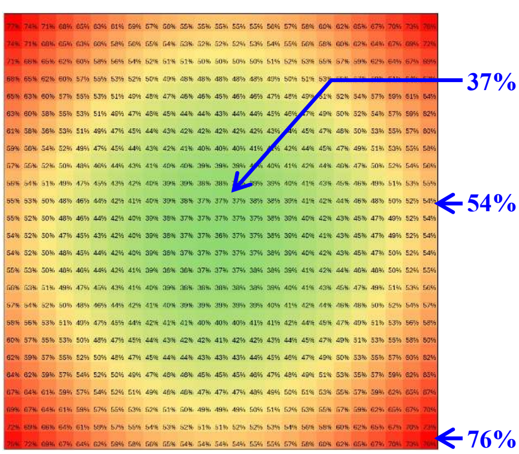

Figure 4: Distribution of Percentage Difference of Estimated Settlement by WM and FEM (Model B5)

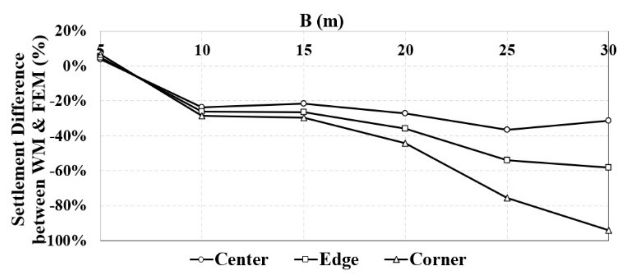

Figure 5: Settlement Difference between WM and FEM at Center, Edge and Corner under Different Footing Sizes

- **Effect of Shear Strength Parameters:** Since shear strength parameters of the founding material such as friction angle (ϕ) and cohesion (c) are not explicitly accounted for in Winkler Model, it is crucial to understand the effects of ϕ and c on settlement and bearing pressure estimation under FEM. Based on a series of FEM sensitive analyses, it is found that higher shear strength parameters could contribute to a reduction in settlement with ranged of 2% to 12% but increased in maximum bearing pressure locally at the edges and corner. However, the reduction trend of settlement with the higher shear strength parameters cannot be well established.

- **Overall Findings:**
  - Accuracy of the Winkler Model with uniform k_s (WM) in settlement estimation decreases as the footing size increase and becomes inaccurate (difference > 10%) when the size of raft footing exceeds 10m x 10m.
  - Accuracy of the WM is affected by the thickness/rigidity of footing, in which a less rigid footing returns less accurate result.
  - Simplified nature of the WM can result in overly conservative estimation of settlement along the edges and corners of raft footings.
  - Accuracy of the WM in settlement estimation radially decreases from the center of the raft footing.
  - The WM tends to underestimate the localized bearing pressure along the outer sides.
  - The WM becomes inaccurate in estimating bending moment when the load pattern is distributed in nature.
  - As the footing size expands with increasing number of column loads, the WM under-estimates the sagging moment and over-estimates the hogging moment, leading to potential under-design of steel reinforcement.

4 SUGGESTED METHODS FOR RAFT FOOTING DESIGN

4.1 Method A: Finite Element Method (FEM) using PLAXIS 3D

Three-dimensional finite element analysis on raft footing design can be conducted using PLAXIS 3D which models entire foundation system and associated geology underneath. Unlike software SAFE which simulate the founding condition based on modulus of subgrade reaction as individual spring support, PLAXIS 3D can simulate the founding condition with intrinsic soil properties including friction angle, cohesion and Young's Modules, etc. Most importantly, it takes into consideration the interaction of soil mass, especially those soil supports beyond the footing footprint, and provide a more realistic estimation on settlement, bearing pressure and structural responses of raft footings.

However, PLAXIS 3D normally requires longer computational time and higher demand on computer power. Furthermore, PLAXIS 3D is less suitable for structural design tasks due to its geotechnical focus especially it is not good at performing analysis under multiple load combinations and detailed reinforced concrete design.

4.2 Method B: Back-calculated k_s from PLAXIS 3D into SAFE

An alternative is to adjust modulus of subgrade reaction (k_s) in WM by adopting the data inferred from PLAXIS 3D. Initially, a PLAXIS 3D model is constructed under a dominant load case, preferably a combination of dead load and live load. The raft footing is virtually segmented into 1m x 1m grids (or smaller for increased precision). Each grid is assigned with its unique subgrade modulus which is back-calculated from the force and settlement within the same grid by PLAXIS 3D. The actual analysis of raft footing is subsequently conducted by Winkler Model in SAFE with the adjusted k_s.

The method numerically simulates the distribution of k_s and applied it in Winkler Model. Not only it can provide more realistic results, but also enable analysis under multiple load combinations, facilitating the structural design of the foundation.

However, the method still requires three-dimensional finite element analysis, leading to long computational time and resources demand. Additionally, since the adjusted subgrade modulus is calculated under one specific load case, the accuracy may be compromised when subjected to different load combinations.

4.3 Method C: Empirical Zoning and Adjusting of k_s Values into SAFE

An empirical method can be used to distribute k_s across the raft. Hans-Georg (2006) suggested multiplying k_s by factors of 1.75 and 3.5 at the edge and corner respectively for a strip width of 0.1B as illustrated in Figure 6 below.

$$k_{s,e} \cdot A_e + k_{s,r} \cdot A_r + k_{s,m} \cdot (A - A_r - A_e) = k_s \cdot A \qquad \text{(Eq. 2a)}$$

$$k_{s,r} = 3.5 \cdot k_{s,m} \ , \ k_{s,e} = 1.75 \cdot k_{s,m} \qquad \text{(Eq. 2b)}$$

where k_{se}, k_{sr}, k_{sm} = subgrade modulus at edge, corner and center respectively, k_s = overall subgrade modulus and A_e, A_r, A = area of edge, area of corner and total area respectively.

According to Figure 3 above, the resulting settlements from WM and FEM not only deviate in terms of shape but also in magnitude. It is observed that WM with k_s derived by Eq. 1 has overestimated the resulting settlement. Considering Eq. 2a and Eq. 2b only caters for the distribution of k_s. This paper introduces an empirical coefficient (N), derived by comparing k_s from Eq. 1 and the average k_s back-calculated from PLAXIS 3D (Method B) based on the size of a square raft footing as described in Figure 7. This adjustment helps align WM results with those from FEM. k_{se}, k_{sr} and k_{sm} are derived from k_s x N and subsequently applied by zone in SAFE.

While this method offers a convenient alternative to obtain relatively realistic results using WM with simplifies modeling and shortens computation time, it is less accurate for irregular footings or complex soil conditions.

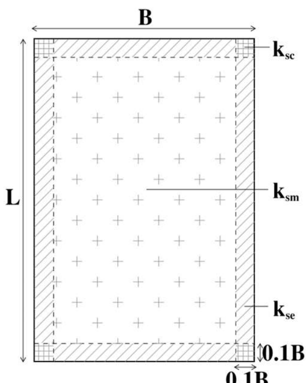

Figure 6: Illustration of k_{se}, k_{sr}, k_{sm}

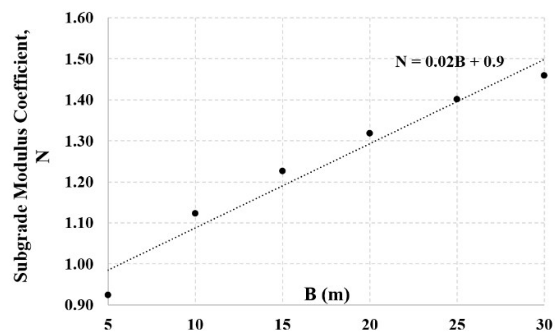

Figure 7: Subgrade Modulus Coefficient, N

4.4 Results Comparison of Method A, Method B and Method C

A comparative study was conducted on Model B5 to examine the accuracy of Method B and Method C. Settlement, bearing pressure and bending moment obtained from the methods are compared. The settlement profiles and bending moment estimations derived from both Method B and Method C exhibit a good level of agreement with the results obtained from the FEM (Method A). As for bearing pressure, while there is a reasonable agreement between the results of FEM and Method B, result from Method C deviates from FEM. The comparison of the advantages and disadvantages of the three suggested methods are listed in Table 3 below:

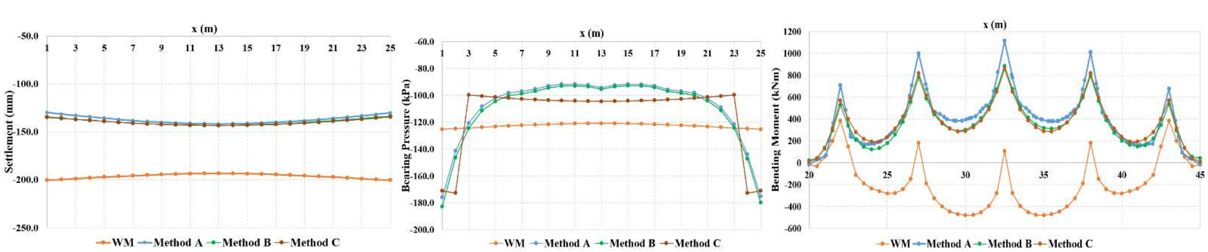

Figure 8: Settlement, Pressure and Bending Moment Comparison of Method A, B and C

Table 3: Summary of Advantages and Disadvantages of Suggested Methods

	Advantages	Disadvantages
Method A (FEM)	1. Most accurate, especially dealing with complicated footing shape, load pattern and geology	1. Very long computational time 2. Less suitable to compute for large amount of load combinations 3. Limited structural design capability
Method B (Back-calculated k_s)	1. Moderately accurate 2. Support multiple load combinations and R.C. design	1. Require FEM modelling 2. Accuracy may reduce for varied load case
Method C (Empirical ks)	1. Generally aligns with FEM results 2. Short computational time (no FEM model) 3. Support multiple load combinations and R.C. design	1. Least accurate 2. Not suitable for complex footings load or varied geology

Given the uncertainties in k_s estimation, sensitivity analyses are recommended under Method B and Method C for both Ultimate Limit State (ULS) structural and bearing design to enhance the robustness of the design. In certain scenarios, a higher subgrade modulus stiffness may result in significant bending moments and shear forces in a raft footing. This phenomenon can be explained by the relative stiffness factor proposed by Meyerhof (1953), which categorizes footings as either flexible or rigid bodies based on the ratio of footing structural stiffness to founding material stiffness. A smaller relative stiffness factor, indicative of a larger subgrade modulus of the founding material, may render the footing more 'flexible', increase of the design forces. It is recommended that sensitivity analyses cover a range of 75% to 150% of the estimated subgrade modulus for bearing capacity and structural checking under Method B and Method C.

5 CASE STUDIES FOR RAFT FOOTING DESIGN

5.1 Case Study 1 – Mixed Foundation Types for a Multi-deck Car Park in Complex Geological Site

The project involved the construction of a new multi-deck car park in Australia. The site was geologically complex, situated on the boundary between two geological formations: Tertiary Older Volcanic (comprising Basalt and Tuff) and Werribee Formation (consisting of Clayey Sand and Silty/Sandy Clay). Site investigation works were conducted in two stages with boreholes and geophysical survey (Multi-channel Analysis of Surface Waves Method). Based on the site investigation works, shallow competent Basalt rock could be found at the northern portion of the site while Silty Clay/Clayey Sand with no bedrock could be founded within 30m depth below ground at the southern portion. The longitudinal geological cross section of the site is shown in Figure 9 below.

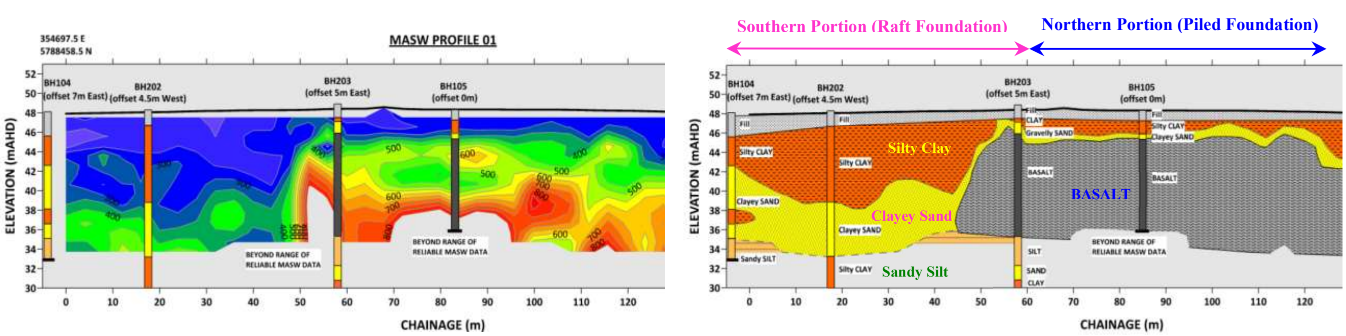

Figure 9: Long Sections show the Geophysical Survey Profile (Left) and Inferred Geological Profile (Right)

Due to highly variable subsurface conditions, a mixed foundation approach was proposed to optimize cost, construction time and manage geotechnical risks from underground uncertainties. For the northern portion of the site with Basalt rock, piled foundation system (600mm to 900mm diameter bored piles) was proposed with slab on grade slab for the ground floor which was cheaper and faster for shallow bedrock situation. For the southern portion of the site with no bedrock encountered, 500mm thick raft footing (35m x 96m) was proposed to prevent deep foundation requirements.

To manage anticipated differential settlement across the two foundation types, structural movement joints (M.J.) were incorporated into the design. However, the initial analysis using the Winkler Model in SAFE with a uniform modulus of subgrade reaction (i.e. k_s = 2250kN/m^3 estimated by Vesic Equation) predicted settlement at the raft footing corners of approximate 50mm, while adjacent pile-supported areas settled only 5mm. This resulted in an estimated differential settlement of 45mm across the M.J. – an unacceptable high value.

To better represent the actual soil–structure interaction, a Finite Element Method (FEM) analysis was conducted using PLAXIS 3D. The raft footing was modeled as a plate element, and variable subsurface conditions were captured through real and dummy boreholes. The results showed maximum settlement of 40mm at the center of the raft under core wall loads, while corner settlement was significantly reduced to approximately 12 mm. This yielded a differential settlement of just 7 mm across the M.J.—substantially less than that predicted by the initial SAFE model.

Based on the results of PLAXIS 3D, iterations with the structural SAFE model had converged at a vertical subgrade modulus of 2250kN/m^3 at the center of the raft slab, 8000kN/m^3 along the perimeter (2 m wide edge, i.e. k_s for edges is about 3.5 times of k_s for center) of the raft slab and 4000kN/m^3 between those two areas. An excerpt from the PLAXIS 3D output shown in Figure 10 presents the estimated raft slab displacements under SLS load case. The results of adjusted k_s SAFE model, which showed consistent settlement values as per PLAXIS 3D model, are presents in Figure 11. Once iterations were complete, the design bearing pressures had been reviewed within the allowable bearing capacity of the founding soil. The structural performance of the raft footing and the M.J. had been assessed under the estimated settlement by considering sensitivity of 75% to 150% of the adjusted k_s values.

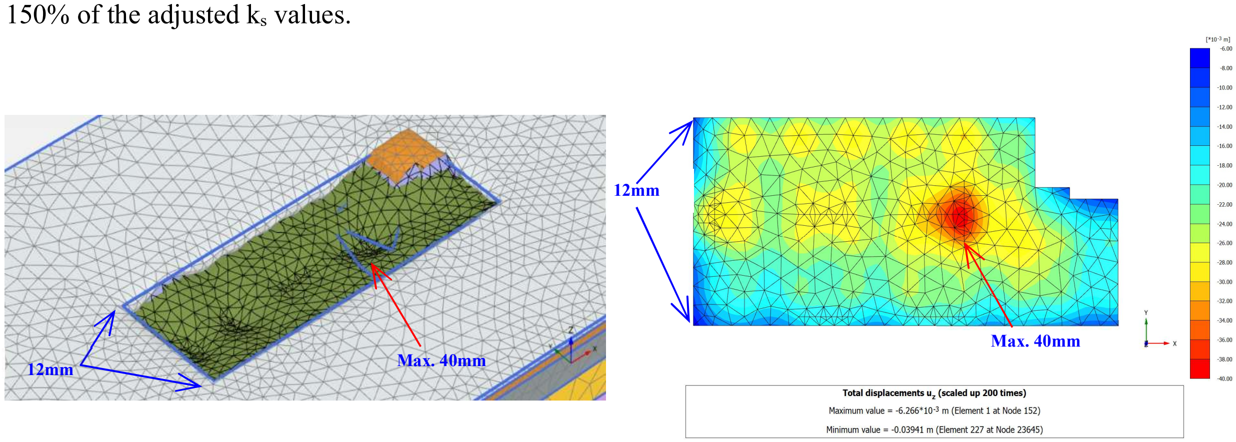

Figure 10: PLAXIS 3D Outputs – 3D View Deformed Shape (Left) and Settlement Contour of Raft Footing (Right)

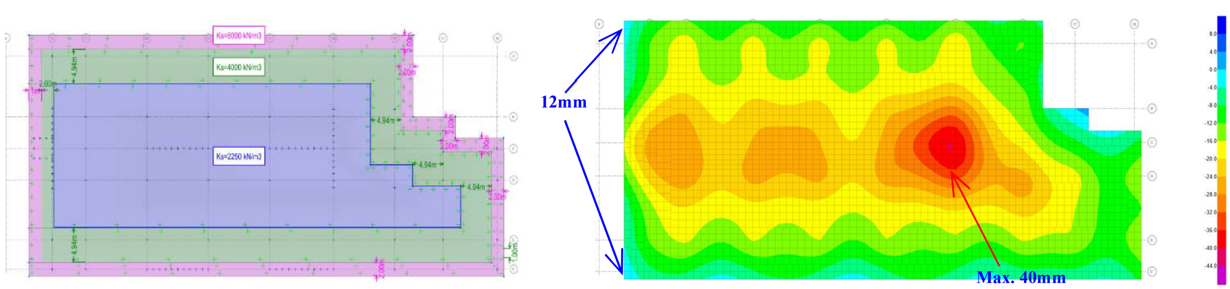

Figure 11: SAFE Model Results – Inputs for k_s (Left) and Settlement Contour of Raft Footing (Right)

5.2 Case Study 2 – Raft Footing on Pulverized Fuel Ash (PFA) in Reclaimed Land

The project involved constructing a plant room on the reclaimed land. The proposed raft footing (size of 23m x 27m x 0.6m thick) was founded on approximate 7m thick of loose PFA fill with silty fine sand and its SPT'N values were less than 5 blows. The design loading of the plant room was relative light with average pressure of 45kPa. Even though the raft footing founding materials were loose in nature, the required bearing capacity could still be achievable based on the bearing capacity equation as per CoP Foundations 2017 because of significant contribution of 23m large width (B) of the raft footing.

The estimated modulus of subgrade reaction (k_s) was 1,650kN/m^3 by hand calculation of settlement assuming 45° load spread pressure on various layers of soil. Winkler Model (WM) by structural software of SAFE was conducted with uniform k_s (adopted 1,650kN/m^3) underneath the entire raft footing footprint. The results revealed that maximum settlement was 33mm at raft footing edge which was marginally over the acceptable limit of 30mm under CoP of Foundations 2017. The SAFE input and output graphs are shown in Figure 12 below.

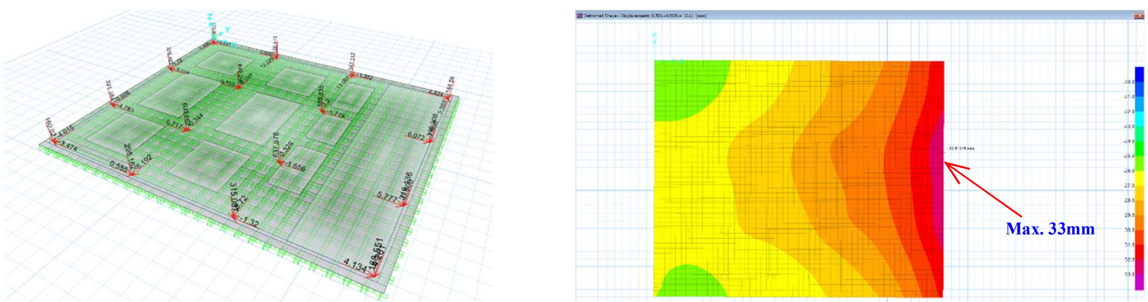

Figure 12: WM (SAFE) Results – Inputs with uniform k_s (Left) and Settlement Contour of Raft Footing (Right)

As discussed previously, Winkler Model with uniform k_s often over-estimates the settlement of raft footing, especially along the edges and corners. To improve accuracy, further analyses using Method B and Method C analyses (referenced in Section 4 of this paper) were conducted to compare with the results of FEM model by PLAXIS 3D (Method A). PLAXIS 3D input and output graphs are shown in Figure 13. The comparison of the results of the following are presented in Figure 14.

- WM – Winkler Model by SAFE with uniform k_s of 1,650kN/m^3 across whole footing footprint
- Method A – FEM Model by PLAXIS 3D
- Method B – Back-calculate k_s from PLAXIS 3D and then Winkler Method (MW) by SAFE where k_s ranged from 1,980kN/m^3 to 6,263kN/m^3.
- Method C – Adjust and Zone k_s Values by Empirical Method and then Winkler Method (WM) by SAFE, i.e. soil subgrade modulus of the center portion, i.e. overall subgrade modulus ($k_{s\text{-overall}}$) = 1,650kN/m^3 x 1.37 (Subgrade Modulus Coefficient from Figure 7 with width of 23m) = 2,260kN/m^3, where k_{sm}, k_{se} and k_{sr}, = 1,582kN/m^3, 2,769kN/m^3 and 5,538kN/m^3 = subgrade modulus at center, edge and corner, respectively.

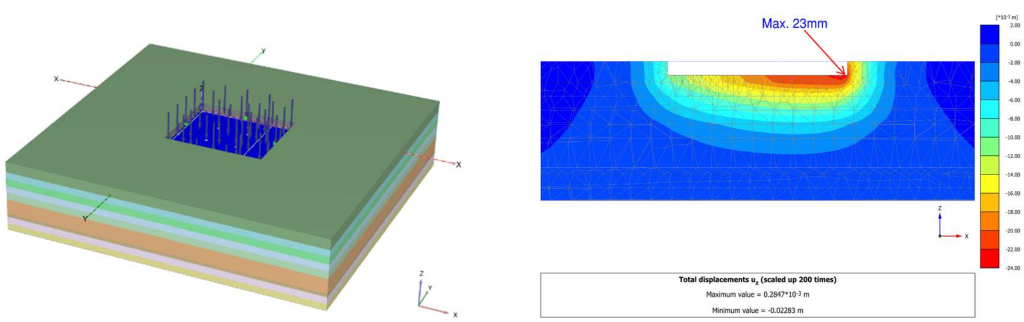

Figure 13: FEM (PLAXIS 3D) Results – Input Graph (Left) and Cross Section Output of Raft Footing Settlement (Right)

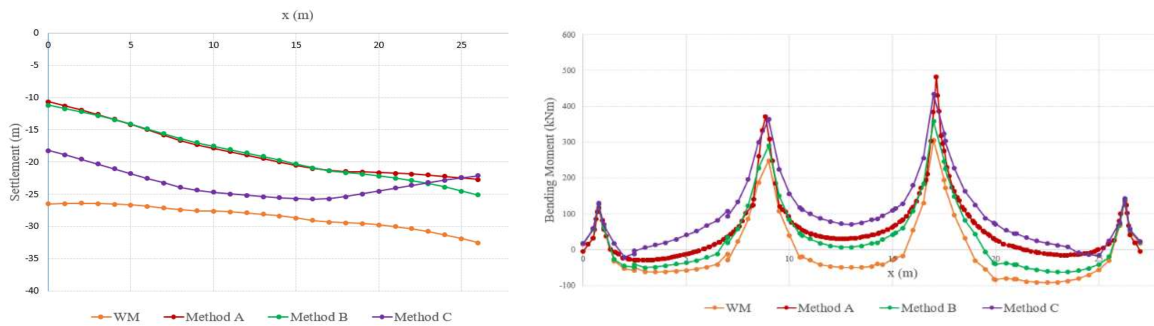

Figure 14: Comparison of the Results with Various Design Methods: Settlement Profile (Left) and BM Profile (Right)

Based on the comparison of the analyses results of various design method, the maximum settlements are 23mm, 25mm and 27mm for Methods A, B and C respectively, which are within the acceptable limit of 30mm. In addition, the bending moment (BM) diagrams are generally in line whereas Winkler Model (WM) by SAFE with uniform k_s shown the under-estimate of the hogging moment while over-estimate of the sagging moment.

6 CONCLUSIONS

Raft footing remains a practical and sustainable alternative to piled foundations, especially in urban developments where cost efficiency, construction time, and environmental impact are critical concerns. However, the traditional reliance on the Winkler Spring Model with a uniform modulus of subgrade reaction (k_s) often proves inadequate in capturing the complex behavior of soil-structure interaction. This is particularly evident in large or irregular shaped raft on heterogeneous ground conditions, where oversimplified assumptions may lead to the premature rejection of raft footing as viable option.

In comparison, the Finite Element Method (FEM) using PLAXIS 3D (referred to as Method A) accounts for the interaction between soil elements and provides a more realistic and accurate prediction of raft behavior. Nevertheless, PLAXIS 3D requires significantly higher computational effort and resources, and it is less suitable for structural design tasks due to its geotechnical focus.

To bridge the gap between geotechnical accuracy and structural practicality, two additional methods—Method B and Method C—have been developed based on the Winkler Model (WM) within SAFE. Method B involves back-calculating k_s values from FEM results and applying them in a grid layout across the raft footprint. Method C employs an empirical zoning approach to vary k_s based on ground conditions and geometry without the need for FEM. Both methods provide improved accuracy over the uniform k_s model and the results align well with FEM outcomes.

Method C offers a simplified and practical approach suited for projects with relatively uniform geology and regular raft geometry. In contrast, Method B, while requiring preliminary FEM analysis, offers a higher level of precision and is better suited for projects with complex soil profiles, foundation shapes, and load distributions.

Ultimately, by adopting suitable analysis methods, designers can unlock the full potential of raft footing systems – maximizing sustainability benefits, optimizing foundation performance, and ensuring resilience in increasingly complex construction environments.

REFERENCES

European Committee for Standardization. *Eurocode 7: Geotechnical design – Part 1: General rules:* European Committee for Standardization

Geotechnical Engineering Office. *GEO Publication No. 1/2006 Foundation Design and Construction:* Civil Engineering and Development Department, HKSAR

Harry G. Poulos, 2000, *Foundation Settlement Analysis – Practice Versus Research*

Hans-Georg Kempfert, H.K. 2006 Chapter 5, *Excavations and Foundations in Soft Soils*: 337-347: Springer
Joseph E. Bowles, P.E., S.E.1996 Chapter 9.6, *Foundation Analysis and Design:* McGraw-Hill Book Co
Karl Terzaghi, 1955. *Evaluation of Coefficients of Subgrade Reaction*
Larkela A., L.A. 2013, *Determination of Distribution of modulus of subgrade reaction:* Proceedings of the 18th International Conference on Soil Mechanics and Geotechnical Engineering. Paris, 2013
Meyerhof, G. G., 1953. *Some Recent Foundation Research and its Application to Design:* Struct. Eng., 31(6) 151–167.
Omer Mughieda, Mohamed Sherif Mehana and Kenan Hazirbaba, 2017, *Effect of soil subgrade modulus on raft foundation behavior:* ASCMCES-17, MATEC Web of Conferences 120, 06010
Samuel E. French, P.E. 1999. *Design of Shallow Foundation;* ASCE Press
Ted Tse, Ka-Ming Lee and Ted Lam, 2024, *Use of Compressible Layer for Raft Footing Design with Winkler Method:* The HKIE Geotechnical Division Annual Seminar 2024
The Buildings Department. *Code of Practice for Foundation 2017*: The Building Department, HKSAR
The Hong Kong Institution of Engineers. *An Explanatory Handbook to the Code of Practice for Foundation 2017:* Civil Engineering and Development Department, The Hong Kong Institution of Engineer
Vesic, A.B. [1961], *Beams on elastic subgrade and Winkler's Hypothesis*, Proc. 5 th. Int. Conf. on Soil Mech. Found. Engrg., Paris, p.p. 845-50.

Numerical Modelling of Deep Shaft Excavations: Bridging The Gap Between 2D And 3D Analysis

Ted Tse, Ted Lan and Kelvin Ng
Binnies Hong Kong Limited

ABSTRACT

It is widely recognized that two-dimensional (2D) analyses for deep shaft excavations tend to be conservative, primarily due to their inability to fully account for corner effects and the arching behavior around shaft walls. Overdesign resulting from 2D analysis can lead to oversized excavation and lateral support (ELS) systems, increasing construction costs and causing greater disturbance to the surrounding environment. This paper presents a comprehensive study on the application of both 2D and 3D numerical modelling in the design and analysis of shaft excavations. The study focuses on how the dimensions, such as breath, length, and depth, influence the comparative outcomes of 2D and 3D analyses. Key outputs, including bending moments, shear forces, wall deformations, and adjacent ground settlements, are analyzed and compared.
The paper also evaluates computational efficiency, cost implications, and the trade-offs between model complexity and accuracy. Practical recommendations are provided for selecting appropriate modelling approaches in design practice. The findings support the integrated use of 2D and 3D models to enhance design reliability and efficiency for complex urban excavations.

1 INTRODUCTION

Rapid urbanization and increasing population density in major metropolitan areas have led to severe congestion in underground spaces. Consequently, urban infrastructure projects, such as water supply, drainage, electricity, and telecommunications, require deeper alignments to avoid conflicts with existing utilities and minimize disruptions to surface activities. Traditional open-cut methods for pipeline installation have become increasingly constrained due to traffic impacts, space limitations, environmental concerns, and public inconvenience. Trenchless technologies, particularly pipe jacking, have emerged as an effective alternative capable of addressing these challenges.

Pipe jacking involves the installation of pipelines through the ground behind a micro tunnelling or tunneling shield. A critical component of this method is the construction of vertical shafts, which serve multiple purposes, including entry and exit points for pipe installation, permanent inspection manholes, and maintenance access points. These shafts typically involve deep excavations supported by robust excavation and lateral support (ELS) systems, such as sheet-pile or pipe pile walls with closely spaced internal steel strutting.

Traditionally, design engineers have relied heavily on simplified two-dimensional (2D) numerical analyses to assess excavation induced soil movements, structural forces in retaining walls, and potential impacts on adjacent structures. While 2D analyses offer computational efficiency and simplicity, the assumption of plane-strain conditions neglects critical three-dimensional (3D) structural interactions. Specially, they overlook phenomena such as corner stiffening effects often referred to as "corner effects" around excavation corners and soil arching, particularly with increasing excavation depth. As a result, prediction from 2D analyses led to be overly conservative.

This conservatism often leads to unnecessarily robust designs, excessive and/or higher grade material use, higher construction costs, and greater environmental impacts, such as noise and vibration from hard driving of sheet piles and extended construction durations. Recognizing these limitations, advanced 3D numerical modelling techniques are increasingly being adopted to better capture complex excavation behavior and optimize ELS design.

This paper systematically investigates and compares 2D and 3D numerical modelling approaches with aid of PLAXIS 2D and 3D respectively for shaft excavation design. The study emphasizes the influence of geometric factors, including shaft length-to-breadth (L/B) and breadth-to-depth (B/D) ratios, and illustrates how explicitly capturing and adopting the corner effects in the 2D analysis based on targeted 3D modelling can result in more realistic and economical designs. Furthermore, practical guidance is provided for integrating the strengths of both modelling strategies to achieve optimized, safe, cost-effective, and environmentally responsible excavation solutions, supported by theoretical insights and a practical case study.

2 TECHNICAL BACKGROUND AND THEORETICAL CONSIDERATIONS

2.1 Deep Shaft Excavation Design Considerations

Deep shaft excavations induce significant stress redistribution in the surrounding soil mass, leading to ground movements, surface settlement, lateral wall deflections, and changes in groundwater pressure. These effects can potentially impact nearby structures, utilities, and infrastructure, necessitating careful prediction and control. Accurate modelling of excavation induced stress paths and soil deformation behavior is essential for designing safe, effective, and efficient excavation support systems.

In urban areas, deep shaft excavation design is typically governed by the wall deflection and associated ground movement, especially to ensure compliance with allowable settlement limits for surrounding structures and utilities. The conservative predictions from 2D numerical analysis often necessitate the use of stiffer wall systems and closer spacing of internal steel struts to control wall deflections, resulting in over-design and less efficient excavation solutions.

2.2 Limitations of Conventional 2D Numerical Analyses

2D numerical analysis assumes plane-strain conditions, meaning the cross-section of excavation is considered uniform and infinitely long in the direction perpendicular to the section. While this assumption enhances computational efficiency, it inherently neglects key 3D phenomena and structural interactions. Specifically, 2D analyses cannot accurately represent the structural stiffening provided by perpendicular walls at corner (i.e. "corner effects") or the beneficial arching of soil that occur at excavation corners.

Several literatures have demonstrated the influence of 3D corner effects on the lateral soil pressure and their role in reducing wall deformation, bending moment and loads on shoring systems such as ground anchors or steel struts (Hsiung et al., 2018, Rabie et al., 2019 and Kosalim & Gunawan, 2023). As a result, 2D analyses typically yield conservative predictions of excavation induced wall deflections, bending moments, shear forces, and adjacent ground settlements, leading to overly robust and costly structural designs especially for deep shaft excavation whose corner effect is way more significant.

2.3 Importance of "Corner Effects" in Excavation and Lateral Support Design

In shaft excavations (see Plate 1 & 2), the perpendicular walls at corners substantially enhance the structural rigidity and reduce lateral deflections compared to plane-strain (2D) scenarios. These corner interactions facilitate the development of soil arching effects, redistributing stresses around the excavation perimeter and further reducing wall deformation and ground movements. The deeper the excavation, the broader the influence zone around the corners, with 3D effects becoming increasingly significant across the entire displacement field (Gianpiero & Marco, 2022). Accurately accounting for corner effects through 3D numerical analysis enables the designers to reliably quantify these beneficial phenomena. This improved representation typically results in significantly reduced predicted structural forces and ground movements, supporting more economical and environmentally sustainable ELS designs.

Relying solely on 2D modeling in shaft excavations without consideration of corner effect leads to over conservatism ELS design. This often results in oversized and less constructible shoring system, with excessive preloading of struts, simply to satisfy settlement, angular distortion and serviceability criteria outlined in general specifications, codes of practice and government publications.


Plate 1: Shaft Excavation – Internal View


Plate 2: Shaft Excavation –Top View

3 NUMERICAL MODELLING AND ANALYSIS

To investigate the influence of excavation geometry on shaft performance comprehensively, a parametric study was conducted, focusing on two critical geometric parameters: the shape factor (length-to-breadth ratio, L/B) and the depth factor (breadth-to-depth ratio, B/D). Numerical analyses were conducted using both 2D and 3D finite element modelling (PLAXIS), and the results are systematically analyzed and compared between the baseline models (PLAXIS 3D) and plane-strain models (PLAXIS 2D) to highlight the significance of 3D effects in terms of maximum ground settlement, wall bending moment and strut forces.

3.1 Numerical Modelling Setup

The parametric analyses presented in this study were conducted using PLAXIS 2D and PLAXIS 3D finite element software to investigate the excavation induced ground settlement and structural responses under varying shaft geometries. Key aspects of the numerical modelling approach are summarized below:

Soil Material Model and Parameters

- The Hardening Soil (HS) constitutive model was selected to realistically represent soil stiffness, stress dependency, and unloading/reloading behavior during excavation processes. Compared to the simpler Mohr-Coulomb model, the HS model provided more accurate predictions for ground response, especially for deep excavations
- Three sets of typical soil parameters, as listed in Table 1 below, were adopted in the numerical modelling.
- The stiffness modulus for primary loading in a drained triaxial test, E_{50}^{ref} is assumed to be Young's Modulus (E_s) of soil at drained condition.
- According to Lim et al. (2010) and Calvello and Finno (2004), the reference moduli for unloading/reloading and oedometer loading were estimated to be $E_{ur}^{ref} = 3E_{50}^{ref}$ and $E_{ode}^{ref} = 0.7E_{50}^{ref}$ respectively.
- The power for stress-level dependency of stiffness (m) and reference stress for stiffnesses (p_{ref}) value are assumed to be 0.5 and 100 kPa respectively.

Table 1: Typical Soil Parameters adopted for Parametric Study

Case	Bulk Unit Weight (kN/m^3)	Cohesion, c' (kPa)	Friction Angle, ϕ′ (deg.)	Young's Modulus, E_s (kPa)
Case 1	19	0	33	10,000
Case 2	19	0	35	10,000
Case 3	19	3	33	10,000
Case 3a	19	3	33	25,000

Boundary Conditions:

- Vertical side boundaries placed sufficiently distant (typically at least 2 to 5 times the excavation depth from the shaft edges) to minimize boundary influence. Horizontal displacements normal to these boundaries are fixed, while vertical movements are allowed.
- The bottom boundary fixed against both vertical and horizontal movements.
- Ground surface boundary is free, simulating realistic surface displacement and settlement.

Groundwater Conditions:

- Groundwater table modelled at 2m below ground level.
- Hydrostatic conditions assigned to excavation faces during the staged excavation.

Excavation Sequences:

- 20kPa applied around the excavation shaft for all stages
- Excavation simulated in sequential stages, mimicking realistic construction practices, which is 500mm below strut level.
- Hydrostatic groundwater conditions are updated at each excavation stage accordingly.

The general input arrangements for PLAXIS 2D and PLAXIS 3D models are presented in Figure 1.

3.2 Effect of Shape Factor (L/B ratio)

The shape factor (L/B), defined as the ratio of shaft length (L) to breadth (B), significantly influenced the magnitude of three-dimensional "corner effects" and related ground settlement patterns. Table 2 summarizes maximum ground settlement obtained from baseline (3D) and plane-strain (2D) model analyses for varying L/B ratios under constant excavation depth of 9m (i.e. B/D = 1).

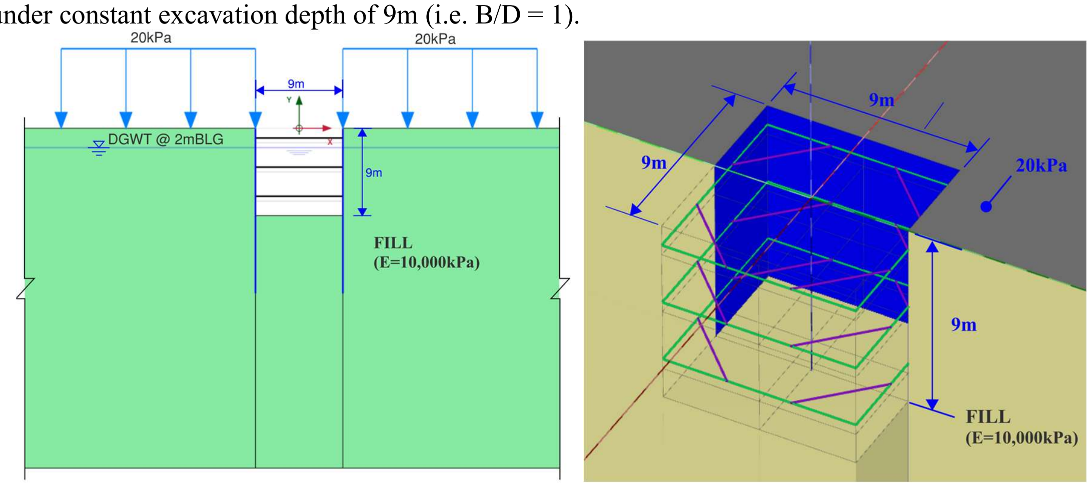

Figure 1: PLAXIS 2D (LHS) and PLAXIS 3D (RHS) Models for Shaft Excavation 9m(B) x 9m(L) x 9m(D)

Table 2: Comparison of Results from PLAXIS 3D and 2D under 3 Sets of Soil Parameters

Shaft geometry (B×L×D) m³	L/B ratio	c=0kPa, ϕ=33˚ (Case 1)			c=0kPa, ϕ=35˚ (Case 2)			c=3kPa, ϕ=33˚ (Case 3 & 3a*)		
		Settlement from 3D (mm)	Settlement from 2D (mm)	Settlement Reduction (3D vs 2D) %	Settlement from 3D (mm)	Settlement from 2D (mm)	Settlement Reduction (3D vs 2D) %	Settlement from 3D (mm)	Settlement from 2D (mm)	Settlement Reduction (3D vs 2D) %
9×9×9	1.00	12.3	21.9	43.9%	11.5	19.1	39.6%	9.4 (7.4)	16.1 (11.5)	41.5% (35.7%)
9×12×9	1.33	16.5	21.9	24.7%	15.1	19.1	20.9%	12.6 (9.8)	16.1 (11.5)	21.7% (14.8%)
9×15×9	1.67	19.3	21.9	11.8%	17.4	19.1	8.8%	15.0 (10.9)	16.1 (11.5)	6.9% (5.2%)
9×18×9	2.00	20.4	21.9	7.2%	18.5	19.1	3.5%	15.8 (11.5)	16.1 (11.5)	1.6% (0.0%)

*Remark: Values in the bracket are the results from Case 3a.

3.2.1 Discussion and Interpretation:

- At low L/B ratios (approaching square shapes), significant reduction in settlements was observed in 3D analyses compared to 2D results (e.g., maximum 43.9% reduction at L/B = 1 as shown in Table 2). This indicates significant corner stiffening and soil arching effects, reducing excavation induced settlements.
- The settlement reduction diminished with increasing L/B ratios. Beyond L/B ≈ 2.00, settlement differences become insignificant (less than 10%), indicating minimal corner effects and effectively plane-strain conditions.
- The reduction in wall bending moment and strut force diminished as the L/B ratio increases, with the maximum reduction being less than 20% when L/B = 1. Beyond L/B ≈ 1.33, wall bending moment differences become insignificant (less than 5%). Benefits on the structural design from 3D analyses seem not significant as per the settlement reduction.
- The chart in Figure 2 illustrates the percentage reduction of maximum settlements (3D vs. 2D) versus the L/B ratio under different soil parameters. A similar trend is observed across all cases, indicating that the effect of the L/B ratio does not vary significantly with changes in soil parameters. However, weaker soil parameters (i.e. lower c-ϕ values) and stiffness (i.e. lower E_s) show a slightly more pronounced reduction in settlement under 3D analyses.

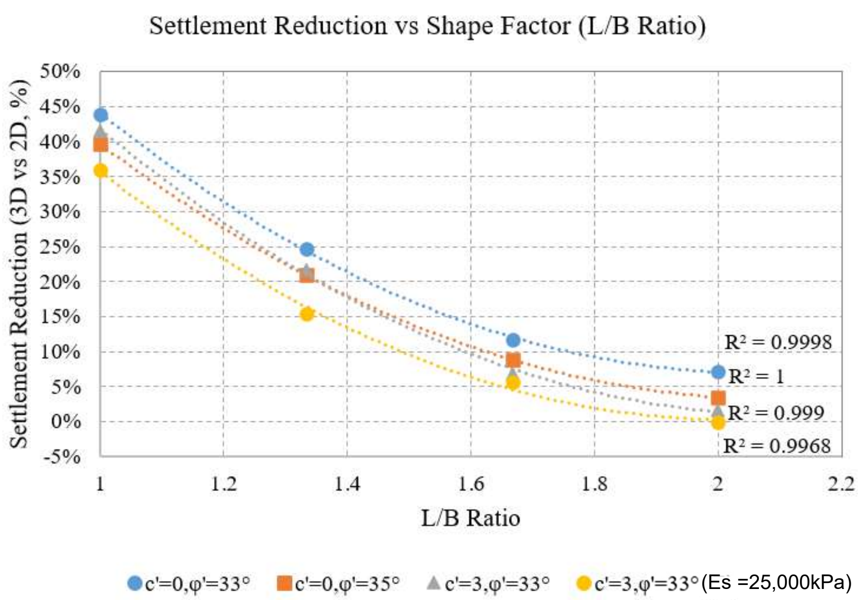

Figure 2: Settlement Reduction vs Shape Factor under different Soil Parameters (with Constant B/D = 1)

3.3 Effect of Depth Factor (B/D ratio)

The depth factor (B/D), defined as the ratio of shaft breadth (B) to excavation depth (D), critically affects excavation induced soil movements due to soil unloading and stress redistribution. Table 3 summarize numerical results from 3D and 2D analyses conducted at varying B/D ratios (constant shaft plan dimensions, i.e. B/L = 1).

Table 3: Comparison of Results from Plaxis 3D and 2D under 3 Sets of Soil Parameters

Shaft geometry (B×L×D) m³	B/D ratio	c=0kPa, ϕ=33˚ (Case 1)			c=0kPa, ϕ=35˚ (Case 2)			c=3kPa, ϕ=33˚ (Case 3)		
		Settlement from 3D (mm)	Settlement from 2D (mm)	Settlement Reduction (3D vs 2D) %	Settlement from 3D (mm)	Settlement from 2D (mm)	Settlement Reduction (3D vs 2D) %	Settlement from 3D (mm)	Settlement from 2D (mm)	Settlement Reduction (3D vs 2D) %
9×9×9	1.00	12.3	21.9	43.9%	11.5	19.1	39.6%	9.4	16.1	41.5%
9×9×12	0.75	18.5	44.3	58.2%	17.6	38.6	54.6%	15.0	36.1	58.4%
9×9×15	0.60	25.8	66.8	61.4%	24.0	57.4	58.2%	20.8	53.0	60.7%
9×9×18	0.50	33.4	94.6	64.7%	31.1	81.2	61.8%	27.2	76.4	64.4%

3.3.1 Discussion and Interpretation:

- Ground settlements predicted by both 2D and 3D analyses increased notably with greater excavation depth. However, the rate of increase in settlements predicted by the 2D model was substantially higher than that by the 3D model.
- For the model with soil parameter c=0kPa, ɸ=33˚, when B/D = 0.5, the 2D analysis predicted a settlement of 95mm, whereas the 3D analysis predicts only 33mm, a substantial difference of approximately 65%. This implies a more significant soil arching effect at greater excavation depths, which had been ignored by 2D analysis.
- There reduction in wall bending moment and strut force by 3D analyses which can be up to 25% in certain cases. However, the reduction trend with the B/D cannot be well established. Similar to shape factor discussion above, benefits on the structural design from 3D analyses seem not significant as per the settlement reduction.
- The chart in Figure 3 illustrates the reduction in maximum settlement (3D vs. 2D) versus the B/D ratio under different soil parameters. A similar trend is observed across all cases, indicating that the effect of the L/B ratio does not vary significantly with changes in soil parameters.
- A 2D axisymmetric model of a circular shaft (9m diameter and 9m deep) was also analyzed as a comparative case. The results showed that the maximum settlement predicted by the axisymmetric model fell between those of the 3D analysis and the 2D plane-strain model, highlighting the necessity for 3D modelling to achieve more accurate settlement predictions.

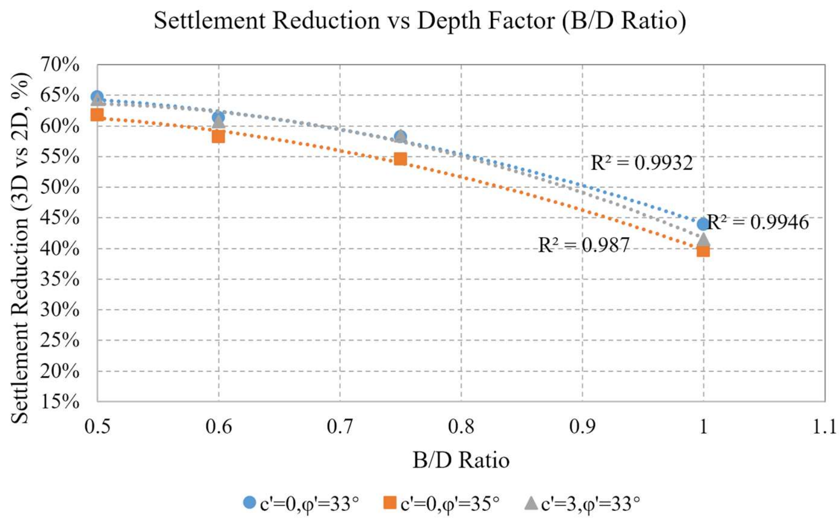

Figure 3: Settlement Reduction vs Depth Factor under different Soil Parameters (with Constant L/B = 1)

4 PARAMETRIC STUDY ON SHAPE AND DEPTH FACTORS OF SHAFT EXCAVATION

4.1 Correlation Between Enhanced Young's Modulus (E_s) and Shape Factor (L/B)

To achieve more realistic settlement results by PLAXIS 2D, an enhancement factor for the Young's Modulus (E_s) of soil is introduced to correlate the results of PLAXIS 2D and PLAXIS 3D, with reference to the shape factor (L/B). This correlation aimed at producing comparable ground settlement predictions. Since settlement is a key performance indicator of an Excavation and Lateral Support (ELS) system, the calibration of Young's Modulus (E_s) in the PLAXIS 2D model is carried out to match the settlement values estimated from the baseline 3D model.

As shown in Figure 4, the Young's Modulus (E_s) in PLAXIS 2D have to be increased by up to five times compared to the original Young's Modulus (E_s) in PLAXIS 3D to achieve similar settlement when the L/B =1.0, for soil with c'= 0 and ɸ' = 33°. However, as the L/B ratio increases to 2.0, the need for E_s enhancement becomes negligible. This indicates that as the shaft becomes more elongated, the 2D plane-strain assumption becomes increasingly valid. A similar trend is observed for soils with varying strength parameters, suggesting consistent behavior in response to changes in shaft geometry.

A lower-bound curve for the enhanced Young's Modulus (E_s) is proposed in Figure 4. The curve illustrates that enhancement is not recommended when L/B exceeds 1.60, as the influence of corner effects becomes minimal and the 2D plane-strain assumption provides sufficient accuracy.

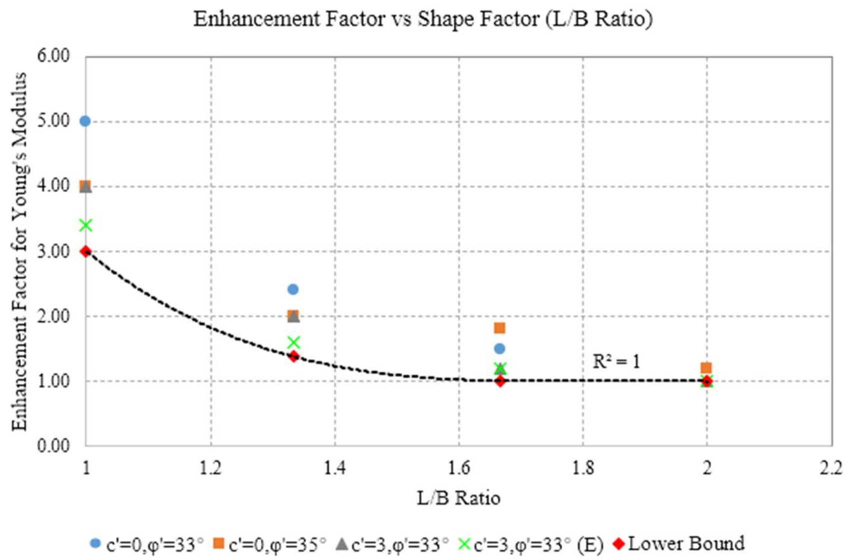

Figure 4: Enhancement Factor for Young's Modulus (E_s) vs L/B ratio (with constant B/D = 1)

4.2 Correlation Between Enhanced Young's Modulus (E_s) and Depth Factor (B/D)

To assess the influence of excavation depth, a similar approach is applied by adjusting the Young's Modulus (E_s) in PLAXIS 2D to match 3D settlement results. As shown in Figure 5, for c'=0 & ϕ' = 33°, the E_s in PLAXIS 2D is increased up to nine times when B/D = 0.6. This reflects the significant 3D confinement effect in deeper excavations. However, as B/D increases beyond 1.5 (i.e. relative shallower excavation), the effect of excavation depth on soil stiffness becomes less pronounced.

Accordingly, a lower-bound enhancement curve is proposed and applied only when B/D ≤ 1.5, as illustrated in Figure 5. Beyond this threshold, 2D modelling without enhancement may adequately reflect the excavation response.

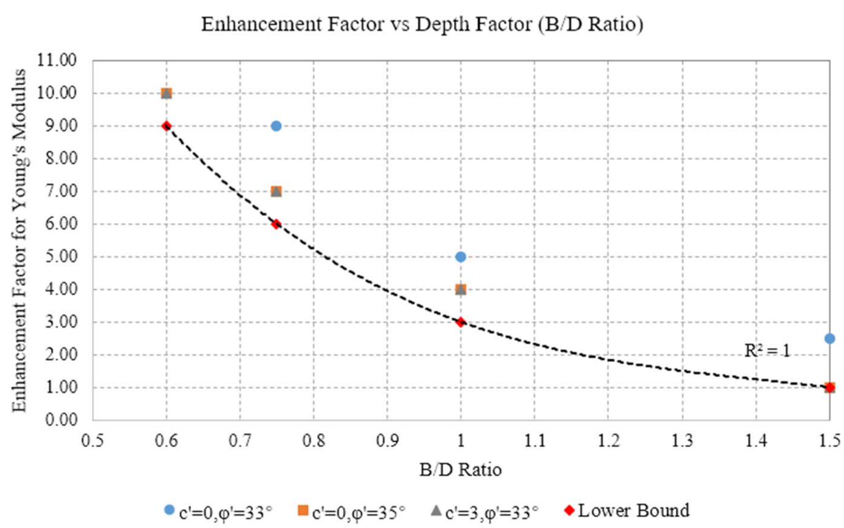

Figure 5: Enhancement Factor for Young's Modulus (E_s) vs B/D ratio (with constant L/B = 1)

4.3 Combined 3D Effects of Shape and Depth on Enhanced Young's Modulus (E_s)

To account for the combined 3D effects of shaft geometry, design lines are proposed in Figure 6, offering enhancement factors for Young's Modulus (E_s) based on the ratios of shaft length, breadth and depth. Analysis revealed that soils with varying strength parameters show consistent deformation trends relative to shaft geometry.

Among the geometric factors, depth factors (represented by B/D or L/D) are found to be the dominant contributor to increase soil stiffness, while shape factors (represented by L/B) play a secondary role. Based on this, it is recommended to apply enhanced Young's Modulus (E_s) in 2D modelling when L/B ≤ 1.6 and L/D ≤ 1.5.

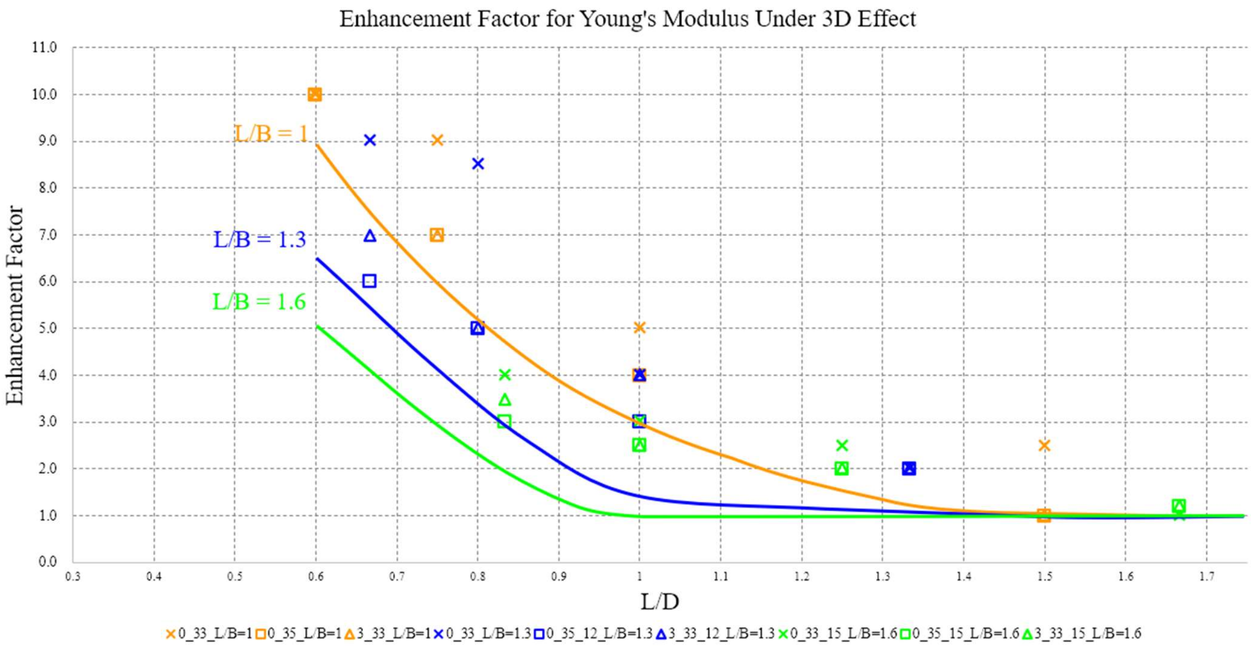

Figure 6: Enhancement Factors for Young's Modulus (E_s) under 3D Effect

5 RECOMMENDED DESIGN APPROACH USING 2D ENHANCEMENT FACTORS

The results of the parametric studies confirm that excavation geometry critically influences ground movements. Notably, 3D numerical analyses reveal that the beneficial effects of three-dimensional confinement are significant when L/B ≤ 1.6 and L/D ≤ 1.5. These 3D effects diminish as the excavation becomes either more elongated or shallower, reducing the influence of corner confinement.

Performing full 3D numerical simulations for every iteration of the Excavation and Lateral Support (ELS) design is not only computationally intensive but may also be inefficient, particularly when the excavation geometry lies outside the effective ranges where 3D effects are insignificant. Moreover, the complexity of 3D models makes it cumbersome to rapidly evaluate multiple design alternatives during the optimization process.

To bridge the gap between the accuracy of 3D analysis and the practicality of 2D modelling, a design framework incorporating 2D enhancement factors (as developed in Section 4) is proposed. This approach allows designers to capitalize on the benefits of 3D effects while maintaining the efficiency and flexibility of 2D modelling tools. The proposed approach advocates for the use of enhancement factors applied to the Young's modulus (E_s) of the surrounding soil strata within 2D models. This allows for a more streamlined and iterative design process, enabling engineers to explore various support system configurations while still accounting for the influence of 3D effects. The proposed design procedures are presented as follows:

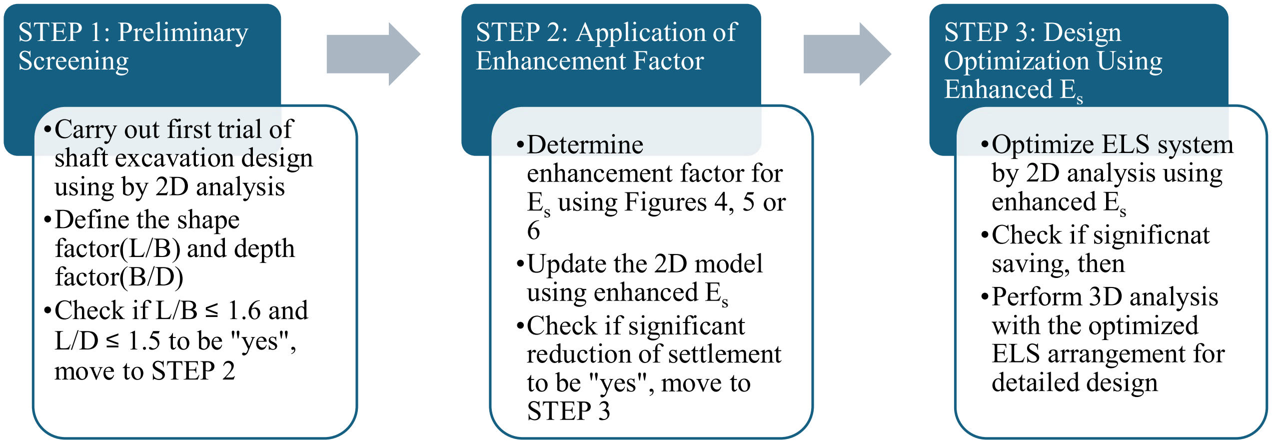

Figure 7: Flow Chart for ELS Design Using Enhancement Factor for Young's Modulus (E_s)

Step 1: Preliminary Screening

Identify shaft configurations with geometry falling within critical thresholds (e.g., $L/B \leq 1.6$ and $L/D \leq 1.5$). These cases are likely exhibit significant 3D effects and warrant further assessment. For configurations outside these ranges, conventional 2D analysis may be sufficient.

Step 2: Application of Enhancement Factors

Apply the corresponding enhancement factor to the Young's modulus (E_s) of the surrounding soil in the 2D model. This modification simulates the increased soil stiffness observed due to 3D confinement effects and provides an improved settlement estimate.

Step 3: Design Optimization Using Enhanced Es

Perform 2D design trial using the enhanced E_s to optimize the ELS system. Once an optimal configuration is selected, validate the final design with a single 3D numerical model to confirm performance and proceed with detailed design documentation.

It is particularly noteworthy that when the length-to-depth ratio (L/D) is less than 0.5, meaning the excavation depth is at least twice the shaft length, the 3D confinement effect becomes especially significant. In these cases, the required enhancement factors can be exceptionally high, leading to substantial reductions in surface settlement. For such configurations, full 3D modelling is strongly recommended, as the potential savings in construction materials and performance improvements justify the added modelling effort.

6 CASE STUDY: APPLICATION OF THE RECOMMENDED DESIGN APPROACH

The project involved a square-shaped excavation (size: 8m(B) x 8m(L) x 9.6m(D)) designed as a launching shaft for pipe jacking works. The subsurface profile consisted of a Fill layer overlaying a layer of Completely Decomposed Granite (CDG), with the bedrock located approximately 14m below existing ground level. The design groundwater table was assumed at 1m below ground level. The adopted design parameters for Hardening Soil (HS) constitutive model are shown in Table 4 below:

Table 4: Input Parameters for Soil (HS Model)

Soil Type	γ (kN/m^3)	c' (kPa)	ϕ' (deg.)	E_{50}^{ref} (kPa)	E_{oed}^{ref} (kPa)	E_{ur}^{ref} (kPa)
Fill	19	0	35	10,000	7,000	30,000
CDG	19	5	39	30,000	21,000	90,000

A benchmark model was developed in PLAXIS 2D as a baseline design for the optimization study. The initial ELS design employed FSP IV sheet piles with five layers of struts and walings, governed by a 25mm settlement limit especially under a high surcharge loading of 50kPa from lifting girder. The model configuration and settlement output are shown in Figure 8, with the maximum predicted ground settlement of 24.1mm.

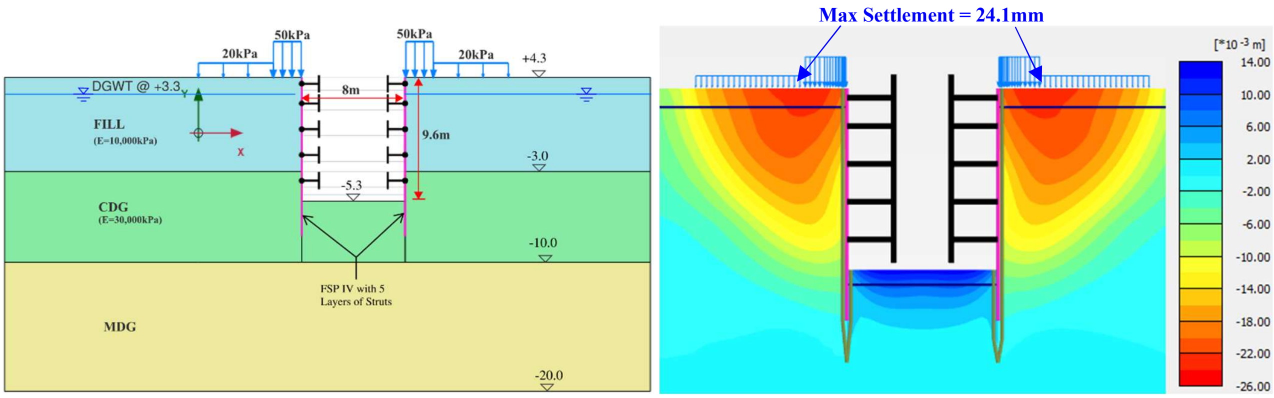

Figure 8: Original Baseline ELS Design – Input Configuration (Left) and Settlement Output (Right)

Step 1: Preliminary Screening

Both the shape factor (L/B = 1 < 1.6) and depth factor (L/D = 0.83 < 1.5) fall within the threshold ranges established in Section 5. Therefore, further exploration using enhancement factor and potential 3D effects are deemed beneficial for ELS optimization.

Step 2: Preliminary Checking with Enhanced Es

Based on Figure 6, enhancement factors for Young's Modulus (E_s) were determined according to the project's shape and depth factors. Incorporating the enhanced Young's Modulus (E_s) into the PLAXIS 2D model led to a reduction in maximum ground settlement from 24.1mm to 14.8mm, i.e. approximate 40% of reduction. This significant improvement by using enhanced E_s revealed opportunity to optimize ELS design by 3D analysis, as ground settlement was typically a critical concern in ELS design. Table 5 summarizes the baseline Young's Modulus (E_s) values and the enhanced E_s values.

Table 5: Summary of Young's Modulus (E_s) for PLAXIS 2D Analysis

Soil Type	Baseline Design (2D Model)		Shape Factor (L/B)	Depth Factor (L/D)	Enhanced E_s Design (2D Model)		
	Original E_s (kPa)	Ground Settlement (mm)			Enhancement Factor	Enhanced E_s (kPa)	Ground Settlement (mm)
Fill	10,000	24.10	1	0.83	4.6	46,000	14.60
CDG	30,000					138,000	

Step 3: Optimizing the ELS System with PLAXIS 2D with Enhanced E_s and Detailed Design in PLAXIS 3D

Several ELS configurations were assessed using PLAXIS 2D with enhanced E_s for rapid optimization. The primary focus was reducing the number of strut layers to lower construction cost and time as well as providing more working spaces. Ultimately, the strut and waling system was reduced from five to three layers (as shown in Figure 9), while still achieving smaller ground settlement (18.6mm) compared to the original baseline (24.1mm).

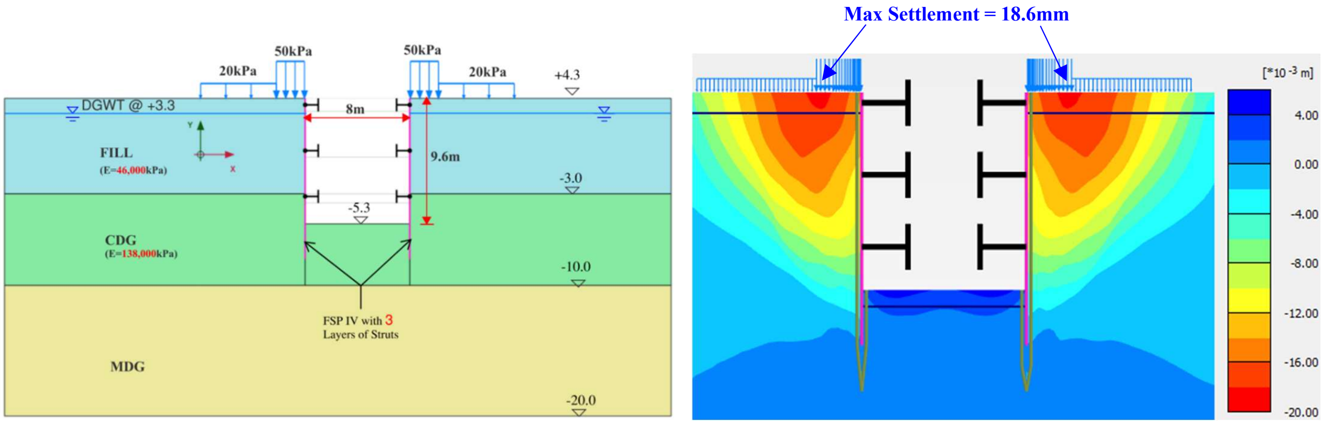

Figure 9: Optimized ELS System – Input Configuration (Left) and Settlement Output (Right)

Following the 2D optimization using enhanced E_s, the proposed arrangement was analyzed in PLAXIS 3D using the original design parameters, refer to Figure 10. The maximum ground settlement was 21.7mm, which closely aligned with the result from the 2D enhanced model, confirming the reliability of the enhancement approach. From a structural optimization perspective, the strut forces in the 3D model were consistently lower than those in the 2D baseline model. Specifically, the total strut force, based on the sum of 5 strut layers in the 2D model versus 3 strut layers in 3D model, was reduced by approximately 45%. Furthermore, the maximum load on individual strut layer showed a reduction of 24%. These reductions suggest potential for further optimization in sizing of strut and waling members. On the other hand, maximum bending moment of sheet pile wall in the 3D model (i.e. 181kNm/m) were about 25% higher than 2D baseline model (i.e. 147kNm/m) due to the greater load width and longer span length between struts following reduction of the strut from 5 layers to 3 layers. Nevertheless, the maximum bending moment from 3D model still remained well within the allowable bending capacity of FSP IV sheet pile (i.e. 325kNm/m for Grade S275). The use of oversized sheet piles in the original baseline design provided additional stiffness, originally intended to control the settlement, and proved sufficient even after design optimization.

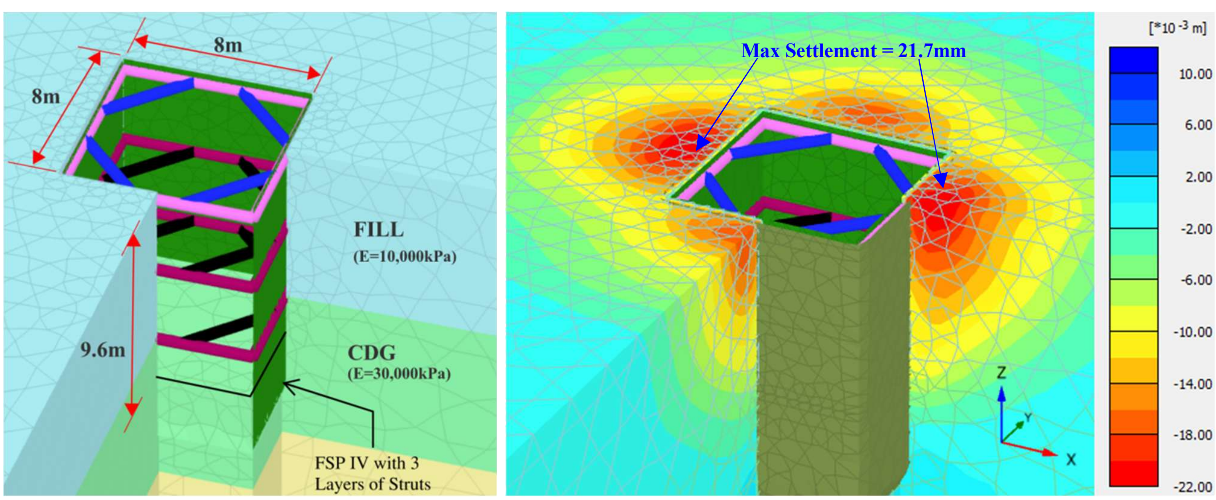

Figure 10: PLAXIS 3D Model of Optimized ELS System – Input Configuration (Left) and Settlement Output (Right)

Figure 11 presents a summary graph of the maximum ground settlements across the various design cases. As discussed, the settlement predicted by the optimized arrangement of PLAXIS 2D model using the enhanced E_s closely aligns with the results from the PLAXIS 3D analysis. This case study demonstrates how the proposed enhancement approach can effectively streamline and optimize the ELS design process for deep shaft excavations with consideration of 3D effects.

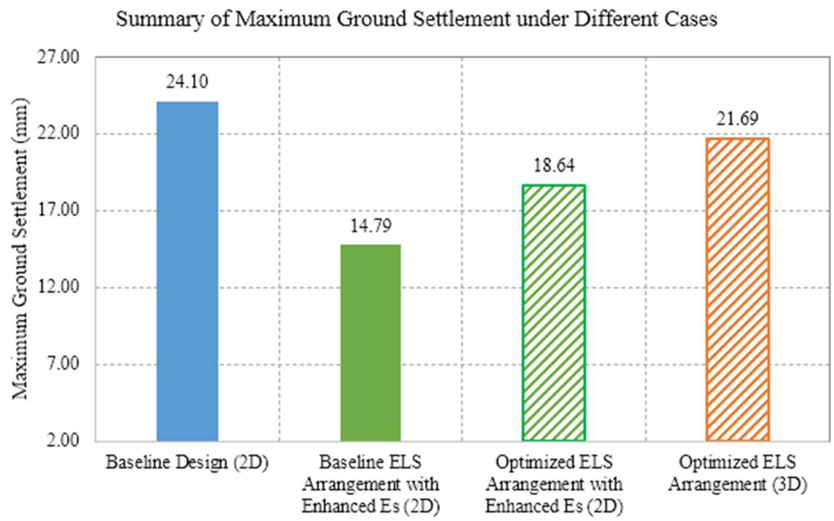

Figure 11: Summary of Settlement Results Across Various Design Cases

7 CONCLUSIONS

This paper presents a simplified and efficient methodology for the preliminary design of Excavation and Lateral Support (ELS) systems in shaft excavations. The approach is particularly beneficial during the serviceability limit state (SLS) design stage, where rapid and reliable assessment of ground movement is normally the controlling factor for ELS design. By incorporating enhancement factors into 2D numerical models to simulate 3D confinement and corner effects, designers can streamline the design process, enabling early-stage optimization of ELS systems prior to comprehensive 3D verification.

The keys findings from the study include:

1. Depth factor (L/D) is the most influential parameter affecting ground movement due to 3D confinement effects. The effect becomes particularly significant when $L/D \leq 1.5$, and is most pronounced when $L/D < 0.5$, where the excavation depth is at least twice the shaft length. In such cases, the vertical confinement induces substantial soil arching and stiffness gains.

2. Shape factor (L/B) also plays a critical role. When $L/B \leq 1.6$, the corner and buttressing effects provide additional lateral support to the retaining walls, leading to reduced lateral wall deflection and associated settlement.

3. When $L/D > 1.5$ and $L/D > 1.6$, the influence of 3D effects diminishes. Under these conditions, the plane-strain assumption in 2D modelling becomes valid, with 2D results aligning closely with those from full 3D analyses.

The integration of 2D enhancement techniques with strategic 3D validation offers a practical, cost-effective, and technically robust framework for shaft excavation design. When applied during early planning stages, this hybrid approach allows designers to efficiently evaluate multiple ELS configurations, reduce reliance on resource-intensive 3D modelling, and ultimately shorten construction timelines and reduce project costs, without compromising safety or performance. This methodology supports the development of resilient and sustainable underground infrastructure in dense urban environments.

REFERENCES

Calvello, N. and Finno, R. (2004). *Selecting parameters to optimize in model calibration by inverse analysis*. Comput. Geotechn. 31, 410–424.

GEO (2023). *Deep Excavation Design and Construction, GEO Publication No. 1/2023.* Geotechnical Engineering Office, Civil Engineering and Development Department, HKSAR Government

Russo G. & Nicotera M. (2022). *Monitoring a deep excavation in the historical center of Napoli: Università Station*. 11th International Symposium on Field Monitoring in Geomechanics (ISFMG2022): 1-8.

Hsiung B-C.B, Yang K.H, Aila W. and Ge L. (2018). *Evaluation of the Wall Deflections of a Deep Excavation in Central Jakarta using Three-Dimensional Modelling*. Tunnelling and Underground Space Technology: 84-96, Vol.72

Kosalim V. and Gunawan A. (2023). *Corner Effects of Retaining Wall on Lateral Stress Distribution and Deformation.* IOP Conf. Ser.: Earth Environ. Sci. 1169 012029

Lim, A., Ou, C.Y., Hsieh, P.G. (2010). *Evaluation of clay constitutive models for analysis of deep excavation under undrained conditions*. J. GeoEng. 5, 9–20.

Ou, C.Y. (2006). *Deep Excavation: Theory and Practice.* Taylor & Francis / Balkema

Rabie M., Ashraf M., El-Hamed M.A. and Bahaa D. (2019). *Comparative Study Between 2D and 3D Analysis for Deep Excavation Case History*. International Conference on Advances in Structural and Geotechnical Engineering, ICASGE'19

Schweiger H. F., Scharinger F. and Luftenegger R. (2009). *3D Finite Element Analysis of a Deep Excavation and Comparison with In-situ Measurements.* Geotechnical Aspects of Underground Construction in Soft Ground – N, Huang & Liu (eds)

PLAXIS 2D 2022, Reference Manual

PLAXIS 3D 2022, Reference Manual

Evaluation of RMR for Meta-Sedimentary Rocks in Hong Kong: Challenges and Potential Solutions

Maggie H.Y. Suen & Cyrus C.F. Chow
AECOM Asia Company Limited

Rachel W. Y. Lau, Alan Y. L. Chau, Patrick P. C. Wong and Thomas H. H. Hui
Geotechnical Engineering Office,
Civil Engineering and Development Department,
Government of the Hong Kong Special Administrative Region, Hong Kong SAR, China

ABSTRACT

Meta-sedimentary rocks are distributed over several areas of Hong Kong, including Sai Kung and Shatin, but are especially prevalent in the Northern New Territories. With the proposed development of the Northern Metropolis in the Northern New Territories in its preliminary stages, there is an increased awareness of the complexity of these meta-sedimentary rocks and how their rock mass and material properties may affect foundation design.

The Rock Mass Rating (RMR) system, developed by Bieniawski, has been adopted in GEO Publication No. 1/2006 for estimating allowable bearing pressure and deformation modulus for foundation design in Hong Kong. Over the years, the RMR system has been proven useful for piling works and applicable to various rock types, including meta-sedimentary rocks. Meanwhile, as the use of the RMR system in meta-sedimentary rocks is becoming prevalent in Hong Kong for estimating the allowable bearing pressures, some practitioners encountered challenges when evaluating RMR for these rocks. These difficulties arise primarily from the inconsistencies in the assessment of the rating of RMR parameters by different practitioners, taking cognisance of the limitations of rock joint descriptions in conventional borehole logging practices.

This paper examines the challenges encountered in RMR assessments for meta-sedimentary rocks in Hong Kong by making reference to the findings of a reviewing exercise conducted by different geologists using conventional borehole logging approaches. It aims to quantify the impact due to inconsistent interpretations of RMR parameters and inadequate rock joint descriptions. Suggestions tailored to address these challenges and inconsistencies in evaluating RMR for foundation purposes are presented for discussion.

1 INTRODUCTION

Meta-sedimentary rocks are distributed over several areas of Hong Kong, including Sai Kung and Shatin, but are especially prevalent in the Northern New Territories where the proposed Northern Metropolis development is located. The published geological information *(Sewell et al., 2000*) indicates that the meta-sedimentary rocks in this region can be highly variable in nature and extent. The Northern Metropolis development covers about one-third of the total area of Hong Kong, with a total area of 30,000 hectares. As an essential platform for Hong Kong's integration into the overall development of the Greater Bay Area, the Northern Metropolis development provides new land for the development of the innovation and technology (I&T) industry and is also one of the main sources of future housing land supply. With the Northern Metropolis development underway, there is a growing awareness of the complexity of these meta-sedimentary rocks and how their rock mass and material properties may affect foundation design.

The Code of Practice for Foundations (*BD, 2017*) currently specifies only one category of presumed allowable vertical bearing pressure for meta-sedimentary rocks on horizontal ground or bedrock. This single presumed allowable bearing pressure with a value of 3,000 kPa is considered conservative for all meta-sedimentary rocks as variations could exist among these rocks. The RMR system, originally developed by Bieniawski (Bieniawski, 1973), has been adopted in the GEO Publication No. 1/2006 – Foundation Design & Construction to estimate the allowable bearing pressure for piles and deformation modulus for jointed rock mass with reference to pile loading test data on instrumented piles within different rock types, including meta-sedimentary rocks, in Hong Kong and US (AASHTO, 2012). Recently, AASHTO (2020) introduced a bearing capacity equation for evaluation of base resistance of drilled shafts for cases where the bearing rock can be characterized by Geological Strength Index (GSI) (Turner and Ramey, 2010). It is noted that GSI was first developed based upon an assessment of the lithology, structure and condition of discontinuity surfaces in the rock mass and was estimated from visual examination of the rock mass exposed in surface excavations (Marinos and Hoek, 2000). There are inherent limitations on interpretation of GSI from boreholes.

The use of RMR system for estimating the allowable bearing pressures in meta-sedimentary rocks has gain popularity in recent years. However, practitioners have encountered challenges in accessing the rating of RMR parameters, particularly for meta-sedimentary rocks. These difficulties arise primarily from the inconsistent interpretations of RMR parameters by different practitioners and inadequate rock joint descriptions in borehole logs due to discrepancies between conventional borehole logging practices and the RMR system.

This paper examines the challenges associated with RMR assessment of meta-sedimentary rocks, focusing on two key issues: 1) inconsistencies in the interpretation from different practitioners regarding the rating of RMR parameters, and 2) inadequate rock joint descriptions resulting from discrepancies between conventional borehole logging practices and the requirements of the RMR system. Suggestions to address these challenges when evaluating RMR for foundation purposes will be discussed. These include standardizing the length of the RMR assessment interval and establishing clear principles for assigning ratings to the respective RMR parameters to reduce inconsistencies across practitioners. Additionally, additional details in rock joint descriptions that build upon conventional borehole logging practices is suggested, thereby enhancing the accuracy of RMR assessments. A case study demonstrating the application of a new approach in RMR assessment will be presented, using a drillhole record from the Northern New Territories.

2 META-SEDIMENTARY ROCKS IN THE NORTHERN NEW TERRITORIES OF HONG KONG IN RELATED TO RMR ASSESSMENT FOR FOUNDATION PURPOSE

Meta-sedimentary rocks are found in several areas of Hong Kong, and especially in the Northern New Territories, where they comprise a significant proportion of the solid geology. In the Northern New Territories, the meta-sedimentary rocks distribute generally along the northeast-southwest trending Tuen Mun- Lo Wu Fold Belt, extending from the Heung Yuen Wai area in the northeast to the northern Tuen Mun area in the southwest. The meta-sedimentary rocks in this area mainly belong to the Lok Ma Chau Formation (Cslm and Cslt), with some belonging to the mylonitised sedimentary rocks under Tai O Formation (Jo) and some belonging to the partially metamorphosed sedimentary rocks under Tuen Mun Formation.

According to GEO Publication No. 1/2006, the RMR system is applicable to sedimentary and metamorphic rocks, except for those rock masses affected by dissolution features (e.g. marble formation). As such, massive marble formations belonging to the Yuen Long Formation as well as the marble clastic bearing rocks under the Tuen Mun Formations, are generally not applicable for the RMR assessment.

The meta-sedimentary rocks exhibit complex geological characteristics such as highly variable lithology or rock types, presences of foliation and highly fractured zones, relatively low rock strength in term of Uniaxial Compressive Strength (UCS) and relatively poor rock mass quality. These complexities of metasedimentary rocks bring challenges to not only the foundation engineers but also the logging geologists. In many cases, the borehole log descriptions are not presented with enough details to facilitate a precise RMR assessment. For example, if a 10m section of rock core is being described as “slickensided planar to rough planar” in the borehole log, the RMR assessment will be forced to use a more conservative assumption of “slickensided planar” for roughness rating estimation over the entire 10m of rock core (i.e. roughness rating = 0 for entire 10m). However, in reality, those “slickensided planar” joints may only occur locally over 2m of the rock core, instead of the entire 10m. In this case, the overall roughness rating of the 10m rock core have been underestimated due to the lack of details about the positions and extent of the “slickensided planar” joints. More details about the inadequate rock joint descriptions for RMR assessment will be discussed in **Section 4**.

3 ROCK MASS RATING (RMR) SYSTEM FOR JOINTED ROCK MASS FOR FOUNDATION PURPOSE IN HONG KONG

The Rock Mass Rating (RMR) system was first developed by Bieniawski in 1973 (Bieniawski, 1973) and has been undergone multiple modifications since then. In addition to Hong Kong, AASHTO (2012) recommended the use of RMR can be used for determination of strength and modulus parameters and allowable bearing pressure for both drilled shaft and spread footing although AASHTO (2020) recently introduced a bearing capacity equation for evaluation of base resistance of drilled shafts for cases where the bearing rock can be characterized by recommended the use of Geological Strength Index (GSI) for estimation of bearing pressures for drilled shafts in rock (Turner and Ramey, 2010). As discussed above, there are inherent limitations on interpretation of GSI from boreholes.

RMR classifies rock mass by using the following six rock mass parameters (Bieniawski, 1974):

A. Strength of Intact Rock
B. Rock quality designation (RQD)
C. Spacing of discontinuities (Joints)
D. Condition of discontinuities (Joints), which include:
   Di: Discontinuity length rating; Dii: Separation rating; Diii: Roughness rating;
   Div: Infilling (gouge) rating; Dv: Weathering rating
E. Groundwater conditions
F. Orientation of discontinuities (Joints)

GEO Publication No. 1/2006 recommends calculating the RMR values for the rock mass beneath the piles according to the guidelines outlined in Table 6.4 of that publication. It is important to note that the ratings for discontinuity length (parameter D(i)) and groundwater conditions (parameter E) are fixed in Table 6.4, while the rating for discontinuity orientation (parameter F) is excluded, as these parameters are deemed irrelevant for assessing allowable bearing pressure.

The RMR assessments presented in this paper were calculated according to the recommendations outlined in Table 6.4 of GEO Publication No. 1/2006. An extraction of Table 6.4 of GEO Publication No. 1/2006 is shown in **Figure 1** for ease of reference.

Table 6.4 – Rating Assigned to Individual Parameters using RMR Classification System (Based on Bieniawski, 1989)

(A) Strength of Intact Rock

Uniaxial compressive strength, σ_c (MPa)	> 250	250 – 100	100 – 50	50 – 25	25 – 5	5 – 1	< 1
Point load strength index, PLI_{50} (MPa)	> 10	10 – 4	4 – 2	2 – 1	σ_c is preferred		
Rating	15	12	7	4	2	1	0

(B) Rock Quality Designation (RQD)

RQD (%)	100 – 90	90 – 75	75 – 50	50 – 25	< 25
Rating	20	17	13	8	3

(C) Spacing of Joints

Spacing	> 2 m	2 m – 0.6 m	0.6 m – 0.2 m	200 – 60 mm	< 60 mm
Rating	20	15	10	8	5

(D) Conditions of Joints

Discontinuity length(1)					
Rating	2				
Separation	None	< 0.1 mm	0.1 – 1 mm	1 – 5 mm	> 5 mm
Rating	6	5	4	1	0
Roughness	Very rough	Rough	Slightly rough	Smooth	Slickenside
Rating	6	5	3	1	0
Infilling (gouge)	None	Hard filling < 5 mm	Hard filling > 5 mm	Soft filling < 5 mm	Soft filling > 5 mm
Rating	6	4	2	2	0
Weathering	Unweathered	Slightly weathered	Moderately weathered	Highly weathered	Decomposed
Rating	6	5	3	1	0

(E) Groundwater

Rating(1)	7

Notes :

(1) Rating is fixed as the parameter is considered not relevant to the evaluation of allowable bearing pressure of rock mass.

(2) RMR is the sum of individual ratings assigned to parameters (A) to (E).

Figure 1: Extraction of Table 6.4 of GEO publication No. 1/2006 for RMR classification System for foundation purpose.

4 CHALLENGES associated with RMR assessment of meta-sedimentary rocks and the corresponding SUGGESTED POTENTIAL solutions

As mentioned in **Section 1**, the challenges of evaluating the RMR of meta-sedimentary rocks are mainly related to the following reasons:

1) inconsistencies in the interpretation of different practitioners regarding the rating of RMR parameters; and

2) inadequate rock descriptions in borehole logs due to discrepancies between conventional borehole logging practices and the RMR system.

In addition, it appears that the degree of opening of the joint has been taken into account in both the infilling (gouge) rating assessment (parameter Div) and the separation rating assessment (parameter Dii). Also, the assessment of the roughness rating (parameter Diii) is challenging due to the typically smaller size of rock cores (less than 84 mm), which results in a low reliability.

The challenges associated with each of the RMR parameters (Parameters A to E) as outlined in Table 6.4 of GEO Publication No. 1/2006, along with issues related to the inadequate precision of the borehole logs, are discussed and listed below. Corresponding suggestions for each issue will also be discussed. These include standardising the rock quality detail assessment intervals and the methodology for rating relevant RMR parameters to minimize inconsistencies in interpretation. To address the issue of inadequate rock descriptions in borehole logs, it is recommended to provide additional details to enhance the rock joint descriptions beyond conventional borehole logging practices in order to improve the accuracy of RMR assessments.

4.1 RMR Parameter Related to Strength of Intact Rock

Challenges Related to Difficulties on Obtaining Representative data for Intact Rock Strength

Uniaxial Compressive Strength (UCS) or Point Load Strength Index (PLI50) are essential for assessing the RMR rating for the Strength of Intact Rock (Parameter A). However, the presence of foliations and other discontinuities, such as bedding or fractures, in meta-sedimentary rocks makes it challenging to obtain suitable samples for carrying out the conventional Uniaxial Compressive Strength (UCS) tests and Point Load Tests (i.e. referring to Diametral Test and Axial Test). Consequently, UCS or PLI50 data (in material failure mode) are not always available to accurately represent the intact rock strength when evaluating the RMR for meta-sedimentary rocks.

Suggestion: Apart from the Diametral Test and Axial Test, ASTM D351-95 (ASTM, 1995) also suggests the Irregular Lump Test as one of the Point Load Tests for determining PLI50. The Irregular Lump Test offers greater flexibility in sample selection, allowing for a greater number of suitable samples to be obtained for determining PLI50 in meta-sedimentary rocks, especially in the presence of foliations and discontinuities. The applicability and practicality of using the results of Irregular Lump Tests for determining intact rock strength in meta-sedimentary rocks should be explored. Further research is required to investigate the correlation between UCS and Irregular Lump Test results, with the aim of establishing the latter as an alternative to the Point Load Test in assessing rock strength.

4.2 RMR Parameter Related to Discontinuities (Joints)

The RMR Parameter B (Rock quality designation (RQD)), Parameter C (Spacing of discontinuities), and the 5 sub-class ratings of Parameter D (Conditions of Discontinuity) reflect the joint characteristics of the rock mass. The challenges and suggestions related to the RMR parameters related to discontinuities are summarised in **Table 1**.

Table 1: Challenges and suggestions related to the RMR parameters related to discontinuities

	Challenge	Suggestion
Rock Quality Designation (RQD) (B)	Drilled cores of metasedimentary rocks are prone to weathering and disintegrate readily due to the prominent foliation. Soon after drilling, the cores tend to obtain high RQD as there are only few joints. After drying for some time, even in term of weeks, the cores may start to disintegrate and become a series of discs leading to a lower RQD.	<u>Existing Borehole Logs</u> In general, RQD ratings can be directly obtained from the RQD values listed in the borehole log. Basically, normal RQD logging practice as mentioned in Geoguide 3 shall be followed. <u>New Borehole Logs</u> It is suggested carry out logging shortly after drilling so to capture the in-situ property as far as practicable, and obtain the RQD ratings directly from the RQD values listed in the borehole log.
Spacing of Discontinuities (C)	There are various methods used by different geotechnical practitioners to estimate the spacing of discontinuities. For example, some practitioners • refer to the spacing outlined in the borehole log, as detailed in Table 7 of Geoguide 3 – Guide to Rock and Soil Description • use the Fracture Index for their calculations • inspect core boxes or analyse core box photographs. These inconsistent practices can lead to differing RMR values for the same borehole.	• Date obtained from Televiewer Test can be used to estimate the joint spacing and therefore the RMR rating. • If televiewer result is not available, the spacing of discontinuities is suggested to be back calculated based on weighted average of the Fracture Index (F.I.) as stated in the borehole log, for an interval of 1 metre or less of intact core pieces with reasonably uniform character, except for those recorded as ‘F.I. >20’ or ‘non-intact’ (NI). The follow equation is used to determine the spacing of joints: $Spacing\ of\ Joint\ (mm) = \frac{1000}{F.I.}$ For rock core sections with F.I. logged to be F.I.>20 or NI, RMR rating of 5 should be adopted.
Discontinuity length	The rating for Discontinuity length is fixed as 2 as per Table 6.4 in GEO Publication No. 1/2006 due to the reason that persistence is considered not relevant to the evaluation of allowable bearing pressure of rock mass.	
Joint Separation (Dii)	The seven (7) descriptive terms for aperture size used in conventional borehole logging practices (Table 9 of Geoguide 3) do not fully align with the five (5) RMR rating classes for Joint Separation outlined in Table 6.4 of GEO Publication No. 1/2006. This may lead to inconsistencies in the interpretation by different practitioners. *The RMR rating classes for Joint Separation include five categories:* None, <0.1 mm, 0.1-1 mm, 1-5 mm, and >5 mm. *The descriptive terms for aperture size defined in Geoguide 3 consist of seven categories:* Wide (> 200 mm), moderately wide (60 - 200 mm), moderately narrow (20 - 60 mm), narrow (6 - 20 mm), very narrow (2 - 6 mm), extremely narrow (> 0 - 2 mm), and tight (0mm) <u>Example</u>:	<u>Existing Borehole Logs</u> • Refer to borehole log description of aperture size • Estimate aperture size based on Table 9 of Geoguide 3 • Suggest referring to the upper bound aperture size the descriptive terms as conservative approach • <u>Example</u>: Suggest assuming 2mm as the aperture size for “Extremely narrow” <u>New Borehole Logs</u> • Indicate exact separation or aperture size in addition to the conventional Geoguide 3 requirements • Refer to the separation range as suggested for the RMR Separation Rating • <u>Example</u>: Very Narrow (2mm); Extremely Narrow (<1mm)

<table>
<tr><th></th><th>Challenge</th><th>Suggestion</th></tr>
<tr><td></td><td>In RMR calculation, descriptive term "Extremely narrow" (> 0 - 2 mm) fall into the classification of three classes (<0.1 mm, 0.1-1 mm, and 1-5 mm).

RMR classification may be interpreted differently by various practitioners, leading to discrepancies in separation rating values that can range from 5 to 1.</td><td></td></tr>
<tr><td>Roughness (Diii)</td><td>The nine (9) descriptive terms for joint roughness in conventional borehole logging practices (Table 8 of Geoguide 3) do not fully align with five (5) RMR rating classes for roughness outlined in Table 6.4 of GEO Publication No. 1/2006. This may lead to inconsistencies in the interpretation by different practitioners

The RMR rating classes for Joint roughness include five categories: Very rough, Rough, Slightly rough, Smooth, and Slickenside

The descriptive terms for roughness defined in Geoguide 3 consist of nine categories: rough stepped, rough undulating, rough planar, smooth stepped, smooth undulating, smooth planar, slickensided stepped, slickensided undulating, and slickensided planar

<u>Example</u>:
The descriptive term “rough undulating” in borehole log could be interpreted as “Very rough”, “Rough”, or “Slightly rough” by various practitioners in RMR assessment, leading to discrepancies in roughness rating values that can range from 3 to 1.</td><td>
<table>
<tr><th>Descriptive Terms in borehole log as per Geoguide 3</th><th>Suggested class of RMR roughness rating</th><th>RMR Rating</th></tr>
<tr><td>Rough Stepped</td><td>Very rough</td><td>6</td></tr>
<tr><td>Rough Undulating</td><td>Very rough</td><td>6</td></tr>
<tr><td>Rough Planar</td><td>Rough</td><td>5</td></tr>
<tr><td>Smooth Stepped</td><td>Slightly rough</td><td>3</td></tr>
<tr><td>Smooth Undulating</td><td>Slightly rough</td><td>3</td></tr>
<tr><td>Smooth Planar</td><td>Smooth</td><td>1</td></tr>
<tr><td>Slickensided Stepped</td><td>Slickenside</td><td>0</td></tr>
<tr><td>Slickensided Undulating</td><td>Slickenside</td><td>0</td></tr>
<tr><td>Slickensided Planar</td><td>Slickenside</td><td>0</td></tr>
</table>
*Refer to Note [1] for details and elaboration of the suggestions.</td></tr>
<tr><td>Infilling (gouge) (Div)</td><td>1) Descriptive terms used in conventional borehole logging practices not fully align with the classifications outlined in Table 6.4 of GEO Publication No. 1/2006.
2) Inadequate descriptions in borehole logs may lead to inconsistencies in the interpretation by different practitioners.

The RMR rating classes for Joint Infilling include five categories: None, Hard filling <5mm, Hard filling >5mm, Soft filling <5mm, and Soft filling >5mm

Conventional borehole logging practices: typically stated with the material name and used wordings of “stained”, “coat” and “infill” to roughly illustrate the thickness of the infilling material.

<u>Example</u>:</td><td><u>Existing Borehole Logs</u>
For infilling hardness:

In the case of no description on hardness of infilling material, the typical states of the infilling material is suggested to be referred.
Suggested RMR Infilling hardness for some of the common infillings are listed as below:

<table>
<tr><th>Infilling Type</th><th>Suggested RMR Infilling Hardness Class</th></tr>
<tr><td>Non-cohesive soil</td><td>Soft Filling</td></tr>
<tr><td>Cohesive soil</td><td>Soft Filling</td></tr>
<tr><td>Kaolin</td><td>Soft Filling</td></tr>
<tr><td>Chlorite</td><td>Soft Filling</td></tr>
<tr><td>Calcite</td><td>Hard Filling</td></tr>
<tr><td>Manganese</td><td>Hard Filling</td></tr>
<tr><td>Quartz</td><td>Hard Filling</td></tr>
</table></td></tr>
</table>

<table>
<tr><th></th><th>Challenge</th><th>Suggestion</th></tr>
<tr><td></td><td>Descriptive term “chlorite coated” could be interpreted as soft infilling or hard infilling by various practitioners.

“Coated” can also be interpreted as <5mm or >5mm in thickness.

This lack of details in the borehole log may lead to discrepancies in infilling rating values that can range from 4 to 0.</td><td>For infilling thickness:
Suggest referring to the description terms of infilling if no details on infilling thickness in the borehole log.
Suggested RMR Infilling thickness for some of the common description terms are listed as below:
“No Infill”, “Clean”, and “Stain” as 0mm
“Coating” as <5mm “Infill” as ≥5mm
<u>New Borehole Logs</u>
Suggest specifying the hardness of the infill (hard or soft) in addition to the standard Geoguide 3 requirements
Note the material thickness or refer to the range of infill thickness indicated in the RMR Infilling Rating
Descriptive terms “Clean”, “Stain” and “No infill” are considered to indicate infilling in thickness of 0mm
<u>Example</u>: Chlorite coated (soft infill, <5mm); Calcite infilled (hard infill, <5mm)</td></tr>
<tr><td>Weathering</td><td colspan="2">The rating for Weathering can be directly obtained from the weathering grading as stated in the borehole log. Basically, normal weathering logging practice as per Geoguide 3 may be followed.</td></tr>
<tr><td colspan="3"><u>Note [1]:</u>
When consider the RMR Roughness Rating, the first terms of “rough”, “smooth” and “slickensided” in Table 8 of Geoguide 3 are considered representing Joint unevenness (i.e. the small scale roughness), while the second terms of “stepped”, “undulating” and “planar” are considered representing the joint undulation or waviness (i.e. the large scale roughness). The Joint unevenness and Joint waviness are referring to as js and jw in the RMi by Palmström and Q system, with the combination of them representing the overall Joint roughness jR.
According to Palmström (2008), the Joint “roughness” under RMR system appears referring generally to the Joint unevenness (i.e. the small scale roughness, js), in which the term “rough, “smooth” and “slickensided” in RMR system are generally “equivalent” to the terms of “rough planar”, “smooth planar” and “slickensided planar” in the Q system (and hence also Table 8 of Geoguide 3).
With that the overall joint roughness jR is the combination of js and jw, it is considered reasonable to imply that the highest rating class of “very rough” should be joint surface which has larger roughness than “rough planar”, which may mean joints described as “rough undulating” and “rough stepped”. On the other hand, the intermediate class of “slightly rough” is considered to be joints with roughness larger than “smooth planar” but worse than “rough planar”, which may be represented by those “smooth undulating” and “smooth stepped” joints.
While it is commonly adopted in the conventional borehole logging system, it should, however, be noted that the waviness of joint is originally intended for larger scale roughness measured on a dm to m scale. As such, engineering judgements may be required, and cores should be reviewed where it is considered necessary when using the suggested RMR rating.</td></tr>
</table>

4.3 RMR Parameter E – Groundwater

The rating for Groundwater is fixed as 7 as per Table 6.4 in GEO Publication No. 1/2006 due to the reason that groundwater is considered not relevant to the evaluation of allowable bearing pressure of rock mass.

4.4 Preciseness of Conventional Borehole logging Descriptions

In addition to the challenges associated with each of the RMR parameters mentioned above, there are also other challenges associated with logging practices for RMR assessment.

Challenge due to Rock Quality Variations at Different Depths Not Indicated Precisely in the Borehole Log:
In conventional borehole logging practices, borehole log descriptions often lack the precise details needed for effective RMR assessment. Specific rock quality characteristics at various positions within the rock cores are not accurately represented. This is particularly common for joint roughness and joint aperture, which are frequently recorded in broad ranges that span multiple RMR rating classes, rather than being distinctly separated based on their actual observed levels. For example, in **Figure 2**, the cores are described as having "smooth planar, rough undulating" and "very narrow to extremely narrow" joints, with calcite and chlorite coatings extending over 20 meters, from 48m to 68m below ground level (mbgl). However, upon examining the actual cores, "smooth planar" joints were found present only in the upper 10 meters, from 48mbgl to 58mbgl, while the "very narrow" joints are found only in the first 5 meters, from 48mbgl to 53mbgl. In this case, conventional rock description practices are too generalized to provide detailed information on rock quality at specific sections of the core for RMR assessment. As a result, the RMR Ratings Dii and Diii may be interpreted differently by various practitioners. Some might use the lower bound of RMR ratings, while others could opt for an average rating for the entire length of the rock core. This variation may lead to inconsistencies in the overall RMR values.

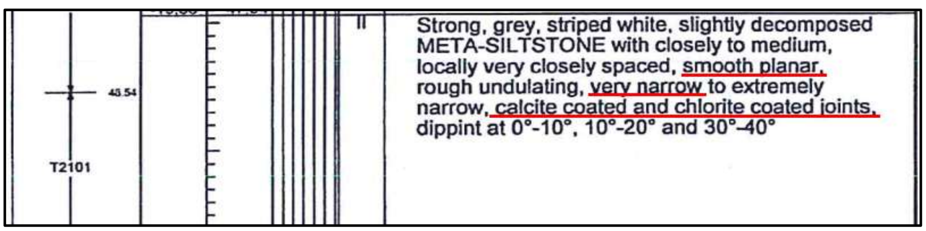

Figure 2: Example of Borehole Logging (from 48mbgl to 68mbgl).

Suggested Solution:

1) For **new borehole logs** – When preparing the borehole log, it is recommended that the logging geologist use a 0.5-meter assessment interval to gather detailed information regarding the RMR parameters discussed in **Section 4**. If any differences can be identified within this 0.5-meter interval, it is advisable to separate the logging descriptions accordingly. Using smaller assessment intervals for logging will yield more precise details for RMR evaluation. Additionally, it is recommended to avoid broad descriptive ranges (i.e. >0.5-meter interval), particularly for sections of rock cores for determination of the founding levels. Instead, it is recommended using specific minor descriptions to indicate local observations and to highlight variations in the RMR parameters.

2) For **existing borehole logs** – As the description of borehole log may not be precise enough for accurate RMR calculation, a conservative RMR rating is suggested to be adopted for those non-precisely described parameters. For instance, in **Figure 2**, the entire 20m rock core under this major description is suggested to be considered as smooth planar, very narrow joints with calcite and chlorite coated for RMR assessment.

4.5 Multifarious Approaches for Calculating RMR

Challenge due to Multifarious Approaches for Calculating the Overall RMR for Rock core:

It is observed that different practitioners may use different methods to calculate overall RMR for rock cores and the calculated RMR could deviate. Some practitioners may simply do the calculation by averaging certain RMR parameters and use the averaged data to come up with the overall RMR for the rock from the borehole log. Others may separate RMR calculation whenever there is a change in the parameters and then estimate the combined RMR for the relevant rock core length. In **Figure 3**, even though the rock description (rock strength, joint aperture, joint roughness) is the same for the selected rock section (from 47.94mbgl to 50.00mbgl), RMR calculations were conducted separately according to the changes in RMR parameters of fracture index and RQD.

Suggested Solution:

1) It is suggested to standardise the RMR calculation approach by calculating RMR separately whenever there is a change in the parameters and then estimate the combined RMR for the relevant rock core length (see the example above in **Figure 3**). Where relevant, RMR calculation is suggested to cover from the engineering rockhead level *(normally category 1(c) or category 2 according to Code of Foundation 2017 (BD, 2017))* to the end of borehole.

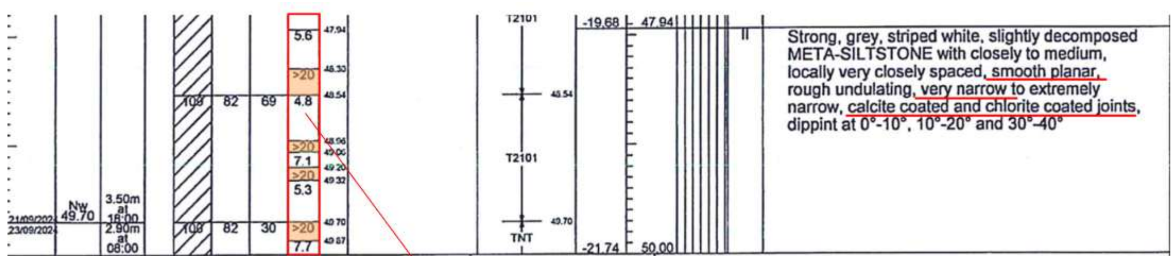

Sample Depth (m)			Sample Length (m)	Rock Grade	Rock Type	Strength of Intact Rock	RQD	Spacing of Joints	Conditions of Joints					Groundwater	RMR	RMR* Length
From	To	mid level mPD							Discontinuity length	Separation	Roughness	Infilling (gouge)	Weathering			
47.94	48.3	-19.86	0.36	II	Meta-Siltstone	7	3	8	2	0	1	2	5	7	35	12.6
48.3	48.54	-20.16	0.24	II	Meta-Siltstone	7	3	5	2	0	1	2	5	7	32	7.68
48.54	48.96	-20.49	0.42	II	Meta-Siltstone	7	13	10	2	0	1	2	5	7	47	19.74
48.96	49.06	-20.75	0.10	II	Meta-Siltstone	7	13	5	2	0	1	2	5	7	42	4.2
49.06	49.2	-20.87	0.14	II	Meta-Siltstone	7	13	8	2	0	1	2	5	7	45	6.3
49.2	49.32	-21.00	0.12	II	Meta-Siltstone	7	13	5	2	0	1	2	5	7	42	5.04
49.32	49.7	-21.25	0.38	II	Meta-Siltstone	7	13	8	2	0	1	2	5	7	45	17.1
49.7	49.87	-21.53	0.17	II	Meta-Siltstone	7	8	5	2	0	1	2	5	7	37	6.29
49.87	50	-21.68	0.13	II	Meta-Siltstone	7	8	8	2	0	1	2	5	7	40	5.2
													Overall Average RMR =		40.85	

Figure 3: Example of RMR Calculation of Selected Rock Portion (from 47.94mbgl to 50.00mbgl)

5 CASE STUDY – APPLICATION OF THE POTENTIAL SOLUTIONS FOR RMR ASSESSMENT OF META-SEDIMENTARY ROCKS

The potential solutions for RMR assessment as mentioned in **Section 4** have been applied to a recently drilled borehole (namely BH-X1 for ease of reference) at a site in the Northern New Territories underlain by meta-sedimentary rocks. During the RMR assessment, it was noted that the log for BH-X1, which was prepared using conventional logging practices, lacked sufficient information to enable an accurate RMR assessment. To facilitate a more precise RMR estimation, the suggestions as mentioned in **Section 4** were applied to BH-X1. A comparison of the RMR assessment results before and after the application of the potential solutions are presented below.

5.1 RMR of BH-X1 Before Applying the Potential Solutions

As shown in the part extraction of the log and photos of BH-X1 (from 36.53mbgl to 42.77mbgl) in **Figure 4**, The descriptions in the log were generic, failing to capture the variations in rock quality at different depths. Thus, a conservative RMR rating was adopted for those non-precisely described parameters (e.g. aperture size of joint and hardness of material infilling at joints). As shown in **Figure 5**, the average calculated RMR for BH-X1 (i.e. based on conventional borehole logging practices) from 36.53mbgl to 42.77mbgl is 38.73.

5.2 RMR of BH-X1 After Applying the Potential Solutions:

To implement the potential solutions for RMR, the cores of BH-X1 were thoroughly inspected, and the log for BH-X1 was reviewed and updated to include relevant details. The borehole log was then revised according to the "suggestions for new borehole log" as mentioned in **Section 4**, aiming to provide a detailed and precise description fitting the RMR classification system, thereby facilitating the RMR assessment. Additional observed details have been included to illustrate the variation in rock qualities at different depths. For example, a more detailed description of joints aperture size ranged from 1-2mm between 36.93mbgl and 40.20mbgl as well as soft manganese oxide coated at rough planar joints from 39.91mbgl to 40.20mbgl were added. The additional precise details in the revised log of BH-X1 are highlighted in red in **Figure 6** for the part extraction of the revised log of BH-X1.

RMR assessment has been conducted again using the revised borehole log by the same practitioner according to the new guideline as proposed in **Section 4**. With a more detailed and precise description, the average calculated RMR on revised borehole log (from 36.53mbgl to 42.77mbgl) was increased by more than 10%, from 38.73 to 43.16. Part extraction of the RMR calculation from 36.53mbgl to 42.77mbgl is shown in **Figure 7**. **Figure 8** displays the calculated RMR results plotted against depth (meters below ground level) for the original borehole log of BH-X1, which was obtained using conventional logging methods, alongside the revised borehole log that incorporates the potential solutions as discussed in **Section 4**. It can be observed from **Figure 8** that the revised borehole log generally exhibits a larger RMR value. This may be due to adoption of a more conservative approach for those non-precisely described parameters in the borehole log, which lacks detail regarding variations in rock quality at different depths.

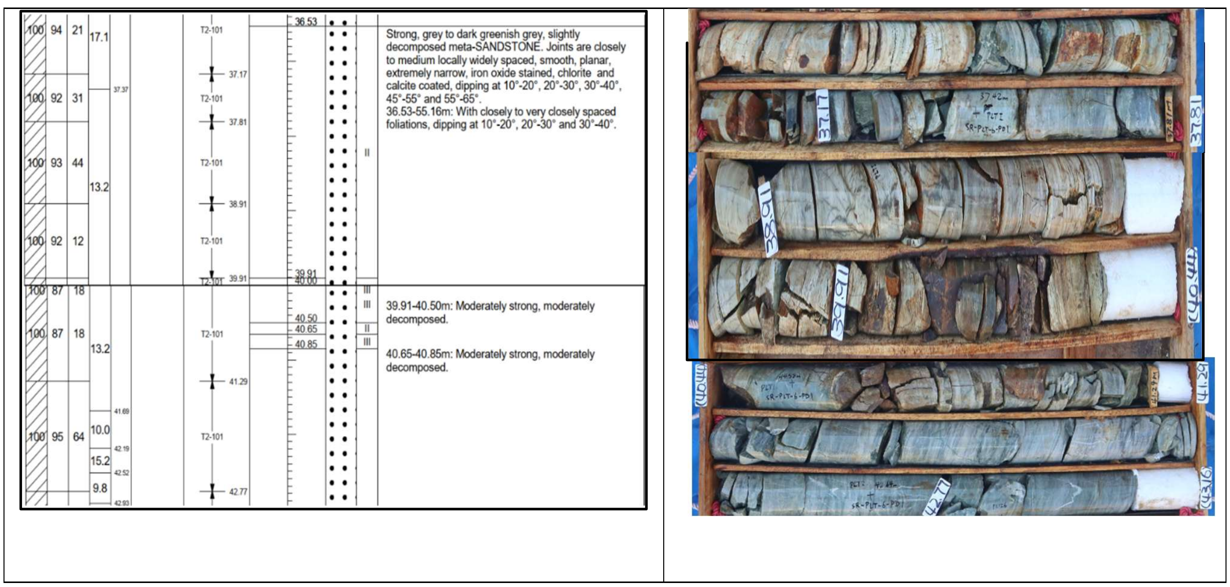

Figure 4: Part Extraction of BH-X1 (from 36.53mbgl to 42.77mbgl) and the corresponding core box photos

Sample Depth (m)			Sample Length (m)	Rock Grade	Strength of Intact Rock	RQD	Spacing of Joints	Conditions of Joints					Groundwater	RMR	RMR* Length
From	To	mid level mPD						Discontinuity length	Separation	Roughness	Infilling (gouge)	Weathering			
36.53	37.17	12.03	0.64	II	7	3	5	2	1	1	2	5	7	33	21.12
37.17	37.37	11.61	0.20	II	7	8	5	2	1	1	2	5	7	38	7.6
37.37	37.81	11.29	0.44	II	7	8	8	2	1	1	2	5	7	41	18.04
37.81	38.91	10.52	1.10	II	7	8	8	2	1	1	2	5	7	41	45.1
38.91	39.91	9.47	1.00	II	7	3	8	2	1	1	2	5	7	36	36
39.91	40.5	8.68	0.59	III	4	3	8	2	1	1	2	3	7	31	18.29
40.5	40.65	8.31	0.15	II	7	3	8	2	1	1	2	5	7	36	5.4
40.65	40.85	8.13	0.20	III	4	3	8	2	1	1	2	3	7	31	6.2
40.85	41.29	7.81	0.44	II	7	3	8	2	1	1	2	5	7	36	15.84
41.29	41.69	7.39	0.40	II	7	13	8	2	1	1	2	5	7	46	18.4
41.69	42.19	6.94	0.50	II	7	13	8	2	1	1	2	5	7	46	23
42.19	42.52	6.53	0.33	II	7	13	8	2	1	1	2	5	7	46	15.18
42.52	42.77	6.24	0.25	II	7	13	8	2	1	1	2	5	7	46	11.5
													Average RMR	38.73	

Figure 5: Part Extraction of RMR Calculation of the BH-X1

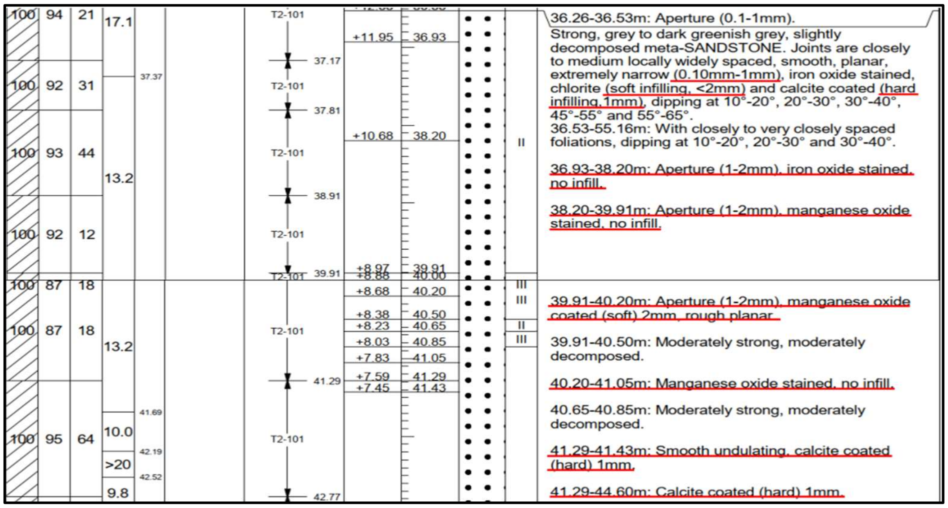

Figure 6: Part Extraction of Revised Borehole Log for BH-X1 for RMR Assessment

Sample Depth (m)			Sample Length (m)	Rock Grade	Strength of Intact Rock	RQD	Spacing of Joints	Conditions of Joints					Groundwater	RMR	RMR* Length
From	To	mid level mPD						Discontinuity length	Separation	Roughness	Infilling (gouge)	Weathering			
36.53	36.93	12.15	0.40	II	7	3	5	2	4	1	2	5	7	36	14.4
36.93	37.17	11.83	0.24	II	7	3	5	2	1	1	6	5	7	37	8.88
37.17	37.37	11.61	0.20	II	7	8	5	2	1	1	6	5	7	42	8.4
37.37	37.81	11.29	0.44	II	7	8	8	2	1	1	6	5	7	45	19.8
37.81	38.2	10.88	0.39	II	7	8	8	2	1	1	6	5	7	45	17.55
38.2	38.91	10.33	0.71	II	7	8	8	2	1	1	6	5	7	45	31.95
38.91	39.91	9.47	1.00	II	7	3	8	2	1	1	6	5	7	40	40
39.91	40.2	8.83	0.29	III	4	3	8	2	1	5	2	3	7	35	10.15
40.2	40.5	8.53	0.30	III	4	3	8	2	4	1	6	3	7	38	11.4
40.5	40.65	8.31	0.15	II	7	3	8	2	4	1	6	5	7	43	6.45
40.65	40.85	8.13	0.20	III	4	3	8	2	4	1	6	3	7	38	7.6
40.85	41.05	7.93	0.20	II	7	3	8	2	4	1	6	5	7	43	8.6
41.05	41.29	7.71	0.24	II	7	3	8	2	4	1	2	5	7	39	9.36
41.29	41.43	7.52	0.14	II	7	13	8	2	4	3	4	5	7	53	7.42
41.43	41.69	7.32	0.26	II	7	13	8	2	4	1	4	5	7	51	13.26
41.69	42.19	6.94	0.50	II	7	13	8	2	4	1	4	5	7	51	25.5
42.19	42.52	6.53	0.33	II	7	13	5	2	4	1	4	5	7	48	15.84
42.52	42.77	6.24	0.25	II	7	13	8	2	4	1	4	5	7	51	12.75
													Average RMR	43.16	

Figure 7: Part Extraction of RMR Calculation of the Revised Borehole Log for BH-X1

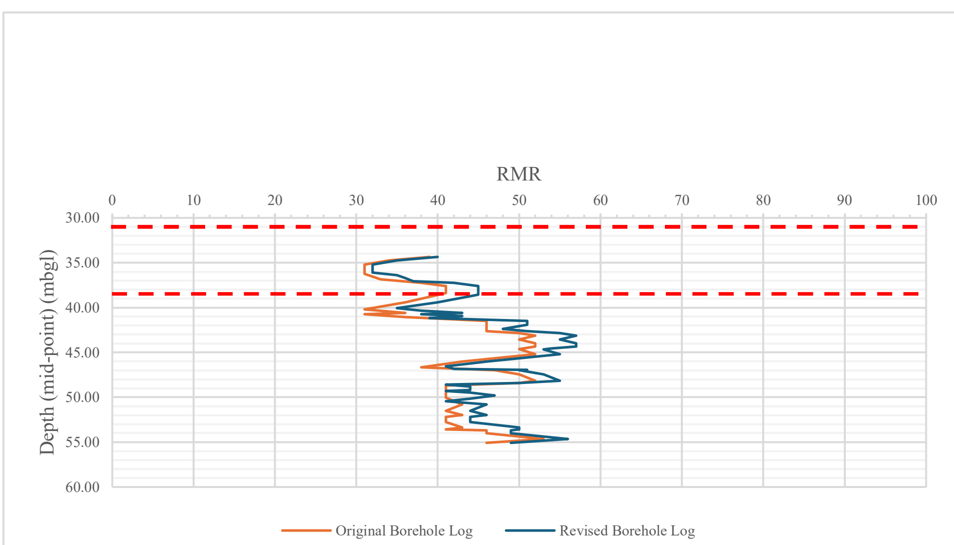

Figure 8: Comparison of Calculated RMR using Original Borehole Log and Revised Borehole Log pf BH-X1

6 SUMMARY

When using the RMR classification system to assess rock mass quality for foundation design, inconveniences often arise with borehole records generated through conventional borehole logging practices. These challenges primarily stem from inconsistencies in the evaluation of RMR parameters by different practitioners, as well as misalignments between conventional borehole logging methods and the RMR system. This issue is particularly pronounced in the case of meta-sedimentary rocks, which exhibit significant variability in rock mass quality. To address these challenges, solutions specifically designed to enhance RMR assessments have been proposed. These suggestions include the standardisation of the RMR parameter rating calculation and the improvement of conventional borehole logs to provide more detailed information, thereby facilitating a more representative RMR assessment.

ACKNOWLEDGEMENTS

This paper is published with the permission of the Head of the Geotechnical Engineering Office and the Director of Civil Engineering and Development, the Government of the Hong Kong Special Administrative Region of the People's Republic of China.

REFERENCES

AASHTO (2012), *LRFD Bridge Design Specifications*. 6th Edition. American Association of State Highway and Transportation Officials. 1661 p.

AASHTO (2020), *LRFD Bridge Design Specifications*. 9th Edition. American Association of State Highway and Transportation Officials. 1914 p.

ASTM (1995), *ASTM D351-95 - Standard Test Method for Point Load Strength Index of Rock*, American Society for Testing and Materials, West Conshohocken, PA, 7p.

Bieniawski, Z.T. (1973). *Engineering classification of jointed rock masses*. Transaction of the South African Institution of Civil Engineers, 15, pp 335-343.

Bieniawski, Z.T. (1974). *Geomechanics classification of rock masses and its application in tunnelling*. Proceedings of the Third International Congress of the International Society for Rock Mechanics, Denver, vol. 2A, pp 27-32.

Bieniawski, Z.T. (1989). *Engineering Rock Mass Classifications – A Complete Manual for Engineers and Geologists in Mining, Civil and Petroleum Engineering.* John. Wiley & Sons, Canada, 250p.

BD (2017). *Code of Practice for Foundations 2017*. Building Department, Hong Kong, 111 p

Fyfe, J.A., Shaw, R., Campbell, S.D.G., Lai, K.W. & Kirk, P.A. (2000). *The Quaternary Geology of Hong Kong*. Geotechnical Engineering Office, Hong Kong, 210p

GEO (2017). *Geoguide 3 – Guide to Rock and Soil Descriptions*. Geotechnical Engineering Office, Hong Kong, 176 p.

GEO (2006). *GEO Publication No. 1/2006 – Foundation Design and Construction.* Geotechnical Engineering Office, Hong Kong, 376 p.

Littlechild, B.D., Hill, S.J., Statham, I. & Plumbridge, G.D. (2000). *Stiffness of Hong Kong rocks for foundation design*. Proceedings of the Nineteenth Annual Seminar, Geotechnical Division, Hong Kong Institution of Engineers, pp 181-190.

NGI (2022). *Using the Q-system – Rock mass classification and support design*. NGI, 56 p.Palmström, A., (2014). *An Introduction to the Rock Mass index (RMi) and its Application*. www.Rockmass.net, 8p

Marinos, P. & Hoek, E. (2000). *GSI: A Geologically Friendly Tool for Rock Mass Strength Estimation.* Proceedings of Geo-Engineering 2000, International Conference on Geotechnical and Geological Engineering, Melbourne, Australia, pp 1422-1440.

Palmström, A., (2008). *Comparing the RMR, Q, and RMi Classification System*s. RockMass as, Oslo, Norway, 10p

Palmström, A., (2009). *Combing the RMR, Q, and RMi Classification Systems.* RockMass as, Oslo, Norway, 25p

Sewell, R.J., Campbell, S.D.G., Fletcher, C.J.N., Lai, K.W. & Kirk, P.A. (2000). *The Pre-Quaternary Geology* *of Hong Kong*. Geotechnical Engineering Office, Hong Kong, 181p

Turner, J. P. and S. B. Ramey (2010). *Base Resistance of Drilled Shafts in Fractured Rock*. Proceedings of The Art of Foundation Engineering Practice Congress 2010. American Society of Civil Engineers, Reston, VA, 2010. pp 687–701.

Advancing Geotechnical Resilience with the Smart Surface Drainage Monitoring System

Raymond P. H. LAW, Jeffrey C. F. WONG
Geotechnical Engineering Office, Civil Engineering and Development Department, HKSAR Government
C. H. CHENG, H. LAM
Logistics and Supply Chain MultiTech R&D Centre

ABSTRACT

The Smart Surface Drainage Monitoring System (SSDMS) is a pilot project developed by the Geotechnical Engineering Office (GEO) of the Civil Engineering and Development Department (CEDD) in collaboration with the Logistics and Supply Chain MultiTech R&D Centre (LSCM). Initiated in early 2023, with site trials commencing in mid-2023, the SSDMS aims to enhance surface drainage maintenance and improve the management of landslide risks associated with extreme rainfall events. During Hong Kong's record-breaking rainstorm in September 2023, the SSDMS successfully detected drainage blockages at one of the trial sites, effectively demonstrating its capability in supporting slope safety management. This system integrates ultrasonic sensors, laser sensors, water-triggering sensors, and verification cameras to provide continuous, real-time monitoring of drainage conditions. Collected data is transmitted via the Government Wide IoT Network (GWIN) or Narrowband Internet of Things (NB-IoT), enabling rapid maintenance responses through a dedicated web application and API. Ongoing enhancements include refining sensor detection algorithms, incorporating artificial intelligence (AI) to further reduce false alarms, and optimizing hardware designs to facilitate easier installation and improved reliability.

1 BACKGROUND

Hong Kong is characterized by its complex topography, dense urban development, and subtropical climate, which together pose unique geotechnical challenges. Over the past several decades, the GEO of the CEDD has successfully established and continuously enhanced a robust slope safety system. This comprehensive system includes stringent geotechnical controls, rigorous engineering standards, and regular preventative maintenance programs, all of which have significantly reduced the risk of slope failures. As a result, Hong Kong is widely recognized internationally for its proactive and effective slope management strategies.

One critical element of Hong Kong's slope safety management strategy is its extensive surface drainage infrastructure, including U-channels, surface channels, and other drainage provisions. These drainage systems play a crucial role in intercepting and diverting surface runoff away from slopes, minimizing infiltration into the soil and reducing potential landslide hazards. For government slopes, regular inspections and maintenance operations are conducted by government maintenance teams, systematically clearing debris and ensuring that drainage channels maintain their designed functions.

However, ongoing global climate trends indicate a potentially increasing frequency and intensity of extreme weather events, with rainfall patterns becoming more intense and less predictable. One example is the record-breaking rainstorm in Hong Kong in September 2023. During this severe weather event, extreme rainfall intensity resulted in significant runoff that rapidly mobilized substantial quantities of vegetation and debris. Under such unforeseeable and exceptional storm conditions, drainage channels may experience rapid accumulation of debris, potentially leading to blockages that are difficult to detect and manage through periodic manual inspections alone. Such challenges highlight the importance of real-time monitoring solutions, as demonstrated by recent IoT-based drainage monitoring initiatives (Gawali et al., 2024).

Recognizing these evolving challenges, GEO proactively initiated the SSDMS project in early 2023. Jointly developed with the LSCM, the primary objective of this project is to complement current practices for inspecting and maintaining surface channels, ensuring that Hong Kong's slope management strategies remain future-proof and capable of addressing emerging threats posed by climate change. The SSDMS leverages state-of-the-art IoT technology, integrating specialized sensors capable of continuous, real-time monitoring of critical drainage systems. This innovative approach enables rapid detection and notification of drainage blockages and related issues, which allows for proactive and targeted maintenance interventions, a method increasingly adopted internationally to enhance drainage management (Diamse et al., 2023).

2 INTRODUCTION OF THE SSDMS

The pilot SSDMS integrates multiple sensing technologies, including water-triggering sensors, ultrasonic depth sensors, laser obstruction sensors, and verification cameras. Each sensor type serves a distinct purpose: water-triggering sensors activate the monitoring system upon initial water detection, ultrasonic sensors provide accurate measurements of water depth within drainage channels, laser sensors detect physical blockages, and verification cameras offer visual confirmation to reduce false alarms. Sensor data is transmitted wirelessly through the GWIN or NB-IoT, as well as LTE network for camera images, which facilitates rapid response from relevant maintenance teams. This multi-sensor integration aligns with recent research advocating sensor-based methods for drainage blockage detection (Narayana et al., 2023).

2.1. Water-triggering sensors

These sensors operate using a dual-float mechanism. As water levels rise within the drainage channel, the first float is lifted, triggering an initial response. If the water level continues to increase and reaches a critical threshold, the second float is activated, triggering the sensor. This activation enhances the system's measurement frequency and prompts image capture, which ensures timely and effective detection of potential drainage issues.

Plate 1 Water Triggering Sensor

2.2. Ultrasonic depth sensors

Ultrasonic sensors measure water depth by emitting high-frequency sound pulses toward the water surface within the drainage channel or catchpit. When these sound waves encounter the water surface, they reflect back to the sensor's receiver. By calculating the time interval between pulse emission and echo reception, and using the known speed of sound in air, the sensor accurately determines the distance to the water surface. The ultrasonic sensors used in SSDMS have an operational range of up to 7 meters. By comparing these measurements with the known dimensions of the channel or catchpit, the system can precisely assess water levels, enabling early detection of abnormal increases that may indicate downstream blockages.

Performance During Extreme Weather:
During the extreme rainstorm in September 2023, the ultrasonic sensors consistently delivered reliable performance despite the challenging conditions. While minor acoustic interference was observed, primarily caused by heavy splashing and turbulent flow, these effects only led to brief fluctuations in depth readings. Importantly, these anomalies did not result in any false alarms or incorrect system triggers.

Plate 2 Ultrasonic Depth Sensor

2.3. Laser obstruction sensors

Laser obstruction sensors installed within the SSDMS utilize infrared laser beams projected sub-horizontally along the length of drainage channels. Under normal, unobstructed conditions, these beams reflect from the channel structure to a receiving photodiode, enabling real-time distance measurement.

When obstructions such as debris, vegetation, or sediment accumulate, the laser reflects from the nearer obstacle, resulting in a shortened measured distance. By comparing these measurements against baseline values, the SSDMS rapidly identifies and locates potential blockages.

Performance During Extreme Weather:
Laser sensors were observed to be more susceptible to signal interference during periods of intense rainfall and fog, primarily due to attenuation and scattering of the laser beam. While these fluctuations fortunately did not trigger any false alerts during the trial period, the possibility of false positives under similar extreme conditions cannot be entirely ruled out. To address this, the project team is actively developing algorithmic filtering and data smoothing techniques to minimize the impact of adverse weather on sensor performance and ensure more reliable blockage detection.

Plate 3 Laser Obstruction Sensor

2.4. Verification cameras

The SSDMS is equipped with digital cameras integrated with night vision capabilities and a solar power system. Upon receiving alerts from other sensors (i.e. water-triggering, ultrasonic, or laser sensors), the camera automatically activates and captures images of the monitored area. These images are transmitted wirelessly via the LTE network to the monitoring platform, allowing operators to visually confirm or dismiss alerts as necessary. This visual verification process significantly reduces false alarms, enhances decision-making accuracy, and assists maintenance teams in preparing targeted and effective clearance actions, consistent with findings from recent studies on automated visual blockage classification (Iqbal et al., 2021).

Plate 4 Verification Camera

2.5. Data processing and alert system

When sensors detect a potential blockage event, the measurement period for the sensors is increased, and the gathered sensor and camera data are continuously transmitted to a designated cloud server, where specialized algorithms analyze the information in real-time. These algorithms evaluate incoming sensor readings against predefined thresholds or patterns to identify potential drainage blockages or other abnormal conditions, similar to automated alert systems described by recent IoT monitoring research (Gawali et al., 2024; Suhail et al., 2023). When sensor data indicates an issue, the SSDMS immediately transmits an alert to GEO's dedicated web application for an initial false alarm verification. If the alert is determined to be valid, the system forwards the information to relevant maintenance teams for further review and necessary action. This streamlined process ensures that only genuine issues are escalated, minimizing unnecessary interventions while maintaining an efficient response system.

3 SITE TRIALS

Following the completion of the initial system development in mid-2023, the first-generation SSDMS prototypes were installed at selected trial sites across Hong Kong, marking the beginning of the site trial phase. This phase aimed to evaluate the system's performance and feasibility under real-world conditions. The selection of trial sites was guided by two general considerations. First, comprehensive GWIN coverage was preferred to ensure reliable wireless data transmission and real-time monitoring capabilities. Second, sites were strategically chosen based on assessments indicating potential susceptibility to blockage risks.

Currently, SSDMS prototypes have been installed at several selected locations, including slopes above Lung Cheung Road, Shek O Road, Sui Wo Road, and a slope at Ho Man Tin. In addition to monitoring traditional U-channel drains, the system has also been deployed at one catchwater location. This trial deployment on catchwater aims to enhance monitoring of overflow conditions, particularly given recent experiences indicating that catchwater overflow during extreme rainfall events can lead to increased landslide risks. Accordingly, SSDMS units have been strategically installed at catchwater overflow weirs to evaluate their effectiveness in detecting overflow conditions and potential blockage issues under varying weather scenarios.

The SSDMS prototypes have now been operational at these trial sites for over a year and continuously collecting monitoring data across different weather conditions and seasons. Notably, during this trial period, the SSDMS was subjected to a real and significant test: the record-breaking extreme rainfall event that impacted Hong Kong in early September 2023 (the sensors installed above Shek O Road and the catchwater above Yiu Hing Road were installed after the rainstorm and were not part of this particular test.). At one of the trial sites (Fo Tan), the SSDMS successfully detected an actual blockage event within a monitored U-channel and the collected data is presented in Plate 5. The blockage, caused by a substantial accumulation of vegetation and sediment mobilized during the intense rainfall, was promptly identified through real-time sensor data and visually verified by the integrated verification camera. This demonstration provided valuable validation of the SSDMS's effectiveness and communication reliability under extreme storm conditions.

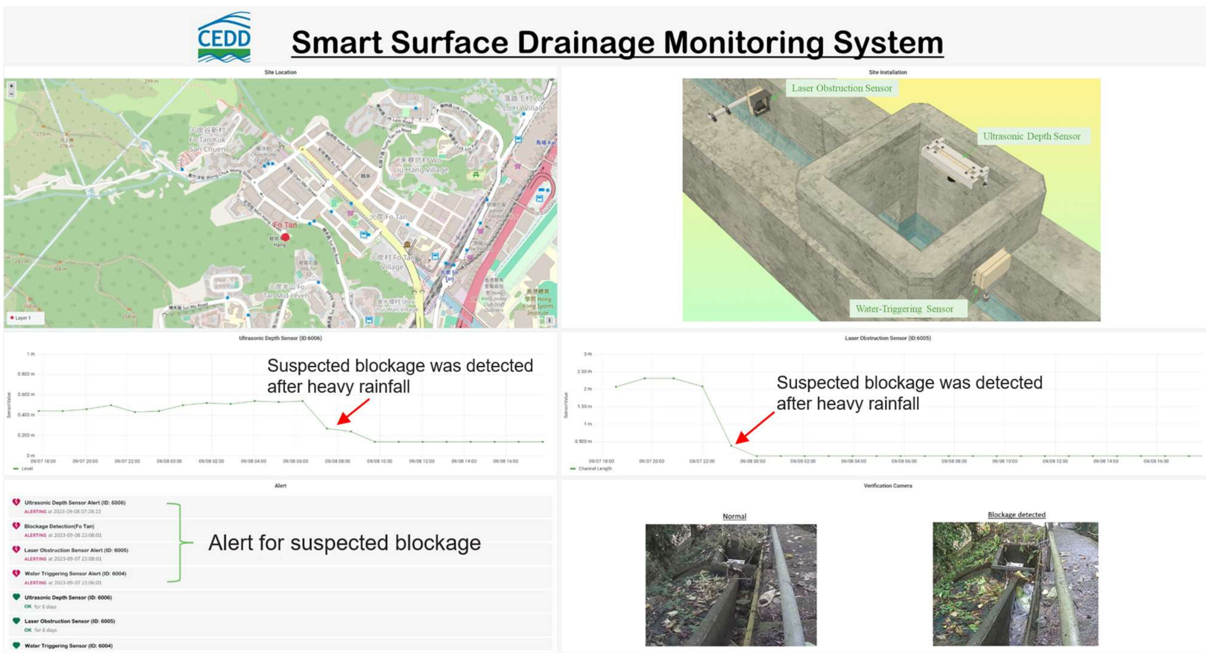

Plate 5 Monitoring platform showing actual blockage detected at U-Channel

Plate 6 Image Captured by the Verification Camera

Performance Summary During Trial:

Wireless Data Transmission:

During the testing site selection process, it was observed that obstructions commonly found in densely populated urban areas present a significant challenge to wireless communication. High-rise buildings and other physical barriers can interfere with signal transmission, reducing coverage and compromising communication reliability. Additionally, severe weather conditions such as heavy rainfall further exacerbate these challenges. During the trial period, serval data packet losses were recorded during periods of intense rain, indicating that wireless communication between sensors and the server was affected. These findings highlight the need for ongoing development of weather-resilient and high penetrating communication solutions to further enhance the performance.

Power Management:
The SSDMS sensors are powered by non-rechargeable batteries, offering a cost-effective solution for IoT system deployments. While each battery can support up to two years of standard operation, battery replacement becomes a time-consuming and labor-intensive process when the system is deployed at scale. To mitigate this limitation, improvements in power management strategies should be prioritized to extend sensor lifespan and minimize maintenance requirements.

4 ONGOING ENHANCEMENTS

Sensor Miniaturization:
Drawing from valuable practical experience and insights accumulated during the ongoing site trials, the SSDMS is currently undergoing continuous enhancements to further improve its effectiveness, adaptability, and resilience. One primary area of enhancement involves the miniaturization and adaptation of sensors specifically tailored for constrained drainage environments. By reducing sensor dimensions and refining their physical profiles, the enhanced SSDMS will be better suited for installation in narrower or more space-restricted drainage channels.

Plate 7 Miniaturized Laser Obstruction Sensor

Power Management Improvement:
Another critical area of ongoing enhancement is optimizing power supply configurations to improve overall energy efficiency. This involves integrating solar energy harvesting technologies along with rechargeable battery modules that feature an automatic power detector and switch within the system design. The switch will manage the power source, alternating between a high-capacity non-rechargeable battery and a solar battery. Such enhancements will significantly extend battery life and reduce maintenance frequency, making the system suitable for remote locations or areas where frequent manual servicing is challenging.

Plate 8 Solar Powered Sensors

In addition, considerable effort is being invested in refining sensor detection algorithms. By analyzing extensive data collected during the trials, the project team aims to enhance the precision of detection algorithms, thereby substantially reducing the frequency of false alarms.

AI-driven Feature for Verification Camera:
The verification camera system is also being upgraded to address practical challenges identified during field trials. Improvements include enhanced camera housing designs for increased durability in harsh environmental conditions. Furthermore, AI capabilities are being integrated into the camera system to assist in automated false alarm verification with pattern and feature detection. This AI-driven feature will help reduce the need for manual intervention, particularly during extreme weather conditions, thereby streamlining the monitoring process.

Plate 9 Captured Image with AI for alarm verification during daytime and nighttime

Enhanced Wireless Communication:
To address the challenges of wireless communication during severe weather conditions, such as heavy rainfall, a private network utilizing low-frequency signals with high penetration capability will be developed and piloted at several test sites. This low-frequency approach is specifically selected to offer extended coverage and improved reliability, particularly in densely built urban environments and under adverse weather conditions.

5 CONCLUSIONS

The SSDMS leverages advanced IoT sensor technologies to deliver real-time, proactive monitoring of slope drainage conditions. By providing continuous and remote assessment capabilities, the SSDMS enhances Hong Kong's slope safety management, especially for slopes adjacent to critical access roads. The system's successful detection and timely reporting of a drainage blockage during the extreme rainfall event in September 2023 validated its practical utility. Ongoing refinements, including sensor miniaturization, robust power management, AI-driven verification, and low frequency communication will further improve its reliability, efficiency, and adaptability. This initiative represents a forward-looking, data-driven approach to geotechnical resilience in the face of climate-related challenges.

ACKNOWLEDGEMENTS

This paper is published with the permission of the Head of the Geotechnical Engineering Office and the Director of Civil Engineering and Development, the Government of the Hong Kong Special Administrative Region of the People's Republic of China.

REFERENCES

Iqbal, U., Barthelemy, J., Li, W. & Perez, P. 2021. Automating visual blockage classification of culverts with deep learning. Applied Sciences, 2021.

Gawali, V.S., Pande, M., Sayyad, M. & Bhadade, R.S. 2024. IoT-based real-time drainage monitoring system. In Proc. of International Conference on Emerging Smart Computing and Informatics (ESCI). 2024.

Suhail, M.P.P., Joice, T., Venugopal, R. & Rajan, N. 2023. Sewage monitoring system for blockage point detection. In Proc. of International Conference on Innovations in Engineering and Technology (ICIET). 2023.

Narayana, G.L., Sowmya, T., Jyothi, S., Devi, R.A. & Sowmya, Y.S.L. 2023. Sensor-based open channel blockage detection system. In Proc. of IEEE 12th International Conference on Communication Systems and Network Technologies. 2023.

Diamse, M.J., Frasco, J.N., Nogra, B., Venasquez, T. & Arana, J.M.P. 2023. A design of IoT-based capture efficiency monitoring and alert system for storm grate inlets through LoRaWan. In Proc. of IEEE 15th International Conference on Humanoid, Nanotechnology, Information Technology, Communication and Control, Environment, and Management (HNICEM). 2023.

Influence of Imbalance of Earth-pressure on Wall Deflections on a Deep Excavation

L.W. WONG & Y.N. HO
SMEC Asia Limited

ABSTRACT

An undersea vehicular tunnel was constructed by using the cut-and-cover method. The cofferdam supporting the excavation of 35 m maximum in depth and 50 m in width comprised intermittent pipe pile walls of 50 m maximum in depth. The struts were preloaded to the magnitudes as large as 16.4 MN. Due to the difference in the depths to the rockhead levels on both sides of the cofferdam, there is the earth-pressure imbalance effect causing differential lateral wall deflections. The wall on the shallower rockhead side was pushed back by the wall on the opposite side with deeper rockhead levels through the struts. The wall deflections were as large as 194 mm on one side and 22 mm on the opposite side. As a result, the central axis of the excavation trench shifted by as large as 156 mm. The magnitude of shifting of the central axis is proportional to the ratio of the depths to the rockhead on the two sides of the excavation.

Keywords: Wall deflections, Cut-and-cover tunnel, Earth-pressure imbalance, struts preloading.

1 INTRODUCTION

The earth-pressure imbalance effects causing different in wall deflections of deep excavation cases have been reported by the researchers. Moh & Hwang (1997) reported the asymmetrical wall deflections at a basement excavation case located at the northern rim of the Taipei basin. Wong & Yong (2013) reported the earth-pressure imbalance effects for an excavation case for the Central Wanchai Bypass (CWB) cut-and-cover tunnel. In the numerical analysis, the half model assuming the central axis as a fixed boundary along the horizontal direction has often been adopted. The occurrence of the earth pressure imbalance would lead to under-estimation of the wall deflections on one side and over-estimation of those on the opposite side.

The excavation for a 500 m length of a dual-3 lanes vehicular undersea tunnel was constructed by using the cut-and-cover method. The excavation as deep as 35 m was supported by intermittent pipe pile walls on the north and the south sides. The horizontal inward wall deflections as large as 194 mm on the south wall occurred in the final excavation stage. On the opposite side along the north wall, the outward wall deflection as large as 160 mm occurred. The central axis of the excavation trench shifted northward by around 156 mm. In order to understand the mechanism causing the asymmetrical wall deflections and to improve the effectiveness on the design and construction of the infrastructure works, the undersea tunnel case on earth pressure imbalance is critically studied.

2 HYDROGEOLOGICAL CONDITIONS

2.1 Extent of undersea tunnel

The undersea tunnel accommodating the dual-3 carriageways is located on the north shore of the Victoria Harbour. Descending from the ground level of 5 mPD at the at-grade section, the undersea tunnel section has the lowest formation level around -32 mPD. As depicted in Figure 1, the undersea tunnel presented in this paper is 50 m in width and 230 m in length. Eight inclinometers were installed immediately behind the pipe pile walls along 4 monitoring sections. The piezometers were installed near Sections 11 and 12.

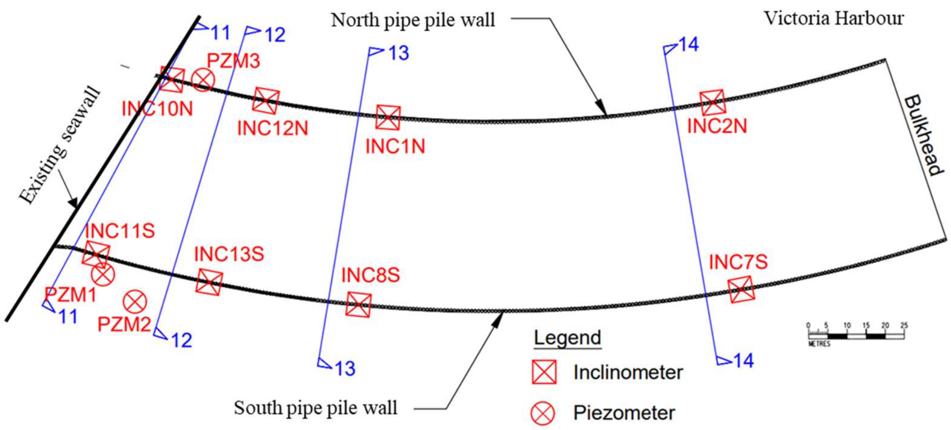

Figure 1: Plan of undersea tunnel showing the locations of the instruments

2.2 *Subsoil conditions*

The subsoils along the tunnel route mainly comprise the marine deposits, the alluvium, the granitic saprolites and the granite bedrock. The seabed level was around -5 mPD. The rockhead levels along the route alignment vary from -22 mPD to -50 mPD. Along the shoreline, there is a fill layer of approximately 7 m in thickness. Figure 2 depicts the soil and rock profiles along the longitudinal direction of the tunnel.

The fill layer overlies the marine deposits clay of 5 m thick, which is underlain by the Quaternary alluvial silty sand of 12 m average in thickness. The alluvium is underlain by the saprolite of completely decomposed granite (Granite V) of 13 m average in thickness and the highly decomposed granite (Granite IV) of 10 m maximum in thickness. The bedrock of moderately decomposed to slightly decomposed granite (Granite III/II) is encountered at elevations ranging from -33 mPD to -68 mPD. The soil and rock conditions at the project site is summarized in Table 1. The mean sea level is 1.2 mPD. The tide level of 2.8 mPD was allowed for the cut-and-cover tunnel construction.

Table 1. Summary of soil profile along the undersea tunnel

Soil strata	Top level, mPD	N value	Description
Fill	4	5 to 12	Greyish silty SAND
Marine deposits	-5	5	Dark grey silty CLAY
Alluvium	-10	11 to 40	Stiff yellowish brown silty SAND
Granite V	-20	28 to 80	Yellowish to reddish brown silty SAND
Granite IV	-50 to -60	90 to 160	Yellowish brown sandy GRAVEL and cobbles
Granite III/II	-33 to -68	-	Pink to brown medium to coarse grained Granite

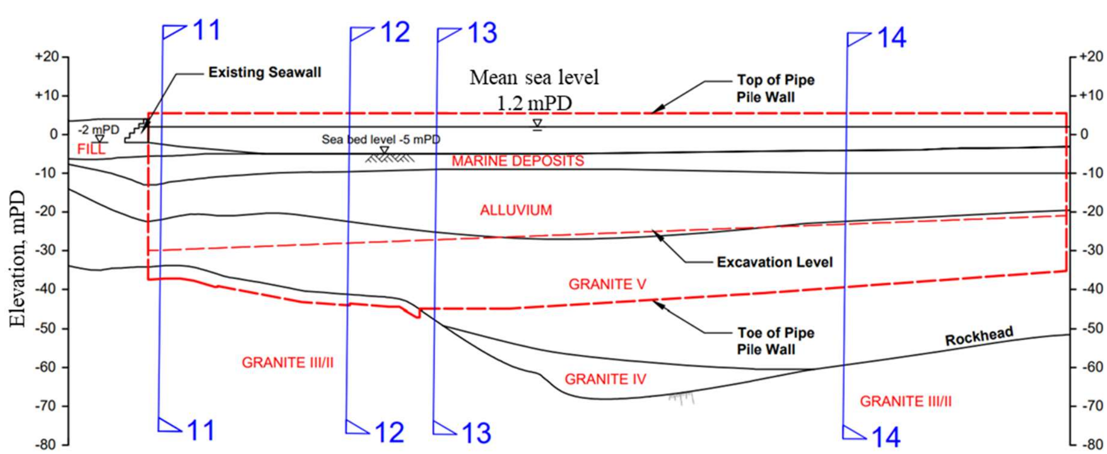

Figure 2: Soil and rock profile along longitudinal section of the cut-and-cover tunnel

2.3 Cofferdam for cut-and-cover construction

As depicted in Figure 3, the tunnel was constructed by using the bottom-up method. The excavation was supported by the intermittent pipe pile walls on the north and the south sides. These walls served as the cofferdam over the sea. The pipe piles had interlocking joints similar to those for sheet piles.

The intermittent pipe pile walls were composed of tubular steel sections of 813 mm in diameter, 16 mm in thickness and spacing at 900 mm. At Section 11 and Section 12, where the excavation depths exceeding 33 m, the pipe piles were strengthened by inserting steel H-section of UB 305 x 305 x 238 kg/m. The stiffnesses of the pipe pile wall, the EI values, were 100 MNm/m and 73 MNm/m for the sections with and without the H-pile insertion respectively. Such stiffnesses are equivalent to the EI value of 93 MNm/m for a concrete diaphragm wall of 0.4 m in thickness allowing a 0.7 reduction factor for cracks in concrete.

The cofferdam was supported with 5 to 9 levels of steel struts. The width of the excavation was 49 m. With the wall top level around 5.5 mPD and the toe levels ranging from -37 mPD to -47.5 mPD, the pipe pile walls were embedded 1.5 m to 7 m into Granite III/II.

The rockhead levels along the south wall are lower than those along the north wall. As summarized in Table 2, the rockhead levels between the north and the south pipe pile walls differ by as large as 9.5 m at Section 12. There were differences in the excavation levels on the north and the south sides. For example, the final excavation levels on the north and the south sides along Section 11 were -32.0 mPD and -31.5 mPD respectively.

Table 2: Embedment of the pipe pile wall and the inclinometers in rock

Section	Pipe pile wall	Rockhead level, mPD	Pipe pile wall		Inclinometer embedment			Final excavation level, mPD
			Toe level, mPD	Embedment in rock, m	Inclino-meter	Toe level, mPD	Embedment in rock, m	
11	North	-30.0	-37.0	7.0	INC10N	-36.2	6.2	-32.0
	South	-34.0	-39.0	5.0	INC11S	-38.2	4.2	-31.5
12	North	-32.0	-37.0	5.0	INC12N	-35.2	3.2	-30.6
	South	-41.5	-43.0	1.5	INC13S	-43.7	2.2	-29.5
13	North	-43.0	-47.5	4.5	INC1N	-63.7	20.7	-29.5
	South	-48.0	-45.0	-	INC8S	-55.7	7.7	-29.5
14	North	-59.0	-39.5	-	INC2N	-57.7	-1.3	-25.7
	South	-59.2	-37.5	-	INC7S	-61.2	2.0	-24.6

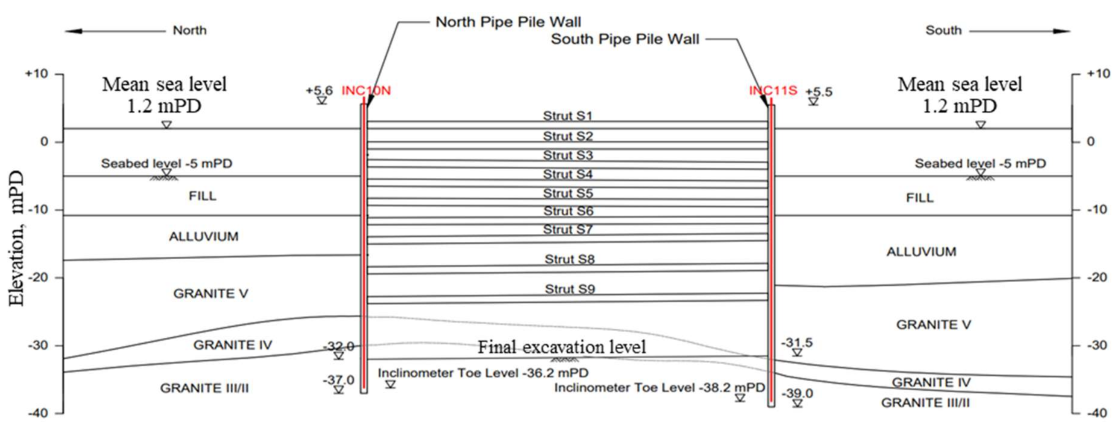

Figure 3: Soil and rock profile along Section 11 of the cut-and-cover tunnel

2.4 Groundwater conditions

As shown in Figure 1, piezometers PZM1 to PZM3 were installed behind the north and the south pipe pile walls in the vicinity of Section 11 and Section 12. Two piezometers were installed at each location. The upper piezometers were installed in the alluvium and the lower piezometers were in the Granite V stratum. Figures 4a and 4b present the variation of the piezometric levels on the south and the north sides of the excavation respectively. The daily readings show that the piezometric levels were under tidal influence with the average level around 1.2 mPD in the beginning stage of excavation.

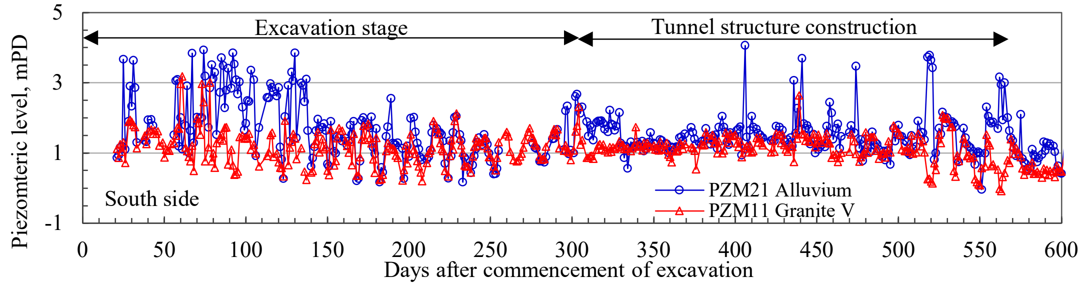

(a) Variation of piezometric levels behind the south pipe pile wall

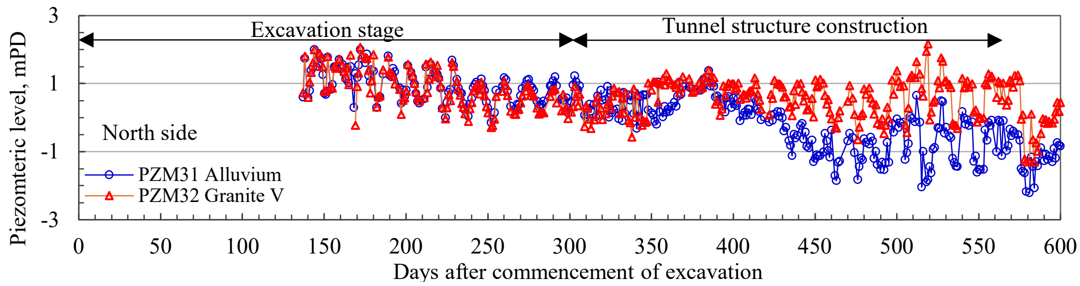

(b) Variation of piezometric levels behind the north pipe pile wall

Figure 4: Variation of the piezometric levels on both sides of Section 11

Figure 4a shows that on the south side of the cofferdam, the average piezometric levels in the alluvium layer were lowered from 1.5 mPD in the excavation stage to 1.0 mPD at the end of the tunnel structure construction stage. In the Granite V stratum, the average piezometric levels were gradually lowered from 1.5 mPD to 0.5 mPD during that period. The piezometric levels as high as 4.0 mPD observed in PZM21 were likely caused by the installation of the grout curtain behind the south pipe pile wall, where sensitive structures were located in the vicinity.

Figure 4b shows that on the north side of the cofferdam, the average piezometric levels in the alluvium layer were lowered from 1.2 mPD in the excavation stage to -1.0 mPD at the end of the tunnel structure construction stage. In the Granite V stratum, the average piezometric levels were gradually lowered from 1.2 mPD to 0 mPD during that period.

3 STRUTS INSTALLATION

3.1 Steel struts

Along Sections 12 to 14 of the tunnel, the twin-struts of level 1 and level 2 were fabricated into a steel truss of 4 m in height and 2.5 m in width. The level 1 twin-struts were the top chords and the level 2 twin-struts were the bottom chords of the steel truss. The upper chords comprised a pair of steel members of 914x4195x388 kg/m UB and the bottom chords comprised a pair of 914x305x289 kg/m UB. The steel trusses were erected at the bulkhead located at the east end of the cofferdam. After fabrication, the steel trusses of 46 m in span length were skidded one by one from east to west with the horizontal spacing around 8.5 m.

The struts below the level 2 were composed of twin-steel struts of 914x419x388 UB, which had the typical length of 12 m per segment. The twin-struts were installed by connecting the 12 m length modular segments with bolted joints. For the lowest struts S8 and S9 at Section 11, the twin struts were strengthened with steel plates of 25 mm in thickness.

Table 3 to Table 6 summarize the properties of the struts supporting the excavation at Section 11 to Section 14 along the undersea tunnel. The struts of 46 m in length were typically composed of 3 segments of 12 m in length and 2 segments with the knee braces at the strut-waling connections. There were 6 bolt connections, at the joints between the struts and waling segment and at those between the strut segments.

Table 3: Strut properties along Section 11

Strut levels	Elevation mPD	Depth, m	Steel member	Horizontal spacing, m	Preload, MN	Stage
S1	2.50	3.3	2-914x305x289 UB	7.0	-	1
S2	-0.50	6.3	2-914x419x388 UB		11.0	2
S3	-3.14	8.9	2-914x419x388 UB		13.7	3
S4	-5.98	11.8	2-914x419x388 UB		15.8	4
S5	-8.82	14.6	2-914x419x388 UB		15.8	5
S6	-11.66	17.5	2-914x419x388 UB		15.8	6
S7	-14.50	20.3	2-914x419x388 UB		15.8	7
S8	-18.90	24.7	2-914x419x388 UB & Plates		16.4	8
S9	-23.30	29.1	2-914x419x388 UB & Plates		16.4	9
Excavation	-32.00	34.5			-	10

Table 4: Strut properties along Section 12

Strut levels	Elevation mPD	Depth below sea level, m	Steel member	Horizontal spacing, m	Preload, MN	Stage
S1	2.50	0	2-914x419x388 UB	7.8	-	1
S2	-1.50	4.0	2-914x305x289 UB		-	2
S3	-5.40	7.9	2-914x419x388 UB		13.3	3
S4	-9.30	11.8	2-914x419x388 UB		14.0	4
S5	-12.50	15.0	2-914x419x388 UB		15.0	5
S6	-17.23	19.7	2-914x419x388 UB		15.0	6
S7	-23.90	26.4	2-914x419x388 UB		15.8	7
Excavation	-30.56	33.1			-	8

Table 5: Strut properties along Section 13

Strut levels	Elevation mPD	Depth below sea level, m	Steel member	Horizontal spacing, m	Preload, MN	Stage
S1	2.50	0	2-914x419x388 UB	8.4	-	1
S2	-1.50	4.0	2-914x305x289 UB		-	2
S3	-5.10	7.6	2-914x419x388 UB		13.5	3
S4	-8.90	11.4	2-914x419x388 UB		14.5	4
S5	-12.46	15.0	2-914x419x388 UB		14.8	5
S6	-16.21	18.7	2-914x419x388 UB		15.2	6
S7	-21.18	23.7	2-914x419x388 UB		15.2	7
Excavation	-29.73	32.2			-	8

Table 6: Strut properties along Section 14

Strut levels	Elevation mPD	Depth below sea level, m	Steel member	Horizontal spacing, m	Preload, MN	Stage
S1	2.00	0.5	2-914x419x388 UB	8.6	-	1
S2	-2.00	4.5	2-914x305x289 UB		-	2
S3	-6.62	9.1	2-914x419x388 UB		12.5	3
S4	-12.10	14.6	2-914x419x388 UB		15.8	4
S5	-20.00	22.5	2-914x419x388 UB		15.0	5
Excavation	-25.70	28.3				6

3.2 Struts preloading

Struts preloading was applied to the levels 2 to 9 struts along Section 11. For Sections 12 to 14, preloading was applied to the struts starting from level 3. Four hydraulic jacks were used for applying the design strut loads ranging from 11 MN to 16.4 MN. The jacking point was located near the mid portion of the strut. The preload was applied in 3 cycles. In Cycle 1, Cycle 2 and Cycle 3, the 50 %, 100 % and 110 % of the design strut load were applied. The extensions of the jack cylinders at the various applied loads and after their releasing were measured in each cycle. In the final Cycle 3, the applied load was locked-off by inserting a stack of shim plates to the gap at the jacking point between the north and the south strut segments. The thickness of each piece of shim plate ranged from 2 mm to 20 mm.

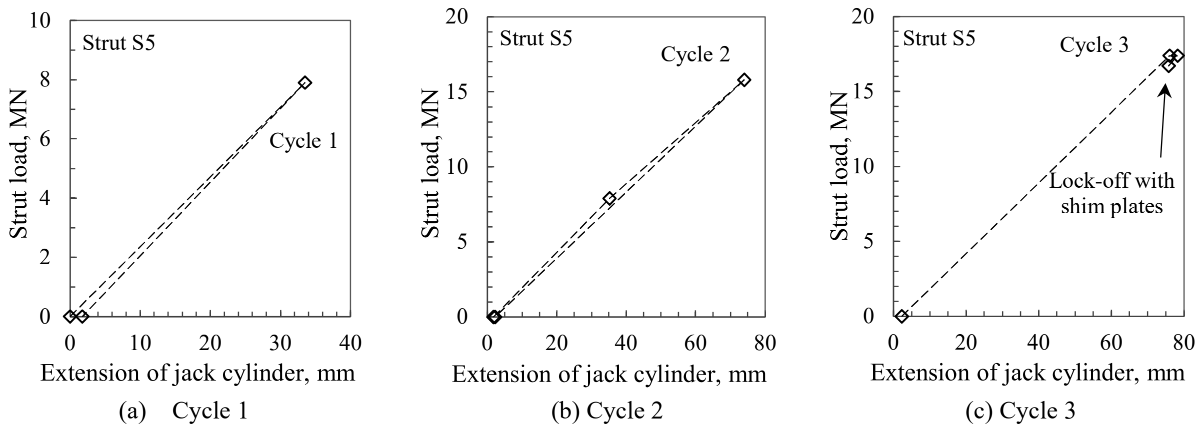

Figure 5: Load versus extension of jack cylinder for strut S5 along Section 11

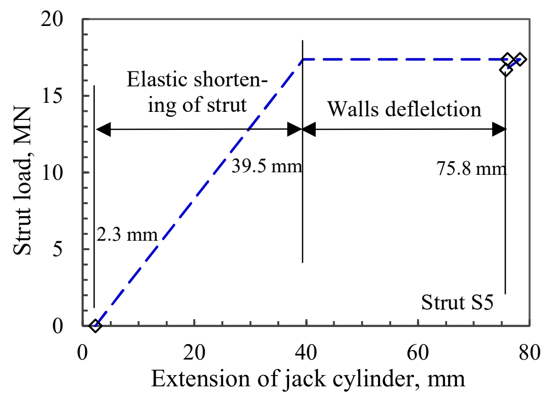

Figure 6: Deduction for walls deflection in Cycle 3 for strut S5 along Section 11

The jack cylinder extension measurements were conducted in the initial stage prior to apply loading, after jacking to the loads in each cycle and after releasing the applied loads. Figure 5 presents the applied loads versus the extensions of the jack cylinders for preloading the struts S5. It is noted that the skim plate has the minimum thickness of 2 mm. Gaps in the stack of shim plates less than 2 mm in width could not be filled up. After the shim plates were placed and the maximum load was released, the strut displacement reduced slightly due to closing of the gaps of less than 2 mm in width. As a result, although the struts were applied to 110 % during the preloading operation, the strut loads were locked-off to around 100 % of the design load after releasing the applied load. For strut S5, the shim plates inserted at the jacking point prior to releasing the applied load had the total thickness of 84 mm.

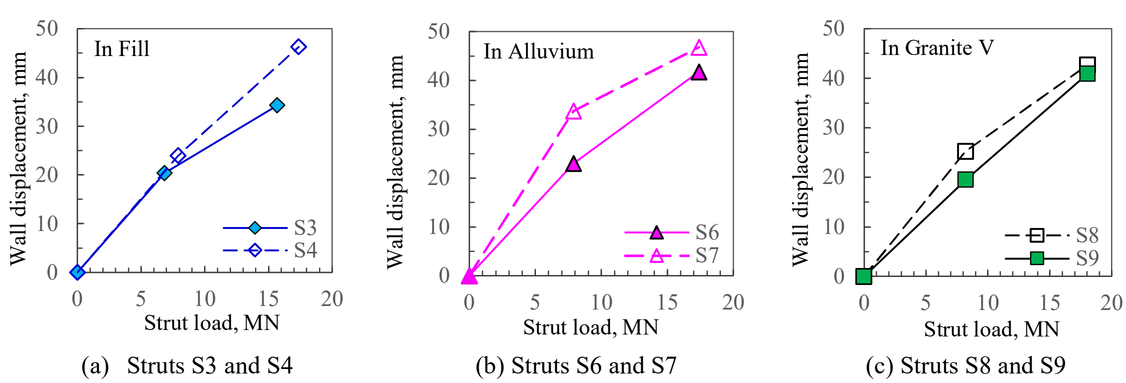

Figure 7: Wall deflections caused by struts preloading at Section 11

3.3 Struts and wall displacements

The extension of the jack cylinder measured comprised 2 portions, the elastic shortening of the steel strut and the pushing back the supporting pipe pile walls under the preloading forces. As shown in Figure 6, using the elastic modulus of steel of 205 GPa and the sectional area of 988 cm^2 for the twin-strut, the elastic shortening of 39.5 mm for the strut S5 of 46 m in length at Section 11 is computed. The wall deflection of 38.8 mm at that strut level is deduced from the measured total extension of the jack cylinder of 78.3 mm. It is noted that the walls on both sides were pushed back by the strut at the same time.

The total wall deflections on 2 sides deduced from the load displacement curves in the various strut levels in the fill, the alluvium, in the Granite V strata are presented in Figure 7a to Figure 7c. The total wall deflections occurring at the north and the south walls due to the 110 % design strut loads ranged from 34 mm to 47 mm, with an average of 40 mm. There is not much difference in the wall deflections occurring between the fill, the alluvium and the Granite V strata, probably due to the fact that these 3 types of soil have similar stiffness values.

3.4 Wall displacements due to preloading observed by inclinometers

The wall deflections due to struts preloading are also assessed by the inclinometer readings. The magnitudes of wall deflections due to struts preloading have been deduced from the inclinometer profiles measured at 1 day prior to and 1 day after the preloading of the struts. The differences in wall deflections measured in these 2 days were the wall deflections caused by preloading the struts. Figure 8 presents the wall deflection profiles due to preloading struts S2 to S9. It is noted that the positive and the negative wall deflection values denote the southward and the northward wall movements respectively.

The wall deflections assessed by measuring the jack cylinder extensions during the struts preloading operation are consistent with those observed in the inclinometers 1-day after preloading. As summarized in Table 7, the relative wall deflections, the summation of the deflections measured in the north and the south walls, range 12 mm to 27 mm, with an average of 19 mm. Table 6 summarized that the wall deflections on the north wall and the south wall had the average of 13.9 mm and 5.1 mm respectively. The wall deflections occurring in the north wall contributed 3 quarter of the total wall deflections.

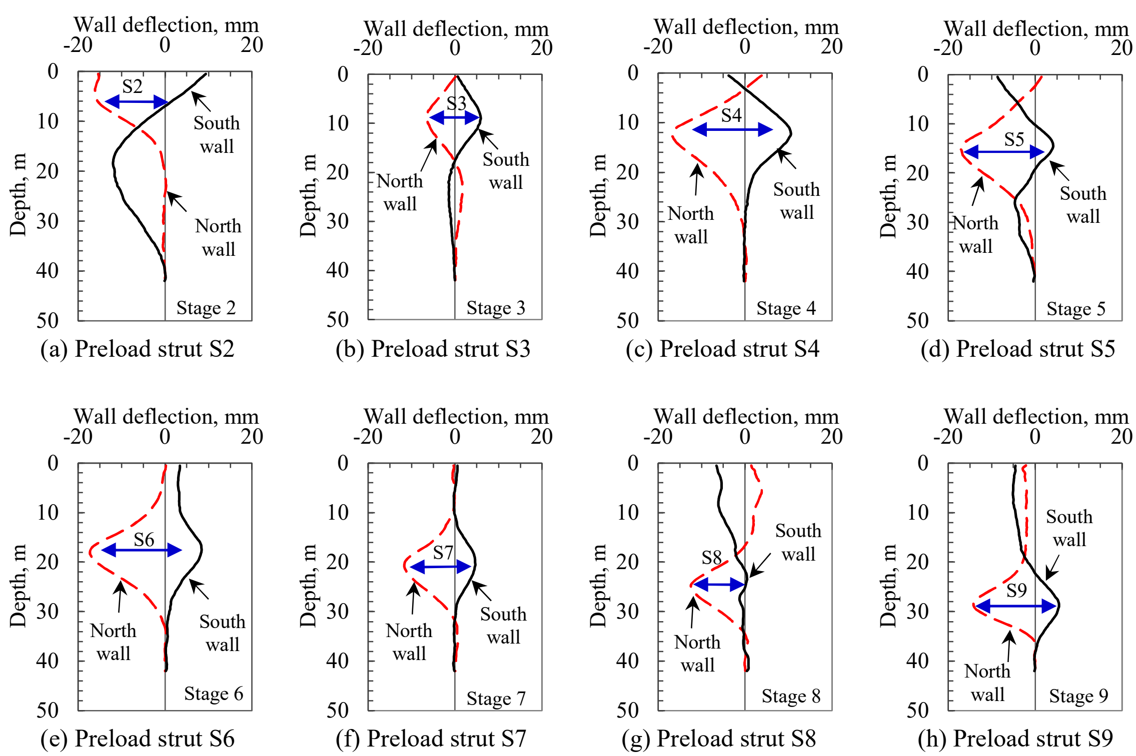

Figure 8: Wall deflections caused by struts preloading observed by the inclinometers at Section 11

Table 7: Wall deflections caused by struts preloading at Section 11

Strut	Depth m	Preload MN	Wall deflections, mm				Ratio of north wall deflection
			Deduced from	Measured by inclinometers			
			struts shortening, δ_w	South, δ_s	North, δ_n	Relative, δ	δ_n / δ
S2	6.3	11.0	31	3	-16	19	0.84
S3	8.9	13.7	34	6	-6	12	0.50
S4	11.8	15.8	46	10	-17	27	0.63
S5	14.6	15.8	37	4	-17	21	0.81
S6	17.5	15.8	42	8	-17	25	0.68
S7	20.3	15.8	47	5	-12	17	0.71
S8	24.7	16.4	43	0	-12	12	1.00
S9	29.1	16.4	41	5	-14	19	0.74
Average			40	5.1	-13.9	19.0	0.74

4 LATERAL WALL DEFLECTIONS

4.1 Monitoring along undersea tunnel

Figure 9 to Figure 12 presents the inclinometer profiles along Section 11 to Section 14 of this undersea tunnel. The wall deflections occurred at the one side of the pipe pile wall were larger than those occurred on the opposite side. The differences in wall deflections were due to the imbalance of the earth pressures acting on the two walls. It is noted that in Figures 9 to 12, the wall deflections in positive and in negative values denote the southward and the northward wall movements respectively.

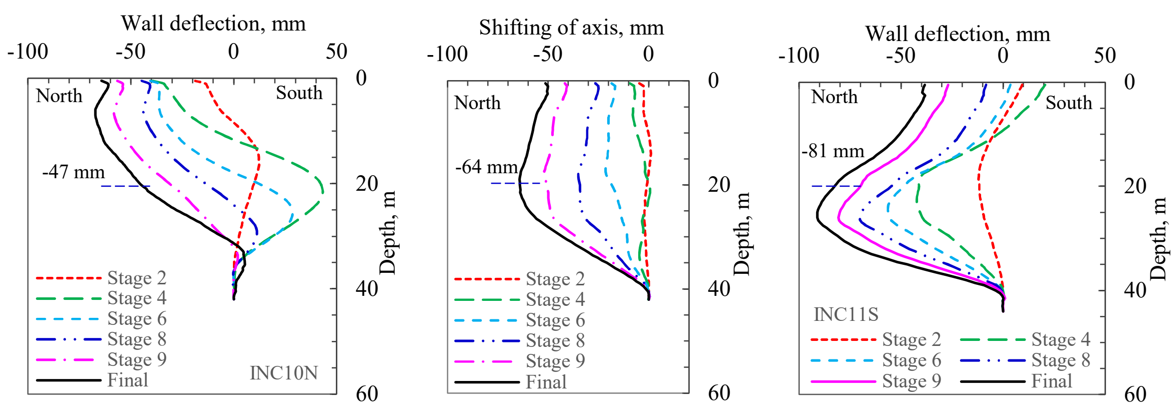

(a) North wall (b) Central axis (c) South wall

Figure 9: Observed wall deflection profiles at Section 11

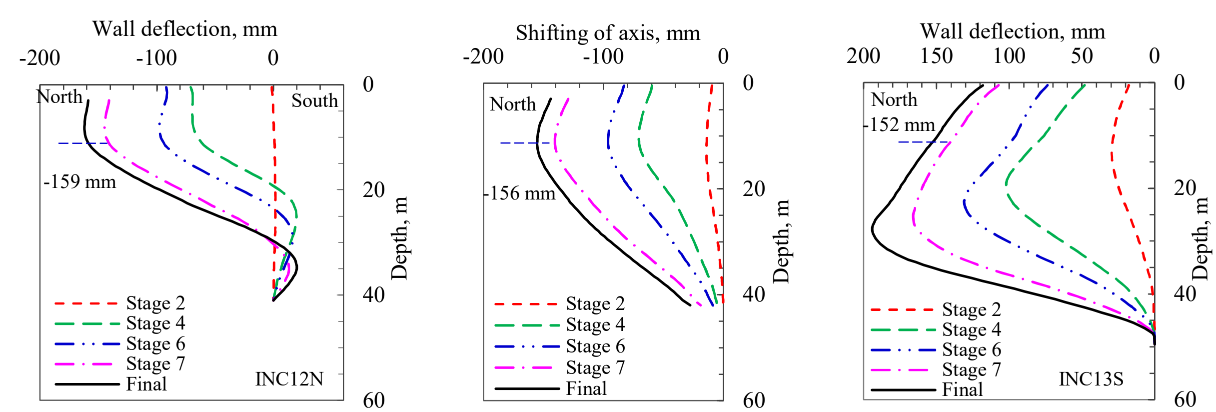

(a) North wall (b) Central axis (c) South wall

Figure 10: Observed wall deflection profiles at Section 12

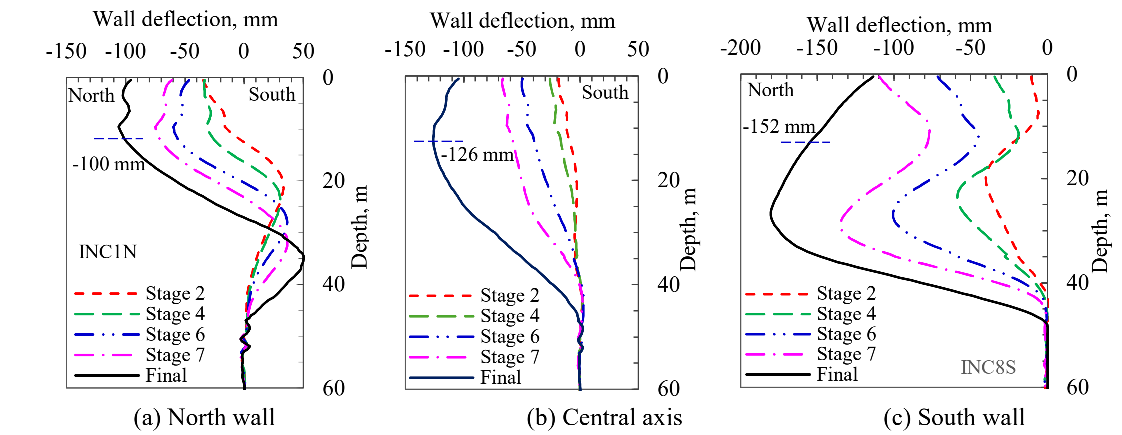

Figure 11: Observed wall deflection profiles at Section 13

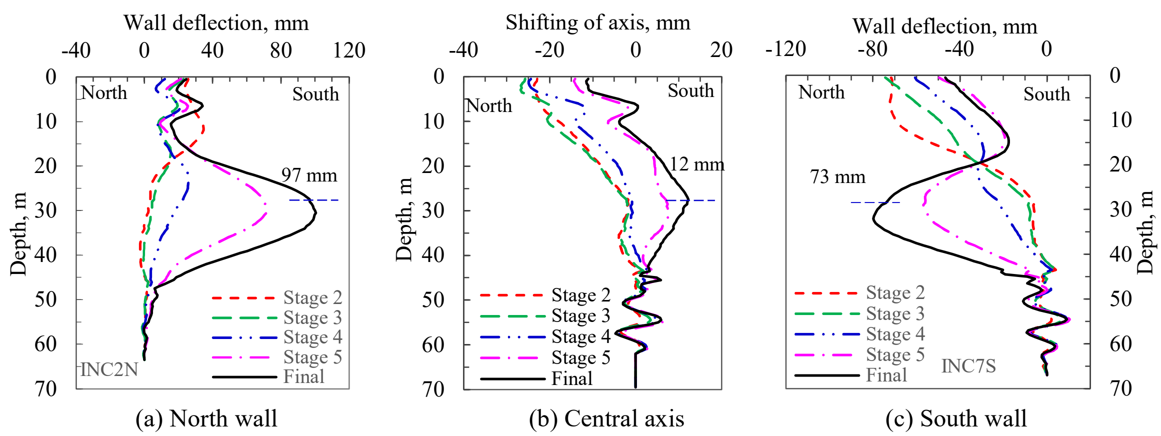

Figure 12: Observed wall deflection profiles at Section 14

Take Figure 9a as an example, there were inward wall movements occurring at the depths between 10 m and 30 m. However, the entire north wall was pushed backward. As a results, net outward wall movements occurred. Figure 9 shows that the maximum inward wall deflections on the south and the north wall in the final stage at Section 11 were -90.6 mm inward and -66 mm outward respectively. The north wall was pushed outward by the multi rows of struts under the active earth pressures acting behind the south wall. The earth pressure imbalance is further discussed in Section 5.1.

4.2 Fixation of the inclinometer toes

It is noted that the inclinometers were installed behind the pipe pile wall at the mid-point between two piles. The toe levels of the inclinometer casings were installed at least 2 m below the rockhead level so that in the interpretation of the inclinometer profiles, the toes of inclinometers can be taken as the fixed points. Table 2 summarizes the toes levels of the inclinometers installed at Section 11 to Section 14. The table shows that the embedment lengths of the inclinometer casings in rock ranged from 2 m to 20.7 m except inclinometer INC2N. At Section 14, the north pipe pile wall encountered the Granite IV at the level of -48 mPD. The toe of inclinometer INC2N was embedded in a core-boulder of 1.3 m in size above the rockhead. As such, the assumption for the inclinometers toes as the fixed point is valid for the inclinometers along the undersea tunnel.

Table 2 also shows that the pipe pile walls at Section 11, Section 12 and the north wall of Section 13 were penetrated 1.5 m to 7.0 m into the rockhead. The excavation level was 2 m below the rockhead at the north side of Section 11.

5 INFLUENCES OF EARTH-PRESSURE IMBALANCE

5.1 Shifting of the axis of excavation

The earth-pressure imbalance effect causes the asymmetrical performance of the wall deflection profiles of the walls on two sides of the excavation. Moh & Hwang (1997) reported the asymmetrical wall deflections at a basement excavation case located at the northern rim of the Taipei basin. Wong & Yong (2013) reported the earth-pressure imbalance effect for an excavation case for the Central Wanchai Bypass (CWB) cut-and-cover tunnel and in the Nicoll Highway case in Singapore.

The shifting of the central axes of the excavation trench in Section 11 to Section 14 are presented in Figure 9b, Figure 10b, Figure 11b and Figure 12b. The shifting of the central axis, δ_c, is defined as:

$$\delta_c = (\delta_1 + \delta_2) / 2 \tag{1}$$

where the δ_1 and the δ_2 values are the deflections of the walls with the deeper and the shallower rockhead levels in the final stage respectively.

Table 8 summarized the shifting of the undersea tunnel along Section 11 to Section 14 and the depths to the rockhead levels on the north and the south walls in those sections. It is noted that the positive and the negative wall deflection values presented in Table 8 denote the southward and the northward movements respectively. The directions of the shifting of the central axis for Sections 11 to Section 13 had the same direction with those occurring at the north wall. The northward movements were caused by the shallower depths to the rockhead, the H_2 values, on the north side. For Section 14 where the inward wall movements occurred on both sides, the central axis shifted toward south, where the south wall had the shallower depth to the rockhead.

In Table 8, the H_1 and the H_2 values are the depths to the rockhead with the deeper and the shallower levels respectively. The central axis shifting values, δ_c, that obtained from Figure 9b to Figure 12b, vary from 12 mm to 156 mm in the final stage.

Table 8: Summary of central axis shifting in the final stage

Case	Location	Excavation depth H, m	Depth to rockhead			Wall deflection			Axis shift δ_c, mm
			Deep side H_1, m	Shallow side H_2, m	H_1/H_2 ratio	Depth, m	Deep side δ_1, mm	Shallow side δ_2, mm	
1	Section 11	30.0	32.0	28.0	1.14	19.5	-81	-47	-64
(This	Section 12	33.1	44.0	34.5	1.27	11.0	-152	-159	-156
study)	Section 13	32.0	50.5	45.5	1.11	12.0	-152	-100	-126
	Section 14	25.7	59.2	59.0	1.00	28.0	97	-73	12
2	CWB tunnel	18.3	41.3	39.6	1.04	20.0	61.2	28.8	16.2
3	Taipei rim	23.3	38	15	2.53	19.0	198	5	97

5.2 Relationship of axis shift with excavation depths

Figures 9c, 10c and 11c show that the south wall had inward movements. The pressures acting on the south wall were in active state. On the opposite side, Figures 9a, 10a and 11a show that the north wall above the excavation levels in each stage had outward movements. The pressures acting on the north wall above the excavation levels were in the passive state and those below the excavation levels were in active state. The division line between the passive and the active state on the north wall propagated downward as excavation proceeded.

Figure 13 shows the relationship between the δ_c values against the excavation depths, the H values, for Section 11 to Section 14. The maximum axis shift values are approximately proportional to the excavation depths. The rates of increase in the shift values with the H values, the δ_c/H ratios, vary between various sections. It appears that the δ_c/H ratios would depend on the ratios of the depths to the rockhead levels on the two sides. The larger of the H_1 /H_2 ratios, the steeper rate of increase in the shift values or the larger the δ_c/H ratios.

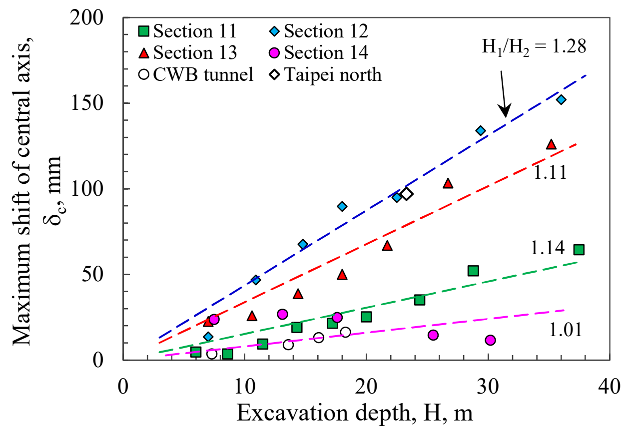

Figure 13: Relationship between excavation depths and the shifts of the central axes

5.3 Relationship of axis shift with depths to rockhead

Due to the uncertainties on the distribution and mobilization of the passive and active pressures on the wall with the outward movements, it is proposed that the variation of the δ_c/H ratios could be related to the H_1/H_2 ratios. The H_1/H_2 would be equivalent the ratio of the earth pressure acting on the two sides of the cofferdam. Figure 14 shows the relationship between the δ_c/H ratios against the H_1/H_2 ratios for Section 11 to Section 14. The δ_c/H ratios for the CWB tunnel and for the Taipei rim cases are included in the correlation. The set of δ_c/H versus H_1/H_2 ratios are fitted into the hyperbolic function that expressed in Equation 2:

$$\delta_c / H = (H_1/H_2 - 1) / [\alpha + \beta (H_1/H_2 - 1)] \tag{2}$$

with the coefficient $\alpha = 0.00002$ and $\beta = 0.00014$. The hyperbolic function of the relationship is an indication of the nonlinearity of the supporting ground. For the excavation Case 3 located at the northern rim of the Taipei Basin, the δ_c value is normalized with the H_2 value of 15 m because the depth to the shallower rockhead, H_2, is less than the excavation depth, H, of 23.3 m.

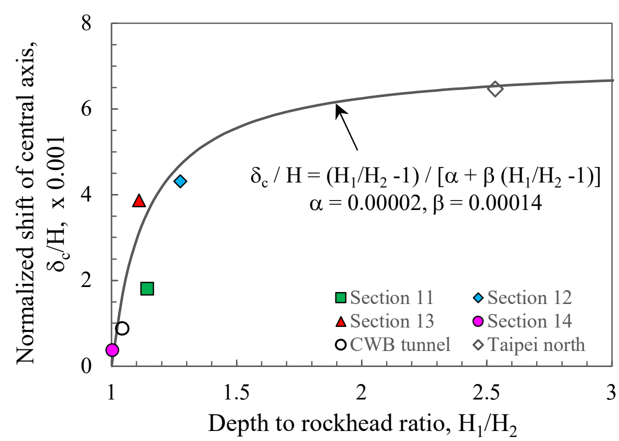

Figure 14: Relationship between depth to rockhead ratios and the normalized shift of the central axis

6 CONCLUSIONS

Based on the wall deflection profiles observed in inclinometers installed on opposite sides of the excavation trench of a cut-and-cover tunnel, the earth pressure imbalance effect has been observed. This issue is very complicated and can only be sorted out by numerical analyses. The following are the preliminary findings:

(5) Mainly due to the difference in the depths to the rockhead levels on both sides of the walls of the undersea tunnel, there is the earth-pressure imbalance effect causing differential lateral wall deflections. The wall on the shallower rockhead side was pushed back by the wall on the opposite side through the struts.
(6) The magnitude of the shifting of the central axis of the excavation trench is proportional to the excavation depths.
(7) The rate of increase in the axis shift values is proportional to the ratios between the depths to the deeper rockhead and the depths to the shallower rockhead levels on the two sides of the cofferdam.
(8) Based on the jack cylinder extension measurements in the preloading operation, the total wall deflections on the 2 sides of wall were around 40 mm measured immediately after locked-off with the shim plates.
(9) Inclinometers monitoring conducted on the following day of preloading showed that the wall movements occurring on the shallower rockhead side contributed around 3 quarter of the total wall deflections.

In the next study, numerical analysis shall be conducted to further examine the earth pressure imbalance effect to the performance of asymmetrical wall deflections. The effects due to wall stiffnesses and the magnitude of the preload are the subjects to be studied.

With the proper understanding the mechanism causing the asymmetrical wall deflections due to the effect of earth pressure imbalance, the design and construction of the underground infrastructures could be refined and the cost-effective solutions to engineering challenges could be formulated.

REFERENCES

Moh, Z.C. & Hwang, R.N. 1997. Geotechnical problems related to design and construction of the Taipei Transit Systems. *Proc. of Keynote Speech, Professor Chun Fung Kee Memorial Lecture*, September 6, 1997, Kuala Lumpur, Malaysia.

Wong, L.W. & Yong, C.C. 2013. Earth pressure imbalance on deep excavation. *Advance in Geotechnical Infrastructure, 18th Southeast Asian Geotechnical Conference*, May, Singapore: 275-281.

Full-scale Pile Load Tests using Osterberg Cells in Meta-sedimentary Rock

Alvin K.M. Lam, Andrew T.F. Wong & Zoe S.T. Leung
Ove Arup & Partners Hong Kong Limited, Hong Kong

Sylvia S.W. Chik, Kian Y.K. Chiu, Eric H.Y. Sze, Patrick P.C. Wong & Thomas H.H. Hui
Geotechnical Engineering Office, Civil Engineering and Development Department, Government of the Hong Kong Special Administrative Region, Hong Kong SAR, China

Andy Y.F. Leung
Hong Kong Polytechnic University, Hong Kong

ABSTRACT

Meta-sedimentary (MS) rocks are the dominant geological formation in the northern district of Hong Kong, an area earmarked for extensive urban development in the upcoming decades. This geological context presents challenges for foundation design, as existing practices typically employ conservative design parameters for piles founded in these formations. To investigate opportunities for optimisation, a series of full-scale pile load tests utilising Osterberg Cells (O-cells) combining with the loading kentledge have recently been conducted. The O-cell method integrates a sacrificial hydraulic jack at the base of the test pile enabling direct transfer of applied load to the rock for accurate measurement of both rock socket friction and end-bearing resistance. Unlike traditional pile load tests by loading kentledge, this eliminates the uncertainty of load shedding to the ground above the rock socket. Furthermore, the experience of using fibre optic technology for real-time strain measurements during the tests will be discussed. This novel approach is rigorously evaluated against the traditional vibrating wire strain gauge with a view to assessing the operational accuracy and overall efficiency of both techniques. The first batch of test piles has been carried out in Yuen Long South and Long Bin. This paper presents details of the test set-up, the loading sequence, the load-movement behavior of the test piles and the mobilised end-bearing capacity in the MS rocks. Rock Mass Rating (RMR) of the MS rocks at the founding levels have been determined, based on information obtained from ground investigation or pre-drill boreholes. The evaluation method of RMR and its applicability will be discussed. The findings of this study contribute valuable insights for future instrumented pile load tests in Hong Kong.

1 INTRODUCTION

Meta-sedimentary (MS) rocks are the predominant geological formation in the northern districts of Hong Kong, including areas within the planned Northern Metropolis, where substantial infrastructure and urban development are anticipated in the coming decades. However, foundation design in MS rocks remains constrained by conservative parameters prescribed in local codes of practice, particularly with regard to the allowable end-bearing pressures and socket bond resistance. It is mainly due to the general lack of geotechnical data for MS rocks in the past. These cautious design assumptions often result in conservative and costly pile foundation works and longer construction time, potentially impeding efficient land development in the region.

While there have been notable local precedents of pile testing in MS rocks, including test piles conducted during the Kowloon-Canton Railway Corporation (KCRC) West Rail Project Phase 1, these data remain limited in scale and applicability. Nevertheless, they provided useful insights into rock socket friction and end-bearing capacity, but a more systematic and instrumented approach is needed to enhance confidence in design parameters, particularly for deep foundations subject to complex geological variability.

Recognising the need to optimise pile design in MS rocks, the Geotechnical Engineering Office (GEO) has launched a full-scale pile testing programme using Osterberg Cells (O-cells) for bi-directional loading. Tests were first conducted at two trial sites in Yuen Long South and Long Bin with comprehensive instrumentation including vibrating wire gauges and fibre optic sensors. Geological conditions were assessed using borehole data and Rock Mass Rating (RMR) classification. This paper presents the details of the test pile design, construction, instrumentation, and testing procedures, followed by interpretation of load-movement behavior and assessment of mobilised end-bearing capacities. The effectiveness of fibre optic technology for real-time strain monitoring is evaluated through comparison with traditional instrumentation. The results of the pile load tests have provided valuable insights into the actual performance of piles in MS rocks under controlled loading conditions, which are vital for the formulation of future foundation design guidelines to support developments in the Northern Metropolis. The overall study plan for reviewing the foundation design of MS rocks is documented in Chik et al. (2025).

2 DESIGN PRACTICE FOR META-SEDIMENTARY ROCKS IN HONG KONG

2.1 Geological Challenges

MS rocks are sedimentary rocks subjected to metamorphism. It is very common to find the presence of closely spaced rock joints in MS rocks in Hong Kong rendering the difficulty of gathering full diameter rock core samples for conducting the conventional Unconfined Compressive Strength (UCS) and/or point load tests to verify the rock strength. In some cases, the rock is so fragmented that it becomes non-intact. Some geologists may describe the non-intact material as Grade IV material. If the thickness is substantial, this will have a major implication to define the engineering bedrock for load bearing piles. Therefore, the feasibility of using irregular lump point load test to determine the strength of MS rocks should be explored.

2.2 Design Practice

In Hong Kong, the Buildings Department (BD) published the Code of Practice for Foundations 2017 (2024 Edition), which classifies MS rocks as Category 2 rock. For moderately decomposed, moderately strong to moderately weak MS rocks of material weathering grade III or better, and with not less than 85% total core recovery (TCR) of the designated grade, a presumed allowable bearing pressure of 3,000 kPa can be adopted. It is noteworthy that there is no specific requirement on the intact rock strength of MS rocks. A presumed allowable bond or friction between rock and concrete or grout of 300 kPa and 150 kPa can be adopted for piles under compression/transient tension and permanent tension respectively. Comparing with igneous rocks, the presumed allowable bearing pressure and bond/friction of MS rocks are much lower than those for igneous rocks. Therefore, GEO has initiated a systematic pile load testing programme to investigate the potential to uplift the presumed allowable bearing pressure and bond/friction of MS rocks, with a view to producing a more cost-effective foundation designs in MS rocks.

2.3 Use of Rock Mass Rating Method

According to Table 6.5 of GEO (2006), the allowable bearing capacity of a pile resting on a jointed rock mass can be evaluated by assessing the respective Rock Mass Rating (RMR). For example, an allowable bearing capacity of 5,000 kPa could be adopted for rock mass with RMR value of 50, and that 14,500 kPa for rock mass with RMR value of 88 (i.e. the maximum value). The RMR method, developed by Bieniawski (1973) and (1989), is a tool to assess the properties of rock mass. Five parameters are considered including the strength of intact rock, Rock Quality Designation (RQD), spacing of joints, conditions of joints and groundwater. The strength is usually determined by UCS or point load test. The joint spacing can be calculated using the fracture index while the condition of joints can be assessed based on visual inspections of the retrieved rock cores and/or the descriptions of the borehole logs. In the current practice, the RMR value shall be assessed to depth of not less than three times the diameter of the pile base. For more details about the RMR method and its potential enhancement for foundation design, please refer to Suen et al. (2025).

3 LOCAL EXPERIENCE OF TEST PILES IN META-SEDIMENTARY ROCKS

3.1 Kowloon-Canton Railway Corporation (KCRC) West Rail Project Phase 1

One of the most extensive test pile program undertaken in Hong Kong could be traced back to 1998 for the Kowloon-Canton Railway Corporation (KCRC) West Rail Project Phase 1, during which a total of 14 numbers of full-scale pile tests were carried out in igneous and MS rocks with various degree of weathering according to Littlechild et al (2000) and Hill et al (2000). The aim of the test piles was to optimise the foundation design so as to save time and cost for the fast-track West Rail project. A total of 2 out of 14 numbers of test piles were tested in MS rocks at Tin Shui Wai. These test piles, namely TSW1 and TSW2, were designed to verify the end-bearing capacity with an effective diameter of 1.2 m and rock socket lengths of 1.6 m and 0.7 m respectively. The test load was applied through a single 850 mm diameter Osterberg cell (O-cell) installed at pile toe combined with the loading kentledge. Similar to the pile construction method at present, the excavation in rock was carried out by the Reverse Circulation Drilling (RCD) apparatus to form the rock socket (see **Plate 1**).

Plate 1: RCD for Construction of Rock Socket for the Test Piles

For the O-cell, a 65 mm thick top and base steel plates were welded to cell prior to welding onto the base section of the reinforcement cage (see **Plate 2**). Grouting beneath and around the O-cell was carried out through 3 sacrificial grout pipes immediately prior to concreting of the pile. The O-cell was instrumented with 3 nos. of displacement transducers to measure the opening of the cell and the hydraulic pressure to operate the cell was monitored through the high-pressure vibrating wire piezometer. Rod extensometers at the top of O-cell (2 nos. per level) and retrievable multi-point borehole extensometer along the pile were installed to monitor the pile movement while vibrating wire strain gauges were installed to monitor the strain at different levels (4 nos. per level). At the pile head, vibrating wire load cells were installed to monitor the applied load through the kentledge while dial gauges were installed to monitor the pile head movement relative to the reference beam (see **Plate 3**). Movement check points were also set at the reference beam to monitor any undue movement of the reference beam during the loading test.

Plate 2: Osterberg Cell at Pile Base

Plate 3: Hydraulic Jacks with Load Cells at Pile Head

3.2 Recent Projects

For the residential projects at Sai Sha, it was proposed to use 813 mm diameter reinforced concrete test bored piles to verify the end-bearing capacity of the founding MS rocks with Rock Mass Rating not less than 45 by a kentledge (SEC Cases 29/2021 and 44/2021). The applied load at the pile base would be monitored by a set of strain gauges near the pile base. When the pile is loaded at the top, the relationship between the applied load and the average strain value can be established. When the same average strain value is measured by the strain gauges at the pile base, it is deemed that the corresponding applied load at the pile base can be determined. The loading kentledge is indeed needed to allow for frictional loss along the pile shaft during the loading test. However, due to the limit of the structural capacity of the pile, the maximum applied load would be limited to about 16,000 kN. The pile details are shown in **Figure 1**. Unfortunately, the test pile has not been proceeded due to tight programme constraint.

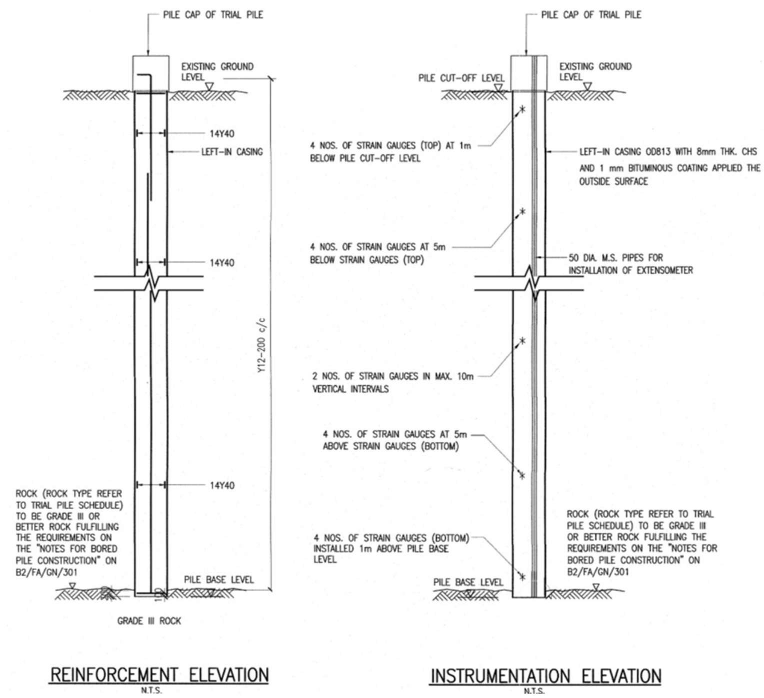

Figure 1: Typical Detail of 813 mm Diameter Test Pile at Sai Sha

Yau et al (2024) reported that full scale load tests on 2 trial piles (with similar set up as the test pile at Sai Sha) with full instrumentations resting on MS rocks with an RMR value above 50 were conducted in Tin Shui Wai. The ultimate bearing pressure of both piles was well in excess of 15,000 kPa. Taking into account of the required factor of safety of 3, the allowable bearing pressure of the site was set at 5000 kPa for rock mass with an RMR value greater than 50.

4 LAUNCHING OF PILE TESTING PROGRAMME IN NORTHERN METROPOLIS

The conservative design parameters for MS rocks can lead to a larger scale and more costly foundation solution, undermining the efficient development of the Northern Metropolis. Because of this, there is a pressing need to improve the current design guidelines with a view to facilitating a more economical yet safe foundation design. In this connection, GEO has initiated a series of full-scale bi-directional pile load tests utilising O-cells in the Northern New Territories (Chik et al. 2025). The first batch of test piles were carried out in trial sites in Yuen Long South (YLS) and Long Bin (LB), with two test piles carried out in each site. Along the pipeline, there would be more test piles to be carried out in other parts of the Northern New Territories (e.g., Lok Ma Chau, Wang Chau, Sandy Ridge, etc.).

In the following sections, one of the test piles in each site will be presented, including the details of the test setup, loading sequences, and load-displacement behavior. The application of the RMR system for geological characterisation will also be briefly discussed. In addition, the implementation of fibre optic technology for real-time strain monitoring during testing will be evaluated.

5 TEST PILE CONSTRUCTION AND DETAILS

5.1 Use of Osterberg Cells

Full-scale bi-directional pile load tests using O-cells were conducted at trial sites in YLS and LB to investigate the performance of bored piles socketed into MS rocks. The O-cell is a hydraulically driven, sacrificial jack embedded within the pile, which applies force simultaneously in upward and downward directions. This enables separate measurement of shaft resistance and end-bearing resistance when the O-cell is placed at the bottom of the pile, offering direct load transfer mechanisms within the test pile.

Compared with the conventional top-down pile load tests, the bi-directional method offers practical advantages, especially for deep pile with substantial shaft friction contribution. It provides direct load transfer among the end-bearing resistance and the rock socket friction. Importantly, the internal loading arrangement allows the mobilisation of maximum available resistance at both the shaft and base within a single test setup.

5.2 Geological Condition at Test Pile Location

The geological conditions at the location of the two test piles were thoroughly investigated through predrilling before the founding levels of the pile were determined.

At the YLS site, predrill borehole YLS-PD07 encountered a thin fill layer at the ground surface, underlain by the alluvial deposit comprising light grey to brown silty clayey sand and sandy silty clay, with Standard Penetration Test (SPT-N) values ranging from 4 to 16. Completely decomposed metasiltstone and metasandstone (Grade V) were encountered starting from approximately 16.5 m below ground level. The founding stratum for the test pile YLS-P2 was located within the bedrock zone classified as Grade II/III, comprising moderately strong to strong, moderately to slightly decomposed meta-siltstone and meta-sandstone, encountered at an elevation of -36.71 mPD. More than three times the pile base diameter below the pile base, slightly decomposed impure marble (Grade II) without evidence of dissolution features was also observed.

At the LB site, predrill borehole PB01 revealed a stratigraphic sequence beginning with a fill layer of greyish brown to dark brown sandy clayey silt, underlain by a layer of light grey, slightly sandy silty clay Alluvium. Below this, the profile consisted of interbedded layers of meta-siltstone and meta-sandstone spanning weathering Grades II to V. The target founding stratum was identified as Grade II/III metasiltstone, characterised as moderately strong to strong and moderately to slightly decomposed at a depth of more than 85 m below ground level. The test pile LB-P1 was socketed into this stratum, with its base located at -87.01 mPD.

In addition to borehole logging and material classification, the geological conditions at each test pile location were further evaluated using the RMR method. For both test piles, individual ratings for each parameter were determined using a length-weighted average method across the depth of influence. The derived RMR values for YLS-P2 and LB-P1 are summarised in **Table 1**. The derived RMR values provide a quantitative assessment of rock mass quality at different depths, which could be used to establish the correlation between pile capacity and rock mass characteristics.

Table 1: Rock Mass Rating Values for YLS-P2 and LB-P1

Test Pile No.	Streng-th (≤ 15)	RQD (%) (≤ 20)	Joint Spacing (≤ 20)	Conditions of Joints					Ground-water (7)	Total (≤ 88)
				Discon-tinuity Length (2)	Separat-ion (≤ 6)	Rough-ness (≤ 6)	Infilling (≤ 6)	Weather-ing (≤ 6)		
In rock socket										
YLS-P2	15	14	9	2	1	1	6	5	7	60
LB-P1	12	8	6	2	4	5	6	5	7	55
Within 1 time the pile base diameter below founding level										
YLS-P2	15	20	10	2	1	1	6	5	7	67

LB-P1	9	3	6	2	4	5	6	5	7	47

5.3 Construction Details of Test Piles

At the YLS site, the diameters of the test pile (YLS-P2) were 813 mm diameter in soil and 750 mm in rock socket. Installation involved advancing a steel casing to rockhead using a MAXA STABOTEC Enviro Flush Casing System, followed by rock socket formation with a down-the-hole hammer. YLS-P2 was constructed with a total length of about 47 m and a rock socket length of 0.91 m. In contrast, the test pile in LB site (LB-P1) adopted a larger diameter of 1,500 mm in soil and 1,350 mm in rock socket. It was formed by soil grab excavation inside temporary steel casing down to rockhead followed by socket drilling using the RCD method. LB-P1 has a total length of about 90 m and a rock socket length of 1.5 m. A relatively short rock socket length was deliberately adopted for both test piles to reduce the available socket bond resistance. This design approach aimed to bring the rock/pile interface closer to ultimate conditions, enabling an assessment of the socket's ultimate bond resistance. To minimise the friction along the pile shaft in soil, permanent steel casing was installed from the ground level down to the top of rock socket. This approach helped reduce the load transfer between the pile and the overlying soil during testing, thus allowing a more accurate assessment of the response of the rock socket.

Instrumentation was installed to monitor strain, displacement, and pile behavior throughout the test. Continuous monitoring was carried out to capture the pile response under each load increment. Measurements from multiple instrumentation sources were recorded and managed via a central data logger. Expansion across the O-cell was recorded by four Geokon Model 4450 linear vibrating wire displacement transducers (LVWDTs). Rod extensometer pipes of 13 mm diameter were fixed onto the reinforcement cage to measure displacements at various locations; above the O-cell, below the base plate, and at the top of the rock socket. The head of the rod extensometers were extended to approximately 1 m above pile cap surface, and additional LVWDTs were installed at the top of the pile cap to monitor the extrusion of the rod extensometers' head throughout the load test. Rebar strainmeters Geokon Model 4911, commonly known as the "Sister Bars" (see **Plate 4**) were positioned in multiple levels along the pile shaft to capture strain profiles. The rebar strainmeter was designed to integrate into the pile by tying it alongside the rebar cage. As the strain behavior near the pile base and within the rock socket was of particular interest, denser instrumentation was employed in that region. The rebar strainmeters were arranged in four-gauge arrays from 1 m above the rock socket down to the pile base with nominal 500 mm interval, and in two-gauge arrays from the pile head to just above the rock socket at nominal 8 m interval. Apart from conventional strain gauges, a fibre optic distributed sensing system was employed to capture real-time strain and temperature data along the pile, providing an extra layer of spatially distributed sensing for verifying strain gauge trends or detecting unexpected responses. In addition, pile head movements were measured by a pair of Leica NA3000 digital levels to a precision of 0.01 mm, with observations taken at fixed backsights and foresights throughout the test. The instrumentation elevation plans for YLS-P2 and LB-P1 are shown in **Figures 2 and 3**, respectively.

Plate 4: Rebar Strainmeter

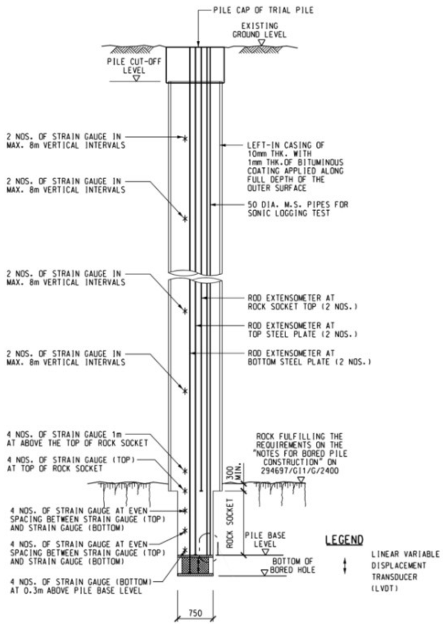

Figure 2: Instrumentation Elevation for YLS-P2

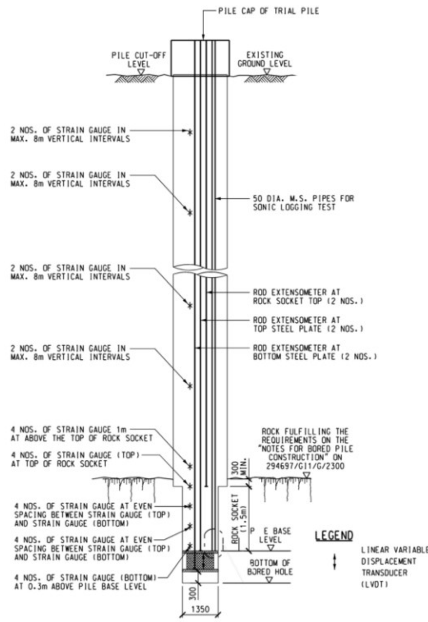

Figure 3: Instrumentation Elevation for LB-P1

The O-cell assemblies were embedded into the reinforcement cages with 50 mm steel bearing plates welded above and below the O-cell to transmit load in opposing directions – upwards to mobilise shaft friction and downwards to mobilise end-bearing resistance. At YLS, a single O-cell with a diameter of 530 mm and a maximum jacking capacity of 10 MN was installed at the pile base. This was paired with 560 mm diameter bearing plates designed to ensure uniform load transfer, with the bottom plate placed in direct contact with the founding rock mass. On the other hand, a higher-capacity setup was adopted in LB, utilising five horizontally arranged O-cells, each 430 mm in diameter and rated to 6.4 MN, yielding a combined jacking capacity of approximately 32 MN. These were installed near the pile base and coupled with steel bearing plates of 1,235 mm in diameter to match the wider pile geometry. Given that such pile was constructed with RCD which typically resulted in a non-uniform rock socket base, a nominal 300 mm thick concrete bedding layer was placed beneath the bottom bearing plate to ensure full and uniform engagement between the pile base and the founding rock mass. To facilitate the placement of this bedding layer, a 300 mm diameter hole was reserved at the centre of the steel bearing plates, allowing insertion of a tremie pipe down to the base of the rock socket. **Plates 5 and 6** demonstrate the O-cell assembled with steel bearing plates and reinforcement cages for YLS-P2 and LB-P1, respectively. **Plate 7** presents the underside of the bottom steel bearing plate installed for LB-P1.

Plate 5: O-cell Assembly for YLS-P2

Plates 6: O-cell Assembly for LB-P1

Plate 7: Underside of Bottom Steel Plate for LB-P1

Both configurations incorporated O-cells with a stroke of 225 mm, allowing sufficient displacement to fully mobilise end-bearing resistance and shaft friction. The hydraulic pressure required to operate the O-cells was delivered via air-driven pumps, using water as the hydraulic medium. This substitution of oil with water not only aligned with environmental protection standards but also mitigated the risk of contamination in the event of leakage during testing. The typical set up for the hydraulic pumps for the O-cell is shown in **Plate 8**.

Plate 8: Set Up of the Hydraulic Pumps for O-cell

5.4 Procedures of Load Testing

The test piles were loaded in a series of cycles with progressively increasing applied load at the O-cell, as shown in **Table 2**.

Table 2: Test Cycles and Maximum Applied Loads

Cycles	Max. Test Load (% of a reference pressure of 7,500 kPa)	Max. Test Load at Pile Base (kN)	
		YLS-P2	LB-P1
1	100%	3,317	10,737
2	200%	6,633	21,473
3	300%	9,950	32,210
4	Up to the practical limit of the O-cell		

The target maximum test load was set to achieve an equivalent pressure of 22,500 kPa at the pile base, corresponding to three times the reference pressure of 7,500 kPa. The loading sequence comprised three primary cycles: Cycle 1 reached 100% of the reference pressure (7,500 kPa), Cycle 2 reached 200% (15,000 kPa), and Cycle 3 reached 300% (22,500 kPa). For each 50% load increment, the holding period continued until the rate of displacement fell below 0.05 mm over a 10-minute interval, sustained for at least 30 minutes. At the maximum test load of 22,500 kPa, a prolonged hold period of 72 hours was adopted to capture time-dependent movements and assess long-term pile behavior under high stress.

At the end of each unloading cycle, residual settlement was recorded to capture the extent of unrecoverable displacement. Following the completion of Cycle 3, an additional Cycle 4 was introduced to further increase the applied load beyond the initial target, with the aim of examining the pile response under extreme loading conditions. For YLS-P2, the maximum test load achieved during Cycle 4 was 390% of the reference pressure, while for LB-P1, the peak load reached was approximately 340%. As Cycle 4 was not part of the original testing objective, only the results from Cycles 1 to 3 are presented and discussed in this paper.

At the start of the test, loading commenced without restraining the pile head – meaning that the pile head was not engaged to any loading kentledge to allow free upward movement when the O-cell was expanded. Under such unrestrained condition, the applied load in the O-cell was resisted by a combination of base resistance and shaft friction along the entire pile, including both the soil shaft and rock socket. This unrestrained phase was designed to assess the mobilised shaft friction, particularly within the rock socket. To ensure that the rock socket resistance could be largely mobilised before the end-bearing resistance became dominant, the test piles were deliberately constructed with relatively short rock socket lengths. Once the available shaft friction was insufficient to counteract the applied load, the expansion of the O-cell could rapidly become excessive. To preserve sufficient O-cell stroke for full load application to the pile base in subsequent loading cycles, two predefined trigger conditions were established to safeguard the test setup: (i) if the O-cell stroke exceeded 80 mm, or (ii) if the upward displacement measured at the top of the rock socket exceeded 4% of the socket diameter. If either condition was met during loading, the test would be paused immediately to turn into restrained phase. The O-cell would be unloaded to zero, and the loading kentledge would be engaged before reloading of the O-cell. These criteria were carefully defined to allow the rock socket friction to be fully mobilised during the unrestrained phase (usually ~ 1 to 2% of the socket diameter), while still preserving adequate O-cell stroke for mobilising the end-bearing resistance in the restrained phase. Given that the maximum allowable stroke of the O-cell was 225 mm, the 80 mm threshold was considered adequate.

The purpose of the loading kentledge system is to restrain the upward movement of the pile head, thereby enabling the full development of the end-bearing resistance. At the pile head, hydraulic jacks were installed to apply a seating load, ensuring full engagement between the pile and the kentledge system at the beginning of the restrained phase. Load cells were used to monitor the load transferred onto the kentledge. When 90% of the kentledge load was mobilised, the test would be ceased for safety concern. **Plate 9** presents the hydraulic jacks with load cells installed at the pile head at LB-P1.

Plate 9: Hydraulic Jacks with Load Cells at Pile Head at LB-P1

The minimum kentledge weights adopted were 10 MN for YLS and 30 MN for LB, in line with the anticipated maximum test loads and overall safety requirements for restrained testing. Conversely, if neither trigger condition was reached throughout all planned load cycles, it would indicate that the shaft friction was sufficient to balance the applied load at the O-cell, and the engagement of the kentledge system would not be required. This was the case for YLS-P2, where the test completed without the need to activate the kentledge system. In contrast, LB-P1 had experienced failure in the shaft friction. During Cycle 3 of the unrestrained phase, the loading was halted at an applied load of approximately 30 MN (~ 280% load) when the pressure started to drop and failed to be maintained. Although the top plate movement at that moment was just around 10 mm which had not reached any trigger conditions, it was considered that the shaft friction had been fully mobilised. The pressure continued to drop until an approximate 35 mm upward movement was recorded. The behavior indicated that the available shaft friction was insufficient to counteract the applied load at the O-cell. The unrestrained phase was then suspended with the O-cell unloaded, and the kentledge system was engaged to allow further loading under restrained conditions.

6 DISCUSSION OF PRELIMINARY LOAD TEST RESULTS

6.1 Load & Movement Behavior

For YLS-P2, the pile base was loaded up to 10,030 kN, which corresponded to slightly above 300% of the reference end-bearing pressure (three times of 7,500 kPa). As illustrated in **Figure 4**, the load-settlement behavior for YLS-P2 demonstrated that at this load level, the corresponding settlement recorded at the bottom plate was 3.91 mm. Notably, during the initial stage of loading, a disproportionately large settlement of 2.03 mm occurred during the first 50% load increment. This behavior deviated from the more gradual settlement trend typically expected in early loading stages and was likely attributed to initial seating effects at the pile base. As discussed in Section 5.3, YLS-P2 was constructed with the bottom steel plate placed directly on the founding rock. The observed seating effects may have resulted from local compression of the slightly uneven rock surface beneath the base plate. Subsequent load increments exhibited smaller and more consistent trend of displacements, indicating that the initial seating had stabilised in the loading process.

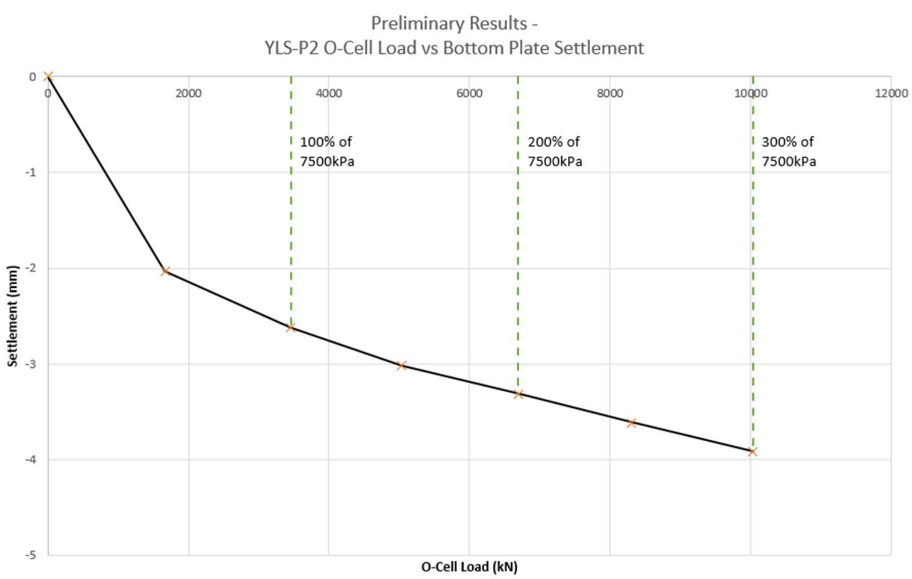

Figure 4: O-cell Load against Bottom Plate Settlement of YLS-P2

For LB-P1, the pile was loaded up to 32,260 kN under the restrained phase, which corresponded to 300% of the reference end-bearing pressure (three times of 7,500 kPa). The load-settlement behavior for YLS-P2 is illustrated in **Figure 5**. The settlement recorded at the bottom plate was 11.53 mm at this load. Unlike YLS-P2, this pile did not exhibit an abnormally large settlement during the initial loading stage. Instead, the overall trend of base settlement remained steady, with the rate of settlement gradually increasing as the applied load intensified. This behavior may be attributed to the presence of a concrete bedding layer beneath the bottom bearing plate, which provided a more uniform interface between the bottom plate and the founding rock. The bedding layer likely helped distribute stress more evenly, reducing localised deformation and minimising seating effects typically associated with direct contact on uneven rock surfaces.

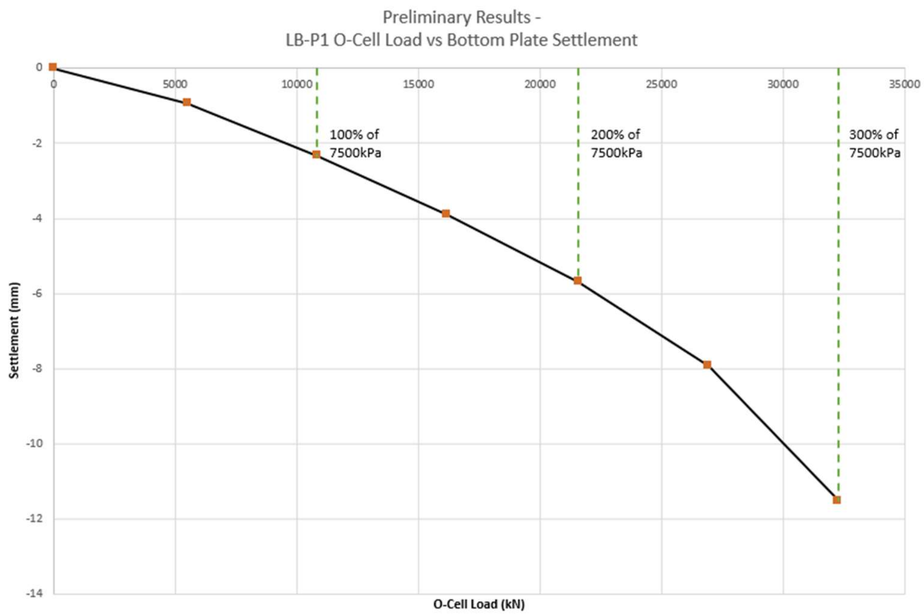

Figure 5: O-cell Load against Bottom Plate Settlement of LB-P1

The mobilised end-bearing resistance derived from the O-cell load and the corresponding settlement of the bottom plate are summarised in **Table 3**. The settlement values were normalised with respect to the pile base diameter to facilitate comparison across different pile sizes. For instance, at 300% load, YLS-P2 achieved an end-bearing pressure of 22,703 kPa with a bottom plate settlement of 3.91 mm (0.52% of rock socket diameter). In contrast, LB-P1 resulted in larger settlements under similar pressure level. The bottom plate settlement at LB-P1 reached 11.53 mm (0.85% of pile socket diameter) under an end-bearing pressure of 22,538 kPa. The larger movements in LB-P1 suggest a more compressible rock stratum beneath the pile base as compared to YLS-P2. Overall speaking, the settlement at one time the reference pressure (7,500 kPa) was found to be less than 1% of the pile base diameter, while the settlement at three times the reference pressure remained below 3% of the pile base diameter.

Table 3: Summary of Mobilised End-Bearing Resistance up to 300% Reference Pressure

Pile No.	Pile Diameter (mm) pile shaft / rock socket	Mobilised End-Bearing Resistance (kPa)	Bottom Plate Settlement (mm) / % of Rock Socket Diameter
YLS-P2	813 / 750	7,832	2.62 / 0.35%
		22,703	3.91 / 0.52%
LB-P1	1500 / 1350	7,524	2.33 / 0.17%
		22,538	11.53 / 0.85%

The test was carried out beyond 300% of the reference pressure, reaching the practical loading limit of the O-cell. During the test, a maximum mobilised end-bearing resistance of approximately 29,000 kPa and 25,000 kPa for YLS-P2 and LB-P1 has been reached respectively, without significant further bottom plate settlement.

These findings indicated that both test piles exhibited relatively stiff end-bearing responses, with limited deformations even under high load levels. The normalised settlement values fell within acceptable performance ranges commonly referenced in local and international design practices, suggesting that the founding MS rocks possessed favorable bearing characteristics. This supports the potential for adopting higher end-bearing design values.

6.2 Young's Modulus of Rock Mass

The Young's modulus of the rock mass (E_m) is a critical parameter for estimating settlement of piles founded on rock. For piles founded on rock, the settlement at the surface of the rock mass can be calculated by the following formula assuming a homogeneous elastic half space below the pile tip:

$$\delta_b = \frac{q(1 - v_r^2)D_b}{E_m} C_d C_s$$

where δ_b = settlement at the surface of the rock mass; q = bearing pressure on the rock mass; C_d = depth correction factor; C_s = shape and rigidity correction factor; v_r = Poisson's ratio of rock mass; D_b = pile base diameter and E_m = Young's modulus of rock mass.

Focusing on the working load range and to mitigate the effects of seating load settlement, the Young's modulus was calculated using the bottom plate settlements between 100% and 200% of the reference pressure. For YLS-P2, with a settlement of 2.62 mm at 100% and 3.31 mm at 200%, the back-calculated E_m value is 10.49 GPa. For LB-P1, with a settlement of 2.33 mm at 100% and 5.70 mm at 200%, the E_m value is 3.85 GPa. These calculated Young's modulus values have been compared and found roughly consistent with the previous test pile results from Figure 6.7 of GEO (2006).

7 DISCUSSION OF FIBRE OPTIC TECHNOLOGY FOR STRAIN MEASUREMENTS

7.1 Use of fibre optic technology for real-time strain measurements

This project adopts distributed fibre optic sensing technology for strain measurements during the load tests. Recent years have seen advances and applications of various types of fibre optic technology in civil engineering instrumentation, including the use of fibre Bragg grating (FBG) sensors or Brillouin optical time domain reflectometry (BOTDR) technology. This study adopts the optical frequency domain reflectometry (OFDR) technology. Compared with FBG and BOTDR, OFDR sensing system can achieve a higher spatial resolution of strain measurements with high sensing frequency for dynamic or real-time strain measurements.

The OFDR sensing technology is based on Rayleigh scattering (Lin et al. 2023). Light output from a tunable laser source in the OFDR equipment is divided into two parts by an optical coupler, with one part used as the reference light and the other used as the measurement light. When the measurement light propagates in the fibre optic cable, backscattered light is generated due to inhomogeneity in the refractive index of the optical fibre. This backscattered light is transmitted back to the equipment and then mixed with the reference light by the optical coupler. The resulting coherent interference is received and demodulated by the photoelectric detector to obtain the strain and/or temperature change along the sensing cable, which is related to the Rayleigh spectral shift by:

$$\Delta v_R = c_\varepsilon \Delta\varepsilon + c_T \Delta T$$

where Δv_R = Rayleigh spectral shift; $\Delta\varepsilon$ = mechanical strain change of the fibre optic cable; ΔT = temperature change; c_ε = coefficient of Rayleigh frequency shift induced by mechanical strain change (= −0.15 GHz/με; and c_T = coefficient of Rayleigh frequency shift induced by temperature change (= −1.25 GHz/K).

Since Δv_R is influenced by changes in both strain and temperature, it is necessary to single out the temperature effects by another loose tube fibre optic cable, where the outer sheath is not mechanically bonded to be fibre optic core. For these cables, the measured Δv_R only arises from ΔT. Therefore, two types of fibre optic cables were utilised and they were both manufactured by NanZee Sensing Technology in Suzhou, China. The strain and temperature sensing cables are referred to as NZS-DSS-C02 and NZS-DTS-C05 cables, respectively. **Figure 6** (Lin et al. 2023) shows the schematic diagrams of the cross sections of these cable types. NZS-DSS-C02 is a type of metal-based funicular strain sensing cable, which is single mode and uses multi-strand metal reinforcement to improve the surface strength of the sensing fibre. The metal reinforcement enhanced its robustness, making it more versatile in construction site environments. The diameter (D) of the cable adopted in this project is 5.0 mm and its weight is 38 kg/km. NZS-DTS-C05 is a type of plastic package armoured cable for temperature measurement, where strain transfer is prevented by a void between the sleeve and the fibre core. Its diameter is about 5.0 mm with an operational range of is from -20 ºC to 85 ºC.

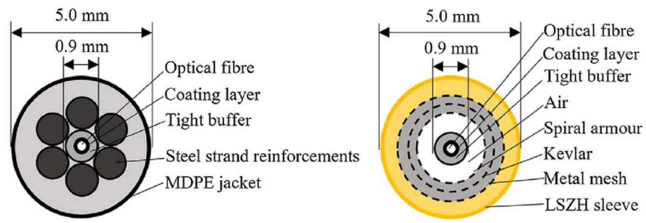

Figure 6: Fibre optic cables for strain and temperature measurements:
(left) NZSDSS-02 cable; (right) NZSDSS-05 cable (adapted from Lin et al 2023)

The equipment used in the load tests was LUNA ODiSI 6102 fibre optic sensing interrogator. It has a maximum spatial resolution of 0.65 mm for strain and temperature measurements. The spatial resolution is adjustable, and for applications in field pile load tests it is typical to adopt the resolution of 1 to 2 cm. During field deployment, the fibre optic cables were mounted onto the longitudinal reinforcement bars along the reinforcement cage, and fixed by plastic cable ties. No pre-straining operation was conducted for the fibre optic cables, as they were expected to be fully embedded in reinforced concrete and hence experience the same strains as the pile material.

7.2 Comparison between fibre optic technology and vibrating wire strain gauges

Figure 7 shows the strain measurements at YLS-P2, obtained by optical fibre sensors after compensating for temperature effects. The data from two cables are plotted together with the average value, at different load stages up to around 9,950 kN. As the Osterberg cell applies an upward load from near the pile tip, compressive strains are induced with maximum values close to the bottom and reduce with elevation. The corresponding data obtained by vibrating wire strain gauges are also plotted for comparison. In general, the strain gauge and fibre optic data match with each other. Such variations of strains at the same elevation might be due to eccentricity of the applied load.

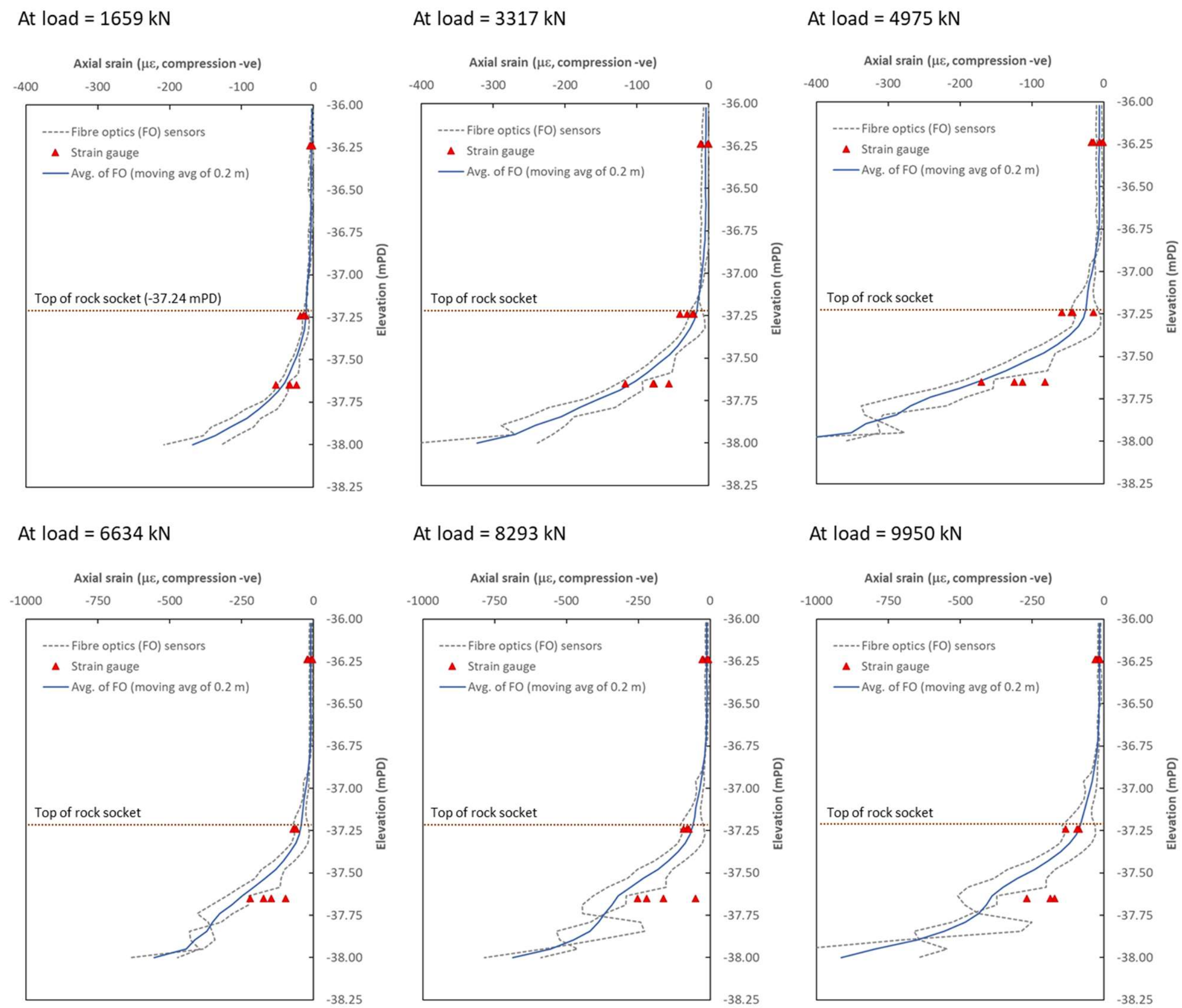

Figure 7: Fibre Optic Strain Measurements Compared with Strain Gauge Data for YLS-P2

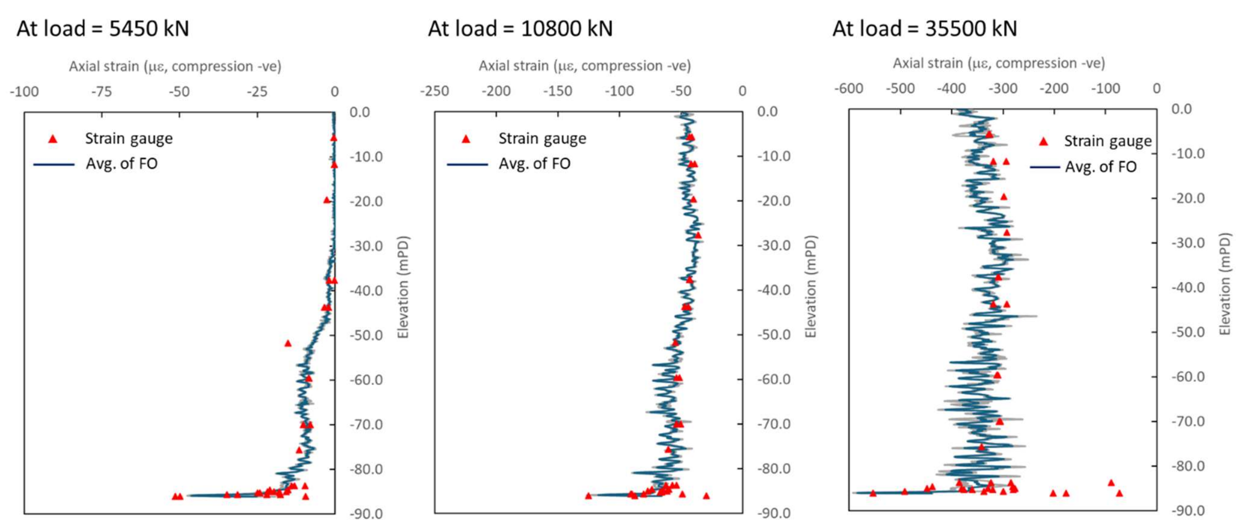

Figure 8: Fibre optic strain measurements compared with strain gauge data for LB-P1

8 CONCLUSIONS

The full-scale bi-directional pile load tests conducted at Yuen Long South and Long Bin have provided valuable, high-quality data on the performance of bored piles socketed into MS rocks in the northern New Territories. Through the use of Osterberg Cells and comprehensive instrumentation including both vibrating wire strain gauges and fibre optic sensors, this study has enabled direct measurement of shaft friction and end-bearing resistance, as well as detailed assessment of load transfer mechanisms and settlement behavior.

Importantly, the mobilised end-bearing capacities and observed settlements from these tests are consistent with, and in some cases exceed, the recommended allowable bearing pressures for jointed rock masses as set out in the Figure 6.8 of GEO (2006). The test results may substantiate the use of higher bearing pressures than those typically adopted in conservative design, subject to further upcoming test piles in other parts of the Northern New Territories.

The successful application of fibre optic technology for real-time strain monitoring, alongside traditional instrumentation, has also been demonstrated, offering enhanced spatial resolution and operational efficiency for future testing programs.

In summary, this study provides strong evidence that pile design in MS rocks can be optimised by integrating detailed geological assessment and full-scale pile load testing. The findings support a leap towards more economical and reliable foundation solutions for major infrastructure and urban development projects in Hong Kong, particularly within the context of the Northern Metropolis.

ACKNOWLEDGEMENTS

This paper is published with the permission of the Head of the Geotechnical Engineering Office and the Director of Civil Engineering and Development, the Government of the Hong Kong Special Administrative Region of the People's Republic of China.

REFERENCES

BD (2024). *Code of Practice for Foundations 2017 (2024 Edition)*. Buildings Department, Hong Kong.

Bieniawski, Z.T. (1974). Geomechanics classification of rock masses and its application in tunnelling. *Proceedings of the Third International Congress of the International Society for Rock Mechanics*, Denver, vol. 2A, pp 27-32.

Bieniawski, Z.T. (1989). *Engineering Rock Mass Classification*. John Wiley, New York, 251 p.

Chik, S.S.W., Chiu, K.Y.K., Lau, R.W.Y., Chau, A.Y.L., Sze, E.H.Y, Wong, P.P.C, Hui, T.H.H. (2025). Trial Piles and Foundation Design in Meta-sedimentary Rocks. *Proceedings of the 45th Annual Seminar.* Geotechnical Division, Hong Kong Institution of Engineers.

GEO (2006). *Pile design and construction GEO Publication No.1/2006*. Civil Engineering Department, Hong Kong.

GEO (2023). *Supplementary Guidelines for Foundation Design and Construction, GEO Technical Guidance Note No. 53*, Geotechnical Engineering Office, Civil Engineering and Development Department, Hong Kong.

Hill, S.J., Littlechild, B.D., Plumbridge, G.D. & Lee, S.C. (2000). End bearing and socket design for foundations in Hong Kong. *Proceedings of the 19th Annual Seminar*, Geotechnical Division, Hong Kong Institution of Engineers, pp 167-178.

Lin, S.Q., Tan, D.Y., Leung, Y.F., Yin, J.H., Li, I., Sze, E.H.Y., Lo, F.L.C., Kan, H.S., Wong, T.C.W. and Chan, E.Y.M. (2023). Fibre optic monitoring of a twin-circular shaft excavation: developments of circumferential forces and bending moments in diaphragm wall. *Journal of Geotechnical and Geoenvironmental Engineering*, Vol. 149 (12), 04023117

Littlechild, B.D., Hill, S.J., Statham, I. & Plumbridge, G.D. (2000). Stiffness of Hong Kong rocks for foundation design. *Proceedings of the 19th Annual Seminar.* Geotechnical Division, Hong Kong Institution of Engineers, pp 181-190.

Suen, M.H.Y., Chow, C.C.F., Lau, R.W.Y., Chau, A.Y.L., Wong, P.P.C., Hui, T.H.H. (2025). Evaluation of RMR for Meta-Sedimentary Rocks in Hong Kong: Challenges and Potential Solutions. *Proceedings of the 45th Annual Seminar.* Geotechnical Division, Hong Kong Institution of Engineers.

Yau, T.L.Y. & Lau, C.K. (2024). Review on the End Bearing Capacity of Large Diameter Bored Piles founded on Meta-sedimentary Rock in Hong Kong. *Proceedings of the Forty-fourth Annual Seminar*. Geotechnical Division, Hong Kong Institution of Engineers, pp 374-385.

Static Plate Load Test in Local Foundation Code – A Case Study

Arthur K O So
Meinhardt Infrastruture and Environment Limited (Email: arthurso@meinhardt.com.hk)
& AKOS Geotechnical Consulting Limited (Email: arthurkoso@hotmail.com)

ABSTRACT

Footings and raft foundations remain widely used in many countries. Local designs often rely on empirical formulae derived over fifty years ago. Prior to construction, a plate load test is required to verify the allowable bearing capacity of the supporting stratum, as stipulated in the Code of Practice for Foundations by the Buildings Department, first issued in 2004 and revised in 2017. Using a large raft foundation from a project as an example, the author proposes a more practical approach: reverting the test load to three times the working pressure, as specified in the 2004 Code, while increasing the allowable settlement by 2.5 mm to account for elasto-viscous deformation under higher loads. For very large raft foundations, the allowable bearing capacity should be capped, and the test may be eliminated entirely. Additionally, soil stiffness is not a material constant as the secant modulus varies with mean stress levels. As soil modulus degrades with increasing strain, the elastic modulus derived from load-settlement data tends to be stiffer than the design value used for settlement calculations at higher strains. The current approach to deducing operational soil stiffness for design purposes requires reconsideration.

1 INTRODUCTION

Footings and raft foundations remain widely used in many countries. Local design practices typically follow the Code of Practice for Foundations (BD, 2017), specifically Clause 2.2. It permits the determination of the allowable bearing capacity (q_a) either through presumed values in Table 2.1 of the 2017 Code or by rational design methods based on sound engineering principles for calculating the ultimate bearing capacity (q_u). Clause 2.2.4 suggests a bearing capacity equation derived from the work of Vesic (1973, 1975):

$$q_u = Q_u/B'L' = c'N_c\zeta_{cs}\zeta_{ci}\zeta_{cg}\zeta_{ct} + qN_q\zeta_{qs}\zeta_{qi}\zeta_{qg}\zeta_{qt}B'L' + 0.5B'\gamma_s'N_\gamma\zeta_{\gamma s}\zeta_{\gamma i}\zeta_{\gamma g}\zeta_{\gamma t} \quad (1)$$

where

where	N_c, N_γ, N_q	= general bearing capacity factors
	Q_u	= ultimate resistance against bearing capacity failure which determine the capacity of a long strip footing
	c'	= effective cohesion of soil
	γ_s'	= effective unit weight of soil
	q	= overburden pressure in the ground adjacent to the foundation and at same level as the base of the foundation
	B	= least dimension of footing
	L	= longer dimension of footing
	B'	= B-e_B
	L'	= L-2e_L
	e_B	= eccentricity of load along B direction
	e_L	= eccentricity of load along L direction
	ζ_{cs}, ζ_{qs} $\zeta_{\gamma s}$	= influence factors for shape of foundation
	ζ_{ci}, ζ_{qi}, $\zeta_{\gamma i}$	= influence factors for inclination of load
	ζ_{cg}, ζ_{qg}, $\zeta_{\gamma g}$	= influence factors for ground surface

ζ_{ct}, ζ_{qt}, $\zeta_{\gamma t}$ = influence factors for tilting of foundation base

According to Clause 13 of the General Requirements for Foundation Works SE-SC1 (BD, 2020) and Section 17(1) of the Buildings Ordinance, engineers must verify the adequacy of the founding stratum's allowable bearing capacity through static plate load tests. The procedures and acceptance criteria for these tests are detailed in Clause 8.2 of the Code of Practice for Foundations (BD, 2004 and revised in 2017). However, recent research suggests that the q_u calculated using Equation [1] may be overestimated for large rafts. Furthermore, the test procedures outlined in the 2017 Code may not adequately verify the founding stratum's suitability. For instance, the elastic modulus E back-calculated from load-settlement data often differs from the design values used in settlement calculations.

2 THE BEARING CAPACITY EQUATION

The analysis of ultimate loads for shallow foundations dates back nearly 170 years. Early work on the subject was initiated by Rankine (1857), followed by Prandtl (1920) who studied the plastic deformation of metals. Caquot (1934) first applied plasticity theory to foundation analysis. Buisman (1940) extended this to soils with weight, introducing the superposition of the weight term (N_γ) with the cohesion (N_c) and surcharge (N_q) terms in the bearing capacity equation. Terzaghi (1943) identified three principal modes of bearing capacity failure and proposed the basic equation $q_u = cN_c + qN_q + ½\gamma BN_\gamma$. Meyerhof (1963) expanded on these ideas and derived practical formulae for designing both rigid and flexible foundations. Hansen (1970) proposed a general bearing capacity equation to account for footings on sloping ground or with tilted bases. Vesic (1973) refined Hansen's equation and derived Equation [1]. The equations developed by Meyerhof, Hansen, and Vesic remain widely used today.

The Bearing Capacity Factors N_c, N_q, and N_γ

Over the years, numerous correction factors for N_c, N_q and N_γ have been proposed. These factors are typically semi-empirical and account for specific effects by multiplying the three terms in the bearing capacity equation. Analytical methods include: the limit equilibrium techniques (Terzaghi, 1943; Meyerhof, 1951), the slip-line methods (Sokolovski, 1960), the limit analysis methods (Chen and Davidson, 1973), and the finite element methods (Griffith, 1982). Experimental methods, such as laboratory tests (Schanz and Vermeer, 1996), full-scale in-situ tests (Briaud and Gibbens, 1994), and centrifuge tests (Okamura et al., 2002), have also been employed. However, these methods have limitations. For example, model footings suffer from scale effects, while full-scale tests are costly and time-consuming. Centrifuge testing, though promising, has not gained widespread adoption due to challenges in accurately simulating soil behaviour.

Okamura et al. (2002) identified three key factors that reduce bearing capacity: the loading conditions, scale effects and footing shape effects. Nguyen et al. (2016) noted that most bearing capacity equations are limited to simple footing shapes and uniform ground conditions, neglecting scale effects. Taghvamanesh and Moayed (2021) reviewed 60 models and found that while N_c and N_q are well-correlated and straightforward to compute, N_γ values vary widely. They attributed this discrepancy to differences in assumptions about the soil wedge beneath the footing (Das, 2004) and the computation of passive earth pressure (Zhu et al., 2001). They concluded that N_γ depends not only on the friction angle (ϕ) but also on footing width (B), dilatation angle (ψ), and relative density (D_r). Specifically, N_γ decreases as B and D_r increase, highlighting the importance of scale and shape effects.

The Scale Effect

Equation [1] suggests that $q_u = ½\gamma BN_\gamma$ when c is zero and q is negligible. This implies that q_u increases linearly with BN_γ or B, which is unrealistic if N_γ depends solely on ϕ. De Beer (1965) was among the first to recognize the scale effect, reporting that the strength envelope in triaxial tests on sand is non-linear and characterized by a secant ϕ that increases with D_r. Vesic (1973) attributed the decrease in strength with foundation size to the curvature of the Mohr envelope, progressive rupture along slip lines, and presence of weak zones or seams in soil deposits. Habib (1974) introduced a modified bearing capacity factor $N^*_\gamma = N_\gamma + 400/n$ where $n = B/\delta$ (with δ being the mean grain size in mm). The Architectural Institute of Japan (AIJ, 1988 and 2001) proposed a modified equation incorporating shape coefficients (α, β) and a scale factor (η). Shiraishi (1990) suggested $N^*_\gamma = 0.71N_\gamma/B^{0.2}$ while Bowles (1997) recommended a reduction factor $r_\gamma = 1 - 0.25\log(B/\kappa)$ where $B \geq 2$m and $\kappa = 2.0$. Ueno et al. (1998) highlighted the stress level effect on shear strength, noting that mean stress beneath foundations ranges from $2\gamma B$ to $10\gamma B$, affecting the internal friction angle. Cerato and Lutenegger (2006) demonstrated that N_γ decreases with B and increases with D_r, with D_r having a more pronounced influence than δ. Lau and Bolton (2011a, 2011b) introduced a variable ϕ analysis, showing that secant ϕ varies linearly with the logarithm of mean effective stress in granular soils.

The Shape Effect

For non-rectangular foundation shapes, obtaining analytical solutions is challenging. Engineers have relied on semi-empirical methods, often based on comparative loading tests with footings of different shapes. These tests show that shape factors depend primarily on ϕ and other parameters, often expressed as constants or simple functions of foundation geometry (B and L). Some examples are given in Table 1. This implies that shape and scale effects are interrelated.

Table 1 – Shape Factors Proposed by Various Authors and the Calculated q_u

Authors	ζ_{cs}	ζ_{qs}	$\zeta_{\gamma s}$	q_u (kPa)
Myerhoff (1963)	$1+0.2K_p(B/L)$ for any ϕ $K_p = \tan^2(45^o+\phi/2)$	1 for $\phi = 0^o$ $1+0.1K_p(B/L)$ for $\phi > 10^o$ $K_p = \tan^2(45^o+\phi/2)$	1 for $\phi = 0^o$ $1+0.1K_p(B/L)$ for $\phi > 10^o$ $K_p = \tan^2(45^o+\phi/2)$	2,507
Hansen (1970)	$0.2(B/L)$ for $\phi = 0^o$ $1+(N_q/N_c)(B/L)$ for $\phi \neq 0^o$	$1+(B/L)\tan\phi$	$1-0.4(B/L) \geq 0.6$	1,381
Vesic (1973)	$1+(N_q/N_c)(B/L)$	$1+(B/L)\tan\phi$	$1-0.4(B/L) \geq 0.6$	1,381
Perau (1997)	-	$1+1.6\tan\phi(B/L)[1+(B/L)^2]$	$1 / [1+(B/L)]$	1,128
Zhu and Michalowski (2005)	-	-	$1+(0.6\sin^2\phi-0.25(B_f/L_f)$ for $\phi \leq 30^o$ $1+(1.3\sin^2\phi-0.5(L_f/B_f)^{1.5}\exp(-L_f/B_f))$ for $\phi > 30^o$	2,308
EN7 (2005)	$1+0.2K_p(B/L)$ for $\phi = 0$ ζ_{cs} $(N_q-1)/(N_q-1)$ for $\phi \neq 0^o$	$1+(B/L)\sin\phi$	$1-0.3(B/L)$	1,532

The Elastic Modulus of Soil

According to Lau and Bolton (2011a), the secant ϕ is not a material constant for granular soils but is highly sensitive to the mean stress level. The vertical stress in the supporting soil ranges from the bearing capacity (q_u) directly underneath the footing to the overburden pressure (q) at the edge. The contact pressure distribution under the footing is also highly non-uniform. Consequently, stress variations cause the mobilized angle of friction (ϕ_m) to vary significantly from point to point. Bolton (1986) attributed this variation in secant ϕ to the strength dilatancy of sands and the crushing of particles at the high end of the stress range. A factor of 50 in confining stress would result in a factor of about 7 in the stiffness of granular soils.

Summary

This literature review has outlined the derivation and limitations of Equation [1], alongside recent findings on scale and shape effects in raft foundation design. Following the implementation of the 2017 Code, feedback from engineers and practitioners has highlighted several practical challenges and concerns. To further explore these issues, the following sections will examine a case study involving the design of a raft foundation from a real-world project. This case study will illustrate key observations related to the 2017 Code and provide actionable recommendations for improvement.

3 THE RAFT FOUNDATION DESIGN

The project involves the design and construction of a 2-storey building with a green roof, as depicted in Figure 1, along with an annex building located nearby. Borehole data reveals that the geology beneath the 2-storey building consists of varying thicknesses of fill, colluvium, alluvium, and completely decomposed granite (CDG) to highly decomposed granite (HDG), followed by rock (Figure 1(b)). Given the relatively low design loading, a shallow raft foundation appears to be the most suitable option. An alternative option, such as large-diameter bored piles on Category 1(d) rock, was considered but deemed less favorable due to the uncertainty in the depth of Category 1(d) rockhead. Driven H-piles were ruled out due to the potential vibration impact on nearby Mass Transit Railway tunnels.

A 0.8-meter-thick leveled raft foundation resting on CDG was designed. The design parameters are summarized in Table 2. The raft is assumed to be rigid, while the CDG is modeled as perfectly elastic-plastic in the analysis. The allowable settlement (S_a) for the project is 30.0 mm. Using the software SAFE, the maximum bearing pressure (q_{max}) of the raft foundation was determined to be 383 kPa at the edge (Figure 1(c)). Assuming $E = 1.5N$ where N is the number of blows in standard penetration test, the maximum settlement (S_{max}) was calculated as 26.2 mm using Schmertmann's (1970) method, as recommended in GEO Publication No. 1/2006 (GEO, 2006). Since the raft foundation is irregularly shaped, the calculation of B and L is based on the largest inscribed rectangle, as per Note (6) of the Clause and Figure 2.4 in the 2017 Code. Thus, B = 14.6 m and L = 19.2 m were adopted, with e_B and e_L ignored (Figure 1(d)). The calculated q_u was applied to the entire raft. Using equation [1], q_u and the q_a were determined to be 1,381 kPa and 460 kPa, respectively, ignoring the 0.8 m overburden. Since $q_a > q_{max}$ (383 kPa), the design is deemed acceptable.

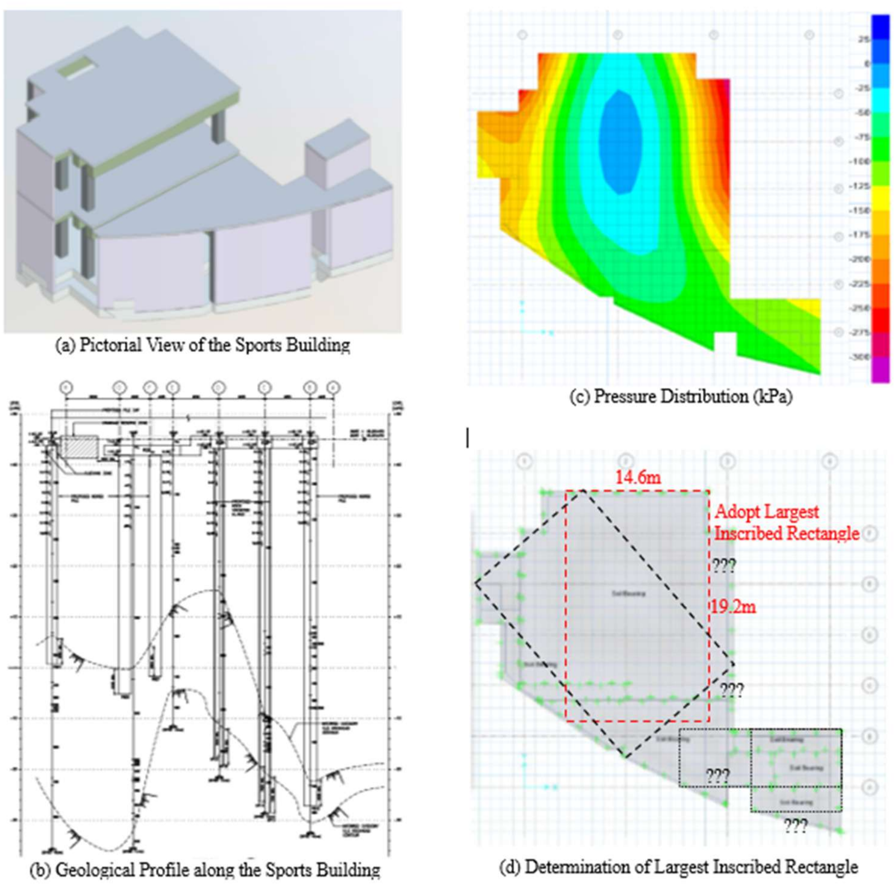

Figure 1 – General View, Geology and Soil Pressure Distribution of the Building Structure

Table 2 – Design Parameters for the Raft Foundation

Design Parameters	Values
Existing Ground Level (mPD)	+45.7
Design Ground Water Level (mPD)	+45.7
Formation Level (mPD)	+44.9
Design Vertical Load (kN)	33,348
Design Horizontal Load (kN)	218
Eccentricity of Load along Least Dimension e_B (m)	4.02
Eccentricity of Load along Longer Dimension e_L (m)	4.33
Friction Angle ϕ' of CDG (degree)	32
Cohesion of c' of CDG (kPa)	0
Bulk Density of CDG (kN/m^3)	19
Poisson Ratio ν of CDG	0.3

4 THE PLATE LOAD TEST PROCEDURES AND ACCEPTANCE CRITERIA

According to Clause 8.2 of the 2004 Code, the maximum test load (proof load) shall be $3W$, where W is the allowable working pressure multiplied by the area of the loading plate: 3 × 383 kPa × π × 0.15 m² = 81.22 kN. This implies that the maximum test pressure under the loading plate is $3q_{max}$ = 3 × 383 kPa = 1,149 kPa, which is less than q_u (1,381 kPa) as determined by the bearing capacity equation [1]. The acceptance criteria specify that S_{max} shall not exceed S_p, calculated as: $S_p = 3\ S_f \times [(B + b) / 2B]^2 \times (m + 0.5) / (1.5m)$, where S_f = allowable settlement of the footing under the allowable working load, b = diameter or least dimension of the plate, and m = length-to-width ratio of the footing ($m \geq 1$). For m = 19.2 m / 14.6 m = 1.3, S_p is calculated as: 3 × 30 mm × [(14.6m+0.3m)/(2×14.6m)]^2 ×(1.3+0.5)/(1.5×1.3) = 21.6mm.

However, the 2017 Code revised the proof load to ≥ $3W_t$, where $W_t = ⅓\ (q_u)_{plate}$ x A_{plate}. Here, $(q_u)_{plate}$ = ultimate bearing capacity of the test plate based on N_c and N_γ, and A_{plate} = area of the test plate. As explained in Clause H8.2(A) of the Explanatory Handbook to the Code (HKIE, 2017), N_q is ignored because no adjacent surcharge is applied during the plate load test. For CDG, c' = 0 kPa and N_c = 0. Equation [1] simplifies to: $(q_u)_{plate} = 0.5B'\gamma_s' N_\gamma \zeta_{\gamma s} \zeta_{\gamma i} \zeta_{\gamma g} \zeta_{\gamma t}$ = 0.5 × 0.3 m × 19 kN/m³ × 30.2 × 0.6 × 1 × 1 × 1 = 52 kPa. The proof load is calculated as: 3 × ⅓ ×52 kPa × π × 0.5 m² = 3.65 kN. The acceptance criteria specify that S_{max} shall not exceed $S_p = 0.15B$ = 0.15 × 300 mm = 45.0 mm. The above calculations are summarized in Table 3. While the designed q_{max} of the raft foundation is 383 kPa, the bearing soil is required to be tested to 1,149 kPa (or 81.22 kN) under the 2004 Code but only to 52 kPa (or 3.65 kN) under the 2017 Code. At the same time, the acceptable S_p increases from 21.6 mm to 45.0 mm. This discrepancy warrants further investigation.

Table 3 – Summary of Design Calculations

	Design Model	Bearing Capacity Equation	Plate Load Test BD (2004)	Plate Load Test BD (2017)
Bearing Pressure	q_{max} = 383kPa	q_u = 1,381kPa q_a = 460kPa	Testing plate pressure = 3*q_{max} =1,149kPa	Testing plate pressure = $(q_u)_{plate}$ = 52kPa
Test Load	-	-	$3W$ = 81.22kN	$3W_t$ = 3.65kN
Settlement	S_{max} = 26.2mm	-	Allowable S_p = 21.6mm	Allowable S_p = 45.0mm

5 OBSERVATIONS AND DISCUSSIONS

The Scale Effect

Figure 2 illustrates the variation of q_u with B, keeping the B/L ratio constant at 0.76 (= 14.6 m / 19.2 m). Assuming no eccentric load for simplicity, and using a mean grain size of 0.1 mm in the Habib (1974) equation and B_0 = 5 m in the AIJ (1988, 2001) equation, the following observations were made: The Habib (1974) prediction closely aligns with Vesic's (1973) results and is insensitive to the mean grain size. The AIJ (1988, 2001), Shiraishi (1990), and Bowles (1997) predictions show an increase in q_u with B, but the rate of increase diminishes as B grows, highlighting the significance of the scale effect for large footings. For the raft foundation in this project, q_u was calculated as 1,381 kPa using equation [1] without considering the scale effect. However, when the scale effect is considered, q_u reduces to 958 kPa (69%), 574 kPa (42%), and 1,079 kPa (78%) based on the AIJ (1988, 2001), Shiraishi (1990), and Bowles (1997) methods, respectively. Consequently, the q_a varies from 193 kPa (= 460 kPa × 42%) to 359 kPa (= 460 kPa × 78%), which is less than the designed q_{max} = 383 kPa. This finding aligns with Table 2.1 in the 2004 and 2017 Codes, which specify presumed allowable vertical bearing pressures of 250 kPa for very dense non-cohesive soil (SPT > 50) and 1,000 kPa for intermediate soil (SPT ≥ 200).

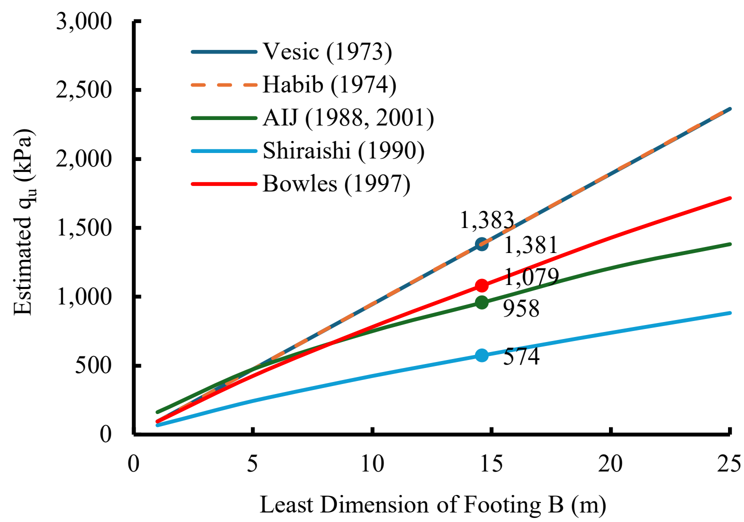

Figure 2 – Variation of q_u with B

The Shape Effect

For irregularly shaped raft foundations, the calculation of B and L in the Code is based on the largest inscribed rectangle. However, several questions arise: Is the largest inscribed rectangle determined by area or perimeter (see Figure 1(c))? Should eccentricities e_B and e_L be ignored or calculated from the largest inscribed rectangle? Should the calculated q_u be applied to the entire raft, or should other areas be ignored? If not, should the raft be divided into multiple rectangles, each with its own q_u? These questions highlight that the calculation of B and L is more of an art than a science, relying heavily on experience and interpretation.

Figure 3 demonstrates the shape effect on q_u. Keeping B constant at 14.6 m, Meyerhoff (1963) suggests an increase in q_u as B/L increases, while Zhu and Michalowski (2005) indicate a decrease in q_u as B/L increases, with a minimum q_u at B/L = 0.6 and a slight increase for B/L > 0.6. Other researchers, including Hansen (1970), Vesic (1973), Perau (1997) and EN7 (2005), show a decrease in q_u as B/L increases. For the raft foundation in this project, q_u ranges from 1,128 kPa to 2,507 kPa for B/L = 0.76, based on shape factors proposed by various authors. However, these values could change if the shape of the raft changes, underscoring the importance of accurately determining the largest inscribed rectangle as per the 2017 Code.

Shape Factor (B/L)

Figure 3 – Effect of Shape Factor on q_u

The Static Plate Load Test

The limitations of the plate load test are discussed in Clause H8.2 of the Explanatory Handbook to the Code of Practice for Foundations (HKIE, 2014 and 2017) and Clause 3.4 of GEO Publication No. 1/2006 (GEO, 2006). According to Clause 8.2(1) of the 2017 Code, the static plate load test is intended to verify q_a and E used in settlement calculations through back-analysis. Figure 4 overlays the test loads and allowable S_p with the typical stress-strain curve of a cohesionless soil. In the 2004 Code, the test load is three times the working pressure $3W$ (1,149 kPa), placing it in the non-linear portion of the stress-strain curve. Since soil is typically modeled as elasto-plastic in design, it is unsurprising that the anticipated S_p may exceed the allowable S_p when the test load approaches q_u (1,381 kPa). In contrast, the 2017 Code reduces the test load to three times the ultimate bearing capacity of the test plate $3W_t$ based on N_c and N_γ only, resulting in a much smaller load (52 kPa, or 4.5% of the value in 2004 Code). This load falls in the early linear portion of the stress-strain curve, yet the permitted S_p increases from 21.6 mm to 45.0 mm, which is counterintuitive. As a result, the test to verify the adequacy of the founding stratum's allowable bearing capacity under the 2017 Code may not be meaningful.

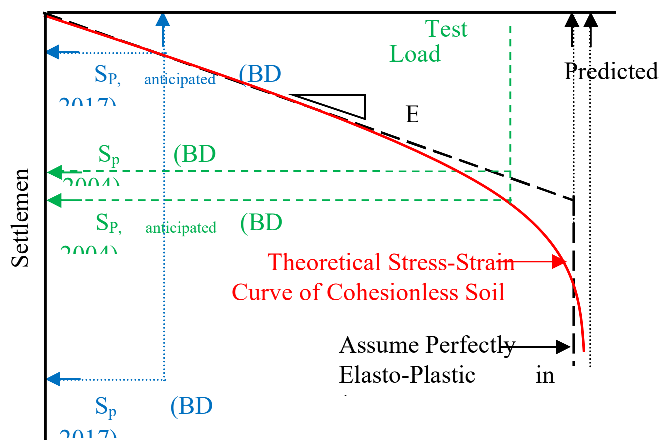

Figure 4 – Schematic Representation of the Static Plate Load Test (Not to Scale)

The Back-Calculated Elastic Modulus

Figure 5(a) illustrates the determination of the elastic modulus or stiffness of soil. In theory, it is equal to the slope of the stress-strain line. If this stress-strain line is linear, the slope is easily determined as the ratio of the stress along an axis to the strain along that axis within the range of elastic soil behavior, and is shown as the initial tangent modulus. However, when the soil behavior becomes non-linear, the gradient of the stress-strain line decreases progressively. The gradient at that point, known as the tangent modulus, represents the soil stiffness at a specific stress level σ. If one connects the end points of the stress-strain diagram at the point of interest with a straight line, the slope of that straight line is the secant modulus, which is traditionally used to back-calculate the soil modulus in the 2017 Code. As shown in Figure 5(b), soil is not a perfectly elastic-plastic material, and the secant modulus determined will therefore decrease as the strain increases. Since the test load in the 2017 Code is very small and should be in the early linear portion of the stress-strain curve, the elastic modulus back-calculated from the load-settlement behavior should be close to the $E_{initial}$. This value is stiffer than the design value at larger strains due to the degradation of the elastic modulus, and the settlement calculation will therefore be underestimated.

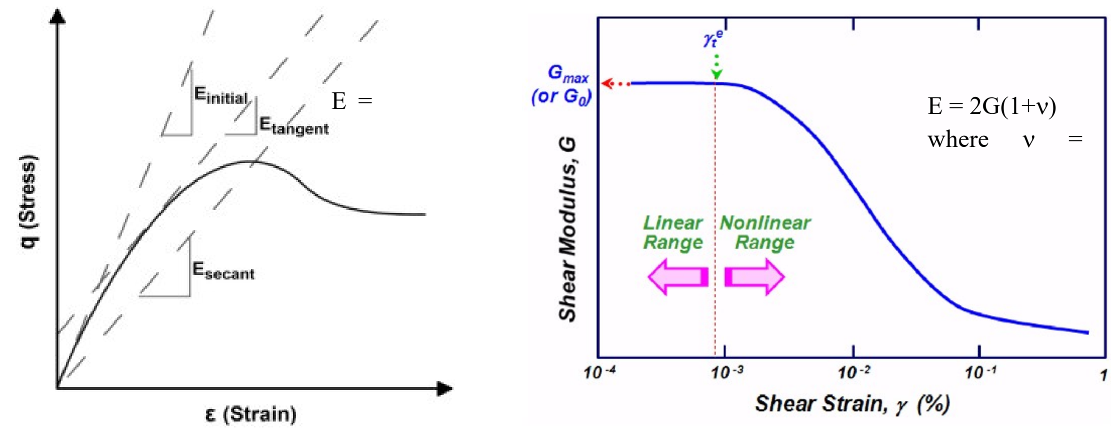

(a) Determination of Elastic Modulus (b) Degradation of Modulus

Figure 5 - Non-Linear Stress-Strain Characteristics of Soil

6 CONCLUSIONS AND RECOMMENDATIONS

The static plate load test is essential for verifying the adequacy of the founding stratum and back-calculating the soil's elastic modulus (E) from load-settlement behavior for settlement analysis. The 2017 Code bases the test load on the working pressure of the test plate, accounting for plate-scale capacity, whereas the 2004 criteria risk overloading the plate due to its requirement of three times the working pressure. Incorporating the plate-size dependent factors could better capture the observed non-linear soil behavior and size effects. However, the discrepancies between the 2004 and 2017 Codes raise concerns about test validity and interpretation.

In the 2004 Code, the test load is set at three times the working pressure, which is often high enough to place the soil in the non-linear portion of its stress-strain curve. Since soil is typically modeled as elasto-plastic for simplicity in design, the anticipated settlement (S_{max}) may exceed the permitted limits (S_p), particularly when the test load approaches the ultimate bearing capacity (q_u). Conversely, the 2017 Code specifies a test load of three times the ultimate bearing capacity of the test plate, derived solely from the bearing capacity factors (N_c and N_γ). This load is often too small, keeping the soil in the linear elastic range, while the permitted settlement (S_p) is significantly larger than that in the 2004 Code. As a result, the test may fail to meaningfully verify the allowable bearing capacity, as the outcomes are almost always deemed acceptable. A more balanced approach is to revert the test load to 3 times the working pressure, but the allowable S_{max} is revised to $\leq S_p = 3S_f$ x $[(B+b)/2B]^2$ x $(m+0.5)/(1.5m) + \delta$. This adjustment δ is not for the purpose to reconcile differences in influence depth, but is the degree of mobilization to cater for the elasto-viscous behavior at large load. For simplicity, δ can be specified as a settlement limit equal to the quake which is the static relative movement between pile and soil that is required to mobilize the plastic resistance. Literature reviews by Soares et al. (1984) indicated that quake equal to 2.5mm is widely used. Larger value can be adopted for larger acceptable viscous behavior. For a very large raft foundation, the allowable bearing capacity should be capped based on local test data and the test can be removed entirely.

Soil stiffness is not a material constant, as the secant modulus (ϕ) varies with mean stress. Due to modulus degradation, the elastic modulus back-calculated from the load-settlement data tends to be stiffer than the design value at larger strains. Thus, the conventional approach to deriving an operational soil stiffness requires reconsideration. Improved estimation methods such as stress-dependent models or advanced testing (e.g., pressuremeter or seismic tests) could be adopted to better reflect design conditions.

In summary, clearer guidelines or alternative methods for calculating B and L should be provided, potentially using probabilistic approaches or case studies to reduce ambiguity. Future research should prioritize large-scale field tests to validate the bearing capacity and settlement predictions, investigate the B/L versus q_u relationship and δ across different soils and loading conditions, and develop standardized methods for estimating soil stiffness under varying stress levels. These advancements would lead to more reliable and efficient raft foundation design practices.

Acknowledgement

I would also like to express my gratitude to The MTR Corporation Limited for the permission to use some raw design data taken from a project.

References

AIJ, 1988, 2001. Recommendations for design of building foundations. *Architectural Institution of Japan*.

BD. 2004, 2017. Code of practice for foundations. *Buildings Department, The Government of the HKSAR.*

BD. 2020. The general requirements for foundation Works – SE-SC1 (9/2020). The Common Conditions and Requirements, *Buildings Department, The Government of the HKSAR.*

Bolton, M. D. 1986. The strength and dilatancy of sands. *Geotechnique*, 36(1), pp. 65-78.

Bowles, J. E. 1997. *Foundation analysis and design*. McGraw-Hill, 5th Edition, McGraw Hill, Singapore.

Briaud, J. L. and Gibbens, R. (1994). Test and prediction results for five large spread footings on sand. *ASCE Geotechnical Special Publication 41, Predicted and Measured Behavior of Five Spread Footings on Sand*, Briaud J L and Gibbens R (Eds) ASCE, New York, pp. 92-128.

Buisman, A. S. K. 1940. *Grondmechanica*. Waltman, Delft, The Netherlands.

Caquot. A. 1934. *Equilibrium des Massifs a frottement Interne*. Gauthier-Villars, Paris, France, pp. 1-91.

Cerato, A. B. and Lutenegger, A. J. 2006. Scale effects of shallow foundation bearing capacity on granular material. *BGA International Conference*.

Chen, W. F. and Davidson, H. L. 1973. Bearing capacity determination by limit analysis. *Journal of the Soil Mechanics and Foundations Division, ASCE* 99(6), pp. 433-449.

Das, B. M. 2004. *Soil Mechanics.* The Engineering Handbook, Second Edition, pp. 81-1 to 81-7.

De Beer, E. E. 1965. The scale effect on the phenomenon of progressive rupture in cohesionless soils. *Proceedings, Sixth International Conference on Soil Mechanics and Foundation Engineering,* Montreal, Canada, 2, pp. 13-17.

De Beer, E E 1970. Experimental determination of the shape factors and the ultimate bearing capacity factors of sand. *Geotechnique,* 20(4), pp. 387-411.

EN7. 1997. *Geotechnical design – Part 1: General rules.* BS EN 1997-1:2004, Eurocode 7.

GEO. 2006. *Foundation Design and Construction. GEO Publication No. 1/2006,* Geotechnical Engineering Office, Civil Engineering and Development Department, The Government of the HKSAR.

Griffith, D. V. 1982. Computation of bearing capacity factors using finite elements. *Geotechnique,* (32)3, pp. 195-202.

Habib, P. A. 1974. Scale effect for shallow footings on dense sand. *Journal of the Geotechnical Engineering Division, ASCE,* 100(GT1), pp. 95-99.

Hansen, J. B. 1970. A revised and extended formula for bearing capacity. *Bulletin of Danish Feotechnical Insitute*, 8, pp. 5-11.

HKIE. 2014, 2017. *An explanatory handbook to the code of practice for foundations*. The Hong Kong Institution of Engineers, The Government of the HKSAR.

Lau, C. K. and Bolton, M. D. 2011a. The bearing capacity of footings on granular soils. I: Numerical analysis. *Geotechnique,* 61(8), pp. 627-638.

Lau, C. K. and Bolton, M. D. 2011b. The bearing capacity of footings on granular soils. II: Experimental evidence. *Geotechnique,* 61(8), pp. 639-650.

Meyerhof, G. G. 1951. The ultimate bearing capacity of foundations. *Geotechnique,* 1(2), pp. 301-332.

Meyerhof, G. G. 1963. Some recent research on the bearing capacity of foundations. *Canadian Geotechnical Journal,* 1, pp. 16-26.
Nguyen, D. L., Ohtsuka, S., Hoshina, T. and Isobe, K. 2016. Discussion on size effect of footing in ultimate bearing capacity of sandy soil using rigid plastic finite element method. *Soils and Foundations, Japanese Geotechnical Society,* 56(1), pp. 93-103.
Okamura, M., Mihara, A., Takemura, J. and Kuwano, J. 2022. Effects of footing size and aspect ratio on the bearing capacity of sand subjected to eccentric loading. *Soils and Foundations, Japanese Geotechnical Society,* 42(4), pp. 43-56.
Perau, E. W. 1997. Bearing capacity of shallow foundations. *Soils and Foundations, Japanese Geotechnical Society,* 37(4), pp. 77-83.
Prandtl, L. 1920. Uber die Eindringungsfestigkeit (Harte) Plastischer Baustoffe und die Festigkeit von Schneiden. *Zeitschrift fur Angewandte Mathematik und Mechanik*, Berlin, 1(1), pp. 15-20.
Rankine, W. 1857. On the stability of loose earth. *Philosophical Transactions of the Royal Society of London*, 147.
Schanz, T. and Vermeer, P. A. 1996. Angles of friction and dilatancy of sand. *Geotechnique*, 46(1), pp. 145-151.
Schmertmann, J. 1970. Static cone to compute static settlement over sand. *Journal of Soil Mechanics and Foundation Division, ASCE*, 96, pp. 1011-1043.
Shiraishi, S. 1990. Variation in bearing capacity factors of dense sand assessed by model loading tests. *Soils and Foundations, Japanese Geotechnical Society*, 30(1), pp. 17-26.
Soares, M. M., Matos, S. F. D. and de Mello, J. R. C. 1984. Pile driveability studies, pile driving measurements. *Proceedings of the Second International Conference on the Applications of Stress-Wave Theory of Piles, Stockholm*, pp. 64-71.
Sokolovski, V. V. 1960. *Statics of soil media*. Butterworth Scientific Publications, London, UK.
Taghvamanesh, S. and Moayed, R. Z. 2021. A review on bearing capacity factor N_γ of shallow foundations with different shapes. *World Academy of Science, Engineering and Technology, International Journal of Geotechnical and Geological Engineering*, 15(8).
Terzaghi, K. 1943. *Theoretical soil mechanics*. 5th Edition, John Wiley and Sons Inc., New York.
Ueno, K., Miura, K. and Maeda, Y. 1998. Prediction of ultimate bearing capacity of surface footings with regard to size effects. *Soils and Foundations, Japanese Geotechnical Society*, 38(3), pp. 165-178.
Vesic, A. S. 1973. Analysis of ultimate loads of shallow foundations. *Journal of the Soil Mechanics and Foundations Division, ASCE*, 99(1), pp. 45-73.
Vesic, A. S. 1975. *Bearing capacity of shallow foundations. Foundation Engineering Handbook*, Edited by Winterkorn, H.F. and Fang, H.Y., Van Nostrand Reinhold, New York, pp. 121-147.
Zhu, D. Y., Lee, C. F. and Jiang, H. D. 2001. A numerical study of the bearing capacity factor N_γ. *Canadian Geotechnical Journal*, 38(5), pp. 1090-1096.
Zhu, M. and Michalowski, R. L. 2005. Bearing capacity of rectangular footings on two-layer clay. *Proceeding of the 16th International Conference on Soil mechanics and Geotechnical Engineering, Osaka*, pp. 997-1000.

Innovative Management of Construction Waste in Hong Kong

Albert T. Yeung
National Yang Ming Chiao Tung University, Hsinchu City, Taiwan
P.L. Ng
The University of Hong Kong, Hong Kong, China
Wing Shun Kwan
California State University, Los Angeles, California, U.S.A.

ABSTRACT

The generation of construction waste is inevitable in coping with the rapid economic growth of municipalities worldwide. Proper construction waste management is critical, as it contributes a significant proportion of waste materials disposed of in landfills. The situation is particularly acute for economies such as the Hong Kong Special Administrative Region (HKSAR), China where land resources for landfilling are scarce. Most economies would thus maximize the reuse and recycling of construction waste to minimize the quantity of construction waste disposed of in landfills. The Government of the HKSAR adopted an innovative approach using information and communications technology (ICT) to achieve the goal. In addition to the quantity maximization and quality control of inert materials in construction waste for reuse and recycling, the approach also prevents illegal dumping of construction waste. Details of the approach and implementation are presented in this paper.

1 INTRODUCTION

Coping with the economic development and living quality improvement, demolition of old facilities and construction of new facilities are inevitable in most economies. Because of demolition and construction activities, tremendous amount of construction and demolition waste is generated. If such waste is disposed of in landfills, not only it is a waste of natural resources, it is also a waste of landfill space. If land resources available for landfills are scarce, the situation becomes more acute. However, the slowing down of demolition and construction activities may hinder the economic development of an economy. The need for proper measures to reduce the amount of construction and demolition waste is evident. The most effective measures to achieve the goal is to increase the amount of reuse and recycling of construction and demolition waste. From a government policy standpoint, incentives must be given to the stakeholders of the construction industry to encourage such activities and penalties be given to those who choose not to perform such activities deliberately. Moreover, monitoring of construction site activities is required to ensure that the incentives have not be abused and illegal activities have not been performed to avoid the penalties. An approach using information and communications technology (ICT) to accomplish these objectives is presented in this paper.

2 BACKGROUND

The Environmental Protection Department (EPD) of the Government of the HKSAR broadly classifies the waste generated in the HKSAR into 8 categories: (1) municipal solid waste; (2) food waste; (3) construction waste; (4) chemical waste; (5) clinical waste; (6) waste cooking oils; (7) special wastes include animal carcasses, livestock waste, radioactive waste, grease trap waste, sewage sludge and waterworks sludges; and (8) other solid waste comprises dredged mud and excavated materials.

The Waste Disposal (Charges for Disposal of Construction Waste) Regulation (Cap. 354N) of the law of the HKSAR defines "construction waste" as *any substance, matter or thing that is generated from construction work and abandoned, whether or not it has been processed or stockpiled before being abandoned, but does not include any sludge, screenings or matter removed in or generated from any desludging, desilting or dredging works.* It is usually a mixture of surplus materials from site clearance, excavation, construction, refurbishment, renovation, demolition, and road works. In the HKSAR, the inert materials in construction waste are denoted as "public fill". Public fill includes debris, rubble, earth, and concrete suitable for land reclamation and site formation. When properly sorted, materials such as concrete and asphalt can also be recycled for use in new construction. The remaining non-inert substances in construction waste include bamboo, timber, vegetation, packaging waste, and other organic materials. In contrast to public fill, non-inert substances in construction waste are unsuitable for land reclamation. After reusable/recyclable items have been extracted, these non-inert substances are disposed of in landfills. In this paper, these non-inert substances disposed of in landfills are denoted as "C&D waste" (Construction and Demolition waste) to distinguish themselves from the reusable "public fill". Therefore, maximization of the quantity of public fill and the extraction of reusable/recyclable items from non-inert substances of construction waste is necessary for proper construction waste management. Disposal of public fill at public fill reception facilities and mixed construction waste at sorting facilities have been the primary approaches for construction waste management implemented by the Government of the HKSAR.

Public fill reception facilities managed by the Civil Engineering and Development Department (CEDD) of the Government of the HKSAR include: (1) public filling areas – designated parts of a development project that accept public fill for reclamation purposes, (2) public filling barging points – strategically located public fill reception facilities that utilize barges to transport public fill, (3) public fill stockpiling areas – newly reclaimed land where public fill is temporarily stockpiled as the surcharging material to accelerate the consolidation settlement process, (4) fill banks – areas allocated for temporary stockpile of public fill for future use, and (5) C&D material recycling facilities – facilities process hard inert materials into recycled aggregates and granular materials for use in construction projects. Four public fill reception facilities are now in operation: Tseung Kwan O Area 137 Fill Bank, Tuen Mun Area 38 Fill Bank, Chai Wan Public Fill Barging Point, and Mui Wo Temporary Public Fill Reception Facility, as shown in Figure 1.

The historical generation rates of public fill and C&D waste are depicted in Figure 2. The generation rate of public fill is the sum of the public fill stored at public fill reception facilities for future use and that reused directly in construction projects. C&D waste includes waste concrete generated in concrete batching plants and disposed of in landfills. It can be observed in Figure 2 that more than 90% of construction waste generated in the HKSAR is recovered as public fill stored at public fill reception facilities or reused directly in construction projects.

The Waste Disposal (Charges for Disposal of Construction Waste) Regulation (Cap. 354N) came into operation on 1 December 2005. Construction waste producers, such as construction contractors, renovation contractors, or premises owners, must open a billing account with the EPD and pay for the construction waste disposal charges before using government waste disposal facilities, i.e., the Charge Scheme. The main contractor undertaking construction work under a contract with a contract sum of $1 million or above must open a billing account solely for the contract. The charge rates, as promulgated by the law, are tabulated in Table 1. It can be observed that the charge rates provide significant financial incentives for construction waste producers to reduce, sort, and recycle construction waste to preserve our valuable landfill space.

3 WASTE MANAGEMENT CHALLENGES IN THE HKSAR

Although more than 90% of construction waste generated in the HKSAR is recovered as public fill, the remaining C&D waste still contributes approximately 25% of the solid waste deposited in landfills, as depicted in Figure 3. Landfill space shortage and the lack of proper operation of the Charge Scheme remain problems facing the Government of the HKSAR. While expansions for the West New Territories (WENT) Landfill and North East New Territories (NENT) Landfill are underway, the additional capacity is projected to accommodate the waste disposal demands of the HKSAR only through the 2040s.

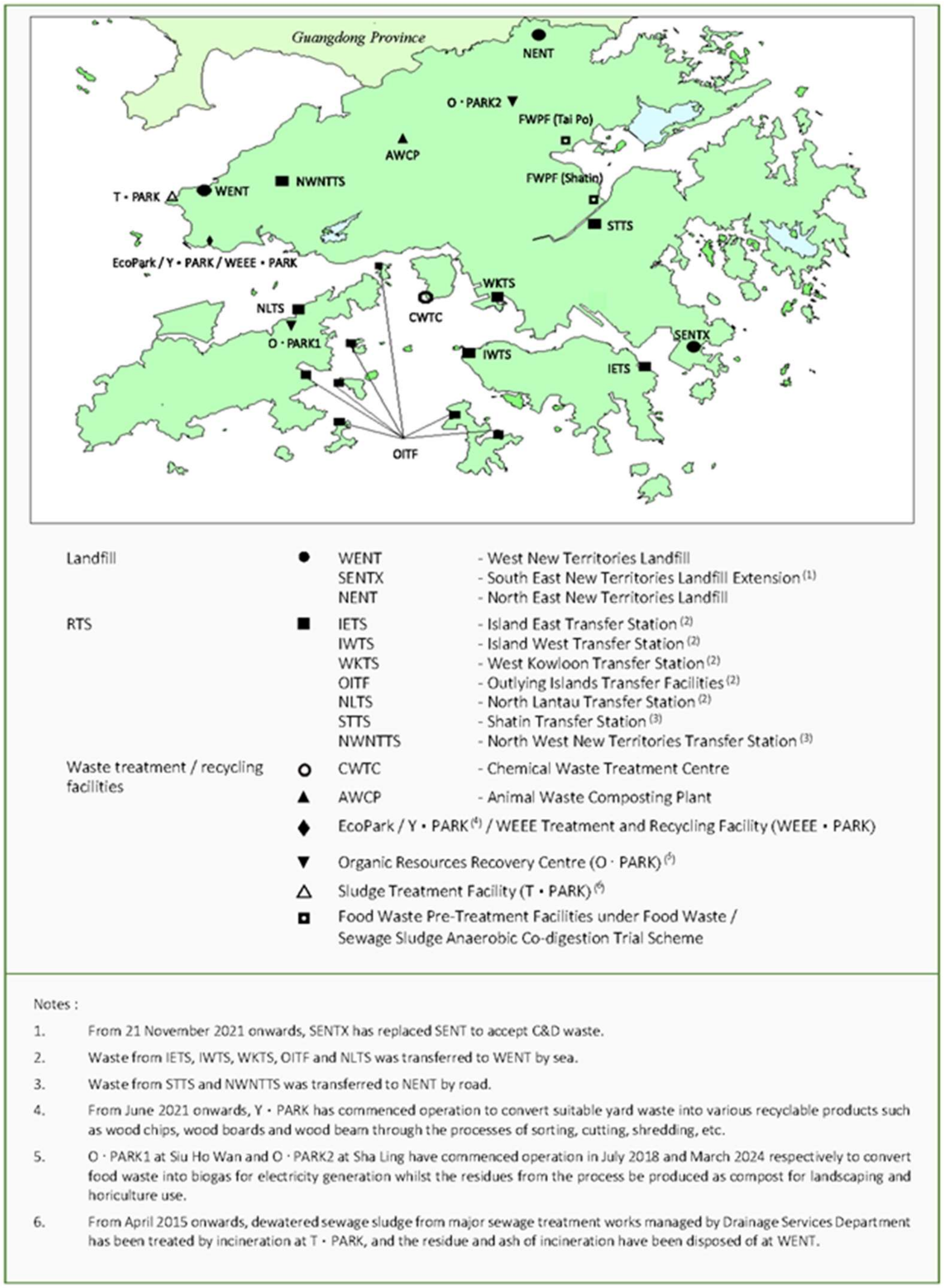

Figure 1: Waste management facility in the HKSAR (after EPD 2024)

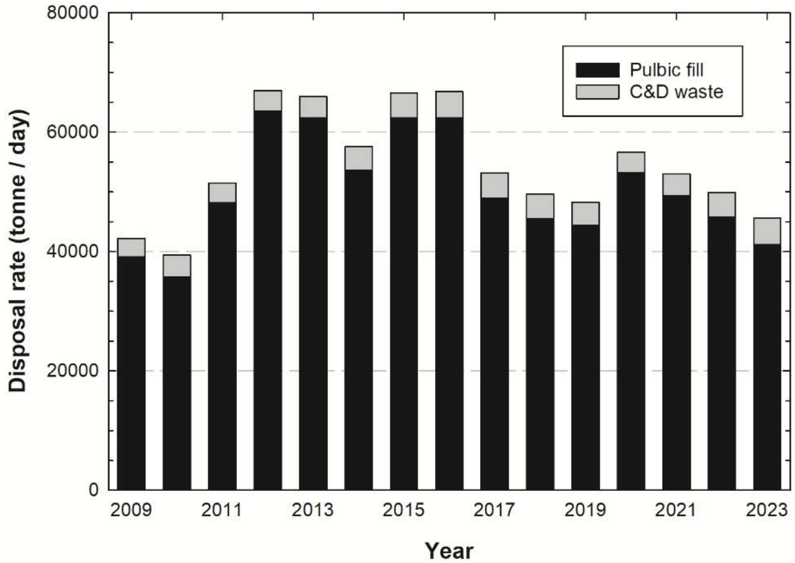

Figure 2: Historical generation rates of public fill and construction waste in the HKSAR

Table 1: Charge rates for construction waste disposal at different government waste disposal facilities

Government waste disposal facilities	Type of construction waste accepted	Charge / tonne
Public fill reception facilities	Consisting entirely of inert materials	\$71
Sorting facilities	Containing more than 50% by weight of inert materials	\$175
Landfills	Containing not more than 50% by weight of inert materials	\$200
Outlying islands transfer facilities	Containing any percentage of inert materials	\$200

3.1 Shortage of reclamation sites and landfill space

The total land area of the HKSAR, China, is 1,114.57 km^2, accommodating a population of 7.53 million (as of mid-2024) and a world-class financial, trading, and business center. However, most of the population is housed in 215 km^2 of urban development because of steep natural terrain and stringent planning controls. Over 400 km^2 of land have been designated protected areas, including country parks, special areas, and conservation zones. The concentration of population and economic activities in such a small area exert intense pressure on the environment. Thus, proper waste management is a significant challenge facing the Government of the HKSAR.

In May 2013, the then Environment Bureau of the Government of the HKSAR published the *Hong Kong blueprint for sustainable use of resources 2013–2022*, which develops a comprehensive strategy, targets, policies, and action plans for waste management for the upcoming 10 years to tackle the waste crisis of the HKSAR. It aims to reduce the per capita municipal solid waste (MSW) disposal rate by 40% by 2022. It proposes policies and actions in three areas to achieve the goal: (1) to undertake multiple and concurrent actions to drive behavioral change to reduce waste at source through policies and legislation, (2) to roll out targeted territory-wide waste reduction campaigns, and (3) to allocate resources to enhance waste-related infrastructure. Examples of newly launched waste-related infrastructure projects include the West New Territories Landfill Extension (WENTX) in Nim Wan, Tuen Mun, and Integrated Waste Management Facilities (IWMF) Phase 1 and 2 on an artificial island near Shek Kwu Chau and at the middle ash lagoon at Tsang Tsui, Tuen Mun, respectively.

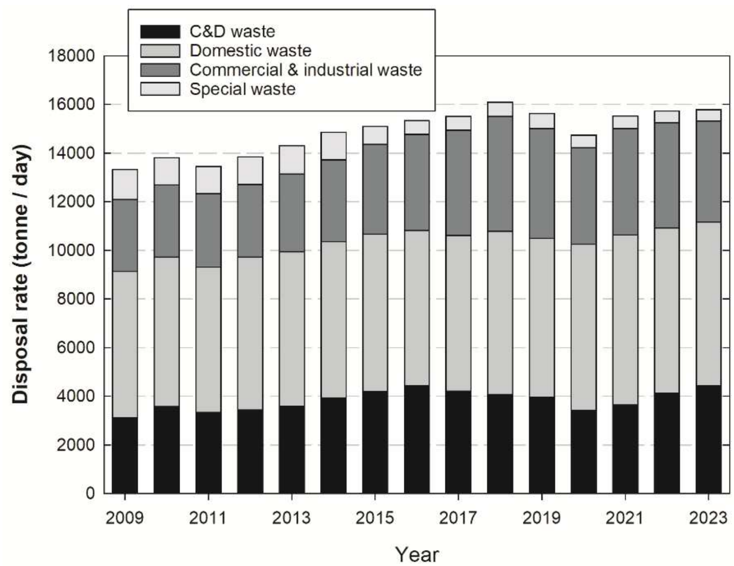

Figure 3: Historical disposal rate of total solid waste at landfills in the HKSAR

In February 2021, building on *Hong Kong: Blueprint for sustainable use of resources 2013-2022*, the then Environment Bureau announced the *Waste blueprint for Hong Kong 2035* (the Blueprint) to set out the vision of "Waste Reduction • Resources Circulation • Zero Landfill." The Blueprint outlines the strategies, goals, and measures to tackle the waste management challenge up to 2035. Under the vision, the Government will work with the industry and the community to move towards two primary goals. The medium-term goal is to gradually reduce the per capita MSW disposal rate by 40-45% and raise the recovery rate to approximately 55% by implementing MSW Charging, while the long-term goal is to move away from the reliance on landfills for direct waste disposal by developing adequate waste-to-energy facilities. The Government of the HKSAR will promote actions in six key areas to achieve these goals: (1) waste reduction, (2) waste separation, (3) resource circulation, (4) industry support, (5) innovation and cooperation, and (6) education and publicity, leading the advancement of various policies and measures and building a circular economy and a sustainable green living environment.

The HKSAR is running out of reclamation sites and landfill space to handle construction waste. If public fill storage capacity is insufficient and construction waste reduction measures are ineffective, more public fill will probably be diverted to landfills for disposal, and the useful lives of landfills will be further shortened. For sustainable development, the HKSAR cannot rely solely on reclamation sites to accept most of the inert construction waste. Therefore, the need for reduction, reuse, and recycling of construction waste is evident. Nevertheless, there will still be a substantial amount of materials that require disposal, either at public fill reception facilities or in landfills.

3.2 Quality control of public fill

It can be observed in Table 1 that there are significant financial incentives for main contractors to dispose of their construction waste at public fill reception facilities or sorting facilities in lieu of landfills. However, they may have to adjust their work processes to sort the inert materials from their construction waste. As a result, the quantity of construction waste disposed of in landfills has decreased tremendously since 2006. However, the disposal quantity fluctuates with the economy and the number of ongoing construction projects.

The Charging Scheme requires that construction waste disposed of at public fill reception facilities be 100% inert materials, i.e., rock, boulder, earth, soil, sand, concrete, asphalt, brick, tile, masonry, or used bentonite. Even construction waste disposed of at sorting facilities must contain more than 50% by weight of inert materials.

During large-scale construction projects, trucks continuously deliver waste to public fill reception or sorting facilities. Moreover, the numbers of public fill reception and sorting facilities are significantly less than the number of construction sites in progress. Therefore, each government waste disposal facility must support many construction sites simultaneously. It is challenging for the resident site staff at these facilities to determine the quality of construction waste, i.e., the proportion of inert materials in the construction waste delivered in trucks. Some unethical contractors may even mix other waste with construction waste to dispose of at public fill reception or sorting facilities to reduce waste disposal costs. However, verifying its original proportion of inert materials is impossible once the construction waste is dumped at these facilities. Mixing non-inert substances with public fill would jeopardize the future use of public fill as construction materials for new construction projects. Therefore, verifying the quality of construction waste is a practical implementation challenge of the Charging Scheme.

3.3 Quantity control of public fill

As tabulated in Table 1, the main contractor is charged by the weights of construction waste disposed of at different government waste disposal facilities. Therefore, it is necessary to determine the weights of construction waste disposed of at different government waste disposal facilities and to register the proper charges to the billing accounts of the main contractors efficiently and accurately. The issue is further complicated as the main contractor of a site may operate many trucks to deliver construction waste to different public fill reception facilities, sorting facilities, or landfills simultaneously depending on the proportion of inert materials in the truckload of construction waste and the progress of the construction work on site. Moreover, a main contractor may also have separate billing accounts for different construction sites as the legislation requires. As a result, it is always a challenge to keep track of the quantities of construction waste of different proportions of inert materials delivered to different facilities by a main contractor accurately.

3.4 Land filling and fly-tipping

Construction waste is sometimes dumped illegally on government or private land without the consent of the concerned landowners. Even the dumping activities are on private land with the consent of the concerned owners, they are still in breach of the town planning, environmental, buildings, drainage, public health, or public safety legislation if such activities contravene the statutory plans, cause adverse environmental impacts or hygiene problems, or result in unstable slopes affecting the safety of adjacent buildings or land. There are also cases where the dumped construction waste becomes an eyesore and has caused environmental degradation in the rural New Territories. There is increasing public concern and calls for the government to extend further control on such irresponsible and illegal activities and to enhance inter-departmental coordination in tackling the problem. Such illegal activities can be broadly classified into two types: (1) land filling, and (2) fly-tipping.

Land filling refers to dumping construction waste as fill material on land to raise the ground level elevation. It also includes filling watercourses, such as stream courses, ponds, etc. Land filling activities are usually carried out for purposes of filling up ponds; leveling off uneven ground surfaces; forming sites for development, e.g., landscaping, roads, village houses, car parks, or recreation facilities; stockpiling in the form of a fill bank; or placing construction waste onto land as dumping ground. Illegal land filling takes place when it contravenes the relevant legislation or is carried out on land without proper authorization of government authorities and/or consent from the land owners/occupiers.

Fly-tipping refers to the illegal dumping of construction waste, often associated with haphazard and casual dumping from vehicles. Fly-tipped construction waste is usually scattered, left in heaps and in small quantities. Most illegal dumping activities occur in urban built-up areas and rural locations with good vehicular access, such as at curbsides or side roads branched off from main roads.

4 THE REAL-TIME ICT SOLUTIONS

Given the practical implementation problems of the Charging System, real-time ICT management systems were developed and implemented simultaneously at public fill reception facilities, sorting facilities, and construction sites. The objectives of these ICT systems are to: (1) control the quality of public fill, (2) improve the efficiency and accuracy of the Charging Scheme, (3) maximize the quantities of reusable and recyclable materials extractable from construction waste, and (4) combat illegal land filling and fly-tipping of construction waste.

Two separate but similar systems co-exist: (1) for delivery of construction waste from construction sites to public fill reception facilities, and (2) for delivery of construction waste from construction sites to sorting facilities. The standard ICT features of the two systems are: (1) delivery truck identification system, (2) entrance and exit records of delivery trucks, and (3) truck weighing system. Different operating features of the two systems are: (1) quality of construction waste, (2) treatment of construction waste upon arrival at the facility, and (3) routing systems of delivery trucks.

Specific computer software has been developed to operate all these ICT features for the two systems. As the computer software is used by resident site staff who may not be proficient in computer operations, the software must be extremely robust and easy to use to minimize the need for troubleshooting and/or human errors. These features are elaborated in detail as follows:

4.1 Delivery truck identification system

A credit-card-sized RFID (radio-frequency identification) tag of unique identification is installed on the windshield of every construction waste delivery truck. Detailed information about the truck, such as its license plate number, ownership, net weight, etc., is recorded on the computer system, as identified by the RFID. Therefore, the RFID tag serves as a unique identifier of the truck, which can be read wirelessly by an antenna when the truck is within a specified range of the facility. The arrangement allows the truck to simultaneously deliver construction waste from different construction sites to various facilities. The truck's information is stored in an on-site notebook computer and a cloud storage system. The data can be accessed by authorized personnel instantaneously through a password-protected system. However, manual verification is required to confirm the RFID tag is installed on the corresponding construction waste delivery truck that is registered.

4.2 Entrance and exit records of the delivery truck

At each construction site exit, an antenna pointing towards the construction site, two cameras, and a weighing bridge are installed. The hardware must be properly selected so that it can be seamlessly integrated. Moreover, it must be weather-resistant. When a delivery truck leaves the construction site with a truckload of construction waste, the antenna reads the RFID tag and extracts the truck's information from the computer system, a camera takes photographs of the license plate of the truck for further verification if needed, and a camera takes photographs of the truckload automatically. The weighing bridge measures the total weight of the truck. The exit time of the truck from the construction site is recorded. All the data are processed, integrated, and recorded by an on-site notebook computer using the specifically developed software and uploaded onto the network cloud server in real time. The specifically developed software also verifies the consistency of the data collected. The data can be accessed by authorized personnel for random manual checking.

Delivery trucks enter or exit the public fill reception or sorting facility through traffic lanes controlled by gates. Two antennas pointing opposite directions, three cameras, and a weighing bridge are installed at each traffic lane of the facility so that the traffic lane can serve as either an entrance or exit. The hardware must be properly selected so that it can be seamlessly integrated. Moreover, it must be weather-resistant.

When a delivery truck enters the facility, one antenna reads the RFID tag to extract the truck's information from the computer system, and the gate is opened automatically upon verification of the truck's information. A camera takes photographs of the truck's license plate for further verification if needed, and a camera takes photographs of the truckload or the truck bed. The weighing bridge measures the total weight of the truck. The truck's entry time is recorded. All the data are processed, integrated, and recorded by an on-site notebook computer using the specifically developed software and uploaded onto the network cloud server in real time. The specifically developed software also verifies the consistency of the data collected.

When a delivery truck leaves the facility, the other antenna reads the RFID tag to extract the truck's information from the computer system, and the gate is opened automatically. A camera takes photographs of the truck's license plate, and a camera takes photographs of the truckload or the truck bed. The truck's exit time is recorded. All the data are processed, integrated, and recorded by the on-site notebook computer and uploaded onto the network cloud server in real time. The data can be accessed by authorized personnel for random manual checking.

4.3 Real-time processing of data recorded

The photographs of the license plate of the delivery truck can be used to check the truck's identity by the software and/or manually whenever necessary. It also provides redundant data to supplement the data provided by the RFID tag in case of malfunctioning of the antenna.

The travel time of the delivery truck between the construction site and the facility can be determined from the exit time of the truck from the construction site and the entry time of the truck into the facility. It indicates the traffic conditions and whether the truck has been driven elsewhere or stopped unnecessarily.

The truck's total weight leaving the construction site and entering the disposal facility can be compared to evaluate whether the truckload of construction waste increased or decreased during transportation without authorization.

The travel time and weight records can deter illegal land filling and/or fly-tipping by the truck driver.

The weight of the construction waste can be determined from the total weight of the truck entering the facility measured by the weighing bridge and the weight of the empty truck leaving the facility or vice versa. The weight of the empty truck is also used to confirm/update the net weight of the truck in the records. The data are also used to monitor the inventory of public fill in the public fill reception facility or the quantity of C&D waste going to the landfill.

The photographs of the construction waste taken at the construction site's exit and the facility's entrance can be used to perform a visual evaluation and/or computerized image processing of the quality of the construction waste whenever necessary.

4.4 Routing of construction waste delivery trucks serving public fill reception facilities

As tabulated in Table 1, the construction waste delivered to public fill reception and sorting facilities is of different quality. Moreover, construction waste delivered to sorting facilities must be processed for further delivery to other facilities. As a result, the delivery trucks going to these disposal facilities are taking different routes.

Construction waste delivered to public fill reception facilities is 100% inert materials, i.e., public fill. The public fill is delivered from construction sites to public fill reception facilities. The empty truck returns to the construction site after unloading the public fill at a public fill reception facility. As a result, the delivery trucks are routed from the construction site to the public fill reception facility and return.

4.5 Routing of construction waste delivery trucks serving sorting facilities

Construction waste delivered to sorting facilities contains more than 50% of inert materials by weight. The construction waste is delivered from construction sites to sorting facilities. The construction waste is sorted into public fill and non-inert substances at the sorting facility. Afterward, public fill is delivered to a public fill reception facility, and non-inert substances are delivered to a nearby landfill. As a result, there are three routes of delivery trucks serving sorting facilities: (1) from the construction site to the sorting facility and return; (2)

from the sorting facility to the public fill reception facility and return; and (3) from the sorting facility to the landfill and return.

Construction waste is delivered from the construction site to the sorting facility by a group of trucks (Group 1), and empty trucks are returned to the construction site upon unloading. A second group of trucks (Group 2) delivers public fill from the sorting facility to the public fill reception facility, and empty trucks are returned to the sorting facility. A third group of trucks (Group 3) delivers non-inert substances from the sorting facility to the landfill, and empty trucks are returned to the sorting facility. The main contractors of construction sites operate Group 1 trucks. The operating contractor of the sorting facilities operates Group 2 and Group 3 trucks. As these three groups of trucks deliver construction waste of different proportions of inert materials from different starting points to various destinations, they must be clearly identified. More importantly, they belong to different contractors. Group 1 trucks can be easily identified as they enter the sorting facility with a truckload of construction waste and leave it with an empty truck bed. However, Group 2 and Group 3 trucks must be differentiated with extreme care as they deliver public fill and non-inert substances from sorting facilities to public fill reception facilities and landfills, respectively. Moreover, they leave the sorting facility with a truckload of public fill or non-inert substances and enter with empty truck beds. As the two sorting facilities in the HKSAR are near the public fill reception facilities and landfills, shown as SENTX in Figure 1, Group 2 and Group 3 trucks are relatively few and can be easily identified.

5 RECENT AND FUTURE DEVELOPMENTS

Although the systems are running smoothly now, there is always room for improvement. Recent advances and recommendations for future developments may include:

5.1 Deployment of GPS technology for real-time tracking of truck locations

As every truck can be identified by an RFID tag, its real-time location can be monitored by a GPS (Global Positioning System). This can further prevent illegal land filling and/or fly-tipping of construction waste, as the truck's location can be monitored in real time. Moreover, the trucks can be steered to use the most efficient routes under current traffic conditions for delivery of construction waste to the appropriate facility, resulting in considerable savings in time and fuel. In recent years, GPS installation and use for truck monitoring have been tried and progressively implemented.

5.2 Image processing of the truckload of construction waste

The photographic images of the truckloads of construction waste can be processed for two purposes. Firstly, the top surface profile of the truckload can be used to estimate the volume of construction waste in the truck. Using the weight measured by the weighing bridge, the unit weight of the construction waste in the truck can be estimated. As the inert materials in the construction waste are typically denser than the non-inert substances, the unit weight of the truckload provides a reasonably good indication of the proportion of inert materials in the construction waste. Moreover, computer visioning can process the images to identify non-inert materials. As a result, the quality control of public fill can be further improved.

5.3 Other future developments

With the rapid advent of ICT, there can be numerous potential developments, such as establishing and utilizing big data and Internet of Things (IoT) technologies to manage public fill. Nevertheless, these developments must be cost-effective to be adopted to improve public fill management. The continuing development of ICT presents opportunities for cross-disciplinary collaborations with academic institutions alongside valuable training for research personnel and engineers.

6 CONCLUSIONS

These conclusions are drawn from the projects of applications of ICT to construction waste management in the HKSAR:

(1) Two automated management systems using ICT have been successfully developed and implemented for the management of construction waste in the HKSAR of China to:
   (a) control the quality of public fill;
   (b) improve the efficiency and accuracy of the Construction Waste Disposal Charging Scheme;
   (c) maximize the quantities of reusable and recyclable materials extractable from construction waste; and
   (d) combat illegal land filling and fly-tipping of construction waste.

(2) The 1st system controls construction waste delivery to public fill reception facilities, and the 2nd system to sorting facilities. Both systems have been installed at multiple public fill reception facilities, sorting facilities, and construction sites. Necessary hardware must be carefully selected so that they can be properly integrated. Moreover, they must be weather-resistant as they are installed outdoors.

(3) Computer software has been specifically developed to operate the two systems. The software must be robust and easy to use to minimize the need for troubleshooting and human errors.

(4) The systems have been successfully operated in the HKSAR for years with necessary routine maintenance. Nevertheless, recommendations for possible future developments are identified and discussed.

(5) It is demonstrated that ICT can effectively manage construction waste in the HKSAR. Moreover, the systems developed can be adapted for other applications in logistics, construction, mining, and other related industries.

REFERENCES

Advisory Council on the Environment 2009. Integrated waste management facilities: Technology review and associated facilities. ACE Paper 22/2009, Advisory Council on the Environment, the Government of the HKSAR, Hong Kong.

Environment Bureau 2021. *Waste blueprint for Hong Kong 2035*. Environment Bureau, the Government of the HKSAR, HKSAR, China.

EPD 2024. *Monitoring of solid waste in Hong Kong: Waste statistics for 2023*. Statistics Unit, Environmental Protection Department, the Government of the HKSAR, HKSAR, China.

Yeung, A.T. 2008. Construction & demolition materials management in Hong Kong. *Proceedings of the Institution of Civil Engineers*, *Municipal Engineer*, 161(ME1), 43-49.

Yeung, A.T. 2009. Extension of the useful lives of constructed facilities: Green management of construction and demolition materials. *Proceedings of the SOE HK Symposium 2009*, the Society of Operations Engineers Hong Kong Region, HKSAR, China, 38-47.

Yeung, A.T., Mok, K.Y., Tham, L.G., Lee, P.K.K., and Pei, G. 2006. Use of inert C&D materials for seawall foundation: A field-scale pilot test. *Resources, Conservation and Recycling*, 47(4), 375-393.

Yeung, A.T., and Ng, P.L. 2025. Real-time management of public fill in Hong Kong using information and communications technology. *Geoenvironmental contamination and waste containment*. Geotechnical Special Publication No. 359, Farid, A., Foye, K., and Khire, M.V., Editors, ASCE, Reston, Virginia, 246-255.

Yeung, A.T., Tham, L.G., Lee, P.K.K., Mok, K.Y., and Pei, G. 2007. Use of inert C&D materials for seawall foundation: Quality control measures. *Waste Management*, 27(6), 768-777.